19th International Conference on Sustainable Energy Technologies

16th to 18th August 2022, Turkey

Sustainable Energy Technologies 2022

Conference Proceedings: Volume 1

Proceedings of the
19th International Conference on
Sustainable Energy Technologies
SET 2022
16th – 18th August 2022, Turkiye

Edited by
Professor Saffa Riffat

SET 2022 Admin Support
Department of Architecture and the Built Environment
Faculty of Engineering, University of Nottingham

Supported by the Conference Organising Committee:

Chair: Professor Saffa Riffat
Professor Zafer Utlu
Dr Yuehong Su
Zeny Amante-Roberts
Celia Berry

Reference to a conference paper:

To cite a paper published in these conference proceedings, please substitute the highlighted sections of the reference below with the details of the article you are referring to:

Author(s) Surname, Author(s) Initial(s), 2022. 'Title of paper'. In: Riffat, Su,. ed., **Sustainable Energy Technologies**: Proceedings of the 19th International Conference on Sustainable Energy Technologies, 16th – 18th August 2022, Turkey. University of Nottingham: Buildings, Energy & Environment Research Group. Pp XX-XX. Available from: nottingham-repository.worktribe.com/ [Last access date].

Foreword

SET2022 in Istanbul, Turkiye was a great venue to resume the annual conference, having had a 2-year break due to covid-19.

The 19th International Conference on Sustainable Energy Technologies was a significant international academic conference in the domain of world sustainable energy. The conference aimed to provide a forum for the exchange of latest technical information, the dissemination of up-to-date research results, and the presentation of major issues that may shape future directions of human society, such as sustainable energy technology research, its application and energy security.

Held from August 16th to 18th 2022 in Istanbul, Turkiye, the conference was a collaboration between the World Society of Sustainable Energy Technologies (WSSET), Halic University and University of Nottingham. World-renowned experts and scholars in the area, representatives of prominent enterprises and universities attended to discuss new developments and achievements in the field, as well as promoting academic exchange, application of scientific results, university-industry collaboration and government-industry collaboration.

The papers contained in these proceedings focus on topics such as Energy Storage for the Age of Renewables; Research, Innovation and Commercialisation in Sustainable Energy Technologies; Integrating Planning & Policy, Architecture, Engineering & Economics; Energy and Environment; Engineering Thermo-physics; and Systemic Change for Cities.

Over 200 delegates from 42 countries attended SET2022; nearly 400 abstracts were received and 150 papers were presented and along with 71 posters. I hope you enjoy as much as I did the breadth of work you will find in the proceedings.

We would like to thank all participating authors for their contributions to both the conference and to the publishing of this book. We are also indebted to our international scientific committee for their advice and seemingly endless review of papers. We would also like to thank unreservedly Zeny Armante-Roberts and Celia Berry for their tireless efforts in making SET2022 one of the most successful conferences we have held. Also a huge thanks to our sponsors PCM Products Ltd., RePG, Terry Payne, Turkish Airlines, Arkaya and SUNUM Engineering.

Professor Saffa Riffat
Chair in Sustainable Energy Technologies
President of the World Society of Sustainable Energy Technologies
SET 2022 Joint Chair

CONTENTS

#25: Thermodynamic assessment of the natural gas liquefaction plant

Arif KARABUGA[1], Zafer UTLU[2]

[1] Haliç University, Sustainable Energy Systems Application and Research Center, Istanbul, Turkey
arif.karabuga @gmail.com
[2] Halic University, Faculty of Engineering, Mechanical Engineering Department, 34445, Istanbul, Turkey,
zaferutlu @halic.edu.tr

Abstract: One of the methods in liquefaction of natural gas is cryogenic liquefaction. The main disadvantage of this method, which is generally preferred due to its high fraction rate, is its high energy consumption. For this reason, it has become necessary to conduct energy and exergy analysis of natural gas liquefaction plants. In this study, an advanced exergy analysis of natural gas liquefaction plants using the cryogenic method was performed. In order to make a detailed analysis of the exergy destruction of the facility, advanced exergy analysis was applied to each component. As a result of the study, the exergy efficiency of the facility was calculated as 53%. It was also found to be the highest unavoidable exergy destruction turbine.

Keywords: advanced exergy analysis; energy analysis; liquefied natural gas; exergy analysis

1. INTRODUCTION

Natural gas can be defined as environmentally friendly as it reduces carbon dioxide (CO_2) emissions by up to 20%, sulphur oxide (SOx) emissions by up to 100%, Nitrogen oxide (NOx) emissions by up to 90% and other harmful particles by up to 99% compared to existing fossil sources (Amalina *et al.*, 2017). In addition to this environmental advantage of natural gas, governments' decarburization and diversification policies in energy resources are expected to increase the share of natural gas in coming years. Liquefaction of natural gas and the active liquefied natural gas (LNG) industry increase the use of natural gas. Trade in natural gas is generally made as the liquefied form of natural gas. According to the 2019 report of the International Gas Union, the global LNG trade was 316.5 million tons in the previous five years. In addition, LNG trade increased by 14.5 million tons in 2018 compared to the previous year. This increase represented 31% of the total gross LNG trade. Although the world's largest natural gas reserves are found in Russia, Qatar and Iran, large capacity liquefaction plants are located in Australia, the USA and Russia. In 2019, forty-three new liquefaction plants were planned to be established in different regions of the world (International Gas Union, 2019).

Apart from the commercial growth in the LNG sector, another issue to be examined is the energy consumption in LNG plants. One of the biggest challenges in natural gas flow is the high energy consumption to liquefy natural gas (Palizdar *et al.*, 2019). For this reason, besides the energy and exergy analysis of the LNG plants, further exergy analysis should be performed. While energy analysis deals with the amount of energy in a system, exergy analysis examines how much of the energy used turns into useful work. However, the importance of advanced exergy analysis defines how much of exergy destruction can be improved (Utlu and Hepbasli, 2007; Akbulut *et al.*, 2016).

In the literature, there has been some research about cryogenic liquefaction system in recent years for LNG production. Palizdar *et al.* (2019) carried out conventional and advanced exergoeconomic analysis of a system using a mini-scale nitrogen dual expansion process for the production of liquefied natural gas. The component with the highest endogenous exergy destruction was found to be expander (59%). Mehdizadeh-Fard and Pourfayaz (2019) did advanced exergy analysis of the heat exchanger network in the natural gas plant. According to advanced exergy analysis, heat exchangers were found to be the most inefficient component. As a result of the advanced exergy analysis, exergy efficiency for heat exchangers increased by 34%. Mehrpooya *et al.* (2018) conducted thermodynamic analysis of the integrated LNG regasification process configuration. Different configurations were compared. The highest energy and exergy efficiencies among all the configurations were 86.3% and 80%, respectively. Mehrpooya *et al.* (2018) investigated advanced exergoeconomic analysis of an integrated cryogenic liquefaction process for LNG. According to the results of the convectional exergy analysis, exergy and exergy destruction of the system were calculated as 41.27% and 89,904 kW, respectively. In terms of advanced exergy analysis, the cost of exergy destruction in the compressor was found to be avoidable.

The aim of this study is to investigate the advanced exergy analysis of the liquefaction of natural gas using the cryogenic method. The convectional exergy analysis should determine the amount and location of the highest exergy destruction and to further calculate how much of the exergy destruction of the components can be improved and avoided by advanced exergy analysis.

2. EXPERIMENTAL STUDY

The LNG liquefaction system is illustrated in Figure 1. The main components of the liquefaction system were the compressor, the booster compressor-turbine pair, the cooler after compressor, the heat exchanger block, heat exchanger-1, heat exchanger-2, heat exchanger-3 and intercooler. The system was fed from two different points and the product was obtained from the 17th point by liquid production.
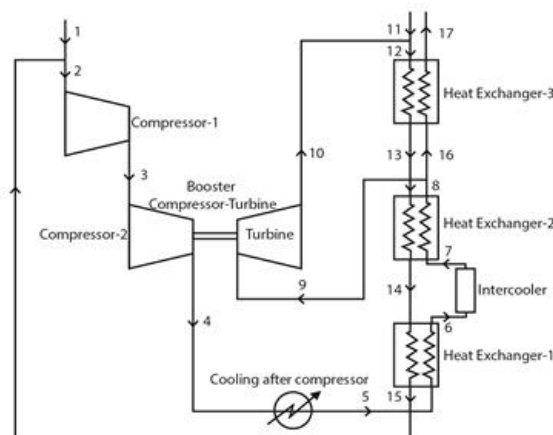

Figure 1: Flow chart for liquefaction of natural gas

Two different methods are generally used in liquefaction systems i.e. cryogenic and non-cryogenic liquefaction systems. Non-cryogenic systems are generally not preferred because their purity rates are low and unsuitable for commercial production. On the contrary, the greatest advantage of the cryogenic method is that high purity products are obtained. However, the disadvantage of the cryogenic method is the high energy consumption (Karabuga *et al.*, 2019). In this study, advanced exergy analysis of LNG system was examined by using the cryogenic method.

3. THERMODYNAMIC MODELLING

Due to the high energy consumption of the cryogenic liquefaction process, it is expected to perform detailed exergy analysis as well as energy analysis. Energy analysis gives the amount of energy spent for liquid production in the cryogenic system, while exergy analysis helps us find out how much of the energy spent for liquid production is transformed into useful work and where exergy destruction occurs. However, further exergy analysis helps to determine how much of the exergy destruction of components occurs with technological limitations and how much is endogenous and exogenous. The convectional and advanced exergy analysis of LNG system was performed with the engineering equation solver (EES) program. The assumptions for the thermodynamic modelling of the aforementioned system are as follows;

•   The system works under steady state conditions;
•   The changes in kinetic and potential energies are neglected;
•   The pressure drops and heat losses in the connecting pipes are neglected;
•   The compressor works with adiabatic compression process;
•   The system operates at atmospheric condition of T0= 25ºC and P0=1 bar as the reference state.

The convectional and advanced exergy analysis was applied to the LNG system show in Figure 1. The most important parameter in enhancing the performance of an LNG plant is the thermodynamic efficiency. Since energy supply is an important parameter in cost planning in the LNG industry, current studies have aimed to minimize facility energy costs by applying numerous optimizations to increase energy and exergy efficiency. Establishing the energy balance is the basic method for examining the energy efficiency. Energy efficiency plays a critical role in improving the system and optimizing it. Energy efficiency can be measured using either economic or physical indicators (Utlu and Parali, 2013). Exergy analysis is a useful tool for evaluating the thermodynamic irreversibilities in the system. Thermodynamic inefficiencies of liquefaction are described and measured by exergy analyses which indicate the location, size and resource use of thermodynamic inefficiencies in a system (Utlu and Hepbasli, 2005; Ishaq *et al.*, 2019). The conventional and advanced exergy analysis of each step of the liquefaction system for LNG production were performed. The exergy of an energy form or a substance is a measure of its usefulness or quality or the potential to cause change. Today an exergy analysis is identified as the most effective method for assessment; the quality of energy carriers and energy conversion processes and the rational use of energy. The analysis of the real thermodynamic inefficiencies in a cryogenic liquefaction system and its components can significantly contribute to its improvement. In conventional exergy analysis the exergy balance for component k and the overall system, in terms of fuel and product exergies, are expressed as follows (Morosuk and Tsatsaronis, 2019; Fallah *et al.*, 2017):

$$\dot{E}_{D,k} = \dot{E}_{F,k} - \dot{E}_{P,k} \qquad (1)$$

The exergy destruction of k component ($\dot{E}_{D,k}$) using in the system (Fallah *et al.*, 2017):

$$\dot{E}_{D,k} = T_0 \dot{m} s_{gen,k} \qquad (2)$$

The exergy efficiency of overall the system can be calculated (Hammad and Dincer, 2018):

$$\eta_{ex} = \frac{\dot{E}_{P,tot}}{\dot{E}_{F,tot}} \qquad (3)$$

The exergetic efficiency for k component can be calculated (Tsatsaronis and Morosuk, 2010):

$$\varepsilon_k = \frac{\dot{E}_{P,k}}{\dot{E}_{F,k}} = 1 - \frac{\dot{E}_{D,k}}{\dot{E}_{F,k}} \qquad (4)$$

Advanced exergy analysis of LNG systems includes splitting the exergy destruction within each component into endogenous/exogenous parts and avoidable/unavoidable parts. Calculations by advanced analysis of the system provides estimates of each potential of component for efficiency improvement. The endogenous exergy destruction (EN) is indicated the exergy destruction occurring within the (k) component when all other components operate in an ideal way and the component being considered operates with its present efficiency. In addition, the exogenous exergy destruction is the difference between total and endogenous exergy destruction.

The endogenous and exogenous exergy destruction can be calculated (Morosuk and Tsatsaronis, 2019) as below:

$$\dot{E}_{D,k} = \dot{E}_{D,k}^{EN} + \dot{E}_{D,k}^{EX} \qquad (5)$$

The unavoidable exergy destruction (UN) can be defined within the (k) component that cannot be further reduced depending on technological limitations such as availability and manufacturing methods. Otherwise, the avoidable exergy destruction is the difference between total and unavoidable exergy destruction. The avoidable and unavoidable exergy destruction can be calculated (Morosuk and Tsatsaronis, 2019) as below:

$$\dot{E}_{D,k} = \dot{E}_{D,k}^{AV} + \dot{E}_{D,k}^{UN} \qquad (6)$$

4. RESULTS AND DISCUSSION

Energy and exergy balance equations were applied to the LNG facility and thermodynamic results were obtained; these values are given in Table 1. The conventional and advanced exergy analysis is applied that each component in LNG system. The obtained results of conventional and advanced exergy analysis shown in Table 2.

Table 1: Obtained results of the LNG

Point	T (K)	P (Bar)	h (kJ/kg)	s (kJ/kgK)	$\dot{E}$ (kW)	Point	T (K)	P (Bar)	h (kJ/kg)	s (kJ/kgK)	$\dot{E}$ (kW)
1	276.4	5.76	-54.35	-1.084	441.2	10	145	5.97	-347.8	-2.549	3281
2	298.9	5.76	-3.946	-0.9087	2825	11	140.4	5.94	-359.2	-2.627	403.4
3	308	32.81	-13.53	-1.819	5573	12	143.3	5.91	-351.8	-2.572	3698
4	354	45.09	96.3	-1.644	6176	13	159.9	5.86	-311.9	-2.305	3345
5	306	45.41	-25.67	-2.018	6065	14	233.3	5.81	-149.1	-1.461	2559
6	251.1	45.3	-168	-2.53	6174	15	303	5.76	5.342	-0.8778	2387
7	235	45.18	-213.3	-2.715	6279	16	190.5	45.09	-509.4	-4.186	1907
8	212	45.09	-287.5	-3.047	6539	17	112.7	45.09	-900.9	-6.68	2812
9	212.6	45.3	-285.9	-3.042	4932						

17 points were determined on the system and pressure, temperature and mass values at the inlet and outlet of the components were measured. The 17th point is the point where the product, the liquid, was obtained. These data were modelled by EES program to determine enthalpy, entropy and specific exergy values. These calculated properties were established exergy balances for each component and applied to advanced exergy formulas. The results obtained are given in Table 2.

Table 2: Results of the conventional and advanced exergy analysis

Component	Conventional exergy analysis			Advanced exergy analysis			
	$\dot{E}_D$ (kW)	$\dot{E}_F$ (kW)	$\dot{E}_P$ (kW)	$\dot{E}_D^{EN}$ (kW)	$\dot{E}_D^{EX}$ (kW)	$\dot{E}_D^{AV}$ (kW)	$\dot{E}_D^{UN}$ (kW)
CM-1	23.56	2748	2724	4.737(20.1%)	18.82(79.9%)	9.317(39.5%)	14.24(60.5%)
CM-2	548.7	1152	603.4	102.2(18.6%)	446.5(81.4%)	172.3(31.4%)	376.4(68.6%)
CAC	110.7	-	-	-	-	-	-
HE-1	63.42	172.1	108.7	7.468(11.7%)	55.95(88.3%)	30.18(47.5%)	33.24(52.5%)
LC	104.5	-	-	-	-	-	-
HE-2	525.9	786.5	260.5	111.6(21.2%)	414.3(78.8%)	-228.5(-43.4%)	754.5(143.4%)
HE-3	552.6	905.6	352.9	164(29.6%)	388.6(70.4%)	2003(362%)	-1451(-262%)
T	1161	1651	490.1	452.6(42.2%)	708.7(57.8%)	-2334(-201%)	3496(301%)

Table 2 shows the main results obtained from the conventional and advanced exergy analysis of the LNG system. It suggests that the turbine had the largest exergy destruction, which is system exergy destruction (37.56%). When all components in the system were examined, most of the exergy destruction was caused by exogenous exergy destruction. The highest exogenous exergy destruction occurred in HE-1 at 88.3%. In the turbine, where the highest exergy destruction occurred, endogenous and exogenous exergy destruction was almost balanced. In addition, unavoidable exergy destruction in the turbine was greater than avoidable exergy destruction.

5. CONCLUSION

In this study, advanced exergy analysis of a LNG system was performed by using the cryogenic method. When the second law of thermodynamics was applied to the system, it was found that the highest exergy destruction (37.56%) in the system was in the turbine. When advanced exergy analysis was performed, the causes of exergy destruction in the turbine were determined. The exogenous exergy destruction, which is a part of the exergy destruction, was found to be approximately 708.7 kW (57.8%) and the exergy efficiency of the whole system was found to be 53%.

6. REFERENCES

Akbulut, U., Utlu, Z., Kincay, O., (2016) Exergoenvironmental and exergoeconomic analyses of a vertical type ground source heat pump integrated wall cooling system, Applied Thermal Engineering, Vol:102, pp 904-921. https://doi.org/10.1016/j.applthermaleng.2016.03.178

Amalina, N. S., Setiawan, T.M., Hadisupadmo, S., Hendradjit, W., (2017) Development of a simulation package of natural gas liquefaction system, Procedia Engineering, Vol: 170, pp:177-181.

Fallah, M., Mahmoudi, S. M. S., Yari, M., (2017) Advanced exergy analysis for an anode gas recirculation solid oxide fuel cell, Energy, Vol: 141, pp 1097-1112. https://doi.org/10.1016/j.energy.2017.10.003

Hammad, A., Dincer, I., (2018) Analysis and assessment of an advanced hydrogen liquefaction system, International Journal of Hydrogen, Vol: 43, No. 2, pp 1139-1151. https://doi.org/10.1016/j.ijhydene.2017.10.158

International Gas Union, 2019 World LNG report. [Accessed: 21/08/2019] URL: https://www.igu.org/sites/default/files/node-news_item-field_file/IGU%20Annual%20Report%202019_23%20loresfinal.pdf

Ishaq, H., Dincer, I., Naterer, G. F., (2019) Multigeneration system exergy analysis and thermal management of an industrial glassmaking process linked with a Cu–Cl cycle for hydrogen production, International Journal of Hydrogen Energy, Vol: 44, No. 20, pp 9791-9801. https://doi.org/10.1016/j.ijhydene.2018.12.140

Karabuga, A., Utlu, Z., Selbas, R., (2019) Examination of the liquefaction system for the use of different cryogenics in terms of thermodynamic analysis, International Journal of Exergy, Vol: 29 No.1 pp 1-21. https://doi.org/10.1504/IJEX.2019.099701

Mehdizadeh-Fard, M., Pourfayaz, F., (2019) Advanced exergy analysis of heat exchanger network in a complex natural gas refiner, Journal of Cleaner Production, Vol: 206, pp 670-687. https://doi.org/10.1016/j.jclepro.2018.09.166

Mehrpooya, M., Sharifzadeh, M. M. M., Katooli, M.H., (2018) Thermodynamic analysis of integrated LNG regasification process configurations, Progress in Energy and Combustion Science, Vol:69, pp 1-27. https://doi.org/10.1016/j.pecs.2018.06.001

Mehrpooya, M., Sharifzadeh, M. M. M., Ansarinasab, H., (2018) Investigation of a novel integrated process configuration for natural gas liquefaction and nitrogen removal by advanced exergoeconomic analysis, Applied Thermal Engineering, Vol: 128, pp 1249-1262. https://doi.org/10.1016/j.applthermaleng.2017.09.088

Morosuk, T., Tsatsaronis, G., (2019) Advanced exergy-based methods used to understand and improve energy-conversion systems, Energy, Vol: 169, pp 238-246. https://doi.org/10.1016/j.energy.2018.11.123

Palizdar, A., Ramezani, T., Nargessi, Z., Afshar, S.A., Abbasi, M., Vatani, A., (2019) Advanced exergoeconomic evaluation of a mini-scale nitrogen dual expander process for liquefaction of natural gas, Energy, Vol. 168, pp 542-557. https://doi.org/10.1016/j.energy.2018.11.058

Tsatsaronis, G., Morosuk, T., (2010) Advanced exergetic analysis of a novel system for generating electricity and vaporizing liquefied natural gas, Energy, Vol: 35, pp 820-829. https://doi.org/10.1016/j.energy.2009.08.019

Utlu, Z., Hepbasli, A., (2007) Assessment of the Turkish utility sector through energy and exergy analyses, Energy Policy, Vol:35, No. 10, pp 5012-5020. https://doi.org/10.1016/j.enpol.2007.04.027

Utlu, Z., Parali, U., (2013) Investigation of the potential of thermophotovoltaic heat recovery for the Turkish industrial sector, Energy Conversion and Management, Vol: 74 pp 308-322. https://doi.org/10.1016/j.enconman.2013.05.030

Utlu, Z., Hepbasli, A., (2005) Analysis of energy and exergy use of the Turkish residential–commercial sector, Building and Environment, Vol:40 No. (5), pp 641-655. https://doi.org/10.1016/j.buildenv.2004.08.006

#26: Thermodynamic evaluation of cryogenic liquefaction system for liquefaction of three different working fluids using the advanced exergy analysis method

Arif KARABUGA[1], Zafer UTLU[2]

[1] Haliç University, Sustainable Energy Systems Application and Research Center, Istanbul, Turkey
arif.karabuga@gmail.com
[2] Halic University, Faculty of Engineering, Mechanical Engineering Department, 34445, Istanbul, Turkey,
zaferutlu@halic.edu.tr

Abstract: In this study, the liquefaction system of various components in the air was investigated by cryogenic method. Advanced exergy analysis was applied to the cryogenic liquefaction system. The study focused on the liquefaction system integrated into the air separation unit (ASU). Three different working fluids were selected i.e. nitrogen, oxygen and argon. In traditional exergy analysis, while calculating exergy efficiency and exergy destruction rates for all three fluids, endogenous, exogenous, avoidable and unavoidable exergy destruction values were also calculated with advanced exergy analysis. As a result of this study, exergy efficiency of argon, nitrogen and oxygen elements were found to be 51.77%, 56.13% and 53.35%, respectively. Therefore, it was calculated that the endogenous exergy destruction, which was one of the advanced exergy components for the whole system and working fluids, was approximately 80-95%.

1. INTRODUCTION

The cryogenic method is used to liquefy gases such as nitrogen, oxygen, argon, hydrogen, helium and it is the most efficient liquefaction system per unit product (Chan, 2015). Despite this advantage, the cryogenic liquefaction method is a chemical industry that uses intensive energy. For this reason, a small performance improvement in cryogenic liquefaction systems provides great economic gain (Mostafa *et al.*, 2022). The most basic approach to determine the performance of a thermodynamic cycle used in the cryogenic liquefaction method is the concept of energy and exergy. Detailed analysis of energy and exergy efficiency is very important for determining the improvement potential in the system and the component to be improved. Advanced exergy analysis is applied to detail the exergy efficiency. Literature studies related to the subject are presented below.

Conventional and advanced exergy analysis of the natural gas liquefaction system for the energy needs of Pakistan was examined by Hamayun *et al.* (2022). Due to the low calorific value of natural gas used in electricity generation in Pakistan, a configuration was developed that allowed it to be mixed with nitrogen. In the study, the traditional air separation unit and the air separation unit integrated into the liquefaction of natural gas were discussed. Traditional exergy analysis determined that the integrated system of natural gas-air separation was better than the single air separation system in terms of both total power consumption and total exergy destruction rate. As a result of the advanced exergy analysis of the natural gas-air separation integrated system, it was calculated that 44.3% of the exergy destruction rate of the system was caused by avoidable exergy destruction.

Thermodynamic evaluation of a new integrated unit to produce liquid helium and hydrogen was carried out by Pakzad *et al.* (2021). As a result of the thermodynamic analysis, it was calculated that the specific energy consumption, coefficient of performance, and figure of merit were equal to 18.96 kWh/kg, 0.03 and 0.37, respectively. In addition, when the second law of thermodynamics was applied to the proposed system, exergy efficiency and exergy destruction in the whole process were calculated to be 67% and 4471 MW, respectively.

Valverde *et al.* (2021) presented a thermodynamic analysis of a cryogenic-based energy storage system. Their study evaluated an adiabatic cryogenic-based 100 MW/400 MWh energy storage system with advanced exergy based analysis method to determine the improvement potential (advanced exergy destruction rate, investment costs and environmental impacts). Rehman *et al.* (2020) presented the thermodynamic analysis of a newly developed modified single mixed refrigerant (MSMR) process for the liquefaction of NG targeted for offshore applications. As a result of the analysis, the unavoidable part of the total exergy destruction was calculated as only 42%, indicating that it was less than the avoidable part.

The aim of this current study was to investigate the advanced exergy analysis of three different cryonic fluids using the cryogenic method. Convectional exergy analysis will determine the amount and location of the highest exergy destruction and to calculate in more detail how much of the exergy destruction of components can be improved and prevented by advanced exergy analysis.

2. EXPERIMENTAL STUDY

The flow chart of the cryogenic liquefaction system integrated into the air separation unit is illustrated in Figure 1. This system consisted of various components: Compressor-2 was a compressor-1 coupled with a booster compressor turbine to compress the fluid coming from the air separation unit; a turbine with post-compression cooling; an intercooler; three heat exchangers and a booster compressor turbine couple. The fluid exiting the compressor line at a temperature of 45 bar and 354 K was liquefied at 112 K without pressure loss, thanks to the heat exchangers. The fluid that came out in liquid form at point 17 was sent to the tanks for storage.
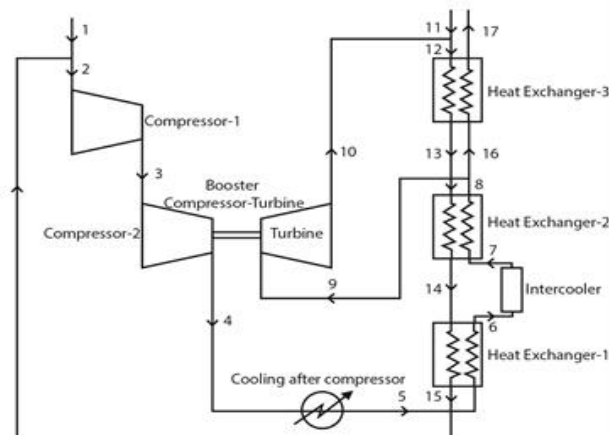

Figure 1: Flow chart of the cryogenic liquefaction unit

Two different methods are generally used in liquefaction systems such as cryogenic and non-cryogenic liquefaction systems. Non-cryogenic systems are generally not preferred because their purity rates are low and unsuitable for commercial production. On the contrary, the greatest advantage of the cryogenic method is that high purity products are obtained. However, the disadvantage of the cryogenic method is the high energy consumption (Utlu and Parali, 2013; Utlu and Hepbasli, 2004; Utlu, 2015). In this study, advanced exergy analysis of three different cryogenic fluids were examined by using the cryogenic method.

3. THERMODYNAMIC MODELLING

Due to the high energy consumption of the cryogenic liquefaction process, detailed exergy analysis, as well as energy analysis, provides both thermodynamic efficiency and economic efficiency. While energy analysis guides in calculating the amount of energy lost on fluid production in the cryogenic system, exergy analysis helps us find out how much of the energy lost on fluid production is converted into useful work and where exergy destruction occurs (Canyurt *et al.*, 2006; Ozturk *et al.*, 2004). However, it does not provide information about the causes of exergy losses and the improvement potential. In contrast, advanced exergy analysis helps determine how much of the exergy destruction of components is due to technological limitations and how much is internal and external. Conventional and advanced exergy analyses of the cryogenic liquefaction system were performed with the engineering equation solver (EES) program. The assumptions for the thermodynamic modelling of the aforementioned system were as follows;

- The system works under steady state conditions;
- The changes in kinetic and potential energies are neglected;
- The pressure drops and heat losses in the connecting pipes are neglected;
- The compressor works with adiabatic compression process;
- The system operates at atmospheric condition of T0= 25 ºC and P0=1 bar as the reference state.

The conventional and advanced exergy analysis was applied to the cryogenic liquefaction system shown in Figure 1. The most important parameter in enhancing the performance of a cryogenic liquefaction plant is the thermodynamic efficiency. Since energy supply is an important parameter in cost planning in the cryogenic liquefaction industry, current studies have aimed to minimize facility energy costs by applying numerous optimizations to increase energy and exergy efficiency. Establishing the energy balance is the basic method for examining the energy efficiency. Energy efficiency plays a critical role in improving the system and optimizing it. Energy efficiency can be measured with economic or physical indicators (Ishaq, *et al.*, 2019). Exergy analysis is a useful tool for evaluating the thermodynamic irreversibilities in the system. Thermodynamic inefficiencies of liquefaction are described and measured by exergy analyses. Exergy analyses indicate the location, size and resource use of thermodynamic inefficiencies in a system (Morosuk and Tsatsaronis, 2019; Fallah *et al.*, 2017; Hammad and Dincer, 2018). The conventional and advanced exergy analyses of each step of the liquefaction system for liquid oxygen, nitrogen and argon production were performed. The exergy of an energy form or a substance is a measure of its usefulness or quality or the potential to cause change. Today an exergy analysis is identified as the most effective method for assessing; the quality of energy carriers and energy conversion processes and the rational use of energy. The analysis of the real thermodynamic inefficiencies in a cryogenic liquefaction system and its components can significantly contribute to improvement. In conventional exergy analysis the exergy balance for component k and the overall system, in terms of fuel and product exergies, are expressed as follows (Tsatsaronis and Mrorsuk, 2010):

$$\dot{E}_{D,k} = \dot{E}_{F,k} - \dot{E}_{P,k} \tag{1}$$

The exergy destruction of k component ($\dot{E}_{D,k}$) using in the system (Hammad and Dincer, 2018);

$$\dot{E}_{D,k} = T_0 \dot{m} s_{gen,k} \tag{2}$$

The exergy efficiency of overall the system can be calculated (Tsatsaronis and Mrorsuk, 2010);

$$\eta_{ex} = \frac{\dot{E}_{P,tot}}{\dot{E}_{F,tot}} \tag{3}$$

The exergetic efficiency for k component can be calculated (Bai *et al.* 2016);

$$\varepsilon_k = \frac{\dot{E}_{P,k}}{\dot{E}_{F,k}} = 1 - \frac{\dot{E}_{D,k}}{\dot{E}_{F,k}} \tag{4}$$

Advanced exergy analysis of cryogenic liquefaction systems includes splitting the exergy destruction within each component into endogenous/exogenous parts and avoidable/unavoidable parts. Calculated by advanced analysis of the system provides estimates of each potential of component for efficiency improvement. The endogenous exergy destruction (EN) indicates the exergy destruction occurring within the (k) component when all other components operate in an ideal way and the component being considered operates with its present efficiency. In addition, the exogenous exergy destruction is the difference between total and endogenous exergy destruction. The endogenous and exogenous exergy destruction can be calculated (Tsatsaronis and Mrorsuk, 2010) as below:

$$\dot{E}_{D,k} = \dot{E}_{D,k}^{EN} + \dot{E}_{D,k}^{EX}$$

(5)

The unavoidable exergy destruction (UN) can be defined within the (k) component that cannot be further reduced depending on technological limitations such as availability and manufacturing methods. Otherwise, the avoidable exergy destruction is the difference between total and unavoidable exergy destruction. The avoidable and unavoidable exergy destruction can be calculated (Tsatsaronis and Mrorsuk, 2010 as below):

$$\dot{E}_{D,k} = \dot{E}_{D,k}^{AV} + \dot{E}_{D,k}^{UN}$$

(6)

4. RESULTS AND DISCUSSION

Energy and exergy balance equations were applied to the cryogenic liquefaction unit and thermodynamic results were obtained and these values are given in Table 1, Table 2 and Table 3. The conventional and advanced exergy analysis was applied to each component in cryogenic liquefaction system. The obtained results of conventional and advanced exergy analysis is shown in Table 2.

Table 1: Obtained results of the Nitrogen gas

Point	T (K)	P (Bar)	h (kJ/kg)	s (kJ/kgK)	Point	T (K)	P (Bar)	h (kJ/kg)	s (kJ/kgK)
1	276.4	5.76	285.4	6.237	10	145	5.97	145.1	5.536
2	298.9	5.76	309	6.319	11	140.4	5.94	140	5.502
3	306	32.81	311	5.81	12	143.3	5.91	143.3	5.526
4	354	45.09	361.3	5.868	13	159.9	5.86	161.5	5.649
5	306	45.41	308.5	5.706	14	233.3	5.81	240	6.056
6	251.1	45.3	246.5	5.483	15	303	5.76	313.3	6.333
7	235	45.18	227.7	5.406	16	190.5	45.09	172.5	5.146
8	212	45.09	200	5.283	17	112.7	45.09	-43.42	3.603
9	212.6	45.3	200.6	5.284					

Table 2: Obtained results of the Argon gas

Point	T (K)	P (Bar)	h (kJ/kg)	s (kJ/kgK)	Point	T (K)	P (Bar)	h (kJ/kg)	s (kJ/kgK)
1	276.4	5.76	-12.58	-0.4046	10	145	5.97	-83.84	-0.7632
2	298.9	5.76	-0.7026	-0.3633	11	140.4	5.94	-86.48	-0.7807
3	306	32.81	-1.819	-0.726	12	143.3	5.91	-84.78	-0.7677
4	354	45.09	23.1	-0.7157	13	159.9	5.86	-75.34	-0.7037
5	306	45.41	-4.046	-0.7996	14	233.3	5.81	-35.48	-0.4965
6	251.1	45.3	-36.49	-0.9161	15	303	5.76	1.459	-0.3561
7	235	45.18	-46.51	-0.9568	16	190.5	45.09	-77.29	-1.102
8	212	45.09	-61.64	-1.024	17	112.7	45.09	-242	-2.224
9	212.6	45.3	-61.32	-1.024					

Table 3: Obtained results of the Oxygen gas

Point	T (K)	P (Bar)	h (kJ/kg)	s (kJ/kgK)	Point	T (K)	P (Bar)	h (kJ/kg)	s (kJ/kgK)
1	276.4	5.76	-21.31	-0.5248	10	145	5.97	-144.8	-1.142
2	298.9	5.76	-0.4767	-0.4523	11	140.4	5.94	-149.3	-1.173
3	306	32.81	-0.1978	-0.8995	12	143.3	5.91	-146.4	-1.151
4	354	45.09	44.05	-0.8467	13	159.9	5.86	-130.3	-1.042
5	306	45.41	-3.093	-0.9917	14	233.3	5.81	-61.25	-0.6842
6	251.1	45.3	-58.4	-1.19	15	303	5.76	3.323	-0.4397
7	235	45.18	-75.25	-1.259	16	190.5	45.09	-126	-1.499
8	212	45.09	-100.4	-1.371	17	112.7	45.09	-363.3	-3.099
9	212.6	45.3	-99.82	-1.37					

17 points were determined on the system and pressure, temperature and mass flow values at the input and output of the components were measured. The 17th point was the point where the product, the liquid, was obtained. These data were modelled by EES program to determine enthalpy, entropy and specific exergy values. These calculated properties were established exergy balance for each component and applied to advanced exergy formulas. The results obtained are given in Table 4.

Table 4: Results of the Nitrogen gas

Component	Conventional Exergy Analysis			Advanced Exergy Analysis			
	$\dot{E}_D$ (kW)	$\dot{E}_F(kW)$	$\dot{E}_P(kW)$	$\dot{E}_D^{EN}$ (kW)	$\dot{E}_D^{EX}$ (kW)	$\dot{E}_D^{AV}$ (kW)	$\dot{E}_D^{UN}$ (kW)
CM-1	32.78	1645	1612	5.65	27.13	4.562	28.21
CM-2	181.8	528.1	346.3	17.91	163.9	74.02	107.8
CAC	45.84	-	-	-	-	-	-
HE-1	37.38	83.69	46.31	3.031	34.35	17.76	19.62
LC	42.43	-	-	-	-	-	-
HE-2	283.2	379.1	95.94	58.53	224.7	-81.14	364.4
HE-3	464.5	163.2	627.7	197.7	266.7	776.7	-312.3
T	593	1033	439.6	154.2	438.8	-556.5	1149

The results of conventional and advanced exergy analysis of the nitrogen liquefaction system are presented in Table 4. Since it had the highest exergy efficiency among the three different fluids, the results of the nitrogen cycle are emphasized. In the nitrogen liquefaction system, the highest exergy destruction occurring in the turbine was 593 kW. Considering the forward exergy analysis, it was found that the largest part of exergy destruction was caused by unavoidable exergy destruction.

5.   CONCLUSION

When the results of the study are examined, it was found that the highest exergy efficiency among nitrogen, oxygen and argon occurred in the nitrogen liquefaction system. The total exergy destruction and exergy efficiency of the nitrogen liquefaction system were calculated as 1681 kW and 56.13%, respectively. Considering the advanced exergy analysis of the nitrogen liquefaction system, it was found that exergy destruction in the whole system resulted from exogenous and unavoidable exergy destruction.

6. REFERENCES

Bai, T., Yu, J., Yan, G., (2016) Advanced exergy analyses of an ejector expansion transcritical CO2 refrigeration system, Energy Conversion and Management, Vol: 126, pp 850-861. https://doi.org/10.1016/j.enconman.2016.08.057

Canyurt O.E., Ozturk H.K., Hepbasli A., Utlu Z., (2006) Genetic algorithm (GA) approaches for the transport energy demand estimation: model development and application, Energy Sources, Part A, Vol: 28 No: 15, pp 1405-1413. https://doi.org/10.1080/15567030600917033

Chang H.M., (2015) A thermodynamic review of cryogenic refrigeration cycles for liquefaction of natural gas, Cryogenics, 72(2), 127-147. https://doi.org/10.1016/j.cryogenics.2015.10.003

Fallah, M., Mahmoudi, S. M. S., Yari, M., (2017) Advanced exergy analysis for an anode gas recirculation solid oxide fuel cell, Energy, Vol: 141, pp 1097-1112. https://doi.org/10.1016/j.energy.2017.10.003

Hammad, A., Dincer, I., (2018) Analysis and assessment of an advanced hydrogen liquefaction system, International Journal of Hydrogen, Vol: 43, No. 2, pp 1139-1151. https://doi.org/10.1016/j.ijhydene.2017.10.158

Hamayun M.H., Ramzan N., Hussain M., Faheem M., (2022) Conventional and Advanced Exergy Analyses of an Integrated LNG Regasification-Air Separation Process, Industrial and Engineering Chemistry Research, Vol: 61(7), pp 2843-2853. https://doi.org/10.1021/acs.iecr.1c03730

Ishaq, H., Dincer, I., Naterer, G. F., (2019) Multigeneration system exergy analysis and thermal management of an industrial glassmaking process linked with a Cu–Cl cycle for hydrogen production, International Journal of Hydrogen Energy, Vol: 44, No. 20, pp 9791-9801. https://doi.org/10.1016/j.ijhydene.2018.12.140

Morosuk, T., Tsatsaronis, G., (2019) Advanced exergy-based methods used to understand and improve energy-conversion systems, Energy, Vol: 169, pp 238-246. https://doi.org/10.1016/j.energy.2018.11.123

Mostafa D., Hamid S., Seyyed M.H., Mehdi M., (2022) Evaluation of small-scale liquefied natural gas (SSLNG) processes: advanced exergoeconomic analysis, Chemical Papers. https://doi.org/10.1007/s11696-022-02408-5

Ozturk H.K., Canyurt O.E., Hepbasli A., Utlu Z., (2004) Three different genetic algorithm approaches to the estimation of residential exergy input/output values, Building and Environment, Vol:39, No:7, pp 807-816. https://doi.org/10.1016/j.buildenv.2003.12.002

Pakzada P., Mehrpooyab M., Zaitsev A., (2021) Thermodynamic assessments of a novel integrated process for producing liquid helium and hydrogen simultaneously, International Journal of Hydrogen Energy, Vol:46(76), pp 37939-37964. https://doi.org/10.1016/j.ijhydene.2021.09.046

Rehman A., Qyyum M.A., Zakir F., Nawaz S., He X., Razzaq L., Lee M., Wang L., (2020) Investigation of improvement potential of Modified Single Mixed Refrigerant (MSMR) LNG process in terms of avoidable and unavoidable exergy destruction, 3rd International Conference on Computing, Mathematics and Engineering Technologies (iCoMET), pp 1-7. https://doi.org/10.1109/iCoMET48670.2020.9073938

Tsatsaronis, G., Morosuk, T., (2010) Advanced exergetic analysis of a novel system for generating electricity and vaporizing liquefied natural gas, Energy, Vol: 35, pp 820-829. https://doi.org/10.1016/j.energy.2009.08.019

Utlu Z., Hepbasli A., (2004) Comparison of Turkey's sectoral energy utilization efficiencies between 1990 and 2000, Part 1: Utility and industrial sectors, Energy Sources, Vol:26 No: 14, pp 1331-1344. https://doi.org/10.1080/00908310490441638

Utlu, Z., Parali, U., (2013) Investigation of the potential of thermophotovoltaic heat recovery for the Turkish industrial sector, Energy Conversion and Management, Vol: 74 pp 308-322. https://doi.org/10.1016/j.enconman.2013.05.030

Utlu Z., (2015) Investigation of the potential for heat recovery at low, medium, and high stages in the Turkish industrial sector (TIS): An application, Energy, Vol: 81, pp 394-405. https://doi.org/10.1016/j.energy.2014.12.052

Valverdea J.I., Hamdya S., Morosuk T., Tsatsaronis G., (2021) Improvement perspectives of cryogenics-based energy storage, Renewable Energy, Vol: 169, pp 629-640. https://doi.org/10.1016/j.renene.2021.01.032

#28: Investigation of the effects of using solar energy on the energy performance of buildings

Ebru HANCIOGLU

Geothermal Energy Research and Application Center, Izmir Institute of Technology, 35430, Urla, Turkey, ebruhancioglu@iyte.edu.tr

Abstract: This research was concerned with the energy analysis of the Narlıdere Nursing Home and Rehabilitation Centre (NNHRC) in İzmir, Turkey, chosen as a sample public building. The Centre was run as a nursing and rehabilitation centre for the aged and it included a geriatric division operating as a hospital. The Centre was analysed using the actual energy consumption data derived from several energy audits. Solar energy is an important technology when considering sustainability and in this study, it was calculated how much the energy load of NNHRC would be reduced if PV Panels were used. The difference between the current situation and that once a 500 kWp PV panel system was installed was discovered. According to the results of the study, with 500 kWp PV panels placed on the roof, approximately 21% of the facility's electricity needs could be provided by these panels. With the use of PV panels, a 2.44% reduction in primary energy and a 4.28% reduction in emissions could be achieved, and an improvement of 2.43% in PER.

1. INTRODUCTION

The crises in energy supply and climate chaos in the world are constantly increasing. In addition to improving the effective use of energy resources, energy should be used efficiently, and targets for more effective use of renewable energy in the energy sector have grown in all countries of the world.

The increase in the effective use of energy sources and the prevention of wasted energy is of great importance for ensuring the security of the energy supply which could only be achieved by decreasing the energy dependency of Turkey, which is more than 70% (Sirin and Ege, 2012; Simsek and Simsek, 2013). According to the Ministry of Energy and Natural Resources (MENR) of Turkey (MENR, 2012), approximately 80% of the total energy demand will be imported by 2030 (Yasar and Kalfa, 2012).

Energy consumption in buildings is responsible for 1/3 of the global energy consumption and this consumption is increasing with the shift of country populations to cities day by day (Famiglietti, 2022,). In the European Union, the largest share of the total energy consumption is in the buildings at 40% (IEA, 2010; EC, 2010). In Turkey, 37% of the total energy is consumed in buildings, followed by 32% by industry, 20% in transportation, and 11% in other areas (MENR, 2012). Based on statistics, the average energy consumption variants of a government office building, non-government office building, hospital building, and school building were 169.98, 197.71, 206.92, and 118.54 kWh/(m²a), respectively (Ma *et al.*, 2017). The potential for saving energy was determined to be 30% in buildings, 20% in the industry sector, and 15% in the transportation sector by MENR (MENR, 2012).

One of the strategic purposes published in the Turkish Energy Efficiency Strategy Document (prepared by the General Directorate of Renewable Energy (EESD, 2012) 2012 was to use energy efficiently. As stated in this document, the aim was to decrease annual energy consumption in buildings by 10% by 2015 and 20% by 2023. In addition, within the scope of the National Energy Efficiency Action Plan implemented between 2017-2023, a target was set to reduce Turkey's primary energy consumption by 14% by 2023 with 55 actions defined in 6 categories, including buildings and services, energy, transportation, industry and technology, agriculture and horizontal issues (EEAP, 2022).

The climate crisis underlines the importance of the Paris Agreement target (IPCC 2018) supported by the Glasgow Climate Pact (UNFCCC, 2021) to strive to limit global climate change to below 2°C of pre-industrial temperatures and to limit it to 1.5°C. Targets have been set to run up to 2050 and the main targets for 2030 are to reduce greenhouse gas emissions by at least 40% (compared to 1990 levels); for renewable energy to be at least 32% of energy generation, and to improve energy efficiency by at least 32.5% (EC, 2022)

In today's conditions, we should take advantage of the potential of renewable energies as much as possible due to the effects of global warming and the increasing demands on energy resources. When evaluated in terms of energy efficiency among renewable energies, solar energy may have low-efficiency levels, but it is a remarkable energy source because it is a resource that can be used all over the world in terms of availability and ease of use. With the developing technologies, the energy efficiency of PV modules increases, and their costs decrease. A study by Baljit *et al.* (2016) can be cited as an example. In this study, an integrated photovoltaic-thermal type that was able to cool PV panels and increase the electrical output was specified as gaining popularity.

In this current study, Narlıdere Nursing Home and Rehabilitation Centre (NNHRC) in İzmir, Turkey, where energy efficiency studies have previously been carried out, was used as a case study. The aim was i) to calculate primary energy and ii) to calculate how much of the electricity needs of the facility could be met with PV modules by integrating 500 kWp PV modules into the facility. In addition, the change in primary energy and CO_2 emissions after the application of the PV module was examined.

2. THE CASE STUDY

2.1. Building description

The facility, located in Izmir, Turkey, served as a nursing and rehabilitation centre for old people. It has been active since 2001 and it was the biggest facility serving in this field in Turkey (Figure 1). The total area of the facility was 114,517 m², total building area was 74,616 m². The facility consisted of one building for management, thirty-four blocks for old people without disabilities, two blocks with nine floors for geriatric care for old people with disabilities, two conference rooms, six cafes, one kitchen, two laundry rooms, one kindergarten, a thirty-two-floor building used for dormitory purposes, one amphitheatre and one greenhouse.

The capacity of the facility was 1,061 people. There were 480 rooms for old people without disabilities and the capacity of the geriatric care centre was 271. In NNHRC, there were 34 blocks for old people without disabilities of which the ambient temperature was 24°C while the geriatric care centre was kept at 28°C since this centre was occupied with people who could not look after themselves, mostly confined to beds and needed greater physical, psychological and social care.

Natural gas was used for heating and the energy systems installed in the NNHRC included a main central system consisting of a natural gas boiler for heating and domestic hot water (DHW), and a steam generator operating with natural gas used for laundry. A chiller driven by electricity for cooling and lighting was also used (Kuzgunkaya, 2019).

Figure 1: Narlıdere Nursing Home and Rehabilitation Centre

2.2. The energy audits

The energy audit initially began by completing the information form of GDRE (GDRE, 2022) so bills and information on the equipment were collected. The information about the facility structure, construction materials, architectural drawings, and installed systems and equipment were provided by the facility's maintenance staff. In the study, the required values were taken from the architectural project and missing values were completed with fieldwork. Bills for natural gas and electricity had been collected over a period of six years (2007-2012). Boiler efficiency was measured and monthly electric counter data were taken.

3. METHOD

3.1. Energy Analysis

The primary energy demand ($E_{p,i}$) is given by Equation 1:

$$E_{p,i} = E_{f,i} + \frac{W_{el,i}}{n_{eg}} \qquad (1)$$

Where:

- I=the final user,
- E_f= the annual fossil fuel demand (assumed as direct primary energy),
- W_{el}=the annual electricity input,
- η_{eg}= the overall energy efficiency of the electric grid.

EP indicator was then calculated using the primary energy input, considering the building floor area, A_f, expressed by Equation 2:

$$EP = \sum_i \frac{E_{p,i}}{A_f} \qquad (2)$$

For a given energy use i, PER_i is defined as the ratio of useful energy at demand ($E_{u,i}$) and primary energy supplied ($E_{p,i}$), as given by Equation 3:

$$PER_i = \frac{E_{u,i}}{E_{p,i}} \qquad (3)$$

$E_{p,i}$ is calculated by Equation 1 and $E_{u,i}$ is defined according to the type of final energy use. General relation of $E_{u,i}$ for heating system and domestic hot water (DHW) is given by Equation 4:

$$E_{u,i} = \sum E_{f,i} n_{hg} n_{de} + \sum W_{el,aux} \qquad (4)$$

Where, $E_{f,i}$ is the fuel input of the heat generator; n_{hg} is the thermal efficiency of the heat generator and η_{de} is the efficiency of distribution network and emission system. $W_{el,aux}$ is the electricity load required for the auxiliaries of space heating process (e.g. pumps, fans).

For the cooling system (cs), a chiller for cold water production/hydraulic distribution–emission distribution system and air conditioning cooling units were used. The formulation is given by Equation 5:

$$E_{u,cs} = W_{el,ch} COP_{ch} n_{de} + \sum W_{el,aux} \qquad (5)$$

$W_{el,ch}$ and COP_{ch} are the supplied electricity and the averaged coefficient of performance for the chiller; $W_{el,aux}$ is the electricity load required for the auxiliaries of space cooling process (e.g. pumps, fans).

For electricity powered equipment (ee) (excluding heating and cooling equipment), such as lighting, ventilation and other NNHRC's electric equipment, the useful energy is given by Equation 6:

$$E_{u,ee} = \sum W_{el} \qquad (6)$$

3.2. PV System

Photovoltaic Geographical Information System (PVGIS) is a web application that allows the user to receive data on solar radiation and photovoltaic (PV) system power generation anywhere in the world (PVGIS, 2022; Figure 2). The PVGIS energy yield model is validated from measurements performed on commercial modules at the JRC's European Solar Test Installation (ESTI). ESTI is an ISO 17025 accredited photovoltaic calibration laboratory for all photovoltaic materials. Using the PVGIS application, the annual amount of energy to be produced by a 1 kWp panel was calculated.
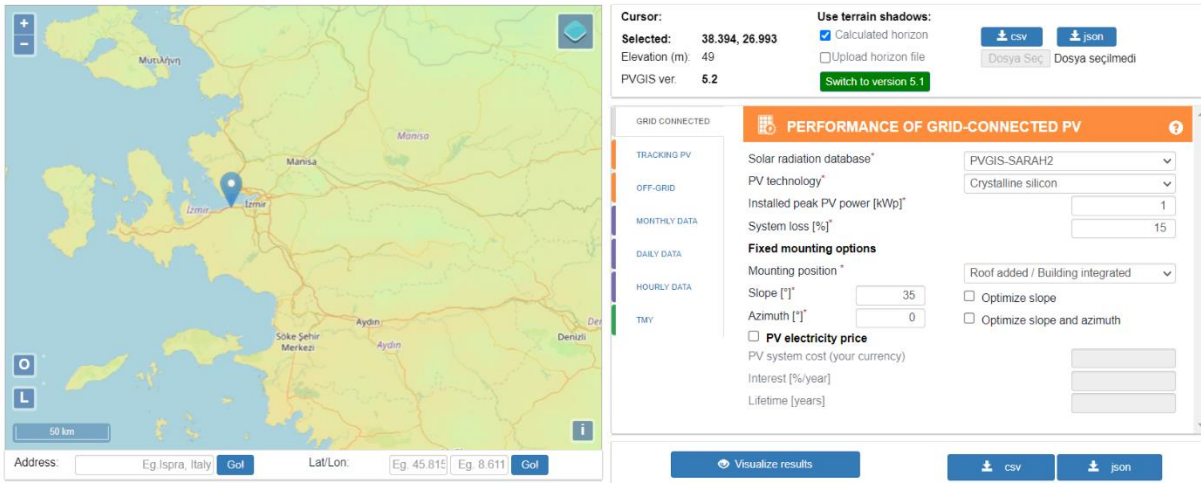
Figure 2: PVGIS

3.3. Emission factors and primary energy factors

Carbon dioxide emission factors and primary energy factors were calculated based on energy consumption. The conversion factors for primary energy and carbon dioxide emission factors were taken from SAP 10.1. The primary energy factor was 1.13 for gas fuels and 1.501 for electricity and the carbon dioxide emission factor was 0.210 kg CO_2 per kWh for gas fuels and 0.136 kg CO_2 per kWh for electricity (SAP 10.1, 2019). In the SAP 10 Technical document (S10TP-15), it was stated that the emission factor was taken as zero for electricity or heat generated from direct solar energy, wind energy, geothermal energy, and hydroelectricity (S10TP-15, 2020).

4. DISCUSSION AND RESULTS

4.1. Energy analysis of NNHRC

The feasibility of energy efficiency for heating and cooling, domestic hot water, steam generation, and electrical equipment (including lightning) was investigated at NNHRC (NNHRC, 2013). The NNHRC's share of energy consumption was analysed considering the invoices and, according to the invoice analysis, the annual natural gas and electricity consumption was 9,289,451 kWh (73%) and 3,430,815 kWh (27%), respectively.

Natural gas was mainly used for space heating, DHW, and steam generation (SG). From the analysis of the natural gas bills for the years 2007–2012, it was seen that from an annual energy consumption of 9,289,451 kWh, 5,229,767 kWh (56%) was associated with space heating, 3,810,708 kWh (41%) with DHW, and 248,976 kWh (3%) with steam generation. Non-heating requirements were assumed from May to October. The results for the monthly natural gas consumption, allocated by space heating, DHW, and steam generation, are shown in Figure 3.
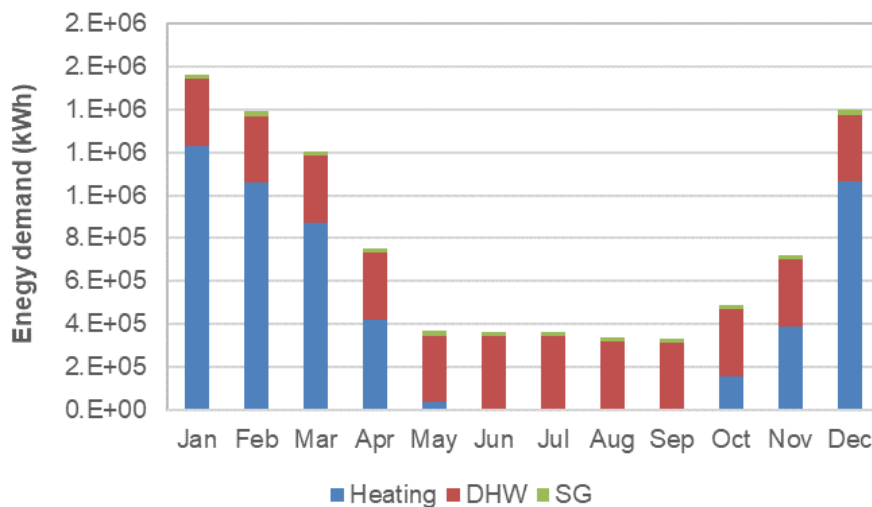
Figure 3: Monthly natural gas consumption

Electricity was used for space heating/cooling, hot/cold water pumping, steam generating, steam pumping, lighting, computers, and other electrical appliances. Figure 4 shows monthly electricity consumption. As a result of the energy audit, it was seen that about 70% of the electricity consumption was used for lighting and other electrical equipment, 22% for cooling, and 8% for heating as seen in Figure 5.
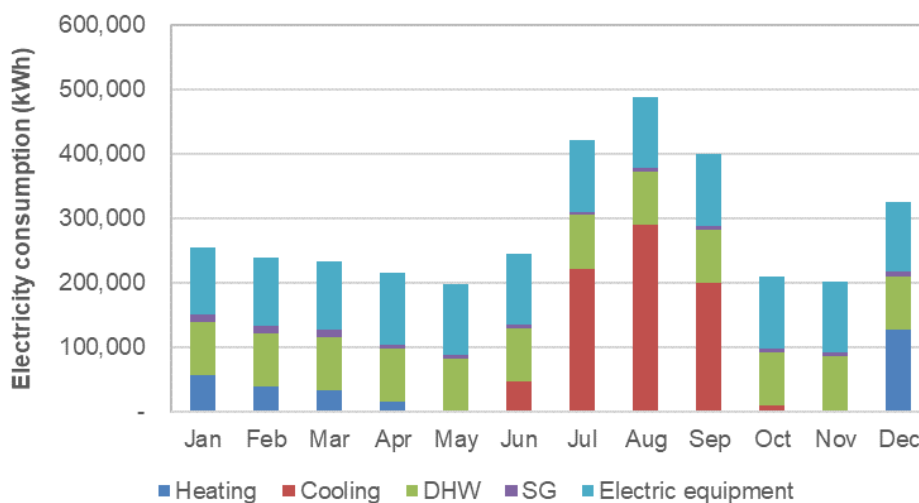
Figure 4: Monthly electricity consumption
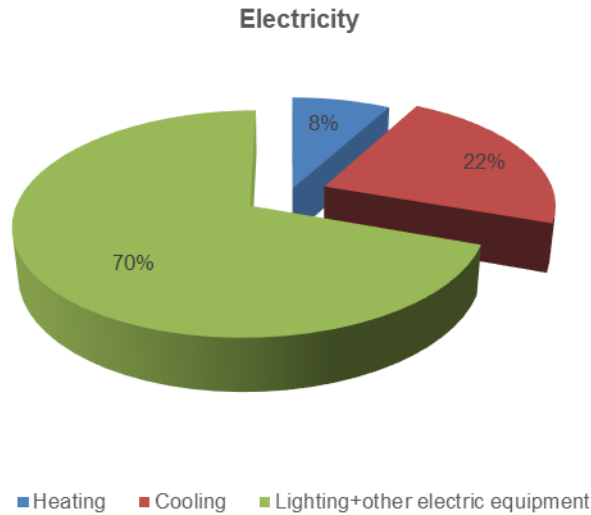
Figure 5: Distribution of electricity use.

4.2. PV system

Using the PVGIS application, the annual amount of energy produced by a 1 kWp panel was calculated. A single crystal silicon PV module was chosen and it was assumed to be fixed at an optimum tilt angle of 35°. In the calculations, building integration was chosen because the panels were planned to be placed on the roof or above the car parking area. The system loss was accepted as 15%, and the simulation output was obtained as 25.88% of the total losses. Annual PV energy production was found to be 1483.03 kWh for a 1 kWp panel. When the calculation was made on a 500 kWp panel, the total annual electrical energy production was 741,515 kWh.

In Figure 6, the monthly energy output and in-plane irradiation amount for the fixed angle PV system obtained with the PVGIS program are shown.
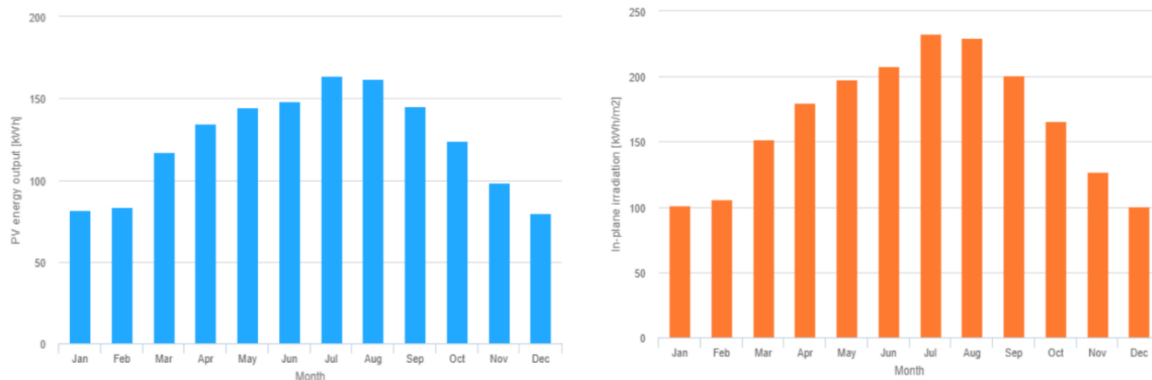
Figure 6: a) Monthly energy output from fix-angle PV system b) Monthly in-plane irradiation from the fix-angle PV system

In Figure 7, the monthly electrical energy requirement of the building and the monthly electricity production from the defined system are compared.
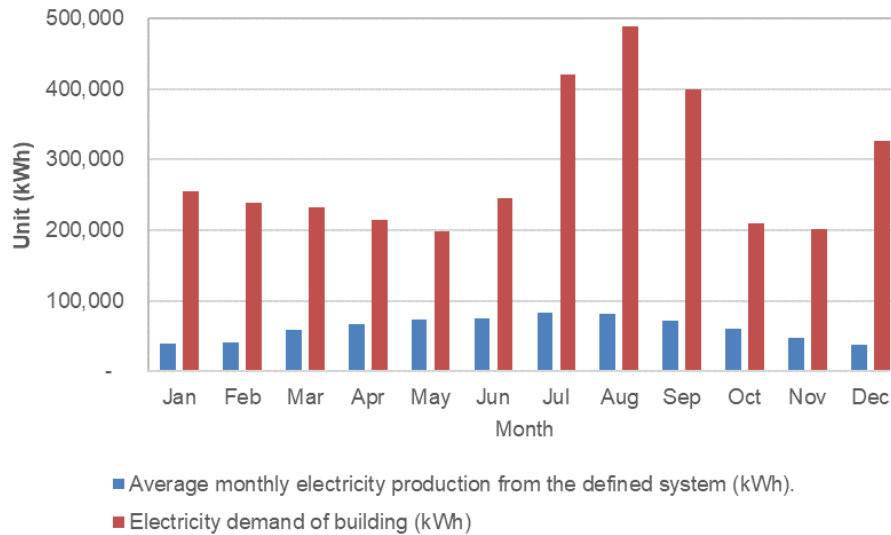
Figure 7: Comparison of the monthly electrical energy requirement of the building with the monthly electricity production from the defined system

4.3. Evaluation of primary energy and CO$_2$ emission

Case 1: Current condition

For the analysis, the energy use was divided into five main groups: space heating; space cooling; DHW; steam production; and electric equipment (including lighting). The division of the annual energy consumption for natural gas and/or electricity and associated primary energy is shown in Figure 8. It demonstrates that the NNHRC's DHW was the major primary energy consumer, followed by space heating and cooling applications.

For the calculation of the monthly consumption (input and useful), it was assumed that the seasonal variation, verified for the natural gas and electricity bills, was exclusively related to the air space conditioning (heating and cooling) process. The assessment of the useful energy in the building's envelope was conducted based on the previous formulation, using estimated efficiencies for the energy systems installed. Based on measurements, the boiler (heat generator) thermal efficiency was measured as 88%. COP of the chiller was 4.5 according to the catalogue but the estimated value was 3.5. The hot/cold water distribution and emission losses were estimated at 15%.
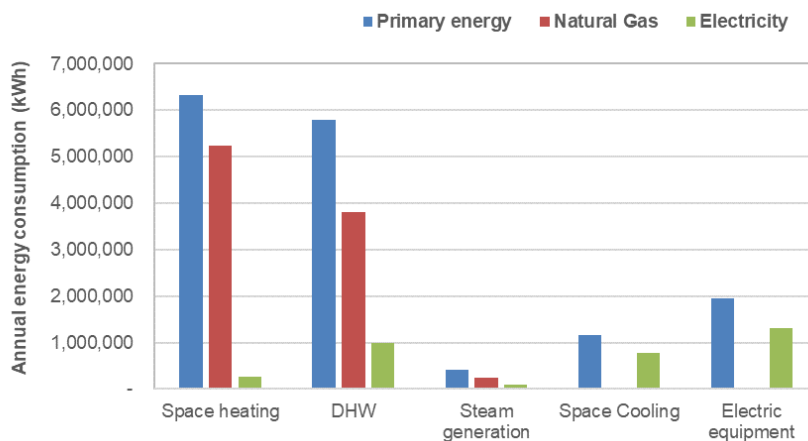
Figure 8: Annual energy consumption for natural gas, electricity, and primary energy

Using the results derived from the Energy Analysis of NNHRC section and assuming an overall efficiency for the electric grid of 30%, the PER was calculated. In Table 1, the results for natural gas, electricity, and related primary energy input, the useful energy, PER indicator, and EP for the tasks: heating, cooling, DHW, steam generation, and NNHRC electric equipment (lighting, elevators, personal computers, and others) are presented. The results derived an overall PER of 0.76, which meant that only 76% of primary energy input was effectively used for the considered NNHRC's tasks. The higher PER value obtained was associated with the chiller, since it had a high COP value. The specific energy demand (EP indicator) and the PER for each unit are shown in Figure 9.

19

Table 1: Estimated annual energy values and PER indicators.

Unit	Primary energy (kWh/year)	Natural Gas (kWh/year)	Electricity (kWh/year)	Useful energy (kWh)	PER	EP (kWh/m²)
Heating (Boiler)	5909637.21	5229767.44	n.a.	3911866.05	0.66	79.20
Heating (auxiliaries)	412672.93	n.a.	274932.00	274932.00	0.67	5.53
DHW	4306099.72	3810707.72	n.a.	2850409.38	0.66	57.71
DHW (auxiliaries)	1490673.12	n.a.	993120.00	993120.00	0.67	19.98
Steam generation	281342.88	248976.00	n.a.	186234.05	0.66	3.77
Steam generation (auxiliaries)	133528.96	n.a.	88960.00	88960.00	0.67	1.79
Cooling (Chiller)	930117.32	n.a.	619665.10	2168827.85	2.33	12.47
Cooling (auxiliaries)	223531.17	n.a.	148921.50	148921.50	0.67	3.00
Electric equipment	1959130.42	n.a.	1305216.80	1305216.80	0.67	26.26
Total	15646733.73	9289451.16	3430815.40	11928487.62	0.76	209.70
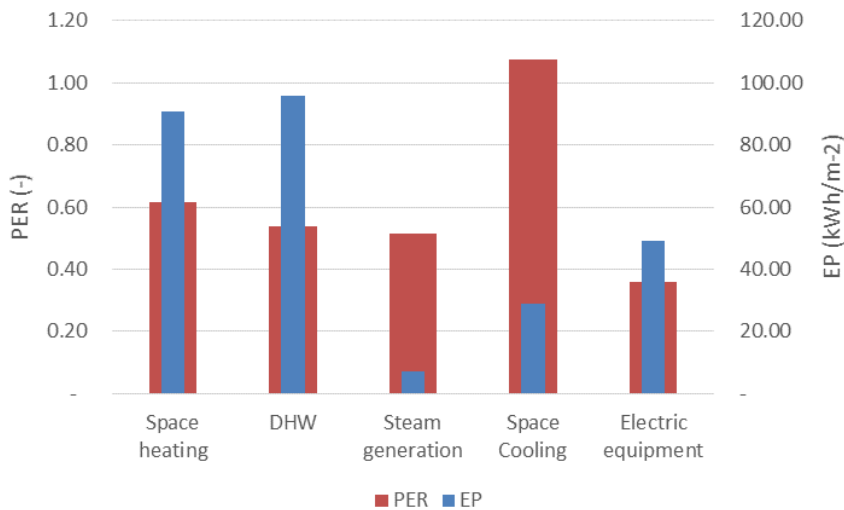
Figure 9. Annual specific primary energy demand and PER.

Case 2: PV use

The effect of electrical energy savings on primary energy and CO_2 emissions, in the case where electrical energy requirements of the facility were met from PVs, was investigated. When 500 kW PV was used in the facility, the annual electrical energy amount to be produced would be 741,515 kWh. Considering that the annual electrical energy need of the facility was 3,430,815 kWh, it is clear that roughly 21% of the annual electrical energy needs of the facility could be met by PV panels. As shown in Table 2, there was a 2.44% reduction in primary energy and a 4.28% reduction in CO_2 emissions. In addition, an increase of 2.43% could be achieved in the PER rate.

Table 2: Evaluation of Case 1 and Case 2.

Unit	Primary energy (kWh/year)	PER	Emissions (kg CO_2/kWh)
Case 1	15646733.73	0.76	2417375.64
Case 2	15265570.12	0.78	2313906.08
Evaluation as a percentage (%)	-2.44	2.43	-4.28

5. CONCLUSIONS

In this study, results derived from an energy audit of NNHRC were used to evaluate the energy performance of the building. The EP and PER were evaluated as 209,70 kWh/m² year, 76% respectively. With 500kWp PV panels to be placed on the roof, approximately 21% of the facility's electricity needs will be provided by PV panels. With the use

of PV panels, a 2.44% reduction in primary energy and a 4.28% reduction in emissions, and an improvement of 2.43% in PER could be achieved.

6. REFERENCES

Baljit, S.S.S., Chan, H., Sopian, K., 2016. Review of building integrated applications of photovoltaic and solar thermal systems. Journal of Cleaner Production, 137, 677-689.

EC (European Commission), 2010. On the energy performance of buildings. Official Journal of the European Union, Directive 2010/31/EU of the European Parliament and of the Council.

EC (European Commission), 2022. 2030 climate and energy framework, https://ec.europa.eu/clima/eu-action/climate-strategies-targets/2030-climate-energy-framework_en.

EEAP (National Energy Efficiency Action Plan), 2022. Republic of Türkiye Ministry of Energy and Natural Resources, https://enerji.gov.tr/evced-enerji-verimliligi-uevep.

EESD (Energy Efficiency Strategy Document, 2012-2023), 2012. Official Gazette, Number: 28215, Turkey, Feb.25.2012.

Famiglietti, J., Toosi, H. A., D´enari´e, A., Motta, M., 2022. Developing a new data-driven LCA tool at the urban scale: The case of the energy performance of the building sector. Energy Conversion and Management, 256, 115389, https://doi.org/10.1016/j.enconman.2022.115389.

GDRE (General Directorate of Renewable Energy), 2022. http://enerjimuh.com/pdf/Etut_bilgi_formu.pdf.

IEA (International Energy Agency), 2010. IEA Policy Pathway: Energy Performance Certification of Buildings, Paris.

Kuzgunkaya, E.H., 2019. Energy performance assessment in terms of primary energy and exergy analyses of the nursing home and rehabilitation center. Energy & Environment, 30(8), 1506–1520, https://doi.org/10.1177/0958305X19862418.

Ma, H., Du, N., Yu, S., Lu, W., Zhang, Z., Deng, N., Li, C., 2017. Analysis of typical public building energy consumption in northern China. Energy and Buildings, 136, 139–150.

MENR (Ministry of Energy and Natural Resources), 2012. <www.enerji.gov.tr/>.

NNHRC , 2013, Narlidere Huzurevi Yaşli Bakim Ve Rehabilitasyon Merkezinde Enerji Verimliliği Fizibilitesi, İzmir Kalkınma Ajansı, 2013.

PVGIS, 2022, PVGIS Photovoltaic Geographical Information System, https://joint-research-centre.ec.europa.eu/pvgis-photovoltaic-geographical-information-system_en

S10TP-15 (SAP 10 Technical Paper), CO_2 And Primary Energy Factors For SAP Version 1.1., 25/11/2020.

SAP 10.1, The Government's Standard Assessment Procedure for Energy Rating of Dwellings, (September 2019).

Simsek, H A, and Simsek, N., 2013. Recent incentives for renewable energy in Turkey. Energy Policy, 63, 521–530.

Sirin, S M, and Ege, A., 2012. Overcoming problems in Turkey's renewable energy policy: How can EU contribute?. Renewable and Sustainable Energy Reviews, 16, 4917–4926.

UNFCCC, 2021. UNFCCC, 2021. The Glasgow Climate Pact – Key Outcomes from COP26https://unfccc.int/process-and-meetings/the-paris-agreement/the-glasgow-climate-pact-key-outcomes-from-cop26.

Yasar, Y., and Kalfa, S.M., 2012. The effects of window alternatives on energy efficiency and building economy in high-rise residential buildings in moderate to humid climates. Energy Conversion and Management, 64, 170-181.

#30: Assessment of the thermodynamic analysis of a unique ejector cooling system

Gamze YAKUT[1], Hasan AYARTÜRK[2], Zafer UTLU[3], Melik Ziya YAKUT[4], Arif KARABUĞA[5]

[1]Isparta University Applied Sciences, Organized Industrial Zone Vocational School, Isparta, Turkey, gamzeyakut@isparta.edu.tr
[2]RePG Energy Systems Inc., Bursa, Turkey, hasan.ayarturk@repg.com.tr
[3]Halic University, Faculty of Engineering, Mechanical Engineering Department, Istanbul, Turkey, zaferutlu@halic.edu.tr
[4]Isparta University of Applied Sciences, Mechatronics Engineering, Faculty of Technology, Isparta, Turkey, ziyayakut@isparta.edu.tr
[5]Haliç University, Sustainable Energy Systems Application and Research Center, Istanbul, Turkey arif.karabuga@gmail.com

Abstract: A significant percentage of energy produced is used for cooling systems. For this reason, improvements in cooling systems can provide significant energy savings. In this study, a comparative result of the energy and exergy changes that occur in the system when different working fluids were used in the ejector cooling system with a unique design is presented. The system comprised different components such as an ejector, a steam generator, an evaporator, an air condenser, and a pump. This study aimed to determine the parameters that affect the thermodynamic performance of different working fluids. As a result, ideal working conditions were found by calculating the working fluid with the highest energy and exergy efficiency.

1. INTRODUCTION

Energy resources have always been important in the world. Today, energy and environmental problems trigger many new developments aimed at improving the performance of industrial processes and reduce greenhouse gas emissions. Research has been ongoing for years to protect existing energy sources and to create alternative energy sources. A significant part of the energy produced is used in cooling systems. Therefore, improvements to be made in cooling systems provide significant recoveries (Al-Sayyab, Navarro-Esbrí & Mota-Babiloni, 2022; Croquer, Poncet & Aidoun, 2016; Direk, İşkan, Tunçkal, Mert & Yüksel, 2022). Multi-generation, as an alternative solution to replace conventional systems, can provide several products simultaneously. One way to improve the performance of energy systems could be their integration in forms suitable for multi-generation purposes using low-temperature heat sources such as waste heat from industrial processes and renewable energies (Ghaebi, Namin & Rostamzadeh, 2018; Bhowmick & Kundu, 2022). A polygeneration system using geothermal energy was designed consisting of an Organic Rankine Cycle (ORC), an ejector cooling loop (ERC), liquid natural gas (LNG), a power generation unit and a PEME. According to the results obtained, the energy and exergy efficiencies and the total unit cost (SUCP) of the products were calculated as 38.3%, 28.9% and 347.9 $/GJ, respectively (Ding, Ai, Sun, Xu & Nedaei, 2022).

Our study was a solar energy-supported multi-energy generation system with unique design. As a result of multi-generation, electrical energy, hydrogen production, thermal energy and cooling energy were obtained. With the cold energy produced, the performance increase of the electricity generation system was provided. There was an Organic Rankine Cycle (ORC) system used in the production of electricity and hydrogen supported by solar energy. In the ORC system, an integrated ejector cooling system was used instead of the fans that consume electricity for cooling. In this system, comparative exergy analyses of different fluids were performed.

2. MULTI-ENERGY GENERATION SYSTEM

The system as illustrated in Figure 1 consisted of a multi-energy production system with solar-supported original design. As a result of multiple production, electrical energy, hydrogen production and cooling energy were obtained. To benefit from solar energy, the vacuum tube heat pipe solar collector (VTHPSC), organic ranking (OR) for electrical energy, ejective cooling system for cold energy production and proton exchanged membrane for hydrogen production (Proton Exchange membrane) were used. The system was as follows:

- Red = thermal energy production
- Blue = electrical energy production
- Green = hydrogen production
- Yellow = ejector cooling
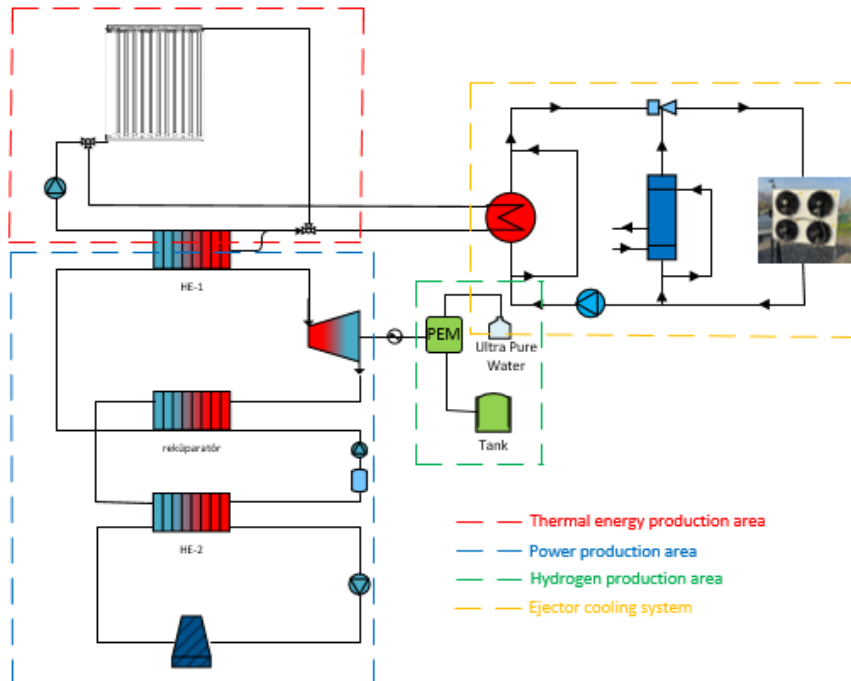
Figure 1: Multi-energy production system

The purpose of the study was the analysis of the ejector used in cold power generation in a multi-power generation system. The infrastructure of this study was supported within the scope of Haliç University Scientific Research Projects and with the contributions of RePG Energy Systems Industry and Trade Joint Stock Company.

2.1. Ejector cooling system

Ejectors have a complex structure therefore geometry design is important for energy efficiency. Ejector behaviour and system performance depend on the selected operating fluids, ejector dimensions and the purpose of cooling, as well as working conditions determined by the heat source and the temperatures of the cooler. Fans were used for cooling in the ORC system, which was used in the production of electricity and hydrogen supported by solar energy. The main reason for this study was the exergy analysis of the cooling system with integrated ejectors as shown in Figure 2 rather than the fans that consume electricity for different refrigerant.
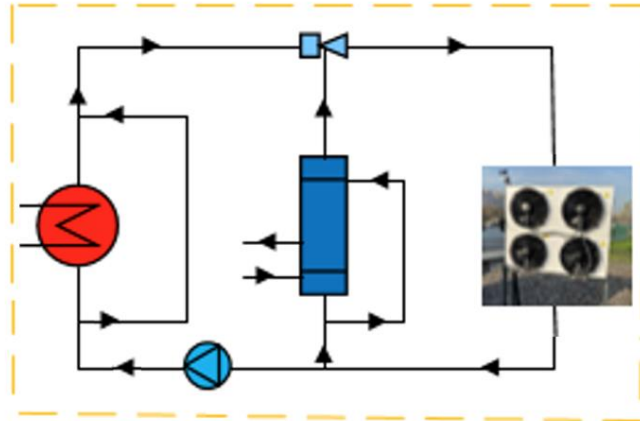
Figure 2: Ejector cooling system

The heat energy obtained from the vacuum tube heat pipe solar collector with medium temperature density was transferred to the boiler. Some of the heat energy stored in the boiler was used as a steam generator for the ejector cooling system.

2.2. Refrigerant

The use of gases with high ozone depletion potential (ODP) has been gradually reduced over the past 20 years. In the coming years, although it does not harm the ozone layer, the use of many gases with high global warming potential (GWP) is expected to be restricted. In this case, finding an alternative fluid for systems containing very large amounts of refrigerant, such as a heat pump, is essential. With the International Montreal Protocol, the production of components that affect the ozone layer, including refrigerants containing chlorine and bromine, has been brought under control. Production of CFC-type refrigerants (such as R11, R12, R113 and R114) was completely discontinued in 1996. R22 production from HCFC (hydrochlorofluorocarbon) type refrigerants has been kept constant at the 1996 production level. It is envisaged that the production of this fluid will be reduced to 0.5% in 2020 and completely stopped in 2030.To operate an energy production system, it must meet thermodynamic criteria (Kabul & Alkan, 2016). Seven different refrigerants were considered as working fluids (namely, R32, R1234yf, R290, R134a, R717, R600a and R245fa). R1234yf, R290, R600a and R717 were considered as low global warming potential refrigerants in European Union regulation (Yilmaz & Erdinç, 2019).

In this study, a comparison of exergy analyses using different fluids was made. First, experiments were carried out using water and R134A. The properties of fluids are given in Table 1.

Table 1: Properties of refrigerant

	Chemical name	Chemical Formula	Molecular weight	Normal boiling point [ºC]	Latent heat of vaporization [kJ/kg]	Critical Pressure[kPa]	Critical Temperature [ºC]
Water	Water	H2O	18.01508	100	2257	101.325	374.3
R134a	Tetrafluoroethane	CF3CH2F	102.03	-26.074	190.7/212.9	4059.3	101.1

2.3. Exergy analysis of ejector cooling system

To operate an energy production system, it must meet thermodynamic criteria. The main purpose of using the ejector as an expander in conventional cooling systems is to reduce irreversibility. An ejector can be used instead of an expansion valve. Exergy analysis shows how much each element of the system reduces the amount of total irreversibility and it is important to determine whether there is any improvement in exergy efficiency compared to the

classical system because with exergy analysis, the severity and location of the reversals in the system can be determined. The physical exergies at each point of the cycles are expressed in Equation 1.

Equation 1: Physical exergies

$$\dot{Ex} = \dot{m}[(h - h_0) - T_0(s - s_0)]$$

Equation 2 calculates the total exergy of the system. The result of the equation are found by summing the exergy of each element in the system.

Equation 2: Total exergies

$$\dot{Ex}_{top} = \dot{Ex}_g + \dot{Ex}_e + \dot{Ex}_c + \dot{Ex}_{ej}$$

The reference state was denoted as "0" and the ambient pressure was assumed to be 100kPa and the temperature to be 20ºC.

In Table 2, the temperature and pressure values are given as input parameters.

Table 2: Input parameters

	values
T_g- P_g	90ºC – 30 bar
T_e- P_e	4ºC – 2 bar
T_c- P_c	30ºC – 8bar

For each system element, the exergy value was calculated from the equation. Calculations were made according to the refrigerants used and the results are obtained. In Table 3, the exergy value of the ejector, the total exergy value, the exergy efficiency of the ejector, and the total exergy efficiency are calculated as the result parameters.

Table 3: result parameters

	$\dot{Ex}_{ej}$ (kW)	$\dot{Ex}_{top}$ (kW)	φ_{ej} (%)	Top (%)
Water	7.98	16.02	49	40.9
R134a	6.432	15.703	64	49.7

3. CONCLUSION

In this study, the solar energy assisted multi-generation system was investigated. An evacuated tube solar collector was used for solar energy. The study consisted of four stages: thermal power generation; electricity generation; hydrogen generation and an ejector cooling system. The main subject of this study was the comparison of the exergy values of two different fluids used in the ejector cooling system. As a result of the study, although the highest total exergy value was found in the water fluid in the ejector cooling cycle, exergy efficiency was obtained with R134a fluid with 49%.

4. REFERENCES

Al-Sayyab, A. K. S., Navarro-Esbrí, J., & Mota-Babiloni, A. 2022. Energy, exergy, and environmental (3E) analysis of a compound ejector-heat pump with low GWP refrigerants for simultaneous data center cooling and district heating. International Journal of Refrigeration, 133, 61-72.

Bhowmick, A., & Kundu, B. (2022). Extremum analysis based on exergy and economic principle for ejector-absorption cycles combined with regenerative organic-Rankine and gas-turbine cycles. Energy Conversion and Management, 253, 115174

Croquer, S., Poncet, S., & Aidoun, Z. (2016). Turbulence modelling of a single-phase R134a supersonic ejector. Part 2: Local flow structure and exergy analysis. International Journal of Refrigeration, 61, 153-165.

Direk, M., İşkan, Ü., Tunçkal, C., Mert, M. S., & Yüksel, F. (2022). An experimental investigation of ejector employed a dual-evaporator vapor compression refrigeration system under various entrainment ratios using R134a as the refrigerant. Sustainable Energy Technologies and Assessments, 52, 102293.

Ghaebi, H., Namin, A. S., & Rostamzadeh, H. (2018). Performance assessment and optimization of a novel multi-generation system from thermodynamic and thermoeconomic viewpoints. Energy Conversion and Management, 165, 419-439.

Kabul, A. & Alkan, R. (2016). Farklı Soğutucu Akışkanlar için Toprak Kaynaklı Isı Pompasının Termodinamik ve Termoekonomik Analizi. Isı Bilimi ve Tekniği Dergisi, 36 (1), 119-131. Retrieved from https://dergipark.org.tr/en/pub/isibted/issue/33974/37605

Li, K., Ding, Y. Z., Ai, C., Sun, H., Xu, Y. P., & Nedaei, N. (2022). Multi-objective optimization and multi-aspect analysis of an innovative geothermal-based multi-generation energy system for power, cooling, hydrogen, and freshwater production. Energy, 245, 123198.

Yilmaz, T., & Erdinç, M. T. (2019). Energetic and exergetic investigation of a novel refrigeration system utilizing ejector integrated subcooling using different refrigerants. Energy, 168, 712-727.

#31: Evaluation of the CFD analysis of a unique ejector

Melik Ziya YAKUT[1], Zafer UTLU[2], Hasan AYARTURK[3], Arif KARABUGA[4]

[1]Isparta University of Applied Sciences, Mechatronics Engineering, Faculty of Technology Isparta, Turkey,
ziyayakut@isparta.edu.tr
[2] Halic University, Faculty of Engineering, Mechanical Engineering Department, Istanbul, Turkey,
zaferutlu@halic.edu.tr
[3]RePG Energy Systems Inc., Bursa, Turkey, hasan.ayarturk@repg.com.tr
[4]Haliç University, Sustainable Energy Systems Application and Research Center, Istanbul, Turkey
arif.karabuga@gmail.com

Abstract: The ejector is a cooling system component developed to prevent energy losses in the throttling valve in conventional cooling systems. Since the cooling systems have a wide application in many different areas, any improvements to be made could have significant energy savings. For this reason, detailed simulation of the ejector system is important. In this study, CFD analysis of the ejector, which is a part of the ejector cooling system with a unique design, was made. It was aimed to prevent energy losses and produce the ideal design by modelling the flow occurring in the ejector with a unique design. The ideal values were evaluated by simulating according to the computational flow design made with the calculated preliminary values. The temperature, pressure and velocity graphs were analysed in 3D and the draft work was detailed. As a result, an ejector with ideal dimensions has been designed for the system.

1. INTRODUCTION

Ejectors are preferred because of their simple structure and working principle, low maintenance costs due to non-moving parts, high reliability and especially cheap welding advantages. Performance and efficiency increase is realized according to its sizing therefore, different studies have been carried out to determine the appropriate design. Ouzzane and Aidoun (2003) used a mathematical model and computer program for the ejector required for the refrigeration cycle in their article. The program was prepared by planning two different fluids, R141b and R142b, in a compressible dimension. By changing the diameters of the ejector according to the pressure, temperature and Mach number, the conditions of the fluid being close to supersonic and sonic were investigated. Besagni *et al.* (2021), using ANSYS CFD program Lumped Parameter Model, analysed ejector cooling systems with five different ejector geometries according to fourth generation natural coolers, nozzle exit position and mixing chamber throat dimensions. They divided refrigerants into three groups according to their performance: first group R1270 and R290 had higher COP (0.5–1.03) but lower critical temperature (20.7–25.0°C); second group R134a, R152a, R1234yf, R1234ze and R600a, had efficiency in the range of COP (0.27–0.83) and critical temperature (22.8–28.0°C); in the third group R245fa and R1233zd had lower COP (0.25–0.58) but a higher critical temperature (26.0–31.0°C). They found that an increased nozzle exit position resulted in 5% higher COP performances, while the ejector entrainment process increased efficiency by up to 35% COP to a high mixing chamber diameter. Hakkaki-Fard *et al.* (2015) showed that with the method applied to two different ejectors, the entrainment rates could be improved by up to 29% without greatly affecting their critical pressure, which was reduced by less than 2.6%. Khalil *et al.* (2011) analysed mathematically boiling, condensing and evaporating temperatures, nozzle and diffuser efficiencies and degrees of superheating on performance characteristics of R134a fluid in a vapour jet cooling system. Hassanain *et al.* (2015) investigated the effects of design parameters for R134a using the EES program. The COP of the system increased by 87.5% as evaporation temperature changed from -10°C to 10°C. Finally, correlations to size ejector main diameters as a function of operating conditions, system cooling capacity and ejector internal efficiencies were reported.

Increased ejector performance improves the performance of ejector cooling systems and increases their competitiveness in real applications. In this study, a new ejector geometry concept different from conventional geometry is proposed to improve performance characteristics and dimensional compactness. The proposals were first analysed as a draft, and it was observed that the most suitable design and the latest model with double suction were a solution that was suitable for both efficiency and system. The proposed final design was also modelled in more detail with ANSYS CFD.

2. EJECTOR DESIGNS AND ANALYSIS

The pressure and flow rate of the fluid circulating in ejector systems decreases due to the processes performed. In this study, four different geometry designs were made and simulated through assisted flow analysis and modelling related to these designs. The efficiency of the designed ejectors was modelled by computer-aided flow analysis. The initial parameters used in computer aided analysis programs are given in Table 1.

Table 1: The ejector input parameters

Parameters	Value
Pressure	30 Bar
Temperature	363 K
Mass Flow	0.25 kg/s
Type of Fluid	R134a

2.1. Box type ejector design

The outer geometry of this designed ejector type formed a compact box-shaped ejector system as seen in Figure 1. The ejector geometry, which had a standard interior design, had an inlet and a suction line.
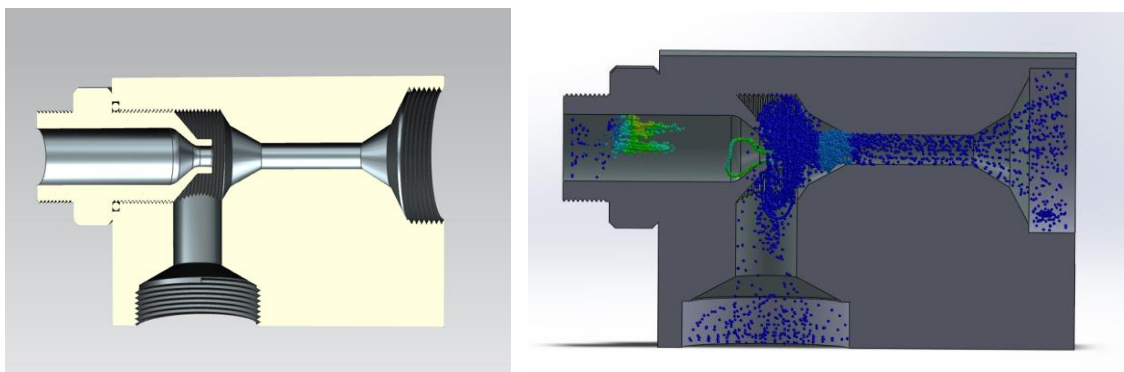
Figure 1: Box type ejector design and results of pressure analysis

As a result of the analysis, it was determined that this ejector design did not provide sufficient efficiency to reduce the pressure.

2.2. Tubular ejector design

The tubular ejector design, shown in Figure 2, was lighter, easier to manufacture, and more efficient than the box type, and it was planned to be designed in such a way that each part could be produced separately and then assembled. It had a single inlet and a single suction line.
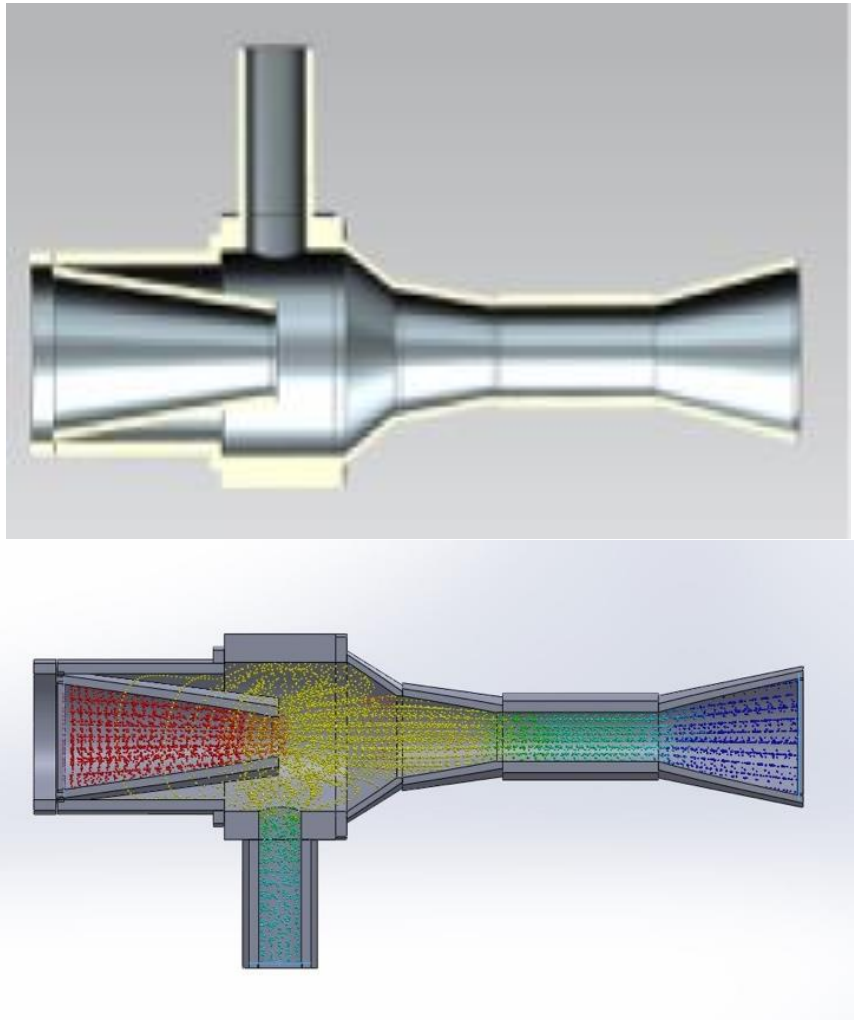
Figure 2: Tubular ejector design and results of pressure analysis

As a result, the final design was continued on this model, although it was not at the desired level.

2.3. Single suction line ejector design

The single suction line ejector design seen in Figure 3, unlike the previous design, was planned to be produced in two parts. The single vacuum line ejector was more compact and lighter than the tube type ejector. Improvements were made in the dimensions of the body in terms of design. In addition, significant changes were made to the nozzle in this design, thereby increasing the efficiency of this system.
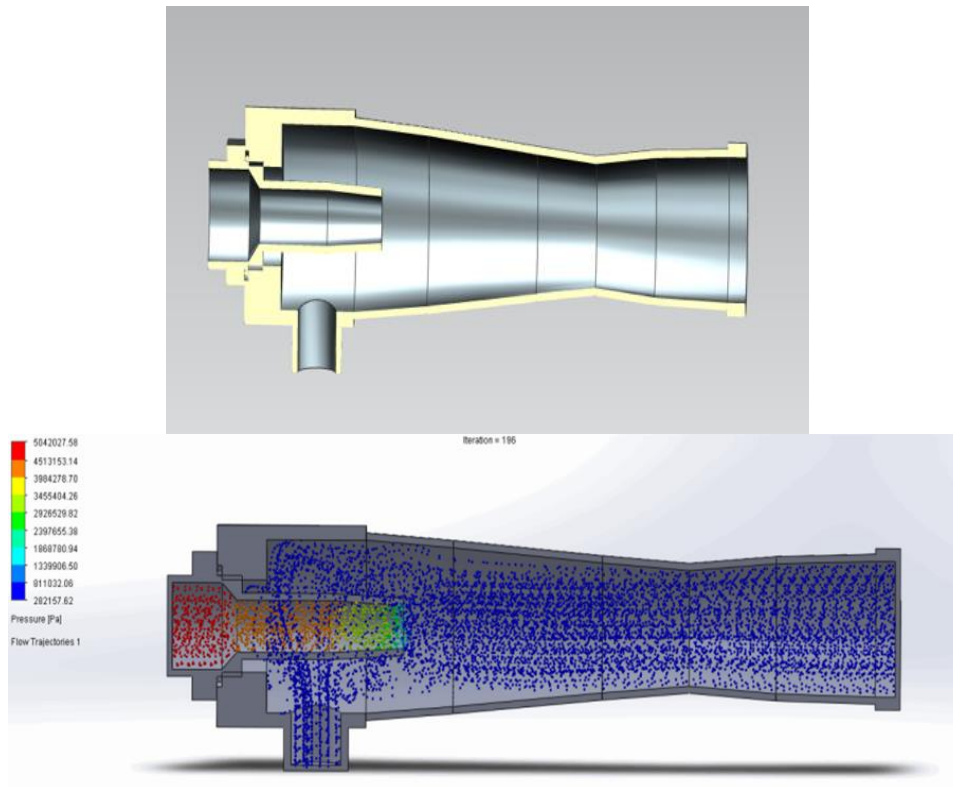
Figure 3: Single suction line ejector design and results of pressure analysis

To make it more suitable for our system, it was concluded that a different model should be modified over this design.

2.4. Double suction line ejector design

This design, shown in Figure 4, was similar to the single suction line ejector design, the main difference being the number of vacuuming lines was doubled and the diameter enlarged for greater suction effect. As a result, more use of the vacuum potential created was achieved.
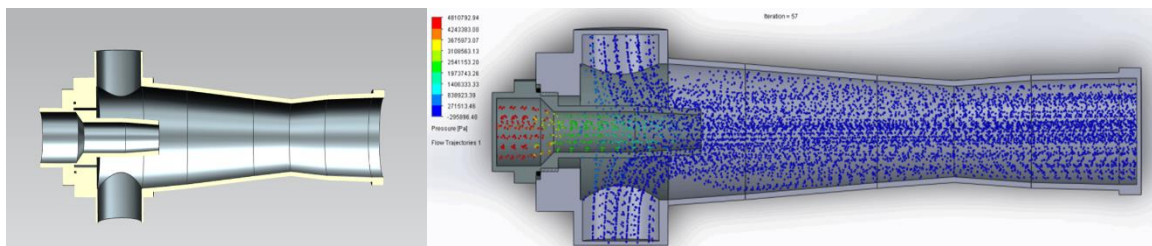
Figure 4: Double suction line ejector design and results of pressure analysis

3. ADVANCED CFD ANALYSIS OF DOUBLE SUCTION LINE EJECTOR DESIGN

This stage was modelled using the computer aided flow analysis program ANSYS Fluent and examined in detail. The thermal, pressure and velocity changes of the designed ejector were investigated by using the initial values in Table 1. The ideal design determined for this study was first subjected to meshing as shown in Figure 5.
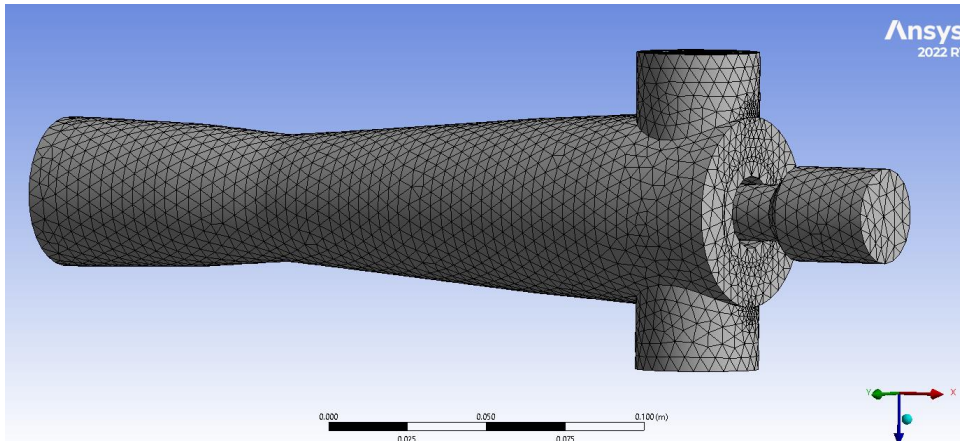
Figure 5: Meshing of double suction line ejector design

According to the analysis results of the model, which was divided into 38063 parts, the maximum skewness result was 0.79656. As a result of the velocity analysis in Figure 6, acceleration of velocity in the narrowing sections and change from the suction lines were observed.
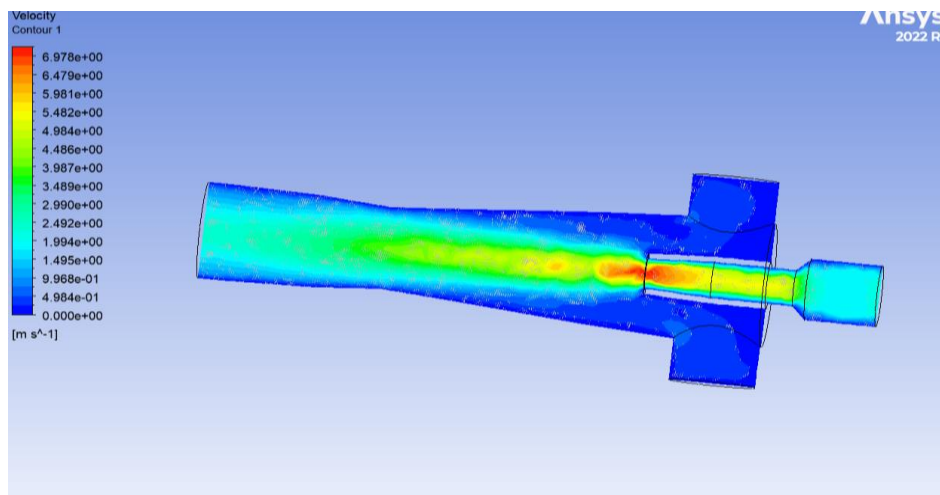
Figure 6: Velocity analysis of double suction line ejector design

In the temperature analysis in Figure 7, the change of the inlet temperature as a result of the cooling analysis developed by the suction effect caused by the pressure and speed was been observed.
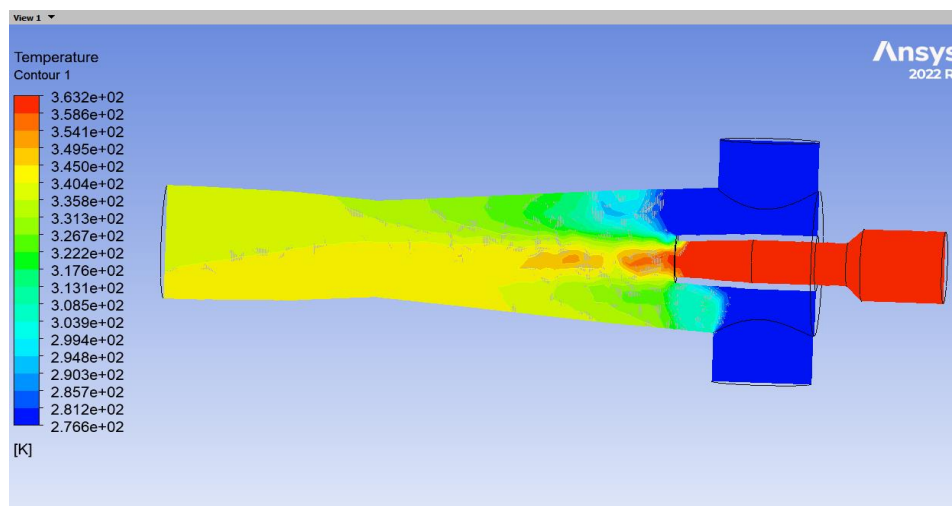
Figure 7: Temperature analysis of double suction line ejector design

In the pressure analysis in Figure 8, the pressure drop effect was observed in the narrowed regions due to the change in the inlet pressure with the design. As a result of the cooling analysis, change was observed with pressure change developed by the suction effect.
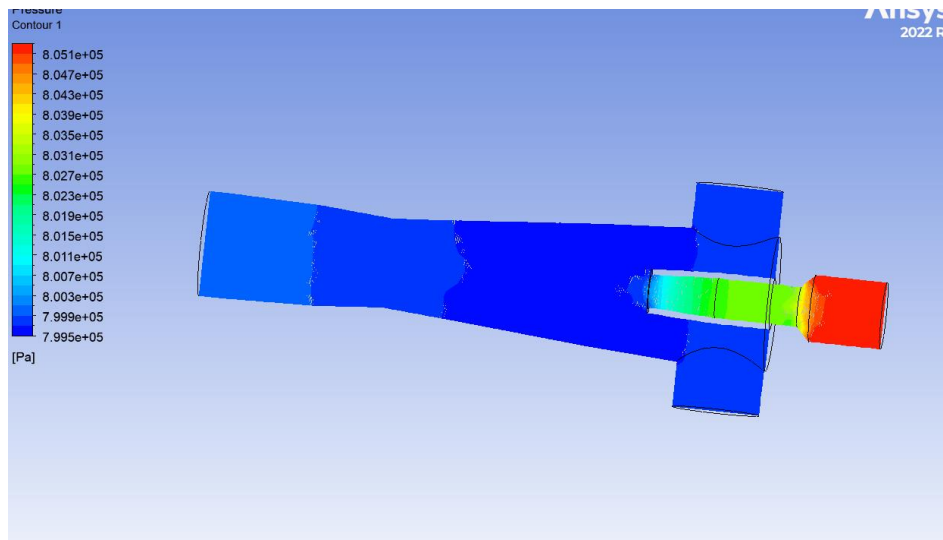
Figure 8: Pressure analysis of double suction line ejector design

When the results were examined, the expected changes of the ejector were seen in the analysis.

4. CONCLUSION

In this study, an ejector was designed to further reduce the pressure and flow of the fluid circulating in the system with high pressure and flow, and to reuse it in the system. At the first stage, the designs of the ideal ejector were tested for ease of manufacturing and its place in the system to be used. The double suction line ejector design was successful. A unique model was presented, both in terms of size and performance and the manufacturing process. This model was produced in the draft manufacturing output and the final output. After determining the dimensions of this successful model, a detailed CFD analysis was made and the success of the system was confirmed.

At the exit of the ejector, the speed changed to 2.492 m/s, the pressure was 7.99 bar, and the temperature was 322 K. It was observed that changes occurred with the effect of changing interior designs and affecting the suction lines.

5. REFERENCES

Besagni G., Cristiani N., Croci L., Guédon G. R., Inzoli F., 2021, Multi-scale evaluation of ejector performances: The influence of refrigerants and ejector design, Applied Thermal Engineering, Volume 186, 116502, ISSN 1359-4311, https://doi.org/10.1016/j.applthermaleng.2020.116502.

Hakkaki-Fard A., Aidoun Z., Ouzzane M., 2015, A computational methodology for ejector design and performance maximisation, Energy Conversion and Management, Volume 105, Pages 1291-1302, ISSN 0196-8904, https://doi.org/10.1016/j.enconman.2015.08.070.

Hassanain M., Elgendy E., Fatouh M., 2015, Ejector expansion refrigeration system: Ejector design and performance evaluation, International Journal of Refrigeration, Volume 58, Pages 1-13, ISSN 0140-7007, https://doi.org/10.1016/j.ijrefrig.2015.05.018.

Khalil A., Fatouh M., Elgendy E., 2011, Ejector design and theoretical study of R134a ejector refrigeration cycle, International Journal of Refrigeration, Volume 34, Issue 7, Pages 1684-1698, ISSN 0140-7007, https://doi.org/10.1016/j.ijrefrig.2011.01.005.

Ouzzane M., Aidoun Z., 2003, Model development and numerical procedure for detailed ejector analysis and design, Applied Thermal Engineering, Volume 23, Issue 18, Pages 2337-2351, ISSN 1359-4311, https://doi.org/10.1016/S1359-4311(03)00208-4.

#32: Exergo-environmental and exergo-enviroeconomic analysis of the solar-based multi-generation system: a case study

Arif KARABUGA[1], Zafer UTLU[2], Melik Ziya YAKUT[3]

[1] Haliç University, Sustainable Energy Systems Application and Research Center, Istanbul, Turkey
arif.karabuga@gmail.com
[2] Halic University, Faculty of Engineering, Mechanical Engineering Department, 34445, Istanbul, Turkey,
zaferutlu@halic.edu.tr
[3] Isparta University of Applied Sciences, Mechatronics Engineering, Faculty of Technology Isparta, Turkey,
ziyayakut@isparta.edu.tr

Abstract: In the present study, a solar power-assisted multi-generation system was experimentally investigated. An evacuated tube heat pipe solar collector was used for thermal energy conversion from solar energy. Electrical energy, hydrogen energy and cold energy were produced from the thermal energy obtained. Conversion from thermal energy to electrical energy was carried out using the Organic Rankine Cycle (ORC) system, PEM electrolyser for hydrogen production and ejector cooling system for cold energy production. In the presented study, the thermo-economic and thermo-environmental analysis of the solar energy-based multi-generation system was examined. The enviroeconomic analysis and exergoenviroeconomic analysis results of the whole system were calculated as \$1.22 and 816.3 $kgCO_2$, respectively.

Keywords: multi-generation; enviroeconomic analysis; exergoenviroeconomic analysis; hydrogen production

1. INTRODUCTION

Today, approximately 1/5 of the electrical energy consumed in buildings is used in cooling systems (Huang *et al.*, 2022) and most of the electricity produced comes from fossil sources (Depren *et al.*, 2022). This situation both poses a risk for countries in terms of energy security of countries and causes us to move away from the scenarios targeted in global warming. The preference of countries for alternative energy sources to fossil fuels stands out as a result of governments' decarbonisation policies. The most powerful renewable energy source is solar energy, as it is an alternative to fossil fuels and is both economical and easily accessible (Utlu *et al.*, 2014; Utlu and Hepbasli, 2007; Akbulut *et al.*, 2016). In this study, a solar energy assisted multiple energy generation system is discussed. In the presented system, vacuum tube solar collector for thermal energy generation, Organic Rankine Cycle (ORC) system for electricity generation, Proton Exchanger Membrane Electrolyser (PEMe) for hydrogen production and ejector cooling system for cooling are examined.

In the literature, there has been some research carried out in recent years around thermo-economic and thermo-environmental benefits of solar based multi-generation systems. In the literature, there has been some thermo-economic and thermo-environmental research in recent years about solar-based multi-generation systems. Fazeli *et al.* (2022) presented a comparative economic and environmental analysis of two cogeneration systems. While gas turbine and ORC units were used in the first system, gas turbine, ORC and ejector systems were used in the second system. When the energy and exergy efficiencies of both systems were compared, the use of the ejector system led to an increase in efficiency in the second cycle. The exergy efficiency and demolition cost of the second system were found to be 40.76% and $151.95/h, respectively. Kasaeian *et al.* (2022) discussed the general evaluation of power cycles with an integrated ejector refrigeration cycle, particularly focusing on the combination of ORC and ejector refrigeration cycle. As a result of the presented study, it was found that the combination of ORC and ejector caused an increase in efficiency for multiple productions. In Zandi *et al.* (2022), Brayton examined the 4E (Energy, Exergy, Economic and Environmental) analysis of an ORC and ejector integrated trigeneration system according to summer and winter conditions. As a result of the 4E analysis of the study, it was found that the output results obtained in the summer were higher than in the winter, while the environmental effects caused less damage. Exergy efficiency was 24.3% and 23.6% in the summer and winter months, respectively.

The aim of this study was to experimentally examine the exergy-based economic and environmental analysis of multi-generation production systems. The aim in the presented system is to determine the parameters affecting the exergy efficiency and to calculate the effect ratios of these parameters have on the efficiency.

2. EXPERIMENTAL STUDY

The solar based multi-generation system is illustrated in Figure 1. The main components of this system were a solar collector, two heat exchangers, a recuperate, a turbine, four pumps, a condenser, a PEMe unit, and an ejector refrigeration unit.
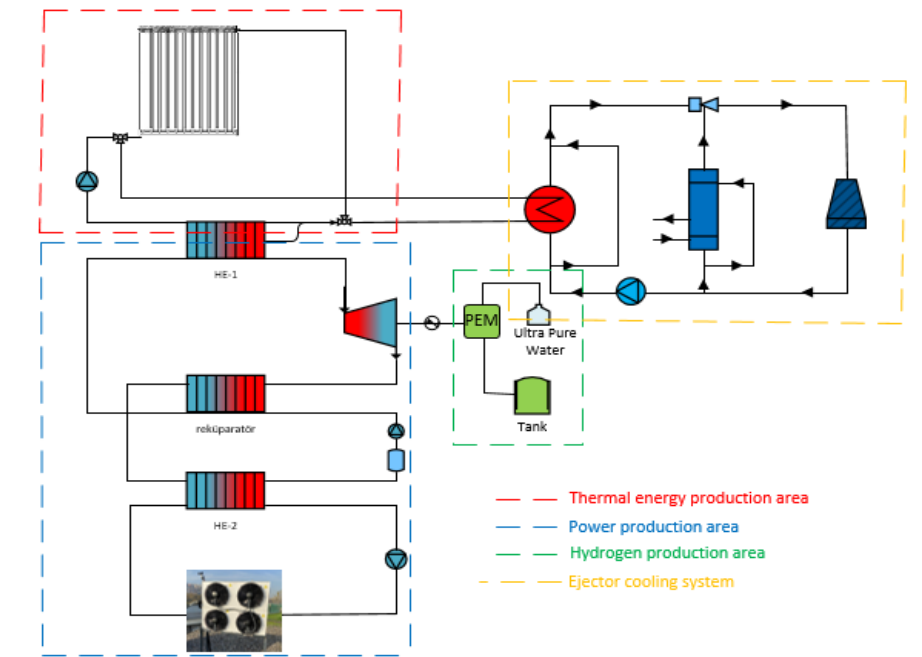
Figure 1: Flow chart of the presented multi-generation system

The thermal energy obtained from solar energy input to the heat exchanger at approximately 96°C and the generator for ejector cooling. R134a was used as the working fluid in the ejector cooling system. The superheated steam obtained from the generator input to the ejector at approximately 50 bar and droped down to 3 bar at the ejector outlet. On the other hand, the hot oil output from the collector input to the heat exchanger and provided the necessary heat energy for the ORC. The microturbine used in the ORC system had a capacity of approximately 1.5 kW. Similar to the ejector cooling system in the ORC system, R134a fluid was used as the working fluid. Some of the electricity obtained from the ORC system was transferred to PEMe for hydrogen production which took place at a capacity of approximately 0.0054 kg/h from PEM. Considering the whole system, electricity, hydrogen and cooling were obtained from solar energy.

3. THERMODYNAMIC MODELLING

Exergy-based economic and environmental analysis of the thermodynamic cycles presented in this study were examined with experimental data. The data obtained from the experimental set were analysed simultaneously with the Engineering Equation Solver (EES) program. In the study, while the solar collector, ORC system and hydrogen production were examined experimentally, the ejector cooling system was optimised based on theoretical calculations. The assumptions for the thermodynamic modelling of the aforementioned system were as follows;

- The system worked under steady state conditions;
- The changes in kinetic and potential energies were neglected;
- The pressure drops and heat losses in the connecting pipes were neglected;
- The compressor worked with adiabatic compression process;
- The system operated at atmospheric condition of T0= 25ºC and P0=1 bar as the reference state.

While thermodynamic modelling of the system was done, energy and exergy efficiency was taken as the basis. All modelling was created taking into account exergy efficiency. The economic and environmental analysis of the system was evaluated according to its exergy value. While designing the ejector, a reverse engineering approach was adopted, so much so that the first and second laws of thermodynamics were applied for the collector system, the ORC system and the hydrogen production system as follows (Utlu and Parali, 2013; Utlu and Hepbasli, 2005; Jadidi *et al.*, 2022; Hai *et al.*, 2022)

$$\sum \dot{m}_{in} = \sum \dot{m}_{out} \tag{1}$$

$$\sum \dot{Q}_{in} + \sum \dot{W}_{in} + \sum \dot{m}_{in} h_{in} = \sum \dot{Q}_{out} + \sum \dot{W}_{out} + \sum \dot{m}_{out} h_{out} \tag{2}$$

$$\sum \dot{m}_{in} s_{in} + \sum \frac{\dot{Q}_{in}}{T} + S_{gen} = \sum \dot{m}_{out} s_{out} + \sum \frac{\dot{Q}_{out}}{T} \tag{3}$$

$$\dot{Ex}_{in}^Q + \dot{Ex}_{in}^W + \sum \dot{m}_{in} ex_{in} = \dot{Ex}_{out}^Q + \dot{Ex}_{out}^W + \sum \dot{m}_{out} ex_{out} + \dot{Ex}_D \tag{4}$$

$$\dot{Ex}_Q = Q\left(1 - \frac{T_0}{T}\right) \tag{5}$$

$$\dot{Ex}_W = \dot{W} \tag{6}$$

$$\dot{Ex}_D = T_0 s_{gen} \tag{7}$$

$$ex_{ph} = h - h_0 - T_0(s - s_0) \tag{8}$$

In the study, the following equations were taken into account while calculating the exergy-based economic and environmental analysis (Caliskan, 2017):

$$x_{exCO2} = y_{CO2} Ex_{solar} t_{working} \tag{9}$$

$$Ec_{exCO2} = x_{exCO2} C_{CO2} \tag{10}$$

One of the basic pieces of equipment that was effective in absorbing heat from the evaporator was the ejector. The ejector generally consisted of three parts: nozzle, mixing chamber and diffuser section. Its operation was assumed to be in steady state. Equation 11 was used to analyse the performance of the ejector (Wang *et al.*, 2009), where μ was the entrainment ratio and η was the efficiency of the nozzle, mixing chamber and diffuser section. Also, h represented the enthalpy of mixed flow (mf) and primary flow (pf) in the inlet (in), outlet (outside), or isentropic state (is).

$$\mu = \sqrt{\frac{\eta_n \eta_m \eta_d (h_{pf,in} - h_{pf,is})}{(h_{mf,out,is} - h_{mf})}} - 1 \tag{11}$$

4. RESULTS AND DISCUSSION

The equations in session 3 were applied separately for each component in the presented study. Both the exergy efficiency of the system and the exergy efficiency of each component were calculated. The exergy efficiency of the system is presented in Table 1.

Table 1: Exergy analysis results of the multi-generation system

Component	Solar collector	ORC	PEMe	Ejector cooling unit	Total efficiency
Exergy efficiency	25.17%	14.08%	17.32%	49.7%	24.08%

In the presented study, the total exergy efficiency was calculated as 24.08%. Considering each component separately, the highest exergy efficiency was obtained in the ejector cooling system. The lowest exergy efficiency in the system was calculated as 14.08%. The results of the exergy-based economic and environmental analysis are given in Table 2.

Table 2: Exergoenvironmental and exergoenviroeconomic analysis of the multi-generation system

Parameters	Solar collector	ORC	PEMe	Ejector cooling unit	Total efficiency
Exergoenviromental ($/kgCO$_2$)	0.123	0.0068	0.0014	0.0006034	0.13
Exergoenviroeconomic (kgCO2/kWh)	67.7	3.8	0.011	0.3329	72

As a result of the exergy-based environmental and economic analysis, the highest environmental impact was calculated as 0.123 $/kgCO$_2$ in the solar collector. In addition, the exergy-based environmental analysis result of the whole system was found to be 0.13 $/kgCO$_2$. Similarly, as a result of the exergy-based economic analysis, the highest economic effect was calculated as 67.7 kgCO$_2$/kWh in the solar collector. The exergy-based economic effect of the whole system was found to be 72 kgCO$_2$/kWh.

5. CONCLUSION

In this study, thermo-environmental and thermo-economic analyses of a solar-based multi-generation system were performed by using the exergy concept. As a result of the study, the exergy efficiency of each component in the proposed system was calculated. Although the highest exergy efficiency among all components was in the ejector cooling system, when the economic and environmental effects were examined, it was found that the lowest exergoenviromental value was in the ejector cooling system. The exergoenviromental analysis result of the whole system was calculated as 0.13 $/kgCO$_2$. It was calculated that the highest exergoenviroeconomic value in the presented system was in the solar collector with 67.7 kgCO$_2$/kWh

6. REFERENCES

Akbulut, U., Utlu, Z., Kincay, O., (2016) Exergoenvironmental and exergoeconomic analyses of a vertical type ground source heat pump integrated wall cooling system, Applied Thermal Engineering, Vol:102, pp 904-921.

Caliskan H., (2017) Energy, exergy, environmental, enviroeconomic, exergoenvironmental (EXEN) and exergoenviroeconomic (EXENEC) analyses of solar collectors, Renewable and Sustainable Energy Reviews Vol: 69, pp: 488-492.

Depren S.K., Kartal M.T., Ertugrul H.M., Depren O., (2022) The role of data frequency and method selection in electricity price estimation: Comparative evidence from Turkey in pre-pandemic and pandemic periods, Renewable Energy, Vol. 186, pp 217-225.

Fazeli A., Zandi S., Mofrad K.G., Salehi G., Manesh M.H.K., Shirmohammadi R., (2022) Comparative thermoeconomic optimization and exergoenvironmental analysis of an ejector refrigeration cycle integrated with a cogeneration system utilizing waste exhaust heat recovery, Environmental Progress and Sustainable Energy. https://doi.org/10.1002/ep.13875

Hai T., Dhahad H.A., Attia E.A., Zakaria Z., Rashidi S., Simgh P.K., Shamseldin M.A., Almojil S.F., Almohana A.I., Alali A.F., Farhang B., Cao Y., (2022) Design, modeling and multi-objective techno-economic optimization of an integrated supercritical Brayton cycle with solar power tower for efficient hydrogen production, Sustainable Energy Technologies and Assessments, Vol:53, pp: 102599.

Huang Y., Jiang P., Zhu Y., (2022) Analysis of a novel combined cooling and power system by integrating of supercritical CO2 Brayton cycle and transcritical ejector refrigeration cycle, Energy Conversion and Management, Vol. 269, pp 116081.

Jadidi H., Keyanpour-Rad M., Haghgou H., Chodani B., Rad S.K., Hasheminejad S.M., (2022) Energy and exergy simulation analysis and comparative study of solar ejector cooling system using TRNSYS for two climates of Iran, Heliyon, Vol:8, pp:e10144. https://doi.org/10.1016/j.heliyon.2022.e10144

Kasaeian A., Shmaeizadeh A., Jamjoo B., (2022) Combinations of Rankine with ejector refrigeration cycles: Recent progresses and outlook, Applied Thermal Engineering, Vol:211, pp 118382.

Utlu Z., Aydin D., Kıncay O., (2014) Comprehensive thermodynamic analysis of a renewable energy sourced hybrid heating system combined with latent heat storage, Energy Conversion and Management, Vol. 84, pp 311-3225.

Utlu, Z., Hepbasli, A., (2007) Assessment of the Turkish utility sector through energy and exergy analyses, Energy Policy, Vol:35, No. 10, pp 5012-5020.

Utlu, Z., Hepbasli, A., (2005) Analysis of energy and exergy use of the Turkish residential–commercial sector, Building and Environment, Vol:40 No. (5), pp 641-655. https://doi.org/10.1016/j.buildenv.2004.08.006

Utlu, Z., Parali, U., (2013) Investigation of the potential of thermophotovoltaic heat recovery for the Turkish industrial sector, Energy Conversion and Management, Vol: 74 pp 308-32. https://doi.org/10.1016/j.enconman.2013.05.030

Wang, J., Dai, Y., Sun, Z., (2009) A theoretical study on a novel combined power and ejector refrigeration cycle, International Journal of Refrigeration, Vol. 32, No. 6, pp.1186–1194.

Zandi S., Fazeli A., Mofrad K.G., Salehi G., Manesh M.H.K., (2022) Enhanced exergy analysis and optimisation of a trigeneration system, International Journal of Exergy, Vol: 39, No:1 pp 97-116.

#34: Investigation of two-stage cascade refrigeration systems from an energy and exergy point of view

Ali KILICARSLAN

Hitit University-Department of Mechanical Engineering, 19030 Corum-TURKEY
Telephone: +90(364) 2274536/1236, Fax: +90 (364) 2274535, e-mail: alikilicarslan@gmail.com

Abstract: Vapour compression cascade refrigeration systems are comprised of two or more systems that are coupled to each other in which the evaporator of the higher stage refrigeration system serves as a condensing medium for the lower stage system. Vapour compression cascade refrigeration systems are used to achieve low temperature refrigeration and are used for applications down to -80°C. In this study, a two-stage vapour compression cascade refrigeration system was modelled from a thermodynamics point of view including first and second law of thermodynamics. R134A was used as the refrigerant in the higher stage system and R404A was used in the lower stage refrigeration, and they were experimentally investigated according to different condenser temperatures ranging from 47°C and 57°C. The results obtained were inserted into a computer program developed with the help of Engineering Equation Solver (EES). It showed that the coefficient of performance of two-stage vapour compression refrigeration system decreased by 8% and the total amount of exergy destruction decreased by 50%.

Keywords: compression refrigeration; cascade; energy; exergy; exergy destruction

1. INTRODUCTION

Today, although the need for energy has been increasing day by day, limited energy resources have focused humanity on the widespread use of alternative and renewable sources and the efficient use of existing energy resources. One of the areas where energy is widely used is refrigeration. Refrigeration systems are used for comfort in integration with air conditioning systems, as well as for refrigeration of food, products, fluids and materials, liquefaction of gases, medical and industrial purposes.

In the applications where a single-stage vapour compression cooling system is not sufficient, cascade systems are used. Vapour compression cascade refrigeration systems consist of two or more systems connected in such a way that the condenser of the system in the low pressure stage is integrated into the evaporator of the system in the high pressure stage. Cascade refrigeration systems are used in the areas of blood storage, liquefaction of gases, and hardening of special alloy steels (Gupta, K., 1985). Vapour compression cascade cooling systems are used in temperature ranges of -50°C/ -100°C (Yılmaz et al., 2020).

There have been theoretical and/or experimental studies including the energy and exergy analyses of two-stage vapour compression cascade refrigeration systems (TSVCCRS). In an experimental work carried out by Kilicarslan (2004), a different type of TSVCCRS was developed in such a way that two separate vapour compression refrigeration systems were connected to each other by a water loop. The result was that the coefficient of performance (COP) of TSVCCRS was higher than the COP of the single stage vapour compression refrigeration system by 21.9%.

A two-stage vapour compression refrigeration system was theoretically investigated from the aspect of first and second laws of thermodynamics for different refrigerant couples including R152a–R23, R290–R23, R507–R23, R234a–R23, R717–R23 and R404a–R23 (Kilicarslan and Hosoz, 2010). It was determined that the coefficient of performance of TSVCCRS increased and exergy destruction rate decreased with increasing polytropic efficiency and evaporator temperature for all of the refrigerant pairs in the study and the maximum COP and minimum exergy destruction rate were achieved by using refrigerant couple R717–R23 in the most of the range of polytropic efficiency and temperature difference.

Energy and exergy analyses of TSVCCRS were carried out by means of a simulation program developed for different refrigerant couples including T2Butene/Toluene, T2Butene/Cyclopen and T2Butene/C2Butene. It resulted that the maximum coefficient of performance and exergy efficiency were obtained by using refrigerant couple T2Butene/Toluene and maximum exergy destruction happened in the condenser (Faruque et al, 2022). The first and second law based analysis of TSVCCRS including an auxiliary refrigeration loop and employing NH_3/CO_2 as refrigerant couple were performed by a computer code with respect to the temperature of low temperature cycle, evaporator temperature and degree of subcooling. It was observed that the maximum coefficient performance of TSVCCRS with the auxiliary refrigeration loop was 4.58% higher than the conventional TSVCCRS for a 10°C of subcooling and the exergy efficiency (Chen et al, 2022). A 4E (energy, exergy, economy and environment) model of TSVCCRS was carried out with respect to the evaporator , condenser and cascade heat exchanger temperatures for the refrigerant couples including R41-R161, R41-R1234yf, R41-R1234ze, R744-R161, R744-R1234yf, R744-R1234ze. It resulted that the highest COP of 2.09 and the highest exergy of 35.32% were achieved at a condensing temperature of 40ºC and evaporating temperature of -30ºC and it also resulted that the optimum refrigerant couples were R41-R161 and R41-R1234ze (Dashtebayaz et al, 2021). In an experimental study, R41/R404A and R23/R404A refrigerant couples were compared from the aspects of energy and exergy in a TSVCCRS. It was observed that the lower values of the power delivered to the compressor and the exergy loss were achieved by employing R41/R404A as a refrigerant couple in the TSVCCRS (Liang et al., 2016).

It was clear from the literature survey that there have been only a few studies investigating the effect of the condenser temperature of two-stage vapour compression. In the current study, the effect of condenser temperature on the refrigeration capacity, the heat rejected by condenser, the power consumed by the compressors, the exergy destructions of the components of TSVCCRS including the compressors, condenser, evaporator, heat exchanger and expansion valves were experimentally investigated in detail.

2. THERMODYNAMIC MODEL

The two-stage vapour compression cascade refrigeration is depicted in Figure 1. It consisted of two compressors, two expansion valves, a condenser, evaporator and heat exchanger. The heat exchanger, where the heat rejected by the vapour compression refrigeration system 1 (VCRS 1) was absorbed by the vapour compression refrigeration system 2 (VCRS 2), connected VCRS 1 and VCRS 2 to each other.
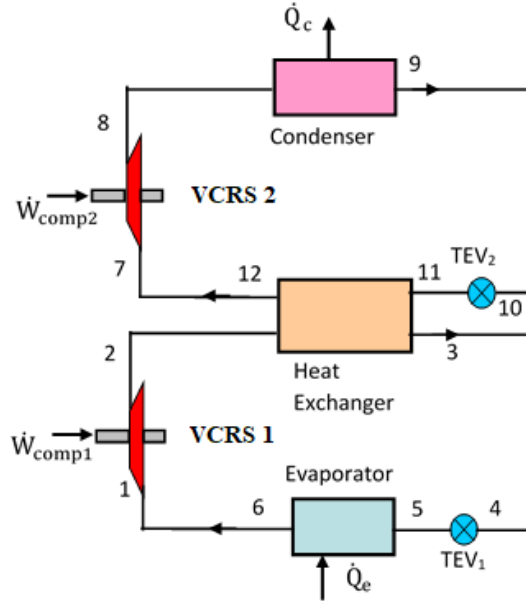
Figure 1: Schematic diagram of a two-stage vapour compression cascade refrigeration system.

In the two-stage cascade refrigeration system, it was presumed that steady-state and uniform flow conditions existed through the components of the cascade refrigeration system, subcooling and preheating occurred at the same time in the liquid line and suction line respectively. The changes in kinetic and potential energies were neglected. The pressure drop through the cycle except at the expansion valves were neglected. The compression processes in the compressors were also assumed to be adiabatic. The pressure–enthalpy (P–h) and the temperature entropy (T–s) diagrams of the two-stage cascade refrigeration system is depicted in Figure 2.
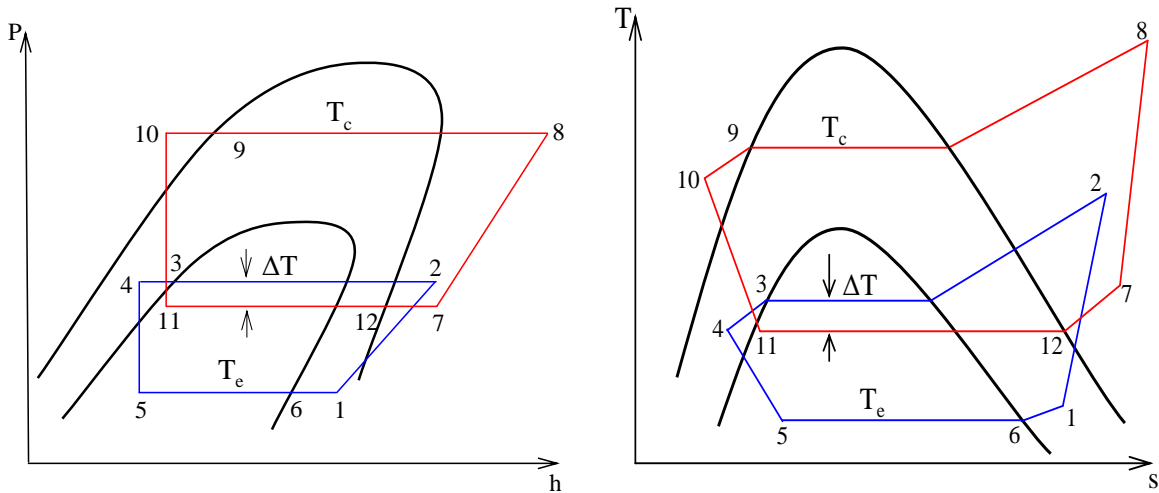
Figure 2: (a) P–h diagram of the cascade cycle and (b) T–s diagram of the cascade cycle.

As the assumptions for the two-stage cascade refrigeration systems were taken into consideration, the system component balance equations for the mass, energy, entropy, exergy and exergy efficiency equations can be expressed as follows,

2.1 Compressors 1 and 2

Equation 1: Mass balance for compressor 1.

$$\dot{m}_1 = \dot{m}_2$$
$$\dot{m}_7 = \dot{m}_8$$

Equation 2:	$\dot{W}_{comp1} = \dot{m}_1 \, (h_1 - h_2)$
Equation 3:	$\dot{W}_{comp2} = \dot{m}_7 \, (h_7 - h_8)$
Equation 4:	$\dot{S}_{gen,comp1} = \dot{m}_1 \, (s_2 - s_1)$
Equation 5:	$\dot{S}_{gen,comp2} = \dot{m}_7 \, (s_8 - s_7)$
Equation 6:	$\dot{E}_{D,comp1} = \dot{m}_1 \, (e_{x1} - e_{x2}) + \dot{W}_{comp1}$
Equation 7:	$\dot{E}_{D,comp2} = \dot{m}_7 \, (e_{x7} - e_{x8}) + \dot{W}_{comp2}$

Where:

- $\dot{m}_1$ = Refrigerant mass flow rate passing through VCRS 1;
- $\dot{m}_7$ = Refrigerant mass flow rate passing through VCRS 2;
- $\dot{W}_{comp1}$ = Power delivered to the compressor in VCRS 1;
- $\dot{W}_{comp2}$ = Power delivered to the compressor in VCRS 2;
- $\dot{S}_{gen,comp1}$ = Entropy generation rate in the compressor 1;
- $\dot{S}_{gen,comp2}$ = Entropy generation rate in the compressor 2;
- $\dot{E}_{D,comp1}$ = The exergy destruction rate in the compressor 1;
- $\dot{E}_{D,comp2}$ = The exergy destruction rate in the compressor 2.

As the exergy destructions caused by the sudden compression and friction in the compressors were taken into account, the exergy efficiencies of the compressors can be written as:

Equation 8:
$$\varepsilon_{comp1} = \frac{\dot{E}_{x1} - \dot{E}_{x2}}{\dot{W}_{comp1}} = \frac{\dot{m}_1\left((h_1 - h_2) - T_0(s_1 - s_2)\right)}{\dot{W}_{comp1}}$$

Equation 9:
$$\varepsilon_{comp2} = \frac{\dot{E}_{x7} - \dot{E}_{x8}}{\dot{W}_{comp2}} = \frac{\dot{m}_7\left((h_7 - h_8) - T_0(s_7 - s_8)\right)}{\dot{W}_{comp2}}$$

Where:

- ε_{comp1} = Exergy efficiency of compressor 1;
- ε_{comp1} = Exergy efficiency of compressor 2;
- $\dot{E}_x$ = Exergy per unit time

2.2 Condenser

Equation 10:
$$T_c = T_{bc}$$

Equation 11:
$$\dot{Q}_c = \dot{m}_7\,(h_9 - h_8)$$

Equation 12:
$$\dot{S}_{gen,c} = \dot{m}_7\,(s_9 - s_8) - \frac{\dot{Q}_c}{T_{bc}}$$

Equation 13:
$$\dot{E}_{D,c} = \dot{m}_7\,(e_{x7} - e_{x8}) + \left(1 - \frac{T_0}{T_{bc}}\right)\dot{Q}_c$$

Where:

- T_{bc} = Boundary temperature between the condenser and environment;
- $\dot{Q}_c$ = Heat rejection rate by the condenser;
- $\dot{S}_{gen,c}$ = Entropy generation rate in the condenser;
- $\dot{E}_{D,c}$ = Exergy destruction in the condenser.

Heat transfer at a finite temperature difference between the condenser and the environment and entropy flow were the main causes of exergy destructions in the condenser. Considering these exergy destructions, the exergy efficiency of the condenser can be expressed as;

Equation 14: The capacity of the evaporator
$$\varepsilon_c = \frac{\left(1 - \frac{T_0}{T_c}\right)\dot{Q}_c}{\dot{m}_7\,(e_{x9} - e_{x8})} = \frac{\left(1 - \frac{T_0}{T_c}\right)\dot{Q}_c}{\dot{m}_7\left((h_9 - h_8) - T_0(s_9 - s_8)\right)}$$

Where:

ε_c = Exergy efficiency of the condenser

2.3 Expansion Valves 1 and 2

Equation 15:	$h_4 = h_5$
Equation 16:	$h_{10} = h_{11}$
Equation 17:	$\dot{S}_{gen,TEV1} = \dot{m}_1 \, (s_5 - s_4)$
Equation 18:	$\dot{S}_{gen,TEV2} = \dot{m}_7 \, (s_{11} - s_{10})$
Equation 19:	$\dot{E}_{D,TEV1} = \dot{m}_1 \, (e_{x4} - e_{x5})$
Equation 20:	$\dot{E}_{D,TEV2} = \dot{m}_7 \, (e_{x10} - e_{x11})$

Where:

- $\dot{S}_{gen,TEV1}$ = Entropy generation per unit time in TEV1
- $\dot{S}_{gen,TEV2}$ = Entropy generation per unit time in TEV2
- $\dot{E}_{D,TEV1}$ = The exergy destruction rate in TEV1
- $\dot{E}_{D,TEV2}$ = The exergy destruction rate in TEV2

Considering the exergy destructions caused by sudden expansion and friction in the expansion valves, the exergy efficiencies of the expansion valves are as follows:

Equation 21:	$\varepsilon_{TEV1} = \dfrac{\dot{E}_{x5}}{\dot{E}_{x4}} = \dfrac{(h_5 - h_0) - T_0(s_5 - s_0)}{(h_4 - h_0) - T_0(s_4 - s_0)}$
Equation 22:	$\varepsilon_{TEV2} = \dfrac{\dot{E}_{x11}}{\dot{E}_{x10}} = \dfrac{(h_{11} - h_0) - T_0(s_{11} - s_0)}{(h_{10} - h_0) - T_0(s_{10} - s_0)}$

2.4 Heat Exchanger

As seen from Figure 2(a), the heat exchanger was a heat exchanger where the amount of heat removed from VCRS 1 is absorbed by the evaporator of VCRS 2. It can be assumed that the heat exchanger was completely insulated from the environment. The energy, entropy and exergy balance equations for the heat exchanger are expressed as:

Equation 23:	$\dot{m}_1 \, (h_2 - h_3) = \dot{m}_7 \, (h_{12} - h_{11})$
Equation 24:	$\dot{S}_{gen,he} = \dot{m}_1 \, (s_3 - s_2) + \dot{m}_7 \, (s_{12} - s_{11})$
Equation 25:	$\dot{E}_{D,he} = \dot{m}_1 \, (e_{x2} - e_{x3}) + \dot{m}_7 \, (e_{x11} - e_{x12})$

Where:

- $\dot{S}_{gen,he}$ = The entropy generation rate in the heat exchanger
- $\dot{E}_{D,he}$ = The exergy destruction rate in the heat exchanger

In the heat exchanger, the entropy generation due to the entropy flow of two refrigerants and friction caused the exergy destruction. In this case, the exergy efficiency of the heat exchanger is expressed as,

Equation 26:	$\varepsilon_{he} = \dfrac{\dot{m}_7 \, (e_{x12} - e_{x11})}{\dot{m}_t \, (e_{x2} - e_{x3})} = \dfrac{\dot{m}_7 \, \big((h_{12} - h_{11}) - T_0(s_{12} - s_{11})\big)}{\dot{m}_t \, \big((h_2 - h_3) - T_0(s_2 - s_3)\big)}$

Where:

- ε_{he} = Exergy efficiency of the heat exchanger

2.5 Evaporator

As seen from Figure 2(a), the heat exchanger is a heat exchanger where the amount of heat removed from VCRS 1 was absorbed by the evaporator of VCRS 2. It can be assumed that the heat exchanger was completely insulated from the environment. The energy, entropy and exergy balance equations for the heat exchanger are expressed as:

Equation 27:	$T_e = T_{be}$

Equation 28:
$$\dot{Q}_e = \dot{m}_1 \, (h_6 - h_5)$$

Equation 29:
$$\dot{S}_{gen,c} = \dot{m}_7 \, (s_6 - s_5) - \frac{\dot{Q}_e}{T_{be}}$$

Equation 30:
$$\dot{E}_{D,e} = \dot{m}_1 \, (e_{x6} - e_{x5}) + \left(1 - \frac{T_0}{T_{be}}\right) \dot{Q}_e$$

Where:

- T_{be} = Boundary temperature between the evaporator and refrigerated space
- $\dot{Q}_e$ = Heat absorption rate by the evaporator
- $\dot{S}_{gen,e}$ = Entropy generation rate in the evaporator
- $\dot{E}_{D,e}$ = Exergy destruction rate in the evaporator

Heat transfer at a finite temperature difference between the evaporator and the refrigerated space and entropy flow were the main causes of exergy destructions in the evaporator. As these exergy destructions were taken into consideration, the exergy efficiency of the evaporator can be expressed as:

Equation 31:
$$\varepsilon_e = \frac{\left(1 - \frac{T_0}{T_e}\right) \dot{Q}_e}{\dot{m}_7 \, (e_{x6} - e_{x5})} = \frac{\left(1 - \frac{T_0}{T_e}\right) \dot{Q}_e}{\dot{m}_7 \left((h_6 - h_5) - T_0(s_6 - s_5)\right)}$$

Where:

- ε_e = Exergy efficiency of the evaporator

3. RESULTS AND DISCUSSION

The effect of the condenser temperature of two-stage cascade refrigeration system on the energy and exergy parameters of the two-stage cascade refrigeration system was experimentally observed and the results were evaluated by a computer code that was developed by means of EES (Klein, 2013) and presented in the following graphs.
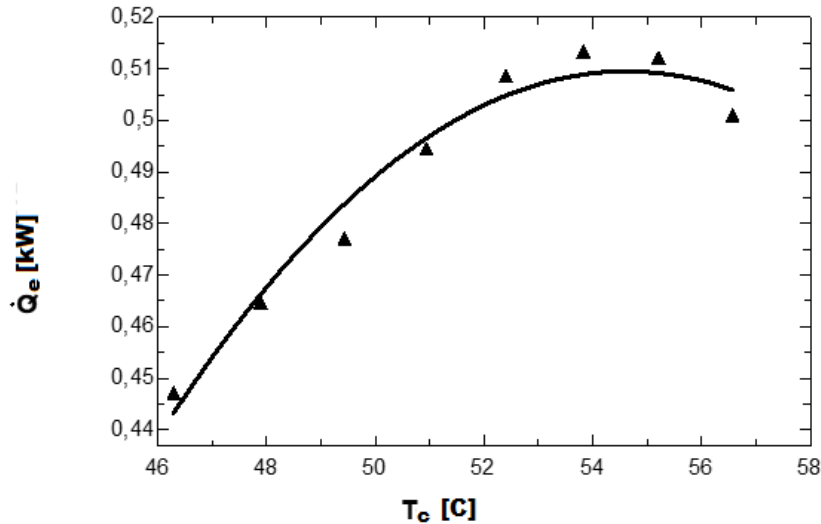
Figure 3: Variation of evaporator capacity according to condenser temperature

Figure 3 shows the variation of the evaporator capacity with respect to the condenser temperature of the cascade refrigeration system. As the condenser temperature increased, the amount of heat absorbed by the evaporator increased. Increasing the condenser temperature caused the evaporator temperature to decrease. As a result of this, the temperature difference between the refrigerated space and the evaporator increased and therefore the amount of heat absorbed by the evaporator increased. As seen in Figure 3, the condenser temperature varied between approximately 47°C and 57°C, while the amount of heat absorbed by the evaporator from the environment varied between 447 W and 501 W.

43
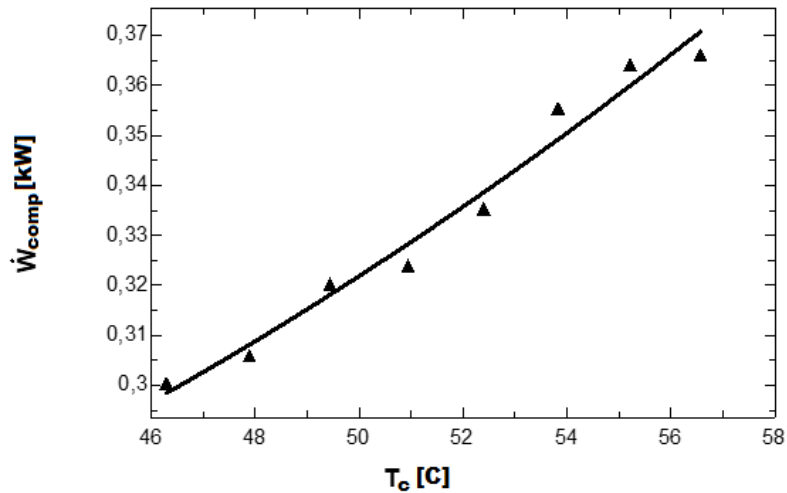
Figure 4: Variation of the total amount of energy drawn by the compressors according to condenser temperature

Figure 4 shows the variation of the total amount of energy drawn by the low and high pressure compressors according to the condenser temperature. As the condenser temperature increased, the total amount of power drawn by the compressors increased. Since the increase in the condenser temperature of the system increased the pressure ratio of the high pressure compressor, this caused the amount of energy drawn by the high pressure compressor to increase. Indirectly, the increase in the condenser temperature increased the compressor pressure ratio on average in VCRS 1 and the energy drawn by the compressor in this region increased. As a result of these, the total amount of energy drawn by the compressors increased. As it was observed from Figure 4, while the condenser temperature increased by 22%, the amount of energy drawn by the compressors also increased by 22%.
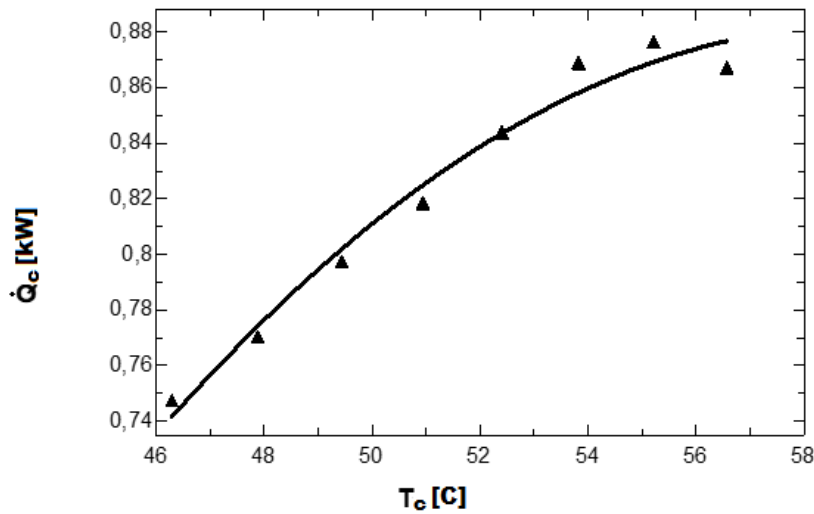
Figure 5: Variation of the heat rejected by the condenser according to condenser temperature

The variation of the amount of heat rejected to the environment by the condenser of the cascade refrigeration according to the condenser temperature is shown in Figure 5. As the condenser temperature increased, the amount of heat rejected by the condenser to the environment increased. Increasing the condenser temperature caused an increase in the temperature difference between the condenser and its surroundings, and as a result of this, the amount of heat rejected by the condenser to the environment increased as seen in Figure 5. While the condenser temperature increased by 22%, the amount of heat released from the condenser to the environment increased by an average of 16%.
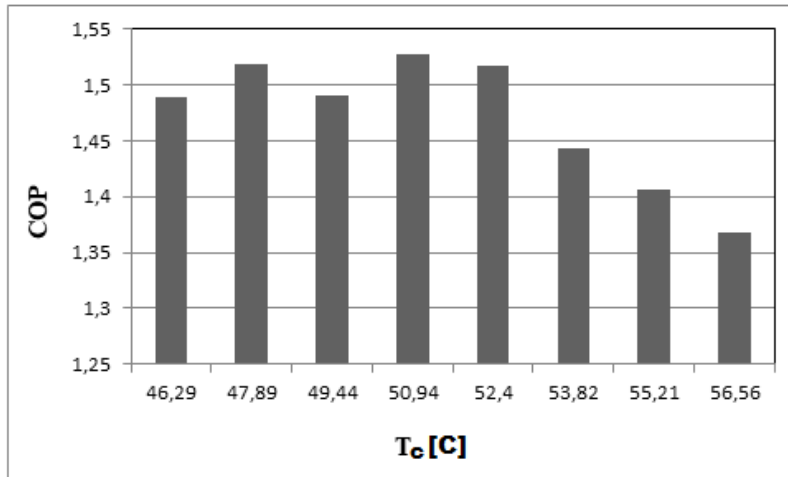
Figure 6: Variation of the coefficient of performance (COP) according to condenser temperature

Figure 6 depicts the change of the COP of the cascade refrigeration system according to the condenser temperature. As the condenser temperature increased, the COP decreased. Increasing the condenser temperature will increase the outlet pressure of the compressor operating in VCRS 2, and as a result of this process, the total amount of energy drawn by the compressors increased. Increasing the condenser temperature also caused the evaporator in VCRS 1 to draw more heat from the environment, but the COP of the system decreased because the compressors drew more power. Although the condenser temperature increased by 22%, the COP decreased by 8%.
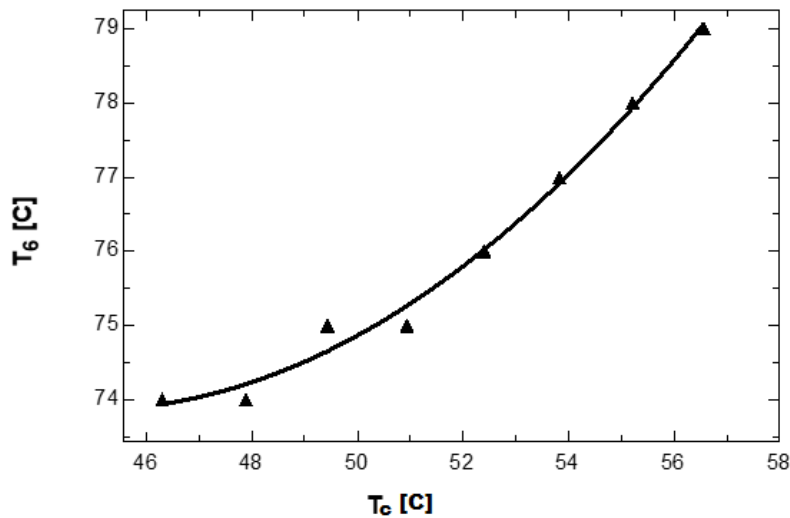
Figure 7: Variation of the outlet temperature of the high pressure compressor according to the condenser temperature

The variation of the outlet temperature of the high pressure compressor with the condenser temperature is shown in Figure 7. As the condenser temperature increased, the outlet temperature of the high pressure compressor increased. As the condenser temperature changed between 46°C and 57°C, the outlet temperature of the high pressure compressor also changed between 74°C and 79°C.
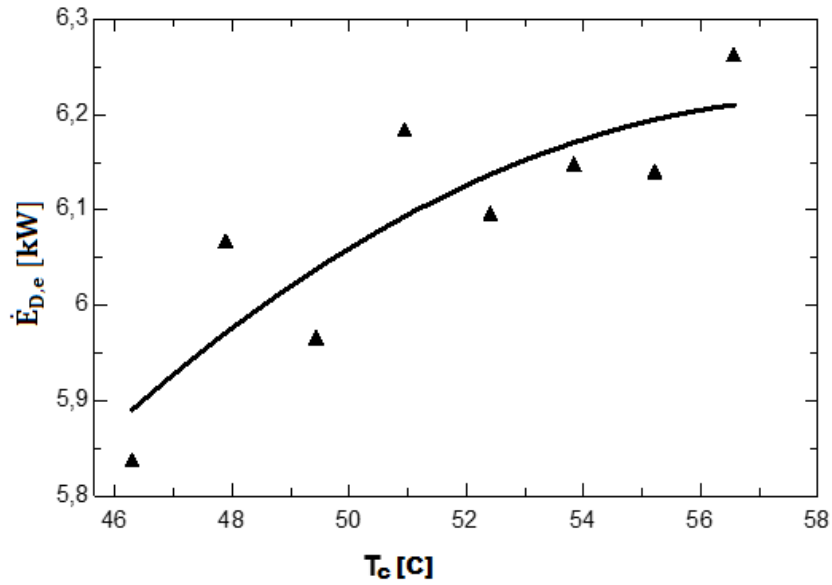
Figure 8: Variation of the exergy destruction of the evaporator according to the condenser temperature

Figure 8 depicts the change of the amount of the exergy destruction of the evaporator of the cascade refrigeration system as a function of the condenser temperature. As the condenser temperature increased, the amount of exergy destruction in the evaporator increased. The reason for this was the heat transfer that occurred due to the finite temperature difference between the evaporator and refrigerated space. As the condenser temperature increased, the amount of heat transfer occurring in the evaporator increased, and as a result of this, an increase in exergy destruction was observed. While the condenser temperature increased by about 22%, the amount of exergy destruction in the evaporator increased by about 7%.
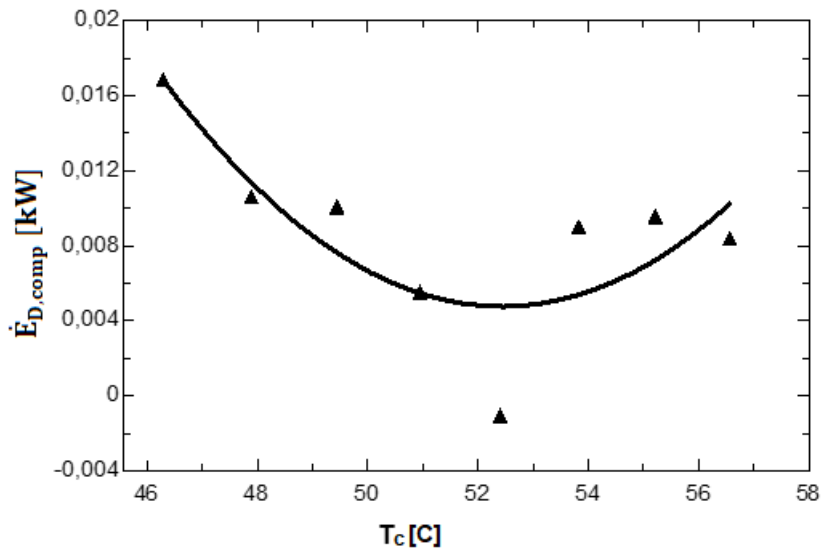
Figure 9: Variation of total exergy destruction in the compressors with condenser temperature

Figure 9 depicts the change of the total amount of exergy destruction in the low and high pressure compressors of the cascade refrigeration system according to the condenser temperature. It was found that as the condenser temperature increased, the total exergy destruction of the compressors decreased. Increasing the condenser temperature caused the outlet pressure and temperature of the compressor to increase in the high pressure region, while decreasing the outlet temperature of the compressor in the low pressure region on average. As a result of these, while the entropy produced in the compressor in the high pressure region increased, the entropy produced in the compressor in the low pressure region decreased. The overall effect tended to decrease overall compressor exergy

destruction. It was determined that while the condenser temperature increased by 22%, the total compressor exergy destruction decreased from 0.01684 kW to 0.008403 kW and decreased by 50% on average.
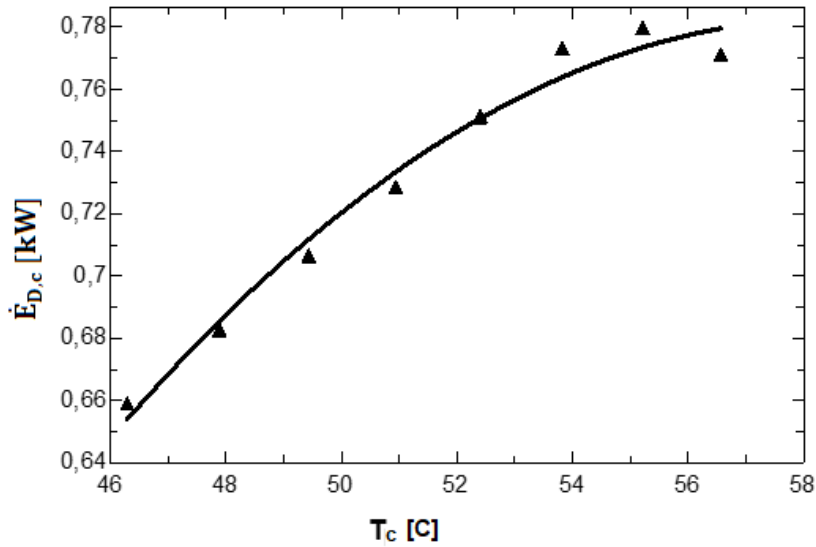
Figure 10: Variation of total exergy destruction the condenser with the condenser temperature

Figure 10 depicts the change of the exergy destruction of the condenser of the cascade refrigeration system according to the condenser temperature. As the condenser temperature increased, the exergy destruction of the condenser also increased. The reason for this was the heat transfer that occurred due to the finite temperature difference between the condenser and environment. An increase in the condenser temperature caused an increase in the temperature difference between the condenser and the environment, thus increasing the heat transfer and consequently increasing the exergy destruction. As seen in Figure 10, while the condenser temperature increased by 22%, the amount of exergy destruction in the condenser increased by 17% on average.
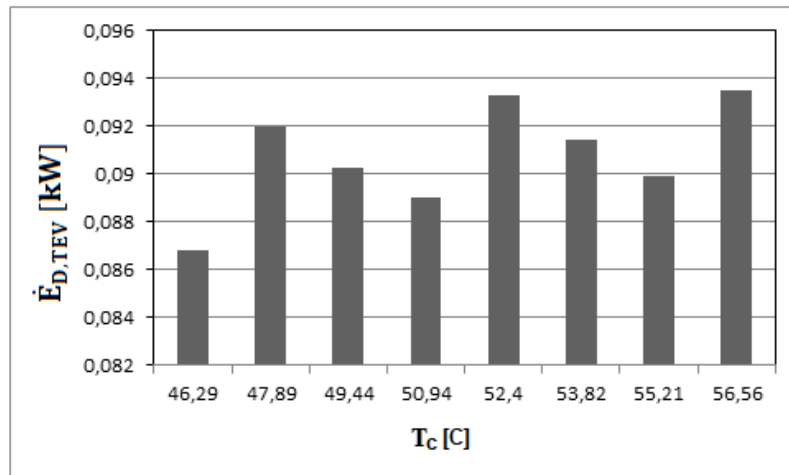
Figure 11: Variation of total exergy destruction in expansion valves with the condenser temperature

Figure 11 depicts the change of the total amount of exergy destruction occurring in the expansion valves in VCRS 1 and VCRS 2 according to the condenser temperature of the cascade refrigeration system. As the condenser temperature increased, the exergy destructions of the expansion valves increased on average. When the condenser temperature increased between 47°C and 57°C, the total expansion valve exergy destruction varied between 0.087 kW and 0.093 kW. When the condenser temperature increased by 19%, the total amount of exergy destruction in the expansion valves increased by approximately 8%.
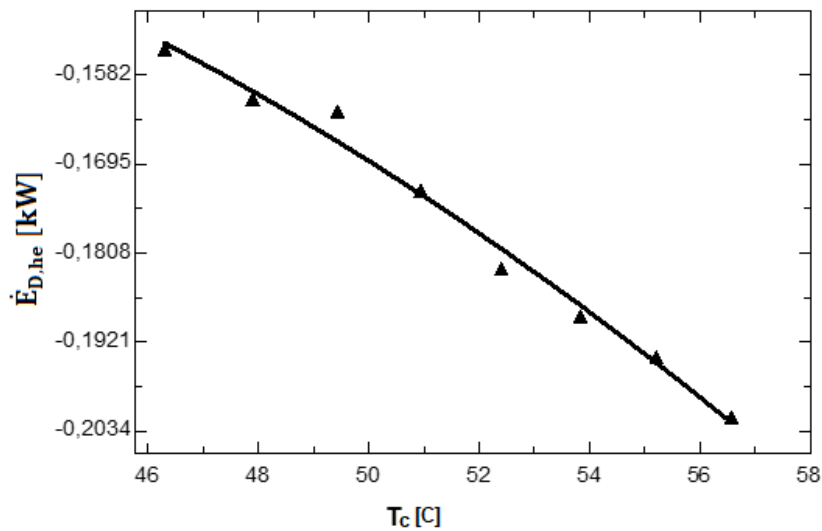
Figure 12: Variation of exergy destruction in heat exchanger with condenser temperature

Figure 12 depicts the change of the amount of exergy destruction occurring in the cascade heat exchanger according to the condenser temperature of the cascade refrigeration system. As the condenser temperature increased, the exergy destruction of the heat exchanger decreased. Since the heat exchanger was assumed to be insulated from the environment, the cause of the exergy destruction was due to the entropy flow between the entropy flow coming from the compressor of VCRS 1 and the one entering the compressor of VCRS 2. The exergy destruction in the heat exchanger varied between -0.15 kW and -0.20 kW on average. When Figure 12 was examined, it was determined that the amount of exergy destruction in the heat exchanger decreased by 30%.

4. CONCLUSIONS

The two-stage vapour compression cascade refrigeration system, in which R134A in VCRS 2 and R404A in VCR 1 were used as refrigerants, was experimentally investigated according to different condenser temperatures, and the obtained results were inserted into the computer program developed with the help of EES, and important conclusions that have been drawn in terms of energy and exergy parameters, can be summarized as follows:

- As the temperature of the condenser increased by 22%, the refrigeration capacity, heat rejected by the condenser, total energy consumed by the compressors and the outlet temperature of the high pressure compressor increased 12%, 16%, 22% and 7%, respectively while the COP of TSVCCRS and the outlet temperature of the compressor of VCR 1 decreased by 8% and 2%, respectively.
- While the condenser temperature increased by 22%, the amount of exergy destruction occurring in the condenser increased by 17%, the amount of exergy destruction occurring in the evaporator increased by 7%, the amount of exergy destruction occurring in the expansion valves increased by 8%, the amount of exergy destruction occurring in the heat exchanger increased by 30%, the amount of exergy destruction occurring in the low and high pressure region compressors increased by 7%. A 50% reduction in the total amount of exergy destruction was observed. Measurements were conducted at the condenser temperatures between 47°C and 57°C.

5. REFERENCES

Chen, X., Yang, Q., Chi, W., Zhao, Y., Liu, G., Li, L., 2022. Energy and exergy analysis of NH3/CO2 cascade refrigeration system with subcooling in the low-temperature cycle based on an auxiliary loop of NH3 refrigerants. *Energy Reports,* 8, 1757-1767.

Dashtebayaz, M.D., Sulin, A., Ryabova, T., Sankina, I., Farahnak, M., Nazeri, R., 2021. Energy, exergoeconomic and environmental optimization of a cascade refrigeration system using different low GWP refrigerants. *Journal of Environmental Chemical Engineering,* 9, 106473, https://doi.org/10.1016/j.jece.2021.106473.

Faruque, M.W., Uddin, M.R., Salehin, S., Ehsan, M.M., 2022. A Comprehensive Thermodynamic Assessment of Cascade Refrigeration System Utilizing Low GWP Hydrocarbon Refrigerants. *International Journal of Thermofluids,* 15, 100177, https://doi.org/10.1016/j.ijft.2022.100177.

Gupta, K., 1985. Numerical optimization of multi-stage cascaded refrigeration-heat pump system. *Journal of Heat Recovery Systems,* 5(4), 305–319.

Kilicarslan, A., 2004. An experimental investigation of a different type vapour compression cascade refrigeration system. *Applied Thermal Engineering,* 24, 2611–2626.

Kilicarslan, A., Hosoz, M., 2010. Energy and exergy destruction analysis of a cascade refrigeration system for various refrigerant couples. *Energy Conversion and Management,* 51, 2947–2954.

Klein S. A., "Engineering Equation Solver", Version 9.478, F-Chart Software, 2013.

Liang Y., Sun Z., Liu S., Ji W., Zang R., Liang R., Guo Z., 2016. Comparative analysis of thermodynamic performance of a cascade refrigeration system for refrigerant couples R41/R404A and R23/R404A, *Applied Energy,* 184, 19-25.

Yılmaz, B., Mançuhan, E., Yılmaz, D., 2020. Theoretical analysis of a cascade refrigeration system with natural and synthetic working fluid pairs for ultra low temperature applications. *Journal of Thermal Science and Technology,* 40(1), 141-153.

#35: Entropy generation of the main components of an air source heat pump using 404A as a refrigerant

Hayati TORE[1], Ali KILIÇARSLAN[2]

[1]Hitit University, Department of Mechanical Engineering, Corum,Turkey hayatitore@hitit.edu.tr
[2]Hitit University, Department of Mechanical Engineering, Corum,Turkey alikilicarslan@hitit.edu.tr

Abstract: Worldwide, approximately 25-30% of electricity is consumed by air conditioning and refrigeration systems therefore energy efficiencies of these systems are very important. Much research on HVAC should be performed in order to increase the efficiency of these systems. In this study, an air-to-air heat pump for cooling purposes using R404A was observed. The entropy generations of the elements of air-to-air heat pump were experimentally carried out in terms of surrounding air temperatures between 25°C to 30°C. In addition, a computer program was improved by means of Engineering Equation Solver (EES) for this purpose; temperatures, pressures, and the power delivered to the compressor and the blowers were also measured. As the surrounding air temperature increased, the entropy generation in the compressor, outdoor unit, and indoor unit increased while the entropy generation in the capillary tube decreased. The maximum entropy generation was obtained in the compressor. Entropy generation of the compressor increased from 0.003026 kW/K to 0.003172 kW/K.

1. INTRODUCTION

As the rate of energy use has increased, researchers look to different methods for solutions. As a consequence, efficiency of energy systems has been developing by the researchers and different institutes in order to conserve energy and minimise energy consumption. For this purpose, a lot of research has been carried out. For instance, air source heat pump technology is widely accepted for energy-saving and in this context, there are studies in which R404A is used as the refrigerant. Also, refrigeration has become very important for a wide range of applications with technological developments and growing population. Especially, refrigeration applications are used in the areas such as food and health.

Yongcai *et al.* (2017) analysed a numerical model to predict the performance of a typical air source heat pump system in China. The numerical results have shown that the ambient air temperature and atmospheric pressure had a great effect on the system performance. A similar work was performed in Jin *et al.*'s study (2016). In order to investigate the effect of ambient temperature ranging from 0 to -26°C on air source heat pump performance, an air source heat pump with an internal heat exchanger using R404A as refrigerant was carried out at low ambient temperatures.

In order to determine the second law efficiency, destruction of exergy, exergy losses and coefficient of performance (COP) stem, a theoretical thermodynamic model was improved in a real vapor compression refrigeration (VCR) using refrigerants R507A and R404A (Akhilesh, A., 2017).

Bukola (2011) carried out experimental research to observe the COP of a window-type air conditioning system using refrigerant including R22, R404A and R507. The results showed that the average energy consumption rates of R404A and R507 were lower by 2.0% than that of R22 while the average energy consumption rates of R404A and R507 were higher by 13,8% than that of R22.

The effect of the relative humidity of the outdoor air on the energy consumption of the air-to-air heat pump integrated using R410A as refrigerant to a direct evaporative cooler was experimentally observed in the summer conditions of South Korea. It was seen that the energy consumption of air-to-air heat pump including direct evaporative cooler was lower by 8.87% than the traditional air to heat pump at a relative humidity of 72% (Kim *et al.*, 2022).

In another study related to the entropic analysis, the analysis of entropy was used to optimize the heat pump system working together with an economizer and injection system (vapour based) and thermodynamic analysis including first and second laws was carried out for different refrigerants, such as R507A, R410A, R404A, R125 and R134A (Ehsan, 2019).

In this study, the effect of surrounding air temperatures between 25°C and 30°C on the performance of the air-to-air heat pump operating for cooling purpose with refrigerant R404A was investigated experimentally. As a result, the entropy generations of the air source heat pump were observed with respect to the surrounding air temperature.

2. MATERIAL AND METHOD

In this experimental study, the air-to-air heat pump operating for cooling purposes included compressor, outdoor unit, capillary type expansion element, indoor unit and four-way valve. A low and high pressure control switch and filter dryer were also used. The outdoor unit, compressor, capillary tube and four-way valve are shown in Figure 1.

Figure 1: Outdoor unit of the heat pump

Additionally, an energy meter measuring the consumed energy by the fans and compressor, Comet MS6D data recorder to record temperatures measured, electric heater and humidifier, and a humidity meter were added. The indoor unit with the associated equipment is shown in Figure 2.

Figure 2: Indoor unit of the heat pump

The refrigerant at low temperature and low pressure was compressed in the compressor and became superheated vapour, which then entered the outdoor unit. It condensed in the outdoor unit by rejecting heat to the environmental air. After leaving the outdoor unit, the refrigerant entered the capillary tube. It left the capillary tube as a liquid vapour mixture. After that, it evaporated in the indoor unit by absorbing heat from the space to be cooled and then returned to the compressor.

According to the first law of thermodynamics for a control volume energy equation can be written as:

Equation 1: Energy equation.
$$\frac{dE_{C.V.}}{dt} = \sum_i \dot{m}h - \sum_e \dot{m}h + \dot{Q}_{C.V.} - \dot{W}_{C.V.}$$

By using the entropy balance for a control volume, entropy generation is expressed as:

Equation 2: Entropy balance.
$$\frac{dS_{C.V.}}{dt} = \sum_i \dot{m}s - \sum_e \dot{m}s + \sum_j \frac{\dot{Q}_j}{T_j} + \dot{S}_{g.j.}$$

In the thermodynamic analysis of the air-to-air heat pump operating for cooling purpose, the following assumptions are taken into consideration:

- It is supposed that homogeneous regime and steady flow conditions exist;
- Changes in kinetic and potential energies are negligible;
- The pressure losses in air-to-air heat pump are neglected.

In the light of the assumptions considered above, applying entropy equations for steady-state steady flow process (SSSF) to the components of the air-to-air heat pump, the following formulas can be written as:

Compressor:

Equation 3: The entropy generations in the compressor.
$$\dot{S}_{gen.\ comp.} = \dot{m}(s_2 - s_1)$$

Where:

- $\dot{m}$ = refrigerant mass flowrate;
- s_1 = specific entropy at compressor inlet;
- s_2 = specific entropy at compressor outlet;
- $\dot{S}_{gen.\ comp.}$ = entropy generation in the compressor.

Outdoor unit:

Equation 4: The entropy generations in the outdoor unit.
$$\dot{S}_{gen.\ ou.} = \dot{m}\left[(s_3 - s_2) - \frac{(h_3 - h_2)}{T_{ou.}}\right]$$

Where:

- h_2 = specific enthalpy at the intlet of the outdoor unit;
- h_3 = specific enthalpy at the outlet of the outdoor unit;
- s_3 = specific entropy of refrigerant at the outlet of the outdoor unit;
- $T_{ou.}$ = outdoor unit boundary temperature;
- $\dot{S}_{gen.\ con.}$ = entropy generation in the outdoor unit.

Indoor unit:

Equation 5: The entropy generations in the indoor unit.
$$\dot{S}_{gen.\ iu.} = \dot{m}\left[(s_4 - s_1) - \frac{(h_4 - h_1)}{T_{iu.}}\right]$$

Where:

- h_1 = specific enthalpy at the outlet of the indoor unit;
- h_4 = specific enthalpy at the inlet of the indoor unit;
- s_4 = specific entropy y at the inlet of the indoor unit;
- T_{iu} = indoor unit boundary temperature;
- $\dot{S}_{gen.\ iu.}$ = entropy generation in the indoor unit.

Capillary Tube:

Equation 6: The entropy generations in the capillary tube.
$$\dot{S}_{gen.\ ct.} = \dot{m}(s_4 - s_3)$$

Where:

- $\dot{S}_{gen.\ ct.}$ = entropy generation in the capillary tube

System:

Equation 7: The coefficient of performance.
$$\dot{S}_{gen.\ tot.} = \dot{S}_{gen.\ comp.} + \dot{S}_{gen.\ ou.} + \dot{S}_{gen.\ iu.} + \dot{S}_{gen.\ ct.}$$

Where:

- $\dot{S}_{gen.\ tot.}$ = total entropy generation in the system

3. RESULTS AND DISCUSSIONS

The influence of the environment air temperature on the entropy generation of the heat pump was experimentally investigated. Also, a computer code was developed to evaluate the results by using EES (Klein S.A., 2020). The results are discussed in detail in the following figures.
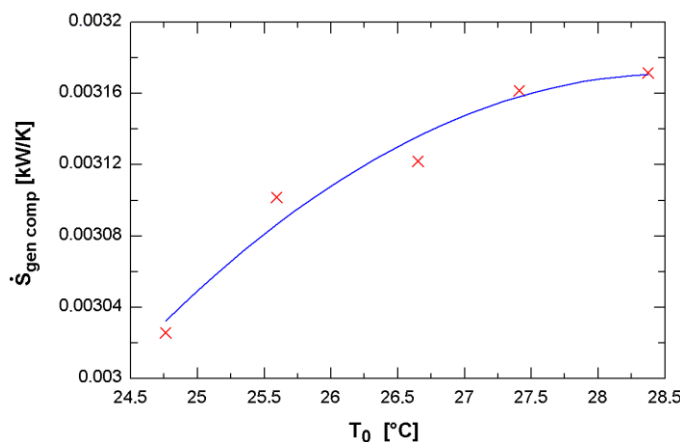
Figure 3: Change of entropy generation in the compressor with environment air temperature

The variation of entropy generation in the compressor unit in terms of the environment air temperature is depicted in Figure 3. As the environment air temperature rose, entropy generation of the compressor increased. The main reason for this was the sudden compression of the refrigerant in the compressor, therefore the increase in the compression ratio caused the entropy generation of the compressor to increase as shown in Figure 3. Entropy generation of the

compressor increased from 0.00303 kW/K to 0.00317 kW/K. The entropy generation of the compressor increased 4.62 % at the temperature range studied.
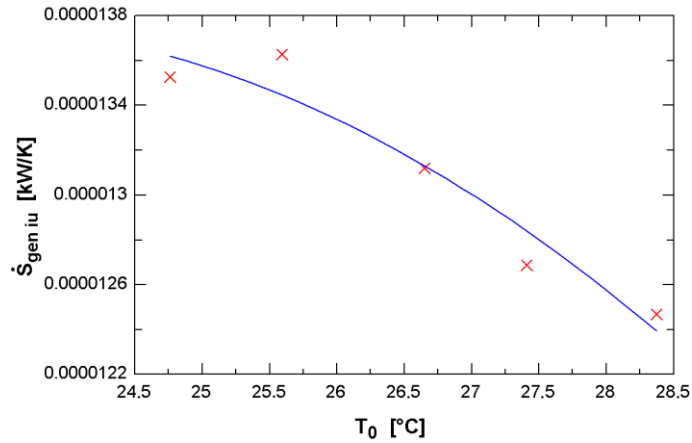
Figure 4: Change of entropy generation in the indoor unit in terms of environment air temperature

The variation of entropy generation of the indoor unit shown in Figure 4 was obtained by varying the environment air temperatures from 24.5ºC to 28.5ºC. As the environment air temperature rose, the entropy generation of the indoor unit did not change so much. As shown in Figure 4, the entropy generation in the indoor unit was approximately constant. The entropy generation decreased by a very small amount. The maximum entropy generation of the indoor unit was 0.000014 kW/K.
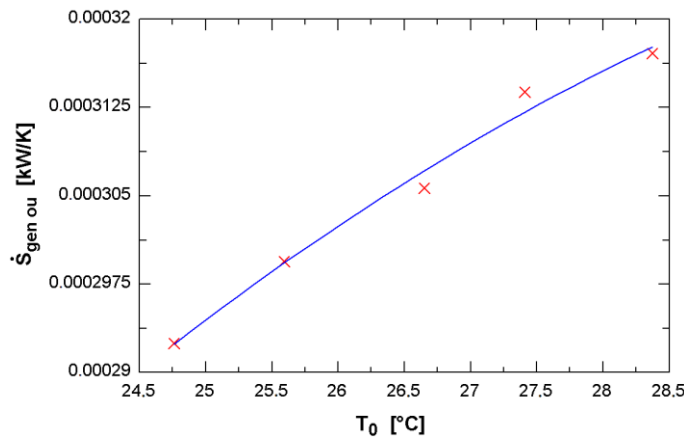
Figure 5: Change of entropy generation in the outdoor unit with environment air temperature

Figure 5 shows the change of entropy generation of the outdoor unit with the environment air temperature. As the environment air temperature rose, entropy generation of the outdoor unit diminished. As shown in Figure 5, due to the small amount of exergy destruction in the outdoor unit, the entropy generation in the outdoor unit was caused by the heat exchange between the outdoor unit and the surrounding air and the entropy flow. The highest values of the entropy generation in the outdoor unit was from 0.000292 kW/K to 0.000317 kW/K. The entropy generation of the outdoor unit decreased 8.56% at the temperature range studied.
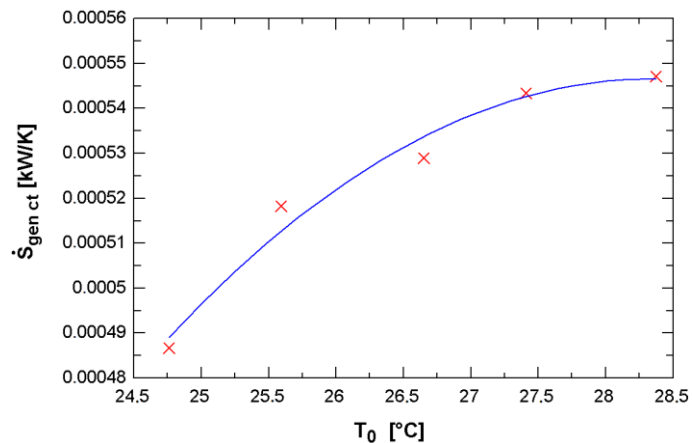
Figure 6: Change of entropy generation in the capillary tube with environment air temperature

The variation of entropy generation of the capillary tube shown in Figure 6 was obtained by changing the environment air temperature from 24.5ºC to 28.5ºC. As the environment air temperature rose, the entropy generation of the capillary tube did not change so much. The entropy generation of the capillary tube increased from 0.000487 kW/K to 0.000547 kW/K and, as the environment air temperature rose, the entropy generation of the capillary tube rose 12.32% at the temperature range studied.
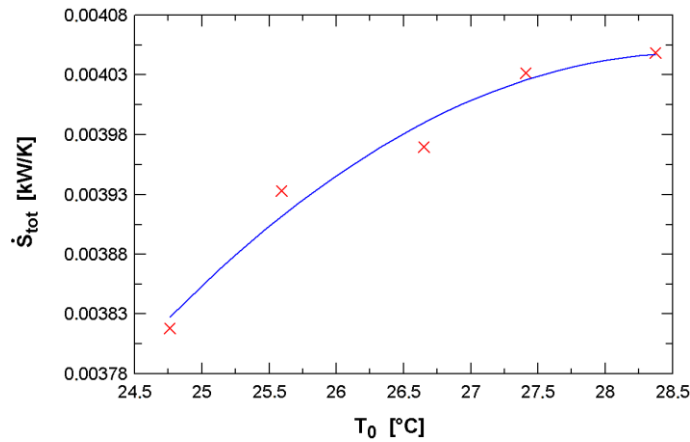
Figure 7: Change of total entropy generation in the system with environment air temperature

The change of the total entropy generation of the heat pump with surrounding air temperature by using R404A as a refrigerant is depicted in Figure 7. The highest entropy generation was in the compressor unit between equipment of the heat pump. The total entropy generation of the heat pump changed from 0.00382 kW/K to 0.00405 kW/K. The entropy generation of the heat pump increased 6.02% at the temperature range studied.

4. ACKNOWLEDGEMENT

5. REFERENCES

Akhilesh, A., Kaushik, S. C., 2017. Theoretical analysis of a vapour compression refrigeration system with R502, R404A and R507A. *International Journal of Refrigeration,* 31, 998-1005.

Bukola, O. B., 2011. Performance investigation of ozone-friendly R404A and R507 refrigerants as alternatives to R22 in a window air-conditioner. Energy and Buildings, 43, 3139-3143.

Ehsan, A. R., Saeed, M., 2019. Entropic optimization of the economizer's pressure in a heat pump cycle integrated with a flash-tank and vapor-injection system. International Journal of Refrigeration, 97, 56-66.

Kim, B.-J., Jo, S.-Y., & Jeong, J.-W. 2022. Energy performance enhancement in air-source heat pump with a direct evaporative cooler-applied condenser. Case Studies in Thermal Engineering,35, 102137.

Klein, S.A., 2020. Engineering Equation Solver (EES) Academic Professional V10.836-3D. F-Chart Software.

Jin, L., Cao, F., Yang, D., Wang, X. 2016. Performance investigations of an R404A air-source heat pump with an internal heat exchanger for residential heating in northern China. International Journal of Refrigeration, 67, 239–248.

Yongcai, L., Wuyan, L., Zongsheng, L., Jun, L., Liyue, Z., Lulu, Y., Ling, X., 2017. Theoretical and numerical study on performance of the air-source heat pump system in Tibet. Renewable Energy, 114, 489-501.

#36: Investigation of a refrigeration cycle as a function of condenser water volume flow rate and refrigeration load

Ali KILICARSLAN[1], Hayati TORE[2]

[1]Hitit University, Department of Mechanical Engineering, Corum,Turkey alikilicarslan @gmail.com
[2] Hitit University, Department of Mechanical Engineering, Corum,Turkey hayatitore @hitit.edu.tr

Abstract: Energy is an important parameter in many applications. The world population and demand for energy have been increasing rapidly day by day. Due to the decline in world resources, scientists have started to research the alternative energy production methods and to use the available energy more efficiently. Refrigeration and air conditioning systems globally consume more than 15% of total energy. In this experimental study, in a vapour compression refrigeration cycle using R134a as the refrigerant, the effect of the water volume flow rate flowing through the water-cooled condenser on the evaporator capacity, condenser capacity, the power delivered to the compressor, coefficient of performance (COP) and the total entropy generation were investigated. Keeping water volume flow rate through the condenser constant, the effect of the evaporator capacity on the condenser capacity, the power delivered to the compressor and COP were also investigated. At the increasing values of the water volume flow rate, the condenser capacity, the evaporator capacity and the COP increased, but the compressor power consumption and the total entropy generation of the system decreased. The total entropy generation of the system decreased by 14.02% and the COP of the system increased by 20.3% at flow rates ranging from 100L/h to 500L/h.

1. INTRODUCTION

Refrigeration systems are widely used to preserve food and medicinal products for a long time without spoiling, thus the need for refrigeration is increasing day by day. The most commonly used refrigeration technique to supply these needs is the vapour compression refrigerating cycle (VCRC). The vapour compression refrigeration cycle is cheap and reliable; in addition to this, it requires virtually minimum maintenance. In general, COP of VCRC can be improved by reducing the power consumed in the compressor by increasing heat released from the condenser to the environment, or by reducing the pressure difference between the condenser and the evaporator.

In the literature, there have been many studies related to the vapour compression refrigeration cycle. Kamil and Nazir (2019) investigated the impact of varying the evaporator load on the performance and parameter characteristics of a heat pump. It resulted that with increasing load on the evaporator, the system pressures and temperatures generally increased. In the study carried out by Ansari *et al.* (2018) on the vapour compression refrigeration cycle, the effect of six different water-cooled condensers and three different ambient temperatures (28°C, 32°C, 36°C) on the coefficient of performance were experimentally investigated. The condensers used in the study were Simple Water-Cooled (SWC), Chilled Water Circulated (CWC), Induced Cooling Tower (ICT), Forced Cooling Tower (FCT), Single Cellulose Pad (SCP), and Double Cellulose Pad (DCP). In conclusion, the COP for SWC at 28°C was found as 4.76. In addition, compared to SWC, COP values for CWC, ICT, FCT, SCP, and DCP were found as 10.23%, 17.62%, 23.57%, 28.33%, and 34.28% higher, respectively.

In another study in which R600a was used as a refrigerant for both a water-cooled condenser and air-cooled condenser, it was observed that the performance of the water-cooled condenser was better than the air-cooled condenser (Shrivastav *et al.*, 2019). Gaikwad *et al.* (2018) experimentally investigated that the COP of the VCRC including the water-cooled condenser was improved more and the power consumption of that was reduced more as it was compared to the VCRC including air-cooled condenser.

In another experimental study, by using a water-cooled condenser in a VCRC system, daily energy consumption was reduced by 17% compared to a conventional VCRC system. Moreover, under similar operating conditions, the irreversibility of VCRC including water-cooled condenser was found as 34% lower than the conventional VCRC. Eventually, it was observed that using water-cooled condensers in domestic refrigerators increased energy efficiency (Shikalgar and Sapali, 2019). Raveendran and Sekhar (2017) experimentally and theoretically investigated the effects of water flow rate and type condenser on the COP and the energy consumption per day. It resulted that, as the water flow rate increased, the COP of the VCRC system with water cooled condenser increased by approximately 66% and the energy consumption reduced by approximately 24% per day compared to the VCRC system with air cooled condenser. Raveendran and Sekhar (2020) also investigated the effects of refrigerants R290/R600a mixture and R134a on the COP and the energy consumption per day. It was seen that the energy consumption of the VCRC system using R290/R600a as refrigerant was lower by 5.9% than that of the VCRC system using R134a as refrigerant while the COP of the VCRC system using R290/R600a as refrigerant was higher by 8.9% than that of the VCRC system using R134a as refrigerant. In order to determine the optimal design of a water-cooled condenser, Taguchi's method and the multi-input, multi-outlet ANFIS inverse model were integrated by Huang & Yu (2016) in a simulation platform developed by using the COMSOL Multiphysics software and Taguchi method was preferred to determine the most critical factors affecting condenser performance.

In this study, contrary to the previous studies in the literature, the effects of both the water volume flow rate flowing through the water cooled condenser and refrigeration capacity of VCRC system on the condenser capacity, the power consumed by the compressor and COP were experimentally investigated. In addition to this, the effect of the water volume flow rate on the total entropy generation was also observed.

2. MATERIAL AND METHOD

Table 1: The components of the vapour compression refrigeration system.

Refrigerant	Component	Type
	compressor	open- reciprocating
	condenser	water-cooled
	TXV (thermostatic expansion valve)	Internally equalized
R134A	evaporator	
	water flow meter	rotameter
	refrigerant flow meter	rotameter
	filter dryer	
	sight glass	

The schematic of the vapour compression refrigeration system used in this experimental work is shown in Figure 1.
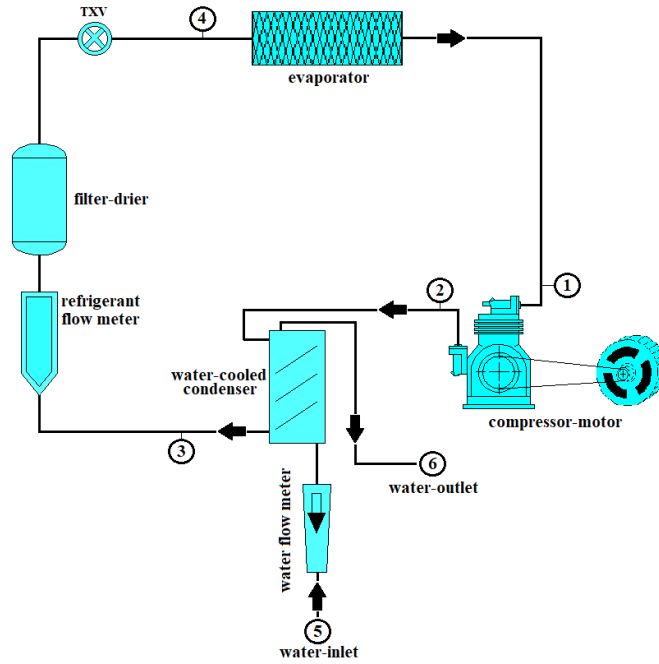
Figure 1: Vapour compression refrigeration cycle

The refrigerant, which had low temperature and pressure, was compressed in the compressor where it became superheated vapour. At this state, the vapour entered the water-cooled condenser where it condensed due to heat rejection to the water. Afterwards, leaving the water-cooled condenser, the refrigerant entered the thermostatic expansion valve where it expanded and became a liquid-vapour mixture. After that, it evaporated inside the evaporator because of the absorption of heat from the environment to be refrigerated and then returned to the compressor finally.

The first law of thermodynamics for a control volume can be written as:

Equation 1: Energy equation.
$$\frac{dE_{C.V.}}{dt}=\sum_i \dot{m}h-\sum_e \dot{m}h+\dot{Q}_{C.V.}-\dot{W}_{C.V.}$$

The entropy balance for a control volume can be expressed as:

Equation 2: Entropy balance.
$$\frac{dS_{C.V.}}{dt}=\sum_i \dot{m}s-\sum_e \dot{m}s+\sum_j \frac{\dot{Q}_j}{T_j}+\dot{S}_{g.j.}$$

In the thermodynamic analysis of the vapour compression refrigeration system under the study, the following assumptions should be taken into consideration:

- Steady flow conditions exist.
- Changes in kinetic and potential energies are negligible in the elements of the vapour compression system.
- The pressure losses in the cycle components, excluding the thermostatic expansion valve, are not taken into account.
- It is also supposed that the entire electrical power taken by the compressor is converted into mechanical power.

By taking into consideration the above assumptions, the energy and entropy balance equations for steady-state steady flow process (SSSF) in the elements of the VCRC, the following equations are written as:

Compressor:

Equation 3: The power delivered to the compressor.
$$\dot{W}_{comp.}=\dot{m}_r(h_2-h_1)$$

Equation 4: The entropy generation in the compressor.
$$\dot{S}_{gen.\ comp.}=\dot{m}_r(s_2-s_1)$$

Where:
  $\dot{m}_r$ = refrigerant mass flowrate;
  h_1 = enthalpy of refrigerant at the compressor inlet;
  h_2 = enthalpy of refrigerant at the compressor outlet;
  s_1 = entropy of refrigerant at the compressor inlet;
  s_2 = entropy of refrigerant at the compressor outlet;
  $\dot{S}_{gen.\ comp.}$ = entropy generation in the compressor.

Condenser:

Equation 5: The capacity of the condenser.

$$\dot{Q}_{con.} = \dot{m}_r (h_2 - h_3)$$

Equation 6: The entropy generation in the condenser.

$$\dot{S}_{gen.\ con.} = \dot{m}_r \left[(s_2 - s_3) - \frac{(h_2 - h_3)}{T_{con.b}} \right]$$

Equation 7: The boundary temperature of the condenser.

$$T_{con.b} = \frac{(T_2 + T_3)}{2}$$

Where:
  h_3 = enthalpy of refrigerant at the outlet of the condenser;
  s_3 = entropy of refrigerant at the outlet of the condenser;
  T_{con} = condenser boundary temperature;
  $\dot{S}_{gen.\ con.}$ = entropy generation in the condenser.

Evaporator:

Equation 8: The capacity of the evaporator.

$$\dot{Q}_{evap.} = \dot{m}_r (h_1 - h_4)$$

Equation 9: The entropy generations in the evaporator.

$$\dot{S}_{gen.\ evap.} = \dot{m}_r \left[(s_1 - s_4) - \frac{(h_1 - h_4)}{T_{evap.b}} \right]$$

Equation 10: The boundary temperature of the evaporator.

$$T_{evap.b} = \frac{(T_1 + T_4)}{2}$$

Where:
  h_4 = enthalpy of the refrigerant at the inlet of the evaporator;
  s_4 = entropy of the refrigerant at the inlet of the evaporator;
  T_{evap} = evaporator boundary temperature;
  $\dot{S}_{gen.\ evap.}$ = entropy generation in the evaporator.

Thermostatic Expansion Valve:

Equation 11: The enthalpy expression in the thermostatic expansion valve.

$$h_3 = h_4$$

Equation 12: The entropy generation in the thermostatic expansion valve.

$$\dot{S}_{gen.\ TXV.} = \dot{m}_r (s_4 - s_3)$$

Where:
  $\dot{S}_{gen.\ TXV.}$ = entropy generation in the thermostatic expansion valve.

COP:

Equation 13: The coefficient of performance.

$$COP = \frac{\dot{Q}_{evap.}}{\dot{W}_{comp.}}$$

Where:
  COP = Coefficient of Performance.

Water side:

Equation 14: The capacity of the water-side.

$$\dot{Q}_w = \dot{m}_w c_{p,w} (T_6 - T_5)$$

Equation 15: Water volume flow rate.

$$\dot{V}_w = \frac{\dot{m}_w}{\rho_w}$$

Where:
  $\dot{m}_w$ = water mass flow rate;
  $\dot{V}_w$ = water volume flow rate;
  ρ_w = density of water;

$c_{p,w}$ = specific heat capacity of water;
T_5 = temperature of water at the condenser inlet;
T_6 = temperature of water at the condenser outlet.

3. RESULTS AND DISCUSSION

The effects of the water volume flow rate on the evaporator capacity, the condenser capacity, the power delivered to the compressor, coefficient of performance (COP), and total entropy generation of the system were experimentally investigated. Also, a computer code was developed to evaluate the results by using EES (Klein., 2020). The results are discussed in detail in the following figures.
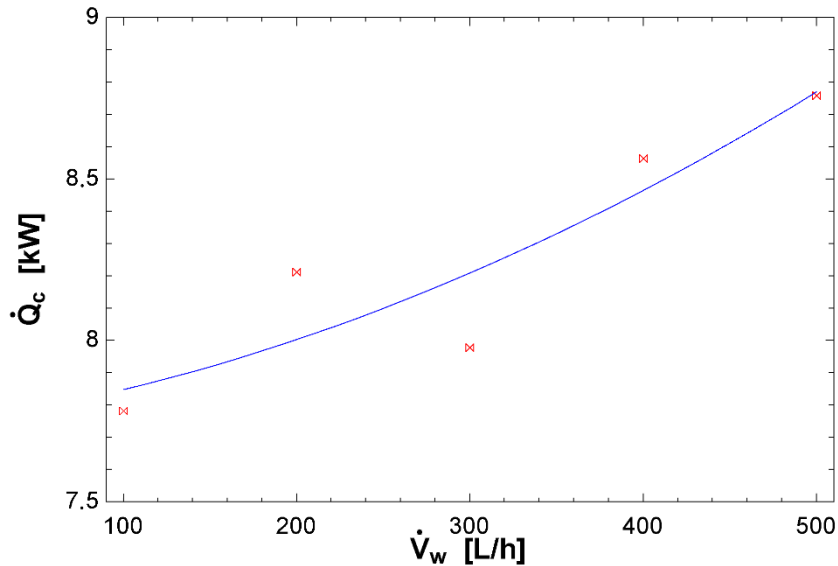
Figure 2: Variation of the condenser capacity with the water volume flow rate

Figure 2 depicts the change of the condenser capacity with the water volume flow rate. As the water volume flow rate rose, the condenser capacity increased. There were two parameters affecting the capacity of the water-cooled condenser: the water inlet temperature and water volume flow rate. As the water inlet temperature was held constant, the water volume flow rate increased causing the capacity of the condenser to increase as shown in Figure 2. The capacity of the water-cooled condenser ranged from 7.7 kW to 8.8 kW as the water volume flow rate increased from 100 L/h to 500 L/h. The maximum condenser capacity was 8.7634 kW. As the water volume flow rate increased by 400%, the percent increase at the condenser capacity was 12.53% in this experimental study.
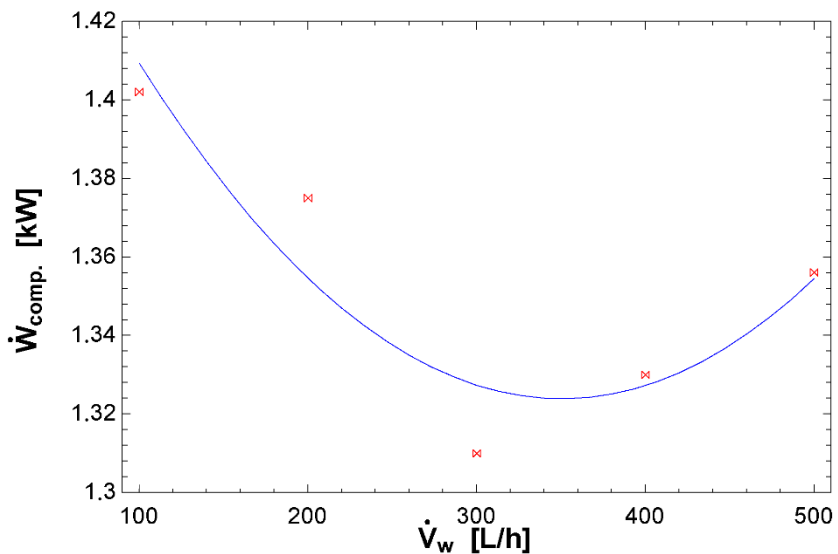
Figure 3: Change of the compressor power consumption with the water volume flow rate

The variation of the compressor power consumption with the water volume flow rate is depicted in Figure 3. As the water volume flow rate through the condenser increased, the condenser pressure decreased, and thereby decreasing the power driven by the compressor on average as depicted in Figure 3. Between the water volume flow rates of 100 L/h to 300 L/h, the compressor power decreased, having the minimum power at the flow rate of 300 L/h. It then increased until it reached the volume flow rate of 500 L/h. As mentioned previously, the power driven by the compressor decreased on average. As the water volume flow rate rose, the compressor power consumption changed from 1.401 kW to 1.3561 kW. The minimum compressor power consumption was 1.3098 kW. The compressor power consumption decreased by 6.56% at the water volume flow rate range studied.
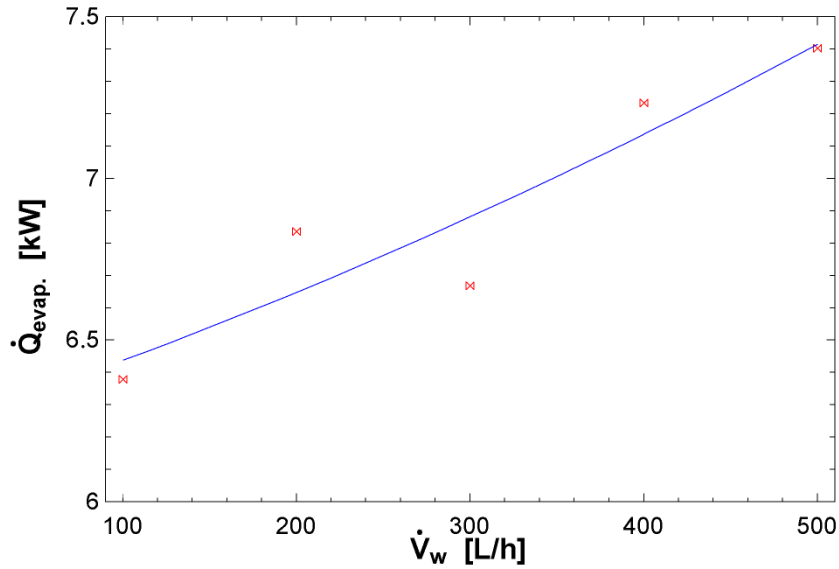
Figure 4: Variation of the evaporator capacity as a function of the water volume flow rate

Figure 4 depicts the variation of the evaporator capacity with the water volume flow rate. As mentioned earlier, the condenser capacity increased as the water volume flow rate passing through the condenser increased. The increase in the water volume flow rate through the condenser also increased the degree of subcooling in the condenser. The increase in the degree of subcooling of the refrigerant caused the evaporator capacity to increase as shown in Figure 4. Also as depicted, the minimum capacity of the evaporator was obtained with a volume flow rate of 100 L/h at 6.3845 kW while the maximum capacity was obtained with a volume flow rate of 500 L/h at 7.3986 kW. The evaporator capacity increased by 15.88% at the studied water volume flow rate range.
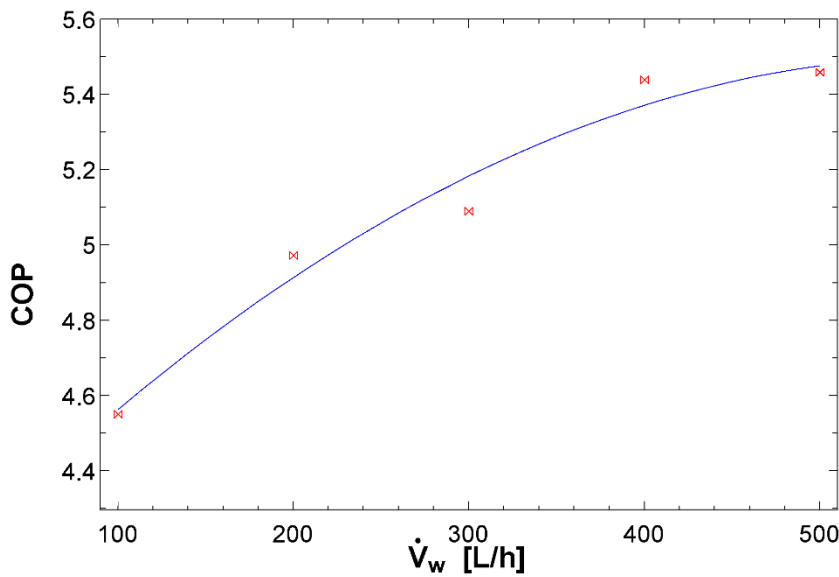
Figure 5: Variation of the COP as a function of the water volume flow rate

Figure 5 shows the change of the COP with the water volume flow rate. As the water volume flow rate increased, the evaporator capacity increased while the power consumed by the compressor decreased. As a result of these processes, the COP of the cycle increased as depicted in Figure 5 because the COP was the ratio of the evaporator

capacity to the compressor power. The highest value of the COP was 5.456 for 500 L/h. As the water volume flow rate increased by 400%, the per cent increase at the COP was 20.03% under these experimental conditions.
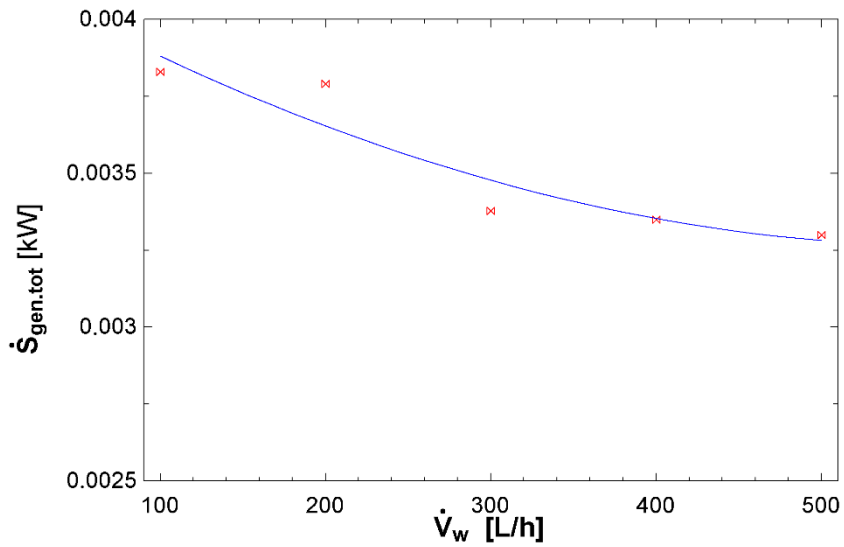
Figure 6: Change of the total entropy generation of the system with the water volume flow rate

The variation of the total entropy generation of the system in terms of the water volume flow rate is depicted in Figure 6. The main sources of total entropy generation of the refrigeration system were the heat transfers with a finite temperature difference in the condenser and evaporator, the sudden compression in the compressor and the sudden expansion in the expansion valve. As the water volume flow rate rose, the entropy generation in the compressor and condenser decreased while it increased in the evaporator and expansion valve. The part of total entropy generation caused by the compressor and condenser was higher than that of evaporator and expansion valve, therefore, the total entropy generation of the system decreased as depicted in Figure 6. The total entropy generation of the system changed from 0.0038 kW/K to 0.0032 kW/K. The entropy generation of the system decreased 14.02% at the water volume flow rate range studied.
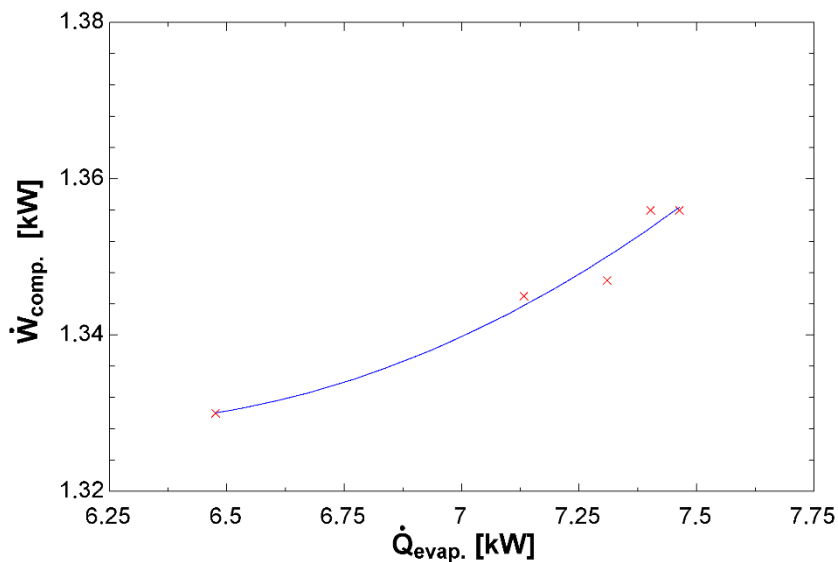
Figure 7: Variation of the compressor power consumption with the evaporator capacity

The change of the power delivered by the compressor with respect to the evaporator capacity is shown in Figure 7. The water volume flow rate was kept constant at 500 L/h. As the refrigeration capacity increased, the amount of mass flow rate of the refrigerant circulating through the system should also increase to meet the additional amount of the refrigeration capacity. The increase in the mass flow rate of the refrigerant caused the power consumed by compressor to increase as shown in Figure 7. The highest compressor power consumption obtained was 1.355 kW while the minimum was 1.330 kW. When the evaporator capacity increased, the percent increase in the compressor power consumption was 1.93%.
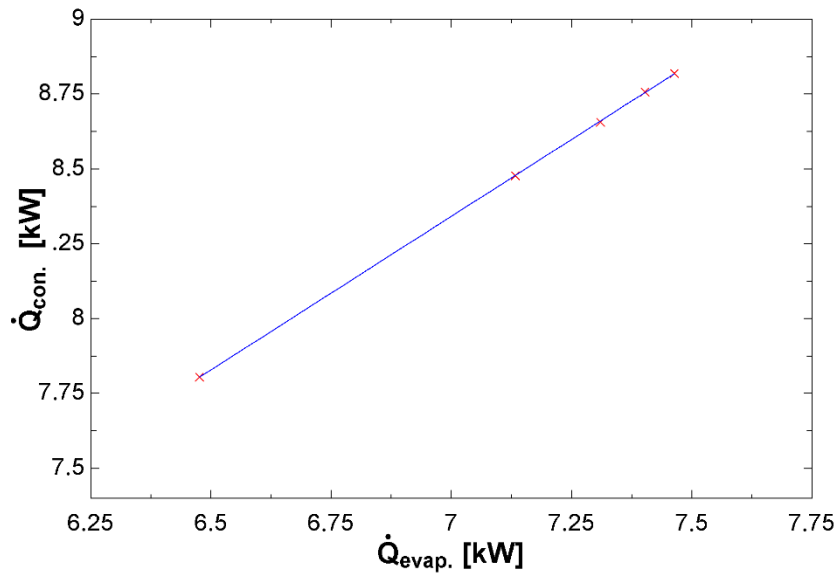
Figure 8: Change of the condenser capacity with the evaporator capacity

Figure 8 depicts the variation of condenser capacity with the evaporator capacity when the water volume flow rate was kept constant at 500 L/h. In a vapour compression refrigeration cycle, the condenser capacity was the summation of the evaporator capacity and the power given to the compressor. As mentioned before, as the evaporator capacity increased, the compressor capacity should also increase. As a result of this, the condenser capacity increased as shown in Figure 8. Also, the minimum condenser capacity obtained was 7.810 kW, while the maximum value was 8.8197 kW. When the evaporator capacity increased, the percent increase in the condenser capacity was 12.93%.
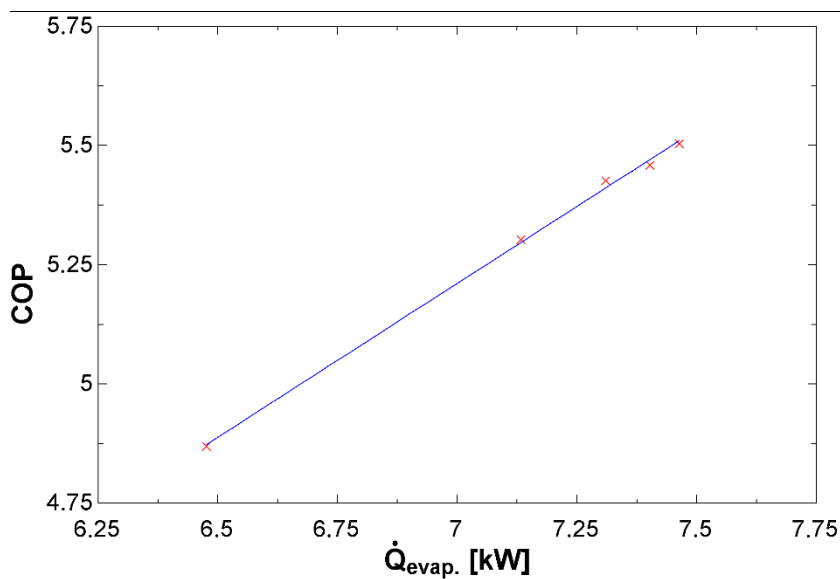
Figure 9: Variation of the COP as a function of the evaporator capacity

The variation of the COP as a function of the evaporator capacity is depicted in Figure 9. The water volume flow rate was kept constant at 500 L/h. The COP was a function of the evaporator capacity and the power consumed by the compressor. As the evaporator capacity increased by 15.27%, it caused the compressor power consumption to increase by 1.93%. This resulted in the increase of the COP of the cycle as shown in Figure 9. The COP changed from 4.868 to 5.5049 as the evaporator capacity ranged from 6.5 kW to 7.5 kW on average. The highest value COP was 5.5049 when the evaporator capacity was 7.4635 kW. As the evaporator capacity increased by 15.27%, the per cent increase at the COP was 13.08% under these experimental study conditions.

4. CONCLUSION

The effects of the water volume flow rates ranging from 100 L/h to 500 L/h on the evaporator capacity, condenser capacity, the power delivered to the compressor, coefficient of performance (COP), and total entropy generation of the system were experimentally determined. In addition to this, the effects of the evaporator capacity ranging from 6.47 kW to 7.46 kW on the condenser capacity, the power delivered to the compressor, and COP were also experimentally investigated.

The main outcomes of this experimental study were as follows:

- As the water volume flow rate increased, the condenser capacity, the evaporator capacity and the COP increased while the compressor power consumption and the total entropy generation of the system decreased. Furthermore, as the evaporator capacity increased, the compressor power consumption, the condenser capacity and the COP increased;
- As the water volume flow rate rose, the COP of the system increased. The highest value of 5.4568 was obtained at a flow rate of 500 L/h, while the lowest COP obtained of 4.5461 was at a flow rate of 100 L/h in the cycle. Furthermore, a 20.03% improvement in the COP was achieved;
- As a result of the increase in evaporator capacity from 647 kW to 746 kW, the COP increased 13.08%;
- Thus, it was determined that the effect of water volume flow rate was more effective than the evaporator capacity on the COP;
- The total entropy generation of the system decreased by 14.02% at the water volume flow rates ranging from 100 L/h to 500 L/h.

5. REFERENCES

Ansari, A. A., Goyal, V., Yahya, S. M., Hussain, T. 2018. Experimental investigation for performance enhancement of a vapor compression refrigeration system by employing several types of water-cooled condenser. *Science and Technology for the Built Environment,* 24(7), 793–802.

Gaikwad, A. P., Tembhune, S. J., Lokhande, P. Y., Mane, R. S. 2018. Experimental Investigation of Performance of VCRS System by Using Air Cooled and Water Cooled Condenser. *International Journal of Scientific Research in Science and Technology,* 4(2), 706–708.

Huang, C. N., & Yu, C. C. 2016. Integration of Taguchi's method and multiple-input, multiple-output ANFIS inverse model for the optimal design of a water-cooled condenser. *Applied Thermal Engineering,* 98, 605-609.

Klein, S.A., 2020. Engineering Equation Solver (EES) Academic Professional V10.836-3D. *F-Chart Software.*

Kamil, M., Nazir, S. 2019. Effect of Evaporator Load on Heat Pump Operating Parameters and Performance. *Journal of Energy and Power Engineering,* 13(3), 124-129.

Raveendran, P. S., Sekhar, S. J. 2017. Performance studies on a domestic refrigerators retrofitted with building-integrated water-cooled condenser. *Energy and Buildings,* 134, 1-10.

Raveendran, P. S., Sekhar, S. J. 2020. Experimental studies on the performance improvement of household refrigerator connected to domestic water system with a water-cooled condenser in tropical regions. *Applied Thermal Engineering,* 179, 115684.

Shikalgar, N. D., & Sapali, S. N. 2019. Energy and Exergy Analysis of A Domestic Refrigerator: Approaching A Sustainable Refrigerator. *Journal of Thermal Engineering,* 5(5), 469-481.

Shrivastav, H. K., Soni, P. S., Namdeo, P. K. 2019. A Review on Comparative Analysis of Refrigerator Using Refrigerant R-134a & R-600a Fitted With Water Cooled Condenser. *International Journal of Innovative Research In Technology,* 5(12), 656-658.

#37: Exergy analysis of a three stage expansion and regenerative Rankine cycle

Ali KILICARSLAN[1], Engin ŞANLI[2]

[1]Hitit University, Department of Mechanical Engineering, Corum,Turkey, alikilicarslan@hitit.edu.tr
[2] Hitit University, Directorate of Construction and Technical Works, Corum,Turkey, enginsanli@hitit.edu.tr

Abstract: The importance of combined heat and power generation systems has greatly increased in recent years because as these systems produce electricity, the waste heat is utilized in processes such as heating, cooling, and process vapor. In this study, the proposed combined heat and power generation system consisted of a three-stage turbine, condenser, boiler, open feed water heater and two pumps. The second law analysis of the elements of the combined heat power system was performed. Exergy destructions of condenser, pumps, boilers, turbines, throttling valves, and open feed water heater were investigated with respect to the turbine inlet temperature and pressure. In this context, a computer program was developed by using EES (Engineering Equation Solver) software. The turbine inlet pressure varied from 8,000 kPa to 18,000 kPa and the turbine inlet temperature ranged from 460°C to 560°C. As the turbine inlet temperature increased, the exergy destructions of the boiler, turbines and condenser increased, while the exergy destructions of the pumps and open feed water heater did not change. As the turbine inlet pressure increased, the exergy destructions of the boiler, turbines and condenser decreased, while the exergy destructions of the pumps and open feed water heater again did not change. The maximum exergy destruction occurred in the boiler, while the minimum exergy destruction occurred in pump1.

Keywords: Rankine cycle; combined heat and power (CHP); exergy analysis; exergy destruction

1. INTRODUCTION

With the increase in technological developments, human comfort conditions have directly increased also. As a natural result of this situation, the need for energy is increasing day by day. In order to meet our energy needs, energy is being produced from many different sources such as fossil, geothermal, nuclear, solar, wind, wave, etc. Nowadays, we need to use the energy obtained from these limited natural resources in the most effective way and make improvements to recover the wasted energy. Energy appears in many different forms such as heat, mechanical, electricity etc. In our country, electricity is produced in steam turbine thermal power plants and the generation of energy with maximum efficiency depends on the use of combined heat and power plants. In this regard, even small improvements in thermal efficiency will contribute to the economy of the country by saving significant fuel. For this reason, in order to increase the thermal efficiency of the cycle on which the steam power plants are based, many studies have been conducted for performance analysis of power plants.

Elhelwa *et al.* (2019) investigated the energy and exergy analysis of the elements of a 650 MW power plant in cases when the power plant was operating at both full load and half load. In both cases, they determined that the most exergy loss among the components in the power plant was the boiler, turbine, condenser, respectively. Sanjay and Mehta (2012) conducted energy and exergy analyses for a 125 MW coal-fired thermal power plant. They found that exergy efficiency was lower than energy efficiency. In addition, they concluded that the highest exergy loss occurred in the economizer at 55.97% and the lowest exergy loss occurred in the turbine at 27.13%.

Kaviri *et al.* (2011) conducted exergy analysis for a steam power plant and investigated the effects of the number of open feed water heaters on other system elements. They determined that the highest exergy loss among the power plant components was in the boiler with 201.37 MW. Rosen and Dinçer (2004) carried out energy and exergy analysis by determining different dead-state conditions in a coal-fired power plant. They applied the energy and exergy analysis to both the system and all components of the system, and analyzed the results.

Naserabad *et al.* (2019) conducted retrofit research for the 4,320 MW Bandar Abbas steam power plant in Iran. They tested five different designs in terms of energy and exergy efficiency related to the power plant and determined that the most efficient design was the parallel feed water-heated production plan. In calculations made with the respect to this design, they found that net exergy and energy efficiency in the cycle could reach 54.49% and 52.98%, respectively. Isam H. Aljundi (2009) conducted energy and exergy analyses for the Al-Huseyin power plant in Jordan. The elements of the system were analysed separately and the areas with the greatest energy and exergy losses were identified by determining the amount of energy destruction. It was found that the exergy loss occurred in the boiler with 77%, in the turbine with 13%, 9% in the condenser and 1% in other system elements.

Kurtaran Ahmet (2019) conducted exergy analyses in İsdemir power plant in Turkey. The thermal efficiency of the cycle was 29% and second law efficiency reached 66.7%. The high pressure closed-feed water heater and condenser had the lowest second law efficiency, while the boiler and condenser pump had the highest second law efficiency. Except for the turbine and boiler, the highest exergy loss was determined in the deaerator.

In the literature, the studies mentioned above conducted energy and exergy analysis in thermal power plants. In this study, unlike other studies, second law analysis of combined heat and power systems (CHP), as a function of high process turbine inlet pressure and temperature were investigated.

2. THERMODYNAMIC ANALYSIS

The combined heat and power (CHP) plant is shown schematically in Figure 1.
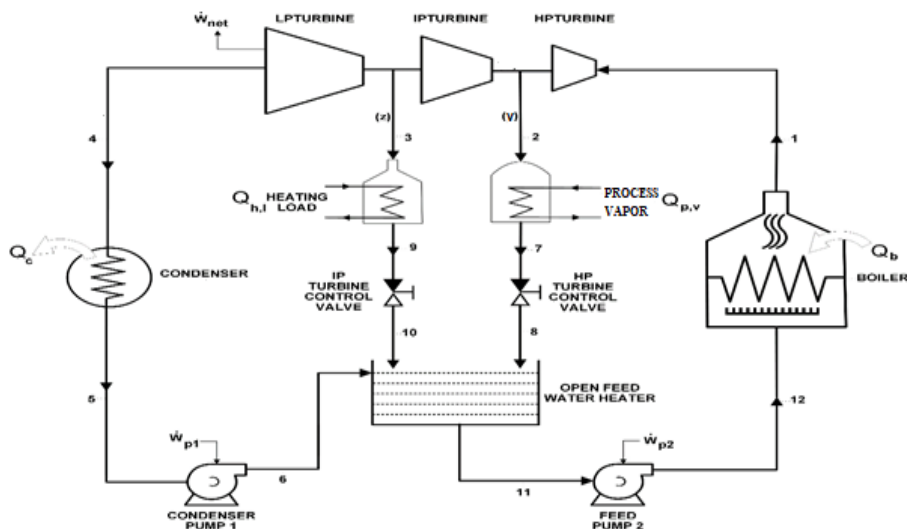
Figure 1: Schematic representation of the combined heat and power (CHP) system plant

The system consisted of 5 main elements including three-stage turbine, a condenser, a boiler, an open-feed water heater and two pumps. The steam at high temperature and pressure entering the cycle from state 1 was expanded through three stages of expansion in the turbine. After this steam was expanded to meet the heating load and process vapor requirements, the remaining steam was used to generate electrical energy connected to the generator at the low pressure stage of the turbine and then became liquid in the condenser. This was collected in the open-feed water heater with the help of the condenser pump. In the open-feed water, the liquid water was mixed with the steam separated from the high pressure and medium pressure turbine, and then liquid water discharged to the boiler by means of feed pump 2. Finally, it returned to the high pressure turbine as superheated steam and the cycle was completed.

The P-h diagram of the cycle is shown in Figure 2.
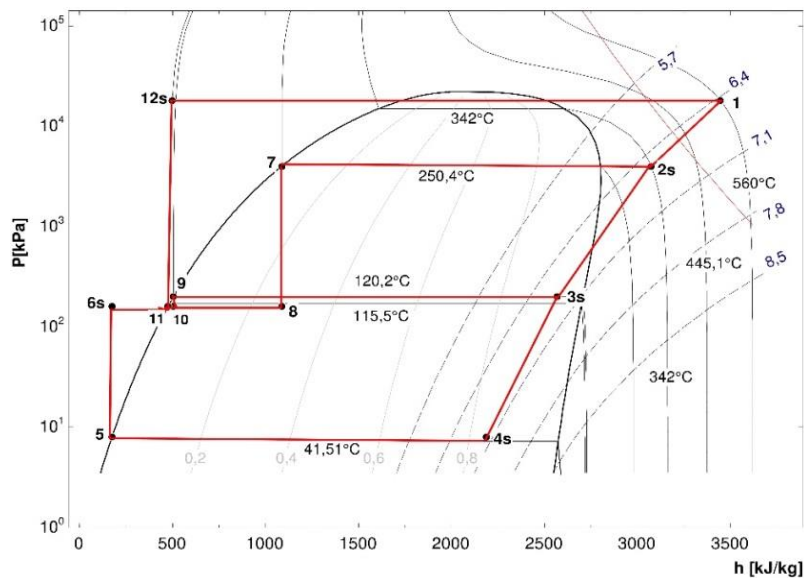
Figure 2: Ideal pressure-enthalpy diagram of the cycle

The assumptions made in the theoretical analysis were as follows:

- Kinetic and potential energy losses were neglected;
- Turbines and pumps were designed adiabatically;
- Pressure losses in the pipelines were neglected;
- It was assumed that the fluid at the condenser outlet was saturated liquid.

In light of all these assumptions, the first and second laws of thermodynamics of the combined heat and power (CHP) plant were performed.

I. Law Analysis

The amount of heat given to the boiler can be written as follows:

Equation 1: The amount of heat given to the boiler.
$$\dot{Q}_b = (h_1 - h_{12})\,\dot{m}_1$$

Where:

- $\dot{m}_1$ = total mass flow rate of steam
- h_1 = enthalpy at the boiler outlet
- h_{12} = enthalpy at the boiler inlet

The amount of heat released through the condenser is determined by using equations below,

Equation 2: The amount of heat released through the condenser.
$$\dot{Q}_c = (h_4 - h_5)\,\dot{m}_4$$

Where:

- $\dot{m}_4$ = mass flow rate of steam through the condenser
- h_4 = specific enthalpy at the inlet of the condenser
- h_5 = specific enthalpy at the outlet of the condenser

The amount of heat utilized from the process vapor is calculated below.

Equation 3: The amount of heat utilized from the process vapor.

$$\dot{Q}_{p,v} = (h_2 - h_7)\, \dot{m}_2$$

Where:

- $\dot{m}_2$ = steam flow rate through the process vapor
- h_2 = specific enthalpy at process steam inlet
- h_7 = specific enthalpy at process steam outlet

The amount of heat given to the heating load is determined by using equations below.

Equation 4: The amount of heat given to the heating load.

$$\dot{Q}_{h,l} = (h_3 - h_9)\, \dot{m}_3$$

Where:

- $\dot{m}_3$ = steam flow rate through heating load
- h_3 = specific enthalpy at the heating load inlet
- h_9 = specific enthalpy at the heating load outlet

II. Law Analysis

The exergy destruction of the elements of the system can be defined as follows:

Equation 1: Exergy lost in the boiler.

$$\dot{E}_{D_B} = T_0\, \dot{m}_1 \left[(s_1 - s_{12}) - \left(\frac{h_1 - h_{12}}{T_{b,g}} \right) \right]$$

Where:

- s_1 = entropy at the entrance to the boiler
- s_{12} = entropy at the boiler outlet
- $T_{b,g}$ = boiler limit temperature

Exergy destruction in the condenser is given in the equation below:

Equation 6: Exergy destruction in the condenser.

$$\dot{E}_{D_C} = T_0\, \dot{m}_4 \left[(s_5 - s_4) + \left(\frac{h_4 - h_5}{T_{b,\varsigma}} \right) \right]$$

Where:

- s_4 = entropy at the condenser outlet
- s_5 = entropy at the condenser inlet
- $T_{c,\varsigma}$ = condenser boundary temperature

Exergy destruction in process steam is shown in the equation below:

Equation 7: Exergy destruction in process steam.

$$\dot{E}_{D_{p,v}} = T_0 \dot{m}_2 \left[(s_7 - s_2) + \left(\frac{h_2 - h_7}{T_{p,v}} \right) \right]$$

Where:

- s_7 = entropy at the condenser inlet
- s_2 = entropy at the condenser out
- $T_{p,v}$ = process vapor limit temperature

Exergy destruction in the heating load is determined by using equations below:

Equation 8: Exergy destruction in the heating load.

$$\dot{E}_{D_{h,l}} = T_0 \dot{m}_3 \left[(s_9 - s_3) + \left(\frac{h_3 - h_9}{T_{h,l}} \right) \right]$$

Where:

- s_9 = entropy in the heating load inlet
- s_3 = entropy in the heating load out
- $T_{h,l}$ = heating load limit temperature

Exergy destruction in turbines is calculated in the equation below:

Equation 9: Exergy destruction in HPT.

$$\dot{E}_{D_{HPT}} = T_0 \, (s_2 - s_1) \, \dot{m}_1$$

Equation 102: Exergy destruction in IPT.

$$\dot{E}_{D_{IPT}} = T_0 \, (s_3 - s_2)(1 - y) \, \dot{m}_1$$

Equation 11: Exergy destruction in LPT.

$$\dot{E}_{D_{LPT}} = T_0 \, (s_4 - s_3) \, \dot{m}_4$$

Where:

- v = process steam inlet mass flow rate ratio

The exergy destruction in the pumps is shown below:

Equation 12: Exergy destruction in the pump 1

$$\dot{E}_{D_{p1}} = T_0 \, (s_6 - s_5) \, \dot{m}_4$$

Equation 13: Exergy destruction in the pump 2

$$\dot{E}_{D_{p2}} = T_0 \, (s_{12} - s_{11}) \, \dot{m}_1$$

Where:

- s_6 = entropy at the condenser pump outlet
- s_{11} = entropy at the inlet water heater pump inlet

The exergy destruction in the valves is shown below:

Equation 14: Exergy destruction in the valve 1

$$\dot{E}_{D_{v1}} = T_0 \, (s_{10} - s_9)(z)\dot{m}_1$$

Equation 15: Exergy destruction in the valve 2.

$$\dot{E}_{D_{v2}} = T_0 \, (s_8 - s_7)(y)\dot{m}_1$$

Where:

- s_{10} = entropy at the inlet of the medium pressure turbine control valve
- s_8 = entropy at the high pressure turbine control valve outlet
- z = heating load inlet mass flow rate ratio

The exergy destroyed in the open feed water heater is shown below:

Equation 16: Feed water heater.

$$\dot{E}_{D_{OFW}} = T_0 \, \dot{m}_1 \, [(s_{11} - (z)s_{10} - (1 - y - z) \, s_6 - (y)s_8]$$

Using the equations above, the computer program was developed with the help of EES (Klein, 2013). The constant values taken during the operation of the computer program are shown in Table 1.

Table 1: Constant values

Component	Value	Component	Value
Plant Load	450 MW	Pomp1 Outlet pressure, P_6	160 kPa
Steam Flow	485,8 kg/s	Pump Isentropic Efficiency	0,85
Boiler Temperature	560°C	Condenser inlet pressure, P_4	8 kPa
YBT Inlet pressure, P_1	18000 kPa	Heating load steam flow, $\dot{m}_3$, z	145,7 kg/s
YBT Outlet Pressure, P_2	4000 kPa	Ambient Temperature, T; T_0	20 °C; 298,2 K
OBT Outlet Pressure, P_3	200 kPa	Heating Load Temperature, $T_{h,l}$	350 K

3. RESULTS AND DISCUSSIONS

With the developed program, the effects of the turbine inlet pressure and temperature on the exergy destruction of the system elements were examined separately. In the graphs shown in Figures 3 and 5, the turbine inlet pressure was increased from 8000 kPa to 18000 kPa, while the turbine inlet temperature was kept constant at 560°C.
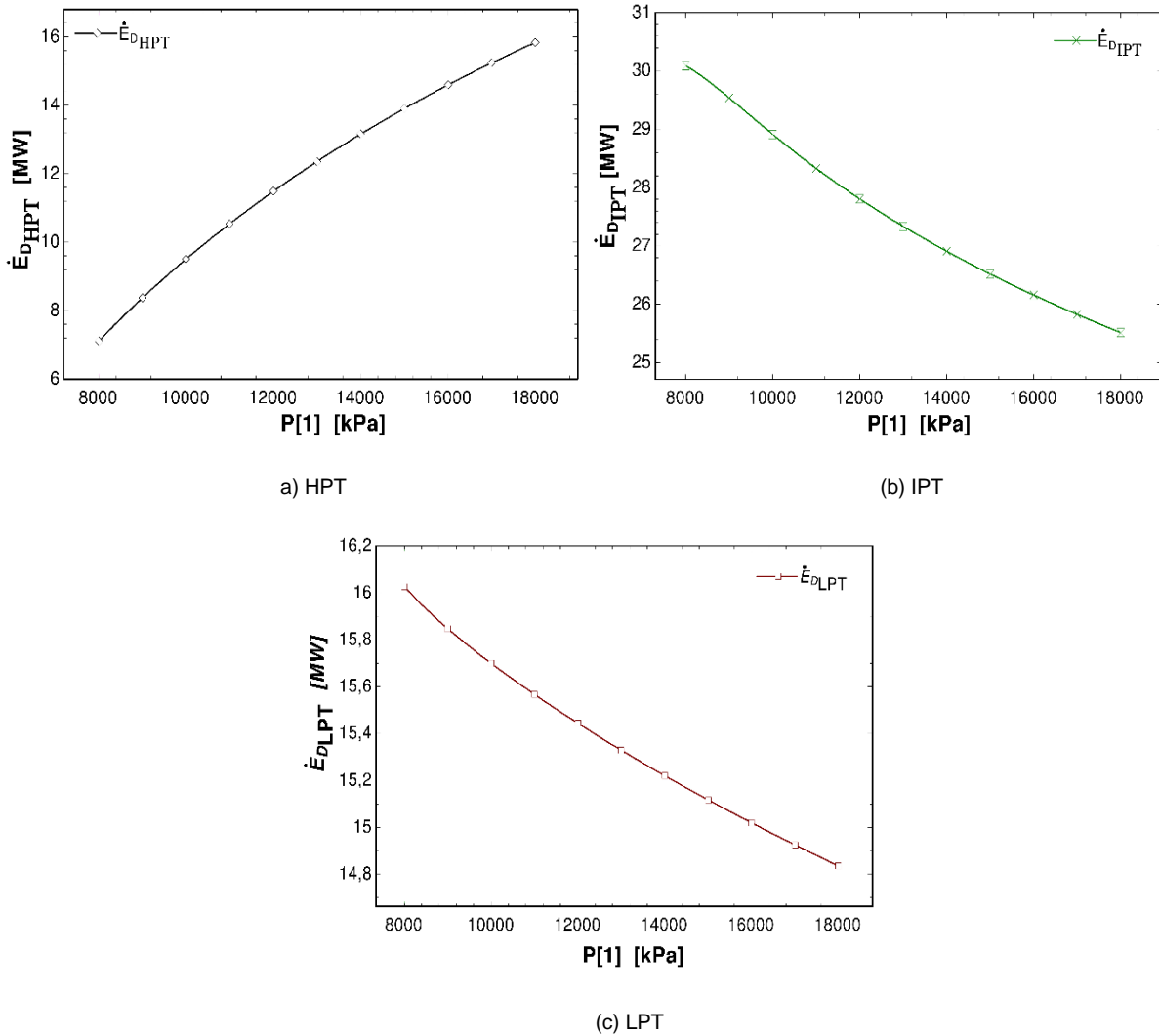
a) HPT

(b) IPT

(c) LPT

Figure 3: Change of exergy destruction in turbines with respect to turbine inlet pressure: (a) HPT; (b) IPT; (c) LPT

Figure 3 shows the change of exergy destruction in the turbines depending on the increase of the turbine inlet pressure. At the constant pressure at the turbine outlets, the temperatures at the turbine outlets decreased as the inlet pressure increased. Irreversibilities decrease with decreasing temperatures at the turbine outlets and exergy in IPT and LPT decrease. The exergy destruction in IPT was 30 MW at 8000 kPa while it was 25.5 MW at 18000 kPa. Figure 3.c shows that exergy loss was 16 MW at 8000 kPa while it was 14.83 MW at 18000 kPa. The maximum exergy occurred in the IPT.

In the meantime, the exergy destruction in HPT increased unlike other the turbines. As can be seen in Figure 3.a, the highest exergy destruction value was 15.84 MW when the pressure value was 18000 kPa and the lowest exergy destruction value was 7.1 MW when the pressure value was 8000 kPa.
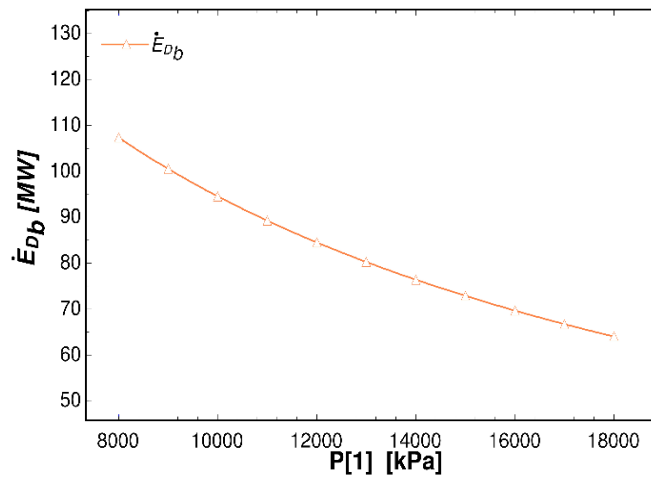
Figure 4: Change of exergy destruction in the boiler with the respect to the turbine inlet pressure

Figure 4 shows the change of exergy destruction in the boiler as a function of inlet pressure. When the turbine inlet pressure was increased, the enthalpy at the boiler outlet reduced, thereby reducing the amount of heat required to be supplied to the boiler, which reduced the irreversibilities occurring in the boiler. As can be seen from Figure 3, the highest exergy destruction was 107 MW when the pressure value was 8000 kPa and the lowest exergy destruction was 64 MW when the pressure value was 18000 kPa.
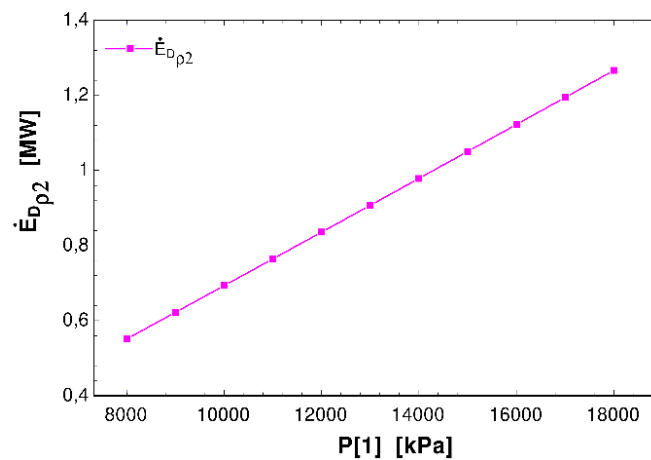
Figure 5: Change of exergy destruction in the pump with the respect to the turbine inlet pressure

Figure 5 shows the change of exergy destruction in pump 2 as a function of turbine inlet pressure. When the turbine inlet pressure increased, exergy destruction in pump 2 also increased. This was due to the fact that with the increase of the pump 2 outlet pressure, the pump work gradually increased, and as a result, the irreversibilities occurring in the pump increased. As can be seen from Figure 5, the highest exergy destruction was 1.266 MW when the pressure value was 18000 kPa and the lowest exergy destruction was 0.55 MW when the pressure value was 8000 kPa. Also, when the turbine inlet pressure was increased, the exergy destruction in pump 2 increased linearly.

In the figures 6, 7 and 8, the turbine inlet temperature can be seen to change between 460°C and 560°C, while the turbine inlet pressure was kept constant at 18000 kPa.
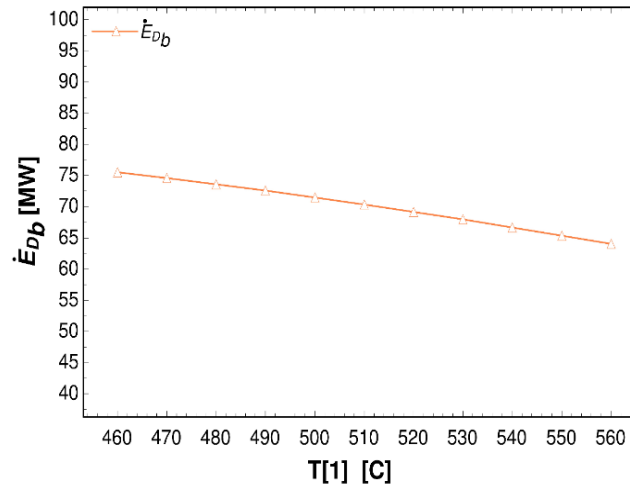
Figure 6: Change of exergy destruction in the boiler with the respect to the turbine inlet temperature

Figure 6 shows the change of exergy destruction in the boiler as a function of the turbine inlet temperature. When the turbine inlet temperature increased, exergy destruction in the boiler decreased gradually. The reason for this was that increasing the turbine inlet temperature caused the exergy destruction of the boiler to decrease. As can be seen from Figure 6, the highest the exergy destruction was 75.5 MW when the temperature value was 460°C, while the lowest the exergy destruction was 64 MW when the temperature value was 560℃.
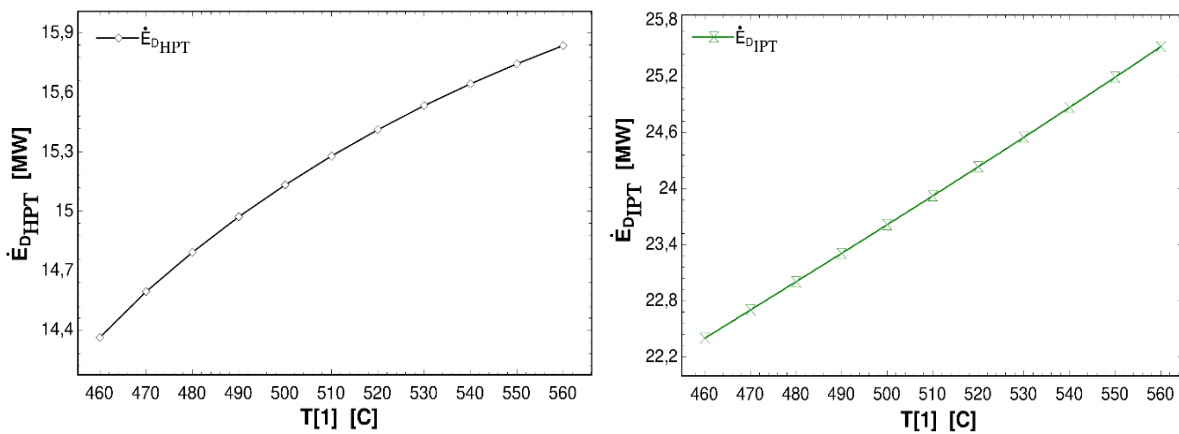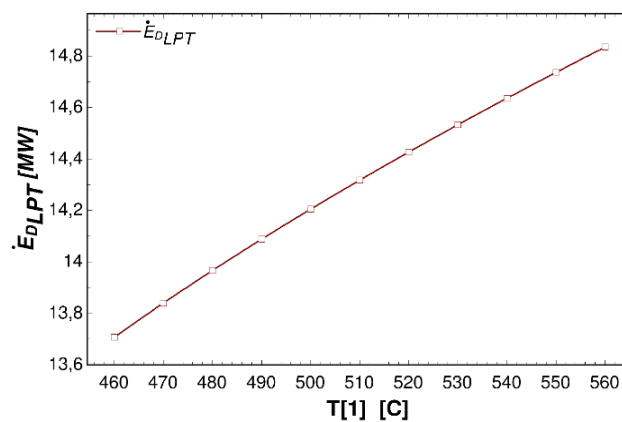
a) HPT

(b) IPT

(c) LPT

Figure 7: Change of exergy destruction with the respect to turbine inlet temperature: (a) HPT; (b) IPT; (c) LPT

Figure 7 shows the change of exergy destruction in the turbines depending on the increase of the turbine inlet temperature. Increasing turbine inlet temperature increased the irreversibilities at the turbines. The increase in the irreversibility caused the exergy destruction to increase in the turbines as shown in Figure 7. Exergy destroyed in HPT was 15.84 MW at 560, while it was 14.36 MW at 460°C. The exergy destroyed in IPT was 25.5 MW at 560, while it was 22.4 MW at 460. The exergy destruction in LPT was 25.5 MW at 560 while it was 13.71 MW at 460°C. Depending on the increase in temperature, exergy destruction tended to decrease gradually in HPT and LPT, while it tended to increase in IPT.
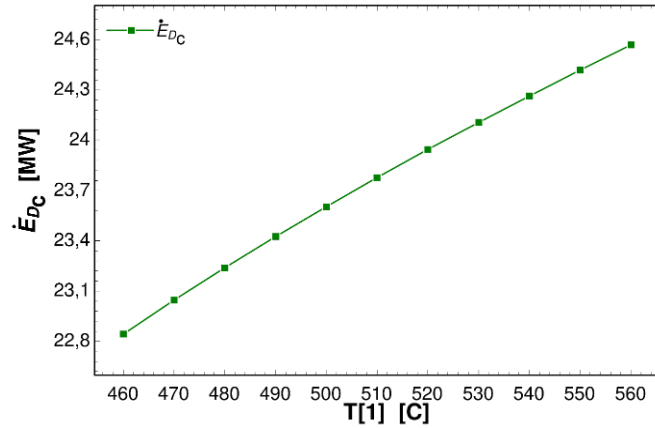
Figure 8: Change of exergy destruction in the condenser with the respect to the turbine inlet temperature

Figure 8 shows the change of exergy destruction in the condenser as a function of the turbine inlet temperature. As the turbine inlet temperature increased, it caused the finite temperature difference between the condenser and the environment to increase, thereby increasing the heat transfer through the surface of the condenser. As a result of this, the exergy destruction in the condenser increased as shown in Figure 8. As can also be seen, the lowest exergy destruction was 22.8 MW when the temperature value is 460°C and the highest exergy destruction was 24.5 MW when the temperature value was 560°C. When the turbine inlet temperature increased, the exergy in the condenser increased linearly.

4. CONCLUSIONS

In the study, exergy destruction of the system elements with respect to the turbine inlet pressure and temperature in the combined heat and power (CHP) system steam cycle were observed. The main results obtained from this theoretical study can be summarised as follows:

The main outcomes of this experimental study are as follows:

- When the turbine inlet pressures and temperatures were increased, the net power produced from the turbine increased in both cases. This increase was limited to a maximum of 450 MW at the inlet pressure;
- When the turbine inlet temperature increased, exergy destruction from the boiler increased while the exergy destruction from the condenser and turbines increased;
- When the turbine inlet temperature increased, the exergy destruction from the pumps, valves and open-feed water heater did not change;
- When the turbine inlet pressure increased, the exergy destruction in the boiler, condenser, IPT and LPT decreased, while the exergy destruction with pump1 and HPT increased;
- As a function of the increase in turbine inlet pressure and temperatures, exergy destruction in the boiler decreased in both cases while exergy destruction in HPT increased;
- Depending on the increase of turbine inlet pressure and temperature, in both cases the exergy destructions in open-feed water heater, pump1 and valves did not change.

5. REFERENCES

Ahmet Kurtaran, İsdemir Kuvvet Santrali Enerji Ve Ekserji Analizi, Yüksek Lisans Tezi, Batman Üniversitesi Fen Bilimleri Enstitüsü Otomotiv Mühendisliği Anabilim Dalı, Ağustos-2019

Aljundi Isam H. Energy and exergy analysis of a steam power plant in Jordan, Chemical Engineering Department, Mutah University, Al-Karak, Jordan, 29: 324-28, 2009

Engin Ş., Kilicarslan A., Üç Kademe Genişlemeli Ve Rejeneratif Rankin Çevriminin Enerji Analizi, 22nd Congress on Thermal Science and Technology (ULIBTK'19)., Book of Fulltext Proceedıngs Volume I, Kocaeli University, Kocaeli, Türkiye, 456-461., 11-14 September 2019

Kaviri A.G., Jafar M.N.M., Tholudin M.L., and Avval H. B., 'Exergy analysis of a Cogeneration heat and Power (CHP) system (First and second law analysis)' ,IEEE First Conference on Clean Energy and Technology CET, 2011

Klein S. A., "Engineering Equation Solver", Version 9.478, F-Chart Software, 2013.

Mali Sanjay D, Dr. Mehta N S, Easy Method Of Exergy Analysıs For Thermal Power Plant, International Journal of Advanced Engineering Research and Studies, April-June, 245-247, 2012

Mohamed Elhelwa, Kareem Saad Al Dahmaa, Abd el Hamid Attiaa, Utilizing exergy analysis in studying the performance of steam power plant at two different operation mode, Applied Thermal Engineering, 150, 285-293, 2019

Naserabad Nikbakht S., Mehrpanahi A., Ahmadi G., Multi-objective optimization of feed-water heater arrangement options in a steam power plant repowering, Journal of Cleaner Production, 220, 253-270, 2019

Rosen M. and Dinçer I., Effect of Varying Dead-State Properties on Energy and Exergy Analyses of Thermal Systems, International Journal of Thermal Sciences, pp. 43, 121-133, 2004

#38: Entropy generation of a cascade refrigeration cycle integrated Linde-Hampson cycle

Selcuk Kızılcaoglu, Ali Kılıcarslan*, İrfan Kurtbaş

Hitit University, Department of Mechanical Engineering, Çorum, Turkey
Email: selcukkizilcaoglu@gmail.com, ikurtbas@gmail.com
*Corresponding author: alikilicarslan@gmail.com
Telephone: +90(364) 2274533/1236, Fax: +90 (364) 2274535

Abstract: In this study, in order to liquefy methane gas, the four-stage cascade refrigeration cycle integrated with Linde-Hampson was proposed. The refrigerants R32, R23, R600, R1234yf, R141b, and R290 were used in the proposed cycle. A computer code was developed using the Engineering Equation Solver (EES-V9.172-3D). Irreversibility of the four-stage cascade refrigeration cycle integrated with Linde-Hampson was investigated according to different evaporator, condenser temperatures, and methane gas mass flow rates. As the evaporator temperature increased, the irreversibility of the cycle decreased. However, the irreversibility of the cycle increased the condenser temperature, and the mass flow rate of methane increased. The minimum amount of irreversibility of the cycle was obtained using R32 as a refrigerant, while the maximum amount of irreversibility was obtained using R23.

1. INTRODUCTION

With technology development, refrigeration systems are available today in many industrial and commercial applications. In these systems, vapour compression refrigeration systems are the most widely used. Cryogenic systems are generally preferred for applications at low temperatures below -150°C. Today, cryogenic systems are used in various areas such as food, energy, medical and space applications. In order to liquefy and store nitrogen, air, argon, hydrogen, and methane, a cryogenic refrigerant cycle is used. During the liquefaction process at very low temperatures, cascade refrigeration systems are employed with the liquefaction systems that are integrated with organic Rankine cycles and geothermal cycles. In the literature, there are systems involving many different methods of liquefaction of gases and studies on thermodynamic analysis of these systems.

The first law of thermodynamics only concerns the conservation of energy. The second law does not provide information about where or how the system performance occurs, or the amount of change (Dincer & Rosen, 2013). In the liquefaction process, cycles such as Linde -Hampson, Kapitza, and Claude or different configurations of these cycles are used. Liquefaction cycles theoretically were examined according to the first and second laws of thermodynamics. The second law efficiencies of these systems have been determined for the liquefaction of different gases. It has been determined that Claude and Kapitza cycles provide better performance than other cycles, while Linde-Hampson cycle has system installation advantages compared to other cycles (Yılmaz, 2019). The performance coefficients of dual pressure and pre-heated Linde-Hampson cycles are two times and 1.8 times higher than the simple cycle, respectively (Dadsetani et al., 2019). A refrigerator cycle using the Linde-Hampson cycle has been theoretically studied with R14 hydrocarbon refrigerant mixture being used as the working fluid.

The system's exergy efficiency increased with a decrease in the refrigeration temperature between -60 and -110°C. As a result of the study, 65% -75% exergy efficiency was achieved. Jerome & Venkatarathnam (2019) investigated the second law analysis of the turbine integral Claude cycle used in helium liquefaction. Irreversibilities of the system and system elements were determined. The most fraction of the irreversibilities occurred in the compressor (Maiti et al., 2019). The exergy efficiency of the three nitrogenous single expansion processes for LNG production was investigated. A large part of the total preventable exergy destruction of the system consisted of compressors and expanders, therefore these components have the highest priority for improvement (Palizdar et al., 2017). It was shown that the hydrogen liquefaction process was affected by different working conditions such as the cycle pressure of hydrogen and helium, pinch point temperature, hydrogen mass flow rate, and the efficiency research and energy, exergy efficiency, and irreversibilities of different designs were investigated. Exergy efficiency in liquefaction increased with pressure in the hydrogen cycle. However, ambient temperature increased from 0 to 40 degrees, reducing the amount of liquefied hydrogen (Yuksel et al., 2017). It was designed in geothermal energy-based cycles for hydrogen liquefaction. They studied a binary cycle for the geothermal energy source and the pre-cooled Linde-Hampson cycle for the liquefaction of the hydrogen. Geothermal source absorption cooling for gas pre-cooling is more advantageous in the gas liquefaction cycle than using geothermal work output (Kanoglu et al., 2008). Many commercial and industrial facilities require very low temperatures for refrigeration, but also high temperatures are required for heating and hot water. Single-stage heat pumps, vapour compression refrigeration systems, and similar systems are insufficient to meet these needs. Cascade systems have been developed to overcome single-stage systems (Boahen & Choi, 2017; Kilicarslan, 2004; Kilicarslan & Hosoz, 2010).

In this study, the irreversibility of the system and its components as a function of mass flow rate type of refrigerants, condenser, and evaporator temperatures in a four-stage vapour compression cascade refrigeration cycle integrated into the Linde–Hampson cycle were studied. A computer program was developed using EES software in the cascade refrigeration cycle integrated into the Linde–Hampson cycle using R1234yf, R600a, R290, R23, R32, and R141b as refrigerants.

2. THERMODYNAMIC ANALYSIS

The four-stage cascade refrigeration cycle integrated Linde-Hampson liquefaction cycle is shown in Figure 1. The cascade refrigeration system consisted of compressors, expansion valves, condenser, and evaporator. The second law analysis of the system was based on the vapour compression refrigeration cycle. Working fluid entered the compressor as saturated vapour at low pressure and temperature in each cycle. In cycles, the effects of subcooling and superheating were not considered. The working fluid compressed in the compressor left the compressor as superheated vapour at high pressure and temperature. It was sent to the condenser, where the constant pressure became the saturated liquid and heated the environment. The working fluid in the form of saturated liquid entered the expansion valve, and its pressure was reduced to the pressure of the evaporator element. It had been used as a condenser and evaporator heat exchanger element in the lower stages of the system. The working fluid entering the heat exchanger element evaporated under constant pressure absorption from the environment. The working fluid leaving the heat exchanger as saturated steam was sent back to the compressor, and the cycle was complete.

The cascade system was integrated into the Linde-Hampson cycle and methane gas was liquefied. The Linde-Hampson cycle included a compressor, heat exchanger, Joule-Thomson (J-T) valve, and storage tank. Methane entering the system as gas was liquefied by the evaporator in the fourth stage of the vapour compression cascade cooling cycle. Methane was combined with the gas from the return line of the Linde-Hampson cycle and isothermally high pressure was compressed in the compressor. Then the working fluid, whose temperature was lowered in the

heat exchanger, passed through the J-T valve and was sent to the storage tank as liquid. Some of the methane gas was sent back and the cycle repeated.
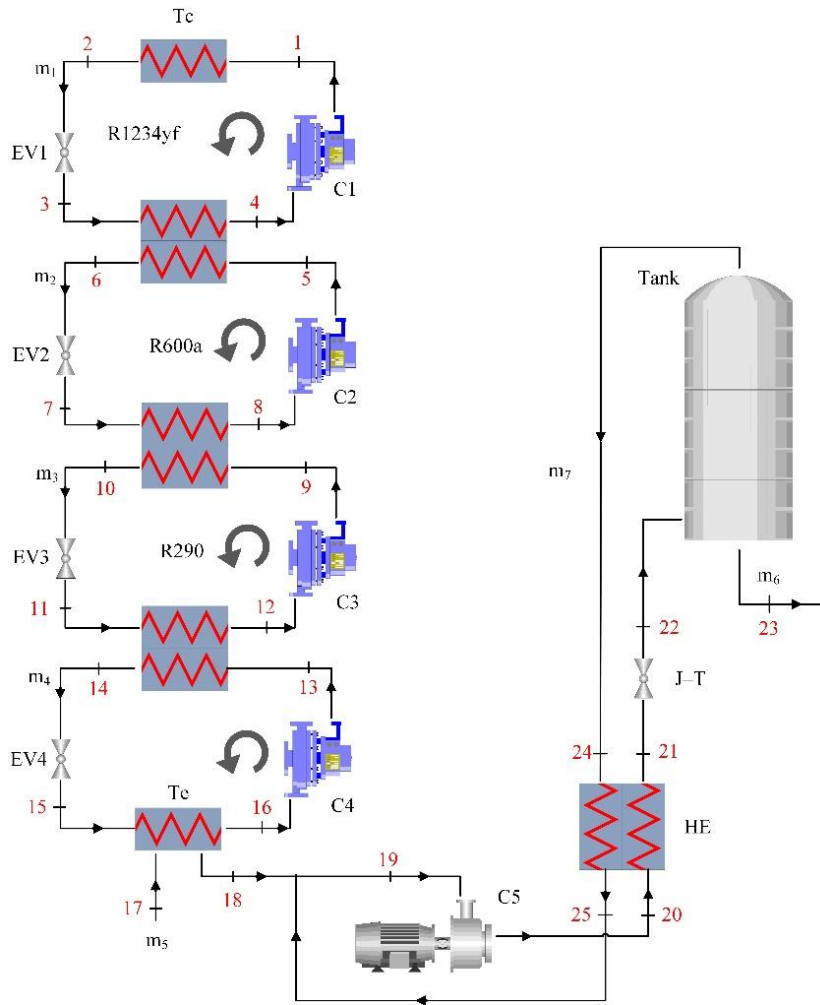
Figure 1: Schematic diagram of the four-stage cascade refrigeration cycle integrated Linde-Hampson liquefaction cycle

In the second law analysis of the four-stage cascade vapour compression integrated Linde-Hampson liquefaction system shown in Figure 1, the following assumptions have been made:

- The effects of variation of kinetic and potential energy were negligible during working fluid flow throughout the system;
- The heat transfers from the pipelines connecting the system elements to the environment was neglected;
- Pressure losses are neglected, and the compressor of each cycle in the four-stage cascade cycle was adiabatic;
- The working fluids in cycles were based on continuous and homogeneous flow conditions;
- The Linde-Hampson cycle compressor was an isothermal compressor and reversible.

In light of these assumptions, according to the first law of thermodynamics, the amount of energy consumed by compressors per unit time was determined by the cycle [12] and using Equations 1 and 2 below.

Equation 1: Conservation of energy

$$\frac{dE_{C.V.}}{dt} = \sum_{in} \dot{m}h - \sum_{out} \dot{m}h + \dot{Q}_{C.V.} - \dot{W}_{C.V.}$$

Where:

- $E_{C.V.}$ = Energy of a control volume
- $\dot{Q}_{C.V.}$ = Heat transfer of control volume
- $\dot{W}_{C.V.}$ = Work of control volume
- $\dot{m}$ = Mass flow rate
- h = Specific enthalpy

Equation 2: Exchange of exergy	$\frac{dS_{C.V.}}{dt} = \sum_{in} \dot{m}s - \sum_{out} \dot{m}s + \sum_s \frac{\dot{Q}_s}{T_s} + \dot{S}_{gen.j.}$

Where:

- $S_{C.V.}$ = Entropy of control volume
- $\dot{S}_{gen.j.}$ = Generation of entropy
- $\dot{Q}_s$ = Heat rate of surface
- T_s = Temperature of surface
- s = Entropy

Since the compressors in the cascade refrigeration system were reversible adiabatic and the compressor in the Linde-Hampson cycle was expressed as the following equations. Equations 3-7: Work of compressions

Equation 3:	$\dot{W}_{C1} = \dot{m}_1(h_4 - h_1)$
Equation 4:	$\dot{W}_{C2} = \dot{m}_2(h_8 - h_5)$
Equation 5:	$\dot{W}_{C3} = \dot{m}_3(h_{12} - h_9)$
Equation 6:	$\dot{W}_{C4} = \dot{m}_4(h_{16} - h_{13})$
Equation 7:	$\dot{W}_{C5} = (\dot{m}_5 + \dot{m}_7)[(h_{20} - h_{19}) - T_{19}(s_{20} - s_{19})]$

Where:

- $\dot{m}$, h, and s = mass flow of refrigerant through at each stage, enthalpy and entropy at the inlet and outlet of the compressor, respectively;
- $\dot{m}_5$ = mass of methane;
- $\dot{m}_6$ = mass of methane sent back to the cycle from the storage tank as gas in the liquefaction process.

Exergy analysis gives information about the losses of the components of the system. Irreversibility can be written as Equation 8;

Equation 8: Irreversibility	$I = T_0 \dot{s}_{gen}$

Where:

- T_0 = Environment temperature
- $\dot{s}_{gen}$ = Entropy generation

Irreversibilities in system components can be written using Equations 9 to 12: Irreversibilities of compressors

Equation 9:	$I_{C1} = \dot{m}_1 T_0(s_4 - s_1)$
Equation 10:	$I_{C2} = \dot{m}_2 T_0(s_8 - s_5)$
Equation 11:	$I_{C3} = \dot{m}_3 T_0(s_{12} - s_9)$
Equation 12:	$I_{C4} = \dot{m}_4 T_0(s_{16} - s_{13})$

Where:

- I_C = Irreversibility of a compressor in the system.

Irreversibilities of condenser and evaporator can be written using equations 13 and 14, respectively.

Equation 13: Irreversibilities of condenser	$I_c = \dot{m}_1 T_0 \left[(s_2 - s_3) - \frac{(h_2 - h_3)}{T_0} \right]$

Equation 14: Irreversibilities of an evaporator	$I_e = \dot{m}_4 T_0 \left[(s_{15} - s_{16}) - \frac{(h_{15} - h_{16})}{T_0} \right]$

Irreversibilities of heat exchangers and expansion valves can be written using equation 15.

Equation 15: Irreversibilities of heat exchanger $I_{HE}=T_0\left[\dot{m}_{cyc,1}(s_{out}\text{-}s_{in})\text{-}\dot{m}_{cyc,2}(s_{out}\text{-}s_{in})\right]$

Irreversibilities of the four-stage cascade refrigeration cycle integrated Linde-Hampson system can be written using Equation 19.

Equation 19: Irreversibilities of system $I_{total} = I_{total,\ C} + I_{total,\ HE} + I_{total,\ EV}$

$$I_{total,\ HE} = I_{HE,1} + I_{HE,2} + I_{HE,3} + I_{HE,4} + I_{HE,5} + I_{HE,6} + I_{HE,7} + I_{HE,8}$$

$$I_{total,\ EV}=I_{EV,1}+I_{EV,2}+I_{EV,3}+I_{EV,4}+I_{EV,5}$$

$$I_{total,C}=I_{C1}+I_{C2}+I_{C3}+I_{C4}+I_{C5}$$

Where:

- $I_{total,C}$= Total irreversibility of compressors;
- $I_{total,EV}$= Total irreversibility of expansion valves;
- $I_{total,\ HE}$= Total irreversibility of heat exchangers;
- I_{total}= Irreversibility of system.

3. RESULTS

The second law integrated cycle proposed above was performed as a function of mass flow rate, condenser and evaporator temperatures for refrigerants such as R23, R32 and R141b. In order to evaluate the results of this study, a computer code was developed with the help of Engineering Equation Solver (EES), a commonly used software EES-V9.172-3D. The effect of the mass flow rate of methane on the irreversibility of the evaporated and condenser was examined.

Table 1: Parameters of cycles

Cycle	Refrigerant
1st cycle	R1234yf
2nd cycle	R600a
3rd cycle	R290
4th cycle	R23-R32-R141b
5th cycle	Methane

In the operation of the computer program, the refrigeration cycle was ideally programmed, and methane gas was liquefied. Some parameters were kept constant; these values are given in Table 1. The refrigerants in 1st, 2nd, 3rd and 5th were not changed, but in the third cycle, R23, R32 and R141b were used.

Figure 2 (a) results were obtained by varying the condenser temperatures from 30ºC to 40ºC, while evaporator temperature and isentropic efficiency were kept constant at -140°C and 0.8, respectively. The highest values of irreversibility occurred in compressor 5 (C5) using R23, R32 and R141b refrigerant, but the lowest irreversibility occurred in compressor 4 (C4) using R32 refrigerant. As shown in Figure 2 (a), as the condenser temperature increased the irreversibility of compressor 1 (C1) increased, while that of compressor 3 (C3) decreased slightly. The irreversibilities such as compressors C2, C4 and C5 were constant.

The results shown in Figure 2 (b) were obtained by varying the evaporator temperatures from -150ºC to -140ºC while condenser temperature and isentropic efficiency were kept constant at 30ºC and 0.8, respectively. The highest values irreversibility occurred in compressor 5 (C5) using R23, R32 and R141b refrigerant, but the lowest irreversibility occurred in compressor 4 (C4) using R32 refrigerant. As shown in Figure 2 (b), as the evaporator temperature increased, the irreversibilities values of all compressors decreased.
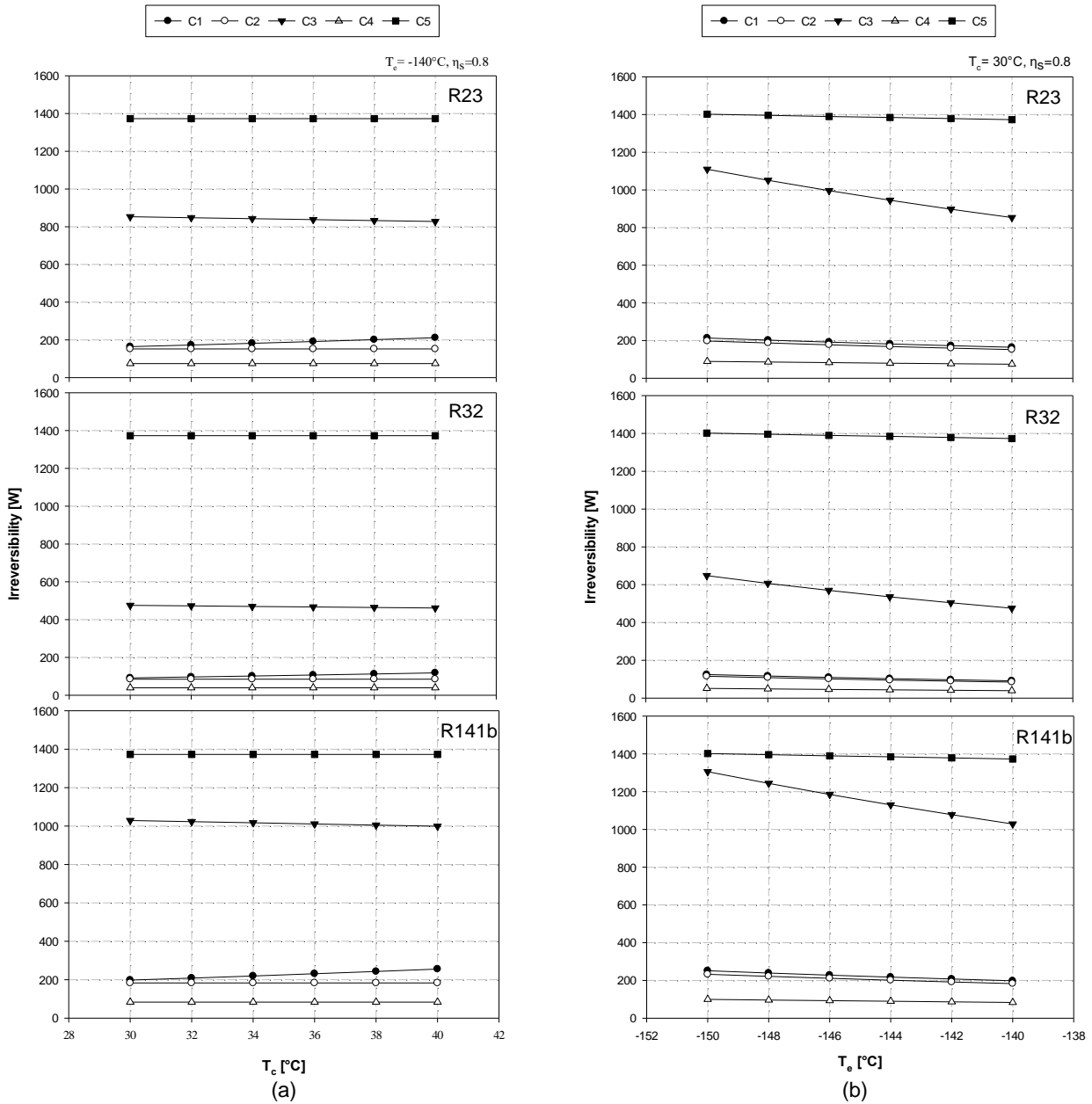
Figure 2: Variation of the irreversibility of the compressors according to condenser (a) and evaporator (b) temperatures

The variation of irreversibility four-stage cascade refrigeration cycle integrated Linde-Hampson with the condenser temperatures as a function of different refrigerants is shown in Figure 3. The condenser temperature varied between 30-40°C. The evaporator temperature of the cascade system was kept constant at -140°C and isentropic efficiency at 0.8. As the condenser temperature increased while evaporator temperature was kept constant, the pressure value at the compressor outlet increased. As a result, the maximum amount of entropy generation was obtained in the fourth stage cycle by using R141b as the refrigerant, while the minimum amount of entropy generation was obtained using the R32 refrigerant. The total entropy values of the system were close to each other by using refrigerants R23 and R141b, for these refrigerants can be alternatives to each other.
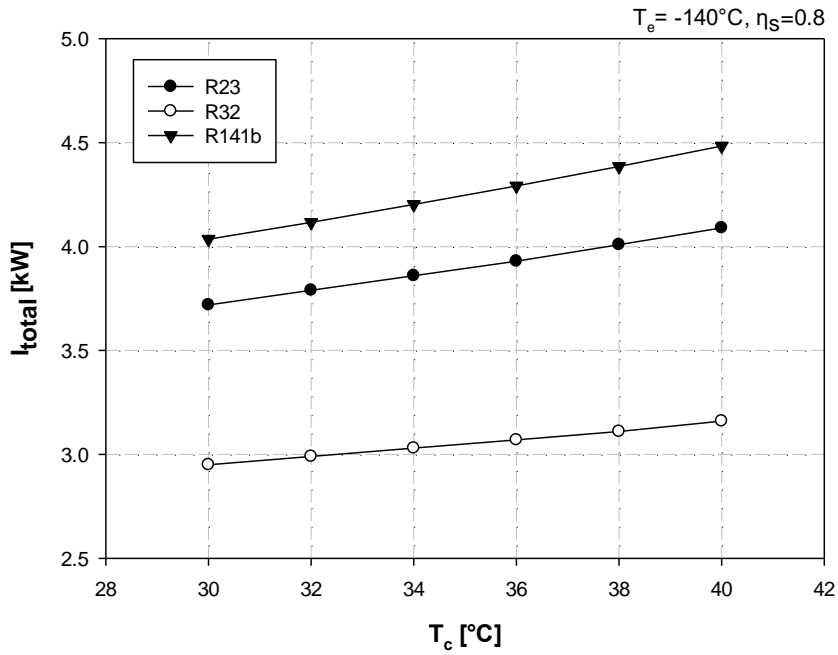
Figure 3: Variation of total irreversibility of the system according to the condenser temperatures

The variation of irreversibility four-stage cascade refrigeration cycle integrated Linde-Hampson with the evaporator temperature as a function of different refrigerants is shown in Figure 4. The evaporator temperature varied from -140°C to -150°C while the condenser temperature of the cascade system was kept constant at 30°C and isentropic efficiency at 0.8. As the evaporator temperature increased, the amount of energy withdrawn from the working fluid to be liquefied increased. The highest system irreversibility occurred when using the R141b refrigerant. The irreversibility of the system decreased by 10% in increasing the evaporator temperature when using R141b refrigerant. The lowest system irreversibility occurred when using R32 refrigerant. The irreversibility of the system was reduced by 7% by increasing the evaporator temperature when using R32 refrigerant.

T_c= 30°C, η_S=0.8
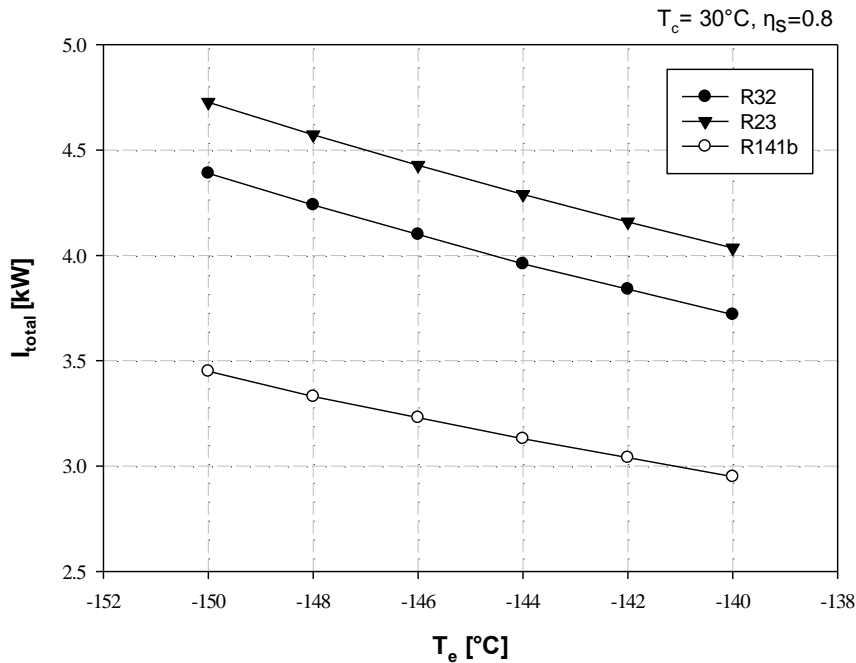
Figure 4: Variation of total irreversibility of the system according to the evaporator temperature
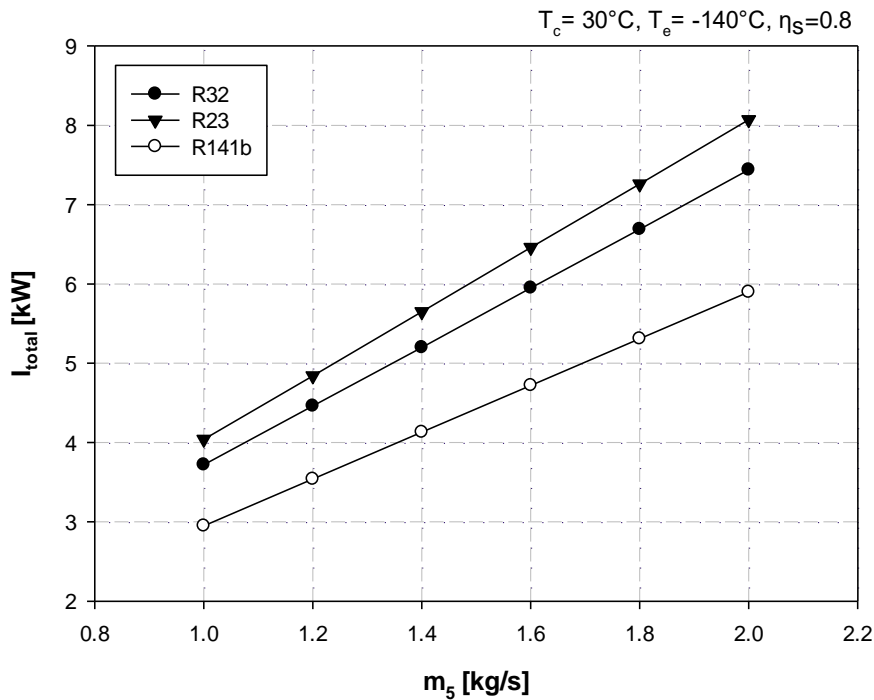
Figure 5: Variation of total irreversibility of the system as a function of the mass flow of methane gas

The change of total irreversibility of the system as a function of the mass flow rate of methane gas is shown in Figure 5. The mass flow rate changed from 1 kg/s and 2 kg/s while the evaporator and condenser temperatures and isentropic efficiency were kept constant. As the mass flow rate of the methane gas increased, the total amount of irreversibility increased for the refrigerants such as R23, R32, and R141b. The total irreversibility of the system in the temperature range studied was almost the same for all refrigerants. When the mass flow rate increased by 100%, the total irreversibility increased by 100%. The highest system irreversibility occurred when using R23 refrigerant, while the lowest system irreversibility occurred when using R141b refrigerant.

4. CONCLUSIONS

The irreversibility of the four-stage cascade vapour compression refrigeration cycle integrated into the Linde–Hampson cycle and the irreversibility of the system components were investigated for the variation of the mass flow rate of liquefied methane gas, the different condenser and evaporator temperatures of the cascade system. The results obtained are summarised below,

- The lowest system irreversibility occurred when R32 refrigerant was used for the increasing values of the condenser. Also, the lowest system irreversibility occurred when R141b refrigerant was used for the increasing values of evaporator and mass flow of methane gas;
- The highest system irreversibility occurred when R141b refrigerant was used for the increasing values of the condenser. Also, the highest system irreversibility occurred when R23 refrigerant was used for the increasing values of evaporator and mass flow of methane gas;
- The highest irreversibility in the compressor (C5) system component occurred when the R23, R32 and R141b fluid was used;
- The lowest irreversibility in the fourth compressor (C4) component of the system occurred when R32 fluid was used.

5. REFERENCES

Boahen, S., & Choi, J. (2017). Research trend of cascade heat pumps. *Science China Technological Sciences*, *60*(11), 1597–1615. https://doi.org/10.1007/s11431-016-9071-7

Dadsetani, R., Sheikhzadeh, G. A., Safaei, M. R., Alnaqi, A. A., & Amiriyoon, A. (2019). Exergoeconomic optimisation of liquefying cycle for noble gas argon. *Heat and Mass Transfer/Waerme- Und Stoffuebertragung*, *55*(7), 1995–2007. https://doi.org/10.1007/s00231-018-2501-5

Dincer, I., & Rosen, M. A. (2013). Exergy and Energy Analyses. In *Exergy*. https://doi.org/10.1016/b978-0-08-097089-9.00002-4

Jerome, S., & Venkatarathnam, G. (2019). Performance of a Linde-Hampson refrigerator operating from –120 °C to –60 °C with optimised R14-hydrocarbon mixtures exhibiting vapour-liquid-liquid equilibria. *Heat and Mass Transfer*. https://doi.org/10.1007/s00231-019-02801-z

Kanoglu, M., Dincer, I., & Cengel, Y. A. (2008). Investigation of geothermal energy use in gas liquefaction. *Heat Transfer Engineering*, *29*(10), 885–892. https://doi.org/10.1080/01457630802125781

Kilicarslan, A. (2004). An experimental investigation of a different type vapor compression cascade refrigeration system. *Applied Thermal Engineering*. https://doi.org/10.1016/j.applthermaleng.2004.04.004

Kilicarslan, A., & Hosoz, M. (2010). Energy and irreversibility analysis of a cascade refrigeration system for various refrigerant couples. *Energy Conversion and Management*, *51*(12), 2947–2954. https://doi.org/10.1016/j.enconman.2010.06.037

Maiti, T. K., Pal, S., Kundu, B., & Ghosh, P. (2019). Evaluation of an existing helium liquefier in refrigerator and mixed-mode operation through exergy analysis. *Cryogenics*, *103*, 102977. https://doi.org/10.1016/j.cryogenics.2019.102977

Palizdar, A., Ramezani, T., Nargessi, Z., AmirAfshar, S., Abbasi, M., & Vatani, A. (2017). Thermodynamic evaluation of three mini-scale nitrogen single expansion processes for liquefaction of natural gas using advanced exergy analysis. *Energy Conversion and Management*, *150*, 637–650. https://doi.org/10.1016/j.enconman.2017.08.042

Yılmaz, C. (2019). THERMODYNAMIC PERFORMANCE ANALYSIS OF GAS LIQUEFACTION CYCLES FOR CRYOGENIC APPLICATIONS. *Journal of Thermal Engineering*, *5*(1), 62–75. https://doi.org/10.18186/thermal.513038

Yuksel, Y. E., Ozturk, M., & Dincer, I. (2017). Analysis and assessment of a novel hydrogen liquefaction process. *International Journal of Hydrogen Energy*, *42*(16), 11429–11438. https://doi.org/10.1016/j.ijhydene.2017.03.064

#40: Engineered Cementitious Composite (ECC) with high-calcium fly ash for sustainable development and energy saving

Indra KOMARA[1,2], Priyo SUPROBO[1], Pujo AJI[1], Data IRANATA[1], Kivanc TASKIN[3]

[1]Institut Teknologi Sepuluh Nopember, Surabaya, Indonesia
[2]Institut Teknologi Adhi Tama Surabaya, Indonesia
[3]Eskisehir Technical University, Eskisehir, Turkey

Abstract: In the near future, the key for the civil engineering community will be to accomplish project objectives in line with the concept of sustainable development and energy-saving, which will require the use of high-performance materials manufactured at a fair price with the smallest possible environmental impact. As a novel eco-friendly material, Engineered Cementitious Composite (ECC) offers to solve the problems both of sustainable development and energy saving because of its potent ability to manage crack width, good behaviour of flexural toughness, and improved durability performance. The partial replacement of fly ash for cement in ECC minimizes environmental pollution and conserves natural resources, and is gaining increased attention in the construction practice. This study presents the experimental findings on the influence of high calcium fly ash on the mechanical properties of ECC. By employing micromechanics-based material design under different w/c content from 0.28 to 0.32, ductility in excess of 3% under uniaxial tensile test can be attained, and the multiple micro cracking behaviour response can be achieved. The experimental program also conducted sorptivity and water absorption tests to determine the capillary suction and its capacity. It was indicated from the experiment that the sorptivity rate off ECC considered by the initial cracking had no relation with w/c (water to cement) ratio using high calcium fly ash. Furthermore, rapid chloride penetration and chloride diffusion also added to corroborate findings. The result for all mixtures satisfied low chloride ion penetrability levels in accordance with ASTM C1202.

Keywords: Engineered Cementitious Composite (ECC); high calcium fly ash; multiple cracking; ductility; durability; sustainable development

1. INTRODUCTION

The first Engineered Cementitious Composites (ECC) were developed in the 1990s. The development of ECC not only enhanced the ductility of conventional concrete and brought a new field of fibre-reinforced concrete, but also displayed good tensile strain capacity and the ability to manage micro-crack width with adequate fibre content (2 percent volume fraction) (Lepech *et al.*, 2008; Li, M. *et al.,* 2009; Li, V.C., 2004a; Li, V.C., 1994). ECC exhibits unique strain-hardening behaviour due to an intentional design based on an understanding of micromechanics between fibre, matrix, and fibre–matrix interface (Li, V.C. *et al.*, 2004b; Wang & Li, 2007). Under tensile stress, ECC exhibits tensile strain-hardening behaviour and generates a tensile strain capacity in the range of 2–7 percent, in contrast to 0.01–0.05 percent for conventional concrete and fibre-reinforced concrete (FRC). Figure 1 illustrates the distinction between the typical tensile stress–strain curves of conventional concrete, FRC, and ECC (Fischer & Li, 2003). Normal concrete is a brittle material, and the emergence of cracks is followed by an abrupt decrease of load carrying capacity. Although the addition of fibre improves tensile strength and fracture toughness to some degree, FRC remains a quasi-brittle material with strain-softening single-cracking behaviour under tension. In contrast, ECC has a metallic quality. After the formation of the first fracture in ECC, the tensile load-carrying capacity rises as strain increases due to a multiple-cracking process with tight control over crack width. Without steel reinforcement, the crack width of ECC is self-controlled to below 100m, which is significantly less than the normal crack width observed in regular concrete and FRC (Wang & Li, 2019; Weimann & Li, 2003; Xiao *et al.*, 2021).
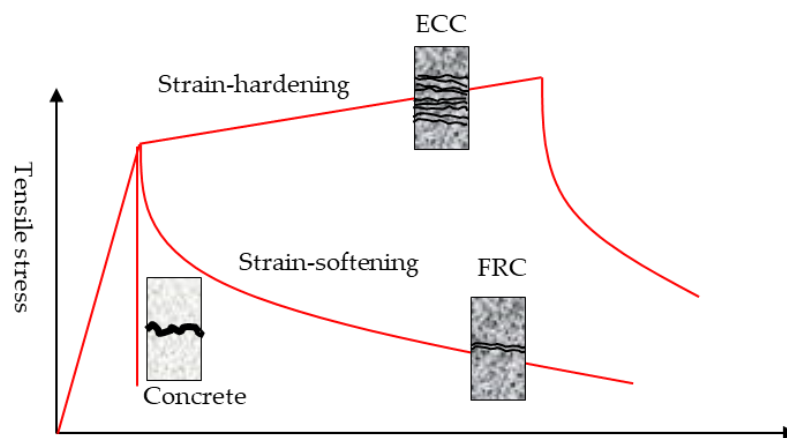
Figure 1: Tensile stress-strain of concrete, FRC and ECC (Fischer & Li, 2003)

ECC's unique tensile strain-hardening behaviour and tight crack width control derive from a complex design using micromechanics to adjust fibre, matrix, and fibre–matrix interface interaction (Li, V.C., 2003). Fibre-bridging qualities affect ECC's tensile strain-hardening. When ECC is stretched, its weakest cross-section cracks. This crack's fibre bears the tensile load. Thanks to engineered steady-state cracking, this fibre can carry a growing load, causing new fractures at other places (Fischer & Li, 2002; Li & Yang, 2017). ECC demonstrates tensile strain-hardening multiple-cracking by repeating this process. In the past few years, due to its exceptional crack-controlling ability, high ductility, high tensile strain, and self-healing capability, ECC has become a potentially ideal material that has been extensively used in civil engineering projects (Hua, 2010; Li, M. *et al.*, 2009), such as for the retrofitting and repair of highway bridges (Lepech *et al.*, 2008). A new use of ECC is as a protection cover to improve structural durability (Bastian *et al.*, 2020; Komara *et al.*, 2020; Komara *et al.*, 2019a; Mooy *et al.*, 2020; Oktaviani *et al.*, 2020), and the results have been reported as positive. In addition, the use of significant quantities of industrial by-products to partially replace the high amounts of Portland cement in the mixture proportions of ECC is a crucial factor in the promotion of ECC. Due to the economic and environmental benefits, the utilization of various supplemental cementitious materials as partial Portland cement substitution has been extensively explored (Li & Yang, 2017; Li, V.C., 2003; Ranade, 2014).

As an industrial pollutant, fly ash (FA) has been employed in civil engineering for almost 50 years, mainly as a replacement for Portland cement in concrete (Zhao *et al.*, 2020). FA has pozzolanic activity, therefore cement-based materials containing FA create secondary calcium-silicate-hydrate (C-S-H) gels by reacting with $Ca(OH)_2$, which increases density and strength (Ammasi & Ragul, 2018; Hu *et al.*, 2019). Many investigations have shown that adding FA and other supplemental cementitious materials can drastically improve fibre-matrix bonding, fill voids, increase compactness, aid expand micro-cracks, and improve ductility and toughness (Atiş, 2003; Bilodeau & Malhotra, 2000; Hwang & Shahsavari, 2019). Previous investigations showed that FA fluctuation affected the workability of ECC mixes. Some researchers studied the impacts of FA type, FA/cement ratio, and water/cement ratio on ECC characteristics (Kusuma *et al.*, 2012; Zeggar *et al.*, 2019; Zhao *et al.*, 2020). Physical and chemical features of FA affected the performance of fresh and hardened composites and class F-FA produced ECC better than class C-FA in this investigation. Yu *et al.* improved ECC's compressive strength and tensile properties. Under the study of FA composition, ECC could achieve 49.4 MPa at 7 days and 69.2 MPa at 28 days, with an ultimate tensile strain of more than 3.5 percent at 28 days (Yu *et al.*, 2018). Şahmaran *et al.* created ECC mixes to study the effect of FA and fibres on cyclic freeze-thaw resistance and microstructure (Şahmaran *et al.*, 2009, 2011, 2012). Both ECC combinations

with significant volumes of FA demonstrated a tensile strain capacity of over 2% after 300 freezing and thawing cycles.

FA also improves self-healing behaviour due to tighter fracture width and a higher volume of hydration reaction cementitious material available for continued hydration (Krykowski *et al.*, 2020). Zhang *et al.* created three ECC mixes with varied amounts of FA to study mechanical characteristics and self-healing (Zhang *et al.*, 2018). ECC mixtures with FA/cement ratios of 4.0, by weight, had the optimum self-healing tendency. Şahmaran found that micro-cracked ECC mixes could still gain high tensile stress and strain and restore practically the original stiffness, demonstrating exceptional self-healing. FA's impact on ECC's mechanical properties cannot be overlooked and is worthy of more study (Yıldırım *et al.*, 2018). Previous research on the effect of FA on ECC performance generally focused on volume, whereas calcium content was neglected. Due to the ready availability of high calcium content fly ash as a waste material from Industrial activities, it is necessary to conduct research on the use of this type of material.

Consequently, to contribute to sustainable development and energy saving by partially using cement, a series of comprehensive experiments were undertaken to determine the influence of the calcium content of FA on ECC. This study aimed to investigate the mechanical properties of ECC with different w/b (water to binder) content to reveal its effect and properties on uniaxial tensile and four-point bending properties of ECCs. First, the micromechanics design of ECC was briefly reviewed, then the proposed mix design and experimental program was conducted. The experimental results of uniaxial tests, bending and compressive test are presented in this paper. Key durability analysis was also addressed to investigate the behaviour such as sorptivity, water absorption, rapid chloride penetration test and chloride diffusion.

2. MATERIALS AND METHODS

The experimental program involved sets of material preparations followed by a set of experimental programs.

2.1. Materials and preparations

In this investigation, four cementitious matrix were used with different water to binder ratios; the proportions are listed in Table 1. The matrix was composed of ordinary Portland cement, fly ash with high calcium content, polyvinyl alcohol (PVA) fibres. Additionally, a polycarboxylate-based high-range water-reducing (HRWR) was used to regulate the fresh characteristics of the mixes to reach flowability. PVA fibres were used in the experimental program, and the properties are given in Table 2. Fibre PVA was the 1.2 w% oil coated PVA fibre with a surface oil coating of 1.2% by weight, and this type of fibre has been widely used as a matrix in ECC concrete. This fibre was manufactured by Kuralon-kuraray, a Japanese manufacturer. The tensile strength and elastic modulus respectively, 41 GPa and 1600 MPa. The fly ash mixed with water to binder ratio accordingly given as 0.28, 0.30 and 0.32. The fly ash taken from, PT Wika Beton Persero Tbk, one of leading industry of concrete manufacture in Indonesia. Table 3 presented the information on the chemical compound of cement and fly ash obtained by XRF.The effect of water to binder ratio on the ECC properties was studied. Considering, PVA fibre content 2% by volume and fly ash to cement ratio accordingly for all mixes.

To process all mixes, in a 5-L mixer, powder materials and water were first combined at low speed for 1 to 2 minutes, followed by 2 minutes at high speed. Then, within one minute of mixing at a slow speed, the fibre was added uniformly. HRWR also added by easy stage to see workability of the ECCs. Lastly, high-speed mixing is continued for a further 2 minutes.

Cube specimens with dimension of 50×50×50 mm was prepared for compression and dogbone shape specimens were prepared for uniaxial tension test, recommended by Japan Society of Civil Engineers (Rokugo *et al.*, 2007), see Figure 2a. In addition, for bending test, plate specimens of 300×75×30 mm was prepared (see Figure 2b). The specimens were then cured in temperature-controlled chamber with 20±5°C and relative humidity 95% for 24-hour. After demoulded, the specimens were placed in water box, fully submerged on the water with temperature 20±5°C until 28-day. For key durability test, cylinder specimens with dimension 300×150 mm was prepared then slices into three specimen as the evaluation parameter.

2.2. Experimental Program

Compression and four-point bending test

Three cube specimens were prepared and used for compression test. Compression tests were conducted using load control distribution with a loading speed of 2400 N/s in accordance with ASTM C109 (ASTM C109/C109M-02, 2020). The loaded area was according to specimen dimension with 50 x 50mm. Each mixture was classified to have three cube specimens, and compressive strength then evaluated and calculated by averaging the result.

Table 1: Mixture design proportion of ECC specimen

Mix proportion of ECC (mass ratio)						
Type No.	Cement OPC	Silica Sand	Fly ash	Water	HRWR[a]	Fibre/vol%
ECC-1	0.707	0.672	0.707	0.172	0.021	2.0
ECC-2	0.690	0.660	0.690	0.182	0.016	2.0
ECC-3	0.673	0.648	0.673	0.190	0.012	2.0

[a] HRWR: high range water reducer

Table 2: Properties of PVA fibre

Density/g/cm³	L/mm	D/µm	Aspect ratio	Strength/MPa	E/GPa	Elongation/%
1.3	8	40	480	1600	41	6

Table 3: Chemical compound of cement OPC and fly ash

Ingredients	Compositions (wt.%)								
	CaO	SiO_2	Al_2O_3	Fe_2O_3	MgO	SO_3	K_2O	P_2O_5	TiO_2
Cement OPC	62.87	20.33	3.1	4.81	0.1	2.5	0.45	0.075	0.43
Fly ash	27.70	23.8	7.0	31.4	1.2	0.5	1.17	0.70	1.20
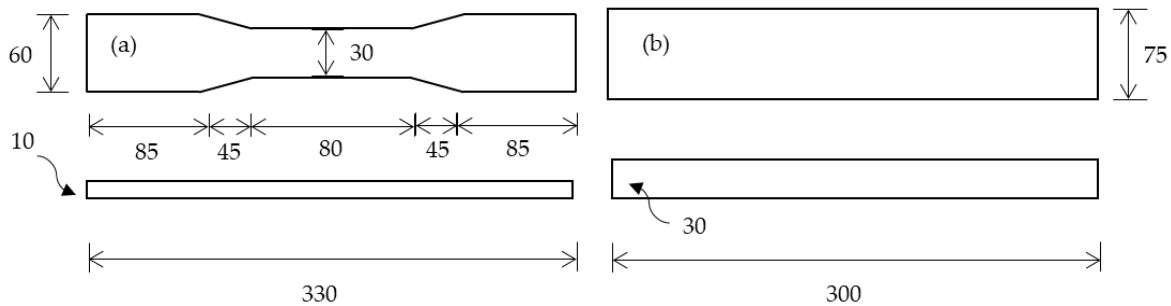
Figure 2: Dimension of ECC specimen; (a) dog-bone for uniaxial tensile test, (b) ECC plate for four-point bending test (all dimensions are in mm)

Then, a plate specimen was used in a four-point bending test for evaluating flexural strength in accordance with engineering fracture mechanics (Wu *et al.*, 2020; Yin *et al.*, 2019). The support span was 270mm, and the loaded point was positioned in between the span near to the mid of support span, which was 90mm each. The test was conducted under load control with a loading speed of 50 N/s. Three specimen were prepared and used for each mixture, and the flexural strength was evaluated by averaging the result of the measurements.

Uniaxial tension test

Uniaxial tensile test with dog bone-shape specimens were conducted to investigate the tensile properties of ECC. The test procedure was almost the same for the two types of specimens. The two ends of the dog bone specimens were placed in steel clamps; the upper and lower clamps were interconnected to the uniaxial loading machine with pin joint and fixed joint, respectively. Two extensometers were attached on the specimen to measure the deformation, and the gauge length was 50mm. The tests were conducted under displacement control with a loading speed of 0.005 mm/s. The evaluation of the experimental results of each mixture were calculated by averaging the data.

Sorptivity and water absorption

The sorptivity test was conducted in accordance with ASTM C1585 (ASTM C1585, 1989). The objective was to measure the rate of absorption by measuring the increase in mass caused by water absorption. Prior to testing, a 300 x 150mm ECC cylinder that had been stored at 50 ± 2°C for three days after curing was split into 67mm thick pieces and each was weighed to determine its mass. Each specimen was covered with weatherproof epoxy except the bottom side, to ensure that the suction come only from one side of the specimen. The specimen's top and circumferential surfaces were also coated in plastic to avoid evaporation caused by environmental exposure. The absorption included levelling tap water to reach 1 to 3mm from the bottom of specimen. The test involved the measurement of mass at given intervals.

The water absorption test was performed according to ASTM C642 (ASTM C642, 2006) as a general method for determining the proportion of absorption and voids in hardened ECC. In this test, the specimen was sliced similarly to sorptivity specimens; however, it was oven-dried at 100 to 110°C for at least 24 hours to calculate its oven dry mass. The measurement was then performed following removal from the oven at a temperature of 25 degrees Celsius. For control reasons, the oven-dry mass was compared with the original mass of the specimen until the maximum difference value of 0.5% was attained. During this technique, the specimen was placed in a container and immersed in water at roughly 21°C for 174 hours, or until two values of mass taken at 24-hour intervals revealed a rise in mass of less than 0.5%, thereby defining the saturated stage.

Rapid chloride penetration

The rapid chloride penetration test is widely recognized as one of the most important factors in determining the durability performance of concrete due to the ingress of a corrosive agent to approve its sustainability and its energy saving parameter. This test followed the designation of ASTM C1202 – 05 (ASTM C1202 - 05, 2005) measures the amount of time it takes for a corrosive agent to penetrate the ECC. The categorization of charge passed in coulombs, as shown in Table 4, was used to determine the qualitative indications of chloride ion penetrability. The charge that was transferred, denoted by Q and measured in coulombs, was determined using the trapezoidal rule and an expression is written in Equation (1).

Table 4: Charge passed chloride ion penetration

(ASTM C1202 - 05, 2005)	
Charge passed (coulombs)	Chloride ion penetrability
> 4000	High
2000–4000	Moderate
1000–2000	Low
100–1000	Very Low
< 100	Negligible

$$Q = 900(I_0 + 2I_{30} + 2I_{60} + \cdots + 2I_{300} + 2I_{330} + I_{360} \tag{1}$$

where I_0 was the current (amperes) immediately after voltage was applied and I_t was the current (amperes) at t (minutes) after the voltage was applied. Aside from the rapid chloride penetration, it was also considered to be important to address the chloride diffusion coefficient as it provides critical information of chloride ions speed penetrating in the ECC concrete, since its mixture proportion is different from normal concrete.

Diffusion coefficient is determined by measuring the concentration of chloride ions on the surface of the cylinder specimen after the rapid chloride penetration and is calculated using these following expressions Equation (2) – (4):

$$D = \frac{RTL}{zFE}\left(\frac{x_d - \propto \sqrt{x_d}}{t}\right) \quad (2) \qquad \propto = 2\sqrt{\frac{RT}{zFE}} erf^{-1}\left(1 - \left(\frac{2C_d}{C_0}\right)\right) \quad (3) \qquad E = \frac{U-2}{L} \quad (4)$$

where D is the non-steady-state chloride diffusion coefficient (m^2/sec); R is gas constant (=8.314 (J/(°K mol))); T is the average (absolute) value of the initial and final temperature (K); z is the absolute value of chloride ion (=1); F is Faraday constant (=9.648×10^4 (J/(V mol))); E is the electric field (V/m); U is the absolute value of the applied voltage (V); L is the thickness of the specimen (m); x_d is the average value of the penetration depth (m); $\propto$ is laboratory constant (m$^{1/2}$) calculated based on equation 2(b); t is test duration (sec); erf^{-1} is the inverse of error function; C_d is chloride concentration at which the colour changes (mol/dm^3); and C_0 is chloride concentration in cathode solution (mol/dm^3).

3. RESULTS AND DISCUSSION

In the design of the combination for ECC materials, it is common to find a high percentage of cement. This study provides evidence that it is possible to develop environmentally friendly ECCs that preserve the tensile and ductile properties of conventional ECCs while also taking into account environmental concerns according to a high amount of fly ash. The effects of using fly ash on the crucial micromechanics parameters governing composite ductility were systematically researched and efficiently used to guide the mixture design. These parameters govern how easily a composite may be deformed. A micromechanics-based method like this one can also be used for the creation of other types of material practice. The development of more environmentally friendly ECCs will boost the sustainability of infrastructure by simultaneously improving the infrastructure's capacity and the material's level of greenness.

Table 5: Average flexural bending test result under the variations of mixture with different w/b ratio at 28-day

Mixture	w/b content	Ultimate load (kN)	Mid-span deflection at ultimate load (mm)	Flexural strength (MPa)	Standard deviation	CV (%)
ECC-1	0.28	3.25	7.45	13	0.16	5.14
ECC-2	0.30	2.98	4.89	12	0.38	5.86
ECC-3	0.32	2.84	2.84	11	0.18	5.54

Table 6: Average uniaxial tensile test and compressive test result under the variations of mixture with different w/b ratio at 28-day

Mixture	Compressive strength (MPa)	First cracking strength (MPa)	Ultimate tensile stress (MPa)	Tensile strain capacity (%)	Standard deviation	CV (%)
ECC-1	50.2	2.27	4.98	3.01	0.67	21
ECC-2	48.7	3.31	5.11	1.82	0.86	29
ECC-3	46.2	3.25	5.35	1.56	0.81	35
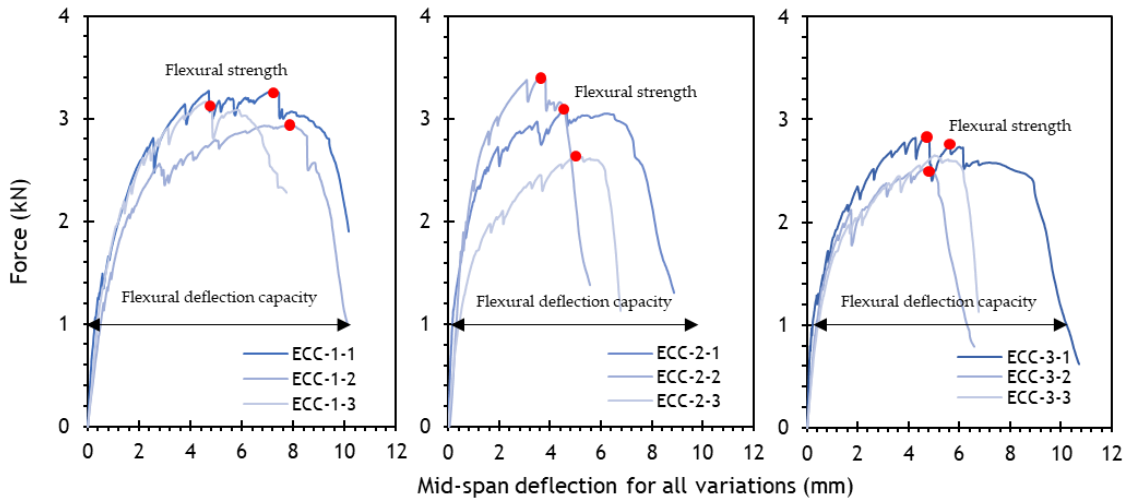
Figure 3: Typical flexural deflection capacity curve of the ECC obtained from flexural bending test of ECC plate under different w/b ratio
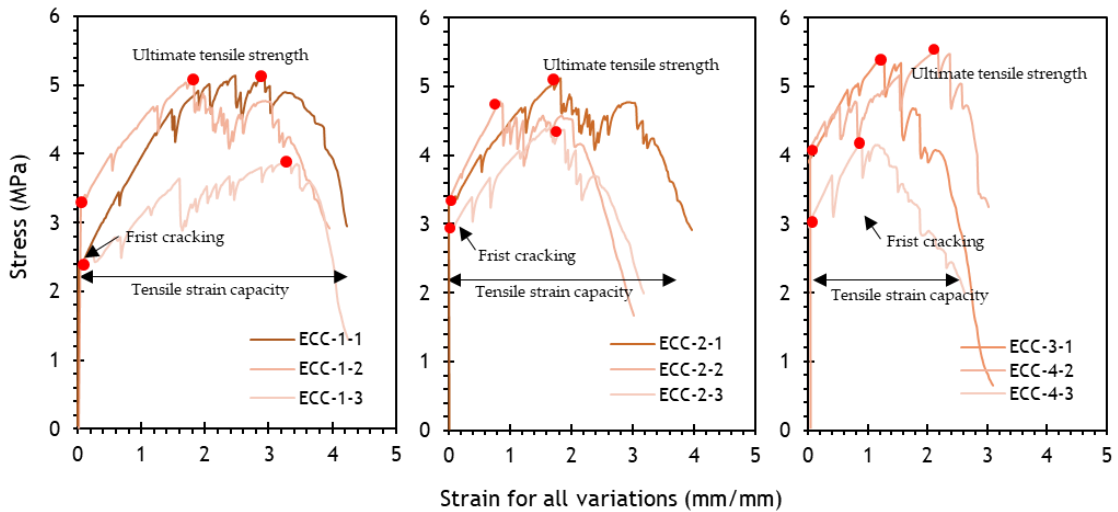
Figure 4: Typical tensile stress-strain curve of ECC obtained from uniaxial test with dog bone specimen under different w/b ratio
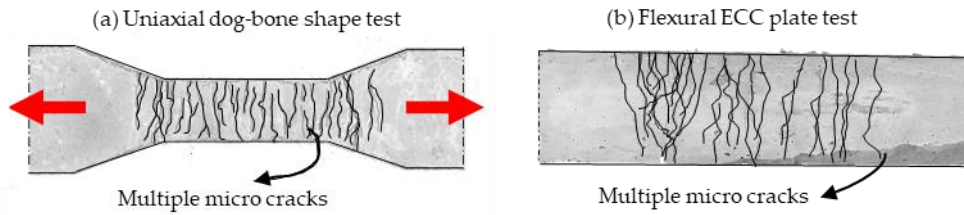
Figure 5: Typical Illustrated crack pattern on the ECC surface after loading application

In general, given the same fly ash content and fibre content with different w/b ratio, the specimens exhibited slightly different results; when the w/b ratio was higher, the flexural strength decreased. The results can be seen in Table 5. The flexural strength under w/b 0.28 was 13 MPa but when it is was w/b 0.32 the flexural strength decreased to 11 MPa. A similar illustration is seen in the ultimate load, where a higher load carrying capacity arrives from a smaller w/b ratio. The variety of result under flexural deflection capacity is illustrated in Figure 3. It can be seen that the degradation of flexural capacity is related to the increasing of w/b content.

Table 6 gives the 28-day tensile properties of developed ECC using different w/b ratios. The same behaviour as seen with flexural strength is also illustrated in this test result, when a lower w/b ration gives higher tensile strain capacity with 3% compared to the other mixtures with the tensile strain below 2%. As w/b ratio increased from 0.28 to 0.32, the ultimate tensile strength increased from 4.98 MPa to 5.35 MPa and then decreased when w/b ratio 0.34 with the value 4.72 MPa. Table 6 illustrates the 28-day compressive strength of ECC with different ratios of w/b. It also presents behaviour typical to the previous two results, which is shows higher w/b content resulting in lower compressive strength, respectively from 50.2 MPa to 45.4 MPa.

A typical tensile stress-strain curve of the ECC obtained from uniaxial tensile test with dog bone-shape specimens is presented in Figure 3. The maximum tensile stress in tensile stress-strain curves is defined as ultimate tensile strength, and the corresponding strain is defined as tensile strain capacity. Regarding Figure 4, all tensile properties met the conditions of ECC concrete with the strain capacity greater than normal concrete: the higher strain capacity was 3% more using w/b content 0.28 while the other mixtures, 0.30 to 0.32 w/b ratio achieved tensile strain capacity of 1.84% to 0.98%. All mixtures with 1.8 FA/C content and 2% fibre exhibited strain-hardening multiple cracking behaviour. Apparently, due to the use of high-calcium fly ash content, the multiple cracking was not as prolific as the ECC using low calcium fly ash content. As w/b ratio increased, the tensile stress-strain became more pronounced to low strain-hardening multiple cracking behaviour, manifested as lowering tensile strain capacity and decreasing the number of cracks. An acceptable strain-hardening multiple-cracking behaviour of ECC was achieved when w/b content was 0.28 and 0.30. The illustrated multiple cracks for both uniaxial dog bone shaped specimen and flexural plate specimen can be seen in Figure 5. From that figure, it can be determined that ECC materials can support sustainable improvement related to its capacity to withstand a certain load with fewer crack width.

Given the same conditions, ECC with variation w/b 0.28 exhibited with 4.98 MPa slightly lower than the ultimate tensile strength of w/b 0.30 and 0.32, with 5.11 MPa and 5.35 MPa, respectively. In fact, comparing all mixtures, ECC with w/b 0.28 implied greater tensile strain capacity, while the number of multiple cracking in w/b 0.28 appeared to present better behaviour than that in the later w/b variations. It was concluded that a developed ECC using high calcium content fly ash to conserve sustainable development and energy saving, up to a certain fly ash content, could exhibit multiple-cracking behaviour and tensile-hardening behaviour. Different w/b content led to different ECC tensile properties.

To see the full behaviour, sorptivity and water absorption tests were also considered as relative measure of water transport associated with capillary suction. Figure 6 presents the volume of penetrable pores from water sorptivity of the ECC mixtures determined by a variety of cycle times under a 28-day curing period. The test involved measuring the mass of cylinder specimens at given time intervals, which were 1, 5, 10, 20, 30, 60, 120, 180, 240, 300 and 360 minutes for the first cycle. Following 30 hours later, the second cycle had time intervals of 30, 54, 102, 126, 150 and 174 hours, allowing for water absorption through capillary suction. The rate of absorption was measured through the change in mass (gram) at the time divided by the cross-sectional area of the specimen (mm^2) and the density of water (g/mm^3).

Typical data of the cumulative sorptivity and water absorption are shown in Table 7 and Table 8. It can be calculated that the cumulative volume of water absorbed per unit surface area in the specimen increased with square root of time. The water absorption was considered to increase fairly when the number of cracks on the surface specimen increased. The initial rate of water absorption was very fast thereby implying that the initial crack of the ECC specimen and capillary pores were saturated in a very short time compared to the immersion after 174-hour. According to a previous study using the same local materials (Bastian *et al.*, 2020; Komara *et al.*, 2019a; Mooy *et al.*, 2020), typical sorptivity was 0.5mm for normal concrete with a w/c ratio of 0.28 and 0.48mm for concrete with supplementary cementitious fly ash under the same w/c ratio. Therefore, the measured sorptivity of about 0.28mm for these ECC specimens with w/cm ratio 0.28 – 0.32 was significantly lower than for normal concrete at nearly half within the value

0.28mm. The variation of w/cm had very little difference. The reason for the lower sorptivity and water absorption of ECC may be attributed to a high amount of calcium fly ash content and absence of coarse aggregate. The use of high calcium fly ash probably resulted in a dense matrix by reducing the pore size and thickness of the transition zone between fibre and surrounding cementitious matrix. According to Mehta and Monteiro, the appearance of microcracks in the interfacial transition zone with coarse aggregate is the principal reason why concrete is more permeable than hydrated cement paste and mortar (Mehta & Monteiro, 2001). Concrete would be poorer and more porous if the aggregate size was larger, all other factors being approximately equivalent.
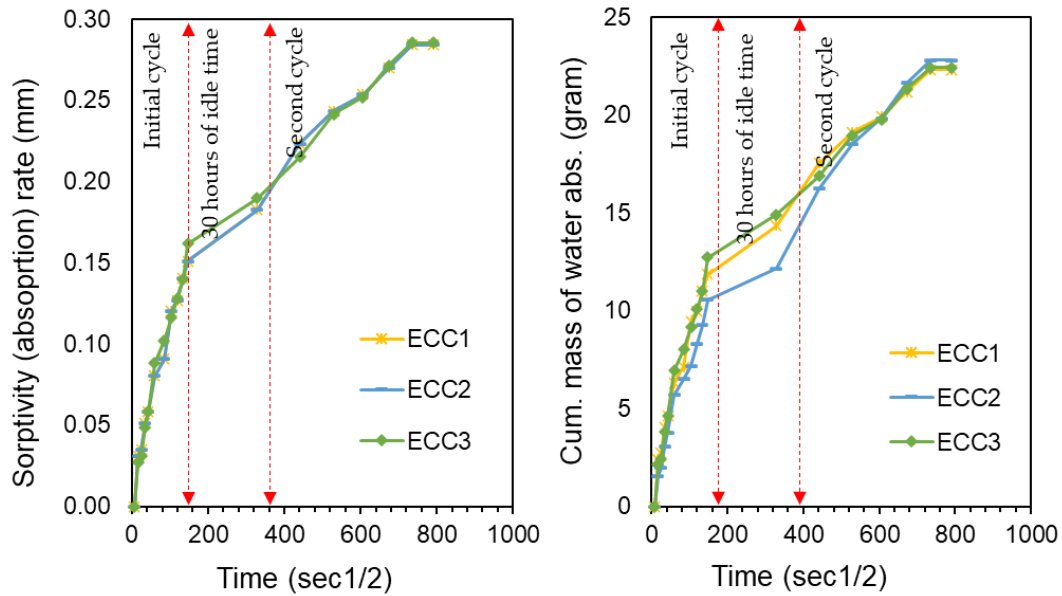
Figure 6: Relationship of sorptivity and water absorption rate vs time

Table 7: Sorptivity rate of ECC specimen under circulated time to 7-day

Test Time		Time	Mass			Δ Mass			Δ Mass/area/density of water, *I*		
Day	s	$s^{1/2}$	(g)			(g)			(mm)		
	Specimen No.		1	2	3	1	2	3	1	2	3
	0	0	966.3	1132.2	990.4	0.0	0.0	0.0	0.00	0.00	0.00
	60	8	966.3	1132.2	990.4	0.0	0.0	0.0	0.00	0.00	0.00
	300	17	968.7	1133.8	992.5	2.4	1.6	2.1	0.03	0.02	0.03
	600	24	969	1134.2	992.8	2.7	2.0	2.4	0.03	0.03	0.03
	1200	35	970.3	1135.3	994.2	4.0	3.1	3.8	0.05	0.04	0.05
	1800	42	970.9	1136	995	4.6	3.8	4.6	0.06	0.05	0.06
	3600	60	972.6	1137.9	997.3	6.3	5.7	6.9	0.08	0.07	0.09
	7200	85	973.4	1138.7	998.4	7.1	6.5	8.0	0.09	0.08	0.10
	10800	104	975.7	1139.4	999.5	9.4	7.2	9.1	0.12	0.09	0.12
	14400	120	976.2	1140.5	1000.5	9.9	8.3	10.1	0.13	0.11	0.13
	18000	134	977.3	1141.5	1001.4	11.0	9.3	11.0	0.14	0.12	0.14
	21600	147	978.1	1142.8	1003.1	11.8	10.6	12.7	0.15	0.13	0.16
1	108000	329	980.6	1144.3	1005.3	14.3	12.1	14.9	0.18	0.15	0.19
2	194400	441	983.8	1148.5	1007.3	17.5	16.3	16.9	0.22	0.21	0.21
3	280800	530	985.4	1150.8	1009.4	19.1	18.6	19.0	0.24	0.24	0.24
4	367200	606	986.2	1152.1	1010.2	19.9	19.9	19.8	0.25	0.25	0.25
5	453600	673	987.5	1153.9	1011.7	21.2	21.7	21.3	0.27	0.28	0.27
6	540000	735	988.6	1155	1012.8	22.3	22.8	22.4	0.28	0.29	0.28
7	626400	791	988.6	1155	1012.8	22.3	22.8	22.4	0.28	0.29	0.28

Table 8: Water absorption rate after 174-hour immersion

Sample	Dimension		Sample Weight (gram)			Percentage of absorption after immersion (%)
	Diameter (cm)	Height (cm)	Initial mass (g)	24-h oven-dry mass, *A* (g)	174-hr mass after immersion, *B* (g)	
ECC1	10.02	6.4	962.55	961.32	988.59	2.0
ECC2	10.02	6.9	1129.5	1128.7	1155.03	1.4
ECC3	10.02	6.7	986.94	985.36	1012.83	2.0

Table 9: Charge passed in coulombs recorded at 30-minute interval

Specimen No.	Current (amperes) ECC		
	1	2	3
0	0.04	0.04	0.04
30	0.04	0.04	0.04
60	0.04	0.04	0.04
90	0.04	0.04	0.04
120	0.04	0.04	0.04
150	0.05	0.04	0.05
180	0.05	0.04	0.05
210	0.05	0.05	0.05
240	0.05	0.05	0.05
270	0.05	0.05	0.05
300	0.05	0.05	0.05
330	0.05	0.05	0.05
360	0.05	0.05	0.05
Q (C)	999	963	999
Mean (C)	981		

(left axis label: Current (amperes))

Table 10: Chloride diffusion coefficient using rapid chloride penetration test method

Parameter	Chloride diffusion coefficient
C_0 (%)	3
C_d (%)	0.84
T (K)	303
$\dfrac{RT}{zFE}$	2.17×10^{-5}
x_d (m)	0.01
t (sec	21600
α (−)	1.96×10^{-3}
D (m^2/s)	9.85×10^{-12}

To identify as a sustainable material, ECC was also studied under rapid chloride penetration test. The evaluation can be observed in Table 9. All data presented were the average of three specimens. The results are expressed in terms of total electrical charge, which is measured in Coulombs and reflects the ability of ECC materials to resist the intrusion of chloride ions. This was carried out to account for findings that were out of the ordinary. However, no significant difference or effect was found. Table 10 presents the chloride diffusion coefficient, which is found by measuring the concentration of chloride ions on the surface of the cylinder specimen after rapid chloride penetration and then using Equations (2) – (4). According to time and NaCl solution concentration, the chloride diffusion depth was within w/c 0.28 – 0.32 implying no significant increase. This was possibly due to the use of high calcium fly ash content with chloride to diffuse in the ECC specimen.

4. CONCLUSIONS

The paper presents the effect of w/b on the compressive and tensile properties of developed ECC using high calcium fly ash content. Based on the experimental results and discussion, the following conclusions can be drawn:

1) Up to a certain fly ash content 1.8 FA/C, the ECC with 0.28 w/b exhibited good behaviour of strain-hardening multiple-cracking behaviour under uniaxial tensile load, with resulting tensile strain capacity 3% and acceptable as ECC with its ductility.
2) Given the w/b 0.28 content, the ECC exhibited higher flexural strength with larger mid-span deflection. It was also supported by a higher compressive strength than the other w/b variations.
3) Cracking normally increased the sorptivity and water absorption of ECC. The extent of such increase was dependent on the microcrack density produced due to the curing time or additional mechanical loading. The sorptivity of ECC was found to not increase significantly with each w/c. It was assumed that high calcium fly ash content helped to preserve capillary suction during the immersion of the specimen.
4) The rapid chloride penetration test showed that the passing charged of each variety of w/c can be omitted. An increment of the passing charged was less than 3%. The diffusion coefficient of ECC was 9.85×10^{-12} m²/s. It was possible that the small crack width and dense pore structure might slow chloride transport.

5. ACKNOWLEDGEMENTS

6. REFERENCES

Ammasi, A. K., & Ragul. (2018). Strength and Durability of High Volume Fly Ash in Engineered Cementitious Composites. *Materials Today: Proceedings*, *5*(11), 24050–24058. https://doi.org/10.1016/j.matpr.2018.10.198

ASTM C109/C109M-02. (2020). Standard Test Method for Compressive Strength of Hydraulic Cement Mortars. *Annual Book of ASTM Standards*, *04*, 9.

ASTM C1202 - 05. (2005). Standard Test Method for Electrical Indication of Concrete's Ability to Resist Chloride Ion Penetration. In *American Society for Testing and Materials.* (Issue C 1202-05, pp. 1–6). https://doi.org/10.1520/C1202-12.2

ASTM C1585. (1989). *Standard Test Method for Measurement of Rate of Absorption of Water by Hydraulic - Cement Concretes* (pp. 51–61).

ASTM C642. (2006). Standard Test Method for Density, Absorption, and Voids in Hardened Concrete Designation C642-06. In *ASTM International* (Issue 3, pp. 1–3). https://doi.org/10.1097/NAN.0b013e31824d1b7a [doi]

Atiş, C. D. (2003). High-volume fly ash concrete with high strength and low drying shrinkage. *Journal of Materials in Civil Engineering*, *15*(2), 153–156. https://doi.org/10.1061/(ASCE)0899-1561(2003)15:2(153)

Bastian, M. A., Tambusay, A., Komara, I., Sutrisno, W., Irawan, D., & Suprobo, P. (2020). Enhancing the Ductility of a Reinforced Concrete Beam using Engineered Cementitious Composite. *IOP Conference Series: Earth and Environmental Science*, *506*, 012044. https://doi.org/10.1088/1755-1315/506/1/012044

Bilodeau, A., & Malhotra, V.M. (2000). High-volume fly ash system: Concrete solution for sustainable development. *ACI Structural Journal*, *97*(1), 41–48.

Fischer, G., & Li, V. C. (2002). Influence of matrix ductility on tension-stiffening behaviour of steel reinforced engineered cementitious composites (ECC). *ACI Structural Journal*, *99*(1), 104–111. https://doi.org/10.14359/11041

Fischer, G., & Li, V. C. (2003). Deformation behaviour of fibre-reinforced polymer reinforced engineered cementitious composite (ECC) flexural members under reversed cyclic loading conditions. *ACI Structural Journal*, *100*(1), 25–35. https://doi.org/10.14359/12436

Hu, B., Zhou, Y., Xing, F., Sui, L., & Luo, M. (2019). Experimental and theoretical investigation on the hybrid CFRP-ECC flexural strengthening of RC beams with corroded longitudinal reinforcement. *Engineering Structures*, *200*(April), 109717. https://doi.org/10.1016/j.engstruct.2019.109717

Hua, X. (2010). Self-healing of Engineered Cementitious Composites (ECC) in Concrete Repair System. *Delft University of Technology*, 62.

Hwang, S. H., & Shahsavari, R. (2019). High calcium cementless fly ash binder with low environmental footprint: Optimum Taguchi design. *Journal of the American Ceramic Society*, *102*(4), 2203–2217. https://doi.org/10.1111/jace.15873

Komara, I., Tambusay, A., Sutrisno, W., & Suprobo, P. (2019a). Engineered Cementitious Composite as an innovative durable material: A review. *ARPN Journal of Engineering and Applied Sciences*, *14*(4), 822–833.

Komara, I., Tambusay, A., Sutrisno, W., Suprobo, P., & Iranata, D. (2019b). The Investigation study of improving Durability Performance of Marine Infrastructure by using the Engineered Cementitious Composite. *The 14th International Student Conference on Advanced Science and Technology (ICAST) 2019*, 8–12. https://doi.org/10.4324/9780367853815-2

Komara, I., Suprobo, P., Iranata, D., Tambusay, A., & Sutrisno, W. (2020). Experimental investigations on the durability performance of normal concrete and engineered cementitious composite. *IOP Conference Series: Materials Science and Engineering*, *930*(1). https://doi.org/10.1088/1757-899X/930/1/012056

Krykowski, T., Ja´sniok, T., Recha, F., & Karolak, M. (2020). A Cracking Model for Reinforced Concrete Cover , Taking Account of the Accumulation of Corrosion Products in the ITZ Layer , and Including Computational and Experimental Verification Tomasz. *Materials*, *13*(5375), 1–17.

Kusuma, G.J., Shimada, H., Sasaoka, T., Matsui, K., Nugraha, C., Gautama, R.S., & Sulistianto, B. (2012). An Evaluation on the Physical and Chemical Composition of Coal Combustion Ash and Its Co-Placement with Coal-Mine Waste Rock. *Journal of Environmental Protection*, *03*(07), 589–596. https://doi.org/10.4236/jep.2012.37071

Lepech, M.D., Keoleian, G. A., Qian, S., & Li, V. C. (2008). Design of green engineered cementitious composites for pavement overlay applications. *Life-Cycle Civil Engineering - Proceedings of the 1st International Symposium on Life-Cycle Civil Engineering, IALCCE '08*, *July 2014*, 837–842. https://doi.org/10.1201/9780203885307.ch130

Li, J., & Yang, E. H. (2017). Macroscopic and microstructural properties of engineered cementitious composites incorporating recycled concrete fines. *Cement and Concrete Composites*, *78*, 33–42. https://doi.org/10.1016/j.cemconcomp.2016.12.013

Li, M.; Li, V.C.; Robertson,R.E.; Lynch, J.P.; Athanasopoulos-Zekkos, A. (2009). *Multi-Scale Design for Durable Repair*. The University of Michigan.

Li, V.C. (1994). From micromechanics to structural engineering -the design of cementitious composites for civil engineering applications. In *Structural Engineering/Earthquake Engineering* (Vol. 10, Issue 2, pp. 1–34).

Li, V.C. (2003). *On Engineered Cementitious Composites (ECC) A Review of the Material and Its Applications*. *1*(3), 215–230.

Li, V C. (2004a). High Performance Fibre Reinforced Cementitious Composites as Durable Material for Concrete Structure Repair. *International Journal for Restoration*, *10*(2), 163–180.

Li, V.C., Lepech, M., & Wang, S. (2004b). Development of green engineered cementitious composites for sustainable infrastructure systems. *International Workshop on Sustainable Development and Concrete Technology*, *1*(September), 181–191. http://core.kmi.open.ac.uk/download/pdf/11346106.pdf#page=192

Mehta, P. K., & Monteiro, P. J. M. (2001). *CONCRETE Microstructure, Properties and Materials*. 1–239.

Mooy, M., Tambusay, A., Komara, I., Sutrisno, W., Faimun, & Suprobo, P. (2020). Evaluation of Shear-Critical Reinforced Concrete Beam Blended with Fly Ash. *IOP Conference Series: Earth and Environmental Science*, *506*, 012041. https://doi.org/10.1088/1755-1315/506/1/012041

Oktaviani, W. N., Tambusay, A., Komara, I., Sutrisno, W., Faimun, F., & Suprobo, P. (2020). Flexural Behaviour of a Reinforced Concrete Beam Blended with Fly ash as Supplementary Material. *IOP Conference Series: Earth and Environmental Science*, *506*, 012042. https://doi.org/10.1088/1755-1315/506/1/012042

Ranade, R. (2014). *Advanced Cementitious Composite Development for Resilient and Sustainable Infrastructure*. 419.

Rokugo, K., Yokota, H., Sakata, N., & Kanda, T. (2007). JSCE Recommendations for Design and Construction of High Performance Fibre Reinforced Cement Composite with Multiple Fine Cracks. *Concrete Journal*, *45*(3), 3–9. https://doi.org/10.3151/coj1975.45.3_3

Şahmaran, M., Lachemi, M., Hossain, K. M. A., Ranade, R., & Li, V. C. (2009). Influence of aggregate type and size on ductility and mechanical properties of engineered cementitious composites. *ACI Materials Journal*, *106*(3), 308–316. https://doi.org/10.14359/56556

Şahmaran, M., Özbay, E., Yücel, H. E., Lachemi, M., & Li, V. C. (2011). Effect of Fly Ash and PVA Fibre on Microstructural Damage and Residual Properties of Engineered Cementitious Composites Exposed to High Temperatures. *Journal of Materials in Civil Engineering*, *23*(12), 1735–1745. https://doi.org/10.1061/(ASCE)MT.1943-5533.0000335

Şahmaran, M., Özbay, E., Yücel, H. E., Lachemi, M., & Li, V. C. (2012). Frost resistance and microstructure of Engineered Cementitious Composites: Influence of fly ash and micro poly-vinyl-alcohol fibre. *Cement and Concrete Composites*, *34*(2), 156–165. https://doi.org/10.1016/j.cemconcomp.2011.10.002

Wang, S., & Li, V.C. (2007). Engineered cementitious composites with high-volume fly ash. *ACI Materials Journal*, *104*(3), 233–241. https://doi.org/10.14359/18668

Wang, S., & Li, V.C. (2019). *Engineered Cementitious Composites with High-volume Fly Ash Engineered Cementitious Composites with High-Volume Fly Ash. March 2017*. https://doi.org/10.1201/b15883-8

Weimann, M. B., & Li, V.C. (2003). Hygral Behaviour of Engineered Cementitious Composites (ECC). *International Journal for Restoration of Buildings and Monuments*, *9*(5), 513–534.

Wu, S., Yang, J., Yang, R., & Zhu, J. (2020). Preparation and Properties of Engineered Cementitious Composites Incorporating a High Volume of Fly Ash. *Transportation Research Record*, *2674*(8), 653–662. https://doi.org/10.1177/0361198120919406

Xiao, J., Long, X., Ye, M., Jiang, H., Liu, L., & Zhai, K. (2021). Experimental Study of Bond Behaviour Between Rebar and PVA-Engineered Cementitious Composite (ECC) Using Pull-Out Tests. *Frontiers in Materials*, *8*(March), 1–15. https://doi.org/10.3389/fmats.2021.633404

Yin, Y., Qiao, Y., & Hu, S. (2019). Four-point bending tests for the fracture properties of concrete. *Engineering Fracture Mechanics*, *211*(March), 371–381. https://doi.org/10.1016/j.engfracmech.2019.03.004

Yıldırım, G., Khiavi, A. H., Yeşilmen, S., & Şahmaran, M. (2018). Self-healing performance of aged cementitious composites. *Cement and Concrete Composites*, *87*, 172–186. https://doi.org/10.1016/j.cemconcomp.2018.01.004

Yu, K., Li, L., Yu, J., Wang, Y., Ye, J., & Xu, Q. F. (2018). Direct tensile properties of engineered cementitious composites: A review. *Construction and Building Materials*, *165*, 346–362. https://doi.org/10.1016/j.conbuildmat.2017.12.124

Zeggar, M.L., Azline, N., & Safiee, N.A. (2019). Fly ash as supplementry material in concrete : A review. *IOP Conference Series: Earth and Environmental Science*, *357*(1). https://doi.org/10.1088/1755-1315/357/1/012025

Zhang, W., Yin, C., Ma, F., & Huang, Z. (2018). Mechanical properties and carbonation durability of engineered cementitious composites reinforced by polypropylene and hydrophilic polyvinyl alcohol fibres. *Materials*, *11*(7). https://doi.org/10.3390/ma11071147

Zhao, N., Wang, S., Wang, C., Quan, X., Yan, Q., & Li, B. (2020). Study on the durability of engineered cementitious composites (ECCs) containing high-volume fly ash and bentonite against the combined attack of sulfate and freezing-thawing (F-T). *Construction and Building Materials*, *233*, 117313. https://doi.org/10.1016/j.conbuildmat.2019.117313

#41: Performance analysis and multi-scenario decision of cogeneration system combined with gasifier under different mixing ratios

Xinzhuang Gu[1,2], Yanjun Dai[1,2]

[1]Institute of Refrigeration and Cryogenics, Shanghai Jiao Tong University, Shanghai, China, xzgu1906@sjtu.edu.cn
[2]Engineering Research Center of Solar Energy and Refrigeration, MOE, China, yjdai@sjtu.edu.cn

Abstract: The gasification cogeneration system with biomass as input energy can help the development of clean heating in rural areas of northern China and implement the "Carbon Neutralization" policy. This research compared and analysed the effects of three typical biomass feedstocks (corncob, wheat straw, and bark) on the system performance under different mixing ratios and proposes the decision-making suggestions of corresponding mixing ratios under different scenarios with the performance evaluation index as reference. The results of the performance analysis of the system were as follows: the optimal equivalence ratio at the m_{cc}:m_{ws}:m_b of 1:1:1 was 0.325, and the corresponding cold gas efficiency was 79.65%. The highest calorific value of syngas was 4.691 MJ/Nm3 at the m_{cc}:m_{ws}:m_b of 1:5:1, while the lowest biomass feedstock consumption was 20.1 kg/h at the m_{cc}:m_{ws}:m_b of 1:5:10. The highest waste heat of jacket water and exhaust gas was 15.94 kW and 17.6 kW at the m_{cc}:m_{ws}:m_b of 1:5:10, and the highest cooling capacity was 6 kW at the m_{cc}:m_{ws}:m_b of 1:5:10. For the scenario with high energy efficiency requirements and insensitive to price, the recommended mixing ratio was m_{cc}:m_{ws}:m_b =1:5:10, and corresponding energy and exergy efficiency were as high as 22.24% and 15.44%. The article has certain significance for expanding the treatment and utilization of biomass feedstocks in multiple scenarios.

Keywords: gasification; combined cooling heating and power; biomass feedstock; mixing ratio; scenario decision

1. INTRODUCTION

There are abundant agricultural and forestry biomass resources in rural areas of China. Taking the northern region as an example, the available farmland biomass resources are corn, wheat straw and other fuels, while the available forestry biomass resources include bark and sawdust. The utilization and processing of agricultural and forestry biomass can reduce accumulation costs and storage pressures (Li; Wu; Dai & Wang, 2021) whilst also reducing the use of some fossil fuels and thus reduce the emission of CO_2 and other greenhouse gases (Mohamed *et al.*, 2021). Therefore, it can help the development of clean heating in rural areas of northern China and the implementation of "carbon neutrality".

At present, part of the research on biomass feedstock utilization focuses on the combined cooling, heating and power system (CCHP) with gasifier, which has the advantages of high-energy efficiency and CO_2 emission reduction rate. For example, Chen *et al.* (2021) designed a cogeneration system based on a fluidized bed gasifier and a Stirling machine, using dried food waste as a single biomass fuel. The designed capacities of the Stirling engine and absorption chiller were 383 kW and 930 kW. The simulation results showed that the levelized total cost of the combined system reduced by 70.5% compared with a conventional reference system. Curcio *et al.* (2021) carried out experiments on sawdust gasification under direct and indirect solar heating and tested the syngas production performance of a 1.5 kW gasifier under mixed heating and self-heating operating modes. The experimental results showed that the cold gas efficiency of the gasification process was 100% at the chamber temperature of 1350°C. Wang *et al.* (2015) conducted an energy and exergy analyses of CCHP systems integrated with biomass air gasification. The simulation results indicated that the largest destruction occurred in the gasification system, which accounted for more than 70% of the total energy and exergy losses.

Most CCHP systems with the gasifier use a single biomass raw material; however, taking into account the storage periods of different agricultural and forestry biomass raw materials can vary from six months to a year, there is a tendency towards mixed combustion of various biomass raw materials in northern rural areas. Meanwhile, the differences in the composition and low heating value of different types of biomass raw materials result in variances in power generation, cooling capacity, and heating capacity of the gasification CCHP system (Li *et al.*, 2020). Therefore, it is necessary to select various typical agricultural and forestry biomass raw materials and conduct the performance analysis of the gasification cogeneration system under different mixing ratios.

2. DESCRIPTION OF THE GASIFICATION CCHP SYSTEM

Figure 1 shows a schematic diagram of the CCHP system with a gasifier based on three typical biomass feedstocks: corncob, wheat straw and bark. The three biomass feedstocks needed to be prepared into pellet fuels with similar shapes and sizes through a hopper and a granulator under different mixing ratios. The pellet fuel underwent a high-temperature gasification reaction under the combined action of moisture and O_2 and produced syngas for combustion and biochar discharged from the gasifier. After passing through the filter, the syngas was sent into the internal combustion engine (ICE), which drove the generator to produce electricity, while the internal combustion engine produced by-products such as high-temperature exhaust gas and jacket water.
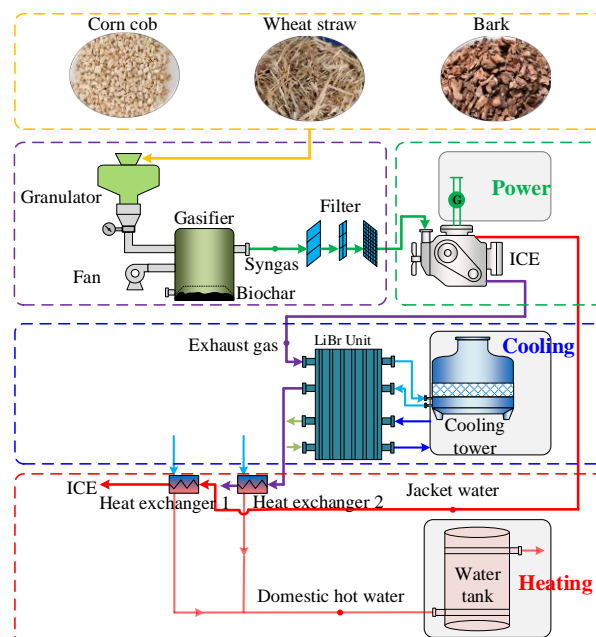
Figure 1: Schematic diagram of cogeneration system combined with gasifier under different mixing ratios of biomass feedstock

The waste heat of exhaust gas was used as the heat source to drive the lithium bromide unit to produce cooling capacity. Then the exhaust gas passed through the heat exchanger to heat the supplementary water to produce a part of domestic hot water, which was discharged into the air after purification. Similarly, the jacket water passed through the heat exchanger to heat the supplementary water to produce domestic hot water.

3. MATHEMATICAL MODEL
3.1. Gasifier

Based on the principles of thermal and chemical equilibrium, the following assumptions were made for the gasification model:

(1) The content of N and S elements in biomass feedstocks was small and could be ignored in the calculation;

(2) The reaction in the gasifier reached thermal and chemical equilibrium;

(3) All oxygen in the air sent by the blower participates in the reaction, and other components do not participate in the reaction.

The chemical equation for the gasification reaction of mixed biomass feedstock under the joint action of moisture and O_2 is shown in Equation 1, (Li, X. $et\ al.$, 2019):

$$C_aH_bO_cN_dS_e + f(O_2 + 3.76N_2) + gH_2O = n_s(x_1H_2$$
$$+ x_2CO + x_3CO_2 + x_4H_2O + x_5CH_4 + x_6N_2 +$$
$$x_7NO_2 + x_8SO_2) + n_{char}C_{char}$$

(1)
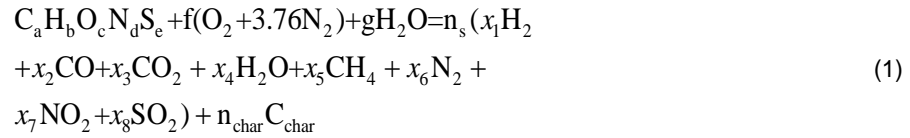
Where:

- $C_aH_bO_cN_dS_e$ = molecular formula of mixed biomass feedstock, calculated in Table 1;
- f = moles of air (mol/s);
- g = moles of moisture (mol/s);
- n_s = moles of syngas (mol/s);
- n_{char} = moles of char (mol/s);
- x_1-x_8 = volume fractions of each gas (%).

The number of moles of O_2 in the gasification process determined the volume fraction of each gas component in the syngas, so the definition of equivalence ratio is shown in Equation 2, (Li, C. $et\ al.$, 2019):

$$E_{er} = \frac{f}{a + \dfrac{b}{4} - \dfrac{c}{2}}$$

(2)

The low heating value and cold gas efficiency of syngas are usually used to evaluate the performance of the gasifier (Chen; Li; Dai & Wang, 2021), as shown in Equations 3 and 4, respectively:

$$Q_{sg} = 0.108x_1 + 0.126x_2 + 0.359x_5$$

(3)

$$\eta_{CGE} = \frac{V_{sg}Q_{sg}}{M_{bio}Q_{bio} + Q_{air}}$$

(4)

Where:

- Q_{sg} = low heating value of syngas (MJ/Nm^3);
- η_{CGE} = cold gas efficiency (%);
- V_{sg} = volume flow rate of syngas (Nm^3/s);
- M_{bio} = consumption of mixed biomass feedstock (kg/h);
- Q_{bio} = low heating value of mixed biomass feedstock (MJ/kg);
- Q_{air} = heat flux of hot air (MJ/s).

Table 2: Proximate analysis, elemental analysis, and lower heating value of corncob, wheat straw, and bark (TNO, 2019)

Parameter	Corncob	Wheat straw	Bark
Proximate analysis (%)			
Moisture	7.04	3	10.9
Ash	2.9	9.02	2.05
Volatile	72.67	68.77	69.59
Fixed carbon	17.39	19.21	17.46
Elemental analysis (%)			
C	43.24	46.27	49.09
H	5.28	5.34	5.61
O	41.02	34.82	31.91
N	0.44	0.39	0.39
S	0.08	0.05	0.04
Low heating value (MJ/Nm^3)	15.05	18.55	18.71

3.2. The internal combustion engine

The power generation efficiency of ICE under the different low heating values of syngas is calculated by Equation 5, (Li, C. *et al.*, 2019):

$$\eta_{ICE} = 28.08 \times \left(6.62 \times 10^{-3} - 6.41 \times 10^{-3} \times 0.824^{E_{ICE}} \right) \times \left(E_{ICE}^* \right)^{0.0563} \times \left(0.102 \frac{Q_{sg}}{Q_{ng}} + 0.897 \right) \tag{5}$$

Where:

- η_{ICE} = power generation efficiency (%);
- E_{ICE} = power generation of ICE (kW);
- E_{ICE}^* = rated power generation of ICE (kW);
- Q_{ng} = low heating value of natural gas (MJ/Nm$^{3)}$.

The heat of exhausted gas at different gas compositions and temperature is calculated by Equation 6, (Wang *et al.*, 2018):

$$Q_{eg} = A_h + \sum_{i=0}^{8} a_{h,i} \left(\frac{T_{eg}}{1000} \right)^i + b_h \times \ln \frac{T_{eg}}{1000} \tag{6}$$

Where A_h, $a_{h,i}$, and b_h are the correlation coefficient.

The heat of jacket water is calculated by Equation (7) (Wang *et al.*, 2018):

$$Q_{jw} = (0.103 + 0.354 \times 0.905^{E_{ICE}}) V_{sg} Q_{sg} \tag{7}$$

3.3. The lithium bromide unit

The energy balance equations of evaporator and condenser are shown in Equations 8 and 9, respectively (Saleh and Mosa, 2014):

$$Q_e = m_e (h_{out,e} - h_{in,e}) \tag{8}$$

$$Q_c = m_c (h_{in,c} - h_{out,c}) \tag{9}$$

Where:

- m_e and m_c = mass flow rate of evaporator and condenser respectively (kg/s);
- $h_{in,e}$ and $h_{in,c}$ = inlet enthalpy of evaporator and condenser respectively (J/kg);
- $h_{out,e}$ and $h_{out,c}$ = outlet enthalpy of evaporator and condenser respectively (J/kg).

3.4. The heat exchanger

The heat transfer of heat exchangers 1 and 2 is calculated by Equations 10 and 11, respectively:

$$c_{p,w} m_{w,1} (T_{out,1} - T_{in,1}) = \eta_{hx1} m_{eg} (Q_{egin} - Q_{egout}) \tag{10}$$

$$c_{p,w} m_{w,2} (T_{out,2} - T_{in,2}) = \eta_{hx2} m_{jw} (Q_{jwin} - Q_{jwout}) \tag{11}$$

Where:

- $c_{p,w}$ is the specific heat capacity of water (kg/s);
- m_w is the mass flow rate of water (kg/s);
- T_{in} and T_{out} are the inlet and outlet water temperature respectively (^{o}C);
- η_{hx} is the heat transfer efficiency (%);
- m_{eg} and m_{jw} are the mass flow rate of exhausted gas and jacket water respectively (kg/s).

3.5. The performance evaluation

In addition to the unit price of different biomass feedstock and equivalent CO_2 gas emission rates in Table 2, the comprehensive performance of the system was evaluated from the perspectives of energy and exergy efficiency, as shown in Equations 12 and 13, respectively (Gao; Dai; Tong & Dong, 2015).

$$\eta_{pe} = \frac{E_{ICE} + Q_H + Q_C}{M_{bio} Q_{bio}} \tag{12}$$

$$\eta_{ex} = \frac{E_{ICE} + Q_H (1 - \frac{T_0}{T_h}) + Q_C (\frac{T_0}{T_c} - 1)}{M_{bio} (Q_{bio} \beta (1 - m_W - m_A) + m_W e_W + m_A e_A)} \tag{13}$$

Where:

- Q_H and Q_C are the heating and cooling capacity respectively (kW);
- T_0, T_h, and T_c are the temperature of ambient, hot water, and chilled water (^{o}C);
- β is the correlation coefficient; m_W and m_A are the proportion of moisture and ash of the mixed biomass feedstock respectively (%);
- e_W and e_A are the exergy values of moisture and ash respectively (kJ/kg).

Table 2: Unit price and equivalent CO_2 emission rate of corncob, wheat straw, and bark (Draugelis and Li, 2012; Aseffe et al., 2021)

Parameter	Corn con	Wheat straw	Bark
Unit price (RMB/t)	750	890	1050
equivalent CO_2 emission rate (g/MJ)	53	58.16	47

4. RESULTS AND DISCUSSION
4.1. Gasification performance at different mixing ratios

In this study, MATLAB software was used for numerical simulation analysis. To ensure the subsequent research on the stability of gasification conditions under different mixing ratios, this section needs to determine the best equivalent ratio under different mixing ratios. As shown in Figure 2, the effects of different equivalence ratios (E_{er}) on the volume

fraction of syngas, reaction temperature (T_r), and cold gas efficiency (η_{CGE}) of biomass feedstock at the m_{cc}:m_{ws}:m_b of 1:1:1 were analysed. The T_r increased from 754.8K to 1308 K when the E_{er} increased from 0.075 to 0.5. The reason was that the increase of oxygen was conducive to the gasification reaction. Since N_2 in the air does not participate in the gasification reaction, the volume fraction increased from 20.34% to 52.03% with the increase of E_{er}. The maximum value of η_{CGE} reached 79.65% at E_{er} of 0.325. Therefore, the E_{er} in gasification reaction was set to 0.325 under different mixing ratios for further analysis and discussion in Figure 3.
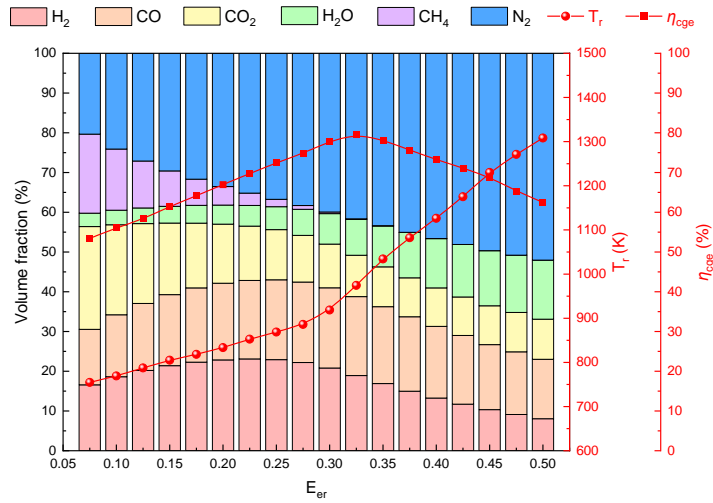
Figure 2: Effects of E_{er} on the gasifier performance at m_{cc}:m_{ws}:m_b of 1:1:1

Figure 3 describes the normalized simulation results of the low heating value of syngas (Q_{sg}) at different mixing ratios of m_{cc}:m_{ws} from 1:5 to 10:5 and m_b:m_{ws} from 1:5 to 10:5. The overall trend of Q_{sg} decreased with the increase of m_{cc}:m_{ws} and m_b:m_{ws}. The maximum and minimum values of Q_{sg} were 4.691 MJ/Nm^3 and 3.679 MJ/Nm^3 at the m_{cc}:m_{ws}:m_b of 1:5:1 and 10:5:10, respectively.
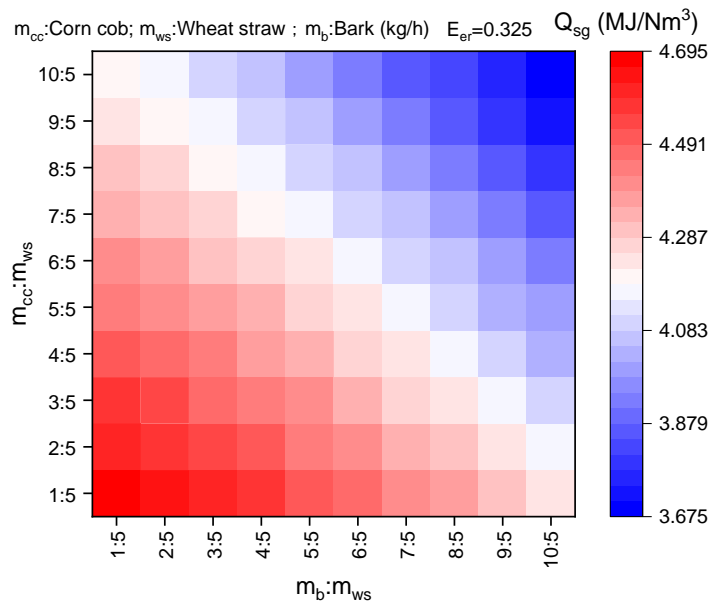
Figure 3: Orthogonal simulation results of Q_{sg} under different mixing ratios

Figure 4 illustrates why Q_{sg} gradually decreased with the increase of m_{cc}:m_{ws} from 1:5 to 10:5 at m_b:m_{ws} of 1:5 and E_{er} of 0.325. With the increase of m_{cc}:m_{ws}, the molar ratio of H to C element increased from 1.394 to 1.433, while the molar ratio of O to C element increased from 0.573 to 0.648, resulting in a gradual decrease in the amount of O_2 involved in the reaction. This is consistent with the trend that the volume fraction of N_2 decreased from 44% to 39.95%. As the water content of 7.04% of m_{cc} was greater than that of 3% of m_{ws}, the increase of m_{cc}:m_{ws} promoted the increase of moles of H_2O in the reaction, making the volume fraction of CO slowly decrease while the volume fraction of CO_2 and H_2O both rose slowly. Therefore, the Q_{sg} decreased from 4.691 MJ/Nm^3 to 4.2 MJ/Nm^3 with the increase of m_{cc}:m_{ws} from 1:5 to 10:5.
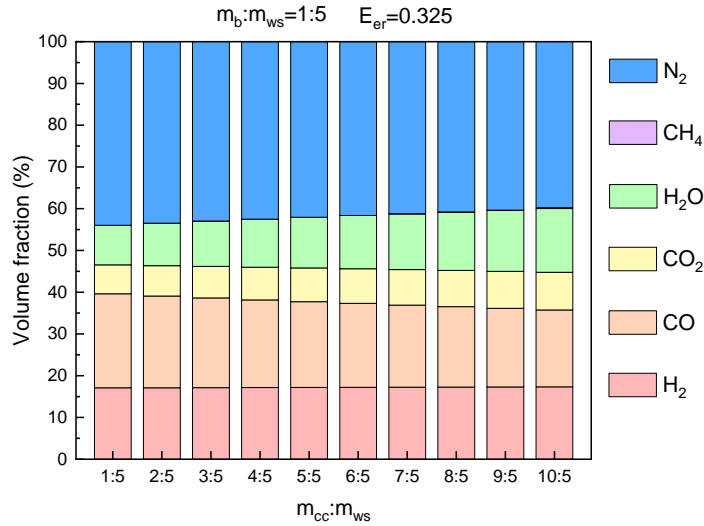
Figure 4: Effect of mixing ratio of $m_{cc}:m_{ws}$ on the volume fraction of different gases in syngas

In addition to selecting the mixing ratio of $m_{cc}:m_{ws}:m_b=1:1:1$ as the control group in Figure 2, the mixing ratio of $m_{cc}:m_{ws}:m_b=1:5:1$, 10:5:1, and 1:5:10 were selected to obtain the maximum low heating value of syngas, the lowest operating cost, and the lowest equivalent CO_2 gas emission rate. Therefore, the above four typical mixing ratios were analysed and are discussed in Sections 4.2 and 4.3.

4.2. Analysis of combined operation of ICE and gasifier

The effect of different power generation on the consumption of mixed biomass feedstock under the four mixing ratios is analysed in Figure 5. The consumption of four mixed biomass feedstocks increased with the power generation increases from 1 kW to 15 kW. Meanwhile, as the power generation efficiency increased with the increase of power generation, the growth rate of the consumption of the four biomass raw materials decreased. The maximum and minimum mixed biomass feedstock consumption at the E_{ICE} of 15 kW were 23.2 kg/h under $m_{cc}:m_{ws}:m_b=10:5:1$ and 20.1 kg/h under $m_{cc}:m_{ws}:m_b=1:5:10$, respectively. The reason was that the proportion of corncob under $m_{cc}:m_{ws}:m_b=10:5:1$ was the highest while the low heating value was the lowest. In addition, due to the higher heating value of syngas under $m_{cc}:m_{ws}:m_b=1:5:1$ and the higher heating value of biomass under $m_{cc}:m_{ws}:m_b=1:1:1$, the consumption of biomass feedstock of the two mixing ratios were close, being 21.06 kg/h and 21.51 kg/h respectively.
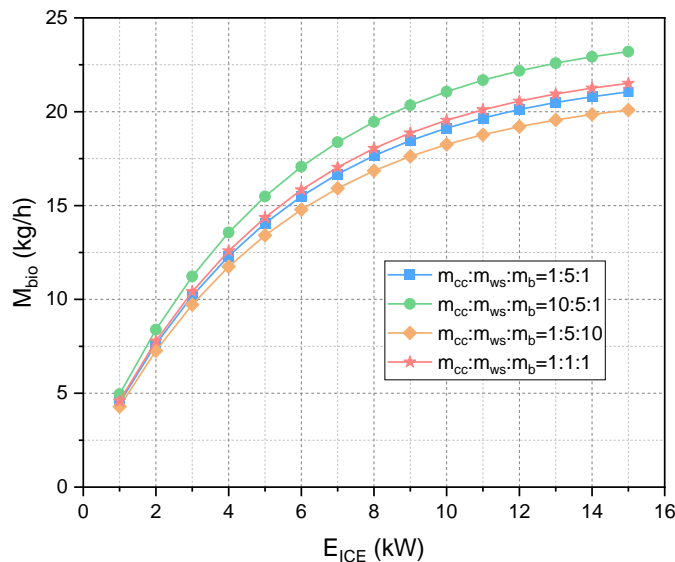
Figure 5: Effect of E_{ICE} on M_{bio} under four mixing ratios

The effects of different power generation on waste heat of exhausted gas and jacket water of ICE under the four mixing ratios are described in Figure 6. The growth rate of waste heat decreased gradually as the efficiency of the internal combustion engine increased. The heat of exhausted gas (Q_{eg}) at $m_{cc}:m_{ws}:m_b$ of 1:5:10 and 1:5:1 were the largest and smallest, which increased from 6.37 kW to 15.94 kW and from 5.74 kW to 14.37 kW with the increase of power generation respectively. Taking $m_{cc}:m_{ws}:m_b=1:5:1$ as an example, the reason for the lowest Q_{eg} under this mixing ratio was that its own moisture content, H/C and O/C element ratio make the mass flow rate the least among

101

the four mixing ratios. Similarly, the heat of jacket water (Q_{jw}) at m_{cc}:m_{ws}:m_b of 1:5:10 and 10:5:1 were the largest and smallest, increasing from 10.44 kW to 17.6 kW and from 9.9 kW to 16.67 kW with the increase of power generation respectively. Taking m_{cc}:m_{ws}:m_b=10:5:1 as an example, the reason for the lowest Q_{jw} at this mixing ratio was that the low heating value of syngas entering the internal combustion engine was the lowest.
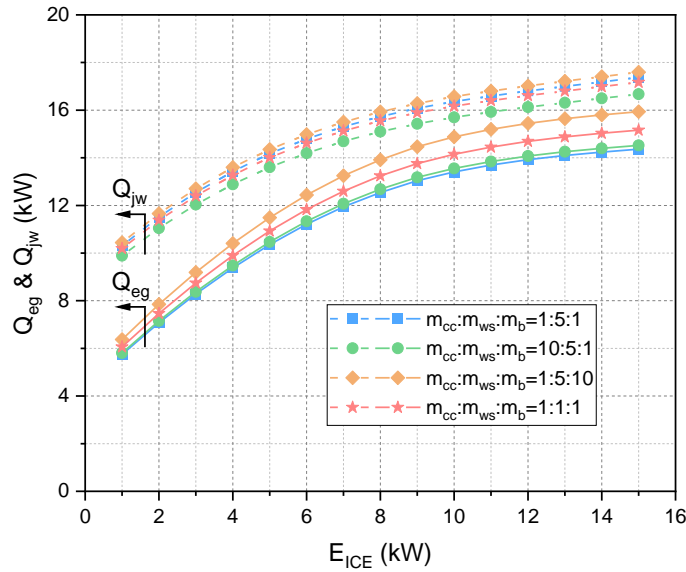
Figure 6: Effect of E_{ICE} on Q_{eg} and Q_{jw} under four mixing ratios

4.3. Comprehensive performance analysis

The effect of different power generation on the cooling capacity (Q_C) and heating capacity (Q_H) under the four mixing ratios is analysed in Figure 7. The difference in Q_C under different mixing ratios was consistent with the trend of Q_{eg} shown in Figure 6. The reason was that higher Q_{eg} was beneficial to COP and cooling capacity of the lithium bromide unit. The Q_C at m_{cc}:m_{ws}:m_b of 1:5:10 and 1:5:1 were the largest and smallest, which increased from 2.2 kW to 6 kW and from 2.2 kW to 5.48 kW with the increase in power generation, respectively. The Q_H under the four mixing ratios was relatively close. The reason was that most of the Q_{jw} was returned to the internal combustion engine for reuse, leaving only a small part of the Q_{jw} for heating.
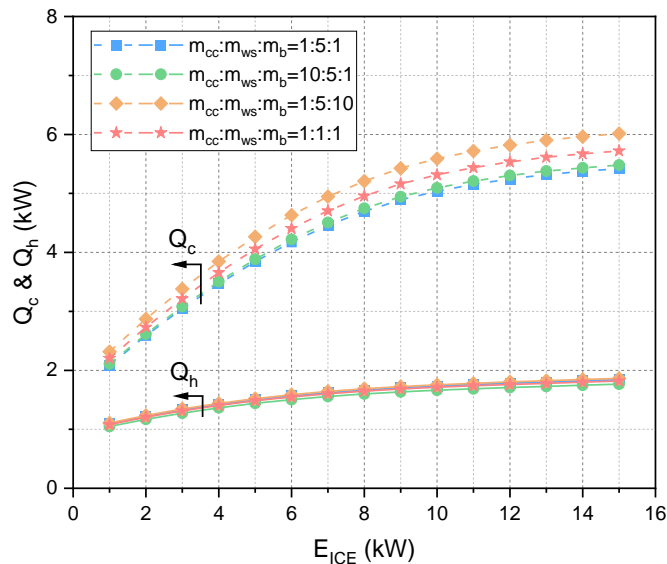
Figure 7: Effect of E_{ICE} on Q_C and Q_H under four mixing ratios

Figure 8 illustrates the influences of different mixing ratios at E_{ICE} of 15 kW on the low heating value of syngas, biomass feedstock consumption, operating cost, energy efficiency, and exergy efficiency. The advantage of the mixing ratio m_{cc}:m_{ws}:m_b=1:5:1 was that the low heating value of syngas was as high as 4.691 MJ/Nm^3. At the same time, under the same power generation, it had lower biomass feedstock consumption and the lowest operating cost, which were 21.06 kg/h and 18.8 RMB/h, respectively. The mixing ratio m_{cc}:m_{ws}:m_b=1:5:1 can be applied to scenarios sensitive to the price of biomass raw materials. The advantage of the mixing ratio m_{cc}:m_{ws}:m_b=10:5:1 was that the

operating cost was low at 18.85 RMB/h, useful in scenarios with rich materials such as corncob and price sensitivity. The advantages of $m_{cc}:m_{ws}:m_b=1:5:10$ were that biomass feedstock consumption, energy efficiency, and exergy efficiency were all optimal, being 20.1 kg/h, 22.24%, and 15.44%, respectively. However, the operating cost was as high as 19.72 RMB/h, suitable for scenarios with high energy efficiency requirements and insensitive to price. For the control group, the five indicators of $m_{cc}:m_{ws}:m_b=1:1:1$ were relatively balanced. The low heating value of syngas, energy efficiency, and exergy efficiency were better, which were 4.277 MJ/Nm^3, 21.63%, and 14.9%, respectively.
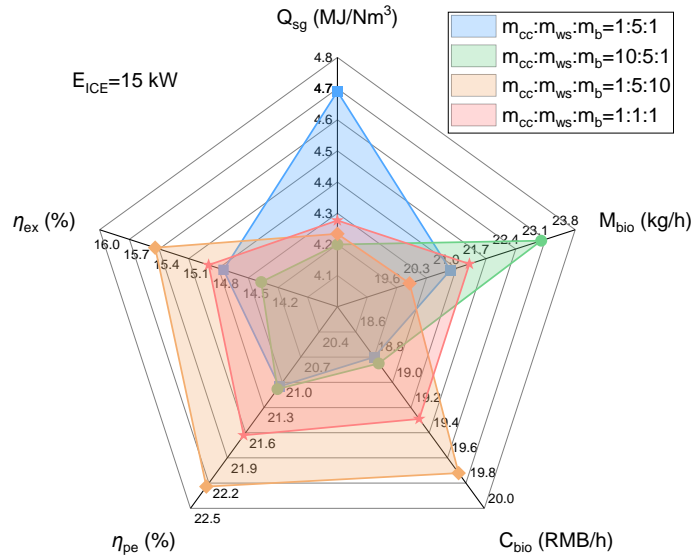
Figure 8: Effect of four mixing ratio on performance evaluation indexes at E_{ICE} of 15 kW

5. CONCLUSION

In this paper, four typical mixing ratios of biomass feedstock were selected for systematic comprehensive analysis of the CCHP system with a gasifier, and the comparison and analysis were carried out based on the performance evaluation indexes. The conclusions were as follows:

1. Among the four mixing ratios, the low heating value of syngas at $m_{cc}:m_{ws}:m_b=1:5:1$ was the highest (4.691 MJ/Nm^3), while the biomass feedstock consumption at $m_{cc}:m_{ws}:m_b=1:5:10$ was the lowest (20.1 kg/h);

2. The mixing ratio $m_{cc}:m_{ws}:m_b=1:5:10$ had the highest heat of exhausted gas, jacket water, and cooling capacity at 15.94 kW, 17.6 kW, and 6 kW;

3. For price-sensitive scenarios, the recommended mixing ratio was $m_{cc}:m_{ws}:m_b=1:5:1$, which had the lowest operation cost of 18.8 RMB/h; For the scenario with high energy efficiency requirements and price insensitivity, the recommended mixing ratio was $m_{cc}:m_{ws}:m_b=1:5:10$, with the energy efficiency and exergy efficiency as high as 22.24% and 15.44%.

6. ACKNOWLEDGEMENT

7. REFERENCES

Aseffe, J., González, A., Jaén, R., Lora, E., 2021. The corn cob gasification-based renewable energy recovery in the life cycle environmental performance of seed-corn supply chain: An Ecuadorian case study. Renewable Energy, 163, 1523-1535.

Chen, J., Li, X., Dai, Y., Wang, C., 2021. Energetic, economic, and environmental assessment of a Stirling engine based gasification CCHP system. Applied Energy, 281, 116067.

Curcio, A., Rodat, S., Vuillerme, V., 2021. Abanades, Experimental assessment of woody biomass gasification in a hybridized solar powered reactor featuring direct and indirect heating modes. International Journal of Hydrogen Energy, 46(75), 37192-37207.

Draugelis, G., Li, S., 2012. District heating reform. Sustainable Low-Carbon City Development in China , 205.

Gao, P., Dai, Y., Tong, Y., Dong, P., 2015. Energy matching and optimization analysis of waste to energy CCHP (combined cooling, heating and power) system with exergy and energy level. Energy, 79, 522-535.

Li, C., Shen, Y., Wu, J., Dai, Y., Wang, C., 2019. Experimental and modeling investigation of an integrated biomass gasifier–engine–generator system for power generation and waste heat recovery. Energy Conversion and Management, 199, 112023.

Li, C., Wu, J., Dai, Y., Wang, C., 2021. Multi-criteria optimization of a biomass gasification-based combined cooling, heating, and power system integrated with an organic Rankine cycle in different climate zones in China. Energy Conversion and Management, 243, 114364.

Li, S., Zhu, L., He, Y., Fan, J., Lv, L., 2020. Thermodynamic evaluation of CCHP system based on biomass gasification by exploring the feasibility of using CO_2 as gasification agent. Sustainable Energy Technologies and Assessments, 42, 100867.

Li, X., Kan, X., Sun, X., Zhao, Y., Ge, T., Dai, Y., Wang, C., 2019. Performance analysis of a biomass gasification-based CCHP system integrated with variable-effect LiBr-H2O absorption cooling and desiccant dehumidification. Energy, 176, 961-979.

Mohamed, U., Zhao, Y., Yi, Q., Shi, L., Wei, G., Nimmo, W., 2021. Evaluation of life cycle energy, economy and CO2 emissions for biomass chemical looping gasification to power generation. Renewable Energy, 176, 366-387.

Saleh, A., Mosa, M., 2014. Optimization study of a single-effect water–lithium bromide absorption refrigeration system powered by flat-plate collector in hot regions. Energy conversion and management, 87, 29-36.

TNO, E., 2019. database for biomass and waste. Phyllis2.

Wang, J., Yang, K., Xu, Z., Fu, C., 2015. Energy and exergy analyses of an integrated CCHP system with biomass air gasification. Applied energy, 142, 317-327.

Wang, J., Chen, Y., Dou, C., Gao, Y., Zhao, Z., 2018. Adjustable performance analysis of combined cooling heating and power system integrated with ground source heat pump. Energy, 163, 475-489.

#42: A review of housing in Indonesia

A case for the integration of sustainable design strategies in low-cost apartments

Irma Handayani Lubis[1], Lucelia Rodrigues[2], Lorna Kiamba[3]

[1]University of Nottingham, University Park NG7 2RD, irma.lubis@nottingham.ac.uk
[2]University of Nottingham, University Park NG7 2RD, Lucelia.Rodrigues@nottingham.ac.uk
[3]University of Nottingham, University Park NG7 2RD, lorna.kiamba@nottingham.ac.uk

Abstract: In the last few decades, housing in Indonesia has been developed from time to time. It has been changing from traditional to modern building, sloping to flat roof, single to multiple storeys, wood to concrete, elevated to landed, and low to high-cost building. Some changes give improvement to the performance of the building, but some might have negative impacts to the building and the environment. The reason for the change might vary from the trends, occupants' comfort, and force by nature. The factor of nature that was influenced by the microclimate conditions such as temperature and humidity made some adjustments in the house design. However, there has been a growing concern about the spreading of informal and unplanned housing in Indonesia which accommodate the majority of low-income people in Indonesia. To solve the social gap between high-income people and low-income communities, the government directs the housing policy in the context of providing access to decent, safe, and affordable housing and settlements without slums by three main approaches, namely the demand side, the supply side, and the enabling environment. On the other hand, climate change affects the thermal performance of housing. As the temperature rises, the energy consumption also increases due to the use of active means. Therefore, this paper tries to review about the development of housing in Indonesia from several aspects such as political and climatic context, vernacular to the upraise of low-cost apartment buildings. This study aims to look at the challenges, acceptability, and opportunities of low-cost apartment buildings in the future.

1. INTRODUCTION

The population of several cities in Indonesia have been growing rapidly. Many cities have become urbanized and occupied by low-income communities. It has changed the cities' view in Indonesia, from planned to unplanned, from compact to scattered, from legal to illegal settlement, and from proper to improper houses. To solve the social disparity between high-income people and low-income communities, the local government started to develop a new lifestyle of living vertically. They developed public-rented flats or low-cost apartments to increase access for low-income people to decent, safe, and affordable housing and supported by the provision of adequate infrastructure, facilities, and utilities.

However, the development of low-cost apartments cannot afford to resolve climate change issues. The rise of air temperature and the decrease of precipitation influence the microclimate condition. The increased air temperature caused a long drought making it hard for occupants to achieve thermal comfort. People use active means of space conditioning to respond to these conditions resulting in increased energy consumption. Therefore, there should be attention from the local government to create regulation and policies to solve these problems.

This paper aims to review housing in Indonesia. This study is focused on the rise of low-cost apartments to create a sustainable city. The houses are reviewed in several contexts, i.e., political, geographical, or climatic, vernacular houses, modern landed houses, and low-cost apartments.

2. POLITICAL AND GEOGRAPHICAL/CLIMATIC CONTEXT

In Indonesia, housing policy is regulated by the Ministry of Public Works and Public Housing. Any plans and policies regarding housing in Indonesia are managed by the Directorate General of Housing. The house planning and policies are written in the national level, including:

- Strategic Plan of the Ministry of Public Works and Human Settlements 2020-2024 (RENSTRA DITJEN PERUMAHAN 2020-2024)
- Strategic Plan of the Directorate General of Housing 2020-2024 (RENSTRA DITJEN PERUMAHAN 2020-2024)
- Ministerial Regulation No. 14/PERMEN/M/2007, regarding simple rental flats

The housing sector policies in Indonesia are intended to expand access to decent housing equipped with adequate facilities and infrastructure for all community groups in an equitable manner. These policies are expected to be satisfied through the development of a complete and balanced multi-system housing provision which includes controlling Commercial Housing, strengthening public housing, flats, the empowerment of self-help housing and Special Housing facilitation. Those are written in the Medium-Term National Development Plan (RPJMN) for the Housing Sector 2020 – 2024. The policy direction in the context of providing access to decent, safe, and affordable housing and settlements is to gradually increase public access to decent, safe, and affordable housing to create a city without slums. The strategy is being carried out through three main approaches, namely from the demand side, from the supply side, and the enabling environment.

Regarding the policy of climate change mitigation, Indonesia has written the green economy as a foundation of Indonesia's development programme in the Medium-Term National Development Plan (RPJMN) 2015-2019. The highlight is to be on 'inclusive and sustainable growth, increasing value-added of natural resources with the sustainable approach, increasing quality of the environment, disaster mitigation and tackling climate change'.

Figure 1: Map of Indonesia (Sardon, 2010)

Indonesia is an archipelagic country that lies in the tropical rainforest climate and has enormous challenges to adapt (see Figure 1). It is surrounded by water and some active volcanoes that lead to frequent earthquakes. It has very hot weather during the dry season which leads to a long drought and high precipitation that periodically causes flooding during the rainy season. Indonesia also has a high population centralised in the Java Island which causes uneven development of building construction. Meanwhile, some researchers have predicted the future climate conditions of Southeast Asia and warmer climates will increase in mean temperature and annual precipitation. Jakarta, the capital city of Indonesia, is located at 6.18°South and 106.83°East. Its elevation varies between -2 and 50 metres (-7 ft to 164 ft) above sea level and the average is 8 metres (26 ft) which is relatively low and flat. According to the 2020 Census, Jakarta has the largest population in Indonesia with 10,562,088 population (BPS, no date a). It has a tropical rainforest climate with two typical seasons, wet and dry seasons.

Based on the historical climatic data (2007-2021) that is depicted in Table 21, the monthly average of dry bulb temperature ranged from 27°C to 29°C. It was recorded that the highest temperature reached was 36°C in January and June and the lowest temperature was 16°C in May. The monthly average of relative humidity varied from 66% to 80%. According to sky cover range, the cloudiest sky conditions occurred between November to March, while the clearest sky condition occurred between April to October. From the wind speed data, this city experienced relatively calm conditions, with the monthly average between 1 and 2 m/s.

Table 1: Weather data summary of Jakarta (generated from epw. files)

Monthly means	Jan	Feb	Mar	Apr	May	Jun	Jul	Aug	Sep	Oct	Nov	Dec
Global Horizontal Radiation (Avg Daily Total in W/m^2)	4706	5085	5272	5163	5276	4929	5316	5889	6196	6057	5436	4926
Dry Bulb Temperature (Avg Monthly in °C)	27	27	28	28	29	28	28	29	29	29	28	28
Relative Humidity (Avg Monthly in %)	75	80	74	77	74	72	72	66	69	72	74	77
Wind Direction (Monthly Mode in Degrees)	250	290	240	310	70	80	90	40	20	330	350	320
Wind Speed (Avg Monthly in m/s)	2	1	2	1	1	1	1	1	1	1	1	1

3. VERNACULAR HOUSES

Indonesia has five big islands which contain several ethnic groups that have different types of traditional houses. There are approximately 50 traditional houses (namely *Rumah Adat*) spread across 33 provinces. These houses commonly occur in suburban and remote areas where traditional values are still important to the people. Some elements are dominant in the building such as high and wide pitched roof, elevated ground floor, and wood construction (see Table 22). It is also noticeable that the houses are mostly built symmetrically.

Table 2: Traditional Houses in Indonesia

Umah Pitu Ruang, Aceh (Azizah, no date)	*Rumah Bolon, Batak Toba* (Marpaung, 2019)	*Rumah Gadang, Minangkabau* (MichaelJLowe, 2005)	*Rumah Kajang Leko, Jambi* (Wahyupratama159, 2021)	*Sundanese Traditional House, West Java* (Julie, 2011)
Joglo Situbondo, East Java (Vannisa, 2019)	*Rumah Panjang West Kalimantan* (Prasstyle.com, 2021)	*Rumah Tongkonan, South Sulawesi* (Dmitrieval, no date)	*Rumah Mbaru Niang, East Nusa Tenggara* (Prasetyo, 2022)	*Rumah Honai, Papua* (superadventure.co.id, no date)

As an example, Joglo which is a traditional house from Java, Indonesia, is primarily constructed from wooden structures, brick walls, and corrugated metal roof. According to Idham (2018), there are some passive strategies applied in this house to promote thermal comfort i.e., south facing façade and cross-ventilation in the prevailing wind direction. Idham argued that elevated floors can decrease the relative humidity and the building envelope has a role

to play in controlling air comfort. The use of permeable wooden or woven bamboo walls allows the air to circulate inside the house. The presence of the high-pitched roof in the middle of the house creates a stack effect by releasing the hot air through the permeable clay tile roof to promote thermal comfort (Idham, 2018). In addition, it is noticeable that the big veranda at the front of the house provides sun shading in the entrance area. Additionally, the open layout also supports the idea of cross ventilation.

4. MODERN HOUSES

Modern houses in Indonesia are classified by several sectors such as social economy, typology, and floor area. Based on social economy, there are 2 classifications of modern houses: planned house and unplanned house. According to typology, there are 5 types of houses, i.e., detached house, semi-detached house, shop house, flat (affordable vertical housing), apartment (luxury vertical housing). Based on floor area, house developers in Indonesia typically classify houses by the size as described below (Table 3).

Table 3: Housing Classification in Indonesia (based on floor area)

No.	Floor Area	Ground floor area/ Unit Area	Building Storey	Typical Room	Open Area
Detached house, semi-detached house (Arsitur Studio, 2020)					
1.	Type 21/24 m^2	6 x 10 m^2 = 60	1-storey	A living dining room A bedroom A bathroom Small kitchen	Carport, patio, garden
2.	Type 36 m^2	6 x 10 m^2 = 60 6 x 12 m^2 = 72	1-storey	A living room A dining room 2 bedrooms A bathroom Small kitchen	Carport, patio, garden
3.	Type 45 m^2	7 x 13 m^2 = 91 7 x 15 m^2 = 105 8 x 13 m^2 = 104	1-storey	A living room A dining room 2 bedrooms A bathroom Kitchen	Carport, patio, big garden
4.	Type 70 m^2 or 2 x 35 m^2	7 x 11 m^2 = 77 9 x 16 m^2 = 144 10 x 17 m^2 = 170	1-storey 2-storey	A living room A dining room 2-3 bedrooms 2-3 bathrooms Kitchen	Carport, patio, big garden
5.	Type 90 m^2 or 2 x 45 m^2	7 x 12 m^2 = 84 10 x 13 m^2 = 130 10 x 14 m^2 = 140	1-storey 2-storey	1-2 living rooms A dining room 3-4 bedrooms 2-3 bathrooms Kitchen	Carport, patio, big garden
6.	Type 120 m^2 or 2 x 60 m^2	9 x 20 m^2 = 180 10 x 15 m^2 = 150	1-storey 2-storey	1-2 living rooms A dining room 4-6 bedrooms 3-5 bathrooms 2 Kitchen	Carport, patio, big garden
Shop house (Wihardjono, 2012)					
1.	Type 130 m^2	11.2 x 7.2 m^2	2-storey	Open layout 2 bathrooms	None
2.	Type 131-137 m^2	5 x 14 m^2	2-storey	Open layout 2 bathrooms	None
3.	Type 139-152 m^2	5.2 x 14 m^2	2-storey	Open layout 2 bathrooms	None
4.	Type 169 m^2	6.5 x 14 m^2	2-storey	Open layout 2 bathrooms	None
5.	Type 185-187 m^2	7 x 14 m^2	2-storey	Open layout 2 bathrooms	None
6.	Type 180-240 m^2	5 x 12 m^2 5 x 16 m^2	3-storey	Open layout 3 bathrooms	None
Flat/ low-cost apartment/ luxury apartment (Tridya, no date; Sing, 2011; Adisurya, 2016; Khairunisa, 2018)					
1.	Studio Type 18 m^2	3 x 6 m^2 = 18	Multi-storey	Bedroom, living room, kitchen together A bathroom	Communal area
2.	Studio Type 21 m^2	3 x 7 m^2 = 21 3.5 x 6 m^2 = 21	Multi-storey	Bedroom, living room, kitchen together A bathroom	Communal area
3.	1-bedroom Type 24-27 m^2	4 x 6 m^2 = 24 4.5 x 6 m^2 = 27	Multi-storey	A bedroom A bathroom Living room, kitchen together	Communal area

4.	1-bedroom Type 30 m^2	4.5 x 7.5 m^2 = 30 5 x 6 m^2 = 30	Multi-storey	A bedroom A bathroom Living room, kitchen together	Communal area
5.	2-bedroom Type 36 m^2	4.5 x 8 m^2 = 36 6 x 6 m^2 = 36	Multi-storey	2 bedrooms A bathroom Living room, kitchen together	Communal area
6.	2-4 bedroom Type 49-54 m^2	7 x 7 m^2 = 49	Multi-storey	2-4 bedrooms A bathroom Living room, kitchen together	Communal area

The classification of social economic are divided based on basic income, planned house is usually for mid-high-income people while unplanned house is used for low-income people (see Figure 2). Planned house is identified by a good planning, similar building size and material, a decent size of street and located in an appropriate area. On the other hand, an unplanned house is known as an urban village, which is an unplanned, small alley, uninhabitable house, and located in a slum area.

| (1) | (2) |

Figure 2: Housing Classification in Indonesia (based on social economic): (1) planned houses (Patriella, 2022) ; (2) unplanned houses (Tempo.co, 2015)

In general, there are 5 types of houses in Indonesia: detached house, semi-detached house, shop house, flat, and apartment (see Figure 3). The most common types of house in Indonesia are detached and semi-detached houses with 1-2 storey high. This is due to the location of Indonesia, which is in a ring of fire, a home of more than 127 active volcanoes that causes a high frequency of earthquakes (LIPI, 2012). The development of massive unplanned houses in high-density cities potentially causes the spread of slums. Shop houses are also familiar in downtown areas where they combine 2 functions: retail and housing. Flats and apartments are a new style of housing in high density cities. Flats or public-rented apartments are usually subsidised by the government, are low rise (3-4 storeys), with limited facilities, and occupied by low-income tenants.

| (1) | (2) | (3) |

| (4) | (5) |

Figure 3: Housing Classification in Indonesia (based on type): (1) detached house (lingkarwarna.com, no date); (2) semi-detached house/ town house (kompas.com, 2021); (3) shop house (Shopee, no date); (4) public rented flat/ low-cost apartment (Martinus, 2018); (5) luxury apartment (All-jakarta-apartments.com, no date)

5. CHALLENGES

Over the last decades, there have been shortages of traditional houses and modern landed houses in Indonesia that make them vulnerable to the climate conditions. The traditional houses in the urban area have been removed gradually due to social and economic reasons. According to Schefold and Nas (2008) Indonesian traditional houses became hard to sustain because of modernity, high frequency of natural disasters, and lack of maintenance. Wibowo (2020) stated that traditional houses were hard to retain due to exploitation issues on the use of natural resources such as wood, bamboo, stone, etc. Suprapti *et al.* (2022) believed that the decrease of traditional houses was caused by the lack of action on preservation and maintenance by the local government.

The warm and humid climate also has a huge impact on building performance. The hot weather delivers overheating during daytime while the relatively high humidity affects health problems. According to the National Electricity Company (PLN, 2017, 2021; PT PLN, 2018; PT PLN Secretariat Company, 2018; PT PLN (Persero), 2019), the energy consumption of the household sector has increased in the last 8 years from 72,132.47 GWh to 112,155.85 GWh between 2012 and 2020 (see Figure 4). According to Surahman *et al.* (2022), looking at the source of energy used, households mostly used energy from electricity rather than gas. However, regarding the house classifications, the higher the cost of houses the more cooling was consumed (Surahman *et al.*, 2022). It was also reported that the cooking and cooling sectors were dominant in Jakarta and Bandung (Surahman *et al.*, 2022). Despite the low percentage of AC unit ownership in Indonesia with less than 10% compared with Malaysia and Singapore which have more than 80%, Indonesia is predicted to contribute more than 50% to the growth of the stock of ACs in Southeast Asia (International Energy Agency (IEA), 2019). This should be a caution for the increase in global energy consumption and carbon emissions.
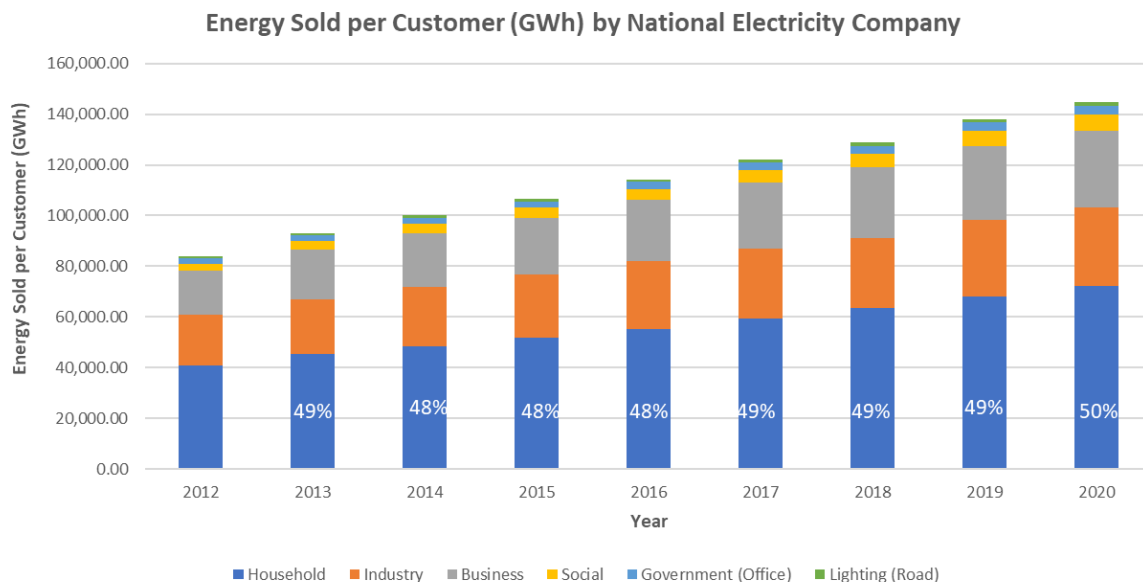
Figure 4: Energy sold by customer (GWH) from 2012 to 2020 (PLN, 2017, 2021; PT PLN, 2018; PT PLN Secretariat Company, 2018; PT PLN (Persero), 2019)

However, the presence of modern houses apparently raises some problems for low-middle income society. It is reported by the Central Bureau of Statistic of Indonesia that the average price/unit of housing construction by perumnas (Million Rupiah) was 93.52 rupiah (USD 6264.40) in 2018 (BPS, no date b). Nursiyono and Dewi (2021) found that the average index of property rate has increased 209.8 points from 2015 to 2019. People from the suburbs are challenging themselves with the aim of getting a proper job but ending up homeless. According to the Central Bureau of Statistics of Indonesia, approximately only 58% of communities have access to adequate and affordable housing (see Figure 5).

To survive living in the metropolitan cities, low-income people try to build their own house illegally with the limitation of budget and poor conditions. Slums in most big cities in Indonesia are identified by limited urban space, are unplanned and scattered (Pandelaki and Shiozaki, 2010; Kubota, Surahman and Higashi, 2014). Murtyas, Hagishima and Kusumaningdyah (2020) found that vulnerable dwellings such as slums are prone to heat risk. Parisi, Kubota and Surahman (2021) proved that the poor environment in slums caused respiratory diseases due to severe dampness and mould risk. Willetts *et al.*, (2019) indicated that poor sanitation in urban houses increased diarrhoea during floods in the rainy season.
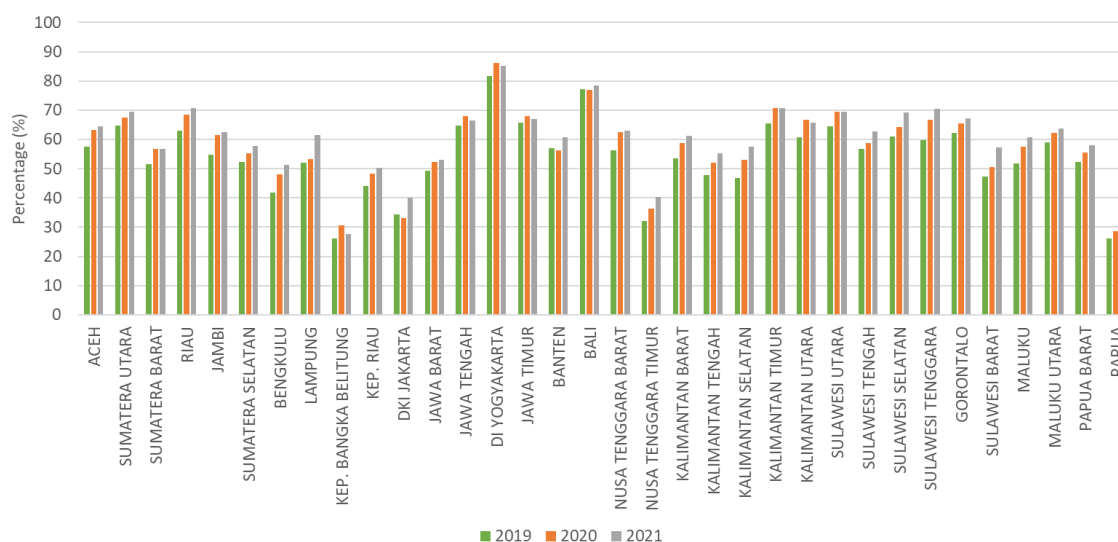
Figure 5: The percentage of households with access to adequate and affordable housing by province
(source: Central Bureau of Statistics of Indonesia)

Recently, the government continued "the Million Houses Program" that was written in the Medium-Term National Development Plan (RPJMN) 2015-2019. It was reported that this program proposed to address the housing needs, especially for low-income people. The government has a target to improve the liveable housing through the construction of flats, special houses, self-help houses and distribution of government-subsidised housing infrastructure, facilities and utilities (PUPR, 2021). In order to do that, there are some strategies that have been developed by the government as follows:

a) Increased access for low-income people to decent, safe, and affordable housing and supported by the provision of adequate infrastructure, facilities and utilities.
b) Construction of flats for low-income people equipped with supporting PSU (Guideline for Public Infrastructure, Facilities, and Utilities Aid) as many as 550,000 units.
c) Controlling the construction of landed houses and accelerate the construction of flats in urban areas.
d) Accelerate provision of flats by new building construction or revitalization (Retrofitting)

The government has implemented a policy of promoting the development of *Rusunawa* (public rented flats) due to urban problems with an ever-increasing population. This government action is appropriate because the land area in urban areas is increasingly limited and it is not possible to build settlements horizontally. Existing development is now more focused towards vertical development (Kementerian PUPR, 2016).

6.   THE UPRISE OF LOW-COST APARTMENTS

The development of low-cost apartments or flats is a logical solution to fulfil the lack of housing in low-middle income communities in the middle of limited urban land with environmental quality degradation problems, poor public transport, traffic jams; aiming for a healthy living environment and to reduce socioeconomic disparity (Kementerian PUPR, 2016). According to the Ministry of Public Works and Public Housing, flats (namely *Rumah Susun* or *Rusun)* are mid-high-rise buildings that are built in an environment that is divided into functionally structured parts, good in both horizontal and vertical directions and where the units can each be used separately, but with places furnished with shared parts and with common ground (Pekerjaan *et al.*, 2016). Public Flats are flats that are organized to meet the housing needs of low-income people (Pekerjaan *et al.*, 2016). In general, there are two types of public flats in Indonesia: state owned public flats (namely *Rusunami*), and rented public flats (namely *Rusunawa*).

Generally, *Rusunawa* have certain areas and facilities that support the function of the apartment. Some of the facilities are the main room area, lobby, shared kitchen, healthcare centre, retails, prayer room, and open spaces. Some points of the technical specifications of the *Rusunawa* building are as follows (Kementerian PUPR, 2016):

1) A five-storey vertical building is permitted without the addition of an elevator.
2) The building units are called twin blocks which contain 48 condominium units each block or 96 units in total. Each twin block has to have three residential units on the ground floor for people with disabilities.
3) Infrastructure and facilities in buildings and environment and areas are provided in accordance with the requirements considering the number of users and the length of time used.
4) They should be implemented through a prototype design that is being developed but allows for a touch of local architecture and adaptation to other local areas and conditions that have little influence on the policy line determined by the Ministry of Public Works.

5) The apartment unit area is 24 m² equipped with a pantry and bathroom and WC.
6) Building requirements including the provision of internal installations must comply with existing regulations.
7) Using the precast system in accordance with the requirements determined by the Ministry of Public Works.

7. ACCEPTABILITY AND OPPORTUNITY

Communities respond to the presence of low-cost apartments in many ways. Some give positive responses while others deliver negative feedback. Lian (2022) found that location of the high-rise public housing was the main factor influencing resident satisfaction. Triyuliana and Prakoso (2020) indicated that there was an opportunity to develop a live-work concept into vertical public-rented housing in Indonesia. Lian and Adianto et al., (2022) stated that the reasons people moved to vertical housing varied with the most frequent answers being the short distance to the workplace (44.29%), affordable price (35.71%), and access to public facilities (20%).

On the other hand, communities who live in public rented flats experience some unpleasant conditions. Adianto et al. (2022) found that the shared facilities in public rented flats provoked conflict among residents. The conflicts arose for several reasons such as maintenance (46%), privacy (29%), time used (16%), and other reasons such as kitchen utensils (Adianto et al., 2022). Nugroho, Triyadi and Wonorahardjo, (2022) commented that vertical housing, which is typically a high-rise building, decreased the thermal performance of surrounding buildings through turbulence, cooling, and overheating. In addition, some residents acknowledged that the limitation on rental period (5 years) was too short a time to improve their economic condition while obtaining a replacement home (Adianto and Gabe, 2022).

However, the development of low-cost apartments may overcome the problem of slum area expansion but cannot contribute to conquering climate change issues which have a huge impact on the housing sector. Much research has been conducted in hot humid climates to predict the future climate conditions. Manton et al. (2001) have analysed 91 stations from 1961 to 1998 in 15 countries of Southeast Asia and the South Pacific and argued that significant increases were detected in the annual number of hot days and warm nights, with significant decreases in the annual number of cool days and cold nights. A few years later, Caesar et al. (2011) made the same observation in 13 countries in Indo-Pacific regions between 1971 and 2005 with an extreme warm increase and cold decrease at night, and trends of significantly less precipitation across the region. Supharatid et al. (2022) also summarised the same result, forecasting that there will be gradual warming trends and decreasing precipitation trends after 2050 in Cambodia, Laos, Myanmar, Vietnam, and Thailand.

In the regard to climate change impact, houses are prone to experience overheating. Thapa (2022) stated that in the future climate projection, social housing with no addition of AC in a cold climate region in India will have more discomfort hours, where the annual overcooling hours will exceed the annual overheating hours. Watkiss (2013) predicted that climate change will increase the amount of additional electricity required for cooling, reaching 89 billion euros per year by 2050, while the money required to purchase air conditioning will be close to 8 and 20 billion by 2050 and 2100 respectively. Santamouris (2016) investigated the demand for air conditioning and the increased rise of population in developing countries and predicted that by 2030, there will be a growth in population about 52% and 34% in Asia and Africa respectively.

Based on the Central Statistics Agency (BPS), in the last 61 years, Indonesia's population increased by 1.90% from 93.9 million in 1961 to 272.2 million in 2021. As the population keeps rising, the requirement of affordable and liveable housing is increasing. It was reported from The Ministry of Public Works and Housing of Indonesia that the total housing backlog in 2019 was 6.8 million units and the number of unhabitable homes was 1.9 million units. The Central Statistics Agency (BPS) also reported that 80% of the population in Indonesia were low-middle income people who cannot afford to install air conditioning in their house in the global warming crisis. Therefore, increasing access for low-income people to decent, safe, and affordable housing and supported by the provision of adequate infrastructure, facilities and utilities, the Ministry of Public Works and Housing are planning to build more flats or affordable vertical housing for low-income people.

There are opportunities to living in public rented flats when viewed from the economic, land use, and technology perspectives. From the economic point of view, public rented flats are cheaper and affordable for low-income communities because they are subsidised by the government. It is also a legal and decent settlement which can reduce the spread of slums. In terms of land used, they are efficient because they are built vertically which means saving more area for green and open spaces and implementing the one-stop living that provides residential, work-place, retail, and prayer hall together in a compact area. For future developments, it is also applicable to apply technologies such as solar PV, kinetic facade, and shading devices but at a more economic price.

8. CONCLUSIONS

Housing in Indonesia has been shifting from traditional to modern landed houses and low-cost apartments. The change was caused by social, culture, and economic factors. The degradation of the traditional houses was the beginning of modern landed houses. The presence of landed houses leads to the limitation of land properties in many big cities and to a significant increase in property prices. In addition, along with the rise of high-cost properties, low-income communities are starting to try to find career opportunities in some big cities in Indonesia. They are trying to

build their own houses illegally due to the inability to buy their own house. This is the beginning of slums spreading in some cities in Indonesia. To solve the social disparity between high income people and low-income communities, the local government started to develop a new lifestyle of living vertically. They developed public-rented flats or low-cost apartments to increase access for low-income people to decent, safe, and affordable housing supported by the provision of adequate infrastructure, facilities, and utilities.

However, the development of low-cost apartments cannot resolve climate change issues. The rising air temperature and the decrease of precipitation influence the microclimate conditions causing a long drought. It makes it hard for occupants to achieve thermal comfort and people increasingly use active means of space conditioning to respond to these conditions. Energy consumption is rising due to the increase of air condition utilisation, however, low-income communities cannot afford to install air conditioning in their homes. Therefore, there is a need to anticipate the requirement to address comfort within those homes using low-tech low-cost energy efficient solutions. Housing policies and regulations need to be reviewed to address this issue and include comfort targets

9. ACKNOWLEDGEMENTS

10. REFERENCES

Adianto, J. and Gabe, R.T. Alternative housing priorities for low-income migrants in Jakarta, Indonesia https://doi.org/10.1080/12265934.2022.2072939

Adisurya, S.I. (2016) 'KAJIAN BESARAN RUANG PADA UNIT RUMAH SUSUN DI JAKARTA, Studi Kasus: Rusun Tebet, Rusun Tanah Abang dan Rusunami Kalibata', Jurnal Dimensi Seni Rupa dan Desain, 13(1), pp. 93–112. doi:10.25105/dim.v13i1.1781.

All-jakarta-apartments.com (no date) Apartemen Jakarta. Available at: all-jakarta-apartments.com (Accessed: 30 June 2022).

Arsitur Studio (2020) rumah tipe 21/24 m2. Available at: www.arsitur.com (Accessed: 30 June 2022).

Azizah, L.N. (no date) Rumah Adat Aceh dan Filosofinya. Available at: gramedia.com (Accessed: 30 June 2022).

BPS (no date a) Jumlah Penduduk Provinsi DKI Jakarta Menurut Kelompok Umur dan Jenis Kelamin 2019-2021. Available at: jakarta.bps.go.id (Accessed: 30 June 2022).

BPS (no date b) Rata2 harga/ unit pembangunan rumah oleh perumnas. Available at: www.bps.go.id (Accessed: 30 June 2022).

Caesar, J. *et al.* (2011) 'Changes in temperature and precipitation extremes over the Indo-Pacific region from 1971 to 2005', International Journal of Climatology, 31(6), pp. 791–801. doi:10.1002/joc.2118.

Dmitrieval (no date) Rumah adat tongkohan, Toraja. Available at: stock.adobe.com (Accessed: 30 June 2022).

Hisham, N.N. and Amin, N.D.M., (2019) Housing Design for Urban Poor in Kuala Lumpur: A Literature Review - Improving natural ventilation for an energy-efficient low-income apartment in the tropic Behavioural and functional based design of high-rise public housing project in Jakarta, Indonesia'. doi:10.1088/1757-899X/615/1/012064.

Idham, N.C. (2018) 'Javanese vernacular architecture and environmental synchronization based on the regional diversity of Joglo and Limasan', Frontiers of Architectural Research, 7(3), pp. 317–333. doi:10.1016/j.foar.2018.06.006.

International Energy Agency (IEA) (2019) 'The Future of Cooling in Southeast Asia', The Future of Cooling in Southeast Asia [Preprint], (October). Available at: https://www.iea.org/reports/the-future-of-cooling-in-southeast-asia.

Julie, D. (2011) Kampung Naga. Available at: en.wikipedia.org (Accessed: 30 June 2022).

Kementerian PUPR (2016) 'Pemanfaatan Rusunawa', pp. 1–80. Available at: https://bpsdm.pu.go.id/center/pelatihan/uploads/edok/2018/11/7920a_3_-_Modul_Pemanfaatan_Rusunawa.pdf.

Khairunisa, A. (2018) 'Kampung Vertikal Sebagai Sentra Industri Bakpia Pathuk Di Purwodiningratan, Yogyakarta', pp. 14–52. Available at: https://dspace.uii.ac.id/handle/123456789/10408.

Kompas.com (2021) Semi-detached house. Available at: www.kompas.com (Accessed: 30 June 2022).

Krisnanto, E. *et al.* (2018) 'The analysis of household energy consumption of public apartments in Indonesia: A case study of rusunawa buildings in bandung city', Journal of Engineering Science and Technology, 13(7), pp. 1926–1938.

Kubota, T., Surahman, U. and Higashi, O. (2014) 'A comparative analysis of household energy consumption in Jakarta and Bandung', 30th International PLEA Conference: Sustainable Habitat for Developing Societies: Choosing the Way Forward - Proceedings, 2(December), pp. 260–267.

Lian, Y. *et al.* (2020) 'Conceptual Housing and Housing Prices: An Empirical Study Based on Micro-big Data of Hangzhou Newly-built Housing Market' Journal of Physics: Conference Series, Volume 1616, 3rd International Symposium on Big Data and Applied Statistics 10-12 July 2020, Kunming, China

Lingkarwarna.com (no date) detached house. Available at: lingkarwarna.com (Accessed: 30 June 2022).

LIPI (2012) LIPI. Available at: lipi.go.id (Accessed: 29 June 2022).

Manton, M.J. *et al.* (2001) 'Trends in extreme daily rainfall and temperature in southeast Asia and the south Pacific: 1961-1998', International Journal of Climatology, 21(3), pp. 269–284. doi:10.1002/joc.610.

Marpaung, R. (2019) File:Rumah Bolon (Batak Traditional House).jpg. Available at: commons.wikimedia.org (Accessed: 30 June 2022).

Martinus, Y. (2018) Rusun. Available at: wartakota.tribunnews.com (Accessed: 30 June 2022).

MichaelJLowe (2005) File:Rumah Gadang.jpg. Available at: commons.wikimedia.org (Accessed: 30 June 2022).

Murtyas, S., Hagishima, A. and Kusumaningdyah, N.H. (2020) 'On-site measurement and evaluations of indoor thermal environment in low-cost dwellings of urban Kampung district', Building and Environment, 184(June), p. 107239. doi:10.1016/j.buildenv.2020.107239.

Nursiyono, J.A. and Dewi, D.M. (2021) 'Determinan Harga Tanah Di Indonesia (Studi Kasus : Www . Lamudi . Co . Id) Determinants of Land Prices in Indonesia', pp. 136–145.

Pandelaki, E.E. and Shiozaki, Y. (2010) 'the Core House Concept and Its Implementation in', Int. Journal for Housing Science, 34(4), pp. 233–248.

Parisi, C. de A., Kubota, T. and Surahman, U. (2021) 'Affordable modifications for sustainable houses in urban informal settlements: a case study of Bandung, Indonesia', International Journal of Urban Sustainable Development, 13(3), pp. 659–689. doi:10.1080/19463138.2021.1946544.

Patriella, Y. (2022) planned house. Available at: ekonomi.bisnis.com (Accessed: 30 June 2022).

Pekerjaan, M. *et al.* (2016) 'JDIH Kementerian PUPR', pp. 1–20.

PLN (2017) 'Statistik Perusahaan Listrik Negara 2016'.

PLN (2021) 'PLN Statistics 2020', Statistik PLN 2020, (1), p. 43.

Prasetyo, B.A. (2022) Rumah Mbaru Niang, Nusa Tenggara Timur. Available at: 99.co.

Prasstyle.com (2021) Rumah Adat Kalimantan Barat. Available at: Prasstyle.com (Accessed: 30 June 2022).

PT PLN (2018) 'PLN Statistics 2018', Sekretariat Perusahaan PT PLN, 53(9), pp. 1689–1699.

PT PLN (Persero) (2019) 'Statistik PLN 2019 [PLN Statistic 2019]', Jakarta [Preprint].

PT PLN Secretariat Company (2018) 'PLN Statistics', p. (in Bahasa Indonesia).

PUPR (2021) 2021, Program Sejuta Rumah Tetap Dilanjutkan Dorong Program Sejuta Rumah, Kementerian PUPR Siapkan Kebijakan dan Strategi Khusus. Available at: perumahan.pu.go.id.

Santamouris, M. (2016) 'Cooling the buildings – past, present and future', Energy and Buildings, 128, pp. 617–638. doi:10.1016/j.enbuild.2016.07.034.

Sardon (2010) Map Indonesia. Available at: commons.wikimedia.org (Accessed: 30 June 2022).

Shopee (no date) Ruko. Available at: shopee.co.id (Accessed: 30 June 2022).

Sing, Y. (2011) KEBERAGAMAN KAMPUNG VERTIKAL. Available at: http://rumah-yusing.blogspot.com/2011/01/keberagaman-kampung-vertikal.html (Accessed: 12 August 2022).

Superadventure.co.id (no date) Rumah Hanoi Papua. Available at: superadventure.co.id (Accessed: 30 June 2022).

Supharatid, S., Nafung, J. and Aribarg, T. (2022) 'Projected changes in temperature and precipitation over mainland Southeast Asia by CMIP6 models', Journal of Water and Climate Change, 13(1), pp. 337–356. doi:10.2166/wcc.2021.015.

Surahman, U. et al. (2022) 'Investigation on household energy consumption of urban residential buildings in major cities of Indonesia during COVID-19 pandemic', Energy and Buildings, 261, p. 111956. doi:10.1016/j.enbuild.2022.111956.

Tempo.co (2015) Urban Kampung. Available at: en.tempo.co (Accessed: 30 June 2022).

Thapa, S. (2022) 'Risk of overheating in low-rise naturally ventilated residential buildings of northeast India–an effect of climate change', Architectural Science Review, 65(1), pp. 14–41. doi:10.1080/00038628.2021.1941748.

Tridya, D.S. (no date) Tipe Rusun. Available at: https://www.rumah123.com/panduan-properti/tips-properti-70316-panduan-lengkap-apartemen-tipe-studio-dari-unit-plan-hingga-harga-sewanya-id.html (Accessed: 12 August 2022).

Utama, A. and Gheewala, S.H. (2008) 'Life cycle energy of single landed houses in Indonesia', Energy and Buildings, 40(10), pp. 1911–1916. doi:10.1016/j.enbuild.2008.04.017.

Utama, A. and Gheewala, S.H. (2009) 'Indonesian residential high rise buildings: A life cycle energy assessment', Energy and Buildings, 41(11), pp. 1263–1268. doi:10.1016/j.enbuild.2009.07.025.

Vannisa (2019) Rumah Adat Jawa Timur. Available at: perpustakaan.id (Accessed: 30 June 2022).

Wahyupratama159 (2021) Rumah Kajang Leko, Jambi. Available at: commons.wikimedia.org (Accessed: 30 June 2022).

Watkiss, P. (2013) 'Energy: the impacts and economic costs of climate change on energy in the European Union'.

Wihardjono, Y. (2012) Ruko. Available at: https://www.flickr.com/photos/chandrayoke/6968414042/.

Willetts, J. et al. (2019) 'Special Issue: Water, Sanitation and Hygiene (WASH) Technologies and Governance in Urban Development Co-developing evidence-informed adaptation actions for resilient citywide sanitation: Local government response to climate change in Indonesia', 0(0), pp. 1–22. doi:10.1177/23998083221098740.

#43: The use of wood for resilient cities

The case of Turkey: investigation on the use of wood in construction sector

Meltem VATAN

Bahçeşehir University, Faculty of architecture and Design, meltem.vatan@arc.bau.edu.tr

Abstract: The World Bank data states that by 2030 the urban population will reach about 5 billion with two thirds of those living in cities. Therefore, it is essential that cities plan their strategies for this quick growth (https://www.un.org/development/desa/dspd/2018/10/inclusive-families/). Within the scope of sustainability in Europe in the 2000s, it was stated that it was necessary to produce new industrial technologies based on the modular, stockpile and reversible elements, as well as to reduce energy use through the form of the buildings, the method of construction and urban design elements (Okşak, 2011). 31st October was designated as World Cities Day by the United Nations General Assembly (2013) and it was followed by the 2015 – 2030 agenda of Sustainable Development Goals (SDGs), accepted in 2015 in Sendai, Japan, which had a critical role in the promotion of the international community's interest in global urbanisation. Within the 17 goals, the 11th is entitled Sustainable Cities and Communities. According to UN data from 2016, 90% of urban dwellers breathe unsafe air and ambient air pollution has caused 4.2 million deaths (https://www.un.org/sustainabledevelopment/cities/). Therefore, minimising air pollution and reducing energy consumption is one of the primary goals to achieve better urbanisation and the well-being of citizens. In this sense, embedded energy and the use of environmentally-friendly materials have become more important than ever. The State Planning Organization of Turkey (DPT), active in the 2000s, supports orientation to renewable energy sources, do-it-yourself systems, pre-fabricated building technologies, and structures suitable for extension (DPT 2001-I), (DPT 2001-II). The aim of this work is to make a comparative study about the use of construction materials such as concrete and wood. These and similar studies are thought to encourage the use of environmentally sensitive and natural materials in future designs. The data will be gathered from official statistical data.

1. INTRODUCTION

Due to the limited natural resources of energy and increase of global population as well as the number of city dwellers there has been a significant intention toward studies in the field of resilience and sustainability in recent decades. This subject includes interdisciplinary studies and approaches related to the economy, industry, society, energy, construction, architectural and urban design and the like. The past, present and surely future of the earth is tightly connected with the sustainable use of its resources. Orientation to the researches, innovations and applications to sustainable growth of the future, next generations and the human well-being is more important than ever. As a result, there have been numerous significant initiatives carried out at international level. Chronologically, the most essential ones may be listed as the designation of 31st of October as World Cities Day by the United Nations General Assembly (2013), the 2015 – 2030 agenda of Sustainable Development Goals (SDGs) signed in Sendai, Japan (2015), the adoption of the UN General Assembly Agenda for Sustainable Development (2015) and numerous national ones in many countries. Additionally, in the 2000s in Europe the importance of new industrial technologies based on the modular, stockpile and reversible elements and reduction of energy use in construction and buildings have been stated within the scope for sustainability (Okşak, 2011; https://www.proholz.at/). The main and deadly effect of energy use to humans is the released carbon and air pollution. According to the UN data from 2016, 90% of urban dwellers now breathe unsafe air and ambient air pollution has caused 4.2 million deaths (https://www.un.org/sustainable development/cities/). Therefore, studies and actions related to the reduction of fuel-based energy consumption and to boost the use of green based, renewable and other alternative energy resources are the main goals to achieve better urbanisation and the well-being of the citizens. Within these goals, the State Planning Organization of Turkey (DPT), established in 1960 and transferred to the Ministry of Development in 2011 and again to the Presidency of the Republic of Turkey of Strategy and Budget in 2018, supports orientation to renewable energy sources, do-it-yourself systems, pre-fabricated building technologies, and structures suitable for extension (DPT 2001-I), (DPT 2001-II).

The aim of this paper is to make a comparative study about the use of construction materials such as concrete and wood in order to investigate the use of wood in the construction sector. Additionally, it is hoped to emphasis the use of wood in the construction sector in order to obtain a low-carbon footprint and low-emission energy use for less environmental impact. The authors believed that these and similar studies will encourage the use of environmentally-friendly and natural materials in future design approaches. This field is significantly important for Turkey as one of the countries that has signed the Sendai Framework agreement and SDGs agenda. The comparison will be made based on the official statistical data.

Although environmental policies come to mind when sustainability is considered, it includes the wider scope such as social, economic and ecological balances. All humans have to feel the obligation to take part in sustainable solutions and to support them due to the rapid increase of the need for shelter. Contributions by architects, engineers or producers to the sector may be possible through technology and materials development to encourage the use of sustainable and local materials. Accordingly, the requirements and local capacity of sustainability need to be determined. Particular intention and priority should be given to local resources and long-term planning of their use. Therefore, the use of wood in the construction sector is the main concern of this study (Somer, 2008).

2. THE IMPORTANCE OF WOOD IN CONSTRUCTION SECTOR FOR SUSTAINABLE CITIES

Sustainability is a broad issue not only in architecture but also in many other fields. In some cases, it is linked to technical, organisational and operational efficiency and in some others it is linked to the improvement of life style, welfare and consumption habits etc. (Somer, 2008). The Sendai Framework formed the 2030 agenda for sustainable development where 17 SDGs were adopted by all United Nations Member States in 2015. This framework aimed to share a blueprint for peace and posterity worldwide for now and future (Sendai Framework for Disaster Risk Reduction 2015–2030, https://sdgs.un.org/goals). The first mention of sustainability dates back to the 70s when Meadows (1972) firstly introduced this concept. Considering the construction sector, the balance parameters are listed as: a sufficient amount of construction that responds to the need for a long time that is suitable for the demand; economic development and ecological balance should be retained; an ecologically sustainable system must protect natural resources and the environment in its production processes; a sustainable system in terms of construction technique must take into account socio-economic trends in order to remain viable for a long time (Somer, 2008).

Within the architectural aspect sustainability includes compatibility with nature, environmentally-friendly materials, green building construction, green energy use, low carbon footprint and so on. Sustainably-designed buildings are sensitive to ecosystems with their design involving a holistic and social-environmental responsibility and understanding; they are climate-responsive and oriented towards renewable energy sources, natural and non-waste-produced materials are used. Therefore, sustainable building design is a holistic approach which includes not only the building but also its environment, and sustainable cities are one of the contemporary fields of architectural design and production. Especially, the quantity and quality of the housing stock directly affects the quality of life in cities. Ecological, economic and social concerns have brought the concept of sustainable urbanisation onto the scene (Somer, 2008).

The United Nations Human Settlements Programme, UN-Habitat, was initiated in 1976 by the United Nations agency for human settlements. It was mandated by the UN General Assembly to promote socially and environmentally

sustainable towns and cities with the goal of providing adequate shelter for all (https://www.un.org). Accordingly, it is possible to say that the first intentions to consider sustainable cities and to improve the life quality by consciousness to the earth was UN-Habitat initiation. However, it was not enough to consider only construction and city planning, adequate policies, acting together (all stake holders), taking into account energy efficiency, carbon footprint and the like. Sustainability needs a holistic approach.

The sustainable cities approach can be dealt with by definition of its concept aiming for a solution to urbanization problems, determination of better solutions considering the Sendai Framework agenda and climate change impacts and reduction of carbon footprint, consideration of embedded energy in construction activities and orientation to the local and recycle material use. The main indicators for this purpose are the improvement and acceleration of construction technologies and the increase in financing opportunities in the construction sector. In order to achieve these, it is necessary to produce modular, stackable, replaceable, element-based new industrial technologies, and to reduce energy use through the form, construction style and urban design of buildings (Okşak, 2011; https://www.proholz.at/).

These facts can be stated as the basis for the importance of the use in wood in the construction sector as a sustainable and environmental friendly material. It has many benefits such as being a renewable and recyclable material. Management of the forest industry makes it an endlessly renewable resource. Additionally, its production requires less energy than other construction materials. It has a carbon absorption capacity and the trees produce oxygen. According to some anonymous data it was stated that a ton of wood production generates approximately 30 kg of net emissions against approximately 264 kg for cement and 694 kg for steel. The production of wood produces less waste and it provides greater energy efficiency.

The importance of wood in the construction sector for sustainable cities can be summarised as being the only construction material that is genuinely renewable and has a carbon absorption capacity; it has better thermal insulation properties than any other construction material; it is healthier and an environmentally-friendly material; it is considered a warm material because of being natural and having a positive impact on the human senses. Additionally, wood is a flexible and light weight material, it has a good earthquake resistance capacity and its construction speed is higher than other materials which helps to reduce the cost of construction.

Taking into account urbanisation and the sustainable city approach, it is clear that the construction sector is one of the leading sectors in this field. So, it is considered to be area for more scope to reduce global carbon emissions and the use of low carbon footprint materials is one of the main solutions. These were the statements included in 2015 – 2030 Sendai Framework agenda. The use of wood in the construction sector and its massive use in city planning has a significant role to be part of solutions for a better future of the world. The use of wood in the construction sector is a leverage for low carbon building construction which will lead to sustainable cities in the long term.

3. THE CASE OF TURKEY – STATISTICAL DATA

The construction industry and accordingly construction materials, innovative approaches and detailed solutions play a more important role than ever among the economic activities in the global scale. The construction sector is a fixed capital investment and needs sustainable, balanced and inclusive economic growth. One of the leverages is to seek a lower environmental impact and a better future which is defined as sustainability in the era of continuous growth in the construction industry. In particular, buildings with higher standards, energy efficiency, low carbon footprint, the use of environmental friendly materials, the digitalization process, smart buildings, cities and systems and the like became crucial in the construction sector. Therefore, investigation on the use and environmental effect of construction materials is a trend topic in this field. The numerical data used in the following graphics were mainly based on the report of IMSAD (Association of Turkish Construction Material Producers which is one the leading NGOs of the Turkish construction materials sector) and data from TUIK (the Turkish Statistical Instıtute).

In 2020, conditions in the world economy were affected by the pandemic and were negative for the construction sector. Accordingly, the global performance of the construction sector has declined. The Covid-19 pandemic caused a contraction in construction expenditure at a global scale; only in China and Indonesia was growth observed (Erkal, Kocabaş, Ermurat, 2021).

3.1. Construction sector in Turkey

The construction sector and the construction materials industry in Turkey has a pioneering role in the economy which has increased in recent decades. The use of innovative technologies and contemporary, environmentally-friendly materials, the construction of mega projects, urban transformation activities and infrastructure investments continue to accelerate the construction sector. Within this context, to monitor the capacity of the construction industry and relevant sectors is of great importance in documenting this rapid change and its effect both in the world and in Turkey. At present, it is only possible to take part in the increasing competitiveness with accurate, sufficient and regular information and data. Therefore, the main goal of this paper is to investigate the material use in the construction sector with particular interest to the wood industry considering sustainability (Erkal, Kocabaş, Ermurat, 2021).

As the world economy and also the economy of Turkey has experienced recession due to the Covid-19 pandemic in 2020, the construction sector has suffered as well. Decrease in support to the construction sector and public building's investment has resulted in a 3.5 percent shrinkage in 2020. The budget of the top 20 largest investments was 10.82 billion TL (approx. 1.5 billion US Dollars). On the contrary, the local market of construction materials grew by 8.1% and reached 408 billion TL (approx. 55 billion US Dollars). Industrial production of construction materials increased by 9.1 percent in 2020. Despite the negative effect of Covid-19 pandemic in 2020, industrial production of construction materials achieved the highest growth in recent years which has been fluctuating since 2015. The main construction material in Turkey is reinforced concrete. The use of wood in construction sector is comparatively rare to reinforced concrete although wooden-framed structures were widely used in traditional Turkish buildings, particularly in houses. Table 1 shows the growth of cement and wood between 2018 and 2020.

Table 1: The growth of construction materials between 2018 and 2020 Ref: Erkal, Kocabaş, Ermurat, 2021

Construction materials industry	Production growth (%) 2018	Production growth (%) 2019	Production growth (%) 2020
Cement	0.6	-10.7	28.4
Wooden construction materials	-23.1	-18.7	2.3

Reinforcing steel bar profiles: the use and production

Iron and steel bar profile industry used as reinforcement is one of the oldest and well-established industries in Turkey. It has a world-class production capacity. By 2020, there were 252 enterprises in the iron and steel bar profile industry. The production of iron and steel bars started to decline after 2017 based on local market contraction but started to increase production again in 2020 by 2.3% which equated to 23.55 million tons. Although the pressure and negative effect of additional customs on exports in the US market and restrictions in the EU, the increase of local market demand supported production. Production of steel reinforcing bars in Turkey between 2017 and 2020 is shown in Table 2.

Table 2: Production and entrepreneurship of steel bars Ref: TUIK, 2022

Year	Entrepreneur (firm)	Production (million tons)
2017	285	27.31
2018	276	26.49
2019	256	23.02
2020	252	23.55

Turkey has an important role in the world economy regarding iron and steel bar export. It reached its peak in 2018 with a 12.5% global share and decreased to 11.5 % in 2019, with a slight increase again in 2020 to 12%. Due to the Covid-19 pandemic as in the global scale Turkey's exports has since dropped significantly (Table 3).

Table 3: The growth of construction materials between 2018 and 2020 Ref: Erkal, Kocabaş, Ermurat, 2021

Years	Turkey's export (billion Dollars)	World's export (billion Dollars)	The share of Turkey (%)
2015	4.239	35.889	11.8
2016	3.696	31.926	11.6
2017	3.915	34.480	11.4
2018	5.425	43.578	12.5
2019	4.694	40.719	11.5
2020	4.147	34.610	12.0

Despite the negative effect of the Covid-19 pandemic and worldwide economy, Turkey ranked first in iron and steel bar global exports in 2020 with 4.1 billion US Dollars, followed by China, Italy, Germany and Spain (Table 4).

Table 4: Top 10 Countries in World Iron and Steel Bar Profile Export - 2019 and 2020 Ref: Erkal, Kocabaş, Ermurat, 2021; TUIK, 2022

2019			2020		
#	Country	Export (US Dollars)	#	Country	Export (US Dollars)
1	Turkey	4,693,544,761	1	Turkey	4,147,440,976
2	China	3,050,486,000	2	China	3,385,347,000
3	Germany	2,754,896,548	3	Italy	2,643,202,000
4	Italy	2,731,200,955	4	Germany	2,635,380,000
5	Spain	2,345,327,000	5	Spain	1,898,962,000
6	Russia	1,438,894,000	6	Russia	1,473,022,000
7	South Korea	1,316,506,286	7	Malesia	1,418,412,000
8	Poland	1,207,653,202	8	Poland	1,204,241,000
9	Japan	1,108,456,142	9	South Korea	1,012,980,000
10	France	946,476,000	10	Japan	863,032,000
TOTAL EXPORT		**40,719,009,000**	**TOTAL EXPORT**		**34,610,113,257**

As it is shown in the above graphics and numerical data, steel material has an important role in Turkey as well as in the world construction sector. Turkey has a significant place in the export market which shows its large production capacity. The other important material in Turkey's construction field is cement.

Cement: the use and production

World cement exports are around 10 billion US Dollars in the last five years, increasing to 11.56 billion in 2019 and decreasing to 8.2 billion US Dollars in 2020. Due to the Covid-19 pandemic, construction activities declined and transportation was restricted and, as a result, export of the cement decreased by 29%.

Turkey is an important producer and exporter in the cement industry and its cement exports in 2019 and 2020 increased repeatedly. The cement sector in Turkey accounts for almost all of the local demand supplies and exports to a large extent. Cement material export is the highest in Turkey in terms of its quantity and the country is among the top 10 countries in the world in terms of cement consumption. Local consumption decreased significantly in 2018 and 2019 but rose by 24.2% in 2020, reaching 59.76 billion tons. Due to the Covid-19 pandemic the local demand decreased dramatically and export became more important which increased considerably together with the clinker. The export capacity of cement is geographically wide-ranging reaching 130 countries in the world. The highest amount is exported to the USA, reaching 221.6 billion US Dollars in 2020, following by Ghana and Israel.

3.2. The use of wood in construction sector in Turkey

Limited stock of local wood and limited investments in the wood industry have had a negative effect on the wood construction production in Turkey. However, production of the materials used in reinforced concrete buildings is based on the energy use which has limited sources and has a negative effect on the earth regarding air pollution and carbon footprint. Therefore, the use of green energy and sustainable energy sources is more important in the global scale as well as in Turkey which makes the use of wood more important than ever.

Wooden products used in the construction industry in Turkey are as follows: plywood, wood veneer panel and similar laminated wood materials (made of bamboo), wooden veneer panels and similar laminated wooden materials, fibreboard, joined parquet and panels, windows, and their frames and doors and their related parts. Additionally, wooden form works for concrete works, tiles and roof shingles and the like.

The wood industry in Turkey has grown in the last decades. Newly-added production capacities have increased the potential for export with new capacity and export amounts in 2018-2019-2020 and increasing in value. Export for 2020 increased by 19% to 1,183,191 tons and 667.5 million US dollars in price. The downward trend in the export has now stopped and in 2020 reached to 0.56 US Dollars. Enterprises involved in production in the wood construction materials industry are shown in Table 5. The increase of numbers of the attempts was limited and there were fluctuations in 2019 and 2020.

Products	2016	2017	2018	2019	2020
Bamboo wooden products	4	4	5	10	12
Plywood, laminated timber, wooden materials	98	111	110	98	98
Fibreboard	56	56	55	45	45
Joined parquet and panels	72	73	83	73	73
Windows and doors	519	525	496	460	545
Concrete form works	11	12	8	8	8
The other veneer and joinery products	61	55	53	49	52

World wood construction materials exports have been in decline since 2018 when exports totalled 42.06 billion US Dollars. It decreased by 9.3% to 38.15 billion US Dollars in 2019 and to 36.19 billion US Dollars in 2020. However, the share of Turkey's exports globally was 1.06% in 2016, increasing to 1.23% in 2017, to 1.47% in 2019, and to 1.84% in 2020. Therefore, Turkey has rapidly increased its market share in the world in recent years. The share of wooden construction materials in world exports for Turkey is shown in Table 6.

Table 6: The share of wooden construction materials in world exports of Turkey Ref: Erkal, Kocabaş, Ermurat, 2021; TUIK, 2022

Years	Export of Turkey (billion US Dollars)	World export (billion US Dollars)	The share of Turkey (%)
2016	425,8	39.963	1,06
2017	506,0	41.170	1,23
2018	515,8	42.066	1,23
2019	559,9	38.148	1,47
2020	667,5	36.190	1,84

4. CONCLUSION

Wood is one of the oldest construction materials and has been used in construction for all of human history and it is still the only one natural and renewable material. Considering the Sendai Framework agenda (2015-2030) and beyond, the use of wood in the construction sector is an imperative for the life cycle and re-use of buildings for a sustainable future and reduction of carbon footprint. Forestry has a direct and indirect effect on human life and the earth is directly dependent on it. Therefore, the use of wood in the construction sector and the management of its industry due to its low impact on the environment is an imperative for the future of the planet.

United Nations data states that the world population is expected to grow by 25% in the next 30 years, rising from 7.7 billion people in 2020 to 9.7 billion in 2050. This fact shows the increasing demand for building construction and particularly housing. So sustainable solutions for building construction, city planning and urbanisation became more critical than ever. Sustainability includes social, economic and ecological balances. Construction materials, technologies, workmanship, transportation, profit and time management are some of the main parameters for this balance.

Another consideration for sustainable development and sustainable cities is climate change as one of the biggest threats for the future of the world and the human race. The rise of overall temperatures in the twenty-first century and the exposure to high heat of the population involving risk to life is anticipated. It is obvious that long-term projections and predictions are underestimated with some long-term events occurring much earlier than expected. One of the main reasons for climate change is rapid urbanisation and the growth of the global population although in some studies the impact of urbanisation is stated as relatively insignificant (Zhang, Li, Li, 2020).

Considering the building construction sector, the need for adaptation to global change including climate change, re-thinking building construction and seeking innovative approaches is significantly important. Reduction of energy use in the construction sector is one of the major precautions that can be taken for example considering embedded energy and building service life; instead of demolishing buildings, having an adaptive re-use approach for their renewal. Additionally, developing and improving new construction technologies and systems, to use light-weight structural systems, sustainable materials, natural and local materials, prefabricated systems, modular production of buildings and the like. Within this concept the main aim of this study was to stress the importance of the use of the wood in construction sector and to have long-term planning for its production industry in order to have a sustainable approach. Particularly, the case of Turkey was investigated and the increase of the use of wood in the construction sector was encouraged.

Migration has a significant impact on the urbanisation in Turkey. Its uncontrolled speed and political decisions without consideration of urbanisation in recent decades decreased the quality of life in cities for their inhabitants. Not only

construction but also infrastructure is a problem waiting for solutions in many urban areas. Therefore, the construction sector is more important than ever. To catch up with global trends and to achieve sustainable solutions are critically important.

In the case of Turkey, achieving the sustainable approach is based on the improvement of construction techniques, development of new building materials and technologies, architectural and structural planning instruments and construction methods (Somer, 2008). The indicators to achieve these goals are universal so the general approach for solutions is universal. However, application of the indicators and their evaluation are conditional. Each place has its own dynamics. In the case of Turkey, the economy and the difficulties in the development of new technologies and innovative approaches are main disadvantages. Application of the theoretical achievements in practice is not easy. Yet, to have a long history of tradition of wooden building construction is a major advantage for this geography, therefore consideration of lessons learned from vernacular and traditional building techniques are invaluable.

The solutions that can help in the case of Turkey are listed below:

- The increase of the use of wood in the construction sector and considered planning of the forestry industry for short and long term processes;
- In rapid and uncontrolled urbanisation, needs and conditions can change rapidly requiring design of flexible spaces, consideration of adaptive re-use and renovation of existing buildings and continued lifecycle approach;
- To ensure sustainable and recyclable construction materials use and waste management;
- Re-think and re-define management of the construction sector including all related industries aiming for reduction of labour costs and time factor;
- Re-think the management of control systems and decision-making actors and processes by considering the gaps of their linkage;
- Standardisation of building construction techniques and the use of modular and prefabricated building construction techniques;
- Increasing the labour quality and rapid construction techniques;
- Development of new construction standards considering environmental impact;
- To encourage the use of recyclable materials and waste management;
- To simplify and develop the standards for do-it-yourself building construction.

Although wood and wooden constructions are defined in different ways depending on geography, its potential for a sustainable future of the construction sector and carbon storage capacity is universal. According to the references, it is estimated that the use and operation of buildings are responsible for approximately 40% of the total energy consumption of EU member states (EU28)—40% and 27.3% in the US and China, respectively —and for 36% of their greenhouse gas (GHG) emissions from energy. Consequently, it is obvious that the construction sector has a large impact on the economy and environment and development of new technologies and the use of materials such as wood having a low carbon footprint is significantly important (Cao, Dai, Liu, 206; Leszczyszyn *et al*, 2022; https://ec.europa.eu/energy/sites).

5. REFERENCES

Cao X., Dai X., Liu J., 2016. Building Energy-Consumption Status Worldwide And The State-Of-The-Art Technologies For Zero-Energy Buildings During The Past Decade. Energy Building. Number: 128, 198–213.

Communications from the Commission to the European Parliament, the Council, the European Economic and Social Committee and the Committee of the Regions. A Renovation Wave for Europe–Greening out Buildings, Creating Jobs, Improving Lives, European Commission, Brussels. 2020. Available online: https://ec.europa.eu/energy/sites/ener/files/eu_renovation_wave_strategy.pdf (accessed on August 1, 2022).

DPT (2001-I) Housing Specialization Commission Report (Konut Özel Ihtisas Komisyonu Raporu). Ankara: Prime Ministry Republic of Turkey, 2000, DPT: 2594 - ÖİK: 606, PDF, ISBN: 975-19-2759-5, http://ekutup.dpt.gov.tr/konut/oik606.pdf (accessed on June 3, 2007).

DPT (2001-II) Local Administrations Special Expertise Commission Report (Yerel Yönetimler Özel Ihtisas Komisyonu Raporu). Ankara: Prime Ministry Republic Of Turkey, 2000, DPT: 2538 - ÖİK: 554, PDF, ISBN: 975-19-2567-3, http://ekutup.dpt.gov.tr/yerelyon/oik554.pdf (accessed on June 3, 2007).

Erkal A. (coordinator), Kocabaş E., Ermurat F. (editors). 2021. Economy and Consultancy Services Company. Türkiye İMSAD - Association of Turkish Construction Material Producers. Construction Sector Report. ISBN 978-605-81691-5-9.

Leszczyszyn E., Heräjärvi H., Verkasalo E., Garcia-Jaca J., Araya-Letelier G., Lanvin J-D., Bidzinska G., Augustyniak-Wysocka D., Kies U., Calvillo A., Wahlströmh M., and Kouyoumji J-L. 2022. The Future of Wood Construction: Opportunities and Barriers Based on Surveys in Europe and Chile. Sustainability 2022, 14, 4358 (https://doi.org/10.3390/su14074358 https://www.mdpi.com/journal/sustainability).

Meadows, D. et al., (1972) https://donellameadows.org/archives/a-synopsis-limits-to-growth-the-30-year-update/

Okşak Y. 2011. Türkiye'de Konut Sektörünün Yapisi Ve Gelişimini Etkileyen Faktörler Toki Uygulamalari Örneği , Master Thesis (In Turkish), Kadir Has University, Social Science Institute, İstanbul.

Sendai Framework for Disaster Risk Reduction 2015 – 2030. UN Report. UNISDR/GE/2015 - ICLUX EN5000 1st edition.

Somer M. E. 2008. "Sustainability of urban residential buildings in emerging economies (Aspekte der Nachhaltigkeit im urbanen Wohnbau von Schwellenländern / Untersuchungen zur Berücksichtigung von Sozialverträglichkeit, Wirtschaftlichkeit, Bautechnik, Ressourcen- u. Umweltschonung / Entwicklung eines mehrgeschoßigen Holzbauprototyps für die Türkei)", Technical University of Vienna, Doctoral Thesis, TU, o.Univ.Prof. DDI Wolfgang Winter; Univ.Prof. Dipl.-Ing. Cuno Brullmann.

TUIK – Turkish Statistical Institute. https://www.tuik.gov.tr/ (accessed on August 1, 2022).

Zhang W., Li Y., Li Z. 2020. Impacts of Climate Change, Population Growth, And Urbanization on Future Population Exposure to Long-Term Temperature Change During The Warm Season in China. Environ SCI Pollut Res 27, 8481–8491 (https://doi.org/10.1007/s11356-019-07238-9).

https://www.un.org/youthenvoy/2013/08/un-habitat-united-nations-human-settlements-programme/#:~:text=The%20United%20Nations%20Human%20Settlements,providing%20adequate%20shelter%20for%20all (accessed on August 1, 2022).

https://www.un.org/sustainabledevelopment/cities/ (accessed on August 1, 2022).

https://www.proholz.at/ (accessed on August 1, 2022).

#44: Implementation of PV/T collectors, controllable crystallisation PCM storage and a second latent heat storage unit on a solar-assisted heat pump to provide heating demand for a dwelling

Cagri Kutlu[1], Emmanuel Tapia-Brito[1], Diana S.N.M. Nasir[2], Osaru Agbonaye[3], Stefan Smith[3], Yuehong Su[1], Ben Hughes[2], Qinghua Lyu[4], Saffa Riffat[1]

[1]Department of Architecture and Built Environment, University of Nottingham, University Park, NG7 2RD, UK
[2]Faculty of Science and Engineering, University of Hull, Hull, UK
[3]Department of Built Environment, University of Reading, Reading, UK
[4]School of Science, Hubei University of Technology, Hubei, Wuhan, China

Abstract: Supercooled phase change materials (PCM) are promising in the use of space heating applications as their latent heat is only released when triggered to induce crystallisation, even when stored at ambient temperature. With this feature, utilisation of solar energy can be maximised and carbon release to the environment can be reduced considerably. However, the phase change temperature of commonly used PCM sodium acetate trihydrate (SAT) is around 56-58°C and the system requires booster heating, especially during cold seasons. In this paper, evacuated PV/T collectors were used for both thermal heat collection for a solar-assisted heat pump and electricity generation for heating resistances. Electric heaters were used for charging the secondary latent heat storage which was filled with erythritol. Since the erythritol had a melting point of 121°C, electric heaters fed by PVs could charge it and be used as a booster heater in the system. Although the SAT storage could be used for a weekly period, erythritol could be used for a daily period but still make an impact on the reduction of storage size and provide heating for peak hours. A comprehensive model was built including PV/T collectors, buffer tank, main heat storage unit with SAT tubes, secondary storage unit and building heating demand model. Real weather data was used for the calculation of heating demand, collector performance and overall system performance. Using 40m² PV/T collectors, 750 litre buffer tank, maximum 6kW heating output heat pump, 252 kg SAT and 31 kg erythritol, the tank was charged and discharged to test its heating potential considering heating demand. Using an additional latent heat storage unit resulted in higher supply water temperature which increased from 30°C to 42°C at night.

Keywords: solar-assisted heat pump; sodium acetate trihydrate; erythritol; dual-latent heat storage

1. INTRODUCTION

Thermal energy storage integration to heating systems can efficiently use renewable energy sources in the building energy infrastructure (Cabeza *et al.*, 2015). In this way, greenhouse gas emissions can be reduced and may lead the systems to be more sustainable. Among latent thermal energy storage materials, SAT has many advantages such as high latent heat capacity, non-toxicity and low-cost. The melting point of SAT at 58°C is suitable for space heating systems and domestic hot water supply to the end users. However, SAT like other salt hydrate PCMs, has some drawbacks such as low thermal conductivity, unstable supercooling, phase separation and corrosion with common materials (Wang *et al.*, 2021). Although there are notable problems, the supercooling feature of SAT is promising for thermal storage applications as the latent heat is only released when triggered to induce crystallisation, even when stored at ambient temperature. This special feature thus provides a PCM installation that can be beneficially integrated with intermittent renewable energy sources such as solar thermal collectors and a heat pump unit. By using controllable crystallisation of the SAT, Englmair (Englmair *et al.*, 2019) carried out a numerical study to show that a solar combi-system including on-demand crystallisation of supercooled SAT composites can provide 56% annual solar fraction of heat supply according to a passive house. Kutlu (Kutlu, Zhang, *et al.*, 2020) presented a simulation study of a solar assisted heat pump unit with PCM tank that showed controllable crystallisation of SAT can reduce daily DHW energy consumption by around 13% on an average solar day. To make the system more applicable for different building types and weather conditions which may call for different heating demands, auxiliary sub-systems and their effective integration into the thermal storage systems are important.

SAT's melting temperature of 58°C is suitable for space heating applications, however, sometimes, the building may need higher temperatures in order to compensate for heat loss during colder days or the fusion temperature of SAT can fall by 3-5°C for other factors. Thus, auxiliary heat input is required such as an electric heater or another heating unit to boost the delivery temperature to the building. As the study also aims to reduce electricity consumption during peak load periods, secondary thermal storage with a higher melting temperature would be effective to increase delivery temperature. Erythritol was chosen as a secondary thermal storage material because it is characterised as high temperature PCM having 121°C melting point with a relatively large latent heat of 340 kJ/kg, good stability, high thermal conductivity, non-toxicity and low price (Cheng *et al.*, 2022). Some studies have been done to adjust the melting temperature of Erythritol to around 80-90°C by mixing different polyalcohols (Hidaka *et al.*, 2004). In this paper, evacuated PV/T collectors were used for both thermal heat collection for solar-assisted heat pump and electricity generation for heating resistances. Electric heaters were used for charging the secondary latent heat storage which was filled with erythritol. Since the erythritol has a melting point of 121°C, electric heaters fed by PVs can charge it and it can be used as a booster heater in the system.

The success of the proposed system also depended on auxiliary sub-systems and effective integration into existing and future building developments. Thus, comprehensive models of solar collectors, SAT storage and secondary erythritol storage tank were built. Space is often a limiting factor in the uptake of heat storage systems, particularly in relation to new builds, but the minimal system heat loss means the PCM storage can be placed both underground or outside without fear of heat loss. Secondary heat storage will guarantee a sufficient delivery temperature to the building. However, the supercooling feature of erythritol was not considered, thus, SAT storage could be used on a weekly storage basis, and erythritol storage would be used on a daily basis. Since the secondary storage unit had a larger latent heat capacity, the total size of the system was reduced. The evening peak load for heating was eliminated by this system which considerably reduced the load from the grid and contributed to carbon reduction targets of the communities.

2. SYSTEM DESCRIPTION AND MODELLING

The proposed system consisted of poly-Si PV/T collectors, a buffer tank, a heat pump unit, SAT storage tank and secondary storage tank. The concept allows the use of many storage tanks which could be charged on high solar radiation days and be used later when solar energy was weak or not available, but in this paper, only one SAT storage and one erythritol storage tank were used to show the proposed idea. The building chosen was an Eco house in order to limit heat losses in daytime. The building model was carried out by IESVE software (*IESVE, 2020*, no date). A case study was conducted to calculate heating loads. The house was one of the Creative Energy Homes at the University of Nottingham Park Campus as well as other several low-carbon buildings. The David Willison Eco-house is a two-story office building with dimensions of 7.9m x 7.9m x 5.0m and an interior floor area of 62.41m^2 for each floor. The IESVE model used real Nottingham, UK, yearly data and real fabric materials used in the building. The house was modelled as a family house with 2 professional parents and 2 children of school age. The occupancy profile, heating profile, ventilation rates, appliances profile and lighting profile were designed accordingly to mention 4 people.

The system configuration is given in Figure 1 and operation of the unit for charging and discharging are explained as follows:

Charging period: As the system had a buffer tank, the solar assisted heat pump charged the SAT tanks at any time during the day, however, in this concept, charging time was limited by daytime to avoid low temperature heat source. Thus, when solar energy was available, poly-Si collectors collected heat to increase buffer tank temperature which were a heat source for the heat pump for higher COP. At the same time, electricity generated by the PVs' charged the erythritol tank.

Discharging period: When heating was required by the building, water was circulated between the building and SAT storage unit. Activated PCMs increased the water temperature to 53-55°C and erythritol storage further increased the delivery temperature.
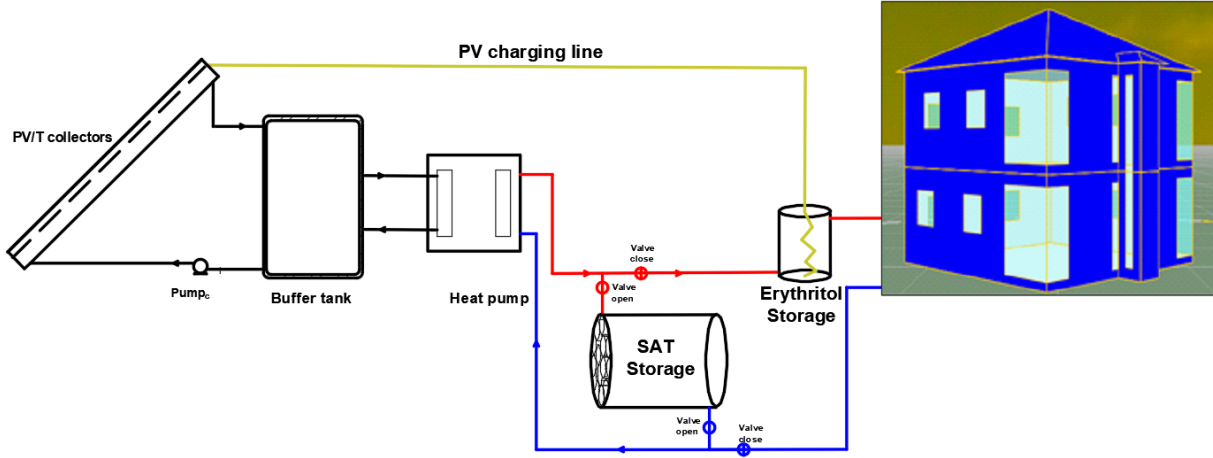
Figure 1: System schematic of solar assisted heat pump with two thermal storage unit

2.1. PV/T collector

PV/T collectors were obtained by incorporating PV cells into the evacuated flat plate (EFP) collectors. TVP SOLAR HT-Power EFP collectors (TVPSOLAR, 2013) were theoretically modified with the poly-Si cells. The equations for PV/T thermal and electrical efficiencies were obtained by deduction method. The calculation procedure can be found in the reference Kutlu, Li, *et al.* (2020). Calculated thermal efficiency equation for the PV/T collector is given in Equation 1.

$$Equation\ 1: Thermal\ efficiency\ of\ collectors \qquad \eta_{th} = 0.6965 - 0.6765 \cdot \frac{T_m - T_a}{G} - 0.004978 \cdot \frac{(T_m - T_a)^2}{G}$$

Where:

- T_a = ambient temperature,
- T_m = mean temperature of the fluid inside the collector and
- G = solar irradiance.

The most common equation to determine the cell temperature is Normal Operating Cell Temperature (NOCT). This value is given by the manufacturer and Equation 2 was used for calculating the cell temperature (Mattei *et al.*, 2006).

$$Equation\ 2: Cell\ temperature \qquad T_{cell} = T_a + (NOCT - 20) \cdot \frac{G}{800}$$

Photovoltaic module electrical efficiency was calculated by the most known model:

$$Equation\ 3: Electrical\ efficiency \qquad \eta_{PV} = \eta_r[1 - \beta_r \cdot (T_{cell} - T_r)]$$

The parameters were given by manufacturers and η_r indicated an efficiency at the reference temperature. Global electrical efficiency of the PV system can be calculated as Equation 4:

$$Equation\ 4: Global\ electrical\ efficiency \qquad \eta_{gPV} = \eta_{PV} \cdot \eta_{DC-AC}$$

126

Where η_{DC-AC} was conversion efficiency of DC to AC and was reported as between 80-95% depending on solar irradiance (Ungureşan *et al.*, 2016, Mulcué-Nieto and Mora-López, 2014).

For $< 300\ W/m^2$, η_{DC-AC} was 80%. For $300\ W/m^2 < G < 500\ W/m^2$, η_{DC-AC} was 85%. This conversion efficiency was used in the calculation of electricity output.

2.2. Buffer tank

The buffer tank maintains the stored solar heat for the heat pump. In order to avoid freezing, Ethylene Glycol water mixture was filled in the buffer tank. The buffer tank was exposed to charging by collectors and discharging by heat pump when they were in operation, besides being exposed to ambient heat losses during the days. Transient performance of the buffer tank was modelled by using one-dimensional temperature distribution model (Duffie and Beckman, 2013).

2.3. Heat pump

The heat pump consisted of four main components namely, compressor, condenser, expansion valve and evaporator. In the modelling, condensation temperature was limited at 75°C as the commercial heat pumps upper level. This temperature was also enough for charging SAT. On the other side, evaporation temperature was affected by the buffer tank temperature which changed the compressor power consumption.

The COP of the heat pump was defined as follows (Equation 5):

Equation 5: *COP of the heat pump*
$$COP = \frac{\dot{Q}_{cond}}{\dot{W}_{comp}}$$

Where:

- $\dot{W}_{comp}$ = compressor consumption
- $\dot{Q}_{cond}$ = condenser load.

The following assumptions were considered for the heat pump simulation: Superheating in the evaporator and subcooling in the condenser was assumed as 3K (Hundy, 2016). For the evaporator, 5K pinch temperature difference approach was assumed (Hundy, 2016) to ensure proper heat was transferred from buffer tank to refrigerant.

2.4. SAT storage

The PCM storage unit was a cylinder shape container with a number of cylindrical PCM tubes placed inside. The horizontal direction of the PCM storage unit was divided into a number of n control volumes. Each control volume was numbered from left to the right to indicate its location as i = 1 being the first element and i = n is the last element. To analyse the temperature gradients with heat transfer process some assumptions have been made:

- Mass transport in the tank was assumed in one dimensional and the tank length was divided into nodes and all node's energy balance equations were solved simultaneously;
- Each element of the tank also contained PCM tube elements and heat transfer occurred between PCM outer surface and water;
- In a water element, water temperature and PCM temperature can be different as charging and discharging occurs;
- PCM tubes were also divided into radial nodes to constitute heat transfer through the PCM centre to the outer edge.

Generalised energy equations of the PCM is given in Equation 6 (Manfrida, Secchi and Stańczyk, 2016)

Equation 6: *Energy equation of PCM*
$$V_{PCM} \cdot \rho_{PCM} \cdot L_{PCM} \cdot \frac{\partial \phi}{\partial t} - V_{PCM} \cdot \rho_{PCM} \cdot c_{PCM} \cdot \frac{\partial T}{\partial t} = h_{w-PCM} \cdot A_{w-PCM} \cdot (T_w - T_{PCM})$$

Where ϕ = PCM liquid fraction, h_{w-PCM} was heat transfer coefficient between PCM and water element.

For the water element, energy balance equation is given in Equation 7:

$Equation\ 7\text{:}\ Energy\ balance$

$$T_{t,n}(i+1) = T_{t,n}(i) + \frac{\dot{Q}_{cond,n}(i) + \dot{Q}_{loss,n}(i) + \dot{Q}_{w-PCM_n}(i)}{M_{st,i} \cdot c_{p,w}} \cdot \Delta t$$

Where $\dot{Q}_{w-PCM_n}(i)$ was heat loss to the ambient via cylinder walls. $\dot{Q}_{w-PCM_n}(i)$ indicated heat transfer rate between water element and PCM material.

The equation for this convection heat transfer is given in Equation 8:

$Equation\ 8\text{:}\ Convection\ heat\ transfer$

$$\dot{Q}_{w-PCM_n}(i) = \alpha_{w-PCM_n}(i) \cdot A_{W-PCM_n} \cdot \left(T_{w_n}(i) - T_{PCM_n}^{wall}(i)\right)$$

Where $\alpha_{w-PCM}(i)$ was convection heat transfer coefficient. It covered the forced convection and natural convection during steady periods, charging and discharging periods. To find the convection heat transfer coefficient, natural convection heat transfer equations for spherical shapes can be valid to use for cylindrical shapes in the water tank (Padovan and Manzan, 2014).

2.5. Erythritol storage

The erythritol storage tank was assumed as a helical coil tank filled with the PCM. The tank was exposed to heat input from PVs, heat rejection from the circulated water to the building and heat loss to the environment. The diagram of the storage tank is given in Figure 2. The simplified model was built to simulate its effect on system performance.
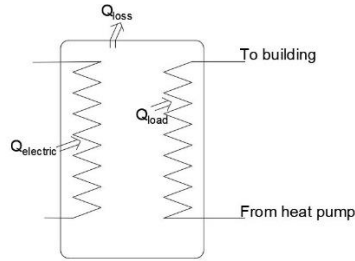
Figure 2: Heat transfer diagram of second PCM tank

For electrical load which charged the tank, Equation 9 was used:

$Equation\ 9\text{:}\ Heat\ input\ from\ PVs$

$$\dot{W}_{PV} = \dot{Q}_{Elect} = G \cdot A \cdot x \cdot \eta_{gPV}$$

Where A and x are collector area and PV cover ratio, respectively. Cover ratio was taken as 0.8.

Transferred heat to the building was calculated by using NTU-effectiveness method. Equation 10 was given:

$Equation\ 10\text{:}\ Heat\ output\ to\ building$

$$\dot{Q}_{load} = m_w \cdot c_p \cdot eta \cdot (T_{coilin} - T_t)$$

Where m_w, eta and T_t were water flow rate, coil effectiveness and tank temperature, respectively.

3. RESULTS AND DISCUSSIONS

The heating requirement of the building was determined based on IESVE simulation considering given weather conditions in Figure 3. The modelled building was a low-energy house on the main campus at the University of Nottingham. The occupancy profile, heating profile, ventilation rates, appliances profile and lighting profile were designed according to aforementioned 4 people. In the building geometry, the thickness of the fabric, voids of the floor and ceiling and the roof were simplified, and the interior structure was supposed to be empty.
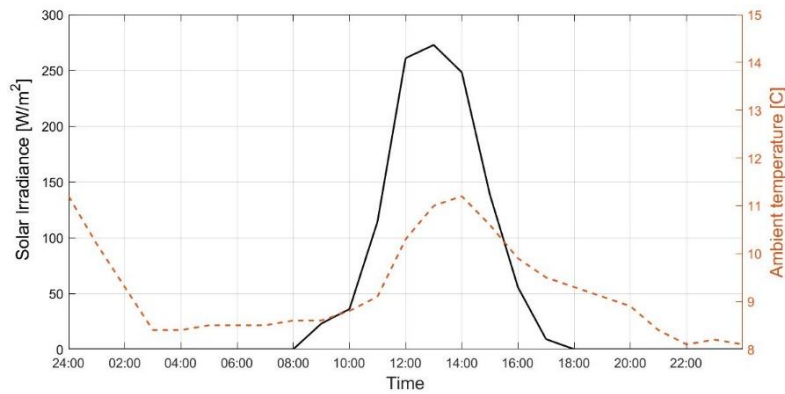
Figure 3: Weather conditions in Nottingham on 1st February

The building materials and their thermal performance specifications were input to the model. The main construction elements and U-values were given as: external wall 0.22 W/m²K; roof 0.19 W/m²K; glazing 1.8 W/m²K; door 2.2 W/m²K and floor 0.2 W/m²K. Set temperature of the rooms were 18°C from 22:00 to 05:30 since winter operating conditions of bedrooms were recommended 17-19°C by CIBSE guide (CIBSE, 2016). When all house members were out, the set temperature was reduced to 15°C as heating was not require during unoccupied hours (7:30 to 18:00). In the remaining times, the set temperature was assigned as 21°C to make an average temperature in the kitchen, hall, bedrooms and living room (CIBSE, 2016).
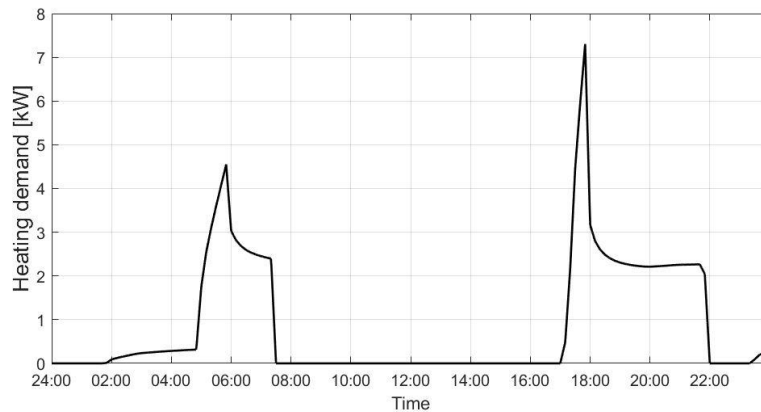
Figure 4: Heating demand profile of the building

Figure 4 shows the calculated heating requirement of the building. Daily 20.73 kWh heating was required in two different time periods: the first was in the morning and the other one in the evening. The PCM tubes were activated at night to increase the PCM storage temperature for space heating purposes. The hot water was circulated in the building and according to the rejected heat (it was heating demand), it returned back to the storage tank but at a lower temperature. Based on calculated heating demand, PCM size was determined as 173 litres. In the storage tank, 14 cylinders having 0.08m of PCM tube diameter were immersed in the water. The big PCM storage tank was also designed as 0.376m diameter with 2.45m length. Erythritol storage was assumed as 5kWh capacity and its mass was decided as 31kg. Table 1 shows determined system specifications. Given parameters were used in the simulations.

Table 1: System specifications

Daily heating load	20.7 kWh	Solar collector area	40 m²
Total SAT mass in tank	252 kg	Collector flow rate	0.033 kg/s per collector
Total PCM volume per tank	173 litres	Heat Pump output	Maximum 6 kW
Erythritol mass	31 kg	H.P. condensation temperature	75°C
Buffer tank	750 litres	Pinch temperature in H.P. evaporator	5°C
Buffer tank fluid	Ethylene Glycol water mixture (30%)	Flow rate between buffer tank and HP	0.33 kg/s
Solar collector type	Evacuated Flat plate PV/T	Water mass in tank	100 kg
One PCM tube volume	12.35 litres	Tank heat loss coefficient	0.8 W/m² K
SAT latent heat	264 kJ/kg	SAT Specific heat	2.9/3.1 kJ/kgK
SAT conductivity	0.6/0.385 W/m K	SAT density	1450 kg/m³
Erythritol latent heat	340 kJ/kg	Erythritol Specific heat	2.7 kJ/kgK
Erythritol conductivity	0.7 W/m K	Erythritol density	1450 kg/m³

3.1. Charging period

During the charging period, the heat pump provided 70°C hot water with a 0.4667 kg/s constant mass flow rate. Although the heat pump heating capacity was a maximum of 6 kW, the highest temperature output was fixed at 70°C which meant the heating load could be lower according to the return flow temperature. The charging period of the SAT storage tank is shown in Figure 5. Initial conditions were taken as PCM and water temperatures were 30°C. The heat pump started to circulate the water coming from one side of the tank, increased the temperature and supplied to the tank on the other side. Figure 5 also shows the supply and return water temperatures to the heat pump with its heating load. The supply temperature increased fast for 2 hours, then the temperature increment stopped because the latent heat of the PCM absorbed all the heat pump load. However, when the outer sides of the PCM tubes melted, the centre of the tubes was still not charged and heat transfer from the water to PCM decreased. As the heat pump output temperature was limited to 70°C, the heat pump heating load decreased. The model shows that SAT can be completely melted in 8 hours and 22 minutes. Regarding erythritol storage, 5kWh of electricity was generated by PVs heating the erythritol tank from 30°C to a fully charged state at 121°C.
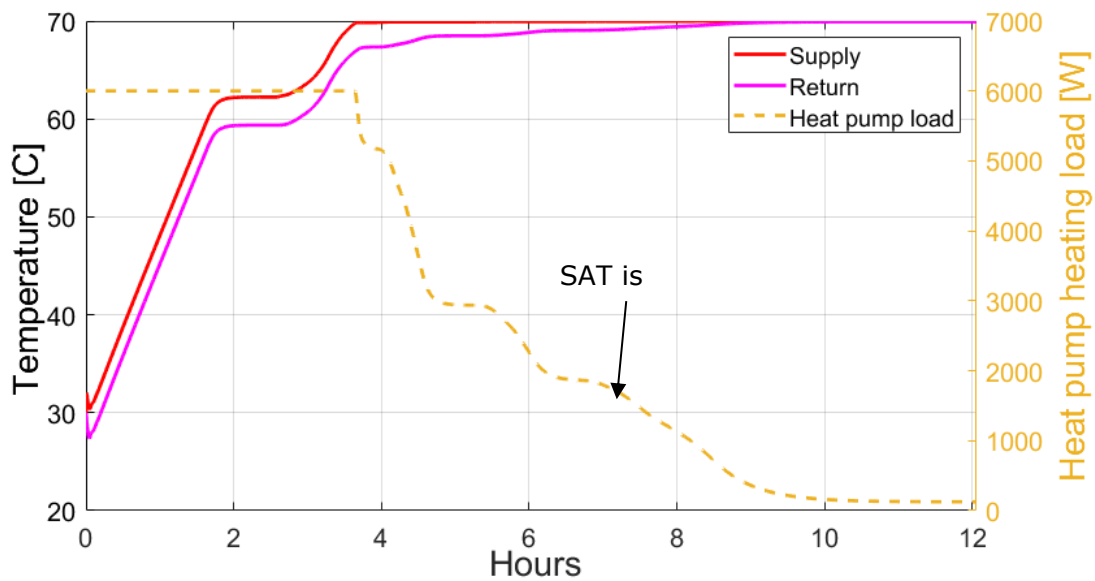
Figure 5: Supply and return temperature of heat pump, and heating load

3.2. Discharging Period

The discharging period simulation assumed that the SAT PCM tank was charged several days previously, and the PCM tubes and water temperature were 20°C at the beginning. PCM tubes were activated at midnight and the water temperature increased within a half-hour. As the tank was assumed to be a thermocline tank, the temperature difference was formed between the inlet and outlet sections. Water temperatures at the inlet and outlet of the tank are given in Figure 6a. During discharge, the water was circulated in the building which resulted in a temperature drop according to heating demand. Heating demand is also given in Figure 6a. Water supply temperature and return water temperature are given in Figure 6b. When heating demand was high, return water temperature decreased significantly. In the figure, the supply temperature fell to below 40°C after 20:00.
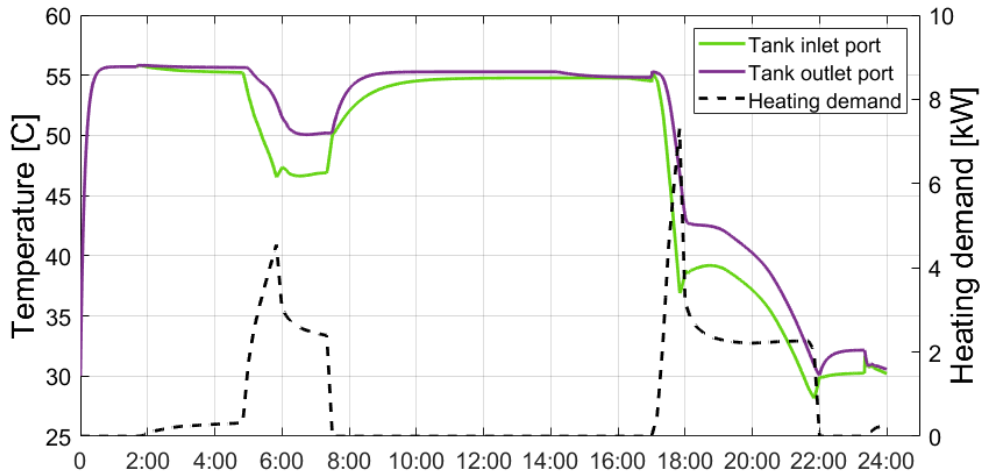
Figure 6 a): Tank temperature variation during discharging, and heating load
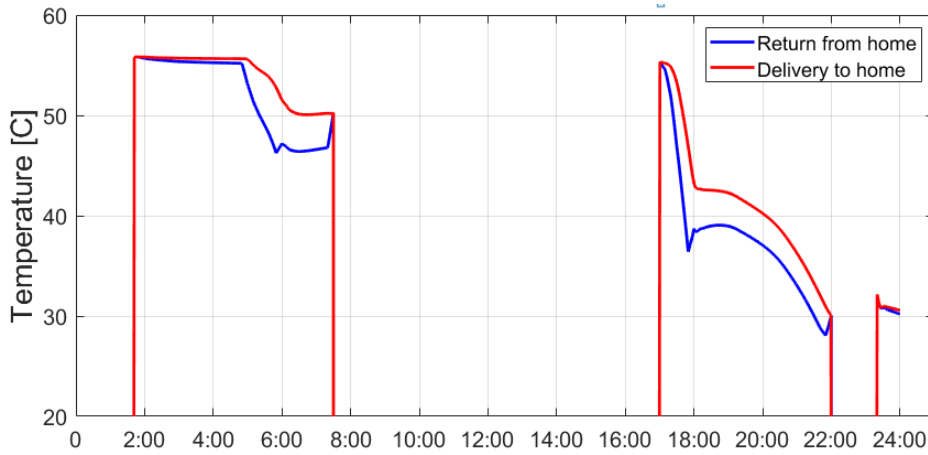
Figure 6 b): Delivery temperature to building and return temperature

In order to overcome the low-temperature water supply to the building, the erythritol tank was used to boost delivery temperature. It also increased the return temperature which helped to maintain a higher temperature in the SAT PCM tank. 2.8kW was chosen as a set heating load to use the erythritol tank. In this way, booster heating was only used for high loads to avoid return temperature drop. In the case without a secondary tank, the delivery temperature decreased to 50°C at 6:00, 40°C at 20:00 and 30°C at 22:00. However, by using a secondary latent heat storage unit when the load was higher than 2.8kW, the delivery temperature was 58°C at 6:00, 45°C at 20:00 and 42°C at 22:00. As additional heating, the secondary storage provided 4.06kWh of heating to the system (Figure 7).
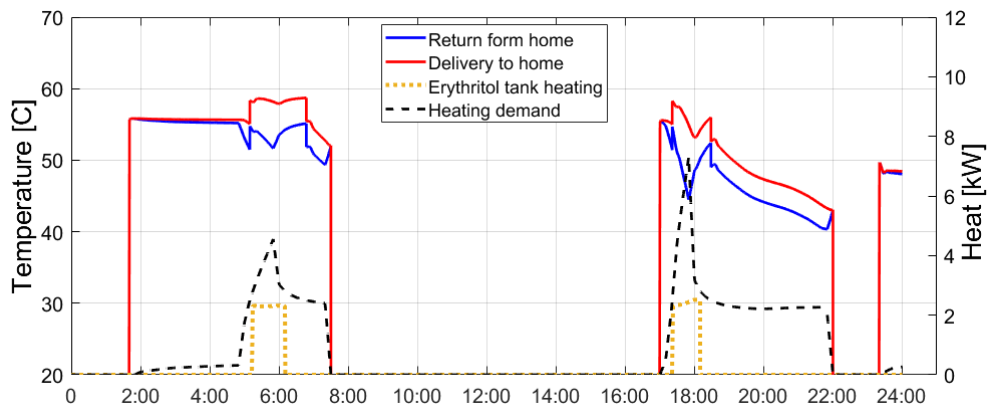
Figure 7: Left: Delivery temperature to building and return temperature; Right: Building heating demand and erythritol storage heating

4. CONCLUSION

Supercooled PCM storage unit integrated into a solar-assisted heat pump unit was modelled to provide the heating requirements of a building. Moreover, an additional latent heat storage tank was adapted to provide a higher water supply temperature to the building. Erythritol was chosen as the secondary storage material because of its high melting temperature and large latent heat capacity. Evacuated flat plate collectors were modified to form PVT collectors. Collected heat was used as a heat source for the heat pump unit and in order to charge the erythritol storage tank, PV electricity output was used in resistant heaters. Using the erythritol storage tank as an additional latent heat storage unit, supply water temperature was increased from 40°C to 45°C in the evening and 30°C to 42°C at night.

5. ACKNOWLEDGEMENTS

6. REFERENCES

Cabeza, L. F. *et al.* (2015) 'CO2 mitigation accounting for Thermal Energy Storage (TES) case studies', *Applied Energy*, 155, pp. 365–377. doi: 10.1016/j.apenergy.2015.05.121.

Cheng, Q. *et al.* (2022) 'Supercooling regulation and thermal property optimization of erythritol as phase change material for thermal energy storage', *Journal of Energy Storage*, 52(PC), p. 105000. doi: 10.1016/j.est.2022.105000.

CIBSE (2016) 'CIBSE Guide A: Environmental Design', *Envrionmental Design*. Available at: www.cibse.org.

Duffie, J. A. and Beckman, W. A. (2013) *Solar Engineering of Thermal Processes*. John Wiley.

Englmair, G. *et al.* (2019) 'A solar combi-system utilizing stable supercooling of sodium acetate trihydrate for heat storage: Numerical performance investigation', *Applied Energy*, 242(December 2018), pp. 1108–1120. doi: 10.1016/j.apenergy.2019.03.125.

Hidaka, H. *et al.* (2004) 'New PCMs prepared from erythritol-polyalcohols mixtures for latent heat storage between 80 and 100°C', *Journal of Chemical Engineering of Japan*, 37(9), pp. 1155–1162. doi: 10.1252/jcej.37.1155.

Hundy, G. F. (2016) *Refrigeration, Air Conditioning and Heat Pumps*. 5th edn. Butterworth-Heinemann.

IESVE,2020 (no date). Available at: https://www.iesve.com/software/virtual-environment (Accessed: 4 September 2021).

Kutlu, C., Zhang, Y., *et al.* (2020) 'A simulation study on performance improvement of solar assisted heat pump hot water system by novel controllable crystallization of supercooled PCMs', *Renewable Energy*, 152, pp. 601–612. doi: 10.1016/j.renene.2020.01.090.

Kutlu, C., Li, J., *et al.* (2020) 'Investigation of an innovative PV/T-ORC system using amorphous silicon cells and evacuated flat plate solar collectors', *Energy*, 203, p. 117873. doi: 10.1016/j.energy.2020.117873.

Manfrida, G., Secchi, R. and Stańczyk, K. (2016) 'Modelling and simulation of phase change material latent heat storages applied to a solar-powered Organic Rankine Cycle', *Applied Energy*, 179, pp. 378–388. doi: 10.1016/j.apenergy.2016.06.135.

Mattei, M. *et al.* (2006) 'Calculation of the polycrystalline PV module temperature using a simple method of energy balance', *Renewable Energy*, 31(4), pp. 553–567. doi: 10.1016/j.renene.2005.03.010.

Mulcué-Nieto, L. F. and Mora-López, L. (2014) 'A new model to predict the energy generated by a photovoltaic system connected to the grid in low latitude countries', *Solar Energy*, 107, pp. 423–442. doi: 10.1016/j.solener.2014.04.030.

Padovan, R. and Manzan, M. (2014) 'Genetic optimization of a PCM enhanced storage tank for Solar Domestic Hot Water Systems', *Solar Energy*, 103, pp. 563–573. doi: 10.1016/j.solener.2013.12.034.

TVPSOLAR (2013) *HT Power product datasheet*. Available at: http://www.tvpsolar.com/files/pagine/HT-Power Datasheet (v4.2x)(ver3).pdf.

Ungureşan, P. *et al.* (2016) 'Potential of Solar ORC and PV Systems to Provide Electricity under Romanian Climatic Conditions', *Energy Procedia*, 85(November 2015), pp. 584–593. doi: 10.1016/j.egypro.2015.12.248.

Wang, G. *et al.* (2021) 'Review on sodium acetate trihydrate in flexible thermal energy storages: Properties, challenges and applications', *Journal of Energy Storage*, 40(May), p. 102780. doi: 10.1016/j.est.2021.102780.

#46: Safety and sustainability of floor coverings in hospitals: a mixed method approach

Gültekin Coşkun[1], Salaheddine Bendak[2]

[1] Cumhuriyet University, Sivas, Türkiye, cgultekin@cumhuriyet.edu.tr
[2] Haliç University, İstanbul, Türkiye,:sbendak@halic.edu.tr

Abstract: It is essential that floor coverings should be adequately slip-proof to sustain the movement of pedestrians. Coverings that are slippery when dry and/or wet can form a safety risk and cause people walking on them to slip and fall. Therefore, it is essential to design safe floor coverings and maintain them in a way that complies with floor covering standards and ensure that existing coverings do not form a safety risk. Hospitals are public places where many people work or visit. To comply with applicable standards, floor coverings in hospitals should have sustainable slip resistant characteristics that ensure the safety of health professionals, patients and visitors. However, little research has been carried out in this area, surprising considering that slips and falls are the most reported work accidents in many countries. This study aimed to investigate slipperiness of hospital floors in Turkey and determine if they form a safety risk to pedestrians based on international standards. Coefficient of friction, which is an important floor covering surface finish characteristic, when dry and wet, at multiple departments/wards in three hospitals in Turkey were measured and statistically analysed using analysis of variance technique. The study also aimed to investigate potential hospital users' opinions using a short questionnaire whose results were analysed using non-parametric Mann-Whitney U-test technique that did not assume normality of data. Results showed that floor coverings in hospitals form a safety risk to pedestrians when wet and that their topographic features do not comply with standards. Respondents to the questionnaire also indicated that hospital floors were slippery especially when wet and that those floor coverings should be made less slippery and safer. It was therefore concluded that topographic features of hospital floor coverings formed a risk to pedestrians and that a change in their surface design was needed to ensure their sustainable use and compliance with safety standards.

Keywords: slip resistance; sustainable floor coverings design; walking safety; hospitals; falling accidents

1. INTRODUCTION

Out of the total number of accidents globally, slips and falls come in the second place after traffic accidents. This problem is widespread in almost all countries. For example, according to US Bureau of Labor statistics, 805 people died and 211,640 people were injured due to slipping and falling at work in 2020 (USBLS, 2021). In another example, Turkey recorded 58,979 slipping and falling accidents at work in 2019 leading to 205 deaths (Turkish Social Security Directorate, 2020).

In order to reduce the risk of slipping, floor coverings should have a safe and convenient surface roughness. Slipping incidents usually happen due to the presence of a combination of factors including the person involved, activity performed, the presence of contaminants (like water, grease, frost and dust), distractions, extreme temperature, poor lighting, pedestrian's mood, characteristics of the footwear and the walking surface (Çoşkun and Sarıışık, 2016; Coşkun and Sarıışık, 2020; Kim et al., 2001; Kim and Bendak, 2021; Mokhtar, 2003). All of these elements can combine to determine whether traction (or slip resistance) is adequate to prevent a slip. Moreover, slip resistance stems from the interaction between the sole of the pedestrian's footwear and the floor covering material. Assessing slip resistance is expected to help in determining the causes of slipping incidents and reduce the risk of slipping and falling of people using these facilities. Various methods are used in measuring this slipperiness. In the current study, a ramp test (DIN 51097 and DIN 51130) was used for determining shoe slip safety.

Walkways should be built to allow safe and comfortable movement and should continuously deliver optimal slip resistant characteristics. Although it is desirable to maintain slip resistant properties of floor coverings, this seems to be difficult in real-life situations. With repeated walking, surface finishes of floor coverings seem to experience considerable changes due to aging of flooring materials, wear and tear, soiling, and maintenance (Kim and Smith, 2000). Consequently, slip resistance functions of floor coverings deteriorate over time.

Surface roughness parameters of both floors and shoes significantly affect slip resistance performance and have been analysed to identify correlations between surface coarseness and slip resistance properties. High surface roughness offers drainage spaces to avoid squeeze film formations under polluted environments. For example, when the shoe sole surface has a distinct macroroughness (tread patterns), the empty spaces between asperities act as reservoirs for the liquid under lubricated conditions, and the pressure distribution at each asperity summit promotes a local drainage effect and increases direct contact area with the floor surface (Li et al., 2004; Ricotti et al., 2009). Therefore, macroroughness or tread patterns are commonly designed into the shoe surfaces but become ineffective quickly after being worn. Nevertheless, surface roughness of floors seems to provide better slip resistance performance than that of the shoe because the floor surface finish may offer sharper, taller, and tougher texture features (Li et al., 2004; Kim, 2015; Kim et al., 2013; Leclercq nd Saulnier, 2002; Ricotti et al., 2009).

Public facilities and buildings have a wide range of floor coverings with different types of materials ranging from highly polished stone in lobby areas to brushed concrete in warehouses. Inadequate floor surfaces can be a significant cause of slip and fall accidents (Çoşkun and Sarıışık, 2016; Findlay-Debeck, 2017; Kim, 2017; Kim, 2021; Kim and Bendak, 2021). According to the US National Floor Safety Institute (NFSI), approximately 55% of slip and fall incidents are attributable to hazardous floor surface materials. For this reason, Spain, for example, introduced mandatory barefoot pedestrian slip safety testing for public facilities (like swimming pools) in 2014. Subsequent assessment of public facility floors showed that more than 60% of floor coverings failed to meet legislatively required slip resistance standards (Findlay-Debeck, 2017).

Floor coverings in public buildings (like hospitals, restaurants, shopping centres, etc.) are of special importance and should get special attention since they are visited by large numbers of people on a regular basis, therefore, the risk of slipping and falling in such places is high. Besides, the presence of dust, water or other agents can exacerbate these risks (Coşkun and Sarıışık, 2020; Hilliard et al., 1999; Kim, 2021; Kim and Bendak, 2021; Oliver et al., 2010). Other studies have reported that community amenities such as recreational centres can potentially inhibit physical activity due to uneven walkways (Nathan et al., 2013; WHO, 2016).

Unfortunately, this issue has not been fully studied in the peer-reviewed scientific literature as is reflected by the very limited number of studies that analysed and discussed the effects of floor coverings in public buildings on the safety of pedestrians as also postulated by Kim (2021). There are also very limited publicly available detailed data on fall incidents ın such places. This study aims to analyse slip resistance of floor coverings in healthcare related facilities in order to determine the slip safety and sustainability of these coverings.

2. METHODOLOGY

To achieve its objectives, the current study involved two phases. The first phase involved a field study where multiple on-site friction measurements were taken. The second phase involved distributing a questionnaire to explore the opinion of potential hospital visitors.

2.1. Field study phase

Friction of the floor depends on the location (Chang *et al.*, 2003). In this phase of the study, three measurements of floor friction (two at opposite sides of the room/space and one at the middle) were taken in 15 different places in each of three big hospitals in Turkey. Measurements were taken under two floor conditions, dry and wet, to try to catch real-life conditions (Chang *et al.*, 2003; Kim and Bendak, 2021). One hospital in Istanbul and two in Sivas (Turkey) were approached to participate in the study and all accepted to take part in it on the condition of anonymity.

There were 90 measurements taken in each hospital (3 measurements/place X 15 different places X 2 conditions). So, the total number of measurements taken in this phase of the study was 270 readings. Such a number is deemed appropriate based on previous studies (Hsu and Li, 2010). Table 1 depicts places where measurements were taken in all hospitals and floor covering types. It should be noted that some floor friction measurements in one of the three hospitals could not be taken due to certain restrictions so friction of identical floors with similar usage purposes and pedestrian population were taken to simulate original floors.

Table 1: Friction measurement places in hospitals.

Measurement Place (all hospitals)	Floor Covering Type
Corridor 1	PVC vinyl
Corridor 2	PVC vinyl
Corridor 3	PVC vinyl
Patient room 1	PVC vinyl
Patient room 1 toilet	Ceramic tiles
Patient room 1 shower	Ceramic tiles
Patient room 2	PVC vinyl
Patient room 2 toilet	Ceramic tiles
Patient room 2 shower	Ceramic tiles
Patient room 3	PVC vinyl
Patient room 3 toilet	Ceramic tiles
Patient room 3 shower	Ceramic tiles
Medical examination room	PVC vinyl
Female guest toilets	Ceramic tiles
Male guest toilets	Ceramic tiles

There are many portable test devices that work according to different standards to determine the dynamic friction coefficients of floor coverings and, in the current study, the SlipAlert instrument was used. It consisted of a gravity-powered rolling trolley which rolled down a specially tailored ramp before contacting the floor surface. The four-wheeled trolley rolled down the ramp and a single rubber slider towards the rear represented the shoe bottom. It included an inbuilt digital display from which the reading was converted to the dynamic coefficient of friction (DCOF) of floor surfaces (DIN, 2014). DCOF is the force (slip resistance) between two objects when one of them is moving. DCOF does not have any unit (Çoşkun and Sarıışık, 2016; Findlay-Debeck, 2017).

DCOF (μ) values are generally evaluated as follows:

- $\mu \leq 0.20$ unsafe
- $0.20 < \mu \leq 0.40$ provisionally safe
- $0.40 < \mu \leq 0.60$ safe
- $\mu > 0.60$ very safe

SlipAlert is considered a reliable and sensitive piece of equipment to measure slipperiness of floor coverings. It has also been found, in general, to be more conservative than other ways to measure slipperiness (Hallas and Shaw, 2006). Figure 1 shows the DCOF measuring process at a patient room toilet with ceramic tiles and Figure 2 shows the same process at a patient room with PVC vinyl floor.

Figure 1: Surface slipperiness measuring process at a patient room toilet with ceramic tiles.

Figure 2: Surface slipperiness measuring process at a patient room with PVC vinyl floor.

2.2. Subjective perception of hospital floor slipperiness

To subjectively assess perception of hospital floor slipperiness, a short floor slipperiness questionnaire of five questions was designed based on questionnaires developed by Hsu and Li (2010), Chang and Chang (2018) and Choi *et al.* (2015). The questionnaire included a brief introduction on the aim of the study and asked respondents about their age and gender. Then it asked respondents to rate their agreement with five different statements as follows:

- I find hospital floors slippery when dry
- I find hospital floors slippery when wet
- People can slip and fall when walking in hospitals when the floors are dry
- People can slip and fall when walking in hospitals when the floors are wet
- Hospital floors should be made less slippery to ensure pedestrians' safety

This short questionnaire was randomly distributed to students studying at two Turkish universities (Cumhuriyet University in Sivas and Halic University in Istanbul). Each participant rated the five statements anonymously and no personal information were sought. Participants rated their agreement with the statements on a 5-point Likert scale ranging from 1 – strongly disagree to 5 – strongly agree.

A total of 297 (168 female and 129 male) students voluntarily participated in the survey. Such a number of participants is deemed appropriate based on previous studies (Hsu and Li, 2010). Mean age of participants was 22.1 (stdev = 1.4) years.

2.3. Data analysis

Descriptive statistics were conducted for both the DCOF readings and the subjective ratings. Analysis of variance (ANOVA) was also used for slipperiness measurement data to test the effects of condition (dry-wet), floor type (PVC vinyl-ceramic) and hospital (1-2-3) on DCOF readings. Subjective ratings of floor slipperiness were tested using non-parametric Mann-Whitney U-test technique that did not assume normality of data.

3. RESULTS AND DISCUSSION

3.1. Field study phase

As mentioned earlier, slipperiness data was recorded in 15 different places in each of three hospitals under two floor conditions, dry and wet. To improve accuracy of data collection, three measurements (replicates) were taken in each place. Slipperiness data (after transforming them to DCOF) of all 90 different places/floors are given in Table 2 (each value representing the average of three measurements in the same place). A crosstabulation of the results is given in Table 3.

Table 2: DCOF values recorded in field study in hospitals.

Place	Floor Cover	H1 Dry	H1 Wet	H2 Dry	H2 Wet	H3 Dry	H3 Wet
Corridor 1	PVC vinyl	0.60	0.29	0.63	0.26	0.41	0.18
Corridor 2	PVC vinyl	0.54	0.30	0.52	0.28	0.42	0.27
Corridor 3	PVC vinyl	0.52	0.30	0.52	0.32	0.44	0.31
Pat. room 1	PVC vinyl	0.52	0.33	0.46	0.31	0.38	0.22
Pat. room 1 toilet	Ceramic tiles	0.36	0.19	0.34	0.18	0.42	0.21
Pat. room 1 shower	Ceramic tiles	0.36	0.18	0.35	0.18	0.41	0.19
Pat. room 2	PVC vinyl	0.51	0.35	0.48	0.33	0.53	0.37
Pat. room 2 toilet	Ceramic tiles	0.36	0.18	0.33	0.18	0.44	0.22
Pat. room 2 shower	Ceramic tiles	0.36	0.19	0.34	0.19	0.33	0.19
Pat. room 3	PVC vinyl	0.49	0.33	0.47	0.29	0.48	0.35
Pat. room 3 toilet	Ceramic tiles	0.35	0.18	0.34	0.18	0.41	0.22
Pat. room 3 shower	Ceramic tiles	0.35	0.19	0.32	0.18	0.36	0.25
Med. Exam. room	PVC vinyl	0.41	0.31	0.38	0.33	0.29	0.19
Female toilets	Ceramic tiles	0.50	0.12	0.39	0.13	0.41	0.16
Male toilets	Ceramic tiles	0.50	0.13	0.44	0.14	0.36	0.21

Guide: Very safe = dark green; safe = green; provisionally safe = orange; unsafe = red.

Table 3: Overall safety conditions of hospital floors recorded.

Floor/Condition (places)	very safe	safe	prov. safe	unsafe
PVC vinyl/Dry (21)	4.8%	81%	14.3%	0%
PVC vinyl/Wet (21)	0%	0%	90.5%	9.5%
Ceramic/Dry (24)	0%	29.2%	70.8%	0%
Ceramic/Wet (24)	0%	0%	20.8%	79.2%

As can be seen in Tables 2 and 3, only one out of the 45 places was found to be very safe when dry and none when wet. When dry, PVC vinyl floors were found to be safer (81% safe and 14.3% provisionally safe) than ceramic floors (29.2% safe and 70.8% provisionally safe). The same was found for wet floors where PVC vinyl floors were found to be, relatively speaking, safer (90.5% provisionally safe and 9.5% unsafe) than ceramic floors (20.8% provisionally safe and 79.2% unsafe).

ANOVA results indicated that PVC vinyl floors were safer than ceramic floors in the three hospitals (p = 0.00). Moreover, and as expected, dry floors were found to be safer than wet floors in hospitals (p = 0.00). ANOVA results also indicated that there were no significant differences between the three hospitals in terms of slipperiness.

Overall results revealed that floors in hospitals were provisionally safe when dry and unsafe when wet. In all cases, these results reflected a worrying finding that hospital floors do not comply with international standards in general and could contribute to pedestrians slipping when walking on them.

3.2. Questionnaire phase

As mentioned earlier, a total of 297 participants, mainly university students, responded to the short questionnaire on slipperiness of hospital floors. Responses were coded 1 for strongly disagree, 2 for disagree, 3 for neutral, 4 for agree and 5 for strongly agree. A summary of the results as well as Mann-Whitney U-test outcome of male-female comparisons is given in Table 4.

Table 4: Summary of questionnaire results and significant gender differences.

Question	Overall average (stdev) (n=297)	Average of male respondents (n=129)	Average of female respondents (n=168)	p-value
Age	22.1 (1.4)	21.6	22.4	-
I find hospital floors slippery when dry	3.47 (0.96)	3.24	3.65	0.03
I find hospital floors slippery when wet	4.40 (0.7)	4.23	4.54	0.03
People can slip and fall when walking in hospitals when floors are dry	3.21 (1.05)	2.96	3.41	0.04
People can slip and fall when walking in hospitals when floors are wet	4.47 (0.67)	4.28	4.60	0.01
Hospital floors should be made less slippery to ensure safety of pedestrians	4.46 (0.71)	4.26	4.62	0.01

As can be seen in Table 3, the average age of respondents was 22.1 (stdev = 1.4) years with male respondents recording a slightly younger age than female respondents (21.6 vs 22.4 years).

In general, respondents indicated finding hospital floors to be slightly slippery when dry with the average of responses being 3.47 (where 3 represents being neutral). Female respondents found floors to be more slippery when dry than male respondents (3.65 vs 3.24, p = 0.03). However, when floors become wet, there was almost a consensus among respondents that they perceived hospital floors to be slippery with the average of responses being 4.4. Even though the general sentiment of all male and female respondents that hospital floors were slippery when wet, female respondents indicated finding them to be even more slippery than male respondents (4.54 vs 4.23, p = 0.03).

Respondents, on average, also indicated their slight belief that people could slip and fall when walking in hospitals when floors were dry with the average of responses being 3.21 (where 3 represents being neutral). Female respondents believed that people could slip and fall when walking on dry floors in hospitals to a greater extent than male respondents who were neutral in this regard (3.41 vs 2.96, p = 0.04). Again, when floors become wet, there was a near consensus among respondents in the belief that people could slip and fall when walking in hospitals with the average of responses being 4.47. As was the case with perceiving wet hospital floors to be slippery, there was a general sentiment that pedestrians could slip and fall when walking on wet floors in hospitals with, however, female respondents indicating an even stronger belief than male respondents (4.60 vs 4.28, p = 0.01).

Finally, respondents indicated their strong agreement that hospital floors should be made less slippery to ensure safety of pedestrians with the average of responses being 4.46. Again, female respondents had stronger views than that of male respondents (4.62 vs 4.26, p = 0.01).

Generally speaking, the results from the questionnaire indicated that respondents perceived hospital floors to be slightly slippery and think that there was a slight potential that people walking on those floors could slip and fall when those floors were dry. Moreover, results indicated that respondents perceived hospital floors to be highly slippery and that there was great potential that people walking on those floors could slip and fall when they were wet. More interestingly, the questionnaire results indicated that female respondents always perceived hospital floors to be more slippery than male respondents under all conditions. This might be attributed to the differences in shoe ware, heel height and sole-floor contact area among genders.

Overall results of both phases of the current study indicated that hospital floors imposed, in general, a low risk of slipping for pedestrians when dry and a high risk when wet. This outcome was revealed through field study measurements and confirmed by people's perceptions and subjective evaluation of those floors.

4. CONCLUSIONS

Slipping and falling accidents caused by slippery floor coverings highlight the importance of slip prevention efforts. In hospitals, patients, staff and visitors should be able to walk on floor coverings that ensure their safety. Determining friction coefficient of those floor coverings and, therefore, the risk of slipping are essential matters in slip prevention efforts. In this study, the risk of slipping was assessed by measuring the friction of floor coverings in 15 different places in each of three hospitals in Turkey. The opinion of pedestrians on the same topic was also sought using a questionnaire survey.

Field study measurements indicated that hospital floors were provisionally safe when dry and unsafe when wet. Such results indicated that those floors were unsafe based on international standards and that they could contribute to pedestrians slipping and falling when walking in hospitals. This yields the conclusion that urgent action is needed to enhance DCOF of those floors in order to ensure their safety and long-term sustainability.

These field study findings were also emphasised by questionnaire findings. People responding to the questionnaire indicated that they found hospital floors to be slightly slippery when dry and slippery when wet. They also indicated their strong belief that hospital floors should be made less slippery in order to ensure the safety of pedestrians.

Overall, findings of both phases of the current study indicated that friction of hospital floors should be enhanced as those floors could not be, generally speaking, considered safe for pedestrians, especially when wet. Results also highlighted the importance of planning and installing safer floor coverings at the design stage of hospitals as this option is more sustainable than improving the friction of floor coverings after installing them. Results also indicated that awareness of architects, civil engineers and hospital administrators deciding on hospital floor coverings should be enhanced to ensure that safe floors are installed at the construction stage of hospitals. Moreover, results of the current study indicated that hospital administrators should enhance slipping resistance of existing floors, especially ceramic tiles (by applying chemicals that enhance slip resistance on them), and make sure that no pedestrians walk on them when wet (by using appropriate signage and barriers).

It should be noted that results of the current study should be taken with caution. Opinion of users and field measurements were all taken from one country (i.e. Turkey). Although it is anticipated that other countries would yield similar results, this has yet to be investigated. Moreover, questionnaire results were based on the opinion of a limited number of hospitals and of young participants and. Future studies should investigate this issue further by incorporating more hospitals and a wider range of people of other ages.

5. REFERENCES

Chang, W-R, and Chang, CC, 2018. Relationship among several measurements of slipperiness obtained in a laboratory environment. *Applied Ergonomics*, 68, 117-124.

Chang, WR, Kim, I-J, Manning, DP and Bunterngchit, Y, 2003. The role of surface roughness in the measurement of slipperiness. In Measuring Slipperiness - Human Locomotion and Surface Factors, Chang WR, Courtney TK, Gröngvist R, Redfern M, Eds.; CRC Press: London, UK. pp. 101-117.

Choi, S-K, Kudoh, R, Koga, J, Mikami, T, Yokoyama, Y, Takahashi, H, and Ono, H, 2015. A comparative evaluation of floor slip resistance test methods. *Construction and Building Materials*, 94, 737–745.

Çoşkun, G, and Sarıışık, A, 2016. "Slip Safety Analysis of Local Afyon Marble", *Afyon Kocatepe Unıversity Journal of Sciences and Engineering*, 16(1), 155-166.

Coşkun, G, and Sarıışık, G,. 2020. Analysis of slip safety risk by portable floor slipperiness tester in state institutions. *Journal of Building Engineering*, 27, 100953.

Findlay-Debeck, R. 2017. Pedestrian Slip Safety: A Guide for Busy Professionals. ASSE Professional Development Conference and Exposition, Denver, Colorado, USA, ASSE-17-661.

German Institute for Standardization (DIN), Prüfung von Bodenbelagen € - Bestimmung der rutschhemmenden Eigenschaft - Verfahren zur Messung des Gleitreibungskoeffizienten [Testing of floor coverings - Determination of the antislip property - Method for measurement of the sliding friction coefficient], DIN, Berlin, 2014. Standard No. DIN 51131: 2014. German.

Hallas, K, and Shaw, R, 2006.Evaluation of the Kirchberg rolling slider and slipalert slip resistance meters. Health and Safety Laboratory.

Hilliard, DJ, Frederick, L, Tierney-Gumaer, R, and Simpson, MJ, 1999. Exploring the relationship between cultural values, beliefs, and practices and patient falls: A Middle Eastern study. *Journal for Healthcare Quality*,21 (1): 42-48.

Hsu, Y-W and Li, KW, 2010. A field assessment of floor slipperiness in a fish market in Taiwan. *Safety Science*, 48, 556–561.

Kim IJ, 2021. Hospital flooring safety and health: knowledge gaps and health. *International Journal of Occupational Safety and Ergonomics*, 27(4), 1116-1135.

Kim, IJ, Smith, R, and Nagata, H, 2001. Microscopic observations of the progressive wear on the shoe surfaces that affect the slip resistance characteristics. *International Journal of Industrial Ergononomics*, 18,17-29.

Kim, I-J, and Smith, R, 2000. Observation of the floor surface topography changes in pedestrian slip resistance measurements. *International Journal of Industrial Ergonomics*, 26 (6): 581-601.

Kim, I-J. 2017. Pedestrian Fall Safety Assessments: Improved Understanding on Slip Resistance Measurements and Investigations. Switzerland: Springer International Publishing AG. pp. 249.

Kim, I-J and Bendak, S, 2021. Emerging Safety Risks from Public Facilities: A Field Study for Ablution Spaces in Mosques. *Facilities*, 39(13/14). 843-858.

Leclercq S, and Saulnier, H, 2002. Floor slip resistance changes in food sector workshops: prevailing role played by fouling. *Safety Science*, 40(6), 59-73.

Li, KW, Chang, WR, Leamon, TB, and Chen, CJ, 2004. Floor slipperiness measurement: friction coefficient, roughness of floors, and subjective perception under spillage conditions. *Safety Science*, 42 (6): 547-565.

Mokhtar, A, 2003. Challenges of Designing Ablution Spaces in Mosques. *Journal of Architectural Engineering*, 9 (2): 55-61.

Nathan, A, Wood, L, and Giles-Corti, B, 2013. Environmental Factors Associated with Active Living in Retirement Village Residents. *Research on Aging*, 35 (4): 459-480.

Oliver, D, Healey, F, and Haines, TP, 2010. Preventing falls and fall-related injuries in hospitals. *Clinics in Geriatric Medicine*, 26 (4) 645–646.

Ricotti, R, Delucchi, M, and Cerisola, GA, 2009. Comparison of results from portable and laboratory floor slipperiness testers. *International Journal of Industrial Ergonomics*, 39, 353–357.

Turkish Social Security Directorate (2020). 2019 Workplace Accidents and Illnesses in Turkey.

US Bureau of Labor (2021). Employer-Reported Workplace Injuries and Ilnesses. USBOL, report number USDL-21-1927.

World Health Organisation (WHO). 2016. Urban Green Spaces and Health - A Review of Evidence. Report available from http://www.euro.who.int/en/health-topics/environment-and-health/urban-health/publications/2016/urban-green-spaces-and-health-a-review-of-evidence-2016.

#48: Developing organic bio-refinery model to achieve sustainable development

Tayyab QURESHI[1], Ussama ALI[2], Muhammad FAROOQ[3]

[1] Department of Mechanical Engineering, University of Engineering & Technology, Lahore, Pakistan,
tayyab1991@outlook.com

[2] Department of Mechanical Engineering, University of Engineering & Technology, Lahore, Pakistan,
ussama.ali@uet.edu.pk

[3] Department of Mechanical Engineering, University of Engineering & Technology, Lahore, Pakistan,
engr.farooq@uet.edu.pk

Abstract: The United Nations' Sustainable Development Goals (SDGs) are designed to revolutionize societies to preparefor the future challenges. However, the practical implementation of such goals in many domains are yet to be achieved despite of unique essence. Sustainable energy production (aligned with SDG 7), sustainable waste services (aligned with SDG 11), and mitigating climate change impacts (aligned with SDG 13) has been the prime focus of SDGs. Scarcityof fossil fuels & the degradation of our environment are the major contributors towards the prompt and necessary development of technology especially. Many developing and/or emerging economies have agriculture-based economy so production of crops at large scale leads to the generation of a by-product known as biomass, which is considered waste at global level. Waste Management has been a neglected sector in emerging or developing regions in the world. The uncontrolled open dumping sites are a threat to the environment, and, in addition to all these recurring issues, the energy demands the need to tap the renewable energy resources. The focus of this research is to develop an Organic Waste Biorefinery Model to achieve Sustainable Development Goals. The waste to energy (WTE) analysis were conducted on the biomass with different ratios. WTE analyses include, Thermogravimetric (TG) analysis, Fourier- transform infrared spectroscopy (FTIR) analysis, Raman spectroscopy, X-ray diffraction (XRD) analysis, Elemental analysis, Proximate analysis, Gross calorific value (GCV), analysis and Scanning electron microscope (SEM) analysis. These analyses investigate different thermo-physical properties which include ignition temperature, ignition delay, mass loss curve, peak temperature, burn out temperature, degradation rate, structural morphology, surface texture and, burning performance and particulate matter. The outcome from this work is to provide a foundation for the development of biomass-based value-added product individually or in a blended form for the purpose of variable usage at the industrial level. Accordingly, it can further facilitate the transition from linear to circular economies and mitigate the major challenges faced, including but not limited to environmental pollution, climate change, and adverse effects on public health.

Keywords: sustainability; waste bio-refineries; environmental pollution; climate change; waste management

1. INTRODUCTION

Whenever power generation is required, we blindly rely on fossil fuels which are not only non-renewable resources -its abundance in Earth is limited - but also their extraction and utilisation is expensive and unstable. After the Paris Climate Accord of 2015, where it was decided to work together as a global community and try to reduce the global temperature by 2°C (United Nations, 2015), further plans were formulated to reduce our dependence on coal-based power plants and switch towards renewable energy sources. Developed countries have considerably reduced their dependency on non-renewable energy resources through the application of wind, solar and biomass energy. At the same time, developing countries are also implementing various initiatives for climate control and reduction of carbon in the environment. One such example is the Billion Tree Tsunami project initiated in the province of Khyber Pakhtunkhwa, Pakistan, as a response to the challenges faced due to global warming with the aim of reversing its adverse effects on our planet (United Nations Environment Programme, 2021). With a higher demand of electrical energy compared to the supply, the government is planning to install new coal-based power plants to tackle the energy shortage issue. Pakistan has 3,064 million tons of proven coal reserves (British Petroleum, 2021) but due to its higher ash and sulfur content and low heating value the quality of the coal reserves is not appropriate for direct consumption. Even with natural reserves the local industry has no choice other than importing coal from Indonesia to meet their demands. Furthermore, between 2005 and 2010 the annual growth of electricity demand on average in Pakistan was 8%. With the increasing population this demand will continue to grow at the same rate until 2035 raising the total demand to 474 GW by 2050 (Farooq and Kumar, 2013). To fulfil this demand the need for alternative and sustainable energy resources and technologies is inevitable in addition to the installation of coal-based power plants. Studies have shownthat by 2050 the energy potential of Pakistan from solar, wind, and biomass will be 169 GW, 13 GW, and 15 GW respectively. Natural energy resources such as solar, wind and biomass have plenty of virtues but there are drawbacks as well. For example, solar and wind have their own geographical challenges. Biomass has a high content of inorganic material that deters the combustion process. Pakistan is an agricultural country producing crops like wheat, rice, sugar cane, maize and cotton. The residues from these crops are generally discarded or ineffectively used. These residues have high heating value and high bulk density which is a positive for transport and handling (Raveendran *at al.*, 1995). Maize production in Pakistan in the fiscal year 2016-2017 was 16.3% higher compared to the previous fiscal year and weighted 6.13 million tons (Asonja et al., 2017; Finance Ministry of Pakistan, 2012). On the global scale, the annual production of corncob is equivalent to 25 billion tons of oil. The annual reduction in CO_2 emissions could amount to 77 million tons if the corncob replaced coal as the energy source (Brunner, 2011). Compared with coal, biomass has a lower ash content and lower CO_2 emissions due to its source and carbon-neutral property (Saidur *et al.*, 2011). The composition of corncob is a mix of 40% hemicellulose, 32–45% cellulose, and 6.7– 14% lignin (Foley, 1978). The calorific value of corncob is 17.45 kJ/kg and 16.4 kJ/kg with 5% and 10% moisture content, respectively (Asonja *et al.,* 2017). Compared with high-grade coal, the heating value of corncob is considerably less, however its added advantages of availability in abundance and carbon neutrality make it a good candidate to replace coal.

In the present study, corncob is being used with the objective of consumption in nearby power plant boilers. The reason behind this is its easy access, high bulk density, and acceptable energy content as compared to other crops being cultivated on a large scale in Pakistan. Combustion of biomass in the raw form is unsuitable as the ash content present in the biomass may cause agglomeration, slagging, and corrosion of the tubes of the boiler. Not only does it reduce the heat transfer rate but also damages the tubes which may lead to a major breakdown of the boiler (Fahmi *et al.*, 2007). The heating value of biomass is affected adversely by its relatively high ash content (Jenkins *et al.*, 1998). Up to 15% of the total biomass weight is composed of alkali and alkaline earth metals (AAEMs) or inorganic minerals such as Ca, Mg, and K (Aslam *et al.*, 2016). If the biomass has high AAEM content, during combustion ash melts at a lower temperature which in turn limits the complete combustion of biomass. Besides this, the base of the furnace has a formation of biomass lumps which greatly affects the fluidizing behaviour of biomass in circulating fluidizedbed boilers. This can lead to complications such as incomplete combustion, loss of raw material, or may require early shutdown maintenance (Jenkins *et al.*, 1998; Easterly and Burnham, 1996; Cui *et al.*, 2010; Sulzbacher and Rathbauer, 2014). To resolve such problems, pre-treatment of biomass is required, e.g., demineralization to leach the minerals out. Leaching reagents such as acids, bases, and even water have been used and turn out to be quite effective. Such reagents have been recommended by various researchers in their studies (Davidsson *et al.*, 2002; Fahmi *et al.,* 2008; Eom *et al.*, 2001). It is crucial to choose a suitable leaching agent for efficient valorisation. Selecting an unsuitable leaching agent may dissolve cellulose, hemicellulose and lignin, thereby devaluing the biomass (Eom *et al.*, 2001). The purpose of this study is to scrutinize the influence of basic and acidic leaching agents on the thermal and physiochemical characteristics of biomass derived from corncob. This in turn will assist in the correct selection of leaching reagents. The biomass becomes suitable for direct combustion in the boilers after it undergoes demineralization. As an alternative, the demineralized biomass can be gasified to produce syngas which can be later transported and used for other activities, such as, for combustion or for electrochemical oxidation in high-temperature fuel cells.

2. METHODOLOGY

Biomass (corncobs) was taken in raw form and shredded using a grinding machine. The grinded sample was passed through a sieve for the generation of powder sample. Then mechano-chemical treatment was applied on the powdered biomass in the acidic medium. The material was then neutralized using distilled water with the confirmation using litmus paper tests. The neutralized sample was de-moisturised using a dehumidifier. It should be noted that samples were demineralized for 30 min, 1hour, and 2 hour process times. After drying, samples were

sent for thermogravimetric analysis (TGA) in co-combustion process, Fourier Transform Infrared Spectroscopy (FTIR) analysis, and X-Ray Diffraction analysis (Figure 1).
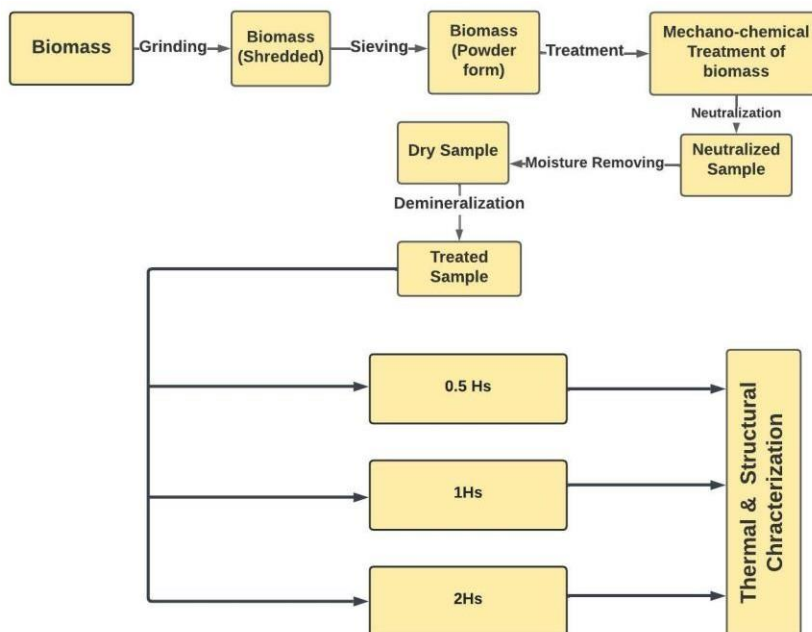
Figure 1: Sample preparation and experimentation

3. RESULTS AND DISCUSSION

In Figure 2, co-combustion profiles at different demineralization process times are shown. It can be observed from the figure that all the profiles were based on multi-stage burning. Analysis further revealed that at higher treatment times more useful burning takes place during the co-burning process, as it can be seen that 2hS demineralization-based process had the longest volatile and fixed carbon degradation period. In all the samples smooth burning was observed in all the profiles of fuel due to efficient treatment. Chemical treatments were directly linked to the kinetic reaction. Higher treatment time led to higher thermal lag, meaning that at a higher demineralization process time, the reaction would be fast but maximum thermal optimization would be achieved. It was observed that at a higher demineralization rate maximum ash removal took place.
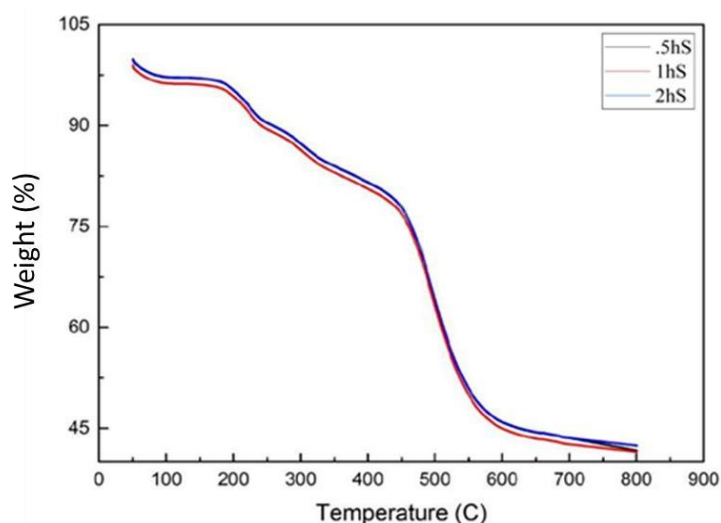
Figure 2: Co-combustion profile of corncob at 20 ml/min, 30 ml/min, and 40 ml/min

The effect of acidic and basic treatments on the chemical structure of raw and selected corncob samples was studied by FTIR, and results are shown in Figure 3. The band variations depict that substantial change was observed in the cross-linkage structure of the samples due to the demineralization effect. Variations in the intensity of the first three peaks is an indication of the changes in the lignin, hemicellulose, and cellulose content in comparison to the raw sample caused byacidic treatment.

144
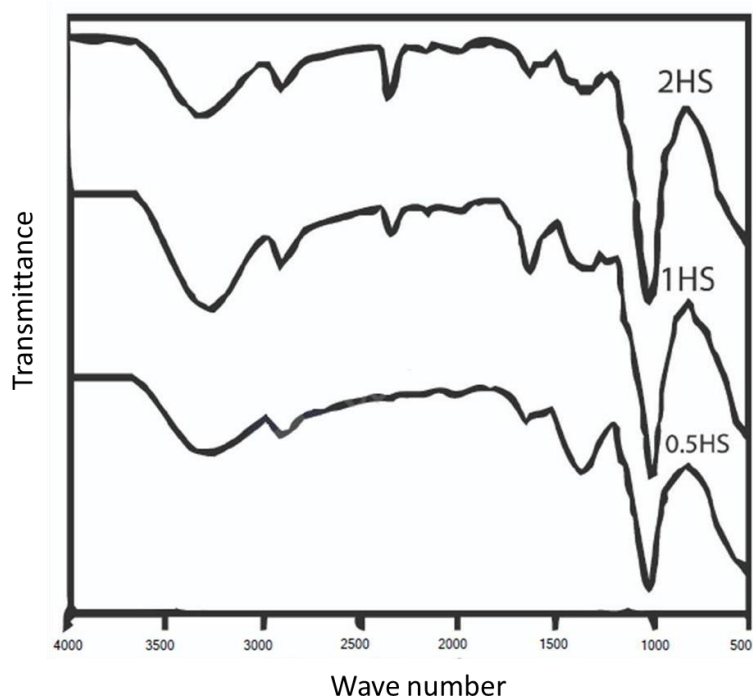
Figure 3: FTIR analysis of corncobs at different demineralization process time

Figure 4 represents the XRD formation of corncob samples. Sharp peaks were detected in all the sample results. The major intensified peaks of all the samples were detected between the range of 20 to 30 degree. The sample 0.5hS showed maximum crystallinity behaviour while the sample 2hS showed the lowest crystallinity behavior. The crystallinity depended upon the wax, cellulose, and bonding at intermolecular level
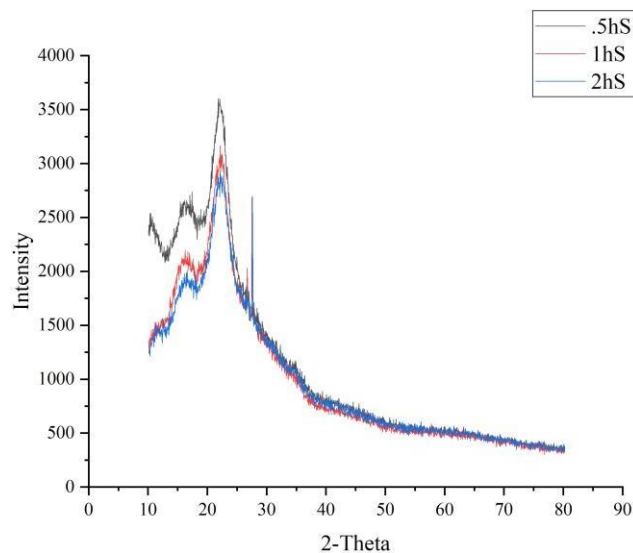
Figure 4: XRD analysis of corncobs at different demineralization process time

4. CONCLUSION

In the current research work, examining the data revealed that at a higher heating rate and higher flow rate, the treatment of fuel has efficient utilisation, which was validated by the thermogravimetric-obtained graphs. It was deduced that at the higher heating rate and flow rate maximum burning of fuel was achieved along with normal working conditions. With the perspective of Structural criteria, it was observed that the crystalline nature of the sample was more noticeable when treated with the lower concertation sample. Overall, acidic treatment has made a vital impact on the reduction process of ash in biomass.

5. REFERENCES

Aslam U, Ramzan N, Iqbal T, Kazmi M, Ikhlaq A (2016) Effect of demineralization on the physiochemical structure and thermal degradation of acid treated indigenous rice husk. Pol J Chem Technol 18:117–121. https://doi.org/10.1515/pjct- 2016-0057

Asonja A, Desnica E, Radovanovic L (2017) Energy efficiency analysis of corn cob used as a fuel. Energy Sources, Part B Econ Planning, Policy 12:1–7

British Petroleum (2021) Statistical Review of World Energy, 70th Edition, https://www.bp.com/content/dam/bp/business- sites/en/global/corporate/pdfs/energy-economics/statistical- review/bp-stats-review-2021-coal.pdf

Brunner T, Kanzian W, Obernberger I, Theissl A (2011) Combustion properties of maize cobs – results from lab and pilotscale tests. In: 19th European Biomass Conference & Exhibition. pp 944–951

Cui H, Turn SQ, Tran T (2010) Biomass pretreatment for gasification. In: 8th International Symposium on Gas Cleaning at High Temperatures, Taiyuan, Shanxi, China. pp 23–25

Davidsson KO, Korsgren JG, Pettersson JBC, Jäglid U (2002) The effects of fuel washing techniques on alkali release from biomass. Fuel 81:137–142. https://doi.org/10.1016/S0016-2361(01)00132-6

Easterly JL, Burnham M (1996) Overview of biomass and waste fuel resources for power production. Biomass Bioenergy 10:79–92

Eom IY, Kim KH, Kim JY, Lee SM, Yeo HM, Choi IG, Choi JW (2011) Characterization of primary thermal degradation features of lignocellulosic biomass after removal of inorganic metals by diverse solvents. Bioresour Technol 102:3437– 3444. https://doi.org/10.1016/j.biortech.2010.10.056

Fahmi R, Bridgwater AV, Darvell LI, Jones JM, Yates N, Thain S, Donnison IS (2007) The effect of alkali metals on combustion and pyrolysis of Lolium and Festuca grasses, switchgrass and willow. Fuel 86:1560–1569. https://doi.org/10.1016/j.fuel.2006.11.030

Fahmi R, Bridgwater AV, Donnison I, Yates N, Jones JM (2008) The effect of lignin and inorganic species in biomass onpyrolysis oil yields, quality and stability. Fuel 87:1230–1240. https://doi.org/10.1016/j.fuel.2007.07.026

Farooq MK, Kumar S (2013) An assessment of renewable energy potential for electricity generation in Pakistan. Renew Sust Energ Rev 20:240–254

Finance Ministry of Pakistan (2012) Economic Survey 2011-12. http://www.finance.gov.pk/survey_1112.html

Foley KM (1978) Chemical properties, physical properties, and uses of The Anderson' corncob products. The Andersons, Cob Division

Jenkins B, Baxter L, Miles T, Miles T (1998) Combustion properties of biomass. Fuel Process Technol 54:17–46.https://doi.org/10.1016/S0378-3820(97)00059-3

Raveendran K, Ganesh A, Khilar KC (1995) Influence of mineral matter on biomass pyrolysis characteristics. Fuel 74:1812–1822

Saidur R, Abdelaziz EA, Demirbas A, Hossain MS, Mekhilef S (2011) A review on biomass as a fuel for boilers. RenewSust Energ Rev 15:2262–2289

Sulzbacher L, Rathbauer J (2014) Maize cobs for energetic use–properties and challenges as fuel for small scalecombustion. In: Proceedings of the International Conference of Agricultural Engineering, 6–10 July, Zurich

United Nations (2015) The Paris Agreement. https://unfccc.int/process-and-meetings/the-paris-agreement/the-paris- agreement

United Nations Environment Programme (2021) Pakistan's Ten Billion Tree Tsunami. https://www.unep.org/news-and- stories/story/pakistans-ten-billion-tree-tsunami

#57: Thermal performance enhancement of a PCM-based heat sink for thermal control of small satellites in the space environment: a numerical study

Abdelrahman M. Elshaer[1,2,*], A. M. A. Soliman[1,2], M. Kassab[3], A. A. Hawwash[1]

[1] Mechanical engineering department, Benha faculty of engineering, Benha University, Benha, Egypt.
[2] Faculty of Engineering and Technology, Badr university in Cairo (BUC), Cairo, Egypt.
[3] Mechanical systems design department, Egyptian space agency, New Cairo, Egypt.

[*] Corresponding author: abdelrahman.alshaier@bhit.bu.edu.eg

Abstract: Thermal control of electronics aims to maintain their temperature within the recommended temperature range. Satellite avionics are getting smaller and have a higher power density. Furthermore, the heat transfer modes in space are limited to conduction and radiation, which makes thermal control more difficult. Thermal energy storage materials are a promising candidate for the thermal control of satellite avionics. Solid-liquid phase change materials (PCMs) are latent heat thermal storage materials that store and release thermal energy during melting and solidification. The best method for using the PCMs in thermal control of satellite avionics is PCM encapsulation. PCM encapsulation refers to packing the PCM into a closed rigid container to isolate it from the surrounding. In the present work, a PCM-based heat sink was adopted for thermal control of a small satellite subsystem. The heat sink was made of aluminium due to its relatively high thermal conductivity and was designed based on the outer dimensions of a small satellite subsystem. RT 35, RT 31, and RT 24 were used as the PCM materials, and thermal conductivity enhancers (TCE) with different geometries were used to get over the lower thermal conductivity of the PCM. The present study delivered a transient numerical investigation of the effect of TCE geometry on the thermal control performance of the PCM-based heat sink. Circular pin fins, triangular pin fins, and novel metal foam geometry were used with a TCE volume fraction of 20%. The electronic subsystem was assumed to be "ON" for 10 minutes generating 20W of heat, and "OFF" for 80 minutes. During the cycle, the heat sink's base plate temperature and the liquid fraction of PCM were recorded. The results showed a significant decrease in the base plate temperature when the PCM was used. RT 24 reduced the temperature by about 46% compared to the case without PCM. The lower melting points recorded higher liquid fraction. RT 24 increased the liquid fraction by 27.7%. The results also concluded that the novel metal foam geometry significantly enhanced thermal performance and delivered the lowest base plate temperature.

1. INTRODUCTION AND LITERATURE REVIEW

Low-Earth-Orbit (LEO) satellites are subjected to a harsh thermal environment. The satellite in low earth orbit exists at various times in both the sunny and eclipse zones. A high amount of thermal energy is received from the sun during the sunny zone resulting in overheating satellite components. In contrast, the lack of solar thermal radiation in the eclipse zone causes a significant temperature drop in satellite subsystems while the satellite is in the eclipse zone (Liu *et al.*, 2016). The following are sources of heat that the spacecraft encounters while in orbit: (1) direct solar radiation; (2) Earth's diffusive radiation (Albedo); (3) the planet's emission of infrared (IR) radiation; (4) friction between spacecraft and gas molecules in the space environment causing the molecular heating effect; (5) energy dissipated from the avionics' systems (Gilmore, 2002). The satellite thermal control subsystem manages the temperature values of the other subsystems. The satellite subsystems have a recommended temperature range within which their temperature values lie. Any excessive heating or cooling of any subsystem can significantly reduce the performance and lead to complete failure. Electronic devices and associated components used in the spacecraft industry, particularly satellite subsystems, have recently become more compact and have a higher power density. These electronic gadgets and satellite subsystems also use more electricity consequently, novel technologies are urgently required for effective thermal control of satellite components (Farrahi & Pérez-Grande, 2017). The satellite subsystems operate cyclically; they are "ON" sometimes and "OFF" for the rest of the cycle. Thermal control of small satellites has some difficulties due to mass limitations, small heat capacity, and power source limitations. Satellite thermal control subsystems are classified into two main categories: passive and active thermal control subsystems. On the one hand, the passive thermal control subsystems require no electrical power, such as radiators, insulation, etc; on the other hand, the active thermal control subsystems require electrical power. Active thermal control subsystems include fluid-looped systems, heaters, coolers, etc. Thermal energy storage materials (TES) are promising candidates for thermal control of small satellites in the low earth orbit environment. There are two types of TES: Latent heat storage (LHS) and sensible heat storage (SHS). The former are materials with higher values of specific heat, while the latter stores the heat during phase change. LHS is called phase change materials (PCM). Solid-liquid PCM, during heating, stores thermal energy and its phase change from solid to liquid. During cooling, the stored heat is released again, and the phase changes from liquid to solid.

Many research works have been dedicated to investigating the feasibility of using phase change materials (PCMs) in the thermal management of electronic devices. Fan *et al.* (2015) investigated the effect of using composite PCMs. The composite PCMs were mixed with a high aspect ratio of carbon nanofillers to enhance their thermophysical properties. Carbon nanofillers were carbon nanotubes and graphene nanoplatelets. The results revealed a great enhancement in PCM thermal conductivity when carbon-based nanoparticles were added. In addition, the heat sink thermal performance was improved greatly. Experimental work was carried out by Gharbi *et al.* (2015) to compare different PCM-based heat sink configurations for cooling electronic devices. This work used four heat sink configurations: pure PCM, PCM with graphite, PCM with silicone matrix, and PCM with fins. The results showed an enhancement in the thermal performance when PCM inserts were used. Humphries (1974) looked at how PCMs change phases in normal and zero-gravity environments. The usage of a honeycomb structure as a filler material in a PCM-based thermal control module was investigated by Abhat and Groll (1974). The authors demonstrated the ability of a honeycomb architecture to keep hardware temperatures within restricted bands, which is essential for satellite operation. Furthermore, the authors reported that natural convection impacts within the PCM were negligible for space applications.

The effect of PCM/fins composite and PCM/nano graphite composite were investigated experimentally by Chang (2017). Results reported a significant enhancement of the PCM thermal conductivity by using PCM/nanographene composite. Andraka *et al.* (2015) presented an experimental study to investigate the effect of using latent heat storage on enhancing the efficiency of a Stirling engine. The findings reported an enhancement in the engine performance by using PCM. Gonzalez-Nino (Gonzalez-Nino et al., 2018) investigated experimentally using PCM in the thermal management of military electronics with high heat flux. The study reported a remarkable enhancement in thermal control performance when PCM was used, which could decrease the component temperature by about $16°C$. An experimental investigation was performed by Ali Mohamed (Ali Mohammadi et al., 2017) to investigate the effect of using nano/PCM composites for the thermal management of electronic chips. An inorganic salt hydrate PCM was used. The nanoparticles were dispersed in the PCM by ultrasonic technique. The findings reported a great enhancement in thermal performance by using nanoparticles/ PCM composite.

2. MODEL

In this section, the model and the associated materials are presented. Section 3.1 presents model design and configuration. Section 3.2 presents the governing equations used during the design and solution stages and the boundary conditions.

2.1. The model configuration and materials

In the current work, an aluminium heat sink was used as a thermal control module for thermal control of a small satellite subsystem. The outer dimensions of the heat sink were based on a small satellite subsystem of 100mm in length, 70mm in width, and 20mm high. The heat sink walls and base plate thickness were all 5mm. Three PCM were

adopted: RT 35, RT 31, and RT 24 (*RUBITHERM (GmbH)*, 2021). The volume expansion of the PCM was neglected; thus, the height of the PCM in the heat sink was 15mm for all cases. Due to the lower values of PCM thermal conductivity, aluminium thermal conductivity enhancers (TCE) were integrated into the heat sink cavity. Three TCE geometries were investigated: triangular pin fins, circular pin fins, and metal foam. The TCE geometries were built at a volume fraction of 20%. TCE volume fraction refers to the volume of the pin fins to the volume of PCM (see Equations 1, 2 & 3). The cover plate of the heat sink was coated with a highly emissive coating with an emissivity of 0.82. Figures 1, 2 and 3 show the configuration of pin fins, the metal foam, and pin fins geometries, respectively. Table 1 presents the properties of the material adopted in the present work for the heat sink and PCM.

$$\Psi = \frac{V_{fins}}{V_{PCM}} \tag{1}$$

$$V_{fins} = \frac{\Psi \cdot V_t}{1 + \Psi} \tag{2}$$

$$V_{PCM} = \frac{V_t}{1 + \Psi} \tag{3}$$

The mathematical equations describing the model for metal foam are presented in equations (4) and (5).

$$V_{removed} = \frac{8}{3}\pi R^3 \tag{4}$$

$$\Psi = \frac{S^3}{\frac{8}{3}\pi R^3} - 1 \tag{5}$$

Where:

S = the basic unit side length and

R = the radius of the cutting circle.
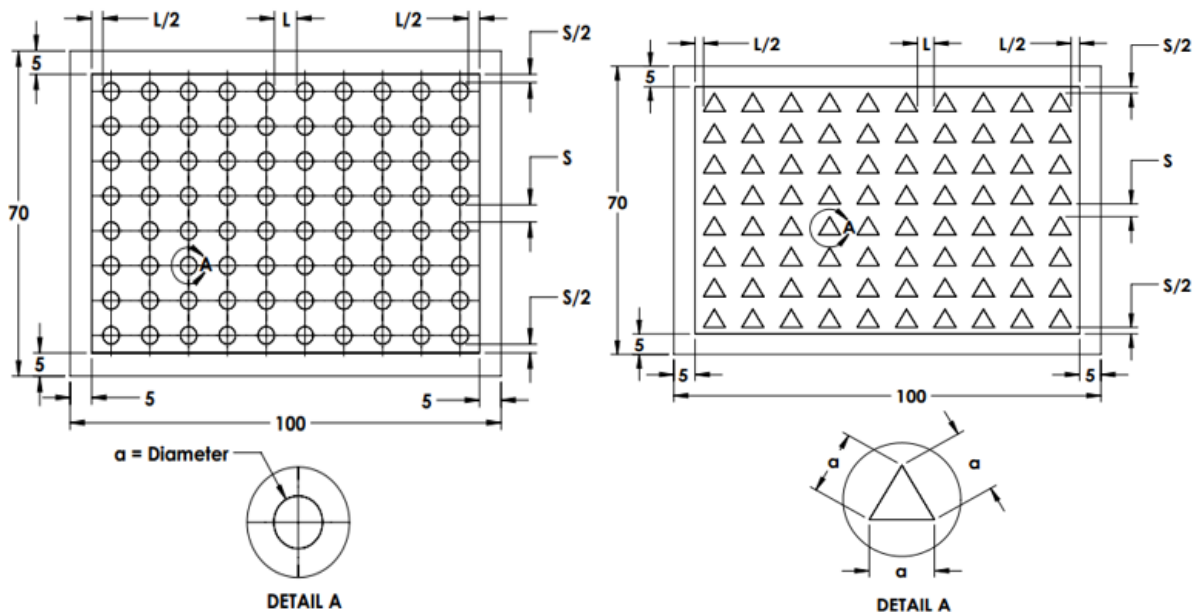
Fin geometry	Circular	Triangular
a (mm)	3.78	5.1
S (mm)	3.72	3.1
L (mm)	5.22	3.91

Figure 1: PCM based heat sink configuration with square and triangular pin fins.
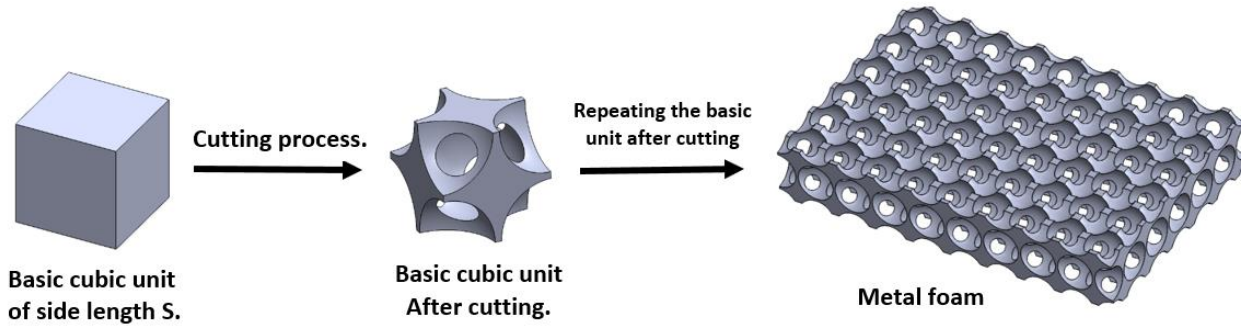
Figure 2: Metal foam modelling methodology
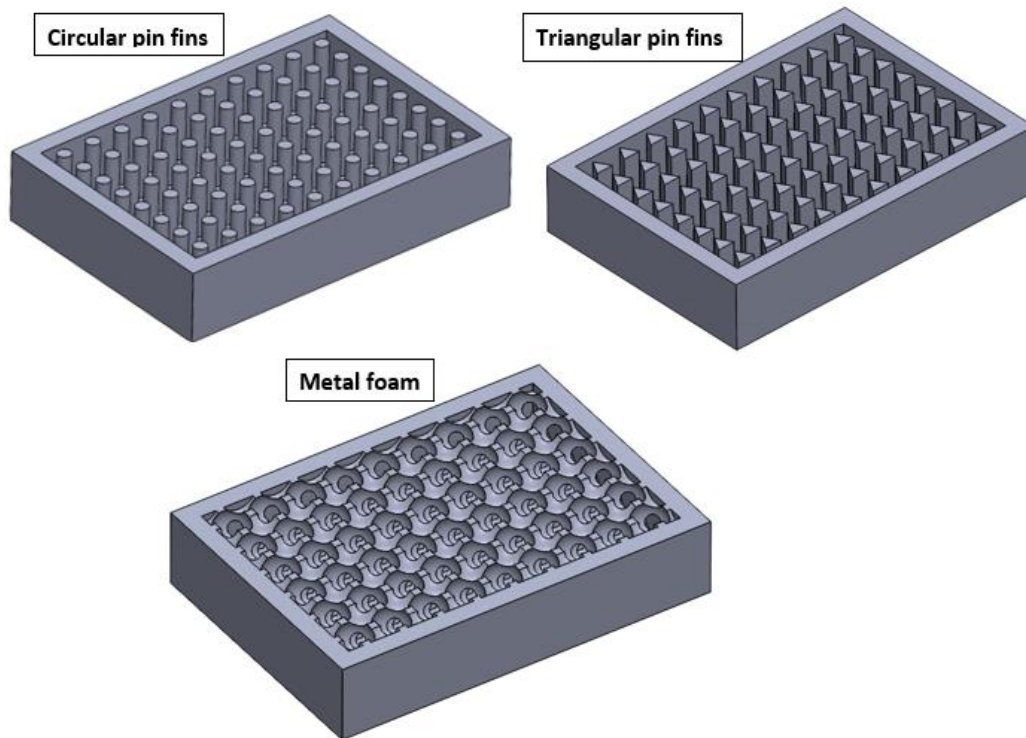
Figure 3: Thermal conductivity enhancers geometries adopted in the present work.

Table 1: Material properties (RUBITHERM (GmbH), 2021)

Materials	Melting point	ρ (kg/m^3)		C_p (KJ/kg)	K (W/m. K)	LH (KJ/kg)
		solid	liquid			
RT 35	29 - 36	860	770	2000	0.2	160
RT 31	27 - 33	880	760	2000	0.2	165
RT 24	21-25	880	770	2000	0.2	160
Aluminium alloy (6061 T6)	–	2770	–	897	167.9	–

2.2. Governing equations and boundary conditions

The finite volume technique was used for numerical simulations on a three-dimensional model of the proposed TCM. The enthalpy-porosity technique was used to model the phase transition process and considered each cell to be a porous zone with a porosity proportional to the melt fraction of the PCM inside the domain (Voller & Prakash, 1987a; Brent *et al.*, 1988). The enthalpy-porosity technique accounted for latent heat storage by providing a latent heat value to each computational grid cell in the energy equation. When a phase transition occurred in the computational cell, it was represented as a porous zone with porosity equaling the melt fraction of the PCM within the medium. The mushy zone constant was set at 10^5. The following are the governing equations used in this investigation.

1. Mass conservation equation 6.

$$div(U) = 0 \tag{6}$$

Where: $U = (u, v, w)$, u, v, and w are the velocities in the x-direction, y-direction and z-direction, respectively.

$$\frac{\partial u}{\partial x} + \frac{\partial v}{\partial y} + \frac{\partial w}{\partial z} = 0 \tag{7}$$

2. Momentum conservation equation.

Momentum in X- direction

$$\rho \left(\frac{\partial u}{\partial t} + u \frac{\partial u}{\partial x} + v \frac{\partial u}{\partial y} + w \frac{\partial u}{\partial z} \right) = \mu \left(\frac{\partial^2 u}{\partial x^2} + \frac{\partial^2 u}{\partial y^2} + \frac{\partial^2 u}{\partial z^2} \right) - \frac{\partial p}{\partial x} + S_x \tag{8}$$

Momentum in Y- direction

$$\rho \left(\frac{\partial v}{\partial t} + u \frac{\partial v}{\partial x} + v \frac{\partial v}{\partial y} + w \frac{\partial v}{\partial z} \right) = \mu \left(\frac{\partial^2 v}{\partial x^2} + \frac{\partial^2 v}{\partial y^2} + \frac{\partial^2 v}{\partial z^2} \right) - \frac{\partial p}{\partial y} + S_y \tag{9}$$

Momentum Z - direction

$$\rho \left(\frac{\partial w}{\partial t} + u \frac{\partial w}{\partial x} + v \frac{\partial w}{\partial y} + w \frac{\partial w}{\partial z} \right) = \mu \left(\frac{\partial^2 w}{\partial x^2} + \frac{\partial^2 w}{\partial y^2} + \frac{\partial^2 w}{\partial z^2} \right) - \frac{\partial p}{\partial z} + S_z \tag{10}$$

Where: S_x, S_y, S_z are source terms which govern the fluid flow in the mushy zone. These source terms reduce the momentum equations to Carman-Kozeny equations to control the flow in the porous media (Voller & Prakash, 1987b). Due to working in zero gravity, the buoyancy source term was neglected.

$$S_x = -A_{mushy} \frac{(1-\Psi)^2}{\Psi^3 + b} u \tag{11}$$

$$S_y = -A_{mushy} \frac{(1-\Psi)^2}{\Psi^3 + b} v \tag{12}$$

$$S_z = -A_{mushy} \frac{(1-\Psi)^2}{\Psi^3 + b} w \tag{13}$$

Where A_{mushy}: is the mushy medium constant that varies from 10^5 to 10^6, Ψ: is the melt fraction of the PCM within each cell, and b: is a constant higher than unity to avoid division by zero and was set at 0.002. Each cell is simulated as a porous medium with porosity equal to the melt fraction.

$$\Psi = \begin{cases} 0 & T < T_m \\ \frac{T - T_{solid}}{T_{liquid} - T_{solid}} & T_{solid} < T < T_{liquid} \\ 1 & T > T_m \end{cases} \tag{14}$$

Where: T_{solid}: is the solidus temperature, T_{liquid}: is the liquidus temperature, and 1℃ was adopted as the temperature difference between the liquidus and solidus temperatures.

1. Conservation of energy

$$\rho \left(\frac{\partial H}{\partial t} + \frac{\partial (uH)}{\partial x} + \frac{\partial (vH)}{\partial y} + \frac{\partial (wH)}{\partial z} \right) = \frac{\partial}{\partial x} \left(k \frac{\partial T}{\partial x} \right) + \frac{\partial}{\partial y} \left(k \frac{\partial T}{\partial y} \right) + \frac{\partial}{\partial z} \left(k \frac{\partial T}{\partial z} \right) + S_h \tag{15}$$

Where: H = the total enthalpy which includes latent and sensible enthalpy.

$$H = h + \nabla H \tag{16}$$

$$h = h_{ref.} + \int_{T_0}^{T} C_p \, dT \tag{17}$$

$$\nabla H = \psi L \tag{18}$$

Where L is the latent heat, ∇H is the latent heat content. S_h: is the enthalpy source term. $h_{ref.}$: is a reference enthalpy at the reference temperature.

$$S_h = \frac{\partial \rho(\nabla H)}{\partial t} + div(\rho U \nabla H) \tag{19}$$

During the phase change process, the energy equation source term is reduced to the latent enthalpy time derivative and the term $div(\rho U \nabla H)$ equals zero. The latent enthalpy is a piecewise polynomial that depends on the temperature and is defined as:

$$\nabla H = \begin{cases} L & T < T_m \\ \frac{T - T_{solid}}{T_{liquid} - T_{solid}} & T_{solid} < T < T_{liquid} \\ 0 & T > T_m \end{cases} \tag{20}$$

Pressure-velocity coupling was represented in the numerical model using the simple scheme. The pressure staggering options (PRESTO) and second-order upwind approaches were used to discretize pressure and energy spatially. The energy equation's convergence criterion was set at 10^-7.
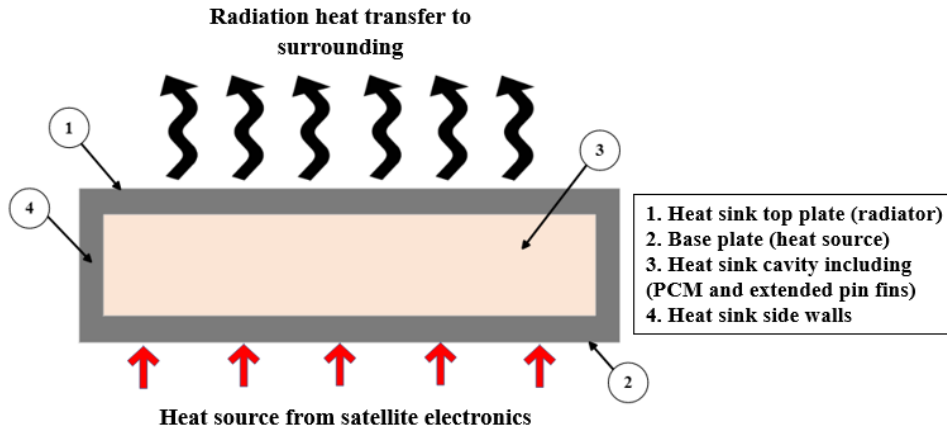
Figure 4: physical problem and boundary conditions

ANSYS fluent 2020 R1 solver was utilised to examine a three-dimensional model of a PCM-based heat sink or TCM. The heat load from the satellite hardware heated the heat sink's base plate. The entire thermal analysis cycle lasted 90 minutes. During the first 10 minute heating phase, the satellite hardware was in (ON) mode. During the cooling phase, which lasted 80 minutes, the hardware was in the (OFF) state. The heat load of satellite gear was 20W or 2857.1 W/m2. During the cooling phase, the TCM dissipates its stored thermal energy via thermal radiation. The ambient temperature to which the heat sink surface emitted heat was set to 20°C. Figure 4 depicts the model elements and explains the physical problem. The properties of the PCM were considered temperature dependent, and the expansion of PCM due to phase change was neglected. Only conduction and radiation heat transfers were regarded in the model due to working in space. The initial temperature was 22°C. Further, the side walls of the heat sink were insulated and the cover plate emitted heat by radiation. The base plate was subjected to heat load from the satellite equipment.

3. RESULTS
3.1. Grid and time step independence study

This model thoroughly examined the influence of the grid element density and the time step for the transient solution. The mesh was produced by employing ANSYS meshing. Body sizing and multizone mesh control methods were applied. The former was employed to generate cell zones with many hexagonal elements. The latter was employed concurrently to regulate the size of the grid elements. Grid and time-step independence were evaluated using RT 35 PCM at 20W heat load. Four scenarios of mesh quality with different element densities were examined: extremely fine, fine, medium, and coarse mesh with 1074921, 765301, 145350, and 21624 grid elements, respectively. The highest inaccuracy in determining the maximum base plate temperature was 0.22% for coarse meshes and 0.027%

for fine meshes. A very fine mesh was employed in this study for data reliability and to catch the precise distinctions across case studies. The results of the grid and time step independence study are reported in Table 2.

Table 2: Grid and time-step independence study

Grid independence investigation				Time step independence study	
Mesh quality	Number of grid elements	Maximum temperature (K)	The liquid fraction at the end of the heating process	Time step (s)	Temperature (K)
Coarse	21625	42.7361	0.712	5	42.736
Medium	145350	42.2825	0.72	3	42.354
Fine	765301	42.13	0.723	1	42.254
Highly fine	1074921	42.0438	0.7237	0.2	42.187

A time-step independence test was conducted based on the extremely tiny mesh's quality. In order to record the phase transition process, the right time step must be specified, as bigger time steps may allow the phase change to be skipped entirely. The adopted time steps were 5, 3, 1, and 0.2 seconds. These were the maximum time steps that the solution can consider. The solution may take into account lower values to satisfy convergence criteria. The highest temperature of the base plate did not change when the time step was reduced from 5 to 0.1 seconds, according to the findings of the time step independence test. Between the 5 second and 0.2 second time increments, the largest achievable error was 0.17%. As a result, a time step of 5 seconds was chosen to accommodate computational time and cost concerns.

3.2. Model validation

Baby and Balaji (2014) conducted an experimental study to investigate the thermal performance of a PCM-based heat sink. The heat sink was made from aluminium by a milling process. The dimensions of the heat sink were 80mm in length, 62mm in width, and 25mm high. The fins were all 1.4mm thick and 20mm high. N-eicosane was used as a PCM material. The validation was performed with the case at which the volume fraction of the PCM was 100%, and the heat load was 7W.

The validation results in Figure 5 show a good agreement between the experimental work performed by Baby and Balaji (2014) and the present numerical model. As shown in Figure 5, the PCM temperature was constant at the corresponding melting temperature before it increased again after the completed melting process. The numerical model could capture the phase transition process effectively. The maximum error obtained between the numerical model and the experimental work results was 4.3%.
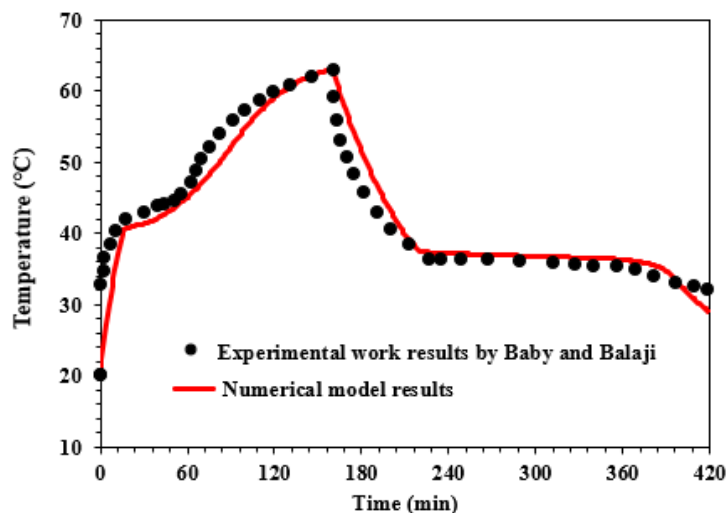
Figure 5: Model validation results with the experimental work performed by Baby and Balaji (2014)

3.3. Effect of latent heat storage on thermal performance

The base plate temperature was reported during the simulation cycle, and the results are shown in Figure 6. Four cases were investigated: heat sink without PCM and heat sink with PCM at three different melting points of 24°C, 31°C, and 35°C. Figure 6 shows that the heat sink temperature increased during the heating process, which lasted

for 10 minutes and decreased again when the heat load was released. The cooling process lasted for 80 minutes. The heat sink without PCM reported a significant increase in temperature. However, the cases at which the PCM was adopted reported a remarkable decrease in temperature.

The heat sink without PCM reported a maximum temperature at the end of the heating process of about 103°C. In contrast, the cases of PCM-based heat sinks reported a lower temperature of 59.3°C, 57.6°C, and 55.8°C for RT 35, RT 31, and RT 24, respectively. The PCM with the lowest melting point, RT 24, recorded the minimum temperature. In addition, RT 24 could reduce the base plate temperature by about 46%. Thermal storage using PCM is a highly effective option for the thermal management of satellite electronics.
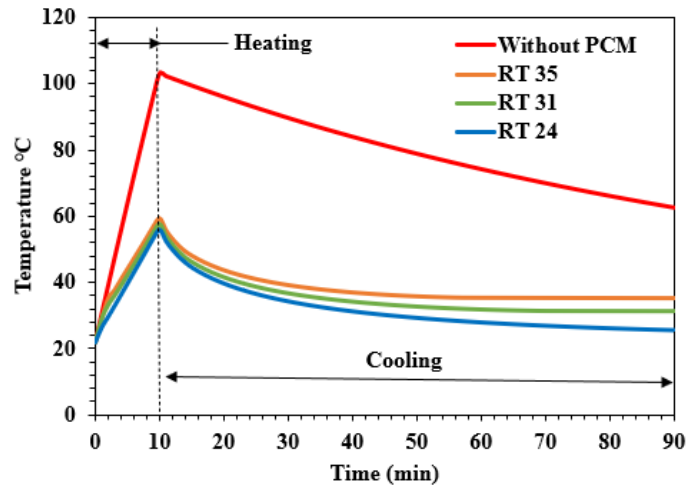
Figure 6: Base plate temperature for heat sink without PCM and with PCM

Figure 7 presents the liquid fraction results of PCM for each melting point. The lower melting point PCM reported the maximum liquid fraction results. RT 35 reported a maximum liquid fraction of 0.65. while RT 31 and 24 reported a maximum liquid fraction of 0.72 and 0.9, respectively. RT 24 could increase the liquid fraction by 27.7%. The liquid fraction results were of great importance. The higher the liquid fraction, the higher the amount of PCM melted; hence, more heat was stored in the form of latent heat. In other words, the liquid fraction indicated the amount of heat stored in latent heat.
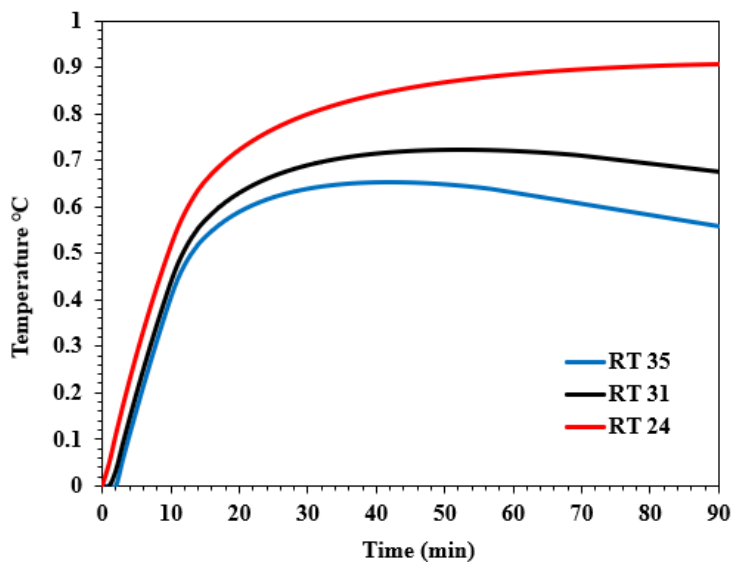
Figure 7: Liquid fraction of PCM at different melting points.

3.4. Effect of thermal conductivity enhancer

This section describes the effect of thermal conductivity enhancers geometry on thermal performance. The base plate temperature results, the temperature contours, and the liquid fraction contours are presented.

The base plate temperature

The effect of TCE geometry was investigated using RT 35, and the results are reported in Figure 8. Three TCE geometries were investigated: triangular pin fins, circular pin fins, and metal foam. The results concluded that the TCE could significantly improve thermal performance. The maximum temperature reached without TCE was 59.3°C while for the cases with TCE, the temperatures were significantly decreased. The results concluded that the metal foam showed the best thermal performance among other geometries: it could reduce the base plate temperature by 20.1°C with a reduction percentage of 33.8%. Triangular and circular pin fins reduced the base plate temperature by 17.8°C and 17°C, respectively. The explanation beyond the significant thermal performance of metal foam returns to the contact area between the TCE metal and the PCM which was remarkably higher for metal foam, hence the metal foam recorded the best thermal performance.
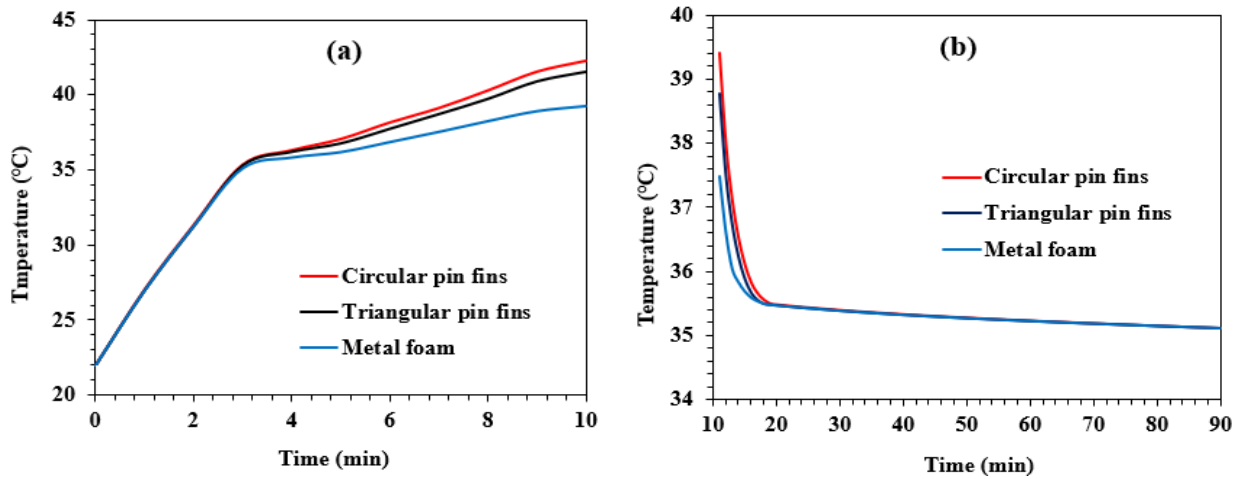
Figure 8: the effect of TCE geometry. (a) during the heating process, and (b) during the cooling process.

Temperature and liquid fraction contours

Figures 9 and 10 present the temperature and liquid fraction contours at the end of the heating process, respectively. Figure 9 shows the temperature contour for circular and metal foam geometries. It was remarked that the metal foam could significantly decrease the temperature of the heat sink. The maximum temperature reached without TCE was 59.3°C while metal foam could reduce the base plate temperature by 20.1°C with a reduction percentage of 33.8%. Triangular and circular pin fins reduced the base plate temperature by 17.8°C and 17°C, respectively. The contact area between the TCE and the PCM was much higher in the case of metal foam compared to other TCE geometries. This contact area promoted the heat transfer process between the TCE and the PCM, which resulted in more latent heat stored in the PCM. So metal foam geometry reported the lower heat sink temperature among other TCE geometries.

Figure 10 shows the PCM liquid fraction contours. The red colour refers to the melted PCM, while the blue one refers to the solid PCM. The TCE significantly improved the contact area between the PCM and the heat sink structure, so the cases with TCE reported a significantly higher liquid fraction of the PCM. Figure 10 shows a remarkable increase in the PCM liquid fraction in the case of metal foam TCE geometry compared to the case without TCE. The case without PCM recorded a liquid fraction of 0.65. At the same time, circular pin fins increased the liquid fraction to 0.84 with a percentage of 29.2%. Triangular pin fins and metal foam increased the melt fraction by 31% and 40%, respectively.

(a) For circular pin fins   (b) For metal foam
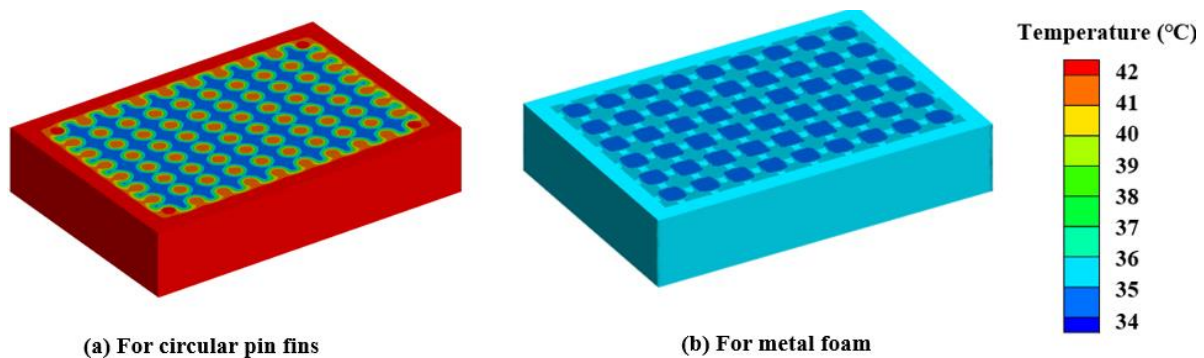
Figure 9: temperature contours at the end of the heating process. (a) for circular pin fins, (b) for metal foam.
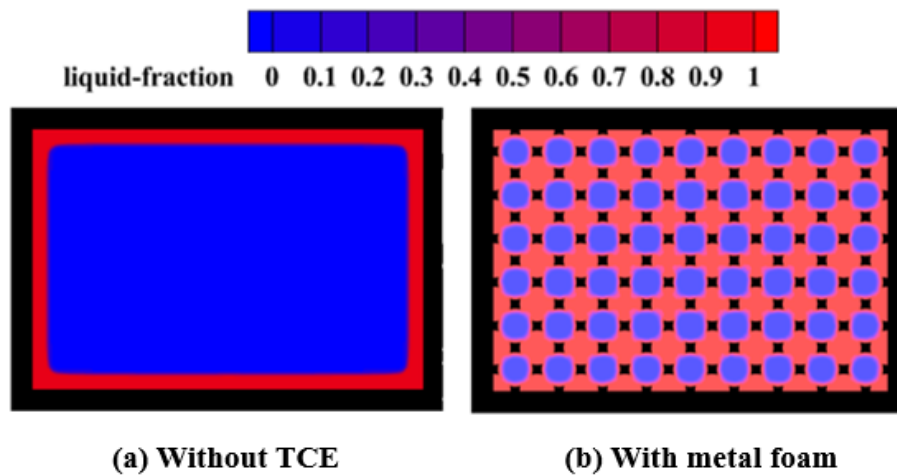
Figure 10: liquid fraction contour for (a) without TCE and (b) with metal foam at the end of the heating process.

4. CONCLUSION

This work investigated the effect of latent heat storage of PCM on the thermal control performance of satellite subsystems. PCM was a promising candidate for the thermal management of electronics. The PCM melting point was a significant parameter of PCM as it influenced thermal performance: the lower the PCM melting point, the higher the performance. Thermal conductivity enhancers were effective for enhancing the PCM thermal conductivity. Novel metal foam was the best TCE as it could significantly decrease the heat sink temperature.

5. REFERENCES

Abhat, A., & Groll, M. (1974, July 15). *Investigation of phase change material /PCM/ devices for thermal control purposes in satellites.* https://doi.org/10.2514/6.1974-728

Alimohammadi, M., Aghli, Y., Alavi, E. S., Sardarabadi, M., & Passandideh-Fard, M. (2017). Experimental investigation of the effects of using nano/phase change materials (NPCM) as coolant of electronic chipsets, under free and forced convection. *Applied Thermal Engineering*, *111*, 271–279. https://doi.org/10.1016/j.applthermaleng.2016.09.028

Andraka, C. E., Kruizenga, A. M., Hernandez-Sanchez, B. A., & Coker, E. N. (2015). Metallic Phase Change Material Thermal Storage for Dish Stirling. *Energy Procedia*, *69*, 726–736. https://doi.org/10.1016/j.egypro.2015.03.083

Baby, R., & Balaji, C. (2014). Thermal performance of a PCM heat sink under different heat loads: An experimental study. *International Journal of Thermal Sciences*, *79*, 240–249. https://doi.org/10.1016/j.ijthermalsci.2013.12.018

Abhat, A., & Groll, M. (1974, July 15). *Investigation of phase change material /PCM/ devices for thermal control purposes in satellites.* https://doi.org/10.2514/6.1974-728

Alimohammadi, M., Aghli, Y., Alavi, E. S., Sardarabadi, M., & Passandideh-Fard, M. (2017). Experimental investigation of the effects of using nano/phase change materials (NPCM) as coolant of electronic chipsets, under free and forced convection. *Applied Thermal Engineering*, *111*, 271–279. https://doi.org/10.1016/j.applthermaleng.2016.09.028

Andraka, C. E., Kruizenga, A. M., Hernandez-Sanchez, B. A., & Coker, E. N. (2015). Metallic Phase Change Material Thermal Storage for Dish Stirling. *Energy Procedia*, *69*, 726–736. https://doi.org/10.1016/j.egypro.2015.03.083

Baby, R., & Balaji, C. (2014). Thermal performance of a PCM heat sink under different heat loads: An experimental study. *International Journal of Thermal Sciences*, *79*, 240–249. https://doi.org/10.1016/j.ijthermalsci.2013.12.018

Brent, A. D., Voller, V. R., & Reid, K. J. (1988). Enthalpy-porosity technique for modeling convection-diffusion phase change: Application to the melting of a pure metal. *Numerical Heat Transfer*, *13*(3), 297–318. https://doi.org/10.1080/10407788808913615

Chang, T. C., Lee, S., Fuh, Y. K., Peng, Y. C., & Lin, Z. Y. (2017). PCM based heat sinks of paraffin/nanoplatelet graphite composite for thermal management of IGBT. *Applied Thermal Engineering*, *112*, 1129–1136. https://doi.org/10.1016/j.applthermaleng.2016.11.010

Fan, L., Zhu, Z., Zeng, Y., Xiao, Y., Liu, X., & Wu, Y. (2015). Transient performance of a PCM-based heat sink with high aspect-ratio carbon nano fi llers. *Applied Thermal Engineering*, *75*, 532–540. https://doi.org/10.1016/j.applthermaleng.2014.10.050

Farrahi, A., & Pérez-Grande, I. (2017). Simplified analysis of the thermal behavior of a spinning satellite flying over Sun-synchronous orbits. *Applied Thermal Engineering*, *125*, 1146–1156. https://doi.org/10.1016/j.applthermaleng.2017.07.033

Gharbi, S., Harmand, S., & Ben, S. (2015). Experimental comparison between different con fi gurations of PCM based heat sinks for cooling electronic components. *Applied Thermal Engineering*, *87*, 454–462. https://doi.org/10.1016/j.applthermaleng.2015.05.024

Gilmore, D. M. (2002). *Spacecraft Thermal Control Hand book*. *1*.

Gonzalez-Nino, D., Boteler, L. M., Ibitayo, D., Jankowski, N. R., Urciuoli, D., Kierzewski, I. M., & Quintero, P. O. (2018). Experimental evaluation of metallic phase change materials for thermal transient mitigation. *International Journal of Heat and Mass Transfer*, *116*, 512–519. https://doi.org/10.1016/j.ijheatmasstransfer.2017.09.039

Humphries, W. R. (1974). Performance of finned thermal capacitators. *NASA Technical Reports*, *July*, 300.

Liu, T., Sun, Q., Meng, J., Pan, Z., & Tang, Y. (2016). Degradation modeling of satellite thermal control coatings in a low earth orbit environment. *Solar Energy*, *139*, 467–474. https://doi.org/10.1016/j.solener.2016.10.031

RUBITHERM (GmbH). (2021). www.rubitherm.eu

Voller, V. R., & Prakash, C. (1987a). A fixed grid numerical modelling methodology for convection-diffusion mushy region phase-change problems. *International Journal of Heat and Mass Transfer*, *30*(8), 1709–1719. https://doi.org/10.1016/0017-9310(87)90317-6

#59: Design and modelling of a small-scale reversible heat pump – organic Rankine cycle system for industrial waste heat recovery

Rahul Velanparambil Ravindran[*], Neil Hewitt, Ming Jun Huang

Centre for Sustainable Technologies, Belfast School of Architecture and the Built Environment, Faculty of Computing, Engineering and the Built Environment, University of Ulster, Newtownabbey, County Antrim, BT37 0QB, United Kingdom.
Corresponding author: velanparambil_ravindran-r@ulster.ac.uk

Abstract: The organic Rankine cycle (ORC) and heat pumps (HP) are technologies well known for industrial waste heat recovery. Considering the similarities in the configurations for both ORC and HP, a system that can be reversed between HP and ORC modes is possible with few modifications. The reversible system according to the requirement of the industry can exploit waste heat in a lower temperature band operating as a heat pump to provide useful process heat or as an organic Rankine cycle system generating power and thus increasing the efficiency of waste heat exploitation. This study discusses the design aspects of a small-scale reversible HP-ORC system, including the system layout, component selection, selection of a low global warming potential (GWP), zero Ozone depletion potential (ODP) refrigerant, the operating conditions for both modes, and sizing of equipment. R1233zd(E) was selected as the preferred refrigerant to replace R245fa in the reversible system and an automotive open drive scroll compressor was found to be suitable which can also be employed as an expander for ORC with minimum modifications. The study also presents the modelling of the reversible system in ORC and HP modes including performance analysis of scroll machine in expander and compressor roles attaining isentropic efficiency values up to 62.4% and 75.4% respectively. The modelling results show a cycle efficiency of 5.9% (T_{ev} = 102°C, M_r = 0.064 kg/s) in ORC mode and a COP of 3.88 in HP mode (for a temperature lift of 50K with T_{source} : 75 - 85°C).

Keywords: waste heat recovery; organic Rankine cycle; heat pump; scroll compressor; scroll expander

1. INTRODUCTION

At the current rate, global warming is expected to cause a temperature increase of 1.5°C between 2030 and 2050 (IPCC, 2018) and unless strict measures are taken, the global surface temperature will continue to rise and global warming could exceed 2°C in the 21st century (IPCC, 2021). The Paris agreement called on its parties to adopt measures to address climate change threats by keeping the global temperature rise below 2°C and taking up efforts to limit the temperature increase to 1.5°C ('Paris Agreement on Climate Change', 2015). In light of the Paris Agreement, the European Commission revised the greenhouse gas emissions reduction target to 55% for 2030 (European Commission, 2020). The European Commission's long-term vision to achieve climate neutrality (zero greenhouse gas emissions) cost-effectively by 2050 (European Commission, 2018) assigns an important role to energy as it is a major contributor to greenhouse gas emissions. Improving energy efficiency in industrial, residential, and service sectors are considered an important strategy to achieve climate neutrality. In the industrial sector, the global energy efficiency rate is 49% which amounts to energy consumption of 52.1 PJ (Forman *et al.*, 2016). The total industrial waste heat potential on a global scale is estimated at 31.9 PJ of which 42% (13.39 PJ) is in the lower temperature band (<100°C) while the medium temperature band (100 -299°C) has a share of 20% (6.38 PJ). In the European Union, the recoverable waste heat is calculated at 304.13 TWh/year (Papapetrou *et al.*, 2018). For the UK, the recoverable waste heat share is 24 TWh/year. A UK-specific waste heat analysis indicates a heat recovery potential of 36 - 71 PJ is available from industries in different temperature bands (McKenna and Norman, 2010).

Among the various waste heat recovery technologies used, a reversible system that can be operated as a heat pump (HP) to upgrade industrial waste heat to useful process heat and as an organic Rankine cycle (ORC) system to generate power increases the efficiency of waste heat utilization. This reversibility allows the system to switch between the two modes to meet the changing needs of the industry. The similarities in both HP and ORC configurations make a reversible system feasible with minimum modifications. Few theoretical and experimental research works based on this reversible concept have been carried out in the domestic and industrial sectors. The feasibility of a reversible HP – ORC system coupled to a solar loop in the domestic sector has previously been evaluated theoretically at three different sites (Schimpf and Span, 2015), with COP values in the 3.63 to 3.92 range and an ORC thermal efficiency range of 5.8% - 6%. An experimental study of a reversible system connected to a solar loop showed encouraging results attaining a maximum COP value of 3.1 (HP mode) and a cycle thermal efficiency of 4.2% in ORC mode with an output power of 3.7 kW (Dumont, Quoilin and Lemort, 2015). The scope of the reversible system as an industrial waste heat recovery technology was examined through a modelling approach (Mateu-Royo, Mota-Babiloni, *et al.*, 2019). The system with R245fa as a working fluid achieved a COP of 2.44 and an ORC efficiency of 8.75% at an evaporating temperature of 100°C. The performance of a system using a screw machine as the expander/compressor with R142b as the working fluid was analysed through experiments (Wu *et al.*, 2019). For a temperature lift of 36K in HP mode, a maximum COP of 2.74, and in ORC mode a cycle thermal efficiency of 4.58% and a power output of 3.7 kW were obtained. The system's reversibility allowed it to be used in pumped thermal energy storage applications in the temperature range of 110 - 160°C (Staub *et al.*, 2018). The design and modelling of a reversible system for thermal energy storage (Carnot battery) showed R1233zd(E) as a suitable refrigerant (Eppinger *et al.*, 2021). The system achieved a maximum power-to-power efficiency of 59%.

This study discusses the design and modelling aspects of a reversible HP-ORC system for recovering waste heat in the lower temperature band (<150°C). The layout, operating conditions, and the selection of components for each operating mode are discussed first followed by modelling of the individual components for HP and ORC modes including the performance analysis of the reversible system under operating conditions.

2. NOMENCLATURE

A	Area, m^2	**Greek letters**		*exp*	*expander*
AU	Heat transfer coefficient, W/K	α	Proportionality factor	*in*	*internal*
d	Diameter, m	η	Efficiency	*is*	*isentropic*
h	Heat transfer coefficient, W/m^2K	**Subscripts**		*leak*	*leakage*
$\dot{M}$	Mass flow rate, kg/s	*amb*	*ambient*	*loss*	*mechanical losses*
N	RPM	*cd*	*condenser*	*pp*	*pump*
$\dot{Q}$	Heat transfer, kW	*comp*	*compressor*	*r*	*refrigerant*
r	ratio	*el*	*electrical*	*sf*	*secondary fluid*
u	Overall heat transfer coefficient, W/m^2K	*ev*	*evaporator*	*su*	*suction*
$\dot{W}$	Power, kW	*ex*	*exhaust*	*v*	*volume*

3. DESIGN

A conventional HP configuration can be modified to a reversible system by the addition of a pump, a volumetric machine that operates as both compressor and expander in each mode, and a series of valves to switch the refrigerant flow between the suction and discharge ports of the volumetric machine. The schematic of such a system is shown in Figure 1. In the selected system layout, the heat exchanger roles (condenser and evaporator) and the refrigerant flow direction remained unchanged when the system operated in both ORC and HP modes. This type of configuration keeps the reversible system compact, simple, and economically viable (Dumont, 2017). The operating conditions which were set by the system performance in MATLAB® in HP and ORC modes are described in Table 1.

Table1: Operating conditions of the reversible system

Operating conditions	ORC	HP
Heat source temperature (°C)	75-140	70-100
Thermal load (Evaporator) (kW)	9.7 – 14.8	5 – 13
Thermal load (Condenser) (kW)	9.5 - 14	5.6 – 14
Evaporating pressure (bar)	4.5 – 17.7	3.7 – 7.5
Condensing pressure (bar)	2.1 – 3	7.6 - 16
Mass flow rate (kg/s)	0.037 – 0.065	0.035 – 0.098

The heat source temperature range for the ORC mode was set to 75-140°C and the heat sink temperature was set to a range of 20-50°C. For HP mode, the heat source and sink temperature ranges were set at 70-100°C and 60-100°C respectively. Construction of a test bed for the reversible system was underway at the laboratory facility and hence the selection of operating conditions, components, and secondary fluids depended on the resources available.
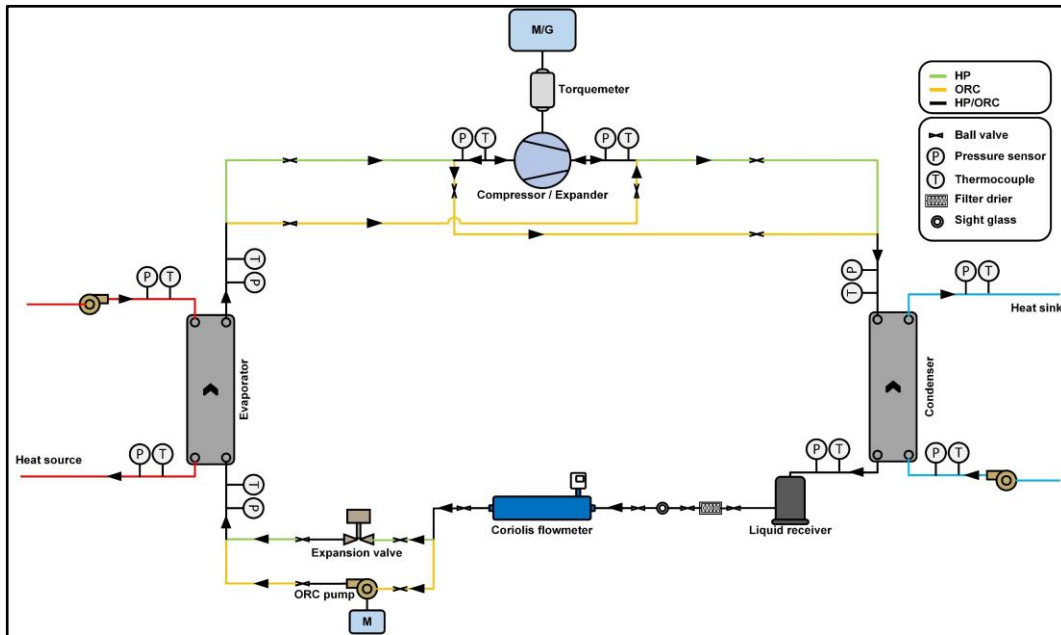
Figure 1: Schematic diagram of reversible HP - ORC system

3.1. Expander/compressor

A compressor that can be reversed to operate as an expander is key to the reversible HP – ORC system. Turbomachinery was excluded at first, as they are generally employed in large-scale power applications. Screw, piston, and scroll machines are commonly used in both ORC and HP systems. Screw and scroll machines offer better handling of two-phase expansion and comparatively lower losses(friction and leakage) than vane machines (Imran *et al.*, 2016). Piston machines can be operated at high pressure and temperatures and at high-pressure ratios, but the lower wet expansion capability limits its application. Screw machines are suitable for higher power applications while piston and scroll machines are preferred for lower power rangers (<2.5kW)(Dumont *et al.*, 2018). A comparison of piston, scroll, screw, and vane machine for various parameters is shown in Table 2.

Table 2: Comparison of various volumetric machines

Volumetric machine type	Scroll	Piston	Screw	Vane
Power range (kW)	1 - 10	1 - 10	15 - 200	1 - 10
Rotational speed (RPM)	Low	Medium	Low	Low
Wet expansion	Yes	No	Yes	Yes
Compactness	High	Medium	High	High
Cost	Low	Medium	Medium	Low

Given the compactness, wet expansion handling ability, and applicability under the mentioned operating conditions the scroll machine was found to be suitable for the reversible system. A scroll compressor used for automotive air conditioning (SANDEN TRSA09) was selected. The compressor had a swept volume of 85.7 cm^3, a built-in volume ratio of 1.9, and could easily be modified to an expander by removing the discharge valve.

3.2. Refrigerant

The refrigerant for this reversible system should perform well with both ORC and HP operating modes. The Kigali amendment agreed to implement new measures to reduce the consumption of hydrofluorocarbons (HFC) (United

Nations, 2016). Under the current regulations, the selection of suitable refrigerants for refrigeration, ORC, and HP applications is becoming increasingly important against the background of global warming (Bobbo *et al.*, 2018). This depends on various refrigerant properties such as global warming potential (GWP), ozone depletion potential (ODP), flammability, and toxicity (Table 3). R245fa is a common refrigerant used in small-scale ORC and HP systems. Despite zero ODP, a high GWP value of 1030 limits its future applications in ORC and HP systems. Theoretical and experimental analysis suggested several refrigerants to replace R245fa in heat recovery applications.

Experimental investigation of an organic Rankine cycle showed higher cycle thermal efficiency and gross power output achieved with R1233zd(E) compared to R245fa (Yang *et al.*, 2018). In the theoretical analysis of a high-temperature heat pump, the most improved COP was achieved with R1233zd(E) followed by R1334mzz(Z) and R1224yd(Z) compared to R245fa (Mateu-Royo, Navarro-Esbrí, *et al.*, 2019). R1233zd(E) and R1224yd(Z) can replace R245fa in high-temperature heat pump applications without changing the compressor at low-temperature sources. R1234ze(Z), R1224yd(Z), and R1336mzz(Z) were also suitable alternatives to R245fa in HP applications (Frate, Ferrari and Desideri, 2019). The T-s, and P-h diagram comparison of R1233zd(E) and R245fa are shown in Figures 2 and 3 respectively. The refrigerant properties were determined using REFPROP 10.0. Considering the performance comparison of both fluids in both HP and ORC systems and the availability of the refrigerant, R1233zd(E) was selected as the working fluid for the system in both operating modes.

Table 3: Comparison of refrigerant properties

Parameters	Ozone depletion potential (ODP)	Global warming potential (GWP)	Critical Temperature (°C)	Critical pressure (bar)
R245fa	0	1030	153.9	36.5
R1233zd(E)	0.00024	1	166.5	36.2
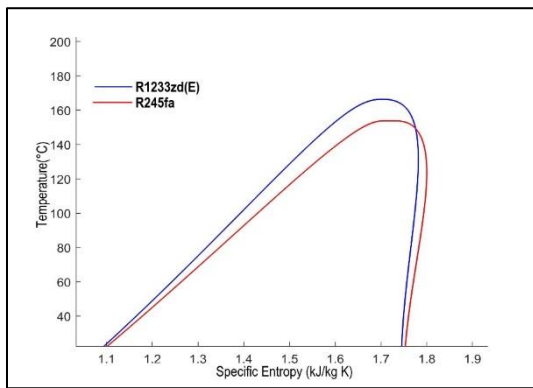
Figure 2: T-s diagrams of R1233zd(E) and R245fa
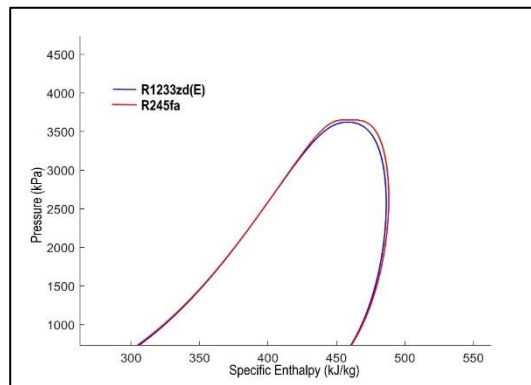
Figure 3: P-h diagrams of R1233zd(E) and R245fa

3.3. Heat exchangers and pump

In the selected system design, the condenser and evaporator conserve their roles in both ORC and HP modes. Water and Therminol 66 were selected as the heat source and heat sink fluid, respectively. The selection of the secondary fluids was based on the resources available in the laboratory. The heat exchanger was selected using the SWEP SSP G8 selection software. For the mentioned operating conditions and subject to availability, SWEP B85x20 was selected for the evaporator and SWEP B25Tx26 for the condenser. A rotary vane pump with a nominal flow rate of 400 l/h was chosen as the pump for the ORC system.

4. MODELLING

4.1. Compressor and expander modelling

Modelling of the components and performance simulation in both HP and ORC configurations was performed on the MATLAB® platform. Semi-empirical models were developed for both the compressor and the expander (Lemort, 2008). The models account for heat transfer during suction and discharge, ambient heat transfer, internal leakage, and pressure drops at the suction and discharge sides. The parameters required for semi-empirical models were taken from previous studies on compressors (Lemort, 2008) and expanders (Twomey, Jacobs and Gurgenci, 2013) and have been modified to account for changes in the swept volume of the selected scroll machine (85.7 cm^3) and the refrigerant (R1233zd(E)) used. The parameters thus obtained are shown in Table 4. Figure 4 and Figure 5 show the schematic of the semi-empirical models of the scroll compressor and scroll expander respectively.

Table 4: Parameters for scroll compressor and expander semi-empirical models

Model parameters	Expander	Compressor
Suction heat transfer coefficient, AU_{su}, (W/K)	42.5	28.4
Exhaust heat transfer coefficient, AU_{ex}, (W/K)	4.3	12
Ambient heat transfer coefficient, AU_{amb}, (W/K)	0.45	9.7
Built-in volume ratio (r_v)	1.9	1.9
Leakage area, A_{leak} (m^2)	3.75×10^{-6}	5.8×10^{-7}
Mechanical loss torque, T_{loss} (N m)	0.84	0.46
Proportionality factor, α	-	0.2
Supply nozzle throat diameter, d_{su} (m)	7.6×10^{-3}	-
Exhaust nozzle throat diameter, d_{ex} (m)	-	7.5×10^{-3}
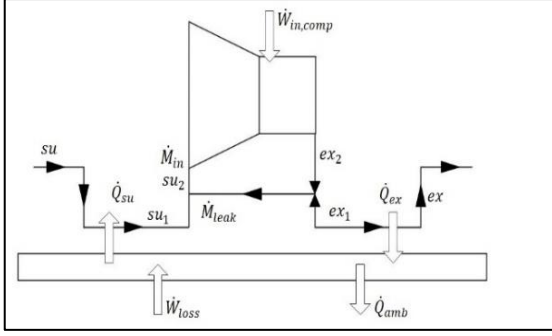
Figure 4: Semi-empirical compressor model (Lemort, 2008)
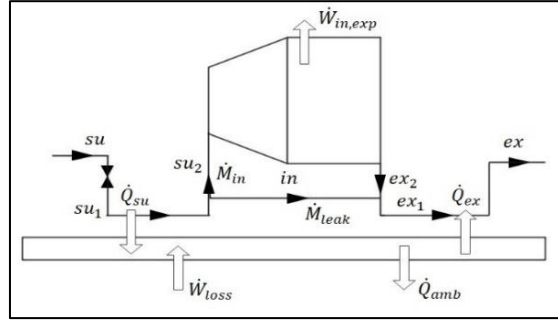
Figure 5: Semi-empirical expander model (Lemort, 2008)

The total power consumption of the scroll compressor was:

$$\dot{W}_{el,comp} = \dot{W}_{in,comp} + \dot{W}_{loss} = \dot{W}_{in,comp} + \alpha \dot{W}_{in,comp} + (2\pi N_{comp} T_{loss}) \quad (1)$$

And the equation for the isentropic efficiency of the compressor is given below:

$$\eta_{is,comp} = \frac{\dot{W}_{el,is}}{\dot{W}_{el,comp}} \quad (2)$$

The equations for power generated and isentropic efficiency for the scroll expander model are given below:

$$\dot{W}_{el,exp} = \dot{W}_{in,exp} - \dot{W}_{loss} = \dot{W}_{in,exp} - (2\pi N_{exp} T_{loss}) \quad (3)$$

$$\eta_{is,exp} = \frac{\dot{W}_{el,exp}}{\dot{W}_{el,is}} \quad (4)$$

$\dot{W}_{el,s}$ is the power consumption (power generated in ORC), when the compression process (expansion in ORC) was assumed to be isentropic.

4.2. Heat exchanger and pump

Heat exchangers were modelled by dividing the exchanger area into three zones (liquid, vapour, and two-phase zones) with the heat transfer coefficient of each zone determined by heat transfer correlations for single and two-phase media (Quoilin, 2011), see Figure 6. Superheating of 10°C at the evaporator outlet in HP mode (5°C in ORC mode) and a subcooling of 5°C at the condenser exit are imposed in the model.
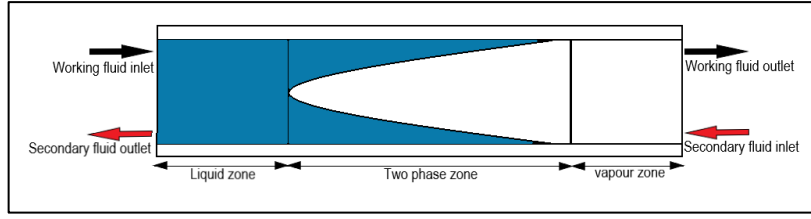
Figure 6: Heat exchanger model (Quoilin, 2011)

The overall heat transfer coefficient for each zone is determined by equation 5:

$$U = \frac{1}{\left(\frac{1}{h_r} + \frac{1}{h_{sf}}\right)} \tag{5}$$

The correlations for boiling (Desideri *et al.*, 2017), condensing (Kwon, Jung and Kang, 2020), and single-phase media (Thonon, 1995) are used to determine the heat transfer coefficients for fluids in each zones. ORC pump was modelled by assuming a constant isentropic efficiency of 50% and the pump power consumption in ORC mode is given by:

$$\dot{W}_{pp} = \frac{\dot{W}_{pp,is}}{\eta_{is,pp}} \tag{6}$$

The COP and cycle efficiency of the system in HP and ORC modes respectively are shown in Equations 7 and 8:

$$COP = \frac{\dot{Q}_{cd,sink}}{\dot{W}_{el,comp}} \tag{7}$$

$$\eta_{ORC} = \frac{(\dot{W}_{el,exp} - \dot{W}_{pp})}{\dot{Q}_{ev,source}} \tag{8}$$

5. RESULTS AND DISCUSSION

5.1. Heat pump configuration

The heat pump model was formed by connecting the scroll compressor, evaporator, and condenser models. The expansion of the working fluid after leaving the condenser was assumed to be isenthalpic. The performance of the reversible system in HP mode was simulated by the varying temperature of the heat sink and keeping the temperature of the heat source constant at a given compressor speed. The compressor set the refrigerant mass flow rate and the HP performance was analysed for different heat source temperatures at different compressor speeds. Figure 7 shows the T-s diagram of the system in HP mode. The mass flow rate varied from 0.035 kg/s at 1400 RPM and 70°C heat source temperature to 0.098 kg/s at 2000 RPM and 100°C heat source temperature. Figure 9 shows the refrigerant mass flow rate at different heat source temperatures at various compressor speeds.
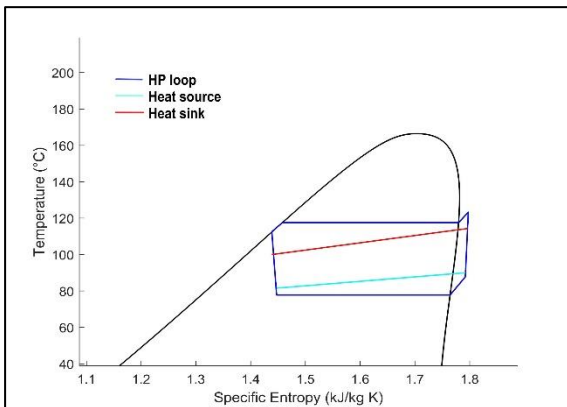
Figure 7: T-S diagram of the system operating in HP mode.
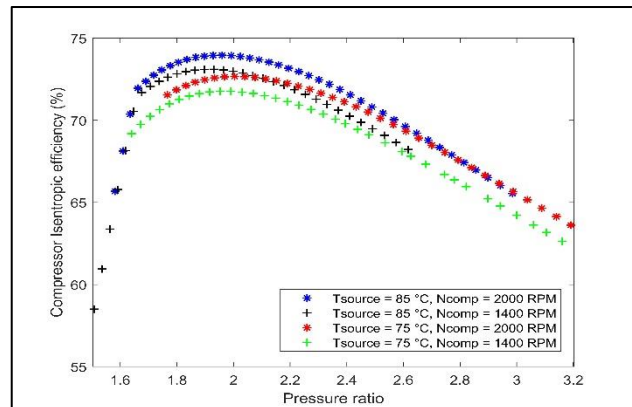
Figure 8: Compressor performance with respect to pressure ratio. The pressure ratio varied by changing heat sink temperature in 60 –100°C range

The performance of the scroll compressor in relation to pressure ratio and heat source temperature is shown in Figure 8 and Figure 9 respectively. A maximum compressor isentropic efficiency of 75.4% was obtained at evaporating and condensing temperatures of 83.2°C and 111°C respectively with compressor speed at 2000 RPM. Lower isentropic

efficiency values at other pressure ratios out of the 1.7 - 2 range could be attributed to under-compression and over-compression losses.

Figure 10 shows the power consumption trend of the scroll compressor at various pressure ratios. The compressor power consumption increased with pressure ratio with values ranging from 576W to 2.3kW. Power consumption was almost steady at lower pressure ratio values (1.5 – 1.7) and increased linearly at higher pressure ratios. The system performance in HP mode with respect to temperature lift is presented in Figure 11.

For a temperature lift of 35K (evaporating temperature =71.7°C & M_r = 0.073 kg/s) and 50K (evaporating temperature = 63.5°C & M_r = 0.039 kg/s) the COP values were 6.59 and 3.88 respectively.
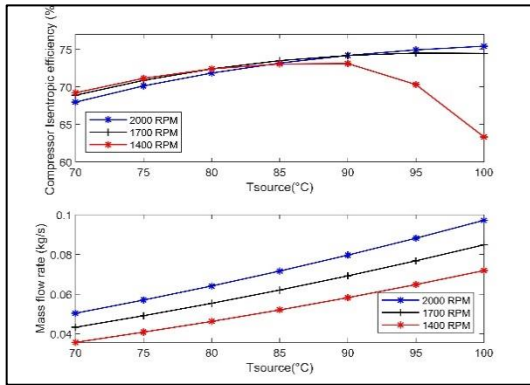
Figure 9: Compressor isentropic efficiency and refrigerant mass flow rate at various heat source temperatures with heat sink temperature at 80°C
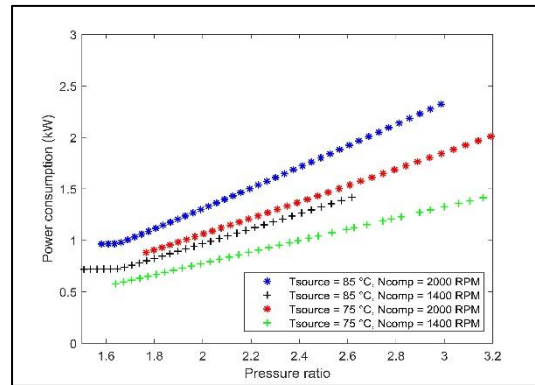
Figure 10: Power consumption of the system at various pressure ratios
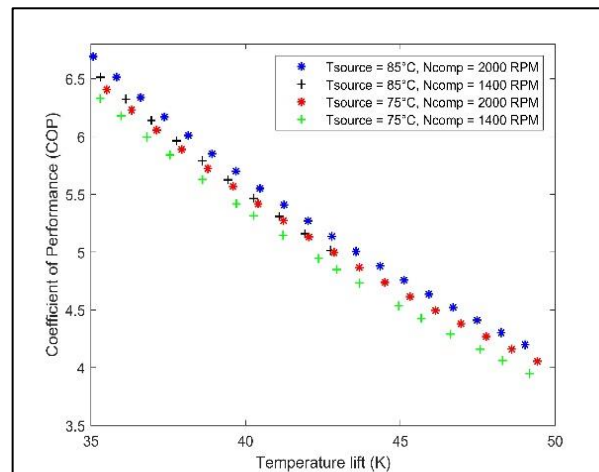
Figure 11: COP vs Temperature lift

5.2. Organic Rankine cycle configuration

The scroll expander, condenser, pump, and evaporator models were interconnected to analyse the system performance in ORC configuration. In ORC modelling, the system performance was simulated by varying the temperature of the heat source and keeping the temperature of the heat sink constant at a given pump speed. The ORC pump set the refrigerant mass flow rate with values varying from 0.037 kg/s to 0.065 kg/s for pump speeds from 400 to 700 RPM. The T-s diagram of the system performance in ORC mode is shown in Figure 12.
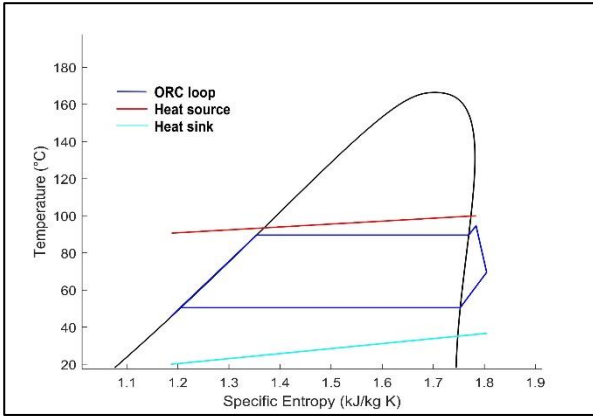
Figure 12: T-s diagram of the ORC system
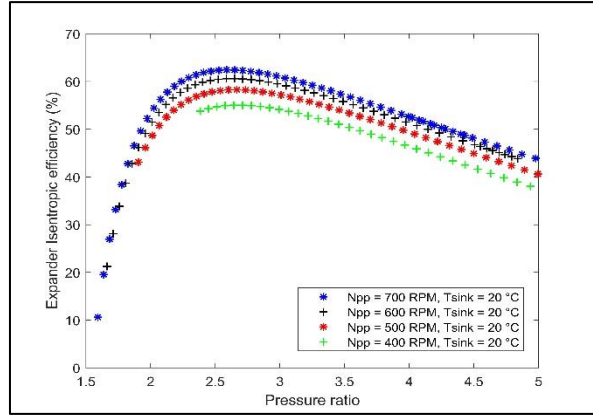
Figure 13: Expander isentropic efficiency vs pressure ratio

The expander performance with respect to the pressure ratio is shown in Figure 13. The isentropic efficiency of the expander reached higher values in the pressure ratio range of 2.3 - 2.7 with the highest achieved efficiency value at 62.4% (r_p = 2.6, evaporating temperature = 88°C, N_{pump} = 700 RPM). Lower isentropic efficiency values at smaller pressure ratios could be due to over-expansion losses. At pressure ratio values higher than 2.7, the efficiency curve showed a decreasing trend and can be attributed to under-expansion losses.
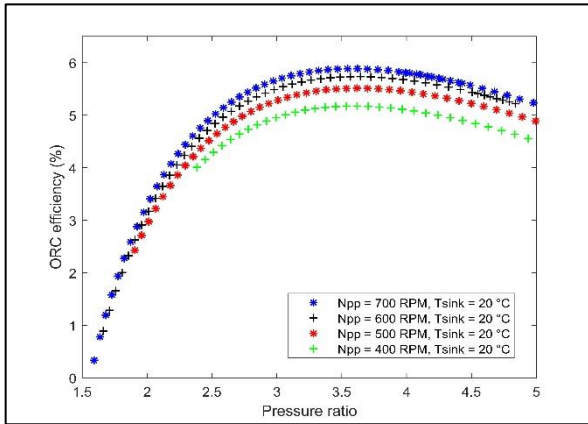
Figure 14: Cycle thermal efficiency vs pressure ratio
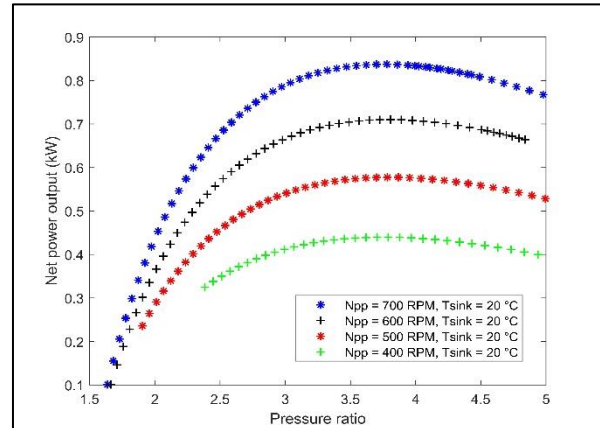
Figure 15: Net Power generation vs pressure ratio
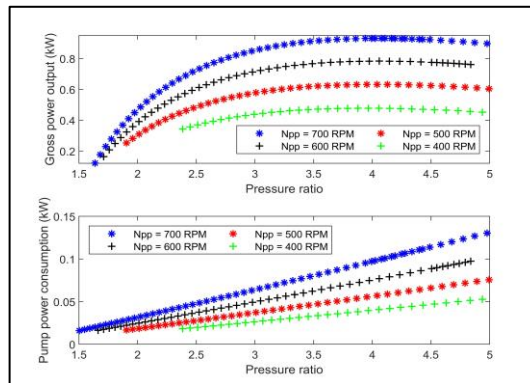
Figure 16: Gross power output and pump power consumption vs pressure ratio

The cycle thermal efficiency increased with pressure ratio and reached a maximum value of 5.9% (evaporating temperature = 102°C, M_r = 0.064 kg/s) with better efficiency values achieved in the pressure ratio range of 2.9 – 3.6 (Figure 14). At pressure ratio values higher than the 2.9 – 3.6 range, the cycle thermal efficiency showed a decreasing trend. The net power output of the system as shown in Figure 15, lay in the 100 – 833W range. The gross power output from the scroll expander ranged from 0.12kW to 0.931 kW with the ORC pump power consumption varying between 20 W to 133 W (Figure 16).

6. CONCLUSION

The study presented the design and modelling aspects of a reversible heat pump – organic Rankine cycle for recovering industrial waste heat lying in lower temperature band (<150°C). R1233zd(E) was selected as the

refrigerant for both operating modes (HP and ORC) considering its near zero ODP, low GWP values, and performance comparison to R245fa in HP and ORC systems. An automotive scroll compressor (Sanden TRSA09) was chosen as the volumetric machine to be used as compressor and expander in HP and ORC modes respectively. Modelling of individual components and system performance in HP and ORC modes were discussed. In HP mode, a maximum compressor isentropic efficiency of 75.4% was achieved with a maximum power consumption of 2.3 kW. The COP of the HP mode lies in the 3.88 – 6.5 range for temperature lifts varying from 35 to 50K (heat source temperature: 75 - 85°C). In ORC mode, the cycle thermal efficiency reached a maximum of 5.9%. A maximum net power generation of 833W was obtained. Expander isentropic efficiency values up to 62.4% were achieved under the mentioned operating conditions.

6.1. Future work

A testbed for the experimental study of reversible HP-ORC system is under construction at Ulster University's Centre for Sustainable Technologies laboratory facility.

7. ACKNOWLEDGEMENT

8. REFERENCES

Bobbo, S., Nicola, G. Di, Zilio, C., Brown, J.S. and Fedele, L. (2018) 'Low GWP halocarbon refrigerants: A review of thermophysical properties', *International Journal of Refrigeration*, 90, pp. 181–201. Available at: https://doi.org/10.1016/j.ijrefrig.2018.03.027.

Desideri, A. *et al.* (2017) 'An experimental analysis of flow boiling and pressure drop in a brazed plate heat exchanger for organic Rankine cycle power systems', *International Journal of Heat and Mass Transfer*, 113, pp. 6–21. Available at: https://doi.org/10.1016/j.ijheatmasstransfer.2017.05.063.

Dumont, O. (2017) *Investigation of a heat pump reversible into an organic Rankine cycle and its application in the building sector.* Available at: https://doi.org/10.13140/RG.2.2.19499.13604.

Dumont, O., Parthoens, A., Dickes, R. and Lemort, V. (2018) 'Experimental investigation and optimal performance assessment of four volumetric expanders (scroll, screw, piston and roots) tested in a small-scale organic Rankine cycle system', *Energy*, 165, pp. 1119–1127. Available at: https://doi.org/10.1016/j.energy.2018.06.182.

Dumont, O., Quoilin, S. and Lemort, V. (2015) 'Experimental investigation of a reversible heat pump/organic Rankine cycle unit designed to be coupled with a passive house to get a Net Zero Energy Building', *International Journal of Refrigeration*, 54, pp. 190–203. Available at: https://doi.org/10.1016/j.ijrefrig.2015.03.008.

Eppinger, B., Steger, D., Regensburger, C., Karl, J., Schlücker, E. and Will, S. (2021) 'Carnot battery : Simulation and design of a reversible heat pump-organic Rankine cycle pilot plant', *Applied Energy*, 288(February), p. 116650. Available at: https://doi.org/10.1016/j.apenergy.2021.116650.

European Commission (2018) 'A Clean Planet for all - A European long-term strategic vision for a prosperous, modern, competitive and climate neutral economy', *Com(2018) 773.* [Preprint].

European Commission (2020) 'Stepping up Europe's 2030 climate ambition Investing in a climate-neutral future for the benefit of our people', *Journal of Chemical Information and Modeling*, 53(9), pp. 1689–1699.

Forman, C., Muritala, I.K., Pardemann, R. and Meyer, B. (2016) 'Estimating the global waste heat potential', *Renewable and Sustainable Energy Reviews*, 57, pp. 1568–1579. Available at: https://doi.org/10.1016/j.rser.2015.12.192.

Frate, G.F., Ferrari, L. and Desideri, U. (2019) 'Analysis of suitability ranges of high temperature heat pump working fluids', *Applied Thermal Engineering*, 150(August 2018), pp. 628–640. Available at: https://doi.org/10.1016/j.applthermaleng.2019.01.034.

Imran, M., Usman, M., Park, B.S. and Lee, D.H. (2016) 'Volumetric expanders for low grade heat and waste heat recovery applications', *Renewable and Sustainable Energy Reviews*, 57, pp. 1090–1109. Available at: https://doi.org/10.1016/j.rser.2015.12.139.

'IPCC: Climate Change 2021: The Physical Science Basis' (2021) *Cambridge University Press. In Press.*, p. 42. Available at: https://www.ipcc.ch/report/ar6/wg1/.

IPCC (2018) *SPM - An IPCC Special Report on the impacts of global warming of 1.5°C, Intergovernmental Panel on Climate Change.* Available at: https://doi.org/10.1002/9780470996621.ch50.

Kwon, O.J., Jung, J.H. and Kang, Y.T. (2020) 'Development of experimental Nusselt number and friction factor correlations for condensation of R-1233zd(E) in plate heat exchangers', *International Journal of Heat and Mass Transfer*, 158, p. 120008. Available at: https://doi.org/10.1016/j.ijheatmasstransfer.2020.120008.

Lemort, V. (2008) Contribution to the characterization of scroll machines in compressor and expander modes.

Mateu-Royo, C., Mota-Babiloni, A., Navarro-Esbrí, J., Peris, B., Molés, F. and Amat-Albuixech, M. (2019) 'Multi-objective optimization of a novel reversible High-Temperature Heat Pump-Organic Rankine Cycle (HTHP-ORC) for industrial low-grade waste heat recovery', *Energy Conversion and Management*. Available at: https://doi.org/10.1016/j.enconman.2019.111908.

Mateu-Royo, C., Navarro-Esbrí, J., Mota-Babiloni, A., Amat-Albuixech, M. and Molés, F. (2019) 'Thermodynamic analysis of low GWP alternatives to HFC-245fa in high-temperature heat pumps: HCFO-1224yd(Z), HCFO-1233zd(E) and HFO-1336mzz(Z)', *Applied Thermal Engineering*, 152(January), pp. 762–777. Available at: https://doi.org/10.1016/j.applthermaleng.2019.02.047.

McKenna, R.C. and Norman, J.B. (2010) 'Spatial modelling of industrial heat loads and recovery potentials in the UK', *Energy Policy*, 38(10), pp. 5878–5891. Available at: https://doi.org/10.1016/j.enpol.2010.05.042.

Papapetrou, M., Kosmadakis, G., Cipollina, A., La Commare, U. and Micale, G. (2018) 'Industrial waste heat: Estimation of the technically available resource in the EU per industrial sector, temperature level and country', *Applied Thermal Engineering*, 138(July 2017), pp. 207–216. Available at: https://doi.org/10.1016/j.applthermaleng.2018.04.043.

'Paris Agreement on Climate Change' (2015) *Reducing Greenhouse Gas Emissions and Improving Air Quality*, pp. 11–22. Available at: https://doi.org/10.1201/9781351116589-2.

Quoilin, S. (2011) *Sustainable Energy Conversion Through the Use of Organic Rankine Cycles for Waste Heat Recovery and Solar Applications.*

Schimpf, S. and Span, R. (2015) 'Simulation of a solar assisted combined heat pump - Organic rankine cycle system', *Energy Conversion and Management*, 102, pp. 151–160. Available at: https://doi.org/10.1016/j.enconman.2015.01.083.

Staub, S. *et al.* (2018) 'Reversible heat pump-organic rankine cycle systems for the storage of renewable electricity', *Energies*, 11(6). Available at: https://doi.org/10.3390/en11061352.

Thonon, B. (1995) 'Recent research and developments in plate heat exchangers', (September), p. 1995.

Twomey, B., Jacobs, P.A. and Gurgenci, H. (2013) 'Dynamic performance estimation of small-scale solar cogeneration with an organic Rankine cycle using a scroll expander', *Applied Thermal Engineering*, 51(1–2), pp. 1307–1316. Available at: https://doi.org/10.1016/j.applthermaleng.2012.06.054.

United Nations (2016) 'Report of the Twenty-Eighth Meeting of the Parties to the Montreal Protocol on Substances that Deplete the Ozone Layer', *Twenty-Eighth Meeting of the Parties to the Montreal Protocol*, p. 72.

Wu, Z., Zhang, Y., He, Z., Yu, X., Ma, X. and Sheng, Y. (2019) 'Performance investigation of a bi-functional integration system for power and heat supply', *Applied Thermal Engineering*, 148(October 2018), pp. 714–721. Available at: https://doi.org/10.1016/j.applthermaleng.2018.11.102.

Yang, J., Sun, Z., Yu, B. and Chen, J. (2018) 'Experimental comparison and optimization guidance of R1233zd(E) as a drop-in replacement to R245fa for organic Rankine cycle application', *Applied Thermal Engineering*, 141(March), pp. 10–19. Available at: https://doi.org/10.1016/j.applthermaleng.2018.05.105.

#60: Sustainable eco-tourism at Gulf of Mannar biodiversity

P SHARAN, Kiruthiga KANDASAMY

School of Planning Architecture and Design Excellence, Hindustan Institute of Technology and Science, India,
sharan02021997@gmail.com
kiruthigak@hindustanuniv.ac.in

Abstract: Oceanic areas are the intermediate areas between land and sea characterised by high biodiversity. Tourists can experience unspoiled nature and sceneries, high-quality environmental products, and services (clean air and water), a healthy community with a low crime rate, and a vibrant, taste of local culture and customs in this area. Eco-tourism is developing and experiencing environmental, cultural understanding and conservation. It can generate income, employment, and contributions to business ventures. The main objective of ecotourism is to create experiences that are equally beneficial to all, not just tourism and stakeholders. At the same time, ecotourism helps to preserve their communities and culture. The study's goal is to create suggestions for long-term ecotourism growth. This might be done from observations of the assorted developments in coastal areas with eco-tourism concepts that are done round the world. The main objectives were to identify the present issues on this area with comparison of eco-tourism parameters and analyse eco-tourism development opportunities in this area. The study spotlights sustainable eco-tourism; it also reveals the link between biodiversity and the local people. The study is limited to a particular part of the Gulf of Mannar biodiversity, focusing more on nature tourism with less priority to adventure tourism and culture tourism.

Keywords: sustainable ecotourism; coastal ecotourism; local community; economic sustainability

1. INTRODUCTION

Ecotourism is a form of tourism that focuses on protecting the environment by supporting the well-being of residents. Ecotourism also provides a responsible travel experience to natural regions without compromising its authenticity, while also conserving the environment and increasing the well-being of local people. Ecotourism has been praised as a viable alternative to mass tourism that promotes community empowerment, environmental conservation, and long-term development (Wondirad *et al.*, 2020). The development of ecotourism provides a unique opportunity to develop strong and magnetic coastal tourism areas in south India, also providing an opportunity to improve the local people's livelihood.

Between longitudes 78008'E and 79030'E and latitudes 8035'N to 9025'N, the Gulf of Mannar Biosphere, the first in South and Southeast Asia, spans southward from Rameswaram to Kanyakumari in Tamil Nadu, India. It covers a total area of 10,500 km^2. Known for its very fertile pearl banks and other religious significance, the Gulf of Mannar region has been a significant place since the 2nd Century AD. Even before UNESCO launched the Man and Biosphere (MAB) programme in 1971, the Gulf of Mannar drew the attention of conservationists. The Gulf of Mannar was designated as a Marine National Park in 1986 due to its remarkable biodiversity of 3,600 species of flora and fauna.

Though the Gulf of Mannar is a place that pulls tourists, other coastal tourist places in the southern part of India, especially in Tamil Nadu have yet to be identified by many. As the biodiversity in the area is very rich, tourism developments must provide measures to protect it (Mallick *et al.*, 2020) so the area's developmental plan must be sustainable and eco-friendly or, in other words, a plan for Ecotourism.

The goal to create ecologically sustainable tourism in Pamban town (Gulf of Mannar marine biodiversity) was taken forward through a stakeholder study on enjoying natural environments that enhance environmental and socio-cultural awareness, appreciation, and preservation, the major. The objectives were to analyse eco-tourism development opportunities in the Pamban area (Gulf of Mannar biosphere) through the stakeholder survey, then to formulate planning, design strategies and guidelines for recreational and cultural activities along the coastal line that applies to the town.

2. LITERATURE

As per the World Travel and Tourism Organization of the United Nations, "tourism comprises the activities of persons travelling to and staying in places outside their usual environment for not more than one consecutive year for leisure, business and other purposes." When it comes to international tourism, this is a crucial economic sector, contributing directly to GDP and employing locals. Furthermore, tourism contributes to the growth and development of a community's stability, wealth, and national and international relationships, all of which contribute to the achievement of sustainable development. In the worldwide tourism business, sustainable tourism development is becoming increasingly important. 2017 was declared as the Global Year of Sustainable Development in Tourism. Essentially, sustainable tourism is described as a nature-based tourist movement that contributes significantly to the destination's ecology, culture, & economic well-being (Clifton and Angela, 2012). As a result, ecotourism is used as an economic and business growth tool to ensure the destination's long-term viability, as well as environmental protection. Current common definitions of ecotourism emphasise on the preservation of the natural environment.

Many researchers have studied this sector and contributed to environmental protection and the growth of nature-based tourism. The ecotourism concept has been created to bridge tourism and natural heritage. The distinction in the base of ecotourism is that it is dependent on individual nature contemplation and activity investigation (Nurhayati *et al.*, 2019). For instance, coastal tourism development constantly promotes certain tourist recreation areas. However, few scholars have questioned sustainability and green tourism. They claim that tourism expansion often affects land use, therefore, sustainability is now a fantasy. Furthermore, the ecotourism concept has already been impacted by a variety of cultural and political factors, including the introduction of strategic planning by numerous local governments to strengthen the ecotourism framework. Ecotourism, on the other hand, is a broad concept with sustainable ecotourism as a kind of acceptance based on development of tourism and GDP creation (Mallick *et al.*, 2020).

The goal of ecotourism is to protect the environment, ensure the well-being of locals, and educate visitors (The international Ecotourism Society, 2018). Human involvement has shifted the nature of ecotourism and severely harmed the environment at times. As a result, the destination should have been a threat in and of itself, destroying the entire system. As a result, the World Ecotourism Summit (2002) established 5 unique criteria: "nature-based product", "minimum effect management", "environmental education", "benefit to conservation", and "participation". Ethics and sustainability have taken the place of 'minimal impact management'.

With its diversified landscape, India offers a wide range of tourism destinations that not only relaxes but also revitalises visitors (Cabral and Rajib, 2020). There are numerous ways to get a true sense of Mother Nature as India is home to a diverse range of flora and fauna. India's surroundings have a plethora of uncommon and endangered animals: the Himalayan Territory, Kerala, northeast India, the Andaman & Nicobar Islands, and the Lakshadweep

Islands are just a few of the places where you can marvel at Mother Nature's immeasurable abundance. Thenmala is the country's first planned eco-tourism resort, with facilities tailored to eco-tourists and nature lovers, it was in Kerala.

3. METHODOLOGY
3.1. Site study

Pamban is a settlement in the Rameswaram taluk of Tamil Nadu's Ramanathapuram district. Figure 1 shows Pamban town area and the Kuntukal coastal area is delineated as the study area. The site was selected based on the preliminary study of the site, issues, and problems of the nature related to the deportation of natural resources mainly the biodiversity of the region, and inferences from the Literature and case studies.
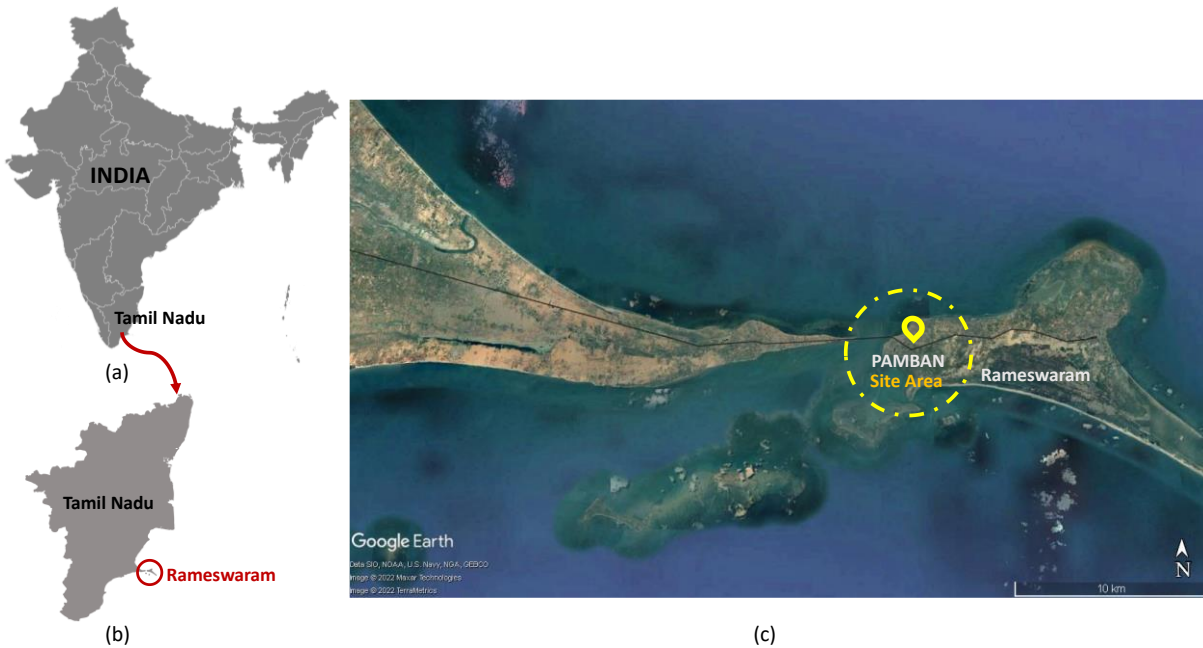
Figure 1: (a) India map showing the location of Tamil Nadu; (b) Tamil Nadu Map showing the location of Rameswaram; and (c) Map showing the location of Pamban (Site Area) at Rameswaram

3.2. Site Study

Data collection consisted of primary and secondary data. A questionnaire was prepared and both quantitative and qualitative methods were used for data collection (Mohd Noh A. N., 2020). Interviews concerning the issues and ongoing planning ideas of the river were conducted with government officials during the physical survey.

3.3. Sampling

A random sampling technique was used. A total of 16 questions and 383 interviews were conducted. The following formula used was for educational purposes (z as the confidence level, e as the margin of error, p as the response distribution, N as the population size):

Equation 1
$$n' = \frac{n}{1 + \frac{z^2 \times \hat{p}(1-\hat{p})}{\varepsilon^2 N}}$$

3.4. Data collection and analysis

The analysis was carried out using the questionnaire survey on the site and the following was recorded as the responses from the respondents.

General information

Using the survey analysis of 303 respondents, Figure 2 indicates that 58% were male and 41% were female with age groups ranging from 17 to 65 and above. It was observed that the majority of the people roaming near the sea shore were aged between 18 and 35 at 66% and the second highest was 29% of people aged between 36 and 64. Figure 2 also indicates that those aged below 17 and above 65 were least likely to visit the river with 1% and 4% respectively in the survey. Out of 303 respondents, men were observed to be more likely to participate than women.

Participants Details

Age Group

■ Male ■ Female ■ Transgender

■ Below 17 ■ 18 to 35 ■ 36 to 64 ■ Above 65
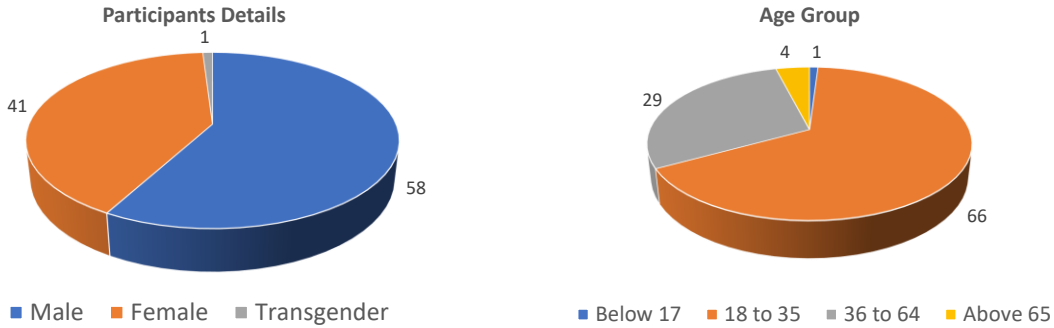
Figure 2: Participants genders and age group

The residing factor

The residing factor analysis showed that most people visiting the seashore were native people of Pamban with the rest being non-natives who had migrated for job opportunities and business purposes. From the analysis, Figure 3 shows that 22% of people had resided locally for 40 years or more; 36% of people had been resident for 20 to 40 years; 37% for 11 to 20 years, and 5% had been resident for less than ten years.

Occupation and annual income

From the survey analysis of 303, 58% of respondents were 'daily wagers' and 38% undertook private jobs. 'Daily wagers' occupations include fishing, making dry fish, collecting seaweed and shells etc. Annual income of this particular group of people was very low (below 3 lakh). Overall 77% of the respondent's annual income was below 3 lakh; 17% was from 3 to 5 lakh, with the remaining 6% being above 5lakh (see Figure 3).

The Residing Factor

Annual Income

■ Residing Factor ■ 1 to 10 ■ 10 to 20 ■ 20 to 30 ■ above 40

■ Above 5 lakh ■ Upto 5 Lakh ■ Below 3 Lakh
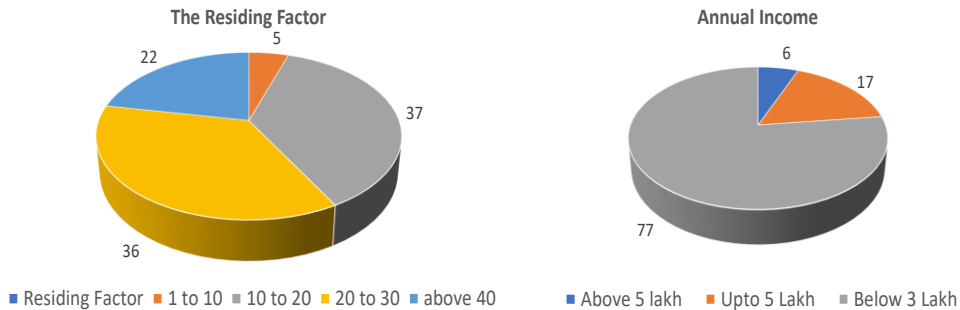
Figure 3: The residing factor and their annual income

Current condition and development of the town

Almost 60% of the population strongly agreed that they would benefit from the development of sustainable eco-tourism. People also felt that Pamban has more potential to develop marine-based tourism and such development would in turn benefit the livelihood of local people. As seen in Figure 4, 70% of the population were satisfied with the current town condition.

Current Condition and Town Development

■ Very satisfied ■ Satisfied ■ Neutral ■ Unsatisfied
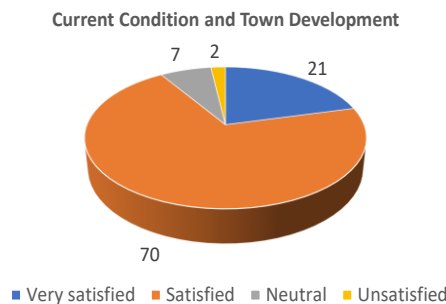
Figure 4: Current condition and town development

Mode of transport & access and linkage

From the survey analysis, the majority of people used bikes daily with the rest using autos and local buses for their transportation. As Pamban is a small town, there are no proper public transport facilities and the majority-used transport were bike, auto and small vans that were used for business purposes. As a contrast, the main type of transportation used by tourists to reach the island was by bus (see Figure 5). Tourists visiting Rameshwaram and surrounding islands generally also visit Pamban but those who visit only the Pamban Island are comparitively few. So for ease of transportation, people mostly prefer cars. As Rameshwaram is one of the famous tourist destination, road connectivity and linkages are good (Figure 5).
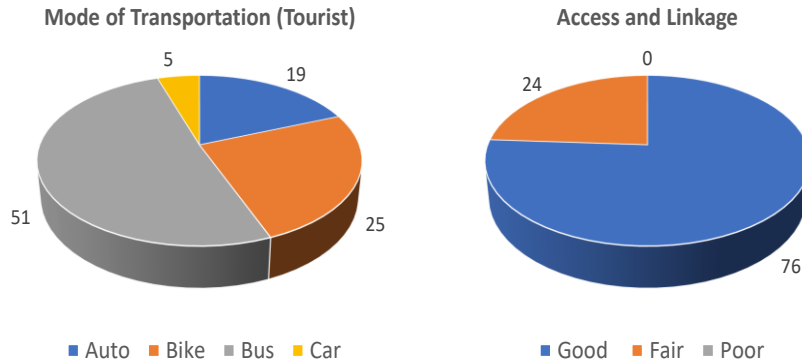
Figure 5: Mode of transport; access and linkage

Frequency of visit

People generally visit Rameshwaram for the following three reasons:

  i.   To witnessing the magnificent Ramanathaswamy temple
  ii. To perform last rites for their ancestors
  iii. Tourism

For Hindus, Rameswaram is one of the holiest destinations and the bulk of visitors make temples their primary destination.The Dhanushkodi Beach is one of the major attractions on this island. The white sand beach is mostly deserted; as a result, tourists enjoy a peaceful walk on the beach without being disturbed by a large crowd of beachgoers. Figure 6 shows the frequency of people visiting Ramaeshwaran. Rameshwaram is a paradise for food lovers. The Rameshwaram platter is an amalgamation of seafood and typical south Indian food. On a visit to Pamban Island or Rameshwaram, one will get to taste exotic fish and a variety of south Indian foods that are prepared with indigenously-found herbs and spices.
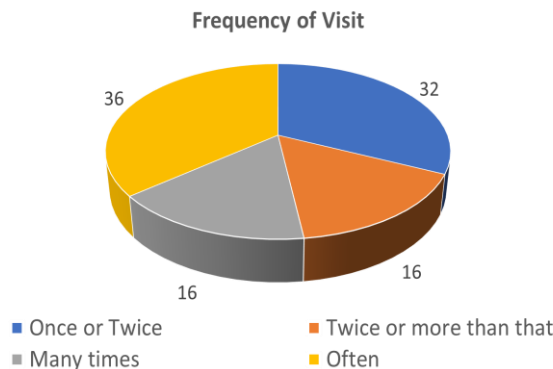
Figure 6: Frequency of visit

Pollution and safety conditions

The major type of pollution found is land pollution (see Figure 7). People throw garbage along the seashore. In the Gulf of Mannar, garbage from fishing ports and processing plants mix with saltwater in the Pamban hamlet. The drainage mixes with the sea water and garbage thrown into the sea leads to water pollution. Regarding the safety conditions, people feel that the area is safe (Figure 7).
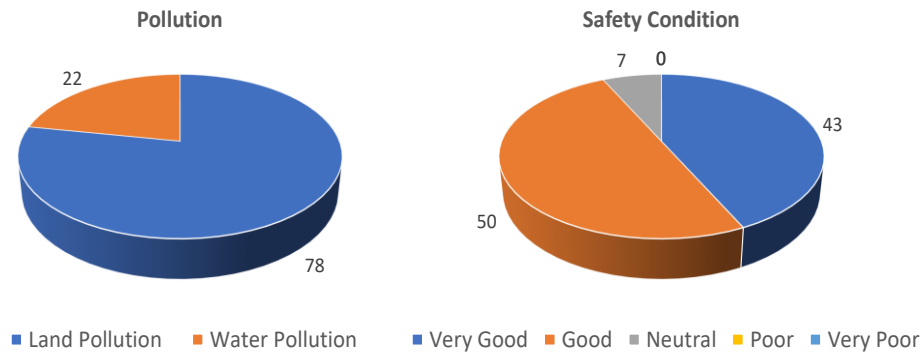
Figure 7: Pollution and safety condition

Tourism-based activities

According to the survey, even though Pamban Island has more places to visit, the only two known places explored by the tourists are Pamban Bridge and Kuntukal beach. Respondents suggested that providing commercial developments such as seafood market, themed restaurants would benefit the tourist and also create various employment opportunities for the local people (see Figure 8). Also, there was no specific place for tourist accommodation in Pamban which was a major criterion that affected the tourism experience of the area. The primary activities that tourists expect in Pamban were boating and water sports. Developments made with regard to all these aspects would result in increased footfall and improved tourism experience in Pamban.
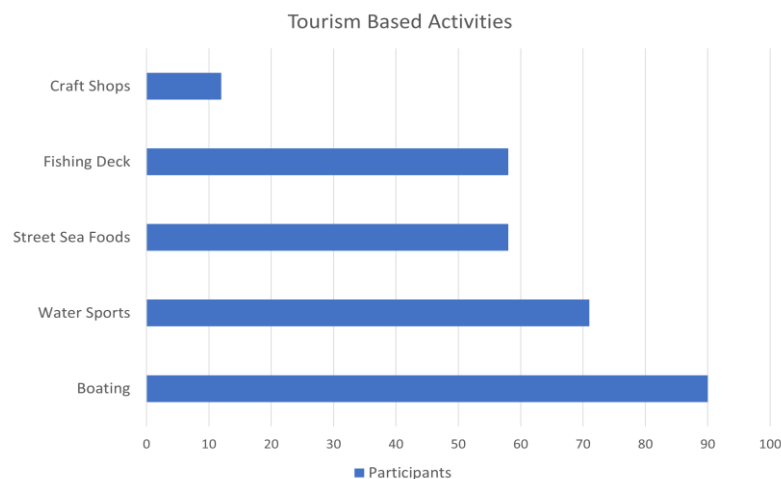
Figure 8: Tourism-based activities

4. RESULTS AND DISCUSSION

Out of 200 respondents, men were observed to be more responsive than women. People of all age groups visited the seashore. The residing factor analysis showed that most people visiting the beach area were natives of Pamban. Tourists usually parked their vehicles in Pamban Bridge for site-seeing which caused traffic and potential accidents. The main source of pollution in Pamban was mainly created by tourists. Though Pamban Island has many places to explore, most tourists visited only Pamban Bridge and Kuntukal Beach. People frequently visit Rameshwaram for the following three reasons (i) For witnessing the magnificent Ramanathaswamy temple (ii) To perform last rites (iii) Tourism. A variety of activities were carried out on the seashore by respondents of all age groups. The uses and activity analysis show the seashore was dotted with a variety of events which makes the Pamban coast a busy place.

From the research, 96% of the respondents earnt income from sea products (fishing, sale of craft materials etc.). This 96% could be divided into 38% doing private business and 58% engaged in daily wage works. The annual income of 77% of respondents' households were below 3 lakhs. The respondents quoted the use of 2-wheelers and auto rickshaws as the major mode of transport. The use of load-auto and load-vans were common for business-related trips. The respondents suggested the need for themed restaurants and eco-friendly accommodation to increase the commercial activities in the area. 36% of the tourist population visited the area frequently for pleasure trips and leisure; 32% of the tourists visited for religious purposes and they visited the area once or twice yearly. The intrusion of sewage water into the sea was witnessed in a number of places, which is a serious issue to be addressed as it impacts the biodiversity of the area. The tourist population also suggested themed restaurants, eco-friendly accommodations, and special markets for sea foods to increase the pull-factor to the area.

5. CONCLUSION

The findings revealed from the survey were that there was a minimal relationship existing between memoir diversity and its original community. Further analysis of this study determined more reasons affecting the interrelation between eco-tourism and its original community: limited or absent programs, guidelines, and regulations; lack of originality in the planning approach and unbridled development; hygienic condition of the biodiversity due to pollution; lack of collaboration and integration among colourful authorities; frequent flooding and performing dikes; lack of awareness, limited vision and personal power over land in foundation areas (Mohd Noh A. N., 2020). This study brings forth intimidating situations and provides recommendations giving attention to the critical problems with the findings from this study. The overwhelmed nature can be brought back from the brink with the creation of infrastructural and recreational installations, making the area more habitable in terms of environmental enhancement and inclusive development whilst saving its character. Ecotourism aims to promote and protect the environment, and both major and small-scale attractions contribute significantly to the local economy. Within the current condition, where there's a requirement to preserve and protect the natural resources, ecotourism development can lead to environmental and native community improvement.

5.1. Recommendations

As a result, to take care of and to create a sustainable ecotourism development, the following recommendations are made to ensure that tourism development is successful. For various reasons, sustainability is critical, including clean air, natural resources, and a nontoxic environment are all things we wish for in our own healthy communities. The most important aspect of research activities is that it is described as the systematic and concentrated observation and assessment of current changes in biodiversity in all of its manifestations (genes, taxa, structures, functions, ecosystems). Raising public awareness and understanding of biodiversity's value and importance, as well as increasing public engagement in its protection and sustainable usage, might make the notice programme mandatory. Marine biodiversity or the diversity of life found in the oceans and seas, could be a vital component of the three pillars of sustainable development — economic, social, and environmental — that supports and provides services that support humanity's health, well-being, and development. Sustainable fishing can be promoted in the following ways: it must be properly managed, being carried out at a level that will allow future generation to continue while also ensuring a productive and healthy fish population, so that other species and habitats in the ecosystem also stay healthy. MSC (Marine Stewardship Council) recognized fisheries must comply with applicable legislation and be adaptable to changing environmental conditions. Artisanal fishing refers to small-scale, low-capital, low-tech fishing activities carried out by individual fishing households. Several of these homes are owned by ethnic communities from the coast or islands. Commercial and subsistence fishing could be carried out in this way. Artisanal fishing differs from modern large-scale commercial fishing in that it is usually less wasteful and less demanding on fish population.

6. REFERENCES

Cabral, Clement, and Rajib Lochan Dhar. "Ecotourism research in India: From an integrative literature review to a future research framework." *Journal of Ecotourism* 19.1 (2020): 23-49.

Clifton, Julian, and Angela Benson. "Planning for sustainable ecotourism: The case for research ecotourism in developing country destinations." *Journal of sustainable tourism* 14.3 (2012): 238-254.

Mallick, Suraj Kumar, Somnath Rudra, and Riya Samanta. "Sustainable ecotourism development using SWOT and QSPM approach: A study on Rameswaram, Tamil Nadu." *International Journal of Geoheritage and Parks* 8.3 (2020): 185-193.

Mohd Noh, A. N., *et al.* "Sustainable Community Based Ecotourism Developement." *PalArch's Journal of Archaeology of Egypt/Egyptology* 17.9 (2020): 5049-5061.

Nurhayati, Atikah, Isah Aisah, and Asep K. Supriatna. "Model Development of A Synergistic Sustainable Marine Ecotourism—A Case Study in Pangandaran Region, West Java Province, Indonesia." *Sustainability* 11.12 (2019): 3418.

The International Ecotourism Society, TIES. (2018). What is Ecotourism?. Retrieved 2018.02.11 from http://www.ecotourism.org/what-is-ecotourism.

United Nation World Tourism Organization (UNWTO), (2017). Sustainable Development. Retrieved from https://www.unwto.org/tourism4development2017

Wondirad, Amare, Denis Tolkach, and Brian King. "Stakeholder collaboration as a major factor for sustainable ecotourism development in developing countries." *Tourism Management* 78 (2020): 104024.

#61: Performance of a solar dryer with storage for drying apples continuously for 24 hours

Ashmore Mawire[1], Masodi Ramokali[1], Molebogeng Mothupi[1], Petros Tegenaw[2], Maarten Vanierschot[2]

[1] North-West University, Material Science, Innovation and Modelling (MaSIM) Research Focus Area, Department of Physics and Electronics, Mmabatho 2745, Mahikeng, South Africa, email:ashmore.mawire@nwu.ac.za
[2] KU Leuven, Department of Mechanical Engineering, Group T Leuven campus, Celestijnenlaan 300, B-3001 Heverlee, email: maarten.vanierschot@kuleuven.be

Abstract: Post-harvest losses can significantly be reduced by drying fruit with solar dryers, thus increasing their shelf life. However, continuous 24-hour operation of solar dryers is not possible due to the lack of thermal energy storage (TES) for operation during non-sunshine periods. Therefore, a solar dryer with latent heat storage for drying apples in a continuous 24-hour cycle was evaluated experimentally in this work. The dryer used DC fans and a flat plate absorber to extract heat from the sun. Twenty aluminium capsules encapsulated with sodium thiosulfate pentahydrate as phase change material (PCM) were used as latent heat storage. The performance of the dryer was evaluated in terms of the temperature profiles and moisture ratios during 24-hour drying cycles with and without latent heat storage. Two average drying chamber airflow velocities of 0.10 m/s (low) and 0.30 m/s (high) were used in the experimental tests. The solar dryer with storage showed lower drying chamber temperatures during the initial solar drying periods compared to the solar dryer without storage due to the heat absorbed by melting of the PCM. On the other hand, the chamber temperatures were higher by up to 10°C after sunset for the solar dryer with storage. For the higher airflow velocity (0.30 m/s), the maximum temperature difference between the storage and the non-storage cases was around 5°C. Slightly lower final moisture ratios (20% min) were obtained with the solar dryer with storage compared to the solar dryer without storage (23% min) during the 24-hour solar drying period with the lower airflow velocity of 0.10 m/s. An increase in the drying chamber airflow velocity reduced the final moisture ratio in the drying chamber for both cases.

1. INTRODUCTION

Food is an essential commodity for human survival in both developed and developing countries. The provision of a sustainable supply of food is a high priority, especially in rural areas of developing regions that are prone to natural disasters such as droughts and floods. To address the issue of sustainable food provision in developing countries, post-harvest processing of crops and fruits can be done to extend their shelf life with the use of food dryers. The cheapest way to dry food in rural communities in developing countries is open sun drying which has disadvantages of non-uniform uncontrolled temperature drying and spoilage due to dust, wind and excessive exposure to solar radiation. Additionally, open sun drying is labour intensive since the food has to be regularly monitored in a large space with long drying periods as the food is prone to insect infestation and it is susceptible to re-absorption of moisture if left on the ground during non-sunshine periods. To tackle the problems associated with open sun drying, different types of indirect solar dryers suitable for the developing world exposed to high solar radiation conditions have been designed, manufactured and evaluated as presented in recent comprehensive reviews (Getahun *et al.*, 2021; Kamarulzaman *et al.*, 2021; Mohana *et al.*, 2020; Udomkun *et al.*, 2020).

As with other solar thermal devices, solar dryers cannot be used effectively with low solar radiation, under cloudy conditions or at night when the sun is not out. To cater for the drawback of solar dryers during non-sunshine periods, thermal energy storage (TES) have been integrated and comprehensively reviewed in the recent papers on solar dryers with TES (Lingayat *et al.*, 2020; Mugi *et al.*, 2022; Nukulwar and Tungikar, 2022; Srinivasan *et al.*, 2021). Other designs of solar dryers with both sensible heat (Andharia *et al.*, 2022; Bhardwaj *et al.*, 2020; Cetina-Quinones *et al.*, 2021) and latent heat storage (Bhardwaj *et al.*, 2021; Chaatouf *et al.*, 2021; Lamrani and Draoui, 2020) have been evaluated recently. Latent heat storage has a higher energy storage density compared to sensible heat storage thus the storage volume can be reduced in dryers where the issue of space is a limiting factor. Drying with TES generally showed better results compared to drying without storage. Continuous 24-hour operation was also possible with solar dryers with storage (Cetina-Quinones *et al.,* 2021; Bhardwaj *et al.*, 2020; Chaatouf *et al.*, 2021) thus enhancing the usefulness at night-time.

The majority of studies on solar dryers with and without thermal storage only considered the thermal profiles with limited temperature measurement locations in the dryer, and a detailed distribution of the temperatures in the different trays of the dryers was not examined. It is essential to know the different thermal profiles in different sections of the drying chamber, which can be useful in the development of strategies to dry different foods in the same drying chamber. Additionally, the air velocity at the inlet of the collector was measured but it is not a true reflection of the airflow velocity throughout the drying chamber due to pressure drop and friction effects as the air passes from the collector to the drying chamber. The effect of the storage during a continuous 24-hour drying cycle has also been rarely investigated. To understand fully the thermal distribution in different levels of a solar dryer, an experimental study of drying apples in continuous 24-hour drying cycles is presented with and without TES. Twenty aluminium phase change material (PCM) capsules encapsulated with sodium thiosulfate pentahydrate above the drying chamber were used as the thermal storage material. This study aims to understand the thermal characteristics inside the drying chamber with and without storage to evaluate the effectiveness of the TES. The thermal profiles at the top, middle and bottom levels (with 2 trays per level) were measured experimentally during 24-hour drying cycles for two different average flow velocities of 0.10 and 0.30 m/s inside the drying chamber. Each drying level had four thermocouples to measure the temperature profiles so that an average drying temperature could be obtained for each level. One central PCM capsule also contained a thermocouple to measure the PCM temperature during the drying tests with storage. The results obtained will be useful in evaluating the effectiveness of the TES on the performance of the solar dryer during continuous 24-hour drying and could be used to validate models for performance optimisation.

2. EXPERIMENTAL METHOD AND PROCEDURE

The isometric and cross-sectional views of the solar dryer used in this study are shown in Figures 1a and 1b, respectively. This solar dryer was a field-scale prototype implementation of the laboratory scale solar food drier used in the study of Tegenaw *et al.* (2021). The solar collector consisted of a flat plate collector with a stainless steel absorber covered with Plexiglas. The length of the collector was 1.740m and the height from the top of the collector to the ground was around 3m. To extract solar radiation incident on the stainless steel absorber plate, six computer CPU cooling DC fans were connected to the inlet to blow air past the absorber, thus heating the drying chamber trays. These fans could be powered directly by a DC power supply or a solar panel with a battery and a charge controller. In the reported experiments, a DC power supply was used to vary the air velocity in the collector. The solar panel mode could not operate continuously for 24-hour due to a thermal switch in the charge controller that shut off the fans after 5 hours of operation. Two DC power supply currents of 0.2A and 0.7A were used which corresponded to average drying chamber air velocities of 0.10 (low) and 0.30 (high) m/s respectively. Two flat K-thermocouples with an accuracy of ± 2°C were placed centrally on the absorber plate to measure the inlet (Tin) and outlet (Tout) temperatures of the collector. Two other flat K- thermocouples were placed on the central axis of the collector to measure the central collector temperature (Tc) and the left-hand side (Tl) collector temperature on the central axis. The heated air from the absorber passed through two honeycomb air diffusers before it entered the dry chamber. These air diffusers were used to make the airflow uniform and improve heat transfer. For the storage case, a row of 20 spherical aluminium PCM capsules (50mm in diameter) was placed on top of the second honeycomb absorber to store thermal energy from the solar collector.
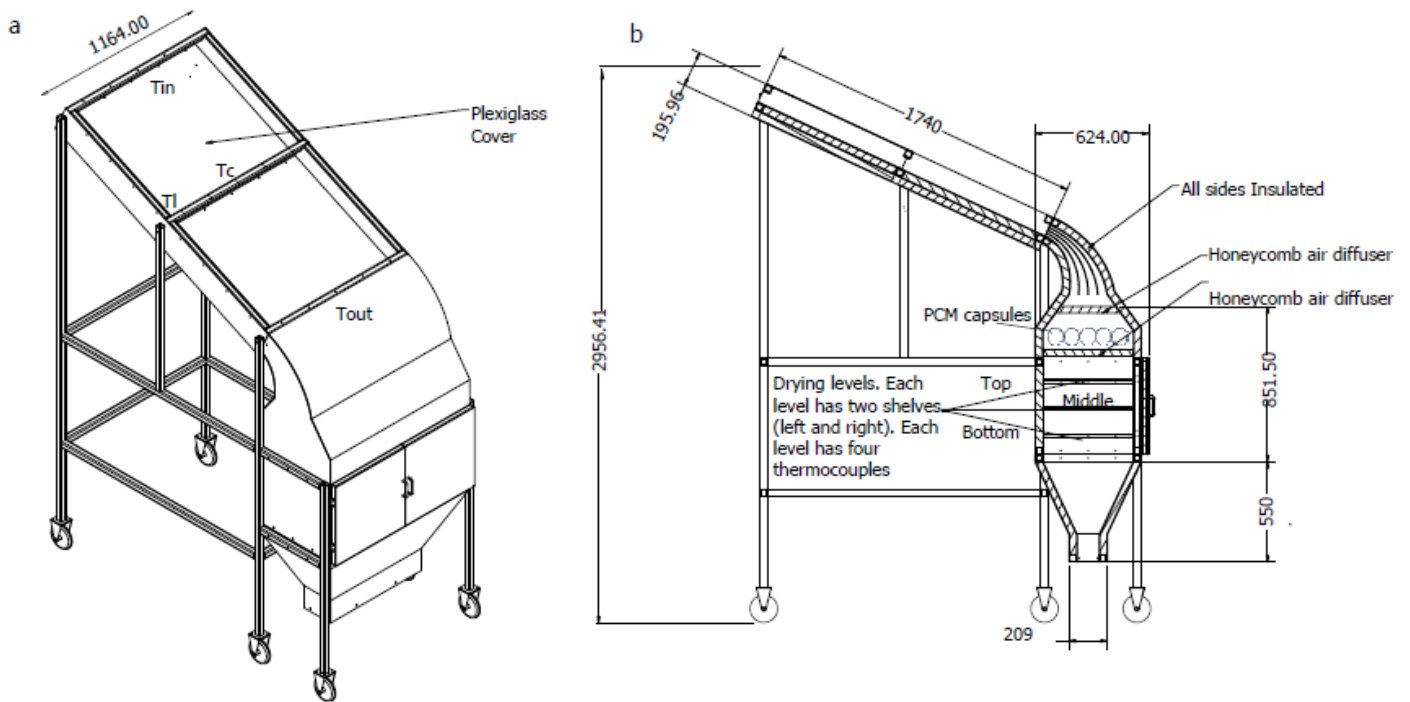
Figure 1: (a) Isometric view and (b) side cross-sectional view of the dryer with PCM capsules showing the dimensions of the different components of the dryer in mm.

Sodium thiosulfate pentahydrate was encapsulated inside the PCM capsules occupying 80% of the volume to cater for thermal expansion after melting. The total mass of PCM in each capsule was around 102g making a total storage mass of around 2.040kg. One central PCM capsule had a K-thermocouple to measure the PCM temperature above the drying chamber during drying tests with storage. Figure 2 shows photographs of an aluminium PCM capsule with a screw cap for pouring PCM and the central aluminium capsule with a thermocouple screw cap for measuring the PCM central temperature. The thermal properties of sodium thiosulfate pentahydrate are presented in Table 1. The PCM had a melting temperature range of 48°C and latent heat of fusion of 200 J/g.
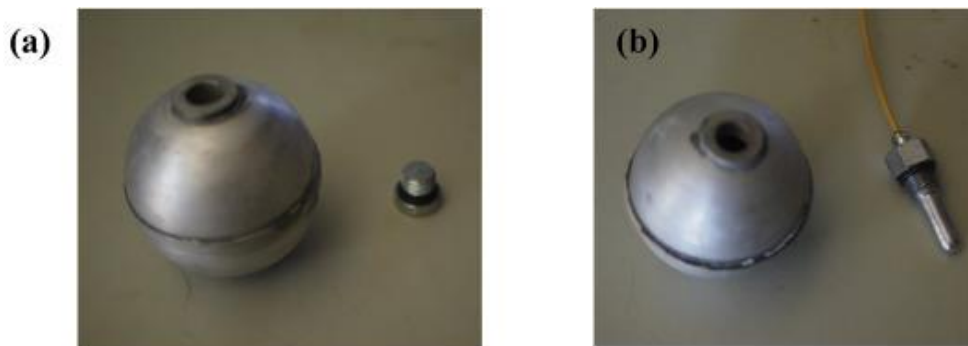
Figure 2: (a) Aluminium PCM capsule with screw cap. (b) Aluminium capsule with thermocouple screw cap.

Table 1: Thermal properties of the sodium thiosulfate pentahydrate (Kenisarin and Mahkamov, 2016)

Melting Temperature (°C)	Latent Heat of Fusion (J/g)	Density (g/cm^3)	Specific Heat Capacity (J/°C	Thermal Conductivity (W/mK)
48	200	1.69-Solid 1.66-Liquid	1.46-Solid 2.38-Liquid	1.153

The drying chamber had three drying levels (top, middle and bottom). Each level had left and right compartments (trays) making a total of six trays inside the dryer. Four K-thermocouples (accuracy ± 2°C) were placed on each level to measure the temperature distribution on the left and right trays of each level. The drying compartment (tray) with and without apples together with the thermocouples are shown in Figure 3. The length and width of each tray were around 51cm and 47cm, respectively. Each tray had a thermocouple placed at the centre and close to the central rear side edge from the door opening. The apples were first treated with lemon juice before drying to limit the growth of microorganisms. Each tray had approximately 35 slices of 5-7 mm thick circular apple slices with a total weight of around 530g. The diameter of the slices ranged from 60-70 mm. The total weight of the apples in the six trays was around 3.18kg.
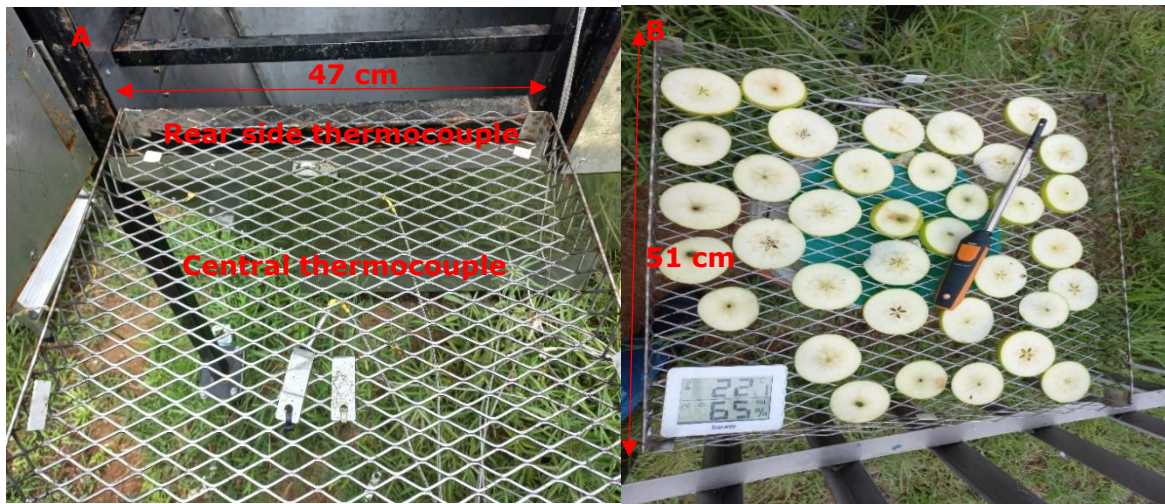
Figure 3: (A) Empty drying tray showing the central and rear side thermocouples and (B) the loaded tray with apples during a drying experiment.

A photograph of the main components of the solar dryer is shown in Figure 4. The airflow velocity inside the chamber and at the inlet was measured with two Testo 450i thermal anemometers with a measuring range of 0-30 m/s, a resolution of 0.01 m/s and accuracy of ± 0.01 m/s for the range of 0-2 m/s. The global solar radiation incident onto the collector was measured with a Kipp and Zonen CMP11 pyranometer with a 95% response time of less than 5s. The wind speed during the experimental tests was measured with a Mastech 625 B anemometer with a range of 0.8-30 m/s, at a resolution and accuracy of 0.01 m/s and ± 2% of the measured value, respectively.
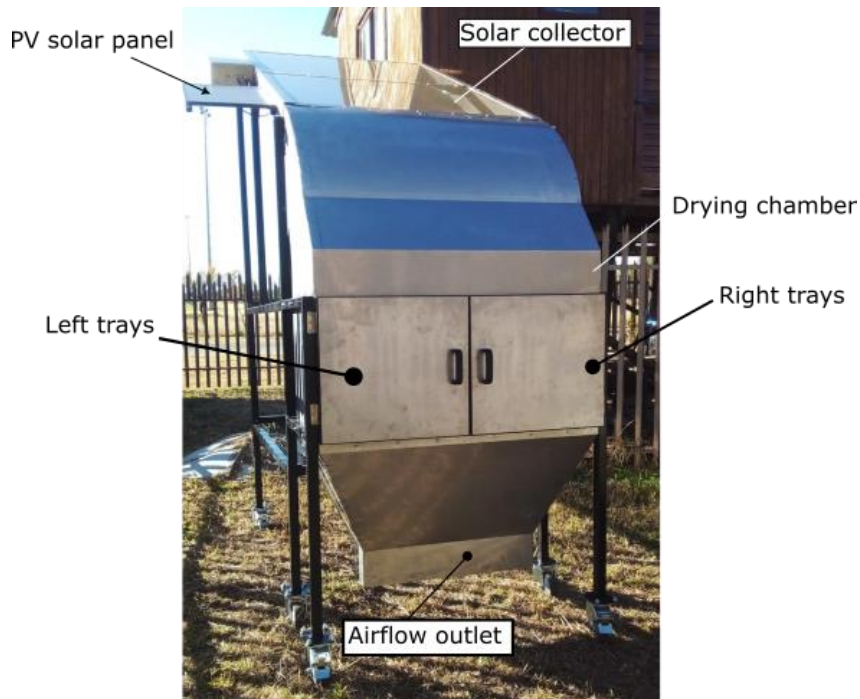
Figure 4: A photograph of the solar dryer.

Two drying experiments with two average chamber drying air velocities (0.10 and 0.30 m/s) were carried out continuously from 9 am one morning to 9 am on the next day for a total drying time of 24-hours with and without storage, making a total of four experiments. During the drying experiments, the data from the thermocouples and the pyranometer were automatically logged to the computer using an Agilent 34970 A data logger. The other remaining measurements were taken manually every hour. The total mass of the apples was measured every hour by opening the dryer so that the moisture ratio could be estimated.

The moisture ratio was estimated (Djebli *et al.*, 2020) as:

$$MR = \frac{M - M_{eq}}{M_0 - M_{eq}} \approx \frac{M}{M_0},$$ (1)

Where:

- M = moisture content,
- M_{eq} = equilibrium moisture content and
- M_0 = initial moisture content.

M_{eq} was much less than M and M_0 therefore it could be neglected as indicated in Equation (1).

3. RESULTS AND DISCUSSION

Solar radiation and wind speed profiles for the 24-hour experimental tests with the low (A1, B1-0.10 m/s) and high (A2, B2-0.30 m/s) airflow velocities are shown in Figure 5. The storage profiles are depicted in red, while the non-storage cases are depicted in black.
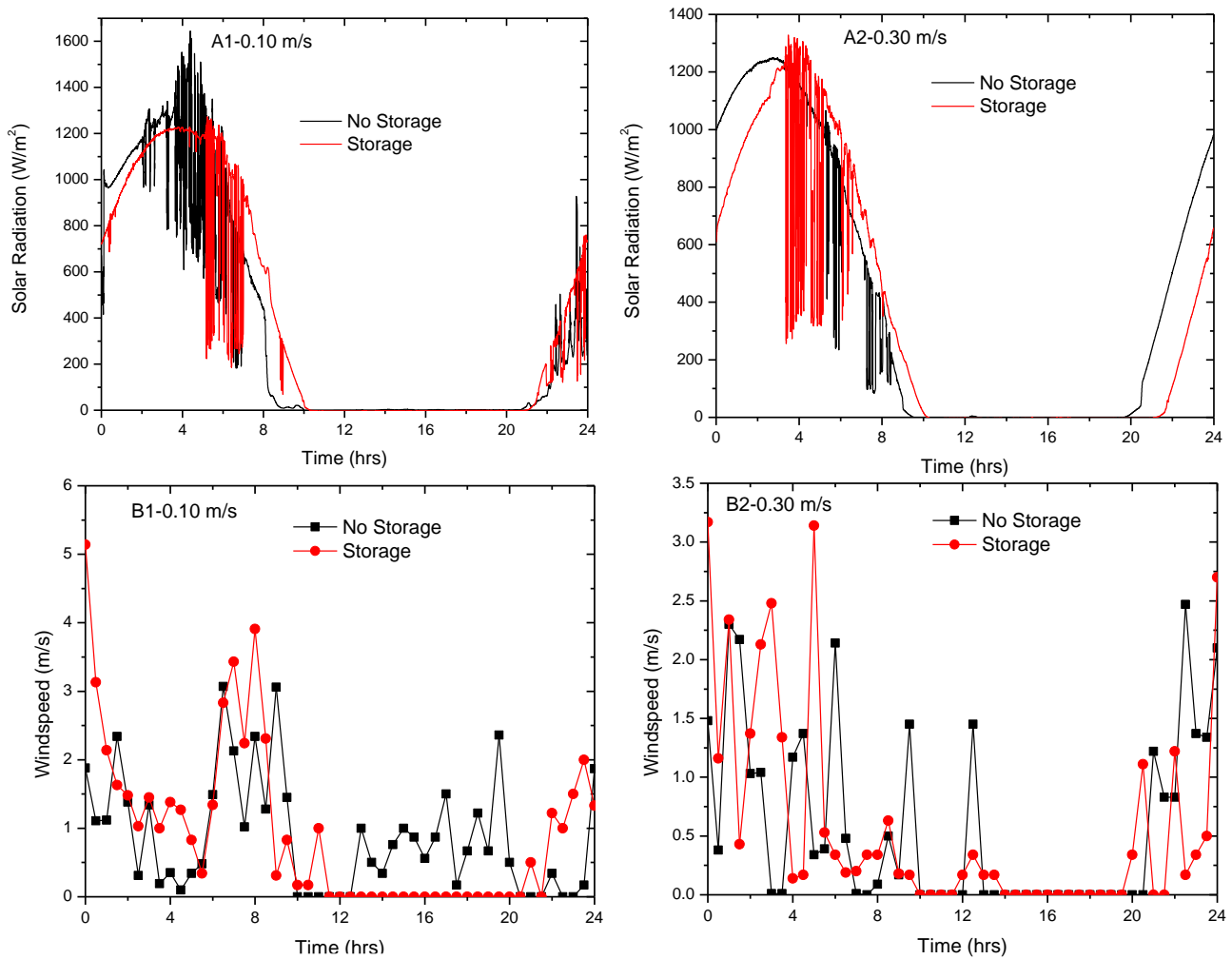
Figure 5: (A) Solar radiation and (B) wind speed profiles during experimental tests using average drying chamber airflow velocities of 0.10 and 0.30 m/s for the storage and non-storage cases. The experimental tests with 0.10 m/s (A1, B1) were carried out on 3-4 December 2021 and 1-2 February 2022 for the non-storage and storage cases, respectively. The experimental tests with 0.30 m/s (A2, B2) were carried out on 30 November-1 December 2021 and 14-15 February 2022 for the non-storage and storage cases, respectively.

The solar radiation profiles for the low airflow velocity case show cloudy conditions for both cases with the storage test showing typical solar radiation fluctuations between 5-7 hours of the experiment compared to 3-7 hours with more fluctuations for the non-storage test. However, the average solar radiation during the non-storage test was around 780 W/m² which was comparable to 850 W/m² for the storage test for 10 hours of sunshine. There were non-clear sky conditions for the whole of December 2021 and February 2022 which were characterised by heavy storms and highly cloudy conditions. The tests with the higher airflow velocity had also a high solar radiation variability between 4-8 hours. The average solar radiation for the non-storage case during sunshine hours was 800 W/m² which was comparable to the storage case of 760 W/m². The wind speed, like the solar radiation, was variable during the experimental tests. The windspeed showed higher values for the storage case during sunshine hours compared to the non-storage case for both airflow velocities. However, the average windspeeds for the low airflow velocity test compared well with values of 0.86 and 0.95 m/s for the non-storage and storage cases, respectively. The average windspeeds for the non-storage and storage tests were almost identical with values of 0.56 and 0.57 m/s, respectively. Controlled experiments under comparable conditions can only be achieved in a laboratory experiment, as recently reported by Tegenaw *et al.* (2021).

Figure 6 shows the collector and ambient temperatures and the storage PCM temperatures during 24-hour drying cycles using the low and high airflow velocities The outlet and inlet collector temperatures were seen to rise and fall in a sequence similar to the solar radiation. Fluctuations in the inlet and outlet collector temperatures were due to the fluctuations in the solar radiation. For the low airflow velocity, the outlet collector temperature for the storage case (T_{OUTST}) shows a higher maximum value of around 95°C compared to 85°C for the non-storage case (T_{OUTNST}). This was a direct result of the higher average solar radiation conditions with fewer fluctuations between 4-5 hours for the storage case. The inlet collector temperatures were also generally higher for the storage case when using the low airflow velocity. The ambient temperature for the non-storage case was generally higher than that of the storage case for the whole duration of drying using the low air velocity. This had a direct influence on the collector temperatures for the storage case which become lower than the case without storage after 10 hours of the experiment.
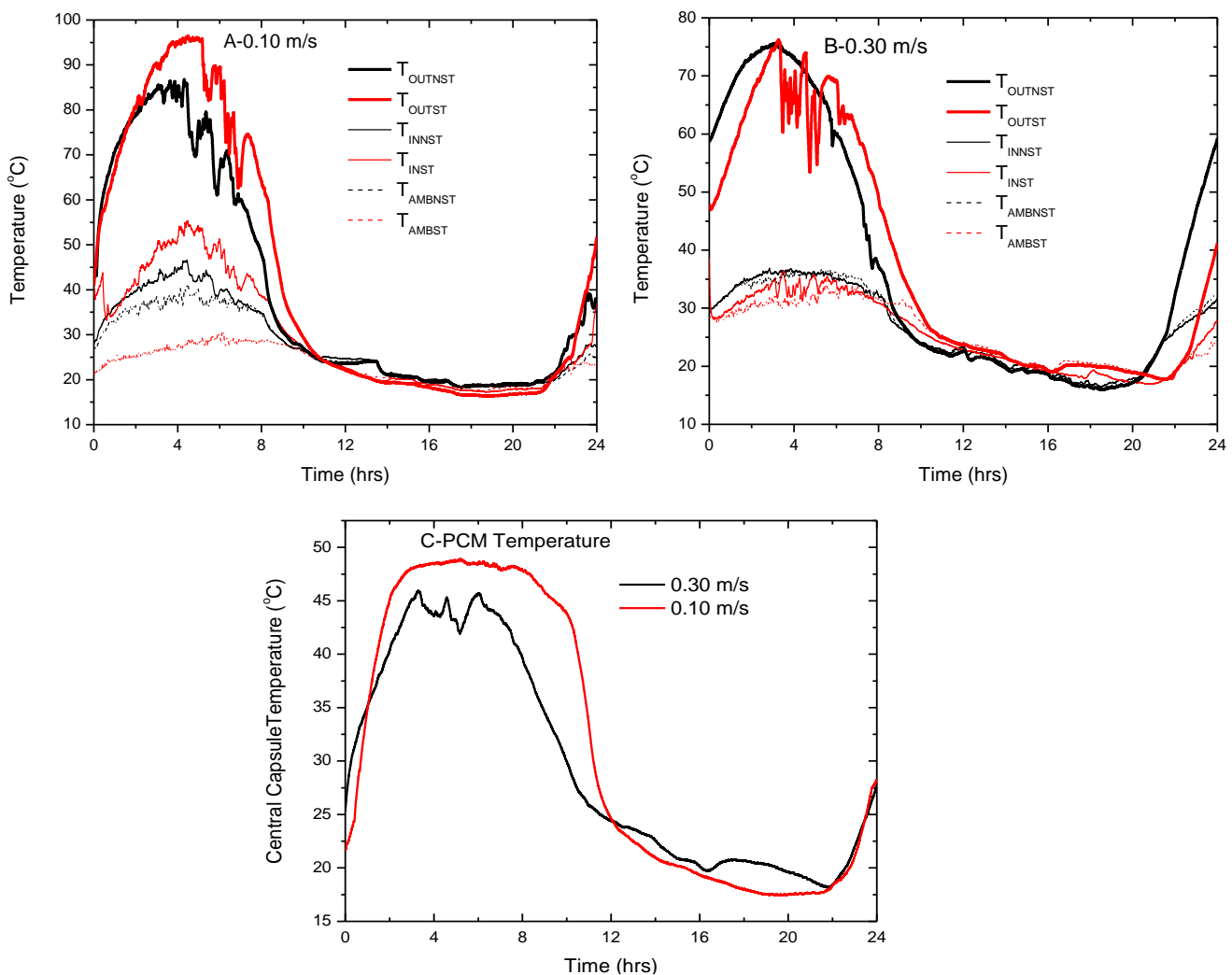
Figure 6: (A) Collector and ambient temperatures for an airflow velocity of 0.10 m/s for non-storage and storage cases, (B) collector and ambient temperatures for an airflow velocity of 0.30 m/s for non-storage and storage cases and (C) central PCM capsule temperatures for airflow velocities of 0.10 and 0.30 m/s.

An increase in the airflow velocity from 0.1 to 0.3 m/s caused the outlet temperatures of the collector to drop as a result of less resident time of the air in the collector. Maximum collector temperatures of around 75°C were obtained for both cases. The rise in the collector temperature was delayed for the storage case, which was a direct effect of heating the additional storage capsules. This delay was also slightly experienced with the lower airflow velocity. The time to achieve the maximum collector temperatures was also reduced with the higher airflow velocity due to increased heat transfer. Unlike the case with the low air velocity, the ambient temperatures for the two cases were comparable. The storage case showed a higher outlet collector temperature between 4-20 hours of the drying test. The temperature profile of the central PCM capsule (Figure 6(C)) showed that melting of the PCM was only possible with the low airflow velocity, which showed an almost constant value of 48°C between 4-8 hours of drying. The higher airflow velocity achieved a lower outlet collector temperature that was not able to melt the PCM thus temperature fluctuated between 4-8 hours at maximum and minimum limits of 46-42°C. A suggestion for future work is to improve the efficiency of the collector so that higher temperatures can be achieved to melt the PCM with a high airflow velocity.
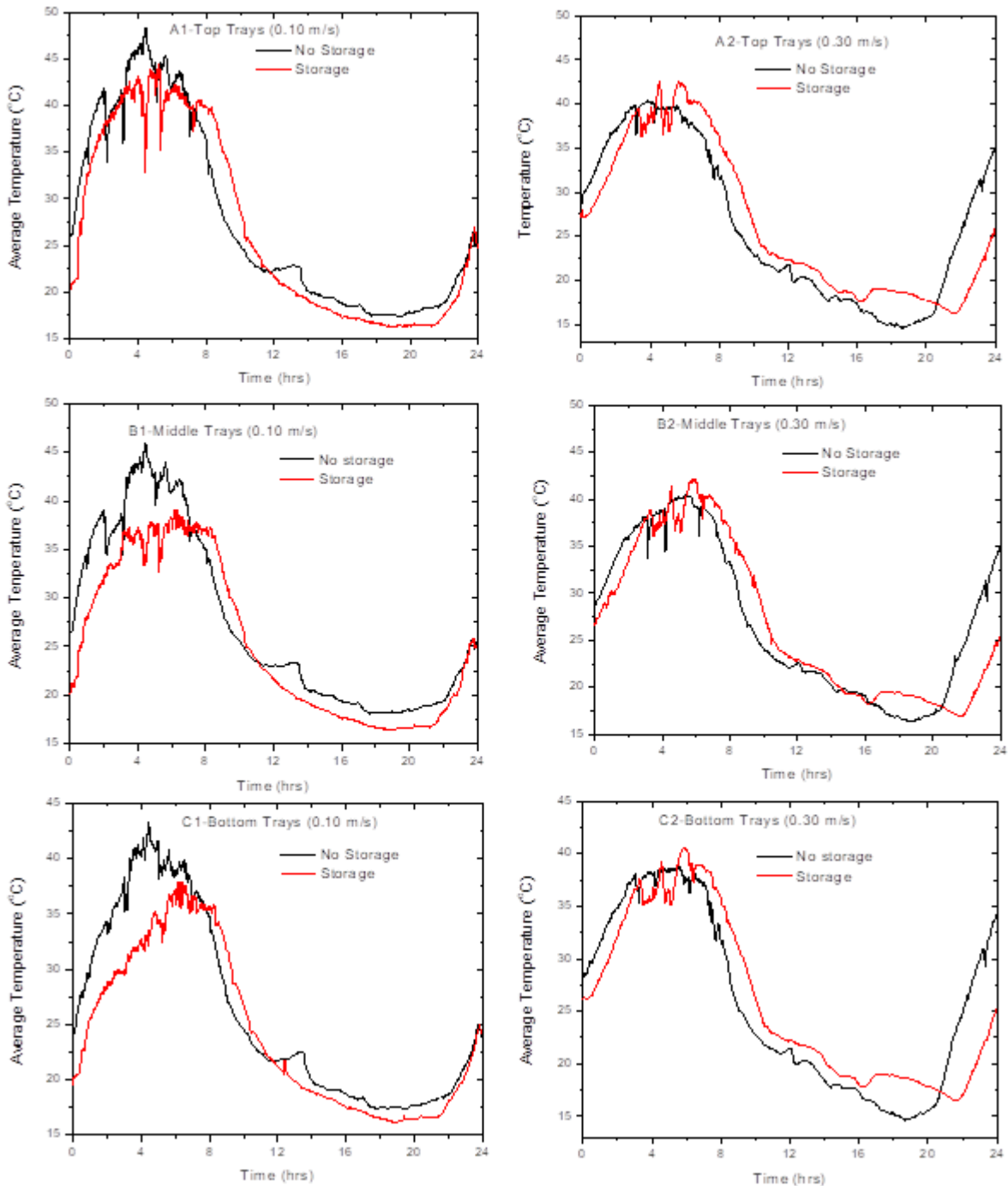
Figure 7: Average drying chamber temperatures for (A) the top, (B) middle and (C) bottom trays using average drying chamber airflow velocities of 0.10 (1) and 0.30 (2) m/s for the non-storage and storage cases.

Figure 7 shows the average temperature profiles inside the chamber for both cases at the top, middle and bottom trays. The temperature profiles in the different trays followed more or less the same trend as the outlet collector

temperatures. For the lower airflow velocity, the non-storage case showed higher average chamber temperatures compared to the storage case possibly due to heat transfer to the PCM before transferring to the apples during the solar drying period. The profiles for the low airflow velocity also rose slightly later for the storage case due to heating of the PCM before transferring heat to the drying chamber. The maximum temperatures achieved in the top trays for the storage and non-storage cases were 44 and 48°C, respectively using the lower airflow velocity. The corresponding maximum temperatures in the middle tray were 38 and 46°C, respectively whereas the bottom trays show maximum temperatures of 37 and 43°C, respectively. During the low and the early non-sunshine hours (8-11 hours), the storage case showed higher dryer average temperatures in all trays for the lower airflow velocity. The temperature difference between the storage and non-storage were as high as 10°C at the top tray after around 8 hours of drying. The temperature difference dropped to zero with the low airflow velocity after 11 hours of drying, and the non-storage case showed higher temperatures between 12-24 hours of drying. This suggested a lower heat transfer rate with the low airflow velocity thus inhibiting the benefits of the PCM storage.

For the higher chamber airflow velocity, the delay in the rise of the temperature profiles of the storage case was lower due to a higher heat transfer rate. The storage case's average drying chamber temperatures rose faster compared to the lower airflow velocity case and the storage case showed higher drying chamber temperatures after 4 hours of drying. The maximum temperatures achieved in the top trays were 42 and 40°C for the storage and non-storage cases, respectively. Generally, even without phase change occurring in the storage case with the higher airflow velocity, the average drying chamber temperatures for the storage case were higher than those of the non-storage case for a longer duration of drying (6-20 hours) compared to the low airflow velocity. This suggested better heat transfer of the stored energy at a higher airflow velocity to fully capitalize the stored thermal energy. However, the maximum temperature difference between the two cases was around 5°C compared to 10°C for the lower airflow velocity. After 20 hours of drying, the non-storage case showed higher drying chamber temperatures during the occurrence of solar radiation on the next day, as there was no storage thermal mass to be heated.

The average moisture ratios in the six trays of the dryer at low and high airflow velocities are shown in Figure 8. For the low airflow velocities, the non-storage case showed a faster drop in the average moisture ratio during the sunshine hours from 0-10 hours. This was expected since the storage heated the PCM as well as the apples in the dryer resulting in a delayed temperature rise in the chamber. This induced a lower rate of moisture removal after 10 hours for the low airflow velocity, the average moisture ratios were almost identical for the two cases and the effect of the storage material seemed insignificant. It was only after 20 hours that the storage case showed slightly lower average moisture ratios. The PCM capsules seemed to show no significant advantage in terms of the reduction in the average moisture ratios with the low airflow velocity. For the higher airflow velocity, the average moisture ratios dropped at a faster rate compared to the low airflow velocity for both cases. The steady-state average moisture ratio was achieved around 8 hours for the higher airflow velocity case compared to 12 hours for the low airflow velocity case.
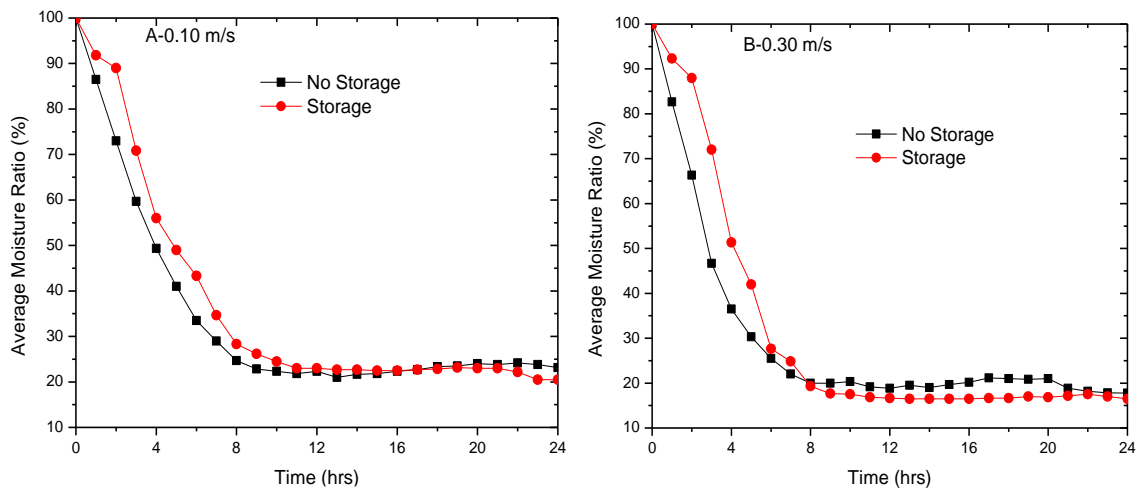
Figure 8: Average moisture ratios in the drying chamber for average drying chamber airflow velocities of (A) 0.10 and (B) 0.30 m/s for non-storage and storage cases.

The average moisture ratios were also lower compared to the low airflow velocity case to due increased heat transfer. The storage case showed lower average moisture ratios from 8 hours to the end of the drying process suggesting performance improvement with the use of PCM storage during non-sunshine periods. The difference in the moisture ratios during non-sunshine periods was not too high, however, this still showed the advantage of TES in terms of improving the performance of the dryer. The highest percentage difference of around 4% in the average moisture ratios for the high airflow velocity occurred at around 19 hours. A suggestion for possible future work to improve the storage performance would be to load the PCM capsules in the collector as reported recently by Andharia *et al.* (2022) since this would ensure that the PCM was melted with the higher temperatures at the collector. This would also ensure the latent heat from the PCM was transferred effectively to the drying chamber resulting in better performance during non-sunshine hours.

Table 2 summarises the results of the 24-hour experiments using the two different airflow velocities. Larger average maximum drying chamber temperatures were seen with the low airflow velocity for the non-storage case compared with the storage case. As the heat transfer rate increased with the higher airflow velocity, slightly higher average chamber temperatures were seen with the storage case compared to the non-storage case. The minimum average moisture ratios were lower for the both airflow velocities for the storage case.

Table 2: Summary of the experimental results with and without storage in the drying chamber.

	Maximum average dryer temperature at the top shelf (ºC)	Maximum average dryer temperature at the middle shelf (ºC)	Maximum average dryer temperature at the bottom shelf (ºC)	Minimum average moisture ratio (%)
0.10 m/s	48 (No storage) 44 (Storage)	46 (No storage) 38 (Storage)	43 (No storage) 37 (Storage)	23 (No storage) 20 (Storage)
0.30 m/s	40 (No storage) 43 (Storage)	40 (No storage) 42 (Storage)	38 (No storage) 40 (Storage)	18 (No storage) 16 (No storage)

4. CONCLUSION

A solar dryer with latent heat storage for drying apples in a continuous 24-hour cycle was evaluated experimentally in this work. The performance of the dryer was evaluated with and without storage. Twenty aluminium capsules encapsulated with sodium thiosulfate pentahydrate as phase change material (PCM) were used as latent heat storage. The performance of the dryer was evaluated in terms of the temperature profiles and moisture ratios during 24-hour drying cycles with and without latent heat storage. Two average drying chamber airflow velocities of 0.10 (low) and 0.30 m/s (high) were used in the experimental tests. The solar dryer with storage showed lower drying chamber temperatures during the initial solar drying periods compared to the solar dryer without storage. On the other hand, the chamber temperatures were higher by up to 10°C after sunset for the solar dryer with storage for the lower airflow of 0.10 m/s. For the higher airflow velocity (0.30 m/s), the maximum temperature difference between the storage and the non-storage cases was around 5°C. Slightly lower final moisture ratios (20% min) were obtained with the solar dryer with storage compared to the solar dryer without storage (23% min) during the 24-hour solar drying period with the lower airflow velocity of 0.10 m/s. The increase in the drying chamber airflow velocity reduced the final moisture ratio in the drying chamber for both cases. A suggestion of possible future work to improve the storage performance would be to load the PCM capsules in the collector. This would ensure that the PCM was melted with the higher temperatures at the collector thus effectively transferring latent heat from the PCM to the drying chamber resulting in better performance during non-sunshine hours.

5. ACKNOWLEDGEMENTS

6. REFERENCES

Andharia K.J., Markam B., Dzhonova D., and Maiti S., (2022). A comparative performance analysis of sensible and latent heat based storage in a small-scale solar thermal dryer, Journal of Energy Storage 45, 103764.

Bhardwaj A.K., Kumar R, Chauhan R, and Kumar S., (2020). Experimental investigation and performance evaluation of a novel solar dryer integrated with a combination of SHS and PCM for drying chilli in the Himalayan region season, Thermal Science and Engineering Progress 20; 100713.

Bhardwaj A.K., Kumar R., Kumar S., Goel B., and Chauhan R., (2021). Energy and exergy analyses of drying medicinal herb in a novel forced convection solar dryer integrated with SHSM and PCM, Sustainable Energy Technologies and Assessments 45,101119.

Cetina-Quinones A.J., Lopez J.L., Ricalde-Cab L., El Mekaoui A., San-Pedro L., and Bassam A., (2021). Experimental evaluation of an indirect type solar dryer for agricultural use in rural communities: Relative humidity comparative study under winter season in tropical climate with sensible heat storage material, Solar Energy 224, 58-75.

Chaatouf D., Salhi M., Raillani B., Amraqui S., and Mezrhab A., (2021). Assessment of a heat storage system within an indirect solar dryer to improve the efficiency and the dynamic behaviour, Journal of Energy Storage 41, 102874.

Djebli A..., Hanini S., Badaoui O., Haddad B., and Benhamou, A., (2020). Modeling and comparative analysis of solar drying behaviour of potatoes, Renewable Energy 145 1494-1506.

Getahun E., Delele, M.A., Gabiye, N., Fanta, S.W., Demissie P., and Vanierschot M., (2021). Importance of integrated CFD and product quality modeling of solar dryers for fruits and vegetables: A review, Solar Energy 220, 88-110.

Lamrani B., and Draoui A., (2020). Modelling and simulation of a hybrid solar-electrical dryer of wood integrated with latent heat thermal energy storage system, Thermal Science and Engineering Progress 18, 100545.

Lingayat A.B., Chandramohan V.P., Raju V.R.K., Meda V., (2020). A review on indirect type solar dryers for agricultural crops – Dryer setup, its performance, energy storage and important highlights, Applied Energy 258, 114005.

Kamarulzaman A., Hasanuzzaman M., and Rahim N.A., (2021). Global advancement of solar drying technologies and its future prospects: A review, Solar Energy 221, 559-582.

Kenisarin M., and Mahkamov K., (2016). Salt hydrates as latent heat storage materials: Thermophysical properties and costs, Solar Energy Materials & Solar Cells 145, 255-286.

Mohana Y., Mohanapriya R., Anukiruthika T., Yoha K.S., and Moses J.A., (2020). Solar dryers for food applications: Concepts, designs, and recent advances, Solar Energy 208, 321-344.

Mugi V.R., Das P., Balijepalli R., and Chandramohan V.P., (2022). A review of natural energy storage materials used in solar dryers for food drying applications, Journal of Energy Storage 49, 104198.

Nukulwar M.R., and Tungikar V.B., (2022). Recent development of the solar dryer integrated with thermal energy storage and auxiliary units, Thermal Science and Engineering Progress 29, 101192.

Srinivasan G., Rabha, D.K., and Muthukumar, P., (2021). A review on solar dryers integrated with thermal energy storage units for drying agricultural and food products, Solar Energy 221, 22-38.

Tegenaw, P.D., Mawire, A., Ramokali M., Mothupi M.., Vanierschot M., (2021). Experimental measurement of heat transfer in a solar-powered food dryer, Proceedings of the Southern African Sustainable Energy Conference (SASEC2021), 17-19 November 2021, Spier, Western Cape, South Africa, 50-56.

Udomkun P., Romuli S., Schock S., Mahayothee B., Sartas M., Wossen T., Njukwe E., Vanlauwe B., and Müller J., (2020). Review of solar dryers for agricultural products in Asia and Africa: An innovation landscape approach, Journal of Environmental Management 268, 110730.

#62: Techno-economic feasibility of a net zero energy retrofit for a multi-unit residential building

In Halifax, Canada

Charlotte Nauss[1], V. Ismet Ugursal[2]

[1] Dalhousie University, Department of Mechanical Engineering, Halifax, NS Canada, Charlotte.Nauss@Dal.Ca
[2] Dalhousie University, Department of Mechanical Engineering, Halifax, NS Canada, Ismet.Ugursal@Dal.Ca

Abstract: The building sector has a large environmental footprint that contributes to current global GHG emissions. Implementing energy efficiency measures in the building sector will assist in reducing energy consumption and has the potential for substantial CO_2 reductions. There is an increased interest for net zero energy buildings to reduce the high energy demands associated with buildings. This paper investigates the techno-economic feasibility of implementing a net zero energy retrofit for a multi-unit residential building (MURB) in Halifax, Canada. An existing and modern 100+ unit MURB was selected and modeled in its current state using a building energy performance software. Iterations of energy efficiency modifications were implemented until the total annual energy consumption was reduced to a level that would allow for the building to achieve net zero energy status by incorporating renewable energy capacity. This paper presents the methodology, the retrofit technologies and renewable energy installation used, and their economic implications. The results show the economic feasibility constraints for a MURB retrofit to achieve net zero status in the cold climate of Halifax.

1. INTRODUCTION

The building sector has a large environmental footprint that contributes to current global greenhouse gas (GHG) emissions. Buildings produce GHG emissions due to their design, location, orientation, and use. Significant policy action towards the promotion of energy efficiency and on-site renewable energy in the building sector is under development all around the world with different levels of intensity and structure. Implementing energy efficiency measures in the building sector assists in reducing energy consumption and has the potential for substantial GHG emission reductions. One of the widely adopted measures that have become part of the energy policy in several countries is the Net Zero Energy Building (NZEB) to reduce the high energy demands associated with buildings. A NZEB produces as much energy as it consumes on an annual basis. This is typically achieved by reducing the loads as much as possible through high performance enclosures and efficient mechanical and electrical systems. The balance of energy is then generated through on-site renewable energy such as solar photovoltaics (PV). NZEB's are often grid-tied, meaning that they draw energy from the grid as needed and supply energy back to the grid as it is produced in excess, the balance over the course of the year being zero or net supply.

The literature shows variations with the definition of NZEB based on the level of the energy chain at which the balance is made, and the requirement for a high level of energy efficiency. Attia (2018) lists several informal and formal definitions of NZEB. In 2014, the U.S. DOE Building Technologies Office contracted with the National Institute of Building Sciences to establish definitions, associated nomenclature, and measurement guidelines for zero energy buildings, with the goal of achieving widespread adoption and use by the building industry (U.S. DOE, 2015). In addition to establishing a definition for Zero Energy Buildings (ZEB), it was clear that definitions were needed to accommodate the collections of buildings where renewable resources were shared. In this work, the U.S. DOE definition is adopted which includes in the building boundary all property premises, and the utility connections and the energy import/export occurring at the building boundary. Thus, the NZEB is one whose total annual energy consumption is equal to the amount of renewable energy generated on-site. This definition can be expanded to include off-site generation if the building owns or leases off-site facilities (Attia, 2018). Another useful concept is the Net Zero Ready (NZR) building, which is built to a high energy efficiency standard but does not incorporate renewable energy to offset the demand. This allows the building owner to incorporate renewable energy generation later at a lower cost due to a reduced requirement for energy.

New construction allows for an integrative design process. It relies on the project team working together to incorporate energy efficiency, renewable energy and green design features into as many aspects of the building as possible. The process enables the team to optimize systems and minimize operating and maintenance costs. Greater energy efficiency begins with planning and designing, allowing new construction to offer more opportunities for integrating efficiency measures. However, implementing energy retrofits in existing buildings is typically a more expensive proposition. New construction allows for design features such as optimal building orientation and window placement to be implemented, as well as opportunities for increased solar production.

The reuse of existing building stock through building retrofits offers greater environmental savings than demolition and new construction. Building retrofits reduce the volume of new material used as well as the emissions created through its construction. Retrofits can include minor, major, and deep retrofits. Minor retrofits include modifications that are low-cost, easy to implement and offer good value for the money and effort invested, whereas major retrofits take a more holistic approach to the upgrades. A deep retrofit involves an extensive overhaul of the building's systems. Deep energy retrofits of multi-unit residential buildings (MURBs) can achieve multiple economic, social, and environmental goals; they can reduce overall costs by renewing near-end-of-life systems and extending building lifespan, lower carbon emissions and operational costs, and provide lower energy bills and better health and comfort for residents.

Due to its northerly location and prevalence of single-family housing, the residential sector in Canada was responsible for about 17% of the energy consumption and 13% of the GHG emissions of total values in 2018 (NRCan, 2018). Improving the end-use energy efficiency in the residential sector would play a major role in Canada's commitment to reduce its GHG emissions. Because of this, research tends to focus on single-family housing (Asaee *et al.*, 2019). In contrast to single-family housing, MURBs are difficult to upgrade and building owners want verifiable proof that the retrofit measures will pay off before they act. The residents may not want the disruption, requiring work to be timed with tenant turnover or other major changes, or, if utilities are included in their rent, they may see no benefit in participating. Finally, industry trades may not fully understand all factors involved or the benefits to be had.

The steps required to achieve NZE status in an existing MURB are:

1. Make improvements to the building envelope. This includes increasing the insulation of the exterior walls and roof, air-tightness improvement, upgrading glazing surfaces and adding insulation to balcony decks to reduce the effect of thermal bridging.
2. Reduce the building's electrical load. Electrical loads include major appliances, water use equipment, receptacle loads, and lighting. Major appliances are upgraded to Energy Star status, and receptacle loads are reduced by implementing sensors. The lighting load is reduced by replacing bulbs with LEDs, as well as using daylighting and occupancy sensors.

3. Improve the HVAC system. Replace the current space conditioning system with an electrified system with a higher efficiency, such as a heat pump and an energy recovery ventilator.
4. Install renewable energy, such as solar photovoltaics or solar thermal, to offset the energy consumption.

A review of the literature indicated that while there are numerous studies that focus on the techno-economic feasibility of retrofitting single family dwellings to NZEBs, there is no such study for MURBs. Therefore, the overall objective of this work is to investigate the techno-economic feasibility of retrofitting an existing multi-unit residential building in Halifax, Nova Scotia, into a net zero energy building.

Nova Scotia (NS) is a maritime province of southeastern Canada, whose weather characteristics are heavily influenced by the Atlantic Ocean. ASHRAE classifies NS as having a climate zone of 6A, which is a cold but humid climate. The average monthly high and low temperatures, as well as the heating degree days for Halifax, the largest city in the province, are given in Table 1. NS receives less solar irradiance than most other Canadian provinces, except British Columbia and Newfoundland. The average solar energy system in NS can produce 1,090 kWh/year of electricity per kW of solar panels (Energy Hub, 2020).

Table 1: Average monthly high and low temperatures, and heating degree days for Halifax

	Jan	Feb	Mar	Apr	May	Jun	Jul	Aug	Sept	Oct	Nov	Dec	Total
High (°C)	0	0	4	9	14	20	23	23	19	13	8	3	
Low (°C)	-8	-8	-4	1	6	11	14	15	12	6	1	-4	
HDD (°C)	681	532	559	416	231	154	22	16	103	301	413	634	4062

2. REDUCING BUILDING ENERGY NEEDS

Building envelope insulation retrofits represent an important starting point for projects seeking to reduce whole house energy consumption to near net zero levels. Building envelope modifications include wall, roof and exposed floor insulation upgrades, window replacement, and air-tightness improvement. The building envelope design should help keep the heating and cooling loads to a minimum, while being practical to build, and make sense from a cost and functional standpoint. The Canadian Mortgage and Housing Corporation (CMHC) suggests insulation levels of RSI-1 for windows, RSI-3.5 for below grade walls, RSI-7 for above grade walls and RSI-11 for roofs when retrofitting homes for NZE (CMHC 2015).

Windows represent a major source of heat loss in the winter, as they typically have the lowest insulating value of the building envelope components. To achieve better performance with windows single- or double-glazed simple windows need to be replaced with highly insulated double- or triple-glazed windows with low-emissivity (low-e) coating and argon fill and insulated frames. Nikooford *et al.*, (2014) found that upgrading all windows in the single-family housing in Canada to triple glazed with low-e coating (emissivity 0.1) and 13mm argon-filled gap windows would result in a reduction of 7% in energy consumption in the housing stock and 8% in GHG emissions.

Air tightening of the building envelope and ducts to reduce air leakage is a core element of energy efficiency programmes and residential retrofit practices. Current best practices in construction seek to make buildings as airtight as possible and provide controlled ventilation with mechanical systems. In general, the literature suggests an air change rate of less than 1.5 ACH at 50 Pa. Air tightening techniques reduce air leakage to the point that contaminants with known health effects are sealed into the unit; therefore, the addition of mechanical ventilation is required to remove indoor-generated pollutants and excess moisture, and to provide a sufficient supply of outdoor air to ensure acceptable indoor air quality (IAQ). The ASHRAE Standard 62.1, 2019 dictates that a dwelling unit requires an outdoor air supply rate of 2.5 L/s.person and an additional 0.3 L/s.m^2. Due to the size of MURBs, balanced ventilation systems which are calibrated to balance the exhaust and supply air flows are used. To minimize the energy consumption required to condition the incoming outdoor air to indoor conditions, heat recovery is added to conventional ventilation systems. Heat recovery can take two forms: transfer of both moisture and sensible heat between the exhaust and outside air streams, and transfer of only sensible heat. The transfer of some of the moisture from the exhaust air to the usually less humid incoming winter air allows for the humidity of the indoor air to stay more consistent. Most moisture and sensible heat recovery devices can recover 70% to 80% of the heat energy from the exhausted air and are most cost-effective in climates with extreme winters and summers.

Due to Canada's cold climate, space heating accounts for more than 60% of the energy used in the average home while space cooling only accounts for 1.9% of the energy used in the average Canadian home. With hot, humid, sunny days becoming more common during the summer months, more Canadians are using cooling. Due to reduced energy consumption, favorable insurance rates, incentive programs and year-round climate control, heat pumps have become increasingly more popular. While the air source heat pump is the most common type of heat pump in Canadian homes, ground-source (geothermal) heat pumps that draw heat from the ground and/or ground water are also chosen due to their higher performance throughout the year. These systems have the potential to reduce heating and cooling energy consumption by 65% compared to standard heating technology.

Incorporating energy efficient lighting is an important step in reducing the electricity demand, which currently accounts for 3.6% of the energy used in the average Canadian home (NRCan, 2010). LEDs are the most efficient, longest lasting light source available since the majority of energy that LEDs consume is used to produce visible light rather than infrared and ultraviolet radiation. In modern buildings, lighting control systems are installed to maximize the energy-efficiency of the lighting system without affecting the comfort of the occupant (Delaney *et al.*, 2009). Dimmers are used to extend the life of the lamp and reduce the energy consumption. Motion sensors, timers and photocells allow for lights to be switched off when not needed, reducing unnecessary lighting energy use by up to 15% (Jinsung *et al.*, 2013).

An average set of major household appliances, which include large stationary appliances used for refrigeration (refrigerators and freezers), cooking (ovens) and cleaning (washing machines, clothes dryers, and dishwashers), consume 2,600 kWh/yr. Clothes dryers are among the largest energy use appliances, with EnerGuide data estimating annual usages of nearly 1,000 kWh for most models (NRCan, 2019a). The most efficient and energy saving method of clothes drying is not having a clothes dryer, and instead installing an interior and/or outdoor clothes drying rack or line for air drying. ENERGY STAR *Most Efficient* designated appliances use the least energy.

Canadian households own 160% more electronics than they did a decade ago, with these electronics accounting for more than 20% of electricity use in homes (NRCan, 2019b). Constant connection through electronic devices has revolutionized society, however all these devices consume electricity. The energy consumption of products is always improving, but the sheer volume of devices used at home and work continue to increase, resulting in more energy consumption. Connected devices are expanding to include products that offer both wired and wireless network functionality such as smoke detectors, security systems, HVAC, and lighting. These network-enabled devices can draw as much energy in standby as when they are fully activated. Standby power consumption can account for 5–10% of household electricity bills. Reducing energy consumption associated with electronics can be achieved by unplugging infrequently-used items and using occupancy sensors, advanced power bars that prevent electronics from drawing electricity when not in use and load shedding devices, which also prevent night plug loads that contribute significantly to wasted energy (Attia, 2018).

Canadians use an average of 75L of hot water each at home every day, with water heaters accounting for 19% of the energy used in the average Canadian home (NRCan, 2019c). Options to reduce domestic hot water (DHW) energy consumption include installation of a water-saving shower head and faucet aerators that reduce the amount of hot water used, as well as technology such as well-insulated electric tanks, heat pump hot water systems and solar water heaters.

3. ON-SITE RENEWABLE ENERGY PRODUCTION

Active solar energy utilization is one of the main strategies used to provide on-site renewable energy to buildings with the intent to achieve net zero energy designation. Photovoltaics (PV) for buildings reduce the electricity demand from the electric grid. PV can be used in a building envelope in two ways: building added PV (BAPV) mounted on the roof or envelope surfaces and building integrated PV (BIPV) that is part of the building cladding units, such as roof cladding, wall siding, skylights, windows and even roof shingles. The best PV efficiency is achieved by monocrystalline cells of commercial modules, which can reach upwards of 20% efficiency. A PV system consists of PV panels, inverters, an electricity meter, a mounting system, and electrical cables. When the PV system produces more electricity than the building requires, excess electricity is exported to the grid. Since the PV system forms a significant portion of the overall cost of a NZEB, sizing and integration of the system should be accomplished after the maximum energy efficiency of the building itself has been achieved. On-site energy storage, such as batteries in connection with advanced controls, allows for the covering of an increased amount of the electrical load by time-shifting utilization of the stored energy generated on-site.

Solar thermal collectors absorb solar irradiation energy as heat, which is then transferred to a working fluid such as air, water, or oil. Solar thermal energy for heating can be collected and stored in hot water tanks used for hot water services or to provide space heating. The two main types of solar thermal collectors are evacuated tube thermal collectors and flat plate collectors. In projects with ambitious energy targets or limited available area for installations, solar thermal collectors and PV modules may be competing for the available space on the building roofs and facades. In this situation a hybrid photovoltaic/thermal (PVT) collector can be used, which simultaneously converts solar energy into electricity and heat. A typical PVT collector consists of a PV module and an absorber plate attached on the back.

Due to the intermittency of most renewable energy, excess energy produced on the site of a net zero energy building must be either stored for later use or exported for off-site use using the electrical grid. Net-metering is the process in which homeowners receive credits for excess electricity that is generated by the renewable energy sources installed on their buildings that do not have on-site renewable energy storage, such as batteries, or has surpassed its maximum capacity of storage. Feeding electricity from on-site generation into utility grids is part of a strategy to increase the overall efficiency as well as increasing the share of power generated by renewables. Electric vehicles (EVs) can also be used as a grid storage tool, by using idle EV battery power as a grid storage unit with which fluctuations from renewable electric power sources are mitigated. On site energy storage for NZEB's typically consists of electrical energy stored in a battery system within the building. Integrating batteries into NZEB is not meant to make them energy independent; however, it assists in shifting periods of peak supply to periods of higher demand.

4. BUILDING ENERGY PERFORMANCE SIMULATION

To identify the retrofit measures that need to be adopted to convert an existing MURB to a NZEB it is necessary to use a building energy simulation software. In this work, OpenStudio was used to model the energy performance of the MURB selected to be retrofitted to achieve NZE status because the software conducts hour-by-hour simulations and provides a large library of common helper functions for creating, querying, and transforming energy models, running simulations, and working with results (OpenStudio, 2022). OpenStudio is an open-source analysis platform that facilitates integrated whole-building energy analysis utilizing the EnergyPlus and Radiance simulation engines. A plug-in for Google Sketch Up enables users to create building geometry and a variety of other input data objects required by EnergyPlus and Radiance. The OpenStudio application is a fully featured graphical interface that includes building envelope, loads, schedules, and HVAC systems. A results view enables browsing, plotting, and comparing of simulation output data. The parametric analysis tool enables users to study the impact of applying multiple combinations of energy efficiency and renewable energy measures to a base model building.

The EnergyPlus program is a collection of many program modules that work together to calculate the energy required for heating and cooling a building using a variety of systems and energy sources (EnergyPlus, 2022). It does this by simulating the building and associated energy systems when they are exposed to different environmental and operating conditions. The core of the simulation is a model of the building that is based on fundamental heat balance principles. EnergyPlus conducts an integrated simulation in which all three of the major parts of a building, i.e. building zones, system, and plant, are solved simultaneously rather than sequentially to account for the feedback from each part onto the other parts. To obtain a simulation that is physically realistic, the elements (zone, system and plant) are linked in a simultaneous solution scheme that are represented as a series of functional elements connected by fluid loops divided into supply and demand sides. EnergyPlus undergoes analytical, comparative and executable testing using industry standard methods as major updates are completed, with the objective of reducing the number of bugs in the software. Version 9.5.0 was available at the time of this research.

Radiance is a suite of programs for the analysis and visualization of lighting in building design (Radiance, 2022). Input files specify the scene geometry, materials, luminaires, time, date, and sky conditions. The calculated values include spectral radiance, irradiance, and glare indices. The primary advantage of radiance over simpler lighting calculation and rendering tools is that there are few limitations on the geometry or the materials that may be simulated. Radiance is used to predict the light levels and appearance of a space prior to construction.

5. TOLERABLE CAPITAL COST

Energy users must determine if it is worthwhile to invest in an energy efficiency or renewable energy upgrade based on the economic feasibility of the upgrade. To evaluate the economic feasibility of energy efficiency or renewable energy upgrades, a variety of tests are used such as payback period, cost-benefit ratio, and return on investment. To reach a conclusion, these tests consider the capital cost of the upgrade. However, it is not always possible to reliably estimate the capital cost of a potential energy upgrade. This could be due to rapidly changing price of technology, the development stage of the upgrade technology, the fluidity of the market, and regional price differences. In these situations, an alternative approach that involves the calculation of a tolerable capital cost (TCC) of the upgrade can be used (Nikoofard *et al.,* 2015). The TCC is the capital cost that one is able to pay for an energy upgrade based on the number of years considered acceptable for payback, the annual savings, and the applicable annual interest and fuel cost escalation rates. The TCC of an energy upgrade is determined by conducting a reverse payback analysis. Using this method, an owner or decision maker can determine the price at which an energy efficiency or renewable energy technology retrofit will be considered economically feasible.

6. METHODOLOGY

The first step was to identify a modern MURB in Halifax that could be used as a case study building. Taking into consideration the trend in the MURBs in Halifax, a relatively new mid-rise residential building with twelve stories and some energy efficient designs and systems was selected. A thorough investigation of potential energy efficient retrofits suitable for the selected MURB that would reduce its energy consumption to a level that would allow net zero operation with the addition of a solar PV array was conducted. The categories for energy upgrade retrofits were building envelope, electrical loads, and HVAC systems. Modifications to the building envelope included increased insulation and the installation of more efficient windows. To reduce electrical loads, replacing major appliances, installing smart sensors, and upgrading lights to LEDs was considered. Lastly retrofit options for the HVAC systems included replacing existing systems with high efficiency versions and more complex systems such as ground source heat pumps. Once all possible retrofit options were listed, the MURB was simulated under its current condition to obtain its baseline energy consumption. Low cost and low disruption energy efficiency improvements were made to the baseline building. These improvements included upgrading major appliances, daylighting and plug load sensors, and the installation of packaged terminal heat pumps. However, this first iteration of energy efficiency modifications did not reduce the energy consumption to a level that would allow for net zero energy status to be met with the addition of solar PV. Therefore, a second iteration of energy efficiency upgrades was applied using more aggressive modifications. This iteration did not consider retrofit cost or potential disruptions to current occupants; instead it focused on reducing the energy consumption as much as possible. The energy improvements of the second iteration

allowed for the building to reach an energy consumption that would allow for net zero energy status, reaching net zero energy operation through the addition of a PV array.

Once the building reached net zero status, a PV system was designed using National Renewable Energy Laboratory's (NREL) PVWatts Calculator (NREL, 2022). A current PV module with a high efficiency was selected (Sunpower M-Series 420-440 W Residential AC Module). To run the PVWatt's Calculator, the user inputs data such as building location, panel tilt and orientation, system losses and array type. Using weather data for the building's location from NREL's database and selecting a panel orientation facing south and a tilt of 45° that would optimize energy production year-round, the number of PV panels required in the array to reach net zero energy operation was determined. The number of panels that would be installed on the roof, and the number of remaining panels that would be installed either on-site or nearby was also calculated. Finally, an economic analysis was conducted using the TCC economic evaluation method.

7. EXISTING MURB

The existing MURB was a 12-storey, 153-unit condominium building with two additional floors of unconditioned, underground parking. The building was a rectangular prism, with dimensions of the above-ground floors of 20m by 85m, and 3m high per floor. The total floor area was 27,050m^2, with 20,400m^2 being conditioned floor space. Unconditioned spaces included the elevators, stairwells and the parking garage levels. The dimensions of the underground levels were 40m by 85m. Exterior walls had a net area of 6,350m^2 and the roof had a net area of 1,615m^2. Windows and glass exterior doors occupied 1,350m^2 of wall space. There were 145 balconies, with various dimensions, attached to the exterior of the building. The long axis of the building including the buildings main entrance was oriented approximately north. The thermal mass of walls, interior partitions, floors, ceilings, and some of the thermal mass of the furniture and parked cars as well as the shading effects of the balconies and a neighbouring condominium building were included in the modelling of the building.

The ground floor contained apartments as well as some common living spaces such as the main lobby and the lounge. The remaining floors, floors two through twelve, were identical and consisted of only apartments. Each of the underground parking levels and the spaces they encompassed were modelled as individual thermal zones. The above ground spaces were broken up so that each apartment had its own thermal zone.

Schedules for building types residential common, residential living and parking published by the California Energy Commission for residential occupancy, lights, receptacles, heating set point, infiltration, and water heating setpoint were used in modelling (CEC, 2019). The building envelope construction details were as follows:

- Above grade walls (heavy weight concrete, polyurethane insulation, air space, gyprock): RSI-3.5
- Roof (roof membrane, polyurethane insulation, heavy weight concrete, gyprock): RSI-4.4
- Below grade walls (heavy weight concrete): RSI-0.24
- Concrete slab (heavy weight concrete): RSI-0.22

Windows and exterior glass doors were double glazed with 6mm air space, no coating and surrounded by vinyl frames with a thermal break. Outdoor air infiltration was based on a rate of flow per exterior surface area equal to 0.014 m^3/min per m^2 at a 50Pa pressure differential.

Heating for the building was supplied through electric baseboards. Any required cooling was done so by opening windows or balcony doors. Ventilation requirements were achieved by centralized air handling units (AHU). Each floor had its own AHU with ducted supply and return to each apartment and common areas. Each unit in the baseline building had its own 170L capacity electric domestic hot water tank. Further details of the existing building are given in Nauss (2022).

8. ENERGY EFFICIENCY IMPROVEMENTS AND PV SYSTEM TO ACHIEVE NZEB STATUS

Energy efficiency improvements were applied in two iterations, described in detail in Nauss (2022). The first iteration included low cost, low disruption retrofits excluding any modifications to the building envelope. Modifications included changing the heating supply, adding sensible and latent heat recovery (76% and 68% effectiveness, respectively) to the ventilation systems, and improving the efficiency of electric loads. All electric baseboard heaters were upgraded to packaged heating only air-source heat pumps with a rated coefficient of performance of 2.5 and low-flow fixtures were incorporated to reduce how water consumption.

The second iteration of energy efficiency modifications represented aggressive modifications made to the building in order to reach near net zero energy status. The energy consumption was reduced as much as possible, with little concern for cost or potential disruptions. Improvements include increased insulation, more advanced heating and ventilation systems, and replacing the elevators. Additional insulation of RSI-3.5 was added to exterior walls to obtain an overall RSI-7, and additional insulation of RSI-6 was added to the roof to obtain an overall insulation of RSI-10.5 All windows and exterior glass doors were upgraded to triple glazing with low-e coating (emissivity of 0.1) and 12mm

argon-filled gap. The frames of the windows and glass doors were insulated to give an overall RSI-0.9. The air tightness of the building and air ducts was increased by reducing the space infiltration by 30%. All balcony surfaces were insulated with 5cm rigid insulation, to minimize balcony heat loss due to the thermal bridge. The air source heat pumps were replaced by a geothermal system with 40 boreholes, each 100m deep and water-to-air heat pumps with a rated coefficient of performance of 3.5 (heating mode) in each unit.

With the energy consumption reduced substantially, a PV system was added to achieve NZEB status of the MURB. The solar panels selected to offset the energy consumption of the near net zero energy building, allowing it to meet net zero energy standard were SunPower Maxeon M-Series SPR-M440-H-AC which has an efficiency rating of 22.8% and a nominal power output of 440W (DC). Each module had a total area of 2m^2 (SunPower, 2022). The solar panels were installed as a fixed array with a support system anchored to the roof of the building. Because the system used a fixed array, the panel orientation was optimized for year-round production with a tilt of 45° and facing south. The system had an inverter efficiency of 96% and a ground coverage ratio of 0.4.

9. RESULTS AND ANALYSIS
9.1. Path to net zero energy building

The total electricity consumption of the existing MURB was 2,273,000 kWh, with a total energy use intensity (EUI) of 111.4 kWh/m^2 of conditioned building area. As shown in Table 2 (columns marked by 1), the four largest consumers of energy were heating, interior equipment, interior lighting, and water systems. Table 2 shows the comparison of monthly electricity consumption in each consumption category between the existing MURB and the MURB after the second iteration of energy efficiency modifications.

Table 2: Electricity consumption comparison: existing MURB (1) and 2nd iteration (2) MURB

	Heating (1)	Heating (2)	Interior Lighting (1)	Interior Lighting (2)	Interior Equipment (1)	Interior Equipment (2)	Fans (1)	Fans+ Pumps (2)	DHW (1)	DHW (2)
January	160,700	12,500	53,100	21,200	46,900	15,700	1,800	6,100	49,500	43,000
February	136,800	10,700	48,900	18,800	42,400	14,200	1,700	5,400	43,700	37,800
March	110,050	8,000	53,000	19,600	46,900	15,700	1,800	5,900	47,600	41,000
April	58,600	4,000	51,700	19,000	45,400	15,200	1,800	5,400	43,300	37,000
May	21,200	460	33,100	8,900	46,900	15,700	1,900	5,300	34,600	28,000
June	3,500	0	31,600	7,800	45,400	15,200	1,900	5,600	30,300	24,000
July	65	0	33,100	8,300	46,900	15,700	2,100	6,100	29,600	23,000
August	60	0	33,000	8,300	46,900	15,700	2,100	6,100	29,600	23,000
September	1,900	0	31,700	8,700	45,400	15,200	1,900	5,700	30,300	24,000
October	26,800	840	33,100	10,200	46,900	15,700	1,900	5,600	34,600	28,000
November	64,300	4,700	51,600	20,700	45,400	15,200	1,800	5,600	33,300	37,000
December	141,200	11,900	53,100	21,600	46,900	15,700	1,800	6,100	49,600	43,000
Total	725,000	53,100	506,900	173,100	552,400	184,900	22,500	68,900	465,900	388,800

The total electricity consumption of the building after the first iteration of energy efficiency modifications was reduced to 1,624,300 kWh, with a total EUI of 79.6 kWh/m^2 of conditioned building area. This represented a reduction in energy consumption of 28.5%. When the second iteration energy efficiency measures were applied, the total energy consumption reduced to 868,800 kWh, with a total EUI equal to 42.6 kWh/m^2 of conditioned building area, representing a reduction in energy consumption of 62%. The change in electricity consumption in each consumption category is shown in Table 3.

Table 3: Electricity consumption comparisons between the existing building and after efficiency modifications

End Use	Electricity Use of Existing Building (kWh)	Electricity Use after First Iteration (kWh)	Electricity Use Reduction of First Iteration (%)	Electricity Use after Second Iteration (kWh)	Electricity Use Reduction of Second Iteration, from Existing Building (%)
Heating	725,000	537,500	26	53,100	93
Interior Equipment	552,400	472,100	15	184,900	67
Interior Lighting	506,900	232,700	54	173,100	66
DHW System	465,900	345,400	26	388,800	17
Fans	22,500	36,600	-63	23,300	-4
Pumps	0	0	0	45,600	n/a
Annual Total	2,273,000	1,624,300	28.5	868,800	62

The second iteration of energy efficiency modifications reduced the total annual energy consumption and allowed the building to reach net zero energy status with the addition of a PV system. To meet net zero energy operation, the building needed to offset the annual energy consumption with a net total energy production through renewable resources either on-site or nearby. To meet the 868,800 kWh electricity generation with 10% excess capacity (to ensure that if the energy consumption of the building varied from year to year, the net PV energy production would still be greater than the total annual energy consumption of the building), the building required a solar array consisting of 1,690 SunPower Maxeon M-Series: SPR-M440-H-AC modules, or 3,260m^2 of solar cells.

The total area of the roof was 1,615m^2, therefore, using a ground coverage ratio of 0.4, 500 PV units could be installed on the roof. The remaining 1,190 units would have to be installed next to the building. The monthly electricity production by the PV array is shown in Table 4. The summary of electricity demand and production for the existing building, the building with energy efficiency modifications and PV electricity production is shown in Table 5. The net zero MURB produced slightly more electricity than it required over the course of the year.

Table 4: Monthly electricity production by the PV array

	Jan	Feb	Mar	Apr	May	Jun	Jul	Aug	Sept	Oct	Nov	Dec	Total
1,000 kWh	62.6	67.2	97	86.2	93.4	88.5	95.8	99.6	92.6	73.2	50.1	49.4	955.7

Table 5: Building summary results

Electricity use of existing MURB	2,273,000 kWh/year
Electricity use after first iteration of energy efficiency measures applied	1,624,300 kWh/year
Electricity use after first iteration of energy efficiency measures applied	868,800 kWh/year
Electricity production by PV system	868,800 kWh/year (+10% excess)
Net electricity (energy) requirement of the net zero MURB	0 kWh/year

9.2. Economic analysis

The difference between the base case energy requirement and the energy requirement with the net zero retrofit (i.e. after the second iteration energy efficiency modifications and PV system implementation) represented the energy savings due to the net zero energy retrofit, which was equal to 2,273,400 kWh/year, since all of the energy requirement was met by the PV system installed. Using the cost of electricity in Nova Scotia of $0.15/kWh for residential customers, the annual energy cost savings was $341,000. Since there was uncertainty in predicting future interest and electricity price escalation rates, instead of using a single value for these parameters, the range of values given in Table 6 were used to demonstrate the impact of these values on TCC. The values of TCC for the net zero energy retrofit for the range of interest and electricity price escalation rates and payback periods are given in Table 7.

Table 6: Range of interest and electricity price escalation rates and acceptable payback periods

	Low	Medium	High
Electricity price escalation rate (%)	2	5	10
Interest rate (%)	3	6	9
Acceptable payback period (year)	10	20	30

Table 7: TCC values of net zero energy retrofit under the range of interest rates, electricity price escalation rates and acceptable payback periods given in Table 4

Payback Period	Interest Rate (%)	TCC with a 2% Electricity Price Escalation (Million CAN$)	TCC with a 5% Electricity Price Escalation (Million CAN$)	TCC with a 10% Electricity Price Escalation (Million CAN$)
10 years	3	3.2	3.6	4.5
	6	2.7	3.1	3.8
	9	2.4	2.7	3.3
20 years	3	6	8	13.3
	6	4.6	5.9	9.4
	9	3.6	4.5	6.8
30 years	3	8.7	13.3	30.1
	6	5.8	8.4	17.4
	9	4.2	5.7	10.7

10. CONCLUSION

The energy consumption and GHG emissions of buildings vary due to their design, location, orientation and use. Implementing energy efficiency measures in the building sector will assist in reducing energy consumption and has the potential for substantial CO_2 reductions. There is an increased interest for Net Zero Energy Buildings (NZEB) to reduce the high energy demands associated with buildings. This paper provided insight into the modifications necessary for an existing MURB to reach net zero energy status. A baseline model was developed, to which upgrades were applied in two iterations. The first iteration included low cost, low disruption modifications using easily accessible technology. The second iteration included more aggressive modifications to the envelope and space conditioning systems, with the goal of reducing the energy consumption as much as possible before offsetting the energy consumption with a net solar production of energy. These results indicated what is required of a MURB retrofit to reach net zero energy status.

The first iteration of energy efficiency modifications showed that simple and readily available technological upgrades can result in significant energy savings. More aggressive energy efficiency modifications such as improving the building envelope and installing a ground source heat pump, as described in the second iteration demonstrated that reducing the energy consumption even further was possible. Net zero energy status was achieved by using the second iteration of energy efficiency modifications and then installing 1,690 solar panels, or 3,260m^2 of solar cells, with 500 being installed on the roof and the remaining 1,190 units being installed on-site or nearby. The required number of PV units to allow for the building to reach net zero energy operation made this PV installation challenging demonstrating the difficulty of achieving net zero energy operation of a MURB with on-site generation.

Economic analysis of the net zero energy retrofit was conducted by calculating the Tolerable Capital Cost under a range of interest rates (3, 6, 9%), electricity price escalation rates (2, 5, 10%) and acceptable payback periods (10, 20, 30 years). The results of the TCC method allowed determination at what price the net zero energy retrofit would be economically feasible.

It was concluded from this research that:

- Simple and readily available technological upgrades can result in significant energy savings,
- Net zero energy status can be achieved through aggressive energy efficiency measures,
- Net zero operation can be achieved through the installation of renewable energy, such as photovoltaics, and,
- The TCC method allows for decision makers to determine at what price the net zero energy retrofit will be economically feasible.

11. REFERENCES

Attia, S, 2018. Net Zero Energy Buildings (NZEB): Concepts, Frameworks and Roadmaps for Project Analysis and Implementation. UK/USA: Butterworth-Heinemann (Elsevier).

Asaee, SR, Ugursal, VI, Beausoleil-Morrison, I, 2019. Development and analysis of strategies to facilitate the conversion of Canadian houses into net zero energy buildings. Energy Policy. 126:118-130.

CEC, 2019. Non-residential ACM Reference Manual Appendices, Appendix 5.4B.
https://www.energy.ca.gov/files/2019-nonresidential-acm-reference-manual-appendices

CMHC, 2015. About Your House Net-Zero Energy Housing. Ottawa, Canada: Canada Mortgage and Housing Corporation. https://www.chba.ca/CHBADocs/CHBA/NZE/2018_CMHC-NZ.pdf

Energy Hub, 2020. Complete Guide for Solar Power in Nova Scotia. https://www.energyhub.org/nova-scotia/

EnergyPlus, 2022. Introduction to EnergyPlus. https://energyplus.net/

Jinsung, B, Insung H, Byoungjoo L, Sehyun, P, 2013. Intelligent household LED lighting system considering energy efficiency and user satisfaction. IEEE Transactions on Consumer Electronics, 59(1), 70-76.

Nauss, C, 2022. Techno-economic feasibility of a net-zero energy retrofit for a multi-unit residential building in Halfax, Nova Scotia. Halifax: Dalhousie University. MASc Thesis.

NRCan, 2018. Energy Use Data Handbook, 2000 to 2018. Ottawa: Office of Energy Efficiency, Natural Resources Canada.

NRCan, 2010. Home Lighting Design Guide Pocket Book: Energy Efficiency Reference Guide. Ottawa: Natural Resources Canada.

NRCan, 2019a. Energy Consumption of Major Household Appliances Shipped in Canada, Trends for 1990-2016. Ottawa: Natural Resources Canada. http://oee.nrcan.gc.ca/publications/statistics/aham/2016/

NRCan, 2019b. Energy Efficiency: Electronics. Ottawa: Natural Resources Canada. https://www.nrcan.gc.ca/energy/products/categories/electronics/13710

NRCan, 2019c. Energy Efficiency: Water Heaters. Ottawa: Natural Resources Canada.

Nikoofard, S, Ugursal, VI, & Beausoleil-Morrison, I, 2014. Technoeconomic Assessment of the Impact of Window Improvements on the Heating and Cooling Energy Requirement and Greenhouse Gas Emissions of the Canadian Housing Stock. Journal of Energy Engineering, 140(2), 04013018.

Nikoofard, S, Ugursal, VI, & Beausoleil-Morrison, I, 2015). Economic Analysis of Energy Upgrades Based on Tolerable Capital Cost. Journal of Energy Engineering, 141(3), 06014002.

NREL, 2022. PVWatts Calculator. https://pvwatts.nrel.gov/pvwatts.php

OpenStudio, 2022. Introduction to OpenStudio. https://openstudio.net

Radiance, 2022. About Radiance. https://www.radiance-online.org/about

US DOE, 2015. A Common Definition for Zero Energy Buildings. U.S. Department of Energy.

#65: Enthalpy determination of phase change material objects by mixing calorimeter

Rajkumar YADAV[1], Nidhi AGRAWAL[1], Harald MEHLING[2], Nalin ARORA[1], Samit JAIN[1]

[1]Pluss Advanced Technologies Pvt. Ltd., B-205, Pioneer Urban Square, Sector 62, Gurgaon 122101, India, rajkumar.yadav@pluss.co.in
[2]Consultant, Weingartenstr, 37, 9702 Würzburg, Germany, harald.mehling@gmail.com

Abstract: Phase change materials (PCMs) store heat or cold by changing phase in a narrow temperature range and with high storage density. They are therefore used in many applications for heat or cold storage, also called thermal energy storage (TES). Many applications use the PCMs encapsulated in pouches made of polymeric film or in solid containers made of plastic or metals. Regarding characterisation, encapsulated PCM in for example a pouch is a PCM object that has a storage capacity. The heat stored by a PCM object could be calculated from the amount of PCM contained in it, but more reliable is a direct measurement as the PCM could change with time by phase separation, or show less supercooling due to larger mass. The heat stored in different types of PCM objects was determined directly using the mixing calorimeter method. For comparison, the heat stored by the PCMs only was also determined using a 3-layer calorimeter (3LC). In addition, the thermal conductivity was determined by the hot-wire method to see if it affected the results. The different methods, setups, measurement and evaluation procedures are described in the paper. The effects of different PCM and encapsulation types were studied. Commercial PCMs and PCM objects, products of Pluss Advanced Technologies Pvt. Ltd., were used in the study. The PCMs were water (to test the setups), organic PCMs of 46°C and 65°C temperatures, and inorganic PCMs of 48°C and 72°C, and the encapsulations were stainless steel balls and HDPE tabs. The heat stored, as measured on the PCM objects, was in good agreement with the cumulative value expected from measurements of PCM alone and literature data of the encapsulation material. The results showed that the mixing calorimeter method reliably presented the heat stored by a PCM object in the desired temperature range. The different thermal conductivities of PCMs did not significantly affect the experiment time of PCM object testing.

1. INTRODUCTION

Thermal energy storage, often also called heat and cold storage depending on the application, plays a crucial role in the energy system and in many common situations. Three basic effects can be used: just raising the temperature of a material as it is, changing its phase, or changing its composition. Just raising the temperature of a material is the effect most frequently used, even in everyday life. The associated heat is also called sensible heat, because the temperature change can be sensed easily. In technical applications solids or liquids are used; the heat stored in gases is comparatively small. If using a phase change, the usual method is between solid and liquid (also called melting and solidification), less often between different solid phases. In contrast to phase change involving a gas phase, these allow the storage of considerable amounts of heat at low pressure and small volume. In addition, these phase changes typically occur in a narrow temperature range. If phase change is at a single temperature, the heat is also called latent heat because it cannot be felt in absence of a temperature change. Materials that are able to store a significant amount of heat by changing phase are called Phase Change Material (PCM), often also latent heat storage material (even if some temperature change is involved). The ability to store a significant amount of heat by changing phase in a small temperature range results in two main fields of use: heat storage (also called thermal energy storage) with high storage density (per unit mass or volume) in a small temperature interval, and passive temperature stabilization (temperature control). Because of these advantages, PCMs are used today in a wide range of applications: in buildings for space heating and cooling as well as to prepare domestic hot water, in logistics, specifically the cold chain, for heating or cooling of the human body, even including medical applications, in mobility, in electronics, as well as industrial processes (Mehling *et al.*, 2022).

The most common PCM is water, changing phase between solid and liquid at 0°C. For many other temperatures other materials are used, e.g. eutectic salt-water mixtures, salt hydrates, salts, paraffins, fatty acids, and alcohols. In an application the PCM is usually encapsulated to avoid loss of the PCM, e.g. the liquid phase flowing away, also to avoid contact with the ambient, and last but not least, encapsulations also serve as heat storage module. Encapsulations vary in size and shape, and capsule wall material. Typical encapsulations of macroscopic size, having dimensions of a few to many centimetres, are flat or spherical containers with plastic or metallic walls, or pouches made from polymer film. They are used in transport boxes for the cold chain, storage for heating and cooling in buildings, even storage in industrial processes, as a module with a fixed capacity to store heat or cold.

The capacity to store heat is the main property of macro-encapsulated PCM. It can simply be calculated from the material properties of the PCM and its amount, and respectively the same for the encapsulation material. However, the properties of the PCM could change with the amount of PCM encapsulated, specifically the degree of supercooling, they could change with time, e.g. by phase separation, or its amount could change by leakage. Further, its properties might not be known at all if macro-encapsulated PCM is bought. Direct measurement of the stored heat on macro-encapsulated PCM is thus more reliable than simple calculation, sometimes even the only option. Doing direct measurements is part of quality control and crucial when buying.

The capacity to store heat in materials is commonly described by the specific heat capacity, for PCM also the latent heat, specific per mass or volume. These are material properties determined on a sample of suitable size. Methods to determine the heat stored are called calorimetric methods. Commonly used for PCM are differential scanning calorimetry (DSC), T-history, and 3-layer calorimetry, or modified heat flow meters (PCM-RAL, 2018: page 25). In contrast, a macro-encapsulated PCM is not a material but instead it is an object (Günther *et al.*, 2006, PCM-RAL, 2018: page 7), so calorimetric measurements must be done on it as a whole, on the whole pouch. However, this is quite difficult. Ideally, the determination of the capacity to store heat, which has to cover a temperature range that includes the phase change, is as a function of temperature. This is because the capacity to store heat strongly varies with temperature due to the phase change. Ideally, measurements give a resolution in the order of 1°C. When doing a calorimetric measurement, the heat flux into or out of a sample is associated inevitably with a heat flux within it, and therefore a temperature gradient. Because of this temperature gradient heat exchanged by the sample can only be attributed to a sample temperature within some temperature range. This effect increases with the heating or cooling rate, as well as sample mass and dimensions (Mehling *et al.*, 2006). For PCM the effect is already relevant in small samples, so even for common DSC measurements on small samples, a heating rate test is needed for good temperature resolution (Mehling *et al.*, 2006, Günther *et al.*, 2006). Heating rate tests are thus required in measurement standards, for DSC (Gschwander *et al.*, 2015) as well as general ones (PCM-RAL, 2018: page 26-28). Calorimetric measurements on whole PCM objects can be carried out with modifications of the above methods on larger samples (PCM-RAL, 2018: page 34, Göbel *et al.*, 2017). For a good temperature resolution, very small heating and cooling rates are however needed for large samples; this makes the development of such modified measurement setups difficult. For this reason, larger PCM objects are often measured by more simple methods that give less temperature resolution or even none at all. An example is the "twin bath" method. It consists of measuring and comparing heating loads of two identical thermostatic baths, one with the encapsulated PCM, the other without (Demirel and Paksoy, 1993, Paksoy, 1996). Straightforward is another method: using heat storage with the PCM object as the heat storage module, and air or water as the heat transfer medium. By integrating the heating/cooling power from initial to final storage temperature, the heat stored between these two temperatures can be calculated (Günther *et al.*, 2006, Günther *et al.*, 2009). The simplest setup, and moreover extremely flexible regarding sample size and shape, is a mixing calorimeter. Here the sample exchanges heat with a reference medium, commonly a liquid, and the heat stored by the sample between initial and final temperature is calculated from the same for the reference (Walcher, 1985, Zheng *et al.*, 2013).

In this paper, we describe the setup of a mixing calorimeter for measurements on macro-encapsulated PCM, results on measurements on four different PCM in two different encapsulations, and a comparison of the results with calculations from measurements on the two PCM by a T-history, respectively 3-layer calorimeter. In addition, the thermal conductivity of the PCM was measured, and its effect on the results of the calorimetric measurements on the macro-encapsulated PCM is discussed.

1. MATERIALS / SAMPLES

Four different PCMs were encapsulated in 2 different encapsulations giving 8 samples in total (all PCM and encapsulations were commercial products of Pluss Advanced Technologies). The four PCMs investigated were the two inorganic, hydrated salt (HS) PCMs HS48 and HS72, and the two organic mixture (OM) PCMs OM48 and OM65. The two macro-encapsulations were ThermoTab600 and Stainless Steel (SS) ball of 80mm diameter. The SS ball encapsulation is shown in Figure 1a. It had a diameter of 80mm, a weight of 132g (empty), and a volume of 235ml (internal). The ThermoTab600 is shown in Figure 1b. It had dimensions of 190mm · 120mm · 35mm, a weight of 114g, and a volume of 548ml. PronGO, sav$E$ and other trademarks are the property of respective companies.

PCM	Mass (g)
sav$E$ OM 46	208
sav$E$ OM 65	194
sav$E$ HS 48	270
sav$E$ HS 72	327

PCM	Mass (g)
sav$E$ OM 46	446
sav$E$ OM 65	451
sav$E$ HS 48	640
sav$E$ HS 72	824
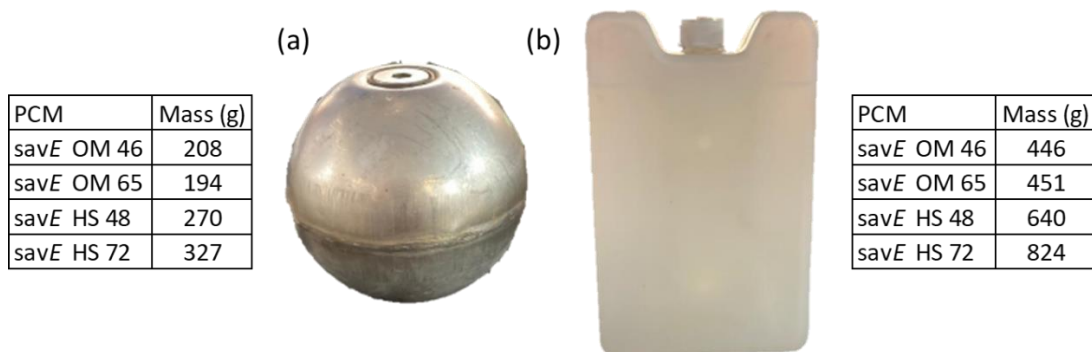
Figure 1: PCM objects; SS ball (a), and ThermoTab600 (b)
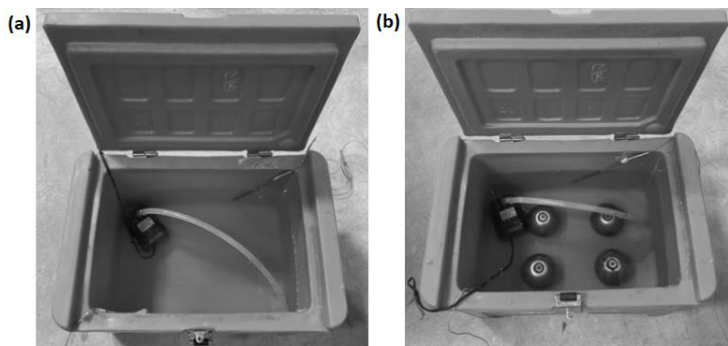
Figure 2: Mixing calorimeter set-up: blank (a) and with PCM objects (b)

2. EXPERIMENTAL METHODS

2.1. Mixing calorimeter to determine the heat stored by encapsulated PCM

Method

In a mixing calorimeter the sample exchanges heat with a reference medium, commonly a liquid. The heat stored by the sample between initial and final temperature is calculated from the same for the reference liquid, for which also its amount and specific heat capacity must be known (Walcher, 1985, Zheng *et al.*, 2013). Ideally, a measurement setup is an adiabatic environment; for a real setup a well-insulated container can be used.

Setup, procedure, and evaluation

Here a well-insulated transport box, PronGo (product of Pluss Advanced Technologies), was used, and demineralised water as the reference medium. Figure 2 shows inside views of the set-up without sample (blank) and with sample (SS balls, 4 numbers). Further on, a datalogger (Process Precision Instruments Pvt. Ltd.), Pt100 RTD temperature sensors (Radix Electrosystem Pvt. Ltd.), and a circulation pump (18W, 780 L/hr output) to stir the reference medium,

water, and a data logger (Columbus Pvt. Ltd.) to record temperature and time data were used. The calculation for enthalpy determination was done by Microsoft Excel. A schematic diagram of the mixing calorimeter setup is shown in Figure 3a.

For preconditioning, a PCM object was put in a water bath, set at a temperature of a minimum of 10°C higher than the phase change temperature (T_{PC}) of the PCM for the freezing enthalpy determination, and lower for the melting enthalpy determination. A measured quantity of water as reference liquid was put in the insulated box. The amount of the reference medium, water, was taken as approximately 10 times the weight of the PCM object to result in well detectable temperature changes. Two ThermoTab600 and four SS Balls PCM objects were used in the experiments to keep the ratio of reference to PCM approximately 10. Two temperature sensors were put in the reference medium, diagonally opposite in corners. The starting temperature of the medium (T_{medium}) was selected 25°C higher and lower than the T_{PC} in case of melting and freezing enthalpy analysis, respectively. Ambient temperature ($T_{ambient}$) was selected 20°C lower than T_{medium}. The temperature sensors were connected to the datalogger. Then, stirring the reference medium, water, in the box with the pump was started. Finally, the PCM objects were immersed in the medium (Figure 2b) to allow heat exchange. The experiment was completed when the thermal equilibrium between the medium and the PCM object was achieved in the box i.e., T_{object} became equal to T_{medium}, an equilibrium temperature (T_{equil}). T_{object} is the starting temperature of the PCM objects.

Water was tested first as a PCM sample in the mixing calorimeter. The trials were performed for 2 hours. The temperature of the medium was recorded as an output from the set-up. Figure 3b shows the temperature profiles of the medium and the PCM objects.
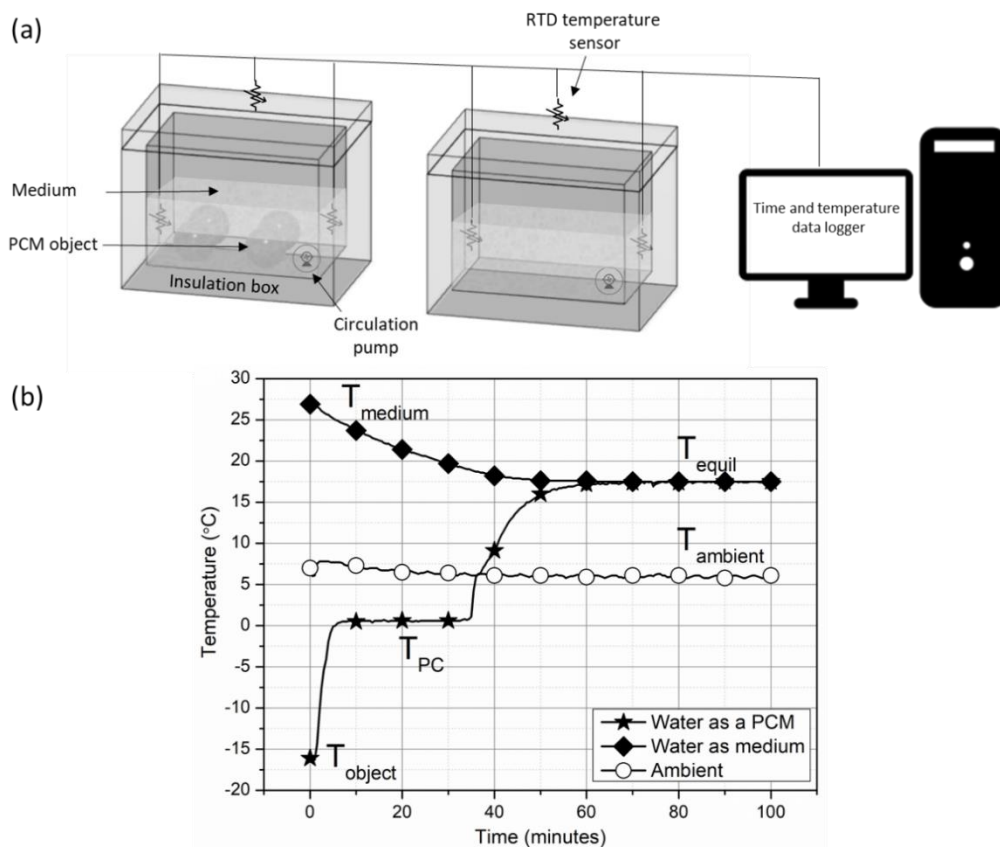
Figure 3: Schematic diagram of the mixing calorimeter set-up (a), and an output graph from a measurement (b) where water was also the PCM in the encapsulation (as indicated by T_{pc} at about 0°C)

A blank trial along with the PCM object sample was also performed in the absence of the PCM object to determine heat exchange of the setup with the ambient (Figure 2a). The experiment was performed for the same duration as with the PCM object. The temperature of the medium, achieved after completion of the trial, was named T_{blank}.

The enthalpy of the PCM was calculated as per the equations explained in the calculation section. It was based on the energy balance between the object tested, the reference medium, and a correction by heat loss to ambient. The sensible heat values of the encapsulation materials were obtained from the literature. The stainless steel (SS ball) and HDPE (ThermoTab600) had a sensible heat value of 0.49 W/m·K and 1.9 W/m·K respectively (Sweet, 1987, Yang et al., 2016).

Calculation

Equation 1: Quantity of heat energy exchanged by the medium with the PCM object, without correction of losses to the ambient (blank).

$$Q_{sample} = m_w \times C_p \times (T_{medium} - T_{equil})$$

Equation 2: Quantity of heat loss to ambient.

$$Q_{blank} = m_w \times C_p \times (T_{medium} - T_{blank})$$

Equation 3: Quantity of stored heat (corrected) of the PCM object in temperature range from T_{object} to T_{equil}.

$$Q_{object} = Q_{sample} - Q_{blank}$$

Equation 4: Quantity of heat energy exchanged by the PCM only.

$$Q_{PCM} = Q_{sample} - Q_{blank} - Q_{encapsulation}$$

Equation 5: Quantity of heat energy exchanged by the encapsulation only.

$$Q_{encapsulation} = m_{w1} \times C_{p1} \times (T_{medium} - T_{equil})$$

Where:

- Q_{sample} = heat exchanged by the medium with the PCM object, without correction of losses to the ambient (blank) (kJ)
- Q_{object} = (corrected) stored heat of the PCM object in temperature range from T_{object} to T_{equil} (kJ)
- Q_{blank} = heat loss to ambient (kJ)
- $Q_{encapsulation}$ = heat exchanged by the encapsulation only (kJ)
- Q_{PCM} = heat exchanged by the PCM only (kJ)
- T_{medium} = initial temperature of the medium (ºC)
- T_{equil} = equilibrium temperature of the PCM object with the medium (ºC)
- T_{blank} = final temperature of the medium in the blank trial (ºC)
- T_{object} = initial temperature of the PCM object (ºC)
- m_w = mass of the water (medium) (kg)
- m_{w1} = mass of the empty encapsulation (kg)
- C_p = liquid specific heat of the water (medium) (kJ/kgºC)
- C_{p1} = specific heat of the encapsulation material (kJ/kgºC)

2.2. 3-Layer Calorimeter (3LC) to determine the heat stored by PCM

Method

The most common method used for calorimetric measurements on PCM is differential scanning calorimetry (DSC) as instruments are available commercially. However, they are expensive. Moreover, DSC typically fit samples in the size of no more than several ten µl, corresponding to several 10mg of PCM, which can significantly affect the result of a measurement for example when measuring salt-hydrates. For this reason, new methods were developed in the past to fit larger samples, and the corresponding equipment is self-built. The most well-known is the T-history method, where a sample is exposed to a sudden temperature step in its ambient, and compared to a reference (typically water) under the same conditions (Zhang *et al.*, 1999). Later an insulation was added to improve measurement results (Lazaro *et al.*, 2006). In a 3-layer calorimeter the same is done, however with two differences: the sample and thermal resistance have a flat geometry (two layers thermal resistance, in between the sample) in contrast to a cylindrical one in the T-history method, and calibration by a reference is done before sample measurement and not in parallel. The 3LC method can use a sample size of as high as 100g but is not limited to.

Setup, procedure, and evaluation

A schematic diagram of the 3LC setup is presented in Figure 4a. It included the 3LC sample box, placed in a temperature-controlled air bath (ambient), the temperature control unit, and a computer with time and temperature data logger. Figure 4b shows a 3LC sample box. A polyurethane foam insulation box was used. The box was covered with an aluminium sheet for uniform heat transfer in the box. A 30g sample was used for the measurement. An air bath (Southern Scientific Pvt. Ltd.) was used to maintain the ambient temperature of the 3LC set-up box. Temperature and time data were recorded using an online data logger (Radix Electrosystem Pvt. Ltd.). The calculation was performed on the Microsoft Excel application.

Figure 4c shows typical 3LC curves, with the sudden temperature step in the air bath (ambient), the resulting temperature development of the reference, and the same of a PCM sample in the melting phase; here it is water. The enthalpy of the sample as shown in Figure 4d was calculated from the 3LC curve. The calculation equations were used as reported in previous literature (Zhang, 1999, Sole *et al.*, 2013).
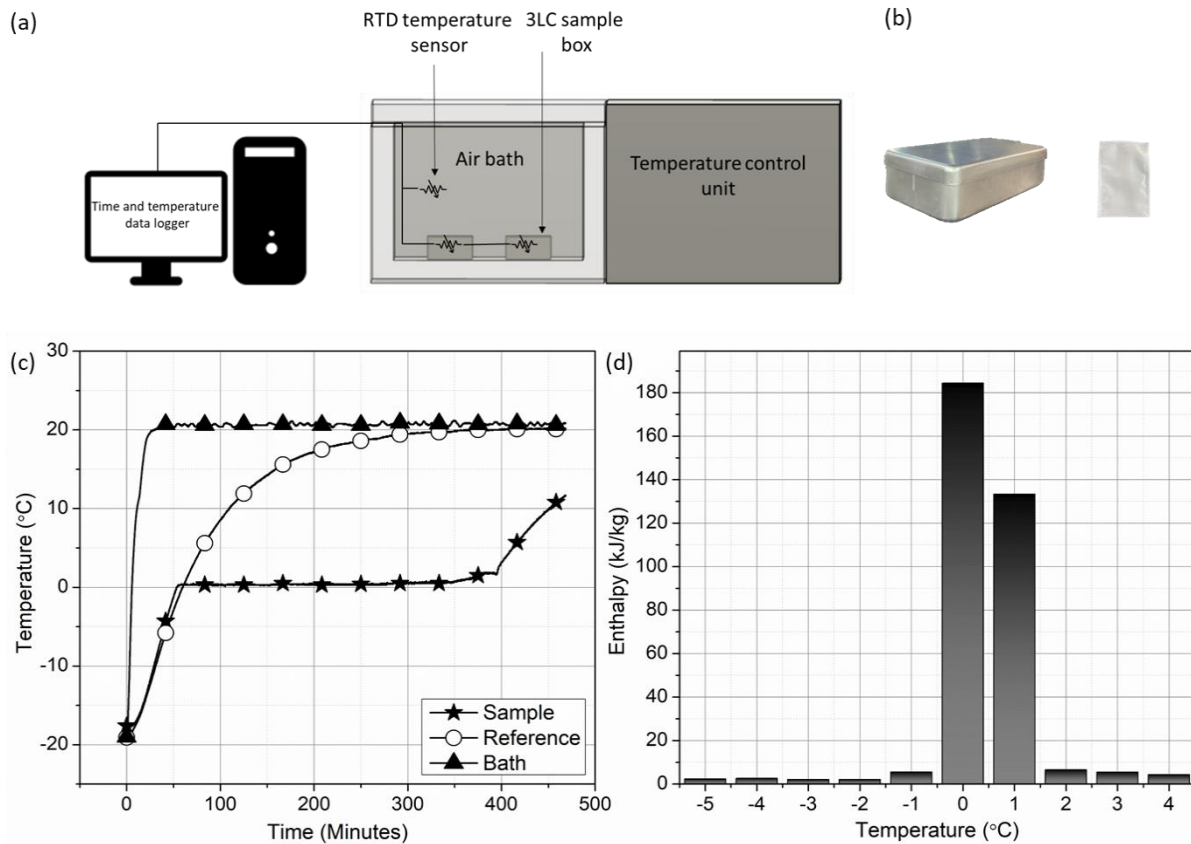
Figure 4: A schematic diagram of a 3LC set-up (a), a 3LC sample box and a sample pouch (b), a typical 3LC curve of a PCM sample in melting phase (c) and an enthalpy curve obtained from 3LC analysis of a PCM in melting phase (d)

2.3. Commercial hot-wire device, KD2Pro, to determine the thermal conductivity of PCM

The thermal conductivity of phase change materials plays an important role in determining their thermal performance in a TES application. The thermal conductivity of a PCM allows understanding the rate of heat ingress and egress from the PCM and PCM object. PCMs have different thermal conductivity in solid and liquid states. When a PCM changes phase from solid to liquid or vice versa, the heat transfer rate changes from the PCM object.

Method

The thermal conductivity of PCMs was determined using the transient hot wire method, which was an accurate, precise technique, and popularly used for various material types. The technique used a thin vertical metal wire (Figure 5) and a step voltage was applied to it. The metal wire acted as electrical heating material and at the same time as a resistance thermometer. Due to a measurement time of approx. 1s, convection plays no role.

Setup, procedure, and evaluation

Here a commercial instrument, the KD2Pro, was used. Figure 5a shows a KS1 type sensor of the equipment which was 60mm long and 0.3mm in diameter. It was used for liquids and thermal insulating materials. TR1 type sensor (Figure 5b) was 100mm long and 2.4mm in diameter and was used for solid, powder, concrete, and rock type materials.
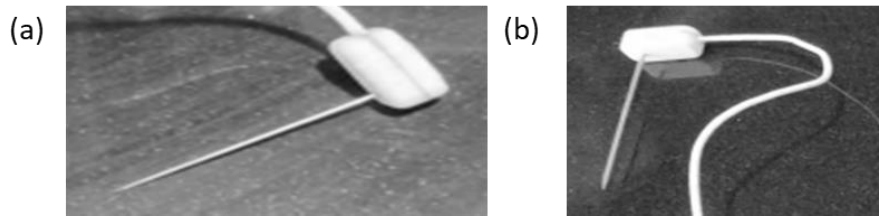
Figure 5: KD2Pro equipment, KS1 sensor (a), and TR1 sensor (b)

3. RESULTS AND DISCUSSION

3.1. Heat stored by PCM, determined using the 3-Layer Calorimeter (3LC)

Table 1 shows the results of the calorimetric measurements on the 4 PCMs, as determined by the 3LC method. Full enthalpy profiles from 3LC measurements are shown in Figure 6, together with results from the mixing calorimeter. The values reported in the Table 1 were the simplified description of the enthalpy profiles shown in Figure 6. The specific heat capacity values were determined by linear fit of the values outside the phase change. The latent heat values were calculated such that they represent a step function with overall the same enthalpy change as the enthalpy temperature function. We performed experiments on two different PCM types; organic mixture (OM) and hydrated salt (HS). Each PCM type had two different temperatures. All the PCMs showed latent heat in a good range and were potential PCMs in high-temperature TES applications and heat recovery.

Table 1: Thermo-physical properties of PCM as determined from the 3LC analysis

PCM	Phase change temperature (°C)	3-layer Calorimeter (3LC)		
		Latent heat (kJ/kg)	Spec. heat capacity (liquid) (kJ/kg·K)	Spec. heat capacity (solid) (kJ/kg·K)
OM46	46	190	2.2	2.6
OM65	65	163	1.6	2.1
HS48	48	176	3.3	3.0
HS72	72	136	2.3	2.0

3.2. Thermal conductivity of the PCM, determined by the hot-wire method

Table 2 shows the thermal conductivity values of the 4 PCMs in their solid and liquid states. Hydrated salt type PCMs had higher thermal conductivity, about twice in both solid and liquid states as compared to organic ones. The higher thermal conductivity of inorganic PCMs was attributed to their smaller molecular size allowing faster movement of molecular thermal motion across directions.

Table 2: Thermal conductivity of PCMs

PCM	Thermal Conductivity in W/m·K	
	Solid	Liquid
OM46	0.20	0.10
OM65	0.22	0.13
HS48	0.44	0.46
HS72	0.58	0.50

3.3. Heat stored by encapsulated PCM, determined by the mixing calorimeter

Calorimetric measurements using DSC, T-history, or 3-layer calorimetry, as done here, characterise PCM alone; the same holds for the thermal conductivity measurements using the hot wire method. A PCM alone is a material; in contrast, a macro-encapsulated PCM is not a material but must be treated as a whole object, i.e. a whole pouch. A PCM might not behave in the same way when it is encapsulated, for example regarding supercooling or phase separation. This makes the measurement on the whole object, for example by a mixing calorimeter, necessary. When measuring the heat stored on an encapsulated PCM, it is important to take into account that the heat stored is not only due to the PCM but also an encapsulation material itself.

Table 3 details the enthalpy (Q_{object}) obtained for the PCM objects in a temperature range from T_{object} at the start of the measurement to T_{equil} at the end (Equation 3 and Table 3). Due to the significant temperature gradient in the encapsulations, and also inherent in the method of a mixing calorimeter, there was no enthalpy as a function of temperature here.

Table 3: Enthalpy data of the 4 PCMs in 2 encapsulations, as determined by the mixing calorimeter

PCM object		T_{object} (°C)	T_{equil} (°C)	Q_{object} (kJ)
	OM46	70.0	38.0	226
SS Ball (4 numbers)	OM65	90.0	40.5	213
	HS48	67.0	49.0	246
	HS72	90.0	41.3	354
	OM46	70.0	33.4	241
ThermoTab600 (2 numbers)	OM65	90.0	35.5	311
	HS48	73.5	38.0	366
	HS72	90.0	42.0	432

Hydrated salts (HS) based PCMs showed comparatively higher enthalpy than organic PCMs. The higher enthalpy of HS PCMs could be attributed to their higher volumetric density as compared to organic ones. T_{object} and T_{equil} could be adjusted according to the requirement of the temperature range of the PCM object use in a TES application. For a cooling measurement, T_{object} should be kept above the phase change temperature of the PCM (T_{PC}) used in the PCM object and T_{equil} should be a lower value than T_{PC}, for a heating measurement reverse. This would ensure a complete phase change of the PCM inside the PCM object.

Enthalpy profiles of the four PCMs from 3LC measurement and mixing calorimeter (Q_{PCM} as per *Equation 4*) are shown in Figure 6, and compared with the enthalpy difference of the PCM alone as determined from the measurement on the encapsulated PCM, taking into account the heat stored in the encapsulation. The results of both methods are given for PCMs cooling phase. The PCM object tests for HS48 in SS Ball encapsulations were repeated three times and showed a variation of 3% (Figure 7). The variation in the repeatability is minimal and is considered highly precise keeping the experimental accuracy in mind. Generally, the enthalpy as predicted by the mixing calorimeter method was in good agreement with the enthalpy profile of 3LC method.

Because measurements with the 3LC, and even more with the mixing calorimeter, were done on large samples, internal temperature gradients in a sample could affect the result of measurements. Despite that, measurements were already done in a way to avoid or at least minimize such effects, a final check was carried out. Since the organic and inorganic PCMs have significantly different thermal conductivity, an effect on the measurement results of the heat stored should show up in a systematic difference in the results of organic and inorganic PCMs. There was no trend in enthalpy values observed with different thermal conductivities of PCMs. There was no significant influence of different PCM types (OM and HS) observed on trial duration.
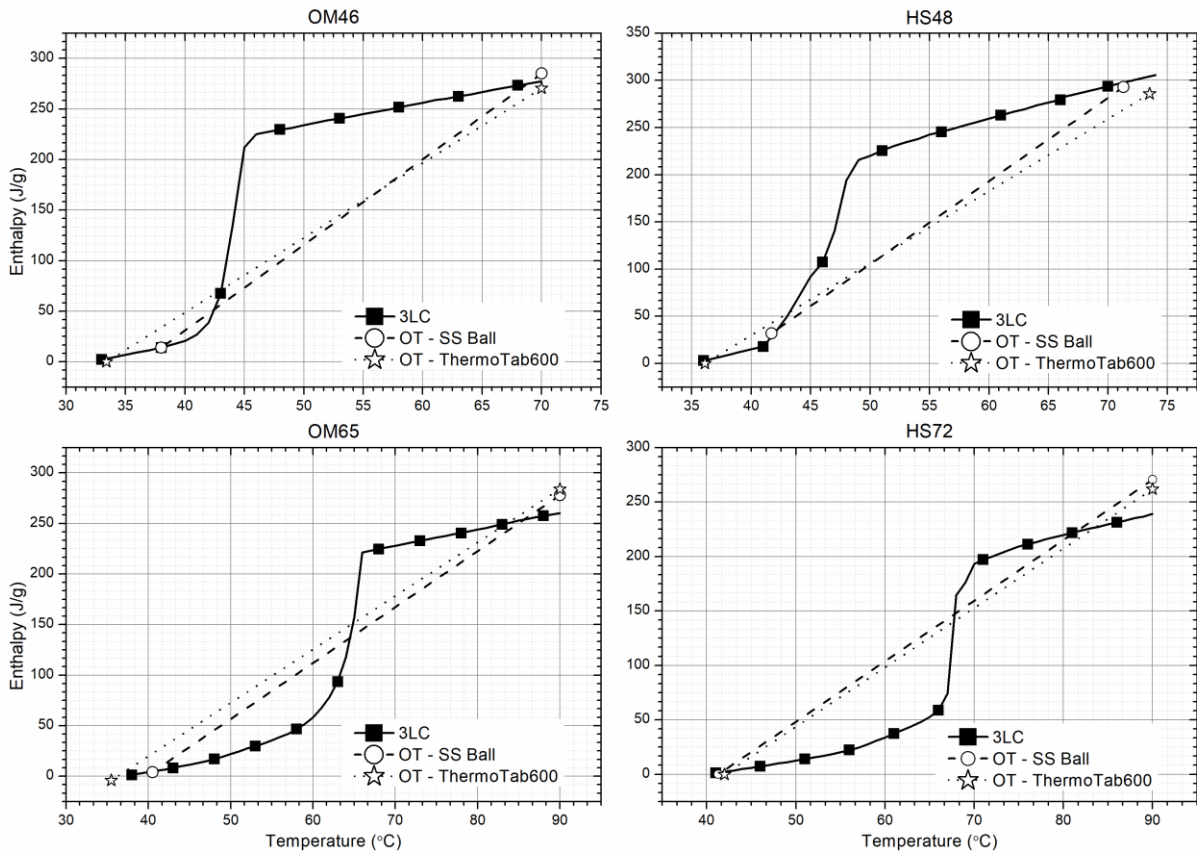
Figure 6: Enthalpy profiles of PCMs only from 3LC and enthalpy differences from mixing calorimeter
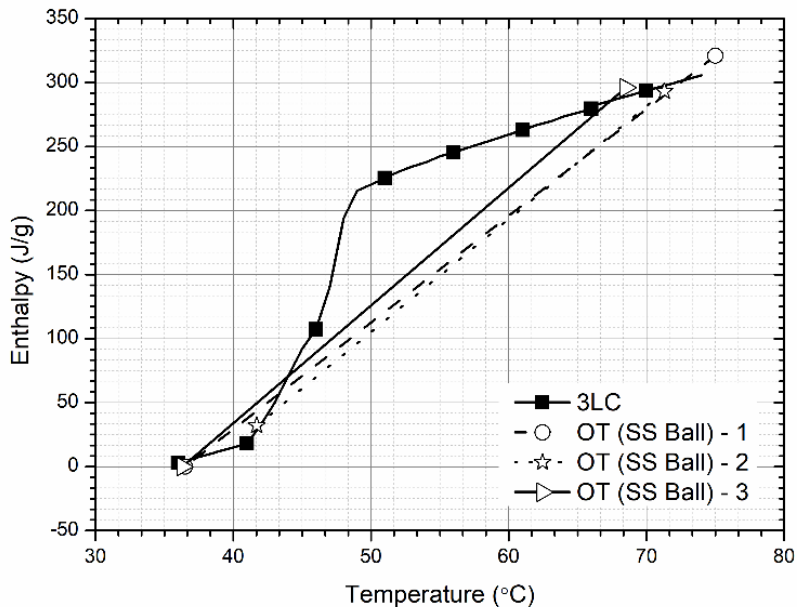
Figure 7: Enthalpy differences of HS48 determined in SS ball using the mixing calorimeter method from multiple trials, and comparison with enthalpy profiles from 3LC method

4. CONCLUSION

The enthalpy of PCM objects was determined by the mixing calorimeter method. The method was successfully tested on 4 PCMs, from two main types of PCMs; organic and inorganic. The enthalpy calculated from the mixing calorimeter matched the value from the 3LC measurement, confirming a reliable enthalpy measurement from the method. The method determined the enthalpy of a PCM object in a temperature range. The temperature range can be selected as

per the object working temperature in a TES application. The study proved that the method was applicable across PCM types, temperatures, and encapsulations geometries. The method duration was much less as compared to the T-history/3LC method. Different thermal conductivity of PCMs showed no significant effect on enthalpy and experiment duration. The PCM investigated here cover a melting point range from 46°C to 72°C; this allowed for the use of water as a reference medium. If temperatures below 0°C were reached in a measurement, the reference medium must be switched from water to perhaps ethylene glycol solution as the reference medium.

5. AUTHOR STATEMENT

Rajkumar Yadav: Conceptualisation, Methodology, Experiments, Software, Characterisation, Writing- Original draft preparation, Data curation, Visualization, Investigation. Nidhi Agrawal: Supervision, Writing- Reviewing and Editing, Visualisation, Investigation. Harald Mehling: Supervision, Writing- Assistance in original draft preparation, Reviewing and Editing. Nalin Arora: Experiments, Characterisation. Samit Jain: Supervision.

6. DECLARATION OF COMPETING INTEREST

The authors report no declarations of interest.

7. ACKNOWLEDGEMENTS

8. REFERENCES

Demirel, Y., Paksoy, H.; 1993. Thermal analysis of heat storage materials. Thermochimica Acta (213), pp. 211-221

Göbel, A., Vidi, S., Klinker, F., Hemberger, F., Brütting, M., Ebert, H.-P., Mehling, H., 2017. Method for the Thermal Characterization of PCM Systems in the Volume Range from 100 ml to 1000 ml. Int J Thermophys (38), p.67 ff., DOI 10.1007/s10765-017-2204-z

Gschwander, S., Haussmann, T., Hagelstein, G., Sole, A., Cabeza, L.F., Diarce, G., Hohenauer, W., Lager, D., Ristic, A., Rathgeber, C., Hennemann, P., Mehling, P., Peñalosa, C., Lazaro, A., 2015. Standardization of PCM Characterization via DSC. 13th International Conference on Energy Storage, Greenstock 2015

Günther, E., Hiebler, S., Mehling, H., 2006. Determination of the heat storage capacity of PCM and PCM-objects as a function of temperature. ECOSTOCK, 2006, Stockton, USA

Günther, E., Hiebler, S., Mehling, H., Redlich, R., 2009. Enthalpy of Phase Change Materials as a Function of Temperature: Required Accuracy and Suitable Measurement Methods. Int J Thermophys (30), p. 1257–1269, DOI 10.1007/s10765-009-0641-z

Lazaro, A., Günther, E., Mehling, H., Hiebler, S., Marın, J.-M. and Zalba, B., 2006. Verification of a T-history installation to measure enthalpy versus temperature curves of phase change materials. Meas. Sci. Technol. 17 (2006) 2168–2174 doi:10.1088/0957-0233/17/8/016

Mehling, H., Brütting, M., Haussmann, T. 2022. PCM products and their fields of application - An overview of the state in 2020/2021. Journal of Energy Storage (51)

Mehling H., Ebert H.-P., Schossig, P., 2006. Development of standards for materials testing and quality control of PCM. 7th IIR Conference on Phase Change Materials and Slurries for Refrigeration and Air Conditioning, France, 2006

Paksoy, H., 1996. Determining thermal properties of heat storage materials using the twin bath method. Energy Convers. Mgmt. vol37, no3, pp261-268

PCM-RAL. 2018. Phase Change Materials - Quality Assurance. RAL-GZ 896, edition 2018.

Solé, A., Miró, L., Barreneche, C., Martorell, I. and Cabeza, L.F., 2013. Review of the T-history method to determine thermophysical properties of phase change materials (PCM). Renewable and Sustainable Energy Reviews, 26, pp.425-436.

Sweet, J.N., Roth, E.P. and Moss, M., 1987. Thermal conductivity of Inconel 718 and 304 stainless steel. International journal of thermophysics, 8(5), pp.593-606.

Walcher, W., 1985. Praktikum der Physik. Teubner, 1985, 5th ed.

Yang, C., Navarro, M.E., Zhao, B., Leng, G., Xu, G., Wang, L., Jin, Y. and Ding, Y., 2016. Thermal conductivity enhancement of recycled high density polyethylene as a storage media for latent heat thermal energy storage. Solar Energy Materials and Solar Cells, 152, pp.103-110.

Zhang Y. and Jiang Y., 1999. A simple method, the-history method, of determining the heat of fusion, specific heat and thermal conductivity of phase-change materials. Measurement Science and Technology, 10(3), p.201.

Zheng, Y., Zhao, W., Sabol, J.C., Tuzla, K., Neti, S., Oztekin, A., Chen, J.C., 2013. Encapsulated phase change materials for energy storage – Characterization by calorimetry. Solar Energy 87 (2013) 117–126

#66: Artificial intelligence assessment of energy efficiency of different refrigerants at low temperatures for storage unit using in medicine

Elif Altintas[1], Ali Kose[2], Alişan Gönül[3], İsmail Cem Parmaksizoglu[4]

[1]Haliç University, Faculty of Engineering, Department of Software Engineering, Istanbul
elifaltintaskahriman@halic.edu.tr
[2]Istanbul Gedik University, Faculty of Engineering, Department of Mechanical Engineering, Istanbul
ali.kose@gedik.edu.tr
[3]Siirt University, Department of Engineering, Faculty of Engineering, Department of Mechanical Engineering, Siirt,
alisan.gonul@siirt.edu.tr
[4]Istanbul Technical University, Faculty of Engineering, Department of Mechanical Engineering, Istanbul,
parmaksizo@itu.edu.tr

Abstract: Nowadays, as a result of the globalisation of epidemics, serious progress is being made in the vaccine sector. However, the storage and distribution of these vaccines to countries is as important as their production. At the same time, more human loss is caused by cancer diseases. It is important to examine cancer cells and to store them under appropriate conditions for studies in this field. In this sense, the cooling cycle is a system that can be used to store vaccines and some types of cancer cells in suitable conditions. This work analyses numerically the energy behaviour of a storage unit designed to be used with R134a, R1234yf, R502, and R717 at low temperatures between 201K and 259K. These data were examined with the help of mathematical formulations of thermodynamics to make an exergy analysis using Engineering Equation Solver (EES) program. Additionally, these applications of energy analysis are important and necessary in terms of sustainability and climate change. For this reason, the Artificial Neural Network (ANN) model was used to forecast different types of energy efficiency problems; a method capable of identifying complex non-linear relationships between input and output data sets. This study proposes a new procedure to identify the structure and parameters of the hidden layer, which can apply the feedforward ANN model to the model and proves the potential of this type of model for thermodynamic values. We compare a model based on an artificial neural network (ANN) with a model based on the principles of thermodynamics as an audit and prediction tool to predict exergy destruction of the cooling cycle system by applying different neural network architecture types. This ANN is trained by using temperature and mass flow as inputs. The results obtained from the method are also compared to the input-output model predictions with good accuracy.

1. INTRODUCTION

Cooling technology absorbs heat from the environment to be cooled to low temperatures and transmits heat to the environment at higher temperatures, creating a cold environment at low temperatures. Cooling systems are widely used in warehouses for vaccine storage in the healthcare industry. The fluid used for cooling in the system has important effects on parameters such as the sustainability of the system, cooling performance and environmental impact. Alexis et al. investigated the performance of an ejector cooling system whose solar panels were driven by R134a as the refrigerant (Alexis, 2005). As a result, they found the COP (coefficient of performance) value between 0.014 and 0.101 by operating between -10 degrees and 0 degrees as the evaporator temperature. Zegenhagen in their study, aimed to derive a simple method representing the operating characteristics of a jet-ejector cooling system for varying boundary conditions, preferring R134a as the fluid (Zegenhagen, 2015). Considering the studies in the literature, although the ozone depletion potential (ODP) of the R134a fluid, which is widely used in many sectors, is zero, its global warming potential of 1430 has led to the search for other fluids to reduce the greenhouse effect (Mota-Babiloni, 2017). Minor shared that the use of R1234yf fluid had environmental properties that would have a long-term positive impact on climate change and was compatible with a smooth and cost-effective transition to existing R134a technology (Minor, 2008). Pabon stated that one of the important current problems faced by cooling systems was the use of refrigerants with high GWP values (Pabon, 2020). In their study, they suggested that the R1234yf fluid, with a GWP value of less than 1 and a low contribution to the greenhouse effect, should be used in cooling technologies. Li et al. compared the energy efficiency of R717, R600, R1234yf, and R134a fluids used in domestic refrigerators (Li, 2019). As a result of their studies, they found that R717 fluid had the highest cooling capacity. They also stated that R1234yf could be an ideal drop-in alternative to R134a for an existing refrigerator due to its similar system performance to R134a. R502 fluid, on the other hand, had a high cooling capacity and was widely used in low-temperature vapour compression refrigeration plants until the end of the 90s (Aprea, 1996). With the Montreal Convention accepted in 1987, the reduction of the use of hydrofluorocarbons (HFC) fluids, which damage the ozone layer of the atmosphere, came to the fore. In 1997, the Kyoto Protocol was signed by many important countries, as the Montreal Convention was developing, which proposed the reduction of CO_2 and other gases which cause the greenhouse effect. With the Paris Climate Agreement signed in 2016 and the United Nations Climate Change Summit held in 2019, the decisions taken to ban fluids that damage ozone and to reduce those that cause global warming have been universalized. In this context, instead of refrigerants with high ODP and GWP values, such as R502, which has been widely used in the literature in the past, alternative fluids are widely researched ((Xuan, 2005), (Arcaklıoğlu, 2005), (Akhilesh, 2008), (Soni, 2021), (Mishra, 2022)).

Kasi et al. stated that higher energy efficiency would be achieved by preferring cascade systems instead of single-stage systems to reach low temperatures (Kasi, 2021). Arafat et al. (2015) mentioned that the improvements made in the cooling systems used in the food, pharmaceutical and vaccine industries can significantly reduce energy shortages and energy hikes and bring an important solution to greenhouse gas emissions (Arafat, 2015). Chojnacky et al. (2010) investigated the cooling effect of refrigerators by performing tests on vaccines kept in medical providers' refrigerators from 2°C to 8°C (Chojnacky, 2010). Santos et al. compared Pfizer, Moderna, CoronaVac, Oxford AstraZeneca, Janssen COVID 19, and Sputnik V. refrigerant fluid options for each storage condition, thermal load to cool each type of vaccine, and environmental impacts of refrigerants. They calculated the total equivalent warming impact and the amount of carbon dioxide produced in the cooling systems where they used R134a, R449a, and R508B fluids. In Table 1, storage temperatures and fluids used in cooling systems are shared according to vaccine types. Considering the high amount of CO_2 created when vaccine storage technologies are used, linking it with energy efficiency and sustainability would be of worldwide importance (Santos, 2021).

Table 1: Storage temperatures according to vaccine types and the type of fluid used in the cooling cycle (Santos, 2021)

Vaccine Storage	Temperature (℃)	Refrigerant Type
Pfizer–BioNTech	-70	R508B & R449A
Moderna	-25	R449A
CoronaVac	2	R134A
Oxford–AstraZeneca	2	R134A
Sputnik V	-18	R449a
Janssen COVID-19	2	R134a

With the development of technology, the methods used in the analysis have changed and progressed. ANN is one of the methods used with these developments. It helps to gain different interpretations and fast processing time with artificial neural networks by processing experimental data. One of these studies was conducted by Yilmaz and Atik, with power consumption, thermal efficiency, and coefficient of performance (COP) of the system in various cooling capacities being examined theoretically by using the data acquired with experimental results using ANN (Yilmaz, 2007). Chouai et al. used the potential application of artificial neural networks (ANN) to represent PVT data within their experimental uncertainty, and then obtain, by numerical derivatives, other thermodynamic properties (Chouai, 2002). Belman-Flores et al. applied ANN techniques to compare the energy of three refrigerants: R134a, R450a, and R513a in terms of the cooling capacity, the power consumption, and the coefficient of performance, as a function of the evaporating temperature and the condensing temperature (Belman-Flores, 2017). Additionally many refrigerant mixtures and their thermodynamic properties have been examined with ANN by Arcaklıoğlu, E. (2004), Sözen A. et al. (2009), Hosoz, M. and Ertunc, H. (2006), Ahmed, R. et al. (2021), and Altintas, E. et al. (2021).

This study was carried out to determine the exergy efficiency of the preferred fluids in the cooling systems used for vaccine storage in the health sector between 201K and 259K and the working ANN algorithms of the exergy destruction caused by the refrigerants.

2. MATERIAL AND METHOD

In this section, the details of the cooling system are presented, see Figure 1. The design of the Artificial Neural Network, which determines the approach of the produced exergy destruction values, is also presented.

2.1. Cooling System

The schematic representation of the cooling system is shown in Figure 1. Calculations with the mass flow rate corresponding to 5 different compressor volumetric flow rates (0.01, 0.15, 0.20, 0.25, and 0.30 m³/s) and temperature range between 201K and 259K, with the help of the EES program, have been made. Calculations were made with 4 different refrigerants R134a, R1234yf, R502, and R717 in the determined cooling system.
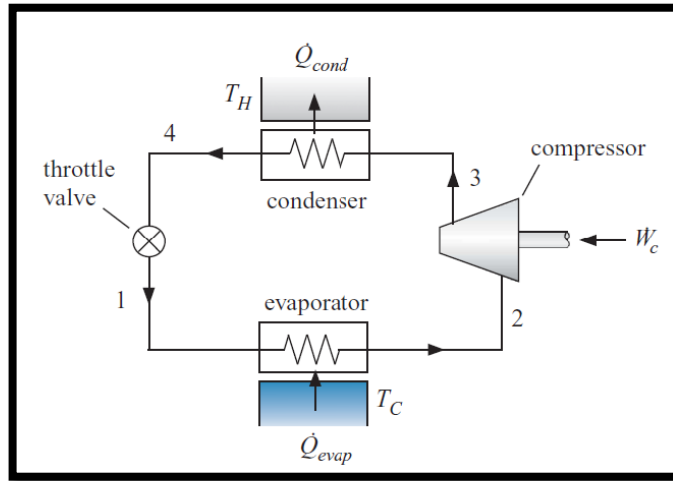
Figure 1: Cooling system

In this study evaporator approach temperature difference, condenser approach temperature difference, degree of superheating and degree of subcooling were kept constant at 5K. In addition, the preferred compressor was the air cooling type, the compressor efficiency (η_{comp}) was 0.78 and the compressor volumetric efficiency (η_{vol}) was 0.75. The temperature value of the air-type condenser in the outdoor environment was accepted as 310K in all cases.

2.2. Thermodynamic Analysis

In this section, exergy destructions and exergy efficiency calculations will be shared to be used for R134a, R1234yf, R502, and R717. The losses that occurred in mass flow rates throughout the system were neglected. The mass flow rate of the system is expressed in $\dot{m}$ (kg/s).

The temperature of the outside environment (T_L), the temperature ranges of the storage where the vaccines would be stored (T_H), the compressor volumetric flow rates ($\dot{V}_{disp}$) to be worked on, and the types of refrigerants, which were determined as the boundary conditions, are shown in Table 2.

Table 2: System details

Parameters	Details
Outdoor Temperature (T_H)	300 K (constant)
Storage Temperature (T_L)	201-259 K (30 different values)
Compressor Flow Rates ($\dot{V}_{disp}$)	0.01, 0.02, 0.03, 0.04, and 0.05 m^3/s
Refrigerants	R134a, R1234yf, R502, and R717

The heat drawn by the evaporator ($\dot{Q}_{evap}$) used in the cooling system from the vaccine storage unit was calculated with the help of Equation 1 where $\dot{m}$ represents mass flows and h enthalpy values:

$$\dot{Q}_{evap} = \dot{m} * (h_2 - h_1) \tag{1}$$

The entropy generation in the evaporator ($\dot{S}_{12}$) was found with the help of Equation 2 where h represents specific entropy value:

$$\dot{S}_{12} = \dot{m} * (s_2 - s_1) - \dot{Q}_{evap}/T_L \tag{2}$$

The power transferred by the compressor used ($\dot{W}_{comp}$) in the cooling system to the refrigerant was calculated with the help of Equation 3:

$$\dot{W}_{comp} = \dot{m} * (h_3 - h_2) \tag{3}$$

The entropy value produced in the compressor ($\dot{S}_{23}$) was found with the help of Equation 4:

$$\dot{S}_{23} = \dot{m} * (s_3 - s_2) \tag{4}$$

The heat value of the condenser ($\dot{Q}_{cond}$), which was located in the outdoor unit of the cooling system and used to remove heat from the fluid to the external environment, was calculated with the help of Equation 5:

$$\dot{Q}_{cond} = \dot{m} * (h_3 - h_4) \tag{5}$$

The entropy value generation in the compressor ($\dot{S}_{34}$) was found with the help of Equation 6:

$$\dot{S}_{34} = \dot{m} * (s_3 - s_4) + \dot{Q}_{cond}/T_H \tag{6}$$

The mass flow rate of the system was calculated with the help of Equation 7. Mass flow rates were obtained according to 5 different compressor volumetric flow rates ($\dot{V}_{disp}$) and the relevant flow rates were used as input parameters in the ANN. In Equation 7, v represents specific volume:

$$\dot{m} = \dot{V}_{disp} * \frac{\eta_{vol}}{v_2} \tag{7}$$

The enthalpy value in the throttling valve($\dot{S}_{41}$) was considered equal before and after the valve ($h_4 = h_1$). The entropy generation in the throttling valve was calculated with the help of Equation 8:

$$\dot{S}_{41} = \dot{m} * (s_4 - s_1) \tag{8}$$

The total entropy production of the system ($\dot{S}_{gen}$) was found by summing the entropy values produced for each component, as seen in Equation 9:

$$\dot{S}_{gen} = \dot{S}_{12} + \dot{S}_{23} + \dot{S}_{34} + \dot{S}_{41} \tag{9}$$

The total exergy destruction of the system was found with the help of Equation 10. Here, T_0 value was the temperature at which the system was in equilibrium with the environment, which was expressed by the dead state temperature. In this study, the dead state temperature was accepted as 300K:

$$Ex_{dest} = T_0 * \dot{S}_{gen} \tag{10}$$

The calculation of the COP (Coefficient of Performance) value is shared in Equation 11:

$$COP = \frac{\dot{Q}_{evap}}{\dot{W}_{comp}} \tag{11}$$

The COP reversible value, which will be calculated by considering the Carnot efficiency of the system, was calculated with the help of Equation 12:

$$COP_{carnot} = \frac{T_L}{T_H - T_L} \tag{12}$$

The exergy efficiency of the system was calculated with the help of Equation 13:

$$\eta_{ex} = \frac{COP}{COP_{carnot}} \tag{13}$$

With 5 different flow rates in the temperature range of 201-259 K using the EES program, the exergy destruction values calculated using 4 different fluids are shown in Table 3. In the exergy destruction calculations, the near ambient temperatures (surface temperature) were accepted at ambient temperatures.

Table 3: The results of thermodynamic analysis of the cooling system

	R134a		R1234yf		R502		R717			R134a		R1234yf		R502		R717	
T (K)	Mass Flow (kg/s)	Exergy Dest (W)	Mass Flow (kg/s)	Exergy Dest (W)	Mass Flow (kg/s)	Exergy Dest (W)	Mass Flow (kg/s)	Exergy Dest (W)	T (K)	Mass Flow (kg/s)	Exergy Dest (W)	Mass Flow (kg/s)	Exergy Dest (W)	Mass Flow (kg/s)	Exergy Dest (W)	Mass Flow (kg/s)	Exergy Dest (W)
201	0.001455	155.79	0.002525	220.05	0.006544	543.3	0.0003318	325.2	231	0.01074	654	0.01546	778.8	0.0336	1608	0.00247	1217.7
201	0.002182	233.67	0.003787	330	0.009816	815.1	0.0004977	487.5	231	0.01611	981	0.02319	1168.2	0.05039	2412	0.003706	1826.7
201	0.002909	311.7	0.00505	440.1	0.01309	1086.6	0.0006636	650.1	231	0.02148	1308	0.03092	1557.6	0.06719	3216	0.004941	2435.4
201	0.003636	389.4	0.006312	550.2	0.01636	1358.4	0.0008295	812.7	231	0.02685	1635	0.03865	1947	0.08399	4020	0.006176	3045
201	0.004364	467.4	0.007575	660.3	0.01963	1629.9	0.0009954	975.3	231	0.03222	1962	0.04638	2336.4	0.1008	4824	0.007411	3654
203	0.001702	175.47	0.002906	244.32	0.007426	594.6	0.000388	362.4	233	0.01199	703.2	0.01711	830.1	0.03684	1698.3	0.002763	1302.6
203	0.002553	263.22	0.004358	366.6	0.01114	891.9	0.0005819	543.9	233	0.01799	1055.1	0.02567	1245.3	0.05526	2547.3	0.004145	1954.2
203	0.003404	351	0.005811	488.7	0.01485	1189.2	0.0007759	725.1	233	0.02399	1406.7	0.03422	1660.5	0.07368	3396	0.005526	2605.5
203	0.004255	438.6	0.007264	610.8	0.01856	1486.5	0.00009699	906.3	233	0.02999	1758.3	0.04278	2075.7	0.0921	4245	0.006908	3249
203	0.005106	526.5	0.008717	732.9	0.02228	1783.8	0.001164	1087.5	233	0.03598	2109.9	0.05133	2490.6	0.1105	5094	0.008289	3909
205	0.001983	196.92	0.003333	270.36	0.008403	648.9	0.0004519	402.9	235	0.01336	754.8	0.0189	883.2	0.04032	1790.1	0.003083	1390.5
205	0.002975	295.38	0.005	405.6	0.0126	973.2	0.0006779	604.5	235	0.02005	1131.9	0.02835	1324.8	0.06049	2685	0.004625	2085.9
205	0.003967	393.9	0.006666	540.6	0.01681	1297.8	0.0009039	805.8	235	0.02673	1509.3	0.0378	1766.4	0.08065	3579	0.006166	2781.3
205	0.004958	492.3	0.008333	675.9	0.02101	1622.1	0.00113	1007.4	235	0.03341	1886.7	0.04725	2208	0.1008	4476	0.007708	3477
205	0.00595	590.7	0.009999	811.2	0.02521	1946.4	0.001356	1208.7	235	0.04009	2264.1	0.0567	2649.6	0.121	5370	0.0925	4173
207	0.002303	220.14	0.003812	283.23	0.009482	705.9	0.0005246	446.4	237	0.01486	807.9	0.02083	937.5	0.04407	1883.4	0.003433	1481.4
207	0.003454	330.3	0.005718	447.3	0.01422	1059	0.0007869	669.6	237	0.02229	1211.7	0.03125	1406.1	0.0661	2825.1	0.00515	2221.8
207	0.004605	440.4	0.007623	596.4	0.01896	1412.1	0.001049	892.5	237	0.02971	1615.8	0.04167	1875	0.08813	3768	0.006866	2962.5
207	0.005757	550.5	0.009529	745.5	0.02371	1765.2	0.001312	1115.7	237	0.03714	2019.6	0.05208	2343.6	0.1102	4707	0.008583	3702
207	0.006908	660.3	0.01144	894.6	0.02845	2118	0.001574	1338.9	237	0.04457	2423.4	0.0625	2812.5	0.1322	5649	0.0103	4443
209	0.002664	245.22	0.004346	327.9	0.01067	766.2	0.0006068	492.9	239	0.01648	862.8	0.02292	993	0.04807	1977.9	0.003817	1574.7
209	0.003996	367.8	0.006519	492	0.01601	1149.3	0.0009103	739.2	239	0.02472	1294.2	0.03438	1489.8	0.07211	2967	0.005722	2361.9
209	0.005327	490.5	0.008692	656.1	0.02134	1532.4	0.001214	985.5	239	0.03296	1725.6	0.04584	1986.3	0.09615	3957	0.007629	3150
209	0.006659	613.2	0.01087	819.9	0.02668	1915.5	0.001517	1232.1	239	0.0412	2157	0.05731	2482.8	0.1202	4944	0.008636	3936
209	0.007991	735.6	0.01304	984	0.03202	2298.6	0.001821	1478.4	239	0.04944	2588.4	0.06877	2979.3	0.1442	5934	0.01144	4725
211	0.003071	272.25	0.004941	359.7	0.01198	829.2	0.0006997	542.4	241	0.01824	919.5	0.02517	1050	0.05236	2073.6	0.004229	1670.7
211	0.004606	408.3	0.007412	539.4	0.01797	1244.1	0.001049	813.6	241	0.02736	1379.4	0.03776	1575	0.07854	3111	0.006344	2505.9
211	0.006141	544.5	0.009882	719.1	0.02396	1658.7	0.001399	1085.1	241	0.03649	1839	0.05035	2100	0.1047	4146	0.008458	3342
211	0.007676	680.7	0.01235	899.1	0.02995	2073.3	0.001749	1356.3	241	0.04561	2298.9	0.06293	2625	0.1309	5184	0.01057	4176
211	0.009212	816.6	0.01482	1078.8	0.02995	2073.3	0.002099	1627.5	241	0.05473	2758.8	0.07552	3150	0.1571	6222	0.01269	5013
213	0.003527	301.2	0.005602	393.3	0.01341	895.5	0.0008041	595.2	243	0.02015	978	0.0276	1107.9	0.05695	2170.2	0.00468	1768.8
213	0.005291	451.8	0.008402	589.8	0.02012	1343.1	0.001206	893.1	243	0.03023	1467	0.04139	1662	0.08542	3255	0.00702	2653.5
213	0.007055	602.4	0.0112	786.3	0.02683	1790.7	0.001608	1190.7	243	0.04031	1956	0.05519	2215.8	0.1139	4341	0.00936	3537
213	0.008819	753	0.014	982.8	0.03354	2238.6	0.00201	1488.3	243	0.05038	2445	0.06899	2769.9	0.1424	5427	0.0117	4422
213	0.01058	903.6	0.0168	1179.6	0.04024	2686.2	0.002412	1785.9	243	0.06046	2934	0.08279	3324	0.1708	6510	0.01404	5307
215	0.004039	332.1	0.006333	428.7	0.01498	964.2	0.0009212	651.6	245	0.02222	1038	0.0302	1167	0.06184	2267.7	0.005168	1869.6
215	0.006059	498.3	0.0095	642.9	0.02248	1446.3	0.001382	977.1	245	0.03333	1557	0.0453	1750.5	0.09276	3402	0.007753	2804.4
215	0.008078	664.2	0.01267	857.1	0.02997	1928.7	0.001842	1332.9	245	0.04444	2076	0.0604	2333.7	0.1237	4536	0.01034	3738
215	0.0101	830.4	0.01583	1071.6	0.03746	2410.8	0.002303	1628.7	245	0.05555	2595	0.0755	2917.2	0.1546	5670	0.01292	4674
215	0.01212	996.6	0.019	1285.8	0.04495	2892.9	0.002763	1954.5	245	0.06665	3114	0.0906	3501	0.1855	6804	0.01551	5610
217	0.00461	365.1	0.007141	465.9	0.0167	1035.9	0.001052	710.7	247	0.02445	1099.5	0.03299	1226.7	0.06706	2365.8	0.005697	1972.2
217	0.006916	547.8	0.01071	699	0.02505	1554	0.001578	1066.2	247	0.03667	1649.1	0.04949	1840.2	0.1006	3549	0.008546	2958.3
217	0.009221	730.2	0.01428	931.8	0.0334	2071.8	0.002104	1421.7	247	0.0489	2199	0.06599	2453.7	0.1341	4731	0.01139	3945
217	0.01153	912.9	0.01785	1164.9	0.04175	2589.9	0.00263	1777.2	247	0.06112	2748.6	0.08248	3066	0.1676	5913	0.01424	4932
217	0.01383	1095.6	0.02142	1398	0.0501	3108	0.003156	2132.4	247	0.07335	3297	0.09898	3681	0.2012	7095	0.01709	5916
219	0.005246	400.2	0.008032	505.2	0.01857	1110.3	0.001198	773.4	249	0.02685	1162.2	0.03599	1287.6	0.07261	2463.6	0.006268	2076.9
219	0.007869	600.3	0.01205	757.8	0.02785	1665.6	0.001797	1160.4	249	0.04028	1743.6	0.05398	1931.1	0.1089	3696	0.009403	3114
219	0.01049	800.4	0.01606	1010.4	0.03714	2220.9	0.002396	1547.1	249	0.05371	2324.7	0.07197	2574.9	0.1452	4926	0.01254	4155
219	0.01312	1000.5	0.02008	1263	0.04642	2775.9	0.002995	1933.8	249	0.06713	2905.8	0.08996	3219	0.1815	6159	0.01567	5193
219	0.01574	1200.6	0.0241	1515.6	0.05571	3330	0.003595	2320.5	249	0.08056	3486	0.108	3861	0.2178	7392	0.01881	6231

T (K)	R134a		R1234yf		R502		R717		T (K)	R134a		R1234yf		R502		R717	
	Mass Flow (kg/s)	Exergy Dest (W)	Mass Flow (kg/s)	Exergy Dest (W)	Mass Flow (kg/s)	Exergy Dest (W)	Mass Flow (kg/s)	Exergy Dest (W)		Mass Flow (kg/s)	Exergy Dest (W)	Mass Flow (kg/s)	Exergy Dest (W)	Mass Flow (kg/s)	Exergy Dest (W)	Mass Flow (kg/s)	Exergy Dest (W)
221	0.005952	437.4	0.009011	546.3	0.0206	1187.4	0.001361	839.4	251	0.02944	1226.4	0.03919	1348.8	0.07852	2561.7	0.006885	2183.4
221	0.008928	656.1	0.01352	819.6	0.0309	1781.1	0.002041	1259.1	251	0.04416	1839.9	0.05878	2032.2	0.1178	3843	0.01033	3276
221	0.0119	874.8	0.01802	1092.6	0.412	2374.8	0.002721	1679.1	251	0.05888	2453.1	0.07838	2697.6	0.157	5124	0.01377	4368
221	0.01488	1093.5	0.02253	1365.9	0.0515	2968.5	0.003402	2098.8	251	0.07361	3066	0.09797	3372	0.1963	6405	0.01721	5457
221	0.01786	1311.9	0.02703	1639.2	0.06181	3561	0.004082	2518.5	251	0.08833	3681	0.1176	4047	0.2356	7686	0.02065	6549
223	0.006734	476.7	0.01008	589.2	0.02281	1266.9	0.001541	908.7	253	0.03222	1291.8	0.04261	1410.6	0.0848	2660.1	0.007549	2291.4
223	0.0101	714.9	0.01513	884.1	0.03421	1900.5	0.002311	1363.2	253	0.04834	1938	0.06391	2116.2	0.1272	3990	0.01132	3438
223	0.01347	953.1	0.02017	1178.7	0.04562	2534.1	0.003082	1817.4	253	0.06445	2583.9	0.08522	2821.5	0.1696	5319	0.0151	4584
223	0.01683	1191.3	0.02521	1473.3	0.05702	3168	0.003852	2271.9	253	0.08056	3231	0.1065	3528	0.212	6651	0.01887	5727
223	0.0202	1429.8	0.03025	1587.9	0.06843	3801	0.004623	2726.1	253	0.09667	3876	0.1278	4233	0.2544	7980	0.002265	6873
225	0.007597	517.8	0.01126	634.2	0.0252	1349.1	0.001741	981.3	255	0.03521	1358.4	0.04626	1473	0.09146	2757.9	0.008263	2400.6
225	0.0114	776.7	0.01689	951.3	0.0378	2023.5	0.002611	1471.8	255	0.05282	2037.6	0.06939	2209.5	0.1372	4137	0.01239	3600
225	0.01519	1035.6	0.02252	1268.4	0.0504	2697.9	0.003481	1962.6	255	0.07042	2716.8	0.09252	2946.3	0.1829	5517	0.01653	4800
225	0.01899	1294.5	0.02815	1585.2	0.063	3372	0.004351	2453.1	255	0.08803	3396	0.1157	3684	0.2286	6894	0.02066	6003
225	0.02279	1553.4	0.03378	1902.3	0.0756	4047	0.005222	2943.6	255	0.1056	4074	0.1388	4419	0.2744	8274	0.02479	7203
227	0.008548	561.3	0.01254	680.7	0.02779	1433.1	0.001961	1056.9	257	0.03841	1425.9	0.05016	1535.7	0.09852	2855.1	0.00903	2511.3
227	0.01282	841.8	0.01881	1020.9	0.04168	2149.8	0.002941	1585.5	257	0.05762	2138.7	0.07523	2303.7	0.1478	4284	0.01354	3768
227	0.0171	1122.3	0.02508	1361.4	0.05558	2866.5	0.003922	2113.8	257	0.07682	2851.8	0.1003	3072	0.197	5709	0.01806	5022
227	0.02137	1402.8	0.03135	1701.6	0.06947	3582	0.004902	2424	257	0.09603	3564	0.1254	3840	0.2463	7137	0.02257	6279
227	0.02565	1683.6	0.03763	2042.1	0.08337	4299	0.005883	3171	257	0.1152	4278	0.1505	4608	0.2956	8565	0.02709	7533
229	0.009594	606.6	0.01394	729	0.03058	1519.5	0.002204	1135.8	259	0.04184	1494.3	0.0543	1598.7	0.106	2951.7	0.009852	2622.9
229	0.01439	909.9	0.02091	1093.5	0.04588	2279.4	0.003305	1703.7	259	0.06276	2241.3	0.08145	2398.2	0.159	4428	0.01478	3933
229	0.01919	1213.2	0.02788	1457.7	0.06117	3039	0.004407	2271.6	259	0.08368	2988.3	0.1086	3198	0.212	5904	0.0197	5247
229	0.02398	1516.5	0.03485	1822.2	0.07646	3798	0.005509	2839.5	259	0.1046	3735	0.1358	3996	0.265	7380	0.02463	6558
229	0.02878	1819.8	0.04182	2186.7	0.09175	4560	0.006611	3408	259	0.1255	4482	0.1629	4797	0.318	8856	0.02956	7869

2.3. Design of Artificial Neural Network

Artificial intelligence (AI) systems are widely used for analysing and comparing the energy behaviour of a storage unit design. ANN is constructed in layers: the input layer, the output layer and some hidden layers. The number of hidden layers depends on the application and type of the problem. In this research, ANNs were implemented in Neural Net Fitting (MATLAB) with 2 hidden layers. In Figure 2, the model of ANN is given.
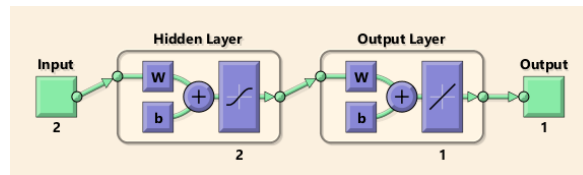
Figure 2: Architecture of a 2–2–1 ANN

Here, T_{Room} (K) and $\dot{m}$ (kg/s) were taken as inputs, and exergy destruction $\dot{Ex}_{dest}$ (W) values from EES program were taken as output value for training. The 150 experimental data were compared with three different ANN algorithms; Levenberg- Marquardt (LM), Bayesian Regularization (BR) and Scaled Conjugate Gradient (SCG). The ANN performance of the data sets dealt with was based on some statistical criteria such as the coefficient of multiple determination (R^2) and the coefficient of variation (r). R Squared formula is the following (Equation 14):

$$R^2 = 1 - \frac{\sum(y-\hat{y})^2}{\sum(y-\bar{y})^2} \tag{14}$$

Where y is the actual value, $\hat{y}$ is predicted of y and $\bar{y}$ is the mean of the y values. The formula of the correlation coefficient is defined as follow (Equation 15):

$$r = \frac{n(\sum xy) - (\sum x)(\sum y)}{\sqrt{[n\sum x^2 - (\sum x)^2][n\sum y^2 - (\sum y)^2]}} \tag{15}$$

Where n equals the number of patterns, x refers to the set of actual outputs and y refers to the predicted outputs. Here in, 104 of 150 data given in Table 3 were used for training, 23 for testing and 23 for validation in the model.

3. RESULTS AND DISCUSSIONS

As a result of the analysis, the exergy efficiencies of the system in the temperature region between 201K and 259K according to different fluids are shown in Figure 3.
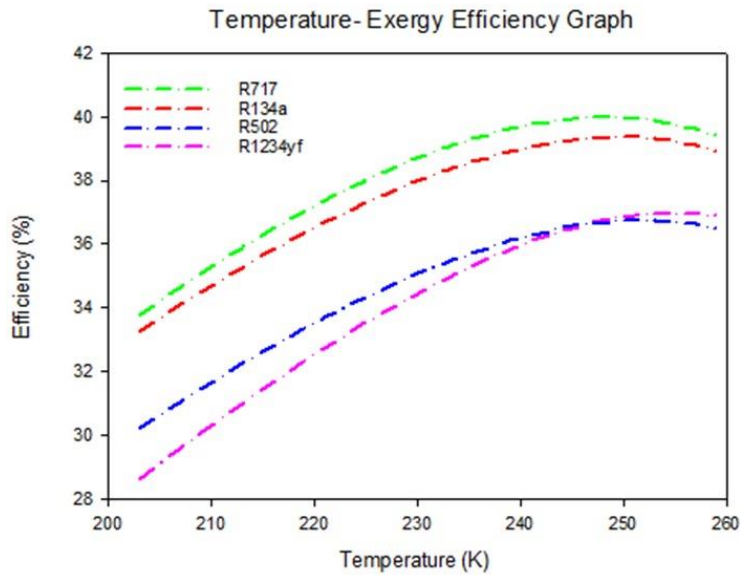
Figure 3: Storage Room Temperature –Exergy Efficiency graph

When examined in Figure 3, it was observed that the order of exergy efficiency was calculated as R717, R134a, R502, and R1234yf, respectively. As a result of the study, the exergy efficiency of R717, which had a high refrigerant capacity between 203K and 259K and within the determined system limits, was found to be high. Although the lowest exergy efficiency was R1234yf, it can be preferred over R-134a since it has very low GWP values compared to R134a.

It was observed that there was a rapid increase in exergy efficiency in the temperature range of 205 to 240K in general for all the fluids considered. For the examined fluids, we approached 250K and it was determined that it offered the best value in terms of exergy efficiency, and after this value, it was determined that the exergy efficiency tended to decrease.

R502 fluid was preferred in this study to make a comparison with R134a, R1234yf, and R717 fluids because it was a fluid with a high ODP and GWP ratio. As a result of the calculations, R717 and R134a achieved higher values than R502 under system conditions in any case. R1234yf fluid, on the other hand, outperformed R502 fluid between increasing 247K and 260K values.

In this study, we examined R717, R134a, R502, and R1234yf fluids by using ANN with Levenberg- Marquardt, Bayesian Regularization, and Scaled Conjugate Gradient algorithms. All the variants with R^2 values studied are given in Table 4.

Table 4: Statistical values of predictions (R^2) for the cooling system using LM, BR, SCG algorithms

	BR	LM	SCG
R717	0.95059	0.95491	0.9291
R134a	0.99991	0.98776	0.99415
R502	0.99115	0.95511	0.96564
R1234yf	0.99977	0.99975	0.98448

Figure 4 shows the results corresponding to LM algorithm: the calculated and predicted Exergy Destruction (W) values are very close to each other for each fluids.
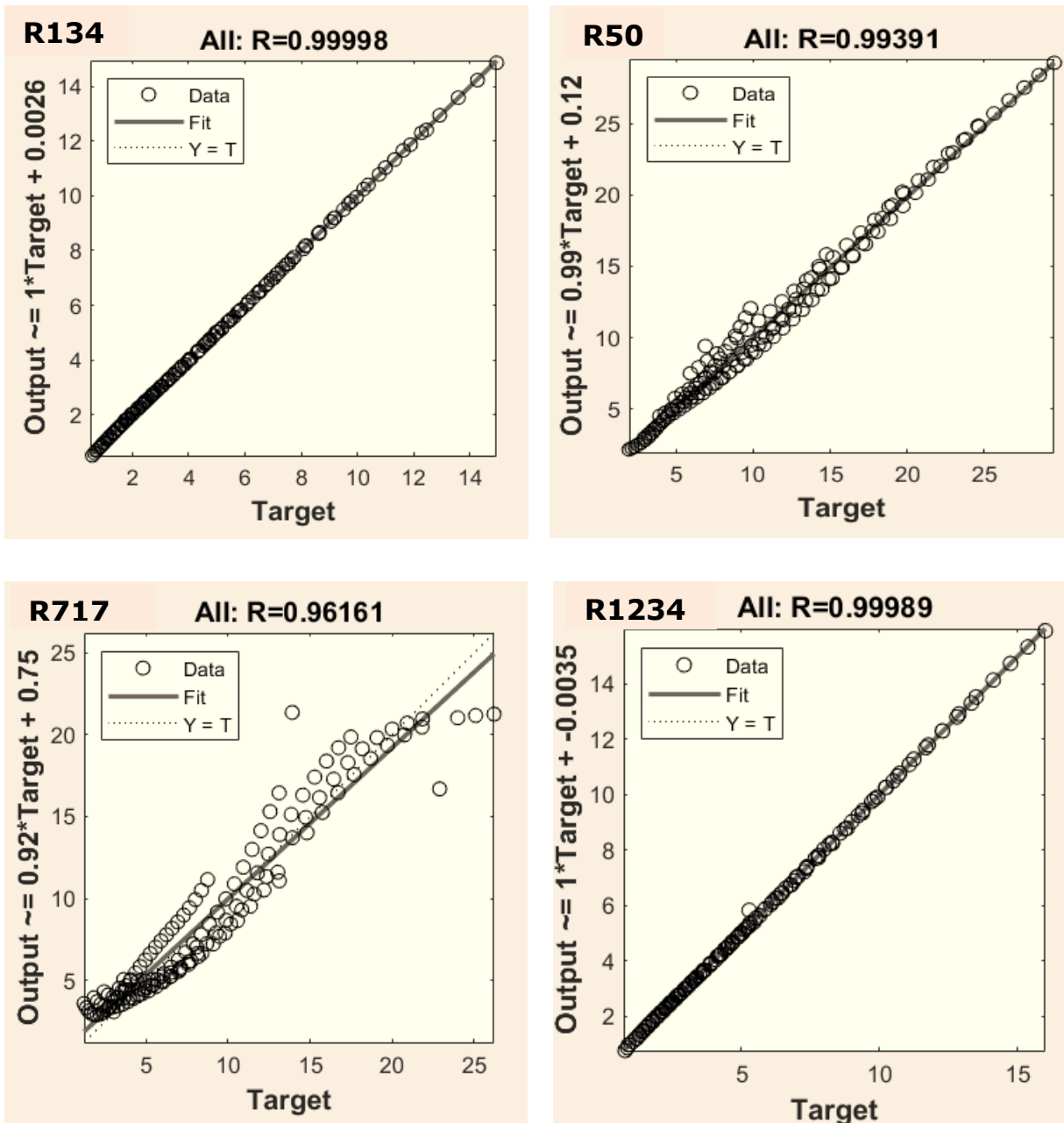
Figure 4: Comparison of calculated and predicted results for the data by using LM algorithm

4. CONCLUSION

In this study, different fluids were preferred and their performance investigated in cooling systems using vapour-compressed compressors kept at very low temperatures, especially for the storage of Pfizer-Biontech vaccine. Exergy efficiency and exergy destruction were considered especially for performance analysis. In this study, four different R134a, R1234yf, R502, and R717 refrigerants were examined for the vapour compression refrigeration system to be used for vaccine storage for exergy efficiency calculation. R717 was calculated as the best result in terms of exergy efficiency. According to the results of these four refrigerants, R134a and R1234yf fluids were recommended as an alternative to R502, in accordance with the Paris Climate Agreement trying to prevent climate change from refrigerants used in the refrigeration sector, preferred for vaccine storage, considering R717 is toxic.

With the study, the exergy destruction calculation of artificial intelligence applications in the vapour compression cooling cycle was examined. Storage room temperature and mass flow rate of refrigerant were taken as input parameters. Exergy destruction was preferred as the output parameter.

Three different algorithms were applied. It was seen that all algorithms made good predictions of R^2 values above 0.9 for all 4 different fluids. In particular, it was observed that the LM algorithm resulted in a sensitivity of over 95%.

In addition to this, the COP, evaporator capacity, entropy generation, and thermodynamic properties of the system were also examined in the ANN approach. It was concluded that the performance of the related systems can be calculated well through artificial intelligence-based programs constructed using the relevant algorithms.

As a suggestion for future studies, Cascade cooling systems can be used instead of single-stage cooling systems, more input parameters can be used in ANN, and alternative fluids can be researched instead of harmful fluids used in the industry. In addition, different condenser temperatures, compressor displacement ratios, supercooling, and superheating values can be studied. Finally, cost analysis and the amount of carbon dioxide production can be examined with both thermodynamic and ANN approaches by choosing input parameters.

5. REFERENCES

Ahmed, R., Mahadzir, S., Rozali, N. E. M., Biswas, K., Matovu, F., & Ahmed, K. (2021). Artificial intelligence techniques in refrigeration system modelling and optimization: A multi-disciplinary review. *Sustainable Energy Technologies and Assessments*, *47*, 101488.

Alexis, G. K., & Karayiannis, E. K. (2005). A solar ejector cooling system using refrigerant R134a in the Athens area. *Renewable Energy*, *30*(9), 1457-1469.

Altintas, E., Tolon, M., Karabuga, A., & Utlu, Z. (2021). Application of artificial neural network model for forecast energy efficiency of the cryogenic liquefaction system in the meaning of sustainability. *International Journal of Global Warming*, *24*(3-4), 420-444.

Aprea, C., Mastrullo, R., 1996. Behaviour and performances of R502 alternative working fluids in refrigerating plants. International Journal of Refrigeration 19 (4), 257–263

Arafat, M. Y., Chakraborty, S., Alen, S. K., & Sarker, M. A. R.(2015) Design and Modeling of a Solar Powered Absorption Refrigeration System.

Arcaklıoğlu, E., Çavuşoğlu, A., & Erişen, A. (2004). Thermodynamic analyses of refrigerant mixtures using artificial neural networks. *Applied energy*, *78*(2), 219-230.

Arcaklıoğlu, E., Çavuşoğlu, A., Erişen, A., 2005. An algorithmic approach towards finding better refrigerant substitutes of CFCs in terms of the second law of thermodynamics. Energy Conversion and Management 46, 1595–1611.

Belman-Flores, J. M., Mota-Babiloni, A., Ledesma, S., & Makhnatch, P. (2017). Using ANNs to approach to the energy performance for a small refrigeration system working with R134a and two alternative lower GWP mixtures. *Applied Thermal Engineering*, *127*, 996-1004.

Chojnacky, M., Miller, W., Strouse, G., & Gallagher, P. D. (2010). Thermal analysis of refrigeration systems used for vaccine storage: report on pharmaceutical grade refrigerator and household refrigerator/freezer.

Chouai, A., Laugier, S., & Richon, D. (2002). Modeling of thermodynamic properties using neural networks: Application to refrigerants. *Fluid phase equilibria*, *199*(1-2), 53-62.

Hosoz, M., & Ertunc, H. M. (2006). Modelling of a cascade refrigeration system using artificial neural network. *International Journal of Energy Research*, *30*(14), 1200-1215.

Kasi, P., & Cheralathan, M. (2021, October). Review of cascade refrigeration systems for vaccine storage. In *Journal of Physics: Conference Series* (Vol. 2054, No. 1, p. 012041). IOP Publishing.

Li, Z., Jiang, H., Chen, X., & Liang, K. (2019). Comparative study on energy efficiency of low GWP refrigerants in domestic refrigerators with capacity modulation. *Energy and Buildings*, *192*, 93-100.

Minor, B., & Spatz, M. (2008). HFO-1234yf low GWP refrigerant update.

Mishra, P., Soni, S., & Maheshwari, G. (2022). Exergetic performance analysis of low GWP refrigerants as an alternative to R410A in split air conditioner. *Materials Today: Proceedings*.

Mota-Babiloni, A., Makhnatch, P., & Khodabandeh, R. (2017). Recent investigations in HFCs substitution with lower GWP synthetic alternatives: Focus on energetic performance and environmental impact. *International Journal of Refrigeration*, *82*, 288-301.

Pabon, J. J., Khosravi, A., Belman-Flores, J. M., Machado, L., & Revellin, R. (2020). Applications of refrigerant R1234yf in heating, air conditioning and refrigeration systems: A decade of researches. *International Journal of Refrigeration*, *118*, 104-113.

Razzaq, M. E., Ahamed, J., Hossain, M., & Hossain, S. (2019). A review on hydrocarbon (HCs) as an alternative refrigerant: based on thermodynamic and environmental approach.

Santos, A. F., Gaspar, P. D., & de Souza, H. J. (2021). Refrigeration of COVID-19 vaccines: ideal storage characteristics, energy efficiency and environmental impacts of various vaccine options. *Energies*, *14*(7), 1849.

Soni, S., Maheshwari, G., & Verma, D. S. (2021). Theoretıcal exergy and second law analysıs of vapour compressıon refrıgeratıon system wıth refrıgerants of low and hıgh global warmıng potentıal. *Journal of Management Information and Decision Sciences*, *24*, 1-11.

Sözen, A., Arcaklioğlu, E., Menli, T., & Özalp, M. (2009). Determination of thermodynamic properties of an alternative refrigerant (R407c) using artificial neural network. *Expert Systems with Applications*, *36*(3), 4346-4356.

Yilmaz, S., & Atik, K. (2007). Modeling of a mechanical cooling system with variable cooling capacity by using artificial neural network. *Applied Thermal Engineering*, *27*(13), 2308-2313.

Zegenhagen, M. T., & Ziegler, F. (2015). Experimental investigation of the characteristics of a jet-ejector and a jet-ejector cooling system operating with R134a as a refrigerant. *International journal of refrigeration*, *56*, 173-185.

Xuan, Y., Chen, G., 2005. Experimental study on HFC-161 mixture as an alternative refrigerant to R502. International Journal of Refrigeration 28 (3), 436–441.

#70: An attempt to design energy efficient buildings with a holistic and multidisciplinary perspective

Yusuf Cihat AYDIN[1], Parham A. MIRZAEI[2]

[1]*Alanya Alaaddin Keykubat University, Kestel District, Üniversite Street, Faculty of Art, Design and Architecture Building, Floor:3 Alanya / Antalya / TURKEY, yusuf.aydin@alanya.edu.tr*
[2]*University of Nottingham, Department of Architecture and Built Environment, Faculty of Engineering, University of Nottingham, NG7 2RD University Park, Nottingham, UNITED KINGDOM, Parham.Mirzaei_Ahranjani@nottingham.ac.uk*

Abstract: Focusing solely on energy efficiency in building design is insufficient to stem the growth of energy demand in the building sector, especially with current market barriers for energy efficient buildings (EEBs). Therefore, when designing EEBs, a holistic and multidisciplinary approach that simultaneously addresses energy efficiency and marketability may yield more efficient results for reducing the building sector's energy demand. Aesthetic features are crucial criteria for marketability and increasing the number of EEBs. However, the effects of parameters affecting energy efficiency on aesthetics and marketability have been barely studied. Window features are a building component that has a major impact on the aesthetics, marketability, and energy efficiency of buildings. Therefore, this study aimed to evaluate the impact of different window features on aesthetics, marketability, and energy consumption of low-rise detached UK residential buildings. For this purpose, the impact of different window features (i.e., position, number, area, width, height, symmetry, and proportion) on annual energy consumption, aesthetics, and marketability were investigated by conducting a series of Design Builder energy simulations and a comprehensive survey study (n=807). According to the results, there was a strong positive correlation between aesthetics and marketability. Window area and number were identified as the most influential window parameters to minimise annual energy consumption whilst improving the aesthetics and marketability of UK residential buildings. Therefore, simultaneous improvement of the energy efficiency, aesthetics and marketability of UK residential buildings could be possible with greater attention to design and the number and area of windows.

Keywords: energy efficient buildings; energy consumption; aesthetics; marketability; window

1. INTRODUCTION

In the design of energy efficient buildings, aesthetic features are as important as energy efficiency. Energy efficiency criteria are important for reducing the operational energy consumption of the designed building, while aesthetic improvement is important for increasing the marketability of energy efficient buildings. Increasing the marketability of energy efficient buildings can elevate the number of these buildings in the existing building stock and therefore help to decrease the energy demand of the building sector (Aydin *et al.*, 2019).

In terms of marketability of buildings, the low market value of energy efficiency in the eyes of clients and other building stakeholders (Johansson *et al.*, 2012; Schnieders & Hermelink, 2006) have been reported in previous studies. On the contrary, architectural features and façade aesthetics are the main driving force in the buying decision-making process (Schnieders & Hermelink, 2006; Aydin *et al.*, 2019). For example, even in socially-conscious Scandinavian countries, the main reason for buyers' preference to purchase 20 low-energy terraced houses in Gothenburg (Sweden) (Isaksson & Karlsson, 2006) and 56 energy-efficient flats in Norway (Hauge *et al.*, 2011) was the buildings' architectural characteristics rather than their energy efficiency. Indeed, the positive effects of the aesthetic properties of buildings on marketability have been widely stated in the literature. For example, in the UK, the rental values of energy-efficient workplaces are significantly associated with buildings' aesthetic while no association with energy-efficiency features were reported (Parkinson *et al.*, 2013). In the US, office buildings with better aesthetic features have attract 7% higher rent and 17% higher selling prices (Fuerst *et al.*, 2011). According to an empirical analysis on the sale data of 5,000 homes in New Zealand, attractive neighbouring buildings provide 37% additional value to a house (Bourassa, Hoesli, & Sun, 2004).

Buildings are complex structures made up of different components. These different components in the building envelope, such as windows, walls, roofs, doors, floors, structures, and balconies, have different levels of impact on aesthetics and energy efficiency. Among the components that affect the aesthetics, energy efficiency (Tsikaloudaki *et al.*, 2015), and marketability of the buildings at the same time, windows are the building elements that have the greatest impact (Aydin *et al.*, 2019). For example, the window is one of the most influential parameters for energy consumption in buildings in the UK, being responsible for 45% of energy consumption in the buildings (20% via the window itself, and 25% via ventilation) (Palmer & Cooper, 2013). In addition, the important role of windows in buyers' dwelling purchasing decision and aesthetic appreciation are mentioned in previous studies (Kwak *et al.*, 2010; Aydin *et al.*, 2019).

Although the effect of windows on building aesthetics and energy efficiency has been investigated in independent studies, the effect of these building elements on aesthetics, marketability and energy efficiency has been barely studied at the same time. Therefore, in this study, the effects of seven different window parameters such as location, number, area, width, height, symmetry and proportion on the energy efficiency and aesthetics of detached buildings in the UK were investigated to determine the dominant window parameters that impact aesthetics, marketability and energy performance.

2. METHODOLOGY

In this study, research was first conducted to determine the most common building typology in the UK. A comprehensive e-mail survey and energy simulations were conducted to determine the impact of the seven window parameters to be studied on aesthetic judgment and energy efficiency.

2.1. Benchmark building

A benchmark building is illustrated in Figure and its properties were defined according to the most common residential properties in the UK, current building regulations, and The Government's Standard Assessment Procedure for Energy Rating of Dwellings calculations (SAP) standards.

The majority of the UK building stock consists of buildings built before the 1919s (EHS, 2016) (age group B in SAP (SAP, 2014)). According to the Department for Communities and Local Government, detached houses represent 25% of UK building stock (DCLG, 2015). In the UK building stock, the vast majority (80%) of the dwellings are two-storeys (DCLG, 2015), and the average usable floor area is 94m^2 (EHS, 2016). The vast majority (98%) of detached residential buildings in the UK building stock have a cavity or solid brick wall (EHS, 2016). The majority (51%) of UK detached dwellings have no wall insulation (32% of cavity walls, 91% with a solid wall), but 80% of them have full double glazing (EHS, 2016). For the age group B buildings, the commonly used wall thickness is 0.22m, and the average window area is 18.3 m^2 (SAP, 2014).

As shown in Figure 1, the reference building was modelled as a 2-storey detached brick residential house with a usable floor area of 94m^2 (from interior wall to interior wall). The overall mass of the building was 7.29m x 7.29m x 5.80m (length x width x height (floor to ceiling - roof height not included)) and the wall thickness was 0.22m. The window area was 18m^2 in total and there were four 1.06m x 1.06m (length x height) square double-glazed windows on the north, east, south, and west facades of the building, all windows have 75% openable area. The base of each

window was located 1.12m up from the floor and 1.52m from the building corner edges. The benchmark building had a 30º gable roof, as rooves also have an impact on operational energy consumption and natural ventilation of buildings (Kindangen *et al.*, 1997).
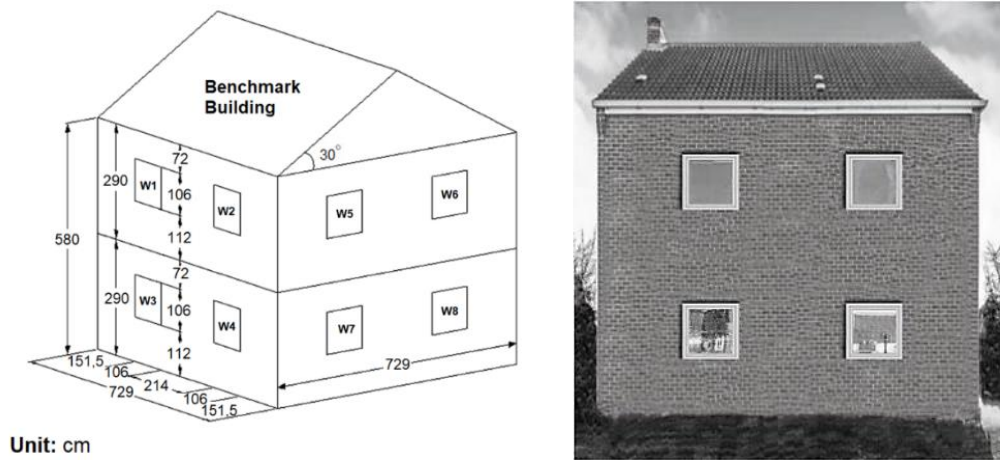
Figure 1: Benchmark building

2.2. Survey

An extensive e-mail survey was conducted to investigate the effect of the seven studied window parameters on aesthetic judgment. In the survey, respondents were only shown one image at a time to rate the aesthetics of the residences shown. Except for the demographic questions and benchmark building (the first picture for the calibration purpose) (Figure 1), the order of the pictures was randomized to minimize the question order bias. In this survey, a bipolar seven-point semantic differential scale was utilized to rate the impact of studied window parameters, in addition, each question was supported by an optional text box to collect participants' additional comments and to let them express a plausible different answer above the given options. In order to prevent misunderstandings and to provide equal conditions for each participant, brief information about the survey and the measurement tool used in the survey was given to the participants.

Participants

This e-mail survey was conducted with all native students studying at the University of Nottingham (UoN). The opportunity to receive a monetary incentive was offered to encourage participants. In total, 1095 responses were received, of which 288 partially completed the questionnaires, only 807 fully completed. Only the fully completed questionnaires were taken into account in this study. Details regarding the demographic distribution of the participants are shown in Table 1.

Table 1: Demographic characteristics of participants

Gender	%	Background	%	Qualification*	%	Age	%	Region ** (σ =1.70)			%
(σ = 0.47)	%	(σ =0.48)	%	(σ =1.35)	%	(σ =0.66)	%	%			%
Male:	32	Architect:	3	Bachelor's degree:	47	Under 18:	0	1:	1	6:	17
Female:	67	Art:	6	Master's degree:	16	18-24:	83	2:	7	7:	18
Other:	1	Other:	92	Ph.D. degree	1	25-34:	11	3:	3	8:	2
				Other:	35	35-44:	4	4:	21	9:	3
						45-54:	2	5:	28	10:	1
						55-64:	1				
						65+:	0				

* Completed or currently enrolled, σ:Standard deviation   Regions from which participants come from

A total of 33 different black and white fully controlled photographic images were produced by editing the benchmark building with GIMP 2.1 Software (Figure 2). Efforts were made to extract the isolated impact of each of the seven window parameters. For this purpose, in each image, only one parameter was changed, and all other parameters were not varied. Each window parameter was configured for three levels and compared with the original benchmark building's results (four levels in total). The maximum and minimum window configuration levels were adjusted according to three considerations: (1) window areas were kept the same in all configurations except for the case of area configurations and the second versions of the window configurations (Ver.2) (see Figure 2), (2) window centre points were considered to be the same in all configurations except for the case of symmetry and position configurations, (3) minimum distances were limited with the UK building regulations (i.e. the minimum window distance from the building corner was 0.39 m, and the minimum distance between windows was 0.325 m (GOV.UK, 2013).

Level 1 (L1) and Level 3 (L3) represent the minimum and maximum configuration levels, respectively. The impacts of the window height, width, position, and energy performance were also investigated with two variations for each parameter, to provide suitable experimental conditions and to examine the isolated impact of those parameters. For example, in the window width configuration version 1, the window width and height were changed to preserve the window area constant, while in version 2 the window height was considered to be the same while the area and width were changed. The distinction between the energy performances when the natural ventilation was applied or not-applied was also considered, to investigate the underlying reasons for energy performance variations with different window configurations.

Benchmark	Area L1	Area L2	Area L3	Height L1	Height L2	Height L3
Height V2 L1	Height V2 L2	Height V2 L3	Number L1	Number L2	Number L3	Number L4
Number V2 L1	Number V2 L2	Number V2 L3	Number V2 L4	Position Hor. L1	Position Hor. L2	Position Hor. L3
Position Ver. L1	Position Ver. L2	Position Ver. L3	Symmetry L1	Symmetry L2	Symmetry L3	Width L1
Width L2	Width L3	Width V2 L1	Width V2 L2	Width V2 L3		

V2: second version of window configurations, Exp: photos that belong to experimental categories

Figure 2: Visual stimuli utilised in the survey

Data analysis

IBM SPSS Version-23 was utilised for all statistical analysis. As the conducted survey had a normal distribution (skewness: *max*: 1.534, *min*: -0.081, kurtosis: *max*: 1.899 -, *min*: -0.804) and large sample size (n = 807), parametric statistical models were utilised. Pearson correlation analysis was utilized to determine the relationships between the configurations of studied window parameters, aesthetic appreciation, and housings' energy consumption. The reliability and internal consistency of the conducted survey were determined by Cronbach's alpha (α) analysis.

2.3. Energy simulation

In this study, Design Builder was utilised for energy simulations. Simulations were performed on all scenarios shown in Figure 2 in order to simultaneously analyse the effect of different window parameters on aesthetics and energy efficiency. The benchmark building was assumed to be in London as it was the region with the highest number of residences. London Gatwick Airport weather data was utilised to model environmental conditions. Most of the thermal and physical properties of benchmark buildings were identified according to age band B buildings (SAP, 2014). In existing UK building stock, 92% of homes have gas central heating (with a gas boiler) (EHS, 2016), thus natural gas central heating systems and electric cooling systems were considered in energy performance simulations and heating setpoint temperatures were arranged between 22°C and 23°C. The internal heat gains from lighting and other equipment were set at 11.77 W/m^2 and the heat gain from the two occupants was set at 123 W/person. Since most UK housing is occupied by two people (EHS, 2016), it was accepted that 2 people live in the house in this study.

In the simulations, the roof was defined as a buffer zone, and eaves were not included in the model used in the simulation, since they can directly affect solar radiation, especially in window position and height configurations. In addition, the effects of interior partition walls, doors, and chimneys were not included in the simulations to simplify the building energy simulations, as these factors do not influence the impact of focused window parameters on annual energy consumption. The calculated approach was utilised in energy simulations, where infiltration and natural ventilation were calculated based on different building and environmental parameters by program, such as window openings, cracks and crack dimensions, wind-driven and buoyancy pressure differences etc. Further thermal properties of building partitions were as illustrated in Table 2.

Table 2: Thermal properties of building partitions

Building partition (From outside to inside)	Thickness (m)	U value $(W/m^2 - K)$	R-Value $(m^2 - K/W)$	Total solar transmittance	Light Transmission
Wall - Brickwork	0,22	2,184	0,458		
Ground floor	0,3327	0,250	4,001		
L1: Urea formaldehyde foam	0,1327				
L2: Cast concrete	0,1000				
L3: Floor screed	0,0700				
L4: Timber flooring	0,0300				
Inner floor	0,1300	2,929	0,341		
L1: Cast concrete	0,1000				
L2: Timber flooring	0,0300				
Roof	0,0500	2,930	0,341		
L1: Clay Tile (roofing)	0,0250				
L2: Air gap	0,0200				
L3: Roofing Felt	0,0050				
Window (double glazing)					
L1: Clear glass	0,0060	3,094		0,7	0,781
L2: Air gap					
L3: Clear glass					

(L= Layer)

3. RESULTS

The effect of the studied window parameters on aesthetic judgment, marketability and annual energy consumption was evaluated according to the mean survey results and the results of building energy simulations. A significantly high positive correlation (r = 0.876, p = 0.000) between housing aesthetic and marketability was observed. This implied that the results of aesthetic judgement for detached house photos can be extended to their marketability. Accordingly, in the remainder of this article, only aesthetic results are discussed.

3.1. The impact of different window parameters on aesthetic judgment

According to Cronbach's alpha (α) criterion, significantly high reliability and internal consistency of the conducted survey were observed (α = 0.95). The mean survey results are shown in Figure 3. In the survey, although illustrations

of buildings with different window configurations were shown to the participants in a mixed order, it was observed that the effect of different window configurations on aesthetic judgment resulted in a particular trend, such as upward, downward, and U-shape trends (see Figure 3). The fact that certain window configurations, which were gradually changed in each window parameter, resulted in gradual changes in the aesthetic appreciation of individuals, clearly shows that different window parameters have different effects on aesthetic judgment and that there was a rationale behind the aesthetic judgments of individuals.

Compared to other window parameters, it was observed that the window area was one of the parameters that had the greatest impact on the aesthetics of the dwelling. As seen in Figure 3, there was a clear inverse U-shape relationship between residential aesthetics and window area configurations. Aesthetic appreciation for benchmark building (M = 2.08) was increased almost two times in the window area configuration level 1 (M = 4.08), then it gradually reduced at the window area configurations of level 2 (M = 3.84) and level 3 (M = 3.22). Increasing the window area up to a certain level increased the aesthetic appreciation (benchmark building (M = 2.08) to level 1 (M = 4.08)), but it decreased after a certain level (level 2 (M = 3.84) to level 3 (M = 3.22)). The enhancing effect of the window area on the aesthetic judgment was also observed in the second versions (V2) of the window configurations. As can be seen in Figure 3, housing photographs with relatively higher window areas, such as the second versions of window configurations (V2) and area configurations, received much higher aesthetic appreciation compared to other pictures.

Aesthetic judgment is a complex phenomenon, in this work aesthetic judgment was the result of the combination of all visible components of the photographs, not just the focused window configuration. In other words, the aesthetic taste for each photograph was influenced by the mutual effects on each window parameters. For example, despite the window height and width configurations having a downward aesthetic appreciation trend from level 1 to level 3, this trend evolved to a slight reverse U-shaped relationship in the second versions (when window area also increased) of the window width and height configurations (see Figure 3 and Table 3). In other words, variations in the different window parameters' combination such as window width – height, and width – area had a mutual impact on each other, and it impacted the aesthetic appreciation.

In addition to the descriptive statistical results, the correlation between aesthetics and the focused window parameters were investigated with Pearson's correlation analysis. According to results, a meaningful positive correlation was found only between aesthetics and window area ($r = 0.330$, $p = 0.031$), height ($r = 0.337$, $p = 0.027$), and position on X-axis (Position_Hor) ($r = 0.351$, $p = 0.053$). Nonetheless, no meaningful correlation was observed between aesthetics and window number ($r = 0.005$, $p = 0.997$), position on Y-axis ($r = 0.055$, $p = 0.748$), symmetry ($r = 0.071$, $p = 0.652$), width ($r = 0.070$, $p = 0.653$), and proportion ($r = -0.288$, $p = 0.061$). In other words, in order to aesthetically enhance residential buildings in the UK, extra care must be taken in the design of these buildings' window area, height and their position on the X-axis.
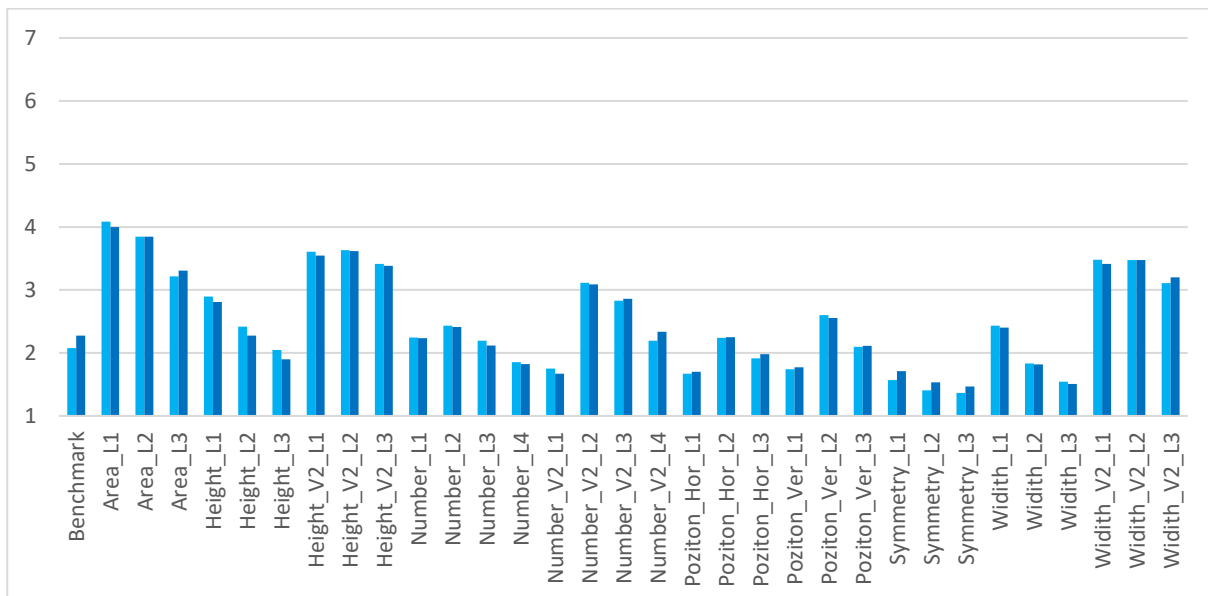
Figure 3: Mean aesthetic appreciation and marketability distribution for each window configurations (Aesthetics light blue, marketability dark blue)

Table 3: Mean aesthetic appreciation and marketability distribution for each window configurations

Configurations	Aesthetics	Marketability	Configurations	Aesthetics	Marketability
Benchmark	2,1	2,3	Height_V2_L1	3,6	3,5
Area_L1	4,1	4,0	Height_V2_L2	3,6	3,6
Area_L2	3,8	3,8	Height_V2_L3	3,4	3,4
Area_L3	3,2	3,3	Number_L1	2,2	2,2
Height_L1	2,9	2,8	Number_L2	2,4	2,4
Height_L2	2,4	2,3	Number_L3	2,2	2,1
Height_L3	2,0	1,9	Number_L4	1,9	1,8
Number_V2_L1	1,8	1,7	Poziton_Ver_L1	1,7	1,8
Number_V2_L2	3,1	3,1	Poziton_Ver_L2	2,6	2,6
Number_V2_L3	2,8	2,9	Poziton_Ver_L3	2,1	2,1
Number_V2_L4	2,2	2,3	Symmetry_L1	1,6	1,7
Poziton_Hor_L1	1,7	1,7	Symmetry_L2	1,4	1,5
Poziton_Hor_L2	2,2	2,3	Symmetry_L3	1,4	1,5
Poziton_Hor_L3	1,9	2,0	Widith_L1	2,4	2,4
Widith_V2_L1	3,5	3,4	Widith_L2	1,8	1,8
Widith_V2_L2	3,5	3,5	Widith_L3	1,5	1,5
Widith_V2_L3	3,1	3,2			

3.2. The impact of different window parameters on annual energy consumption

Figure 4 illustrates the percentage of the difference between all studied window configuration levels and the benchmark building annual energy demand under conditions with and without natural ventilation. The benchmark building had an annual energy consumption of 83.55 MWh and 26.47 MWh, respectively, under natural ventilation included or excluded conditions. It was observed that most of the annual energy consumption of the benchmark building was due to heating loads, especially when natural ventilation was included. Based on London's environmental conditions, the building's heating load was 85% of its total annual energy consumption (71.06 kWh).

According to the simulation results, although almost all window configurations had an impact on the annual energy consumption, compared to the other studied parameters, the window area was determined as the most influential window parameter on the annual energy consumption of low rise detached UK housings. Alterations in other window configurations, not including the window area, caused a change in annual energy consumption of 4% or less. In contrast, up to 24% change in annual energy consumption was observed in simulations where the window area changed, such as window area configurations and second versions of different window configurations (V2) (see Figure 4). When natural ventilation was included in the energy simulations, the second version of the window number configuration level 3 resulted in the highest annual energy consumption change of 24% compared to the annual energy consumption of the benchmark building. Similarly, annual energy consumption was increased up to 21% at the window area configuration level 3 (see Figure 4 and Table 4).

The window area was the most influential parameter on the housing units' annual energy consumption because it simultaneously influences the housings' natural ventilation, infiltration, and direct solar gain. Natural ventilation was mainly related to the opening area, local wind speed, indoor and outdoor dry-bulb temperature difference, and the height from the midpoint of the opening to the natural pressure level (see Equation 1 and Equation 2). The window area was also influential on the amount of solar beams reaching inside houses; it was in accordance with the position of the sun, the height and width of the windows, and the depth of the outside and inside reveal surfaces (see Equation 3 and Equation 4). In addition, the window area had an indirect influence on infiltration, which was generally caused due to the cracks around windows and building elements. The infiltration rate depended on the effective air leakage area, the absolute temperature difference between zone air and outdoor air, and the local wind speed (see Equation 5).
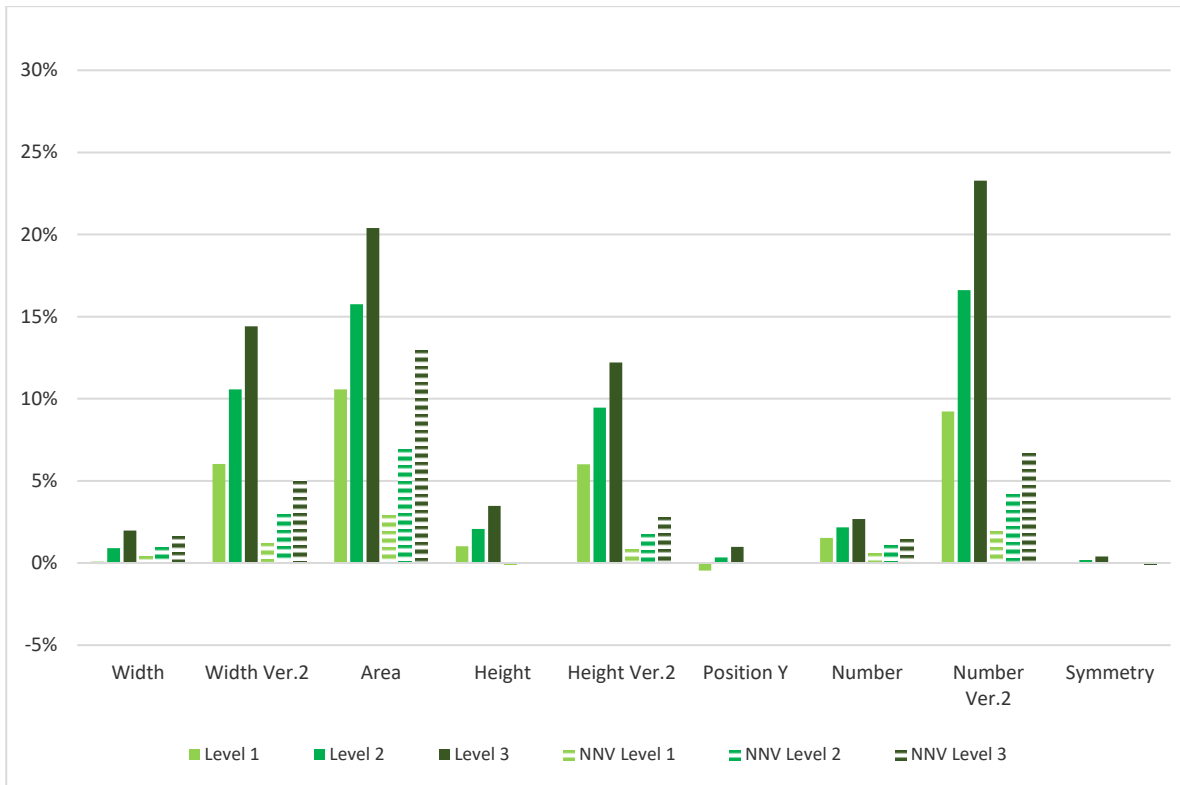
Figure 4: The percentage of the difference between all configuration levels and benchmark building annual energy demand

Table 4: The percentage of the difference between all configuration levels and benchmark building annual energy demand

Natural Vetialtion				No Natural Vetialtion		
	Level 1	Level 2	Level 3		NNV Level 1	NNV Level 2	NNV Level 3
Width	0,08%	0,90%	1,98%	Width	0,43%	1,02%	1,68%
Width Ver.2	6,02%	10,58%	14,40%	Width Ver.2	1,26%	2,99%	5,01%
Area	10,57%	15,75%	20,40%	Area	2,94%	6,98%	13,02%
Height	1,01%	2,08%	3,47%	Height	-0,11%	-0,06%	0,11%
Height Ver.2	6,00%	9,46%	12,21%	Height Ver.2	0,91%	1,77%	2,84%
Position Y	-0,45%	0,33%	0,97%	Position Y	-0,03%	0,03%	0,05%
Number	1,53%	2,17%	2,68%	Number	0,63%	1,10%	1,51%
Number Ver.2	9,22%	16,60%	23,29%	Number Ver.2	1,98%	4,25%	6,70%
Symmetry	0,05%	0,19%	0,40%	Symmetry	-0,03%	-0,05%	-0,07%

Equation 1: Wind-driven natural ventilation (EnergyPlus, 2019). $Qw = Cw.Aopening.Fschedule2.WindS$

Where:

- Q_w = volumetric air flow rate derived by wind (m^3/s),
- C_w = opening effectiveness (dimensionless),
- $A_{opening}$ = opening area (m^2),
- $F_{schedule2}$ = open area fraction (dimensionless), and
- WindS = local wind speed (m/s).

Equation 2: Buoyancy-driven natural ventilation (EnergyPlus, 2019). $$Q_s = C_D.A_{opening}.F_{schedule2} \sqrt{2.\Delta H_{NPL}(|T_{zone}-T_{out}|/T_{zone})}$$

Where:

- Q_s = volumetric flow rate due to stack effect (m^3/s),
- C_D = discharge coefficient for opening (dimensionless),
- ΔH_{NPL} = height from midpoint of lower opening to the natural pressure level (m),

- T_{zone} = zone air dry-bulb temperature (K), and
- T_{zone} = local outdoor air dry-bulb temperature (K).

Equation 3: The size of the shaded areas (EnergyPlus, 2019

$$A_{1,sh} = \tfrac{1}{2}\,(d_1 - p_1)^2 . \tan \alpha$$

Equation 4: The areas by which solar rays reach inside the building through windows (EnergyPlus, 2019)

$$A_{2,sh} = d_2'.L + \tfrac{1}{2}\,(d_1 + d_2)^2.\tan \alpha - \tfrac{1}{2}\,(d_1 + p + d_2'')^2.\tan \alpha$$

Where:

- $A_{1,sh}$ = shaded area at the outside of the window (m^2),
- $A_{2,sh}$ = shaded area at the inside of the window (m^2),
- d_1 = depth of outside revealed surface (m),
- d_2 = depth of inside reveal (m),
- L = window height and width (m),
- α (degree) = solar profile angle for shading on revealed surfaces,
- p_1 = distance from the outside (inside) surface of frame to glazing midplane (m),
- d_1 = depth of shadow cast by top reveal on bottom reveal (m), or by left reveal on right reveal, or by right reveal on left reveal, and
- d_2'' = depth of shadow cast by frame (m).

Equation 5: İnfiltration (EnergyPlus, 2019)

$$\text{İnfiltration} = (F_{schedule})\, A_L/1000 \,\sqrt{C_8}.\,\Delta T + C_w(\text{WindS})^2$$

Where:

- İnfiltration = uncontrolled air leakage through building components,
- $F_{schedule}$ = value from a user-defined schedule,
- A_L (cm^2) = effective air leakage area that corresponds to a 4 Pa pressure differential,
- C_8 = coefficient for stack-included infiltration and
- C_w = coefficient for wind-included infiltration.

Pearson correlation analysis was also used to examine in more detail the relationship between annual energy consumption and the window configurations studied. According to the results, there was a positive correlation between the annual energy consumption and window area ($r = 0.495$, $p = 0.000$), and number ($r = 709$, $p = 0.000$). No meaningful correlation was observed between the annual energy consumption and the rest of the studied window parameters ($p > 0.05$). In other words, in order to reduce the annual energy consumption of residential buildings in the UK, extra care must be taken in the design of these buildings' window area and their number.

4. CONCLUSION

The influence of window position, number, area, width, height symmetry, and proportion on the aesthetics and annual energy consumption of low-rise UK residential buildings was investigated with a comprehensive survey (n=807) and energy simulations. According to the conducted studies, the seven window parameters had an impact on energy efficiency and aesthetics of detached residential houses. The key findings of this research can be summarised below:

- A significantly high positive correlation between housing aesthetic and marketability was observed;

- Window area, height, and position on the X-axis was one of the most influential window configurations that impacted the aesthetic judgement for the low-rise detached residential buildings in the UK;

- In order to reduce the annual energy consumption of low-rise detached residential buildings in the UK, extra attention must be taken to the design of these buildings' window areas and their number;

- Particularly, the windows' area was the most influential parameters that simultaneously impacted the housings' energy consumption and aesthetics. Therefore, in the UK, extra effort should be made to find an optimum level window area in terms of aesthetics and energy efficiency in building design. In this way, energy efficient buildings can be more aesthetic and therefore more marketable compared to conventional buildings, so the number of energy efficient buildings can be increased more quickly in the UK.

5. REFERENCES

Aydin, Y. C., Mirzaei, P. A., & Akhavannasab, S. (2019). On the relationship between building energy efficiency, aesthetic features and marketability: Toward a novel policy for energy demand reduction. *Energy Policy*, *128*, 593–606. https://doi.org/10.1016/j.enpol.2018.12.036

Bourassa, S. C., Hoesli, M. E., & Sun, J. (2004). What's in a View ? *Environment and Planning A*, *36*(8), 1427–1450. file:///C:/Users/Y.C.A/Downloads/unige_5795_attachment01 (2).pdf

DCLG. (2015). *Department for Communities and Local Government Housing Statistical Release: Net supply of housing: 2014-15, England.* https://www.gov.uk/government/uploads/system/uploads/attachment_data/file/475832/Net_Supply_of_Housing_England_2014-15.pdf

EHS. (2016). The English Housing Survey (EHS) Headline Report 2015-2016. Department for Communities and Local Government (DCLG). In *Department for Communities and Local government*.

EnergyPlus. (2019). *EnergyPlus^{TM} Version 9.1.0 Documentation Engineering Reference*. https://energyplus.net/sites/all/modules/custom/nrel_custom/pdfs/pdfs_v9.1.0/EngineeringReference.pdf

Fuerst, F., McAllister, P., & Murray, C. B. (2011). Designer buildings: Estimating the economic value of "signature" architecture. *Environment and Planning A*, *43*(1), 166–184.

GOV.UK. (2013). *The UK Building Regulations Approved Document: A*. https://www.gov.uk/government/uploads/system/uploads/attachment_data/file/429060/BR_PDF_AD_A_2013.pdf

Hauge, Å. L., Thomsen, J., & Berker, T. (2011). User evaluations of energy efficient buildings: Literature review and further research. *Advances in Building Energy Research*, *5*(1), 109–127.

Isaksson, C., & Karlsson, F. (2006). Indoor climate in low-energy houses-an interdisciplinary investigation. *Building and Environment*, *41*(12), 1678–1690.

Johansson, T. B., Patwardhan, A., Nakicenovic, N., & Gomez-Echeverri, L. (2012). *Global energy assessment: Toward a sustainable future, Chapter 10. International Institute for Applied Systems Analysis (IIASA)*.

Kindangen, J., Krauss, G., & Depecker, P. (1997). Effects of roof shapes on wind-induced air motion inside buildings. *Building and Environment*, *32*(1), 1–11.

Kwak, S. Y., Yoo, S. H., & Kwak, S. J. (2010). Valuing energy-saving measures in residential buildings: A choice experiment study. *Energy Policy*, *38*(1), 673–677.

Palmer, J., & Cooper, I. (2013). United Kingdom housing energy fact file. Department of Energy & Cliamte Change (DECC). In *Department of Energy & Climate Change*. https://www.gov.uk/government/uploads/system/uploads/attachment_data/file/345141/uk_housing_fact_file_2013.pdf

Parkinson, A., de Jong, R., Cooke, A., & Guthrie, P. (2013). Energy performance certification as a signal of workplace quality. *Energy Policy*, *62*, 1493–1505.

Reis, A. T. da L., & Lay, M. C. D. (2010). Internal and External Aesthetics of Housing Estates. *Environment and Behavior*, *42*(2), 271–294.

Ryghaug, M., & Sørensen, K. H. (2009). How energy efficiency fails in the building industry. *Energy Policy*, *37*(3), 984–991.

Schnieders, J., & Hermelink, A. (2006). CEPHEUS results: Measurements and occupants' satisfaction provide evidence for Passive Houses being an option for sustainable building. *Energy Policy*, *34*(2 SPEC. ISS.), 151–171.

Tsikaloudaki, K., Laskos, K., Theodosiou, T., & Bikas, D. (2015). The energy performance of windows in Mediterranean regions. *Energy and Buildings*, *92*, 180–187.

#74: An energy management approach with renewable energy sources, electric vehicles and heat pump for electricity demand

Abdullah Dɪᴋ, Cagri Kᴜᴛʟᴜ, Siddig Oᴍᴇʀ, Rabah Bᴏᴜᴋʜᴀɴᴏᴜꜰ, Yuehong Sᴜ, Saffa Rɪꜰꜰᴀᴛ

[1] Department of Architecture and Built Environment, Faculty of Engineering, The University of Nottingham, Nottingham NG7 2RD, UK

Abstract: The electricity demand for domestic and industrial purposes has been consistently increasing. Additionally, it is predicted that e-mobility and heat pumps (HPs) will trigger a mass of additional electricity demand. It is important that energy sources used to meet this electricity demand should be carefully evaluated to reduce carbon emissions from energy generation and to achieve zero-carbon targets. Electrical power storage becomes a critical technology for smoothing out the unpredictable and intermittent nature of Renewable Energy Sources (RESs). For this reason, the vehicle-to-everything (V2X) concept is being evaluated to offer the opportunity to store renewable energy (RE) in electric vehicle (EV) batteries and discharge this stored energy back to the grid (V2G) or homes (V2H) when needed. The present study set out to examine the effect of EV discharge operations on meeting the electricity demand of a house by using 100% of RESs. Firstly, a house in England, which had a high electricity demand at the peak time of the grid due to high electricity and heating needs in the wintertime was modelled in the study. Then, energy analysis was performed to investigate the effectiveness of V2H technology in responding to the peak electricity demand by using an electric vehicle charged by renewables in a workplace plug-in station.

1. INTRODUCTION

Electricity generation from fossil fuels has long been an issue of great interest in the literature related to the environment. The biggest concern with fossil fuels is that they cause carbon dioxide emissions in the atmosphere during combustion due to their high carbon footprint. An extreme amount of fossil fuels has been used due to the increasing heating, electricity, and transportation needs. This situation triggered the increase of greenhouse gases (GHGs) in the atmosphere, namely carbon dioxide (CO_2), water vapour (H_2O), methane (CH_4), nitrous oxide (N_2O), ozone, and chlorofluorocarbons (CFCs), which causes overheating of the earth's surface and therefore global warming. As an effect of global warming, on the 25th of July 2019, Cambridge weather station thermometers showed a record temperature of 38.7°C and it has been recorded as the highest temperature value ever seen in the UK (BBC, 2020). GHG emissions in the UK have decreased by 44% since 1990, but it is insufficient to meet the country's zero-carbon targets (BEIS, 2021). The UK's net-zero strategy might only succeed with the widespread utilisation of heat pumps (HP), penetration of large EV fleets and integration of large-scale RESs.

At the same time, energy consumption for heating buildings is also responsible for CO_2 emissions and it has been reported that 30% of the UK energy usage is consumed by buildings (Prime et al., 2014); this figure increases to 40% of final energy consumption in the EU (EC, 2019). In order to heat the houses, heat pumps have been introduced as an alternative and attractive option as they consume less electricity compared to electrical heaters (Chua et al., 2010). It is also an environmentally friendly system with zero direct carbon release against boiler systems. However, the grid electricity consumption also causes carbon emissions because of carbon-based fuel burning for electricity generation. Thus, performance improvement of the heat pumps is an important issue and a solar-assisted heat pump system has been developed to reach a higher coefficient of performance (COP) than the air-source heat pump (Cervantes and Torres-Reyes, 2002). A comprehensive review of solar-assisted heat pump technology was carried out by Buker and Riffat (Buker and Riffat, 2016) and they concluded that this combination could be a good method to reduce fossil fuel consumption.

Regarding RESs, they have the potential to play a critical role in grid decarbonization and tackling climate change (Sinsel et al., 2020) and have become increasingly popular over the last decade. According to the Department for Business, Energy & Industrial Strategy (BEIS) (BEIS, 2022), RE contributes to around 40% of the country's overall energy supply, with wind energy leading the sector, accounting for 53% of the RE market. Despite significant advances, there is still a tremendous amount of work to be done in order to meet the country's zero-carbon goals. By 2050, it is predicted that 90% of the electricity generated would come from renewable sources, with wind and solar PV power accounting for 70% of this RE supply (Bouckaert et al., 2021). The bulk of the UK's 1,007,427 solar PV systems were installed on small scale with output capacities of less than 4kW (Nedelcheva, 2021). This was because, in large-scale applications, RESs' unpredictable and intermittent nature causes power challenges in the grid. Power stability, for instance, is one of the most frequently stated problems with electrical grids. For a safe grid, the instantaneous energy demand and supply must be equal in the grid. Transmission Network Operators (TNOs) provide ancillary services for the demand-supply balance; otherwise the grid may encounter overloading that can cause blackouts or overgeneration problems that cause energy to waste.

Studies on storage technology indicate that batteries are one of the best options for power quality and power flow concerns in the grid because of their quick reaction times, modular structures, and flexible installation possibilities (Sundararagavan and Baker, 2012; Zhang et al., 2018). Despite the fact that recent studies on battery technology have found favourable results in terms of efficiencies, energy densities, cycle numbers and prices, the use of battery technology is still limited due to high-cost problems. In fact, the cost issue problems of batteries can be overcome by EVs, which are one of the most effective means of achieving zero carbon targets. EVs may store excess RE without incurring additional storage costs due to their battery technology (Kempton and Tomić, 2005). Furthermore, Kempton and Letendre (1997) have proposed V2G which can respond to demand by transferring stored EV battery energy to the grid during periods of high demand. Figure 1 demonstrates the V2G model.
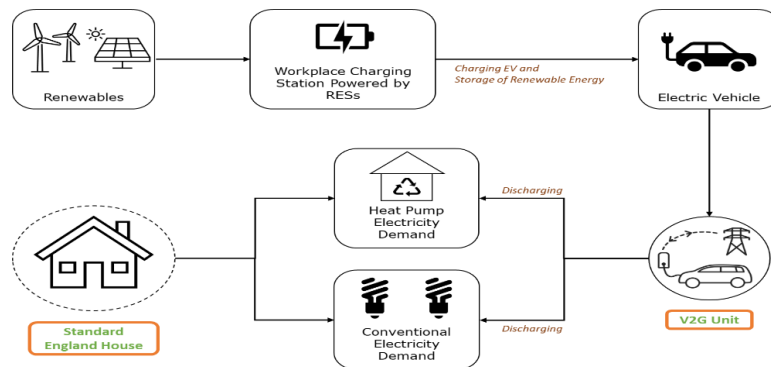
Figure 1: the vehicle-to-grid (V2G) model

The purpose of this paper is to evaluate the effectiveness of EVs with V2G technology in the peak load shaving and demand response in building applications. This study examines whether EVs with V2G can be used to supply the electrical energy needed by HPs and other electronics in a British residence, based on the idea of 100 per cent RES-based power.

2. METHODOLOGY

The use of fossil-based fuels to meet the increasing energy demand has caused environmental problems. Today, the UK government supports the use of HPs for heating and EVs for transport as part of the zero-carbon targets to reduce and end the use of fossil fuels. However, increasing the number of EVs and HPs also may increase the electricity consumption in the grid due to the energy needs of these devices. Therefore, it is essential to use RESs instead of fossil sources in electricity generation not only to end carbon emissions from electricity generation but also to prevent future carbon emissions due to EVs and HPs. Exploring the interaction between EVs, HPs and RESs can eliminate the power problems that high-scale RES integrations will cause in the future. This study is based on the 100% RES concept and investigates the potential of an EV using V2G technology in demand response for a UK traditional detached house with high heating and electrical loads.

In this study, the electric load is investigated across two categories. The first category includes the use of conventional electricity for lighting, cooking, and any other electronics, while the second is based on electricity used by HPs for heating loads.

For the conventional load, the study used the data provided by Energy Saving Trust's (EST) report written by Paula et al. (Owen and Foreman, 2012). The analysis of the energy load patterns of 26 UK residences revealed an average yearly conventional power consumption of 3,638 kWh/year across the nation. The hourly electrical load pattern (excluding the heating load) given by the EST was utilised as a reference in this study. Regarding heating loads, there were two profiles presented with one for average weather conditions (in March), and the other for cold weather conditions (in January). The profiles were sourced from the datasets of the Renewable Heat Premium Payment (RHPP) trial, which monitored heat pump heating loads in about 700 homes considering space heating and domestic hot water demands (Love et al., 2017).
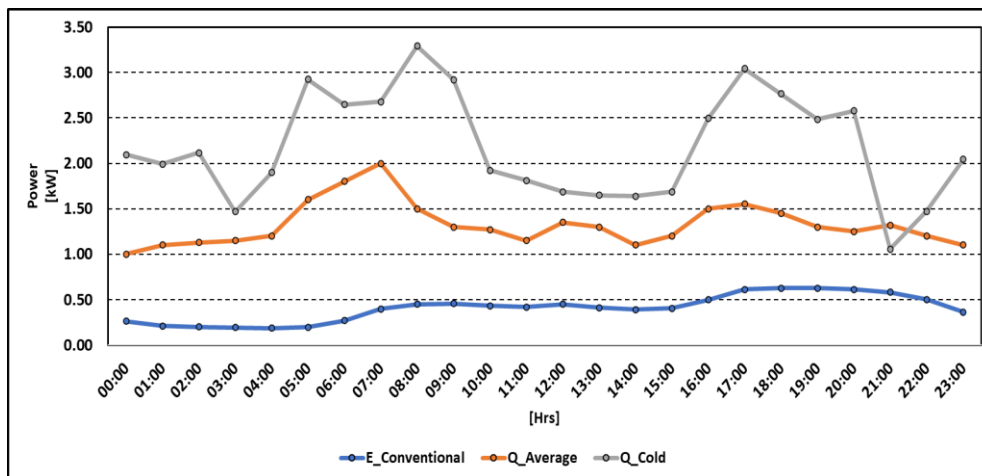
Figure 2: The electricity and heat demand of the house

Figure 2 displays the hourly electrical load pattern as E_Conventional, the heating demand for average weather conditions as Q_Average, and the heating demand for cold weather days as Q_Cold. According to Figure 2, the simulated home's daily conventional electricity use is around 9.75 kWh, with peak power demand occurring between 5 and 10 pm. However, the heating demand profile shows two peaks in the early morning and evening, regardless of the weather. Under average weather conditions, the peak reaches 2 kW in the morning and 1.5 kW in the evening with a daily 31.82 kWh. In the cold weather conditions, the morning peak is 3.3 kW, evening peak is 3 kW with a daily 52.37 kWh.

Since the study was investigating the required electricity to be discharged from the EV, the total electricity demand needed to be calculated on an hourly basis. In order to identify the house's total demand, the HP compressor power consumption was calculated, and it was then added to the conventional electricity demand. Following the determination of the energy requirements, the research analysed UK EV statistics and examined the capability of various EVs to serve the house's load using V2G technology. Once the analysis was completed, the standard air-source HPs were replaced by solar-assisted HPs to explore the interaction of different HPs to the discussed approach, and the analysis was repeated. The case profiles used to evaluate different heat pumps and different air conditions are compared in Table 1.

Table 1: The case profiles of the study

Cases	Ambient Temperature	Heat Pumps
Case 1	Average	Air Source
Case 2	Average	Solar Assisted
Case 3	Cold	Air Source
Case 4	Cold	Solar Assisted

2.1. Description of heat pumps

A heat pump is a device that transfers heat from a low-temperature medium to a high-temperature medium. It consists of four main components namely, compressor, condenser, expansion valve and evaporator. Traditional heat pumps use ambient air as a heat source which makes their performance purely dependent on ambient temperature because heat source temperature directly affects the compressor electricity consumption. The heat pump performance is defined as the coefficient of performance (COP) which is delivered heat to the building over given electricity to the compressor as in Equation (1):

$$Equation\ 1:\ COP\ of\ the\ heat\ pump \qquad\qquad COP = \frac{\dot{Q}_{cond}}{\dot{W}_{comp}}$$

Where $\dot{Q}_{cond}$ and $\dot{W}_{comp}$ indicate condenser heat output and compressor electricity consumption. In the analysis, $\dot{Q}_{cond}$ was building energy demand and compressor consumption was calculated according to weather conditions. As the proposed work considered average and cold weather conditions across the UK, the average COP values were used in the calculation of the electricity consumption of the compressor. For the average heating load profile, 10°C average temperature, for cold weather conditions, 3°C ambient temperature was considered, and electricity requirements were calculated.

In order to improve the performance of the conventional heat pumps, solar-assisted heat pumps were introduced. The solar-assisted heat pump units on the market mostly come with a buffer tank to utilise solar energy at the maximum level. Thus, heat transfer fluid coming from the buffer tank is circulated through the heat pump's evaporator. The collected heat is used as an energy source for the heat pump. In the modelling, maximum condensation temperature was fixed at 70°C, however, evaporation temperature changes by buffer tank temperature and compressor power consumption changes with the operating conditions. Based on a study carried out by our research group, solar-assisted heat pump systems utilise solar energy and increase weekly COP (one week of solar and ambient temperature profiles were used). Using 40m^2 solar thermal collectors with 600 litres of the buffer tank, the average COP increased around 35% under Nottingham real weather conditions. Thus, in this study, a case of adapting a solar-assisted heat pump and its effect on EV battery will be investigated.

2.2. Description of electric vehicles

An International Energy Agency (IEA) finding revealed that there were currently 370-unit EV models with various capacities available (IEA, 2022). The usefulness of V2G to handle the load is strongly affected by the capacity rate of the cars. As a result, EVs with a capacity below the necessary kWh of electrical energy (taking into account daily EV utilisation and V2G efficiency) cannot manage the whole load. Furthermore, the variety of EVs considered in this study by employing 5 distinct EVs, namely, Tesla Model 3, Nissan Leaf, Volkswagen e-Golf, Mercedes C Class and Mitsubishi Outlander, to analyse the effects of different vehicles. To identify these five EVs, the most popular EVs in the UK were first analysed using data from the Department for Transport DfT (DfT, 2022) statistics, and after that, characteristics like their capacity and consumption rates were investigated. Table 2 provides an overview of these EVs and their features.

EVs	Type	Number [Unit]	CAP [kWh]	Consumption [kWh/mile]
TESLA MODEL 3	BEV	54,033	60	0.245
MITSUBISHI OUTLANDER	PHEV	45,956	12	0.27
NISSAN LEAF	BEV	42,174	40	0.264
BMW 3 SERIES	PHEV	34,146	12	0.449
RENAULT ZOE	BEV	20,280	52	0.274
JAGUAR I-PACE	BEV	16,389	84.7	0.36
KIA NIRO	BEV	16,071	64.8	0.278
BMW I3	BEV	13,895	42.2	0.243
BMW 5 SERIES	PHEV	13,256	12	0.285
VOLKSWAGEN ID3	BEV	12,795	55	0.265
AUDI E-TRON	BEV	12,595	85	0.327
MERCEDES A CLASS	PHEV	11,404	15.6	0.251
VOLKSWAGEN GOLF	PHEV	10,849	8.7	0.281
MINI COUNTRYMAN	PHEV	10,720	10	0.243
MERCEDES C CLASS	PHEV	10,518	25.4	0.22
TESLA MODEL S	BEV	10,350	100	0.297
MG ZS	BEV	9,880	49	0.297
HYUNDAI KONA	BEV	9,812	64	0.261
VOLKSWAGEN GOLF	BEV	7,456	32	0.278
HYUNDAI IONIQ	BEV	7,322	54	0.292
KIA NIRO	PHEV	6,280	8.9	0.247

In this research, it was assumed that the EV which will meet the power demands, leaves the house at 8 a.m and returns at 5 p.m., thus the grid will be used to cover all electrical needs between these times. It was also assumed that the EV used in this study was 100% charged at a workplace charging station fully equipped with RESs. These assumptions will be addressed in a future study by using a stochastic approach.

Daily automobile use was assessed using data from the Department of Transportation's National Travel Survey (DfT, 2021). According to the research, a car on UK roads in 2020 travelled 6,700 miles annually, of which 200 miles were for business purposes, 2,400 miles were for commuting, and 4,100 miles were for personal usage. This indicated that a car is typically driven approximately 20 miles per day in the UK. For this reason, discharge operations in the present investigation were restricted to ensure that the vehicle should go at least 20 miles each day. The vehicle was considered to travel half of these 20 miles going away from the house in the morning and the other half on the way home.

Table 3: EV parameters for discharge operations

	TESLA MODEL 3	NISSAN LEAF	VOLKSWAGEN e-GOLF	MERCEDES C Class	MITSUBISHI OUTLANDER
Capacity [kWh]	60	40	32	25.4	12
Distance (Before Arriving Home) [mile]	10	10	10	10	10
Consumption Rate [kWh/mile]	0.25	0.26	0.28	0.22	0.27
Net Power (Before Discharging) [kWh]	57.55	37.36	29.22	23.20	9.3
SOC (Before Discharging) [%]	95.92	93.4	91.31	91.34	77.5
Power Needed (After discharging) [kWh]	2.45	2.64	2.78	2.2	2.7

After calculating the daily travel requirements for the EVs, the efficiency of their electric motors (kWh/mile) was taken into consideration, and the power requirements of the cars before beginning the discharge operations and before leaving the house were computed. Table 3 provides a summary of all these computations. Additionally, in this study, the efficiency of V2G technology was also taken as 90%, while the EVs used were assumed to be suitable for V2G technology.

3. RESULTS

It is almost certain that EVs will be one of the most important power consumers in future grid systems due to their charging needs. On the other hand, HPs, which are one of the most promising low-carbon technologies, will be connected to the grid with high electricity demands in the future. The utilisation of RESs to meet this increasing electricity demand may be possible if EVs are able to be used as a storage medium. This study set out to evaluate

how effective EVs and V2G are in responding to the electricity demand, especially the peak load, of a British household whose heating needs are met by a heat pump.

The first set of analyses examined the electricity consumption by air source and solar-assisted HPs under average weather conditions. While Figure 3a shows the hourly conventional electricity load and calculated electricity consumption by air-source HP under Case 1, the data presented in Figure 3b displays the figures based on Case 2. A closer inspection of the figure comparing air-source and solar-assisted HPs under the same weather conditions shows the preference for solar-assisted HPs which could reduce the total daily electricity consumption in the house by 12.6% from 20.71 kWh to 18.18 kWh. However, in this study, since the EV would only be at home during certain hours, the amount of electricity that must be met by the EV was 14.2 kWh for Case 1 and 12.4 kWh for Case 2.
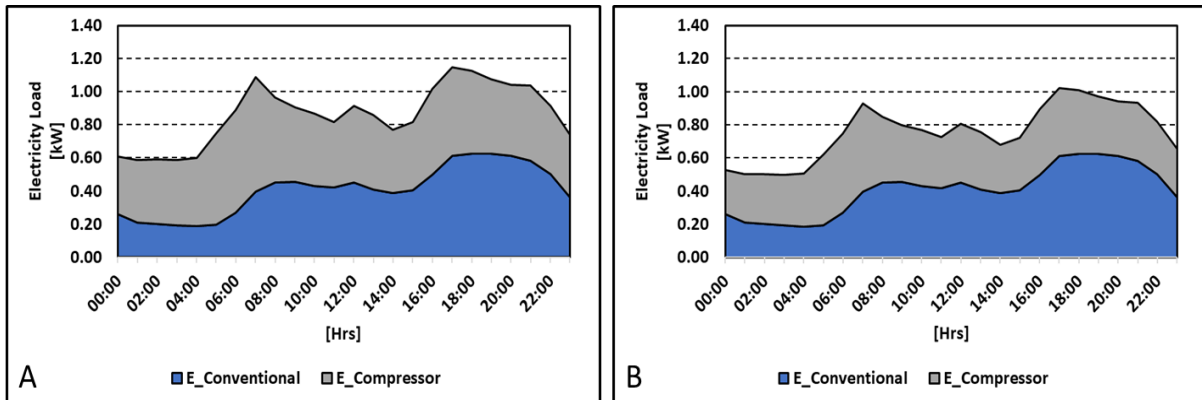
Figure 3: The sum of conventional electricity load and compressor demands in average weather conditions, (a) based on Case 1 (b) based on Case 2

The results from Case 3 and Case 4's analysis for the cold weather conditions are set out in Figure 4a and 4b, respectively. According to the calculation, the total electricity load of the house was 31.2 kWh with air-source HP and 26.42 kWh with solar-assisted HP; therefore, solar-assisted HP provided a 15.6% drop in load in cold weather conditions. What stands out in these figures given above is that by far the greatest demand is under Case 3 which included cold days and air source HP, while Case 2 has the lowest demand because of the warm weather and solar-assisted HP.
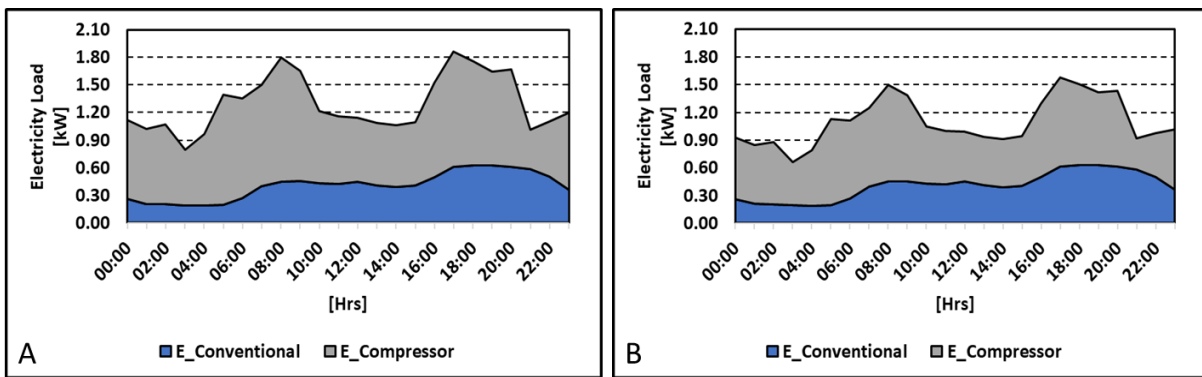
Figure 4: The sum of conventional electricity load and compressor demands in cold weather conditions, (a) based on Case 3 (b) based on Case 4

Figure 5 and Figure 6 show the hourly state of the battery charge profiles of discharged EVs based on the cases analysed in this study. In the figure, the EV's discharging period is shown on the X-axis. Additionally, the right Y-axis illustrates the battery's state of charge, while the left Y-axis displays the battery's available power. The bars on the figures are the indicator of battery capacities in kWh, while the lines display the battery status as a percentage.
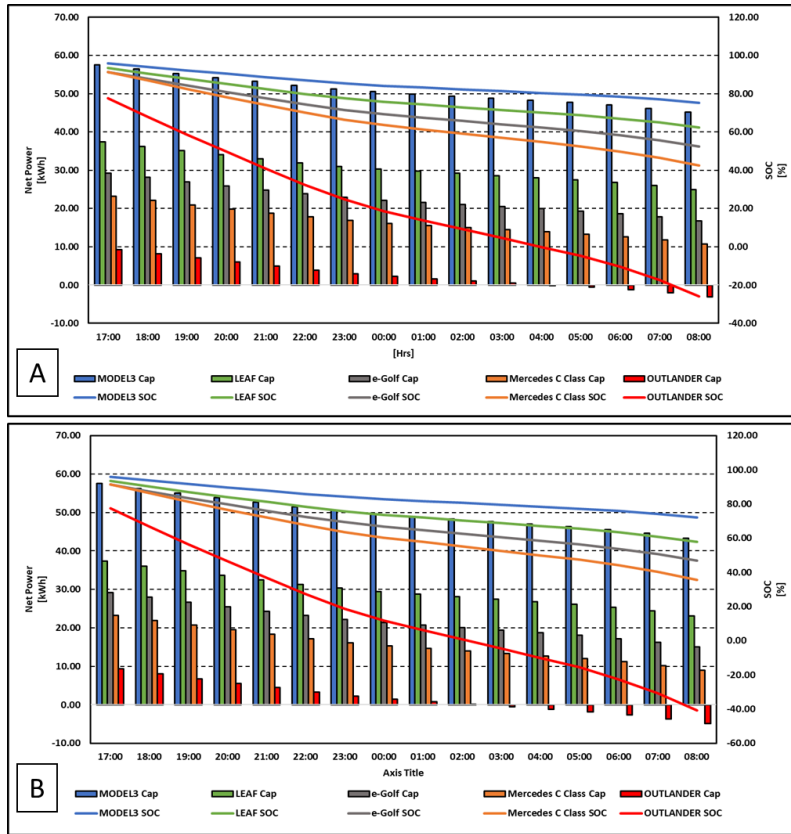
Figure 5: Hourly state of the battery charge profiles of discharged EVs in average conditions; (A) based on Case 1, and (B) Case 2
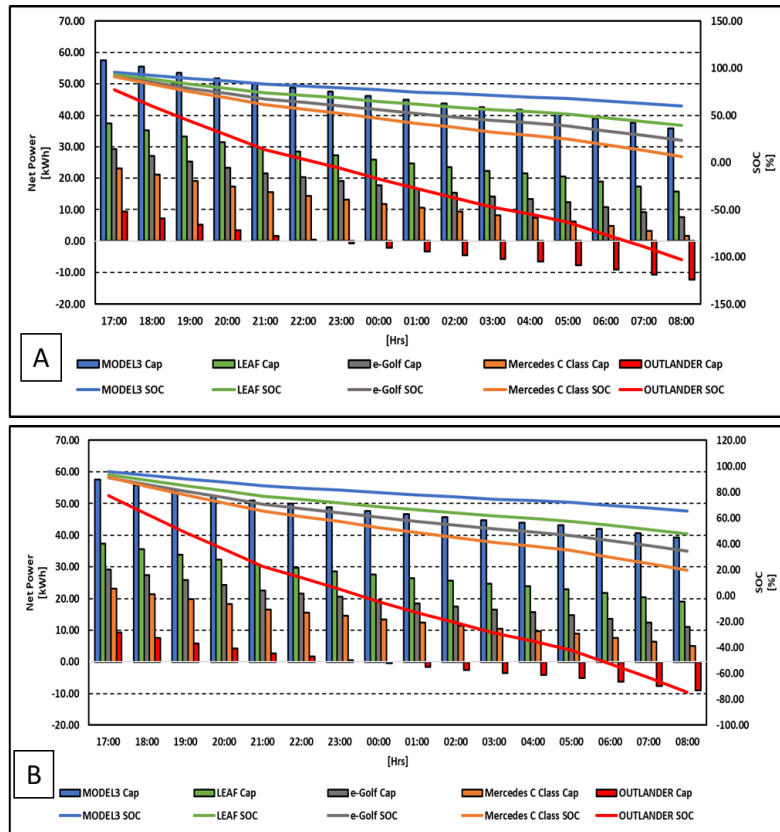
Figure 6: Hourly state of the battery charge profiles of discharged EVs in cold conditions; (A) based on Case 3 and (B) Case 4

Table 4 shows the summary of the findings based on Figure 5 and Figure 6. The results show that Tesla Model 3, Nisan Leaf and VW e-Golf (BEV) were suitable for all cases in the proposed methodology. Tesla Model 3 could achieve two days of operation without re-charging in all cases, whilst the Nissan Leaf could provide two days of service only in average weather conditions. However, VW e-Golf could respond to the load of the house only for one day in all cases, needing to be recharged for the following day.

Results for Mercedes C Class show the importance of using a solar-assisted heat pump unit. Although the battery of the Mercedes successfully covered the loads in average weather conditions (Case 1 and Case 2), the battery failed when the heating demand met by the conventional HP was high (Case 3). However, this EV could be able to supply the whole electricity needs of the building even in cold weather conditions if the house was equipped with a solar-assisted heat pump.

Looking at Table 4, it was apparent that vehicles such as Mitsubishi Outlander PHEV with a small battery were not suitable for the proposed methodology in all cases. However, this PHEV and similar may be able to be used only for peak demand. When the travel needs of the Outlander were considered, the car still had 6.6 kWh of power to discharge to the house during the peak electricity consumption times.

Table 4: The charge status of the EVs at the end of the day

EVs/Cases	Case 1	Case 2	Case 3	Case 4
Tesla Model 3	68.2%	71.1%	55.8%	61.4%
Nissan Leaf	51.3%	55.7%	32.7%	41.2%
VW e-Golf	38.2%	43.8%	15.1%	25.6%
Mercedes C Class	26.7%	33.7%	-2.5%	10.8%
Mitsubishi Outlander	-63.3%	-48.5%	-125%	-97.1%

On the other hand, if the total electricity demand of the house was met through V2G, as mentioned above, the excess renewable generation would be able to integrate into the grid. In addition, with this method, the stress to be created on the grid by HPs, which would increase in number in the future, may be reduced by using EVs. More importantly, zero-carbon targets could be supported by reducing carbon emissions through the cooperation of RESs and EVs.

Table 5: The amount of daily GHG emissions saved and excess RE recovered

Cases	Saved CO2e [kgCO2e]	Integrated RE [kWh]
Case 1	3.02	14.2
Case 2	2.65	12.4
Case 3	4.60	21.6
Case 4	3.88	18.3

The conversion rate of greenhouse gases has been determined as 0.21233 kgCO2e/kWh for the UK grid in 2021 (Hill et al., 2020). It has been observed that the methodology might recover up to 21.6 kWh of excess renewable energy on cold days and prevent up to 4.6 kgCO2e of GHGs per day. However, this study only analysed one house and one vehicle. Therefore, considering the national models in which future scenarios are included, a considerable amount of RE can be integrated into the grid system and emissions from electricity generation can be minimised.

4. CONCLUSION

This project was undertaken to explore the maximum interaction between EVs, RESs and HPs and evaluate the effectiveness of the EVs with V2G technology for demand response by considering the heating loads of the UK buildings in average and cold weather conditions. Air source and solar-assisted heat pumps based on heating profiles provided building heat demand. After calculating the total electricity requirements of the building for different cases, EVs' state of battery capacities were compared by consumption (mile/kWh) and taken into consideration.

The findings indicated that the maximum total electricity demand could reach 21.63 kWh in the highest demand scenario, Case 3. It was identified that the EVs, which had a battery capacity of 25.4 kWh, still could not provide the whole required electricity due to battery efficiency and daily travel needs. However, the current data highlighted the importance of solar-assisted HPs because the same EV was achieved successfully when a solar-assisted heat pump unit replaced the air-source HP. One of the more significant findings to emerge from this study was that the EVs' battery needed to be more than 54 kWh under the proposed methodology to avoid daily recharging even in the worst conditions. Moreover, the most popular EV in the UK, Tesla Model 3, showed promising results in this study by allowing two days of operation before needing to be recharged.

This approach will prove helpful in expanding the understanding of how EVs and HPs might be a solution to minimise carbon emissions and large-scale RES integration instead of being a challenge that adds additional electricity load into the system.

5. REFERENCES

BBC. 2020. *Climate change: Last decade UK's 'second hottest in 100 years'* [Online]. Available: https://www.bbc.co.uk/news/science-environment-50976909 [Accessed 14.07.2022].

BEIS. 2021. Net Zero Strategy: Build Back Greener. Department for Business, Energy & Industrial Strategy (BEIS).

BEIS. 2022. *Energy Trends (June 2022)* [Online]. Department for Business, Energy & Industrial Strategy (BEIS). Available: https://www.gov.uk/government/statistics/energy-trends-section-6-renewables [Accessed 14.07.2022].

Bouckaert, S., Pales, A. F., Mcglade, C., Remme, U., Wanner, B., Varro, L., D'Ambrosio, D. & Spencer, T. 2021. Net Zero by 2050: A Roadmap for the Global Energy Sector.

Buker, M. S. & Riffat, S. B. 2016. Solar assisted heat pump systems for low temperature water heating applications: A systematic review. *Renewable and Sustainable Energy Reviews,* 55**,** 399-413.

Cervantes, J. G. & Torres-Reyes, E. 2002. Experiments on a solar-assisted heat pump and an exergy analysis of the system. *Applied Thermal Engineering,* 22**,** 1289-1297.

Chua, K. J., Chou, S. K. & Yang, W. 2010. Advances in heat pump systems: A review. *Applied energy,* 87**,** 3611-3624.

DFT. 2021. *NTS0901: Annual mileage of cars by ownership and trip purpose: England, since 2002* [Online]. Department for Transport (DfT). Available: https://www.gov.uk/government/statistical-data-sets/nts09-vehicle-mileage-and-occupancy [Accessed 14.07.2022].

DFT. 2022. *Licensed Ultra Low Emission Vehicles by Body Type and Propulsion or Fuel Type* [Online]. Department for Transport (DfT) Statistics. Available: https://www.gov.uk/government/statistical-data-sets/vehicle-licensing-statistics-data-tables [Accessed 14.07.2022].

EC. 2019. *Clean energy for all Europeans Package* [Online]. European Comission (EC). Available: https://ec.europa.eu/energy/topics/energy-strategy/clean-energy-all-europeans_en [Accessed 14.07.2022].

Hill, N., Bramwell, R., Karagianni, E., Jones, L., Maccarthy, J. & Hinton, S. 2020. Government greenhouse gas conversion factors for company reporting: Methodology paper. Department for Business. *Energy and Industrial Strategy.*

IEA. 2022. *Global EV Data Explorer* [Online]. International Energy Agency. [Accessed 15.07.2022].

Kempton, W. & Letendre, S. E. 1997. Electric vehicles as a new power source for electric utilities. *Transportation Research Part D: Transport and Environment,* 2**,** 157-175.

Kempton, W. & Tomić, J. 2005. Vehicle-to-grid power implementation: From stabilizing the grid to supporting large-scale renewable energy. *Journal of power sources,* 144**,** 280-294.

Love, J., Smith, A. Z., Watson, S., Oikonomou, E., Summerfield, A., Gleeson, C., Biddulph, P., Chiu, L. F., Wingfield, J. & Martin, C. 2017. The addition of heat pump electricity load profiles to GB electricity demand: Evidence from a heat pump field trial. *Applied Energy,* 204**,** 332-342.

Nedelcheva, G. 2021. *UK Solar Capacity: Is the Future of Solar Cloudy?* [Online]. GREENMATCH. Available: https://www.greenmatch.co.uk/blog/2019/09/uk-solar-capacity [Accessed 14.07.2022].

Owen, P. & Foreman, R. 2012. Powering the nation: Household electricity using habits revealed. *Energy Saving Trust/DECC/DEFRA, London.*

Prime, J., Khan, S. & Wilkes, E. 2014. CHP 1: Overall Data Tables, Energy Consumption in the UK *Chapter 3: Domestic Energy Consumption in the UK Between 1970 and 2014*.

Sinsel, S. R., Riemke, R. L. & Hoffmann, V. H. 2020. Challenges and solution technologies for the integration of variable renewable energy sources—a review. *renewable energy,* 145**,** 2271-2285.

Sundararagavan, S. & Baker, E. 2012. Evaluating energy storage technologies for wind power integration. *Solar Energy,* 86**,** 2707-2717.

Zhang, C., Wei, Y.-L., Cao, P.-F. & Lin, M.-C. 2018. Energy storage system: Current studies on batteries and power condition system. *Renewable and Sustainable Energy Reviews,* 82**,** 3091-3106.

#75: An evaluation of the UK electricity grid for high RES and EV penetration

Abdullah Dik, Siddig Omer, Rabah Boukhanouf

Department of Architecture and Built Environment, Faculty of Engineering, The University of Nottingham, Nottingham NG7 2RD, UK

Abstract: The carbon intensity of the UK electricity grid is currently experiencing a fast reduction as a result of increasing the share of power generation from renewable sources, particularly wind. The UK energy policy towards achieving zero carbon emissions by 2050 requires both the building and transport sectors to be decarbonised. This, however, presents a huge technical and economical challenge in that all heat generation in buildings needs to be supplied from electrically-driven heat pumps and fossil-fuelled private vehicles be replaced by electric vehicles (EVs) which are affordable to consumers. Achieving such an ambitious goal will require the power generation capacity to more than double which in turn exacerbates the issue of intermittency of renewables and low inertia in the grid system. This paper attempts to analyse the current UK grid system critically and addresses the question of what will happen to the UK's electricity grid under large-scale RES integration and high EV penetration. With the increasing number of EVs connected to the grid for charging, management of plug-in EVs becomes critical to maximise the use of renewables, particularly at times of excess generation.

1. INTRODUCTION

Population growth and technological developments are probably the primary drivers for the increasing electricity demand. An IEA report (IEA, 2022) showed that global annual electricity consumption increased from approximately 11 GWh to 25 GWh between 1990 and 2019. In the UK, the Department for Business, Energy & Industrial Strategy (BEIS) statistics (BEIS, 2022) showed that electricity consumption, which had remained almost constant since 2014, started to increase again in 2021. Additionally, developments in electric vehicle technology and incentives for EV penetration within the scope of zero-carbon targets increased the number of EVs on UK roads, reaching 738,986 units at the end of 2021 (DfT, 2022). Moreover, National Grid (NationalGrid) predicts that the upward trend will accelerate, and EV numbers will reach as high as 36 million by 2040. Therefore, it is an urgent issue whether the UK's grid will be sufficient to deal with this rapid growth in the electricity demand due to increasing daily energy needs in addition to the increasing number of EV charging needs.

Another unanswered question is what types of energy sources will cover the increasing electricity demand in the grid. Today, fossil-based energy sources play a prominent role in the electricity market of many countries. BEIS (Harris *et al.*, 2022) state that the UK's fossil fuel usage for electricity generation reached 43% in 2021. There is no doubt that using fossil fuels for the increasing electricity demand could increase carbon emissions, which is one of today's biggest problems. More importantly, the utilisation of fossil fuels for EVs' charge loads could make the use of EVs conflicting with their primary purpose.

Renewable Energy Sources (RESs) can be instrumental in decarbonising the grids and mitigating climate change (Sinsel *et al.*, 2020) and developed countries have been increasing the usage of RESs in energy markets. For instance, RES production reached a record level in the UK in 2020 (Harris *et al.*, 2022). Along with the growth of RES usage, the UK grid still needs large-scale RES integration to achieve its zero-carbon targets. However, the intermittent and unpredictable nature of RESs causes power quality problems in the grid. Therefore, storage technologies seem necessary for a safe large-scale integration.

EVs, whose number is increasing daily, might be one of the newest and most promising solutions to improve the integration of renewable energy (RE) into the grid. Because of their battery technology, EVs can store excess renewable energy without causing an additional storage cost (Kempton and Tomić, 2005). It might be possible to profit from the EVs' batteries to increase the usage of RES in the UK if the synergy is able to be discovered between RES and EVs as illustrated in Figure 1.
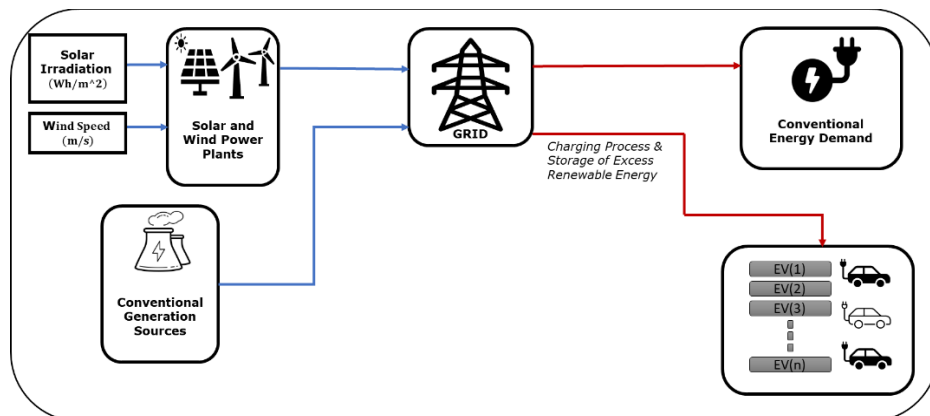
Figure 1: Using EVs to store excess RE during peak generation times for use during peak demand

This study seeks to develop an understanding of the status of the UK's power grid and to estimate the possible future power problems related to EVs and RESs.

2. METHODOLOGY

Today, data analysis is widely available and used in many investigational studies to convert complex raw data into a meaningful form. Descriptive analysis is one of the most common methods to describe, organise and summarise the raw data. The UK's conventional electricity consumption, conventional electricity generation and RE generation values were analysed in the present study. It was decided that the best method to adopt for the dataset analysis was the usage of descriptive analysis. Figure 2 shows the process steps applied for the analysis in this paper. The dataset showing the energy flow on the grid at 5-minute intervals in 2021 was provided by GRIDWATCH (GRIDWATCH, 2022). In the first stage, the figures in the dataset containing thousands of pieces of information were defined, and then the missing, incorrect, or duplicated values were organised and made usable. In the second stage, unnecessary data was removed, and the dataset was converted into the desired format. The graphics were created and interpreted in the final stage through analysis and discussion.
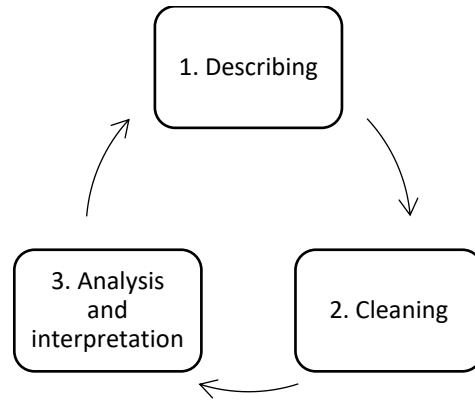
Figure 2: The process used for data analysis

In recent years, two different approaches, deterministic and stochastic, have been used to estimate EV demands. It is obviously necessary to know uncertainties such as battery capacity, energy consumption rate, state of the battery charge (SOC), charge/discharge power, driver behaviours, and charge starting time in evaluating the charge demands. The literature argues that the stochastic approaches might give more realistic results (Kim and Hur, 2020). For this reason, this paper adopted a stochastic approach to calculate the charge load of the UK's EV fleet.

The dataset providing various information such as the number, type, and registration dates of EVs available in the UK was obtained from DfT (DfT, 2022). The model considered three EV battery groups, namely small, medium, and large batteries. Then, an average battery capacity for each battery group was determined by considering the UK's current EV trends. Here, the UK's trends were analysed using data from DfT (DfT, 2022) statistics. Next, taking into account the utilisation shares of the battery capacities in the UK, the model randomly allocated a battery capacity for each car in the dataset. As mentioned above, the parameters such as driving models, charging behaviours, EV types and battery capacity are important variables affecting EVs' SOC. For this reason, there were some uncertainties in calculating the SOC of EVs. Since this was a UK-wide analysis, the Linear Congruence Generator, which was also used in Monte Carlo analysis, was modelled in MATLAB to generate random numbers for the SOCs of each vehicle in the dataset. In this case, it was assumed that the SOCs of the EVs to be charged would range between 20% and 80%. After this stage was complete, the amount of energy needed for each EV whose SOC and total capacities were known were calculated with the help of the simple formula given in Equation 1.

Equation 1: The charge load of each vehicle

$$NE = \left(Battery\ Capacity\ (kWh) \times \left(\frac{100 - SOC(\%)}{100} \right) \right)$$

Where NE (kWh) refers to the electricity demand of the vehicle while SOC stand for the state of charge of the vehicle.

3. RESULTS

The UK electricity grid system, which was first established 120 years ago, has transformed into the interconnected grid system used today. Although the grid networks are complex systems, energy balance is the most crucial issue for these systems. At any time, the electrical energy fed into the network must equal the electrical energy consumed at that moment. Otherwise, the network will fail, and blackouts may occur. The first set of analyses examined the current status of the UK's grid under the existing electricity generation and demand.

Figure 3 shows an overview of the monthly energy flowing in the UK's electricity grid. In the figure, Excess refers to the difference between the electrical energy consumed and the sum of the electrical energy imported and generated from Conventional, Solar Photovoltaics (PVs) and Wind energy sources. As readily apparent, while the UK electricity grid has an excess of up to almost 1.5 TWh per month in the spring and summer periods, there is almost no difference between energy generation and consumption values due to the increase in heating load in winter and autumn. It means that the existing network system may not be suitable for possible additional loads in the winter and autumn periods. Therefore, a potential load increase in these periods may cause additional network investment costs.
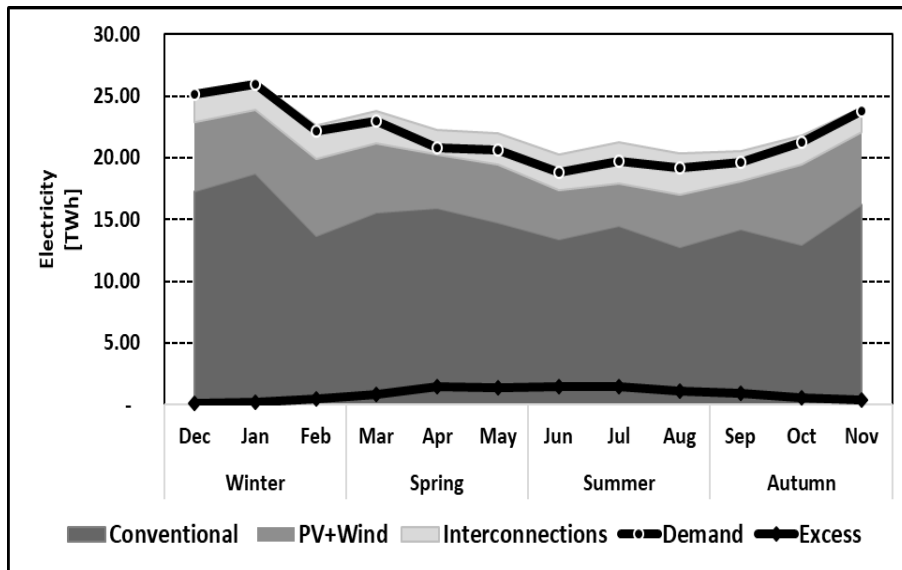
Figure 3: The current status of the UK's grid

Figure 4 displays the hourly distribution of UK electrical energy generation from PVs and wind turbines in 2021. The fact that there is a decline in wind energy generation in the summer season prevents the formation of much higher overgeneration in the grid, however; the decrease in the summer electricity demand caused more than 4 TWh of excess energy in just three months (June, July, and August).
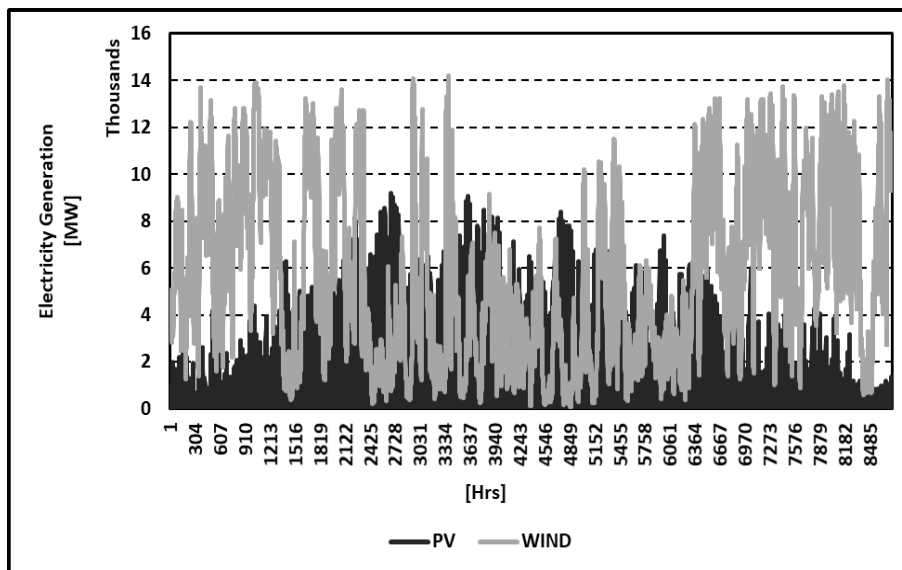
Figure 4: Electricity generation from solar PVs and wind turbines in the UK

Figure 5 presents the variation of the UK annual electricity demand by year. Data provided by BEIS (BEIS, 2022) showed that electricity demand in the UK decreased by almost 50 TWh between 2000 and 2020, despite some breaks in years. There is no doubt that the main reason for this phenomenon is the improvement of energy efficiency day by day. After the downward trend, an increase of about 2% (approximately 5 TWh) was observed in electricity consumption in 2021. A remarkable point here was that if the excess energy generated had been able to be used, the demand increase of 5 TWh in 2021 would have easily been met with excess energy of 10.34 TWh. However, a serious challenge to be emphasised about the electricity demand is that the Balanced Net Zero (BNZ) Pathway scenario modelled by Daly *et al.* (Daly *et al.*, 2022) predicted that the UK's electricity consumption rate will increase by 56% and reach 470 TWh by 2035.
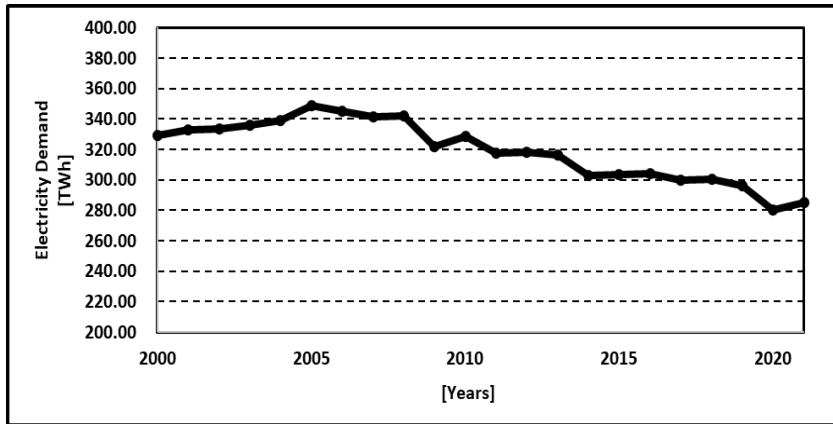
Figure 5: The comparison of the electricity demand of the UK's grid by year

Another formidable challenge is peak demand times when most electrical energy is consumed. As an example, Figure 6 shows the hourly electrical energy consumed in the UK on 15 January. As can be seen, the peak time of the UK grid is at 6 pm, so any additional load at that time can lead to overloading problems in the grid. Peak load is one of the most challenging problems faced by grid networks. Increasing the peak load is an undesirable situation because it requires high energy over a short period of time and causes high energy costs (Ueckerdt and Kempener, 2015). However, in the future, it is expected that many people, especially those commuting, might plug in their cars at the evening peak times of the grid to fill their battery for the next day. This phenomenon likely causes an increase in the peak load, overloading the branches and congestion.
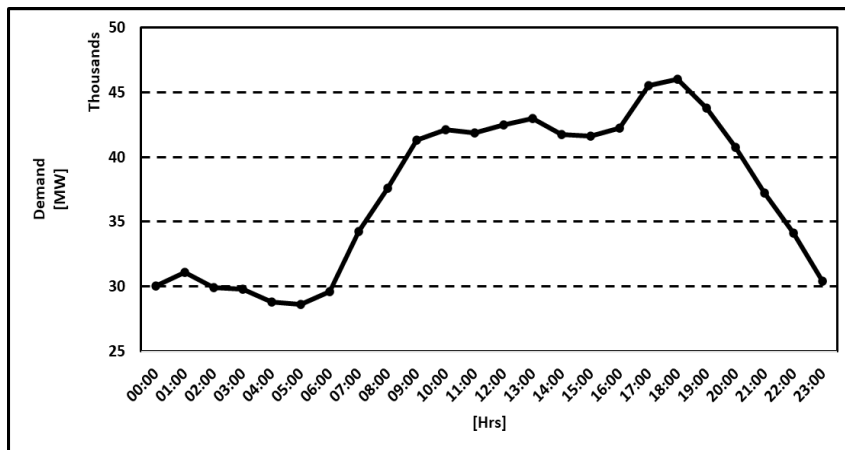
Figure 6: The hourly demand profile on the 15 of January

Further analysis can be made on EVs by using the EV dataset, which was created by modelling EVs stochastically under the UK's EV market status. Table 1 provides information about some of the 637,252 EVs modelled in this study.

Table 1: Some of the modelled EVs and their features

EV Name	Battery Group	Battery Capacity [kWh]	SOC [%]	Daily Energy Demand [kWh]
EV1	Medium	38	50	19
EV2	Small	11	78	2.42
EV3	Medium	38	67	12.54
EV4	Small	11	54	5.06
EV5	Small	11	75	2.75
EV100000	Large	74	67	24.42
EV100001	Small	11	41	6.49
EV100002	Small	11	74	2.86
EV100003	Medium	38	62	14.44
EV100004	Medium	38	48	19.76
EV637248	Medium	38	42	22.04
EV637249	Small	11	68	3.52
EV637250	Small	11	37	6.93
EV637251	Small	11	24	8.36
EV637252	Small	11	72	3.08

Studies show that 87% of EVs in the UK are charged at home (REGEN, 2018), and 70% are charged once a day (Quirós-Tortós *et al.*, 2015). However, if it is considered that all EVs in the dataset charge once per day, EVs on the UK's roads can result in additional electricity demand of 13.2 GWh per day. But, due to peak demand difficulties, the connection period of EVs to the grid is more important than the total load they will cause. The hourly impact of EVs on the UK's grid will be modelled in a future study.

The fossil-based energy sources with high capacity might easily be able to cover future electricity demand, which will increase due to EVs and other energy consumption devices. However, this may increase existing carbon emissions exponentially. To better understand the carbon emissions caused by the charging demands of EVs, the energy mix of the UK grid should be analysed. The UK grid electricity mix by years is presented in Figure 7, created using BEIS (BEIS, 2021a) statistics.
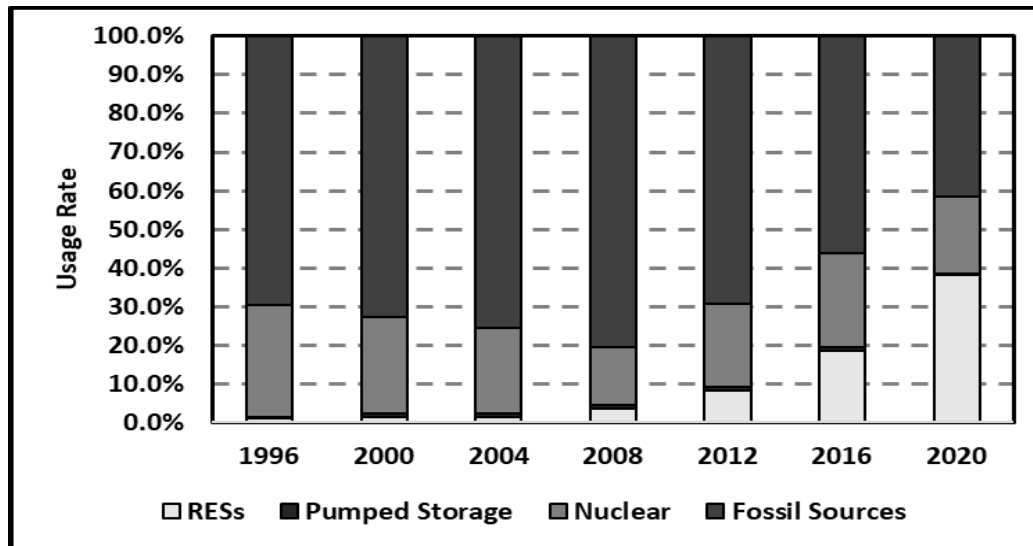
Figure 7: The energy mix of the UK's electricity grid

Additionally, BEIS assessment (Hill *et al.*, 2020) declared that the conversion factors of the greenhouse gas emissions for the grid are 0.55828 kgCO2e/kWh and 0.21233 kgCO2e/kWh in 1996 and 2021, respectively. From the general perspective, if today's grid greenhouse conversion factor had been the same with 1996, today's EVs in the UK would have been able to release an additional 5,000 tCO2e of greenhouse gases per day because of their potential daily charge load of 13.2 GWh. That is, only EVs will release an extra 2 million tCO2 in a year. When considering future EV scenarios, it becomes clear that using RESs to cover EV charging loads is essential for both carbon reduction goals and a clean environment.

The next question that should be asked is whether the total installed RES capacity is sufficient to meet today's and future EV charge demands. The data showed that the UK generated 81.6 TWh of electricity in 2021, and almost 60% came from wind turbines. If the total amount of RES generation had been able to be used for charging the current EV fleet in the UK, such an amount of RES generation would met the potential annual charge needs of the EVs 17 times over.

The data analysed from BEIS (BEIS, 2021b) are set out in Figure 8 and show how the amount of RES installed capacity increased over the years. What is important in this figure is the dominance of wind and PV capacities. These two dominant energy sources have a high potential for large-scale integration and meeting the increasing electricity demand. However, it is impossible to quickly deactivate high-capacity conventional energy sources and replace them with PV and wind turbines due to these two sources' intermittent and fluctuating nature.
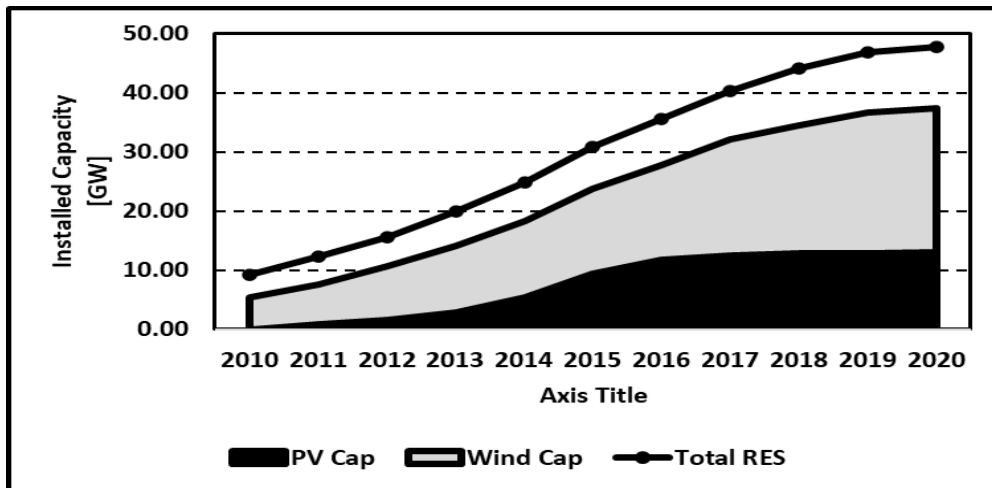
Figure 8: The installed capacities of RESs in the UK

Figure 9 compares the electricity generation from the different RESs in the UK in 2021. Looking at the figure, it is apparent that, unlike wind and PV, hydro and biomass sources generate a near constant amount of electricity each month of the year. Figure 4 can also provide an in-depth reading of the UK's fluctuation of PV and wind energy in the UK.
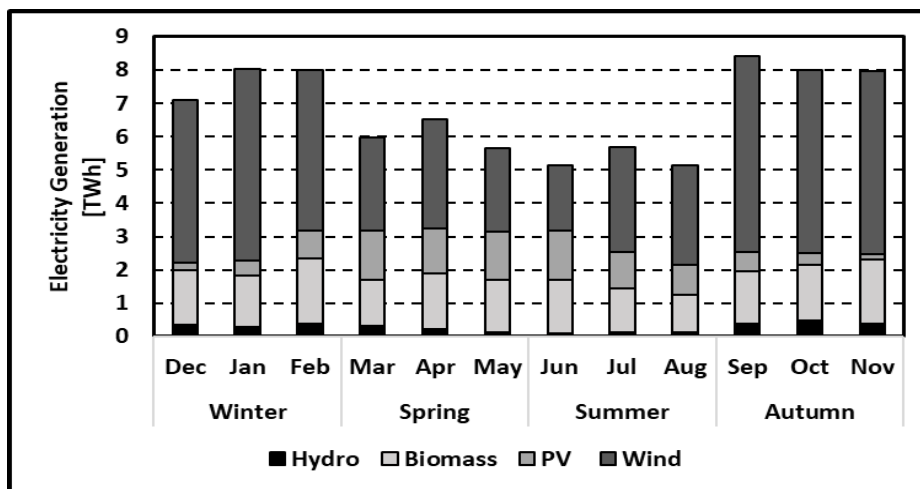
Figure 9: The types of RESs used for electricity generation in the UK in 2021

As shown above, instantaneous fluctuations in solar irradiation and wind speed cause unpredictable electrical outputs from these two sources and, therefore, power quality problems in the grid. Two undesired situations may be encountered in grids with high-capacity RES: overgeneration on days when solar radiation and wind speed are high and overloading on days when these weather conditions are low. These phenomena cause frequency and voltage variations that damage power networks and cause blackouts.

Figure 10 depicts the hourly and monthly surplus electricity generation and electricity shortage conditions in the UK network in 2021 under current conditions. Where the net electricity refers to the difference between the total electrical energy generated and imported and the electrical energy consumed, the excess share curve represents the ratio of the surplus electricity to the total electricity. It is apparent from the figure that although the UK's grid failed to meet the total demand at some points on an hourly basis in 2021, it was generally seen to be sufficient to meet the current electricity demand. However, on average, the interconnection lines accounted for 12% of the monthly demand, therefore, a possible interruption in these lines may cause the UK network to fail to meet the current load. Moreover, one of the most exciting aspects of this graph is that there was almost no difference between the total electricity generated and imported and the current demand in the winter and autumn periods. Hence, when the rapidly increasing EV charging demands were added to the system, a lack of electricity would likely appear, and therefore severe investment costs for expanding existing grid systems are required. If the new demand, including EV loads, massively exceeds the total supply, the grid may face terrible blackouts that destroy the electricity grid.
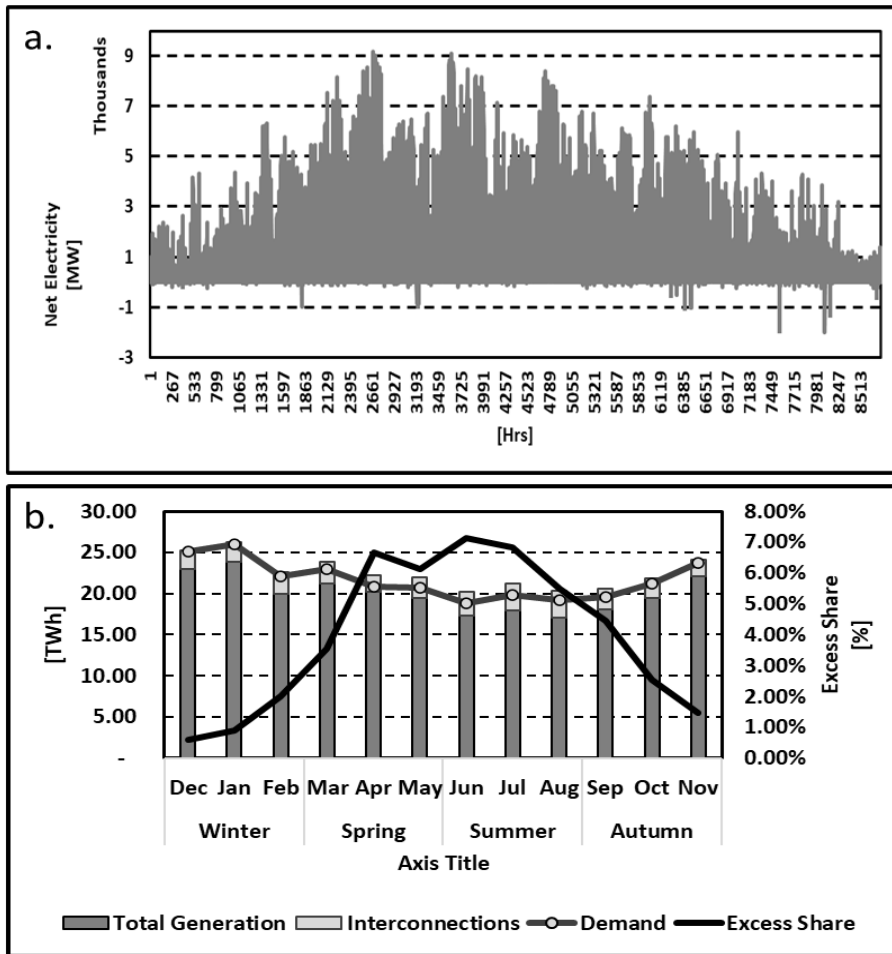
*Figure 10: The cases of excess generation and electricity shortage in UK's grid
on (a) hourly basis and (b) monthly basis*

On the other hand, the massive amount of excess energy due to high PV energy potential and lower demand in the summer and spring months in the UK leads to wasted renewable energy (RE) as it cannot be sold through interconnection networks or stored. In such cases, the RE curtailment phenomenon occurs where transmission network operators allow RES generation to go to waste.

According to the UK's zero carbon targets, it is expected to increase the percentage of electricity generation from RESs from 29% in 2020 to 70% by 2050. Additionally, it is planned that solar and wind energy sources will be responsible for half of the total electricity supply in 2050 (Bouckaert *et al.,* 2021). It is evident that these developments will cause more power quality problems in the future for the UK's grid if no precaution is taken, and much more renewable energy will be wasted during the summer and spring periods.

Even though EVs are one of the main reasons for all the problems mentioned above, they may also be the most effective solution to deal with these problems. There is a strong synergy between EVs and RES. If an effective charging strategy can be developed, excess RE can be stored in EV batteries. Under current conditions, the UK grid generated an excess of 10.34 TWh of energy in 2021. To understand the magnitude of the excess energy production in the UK, if 13.2 GWh of daily charging demand of EVs modelled in this study is considered, the existing annual excess energy production is more than twice the annual EV charge requirements.

4. CONCLUSIONS

The purpose of the present research was to carry out an energy analysis of the UK's grid to understand better the challenges that the grid will face under large-scale RES integration and high EV penetration. In this investigation, the energy flow on UK networks was comprehensively assessed by modelling the potential EV charge demands and discussing EVs' potential to store RE generation. The most apparent findings to emerge from this study are summarised as follows:

1. Currently, the UK's grid system is sufficient to meet electricity demand even if it fails in some hours of the year;

2. The existing EV charge load is not at such a dangerous level that the grid cannot cover it. However, hourly analysis is necessary to examine its effect on evening peak demand;

3. In the autumn and winter, when demand is high, the grid is not quite suitable for the additional electricity demands. Hence, EV charge demands in the future could result in significant investment for capacity expansions. However, increasing only the network's capacity may increase excess generation in the spring and summer periods, thus allowing power problems in the grid;

4. During the spring and summer periods, the UK's grid has serious excess energy as a result of low electricity consumption and high PV generation. The results of this investigation shows that the amount of available excess energy is reasonably sufficient to charge the existing EVs in the UK. However, excess renewable energy, which cannot be spent on the grid, not only endangers the grid security but also causes valuable renewable energy to go to waste.

Overall, this study strengthens the idea that the UK's power grid with large-scale RESs and an increased number of EV fleets might face destructive challenges. The UK needs both high EV penetration and large-scale RES integration to achieve the zero-carbon targets. The paper's findings suggest that the power grid, which tries to deal with many power quality and power flow problems under the current conditions, should take advantage of the synergy between EVs and RES to overcome the new potential problems. It is strongly recommended that appropriate charging strategies such as vehicle-to-grid (V2G) and smart charge (V1G) should be adopted to minimise storage needs and large-scale RES challenges.

5. REFERENCES

BEIS, 2021a. Dukes (5.3): Fuel Used in Generation. Department for Business, Energy and Industrial Strategy (BEIS) Statistics.

BEIS, 2021b. Regional Statistics 2003-2020: Renewable Energy Installed Capacity. Department for Business, Energy and Industrial Strategy (BEIS) Statistics.

BEIS, 2022. Supply and Consumption of Electricity. Department for Business, Energy and Industrial Strategy (BEIS) Statistics.

Bouckaert, S., Pales, A. F., McGlade, C., Remme, U., Wanner, B., Varro, L., D'Ambrosio, D. & Spencer, T., 2021. Net Zero by 2050: A Roadmap for the Global Energy Sector. International Energy Agency (IEA).

Daly, E., Finkel, V., Kar, J. & Pani, M., 2022. Facing the future: Net zero and the UK electricity sector [Online]. McKinsey&Company. Available: https://www.mckinsey.com/industries/electric-power-and-natural-gas/our-insights/facing-the-future-net-zero-and-the-uk-electricity-sector [Accessed 24.06.2022].

DFT, 2022. VEH0133: Licensed ultra low emission vehicles (ULEVs) at the end of the quarter by body type and fuel type, including breakdown of generic models: Great Britain and United Kingdom. Department for Transport (DfT) Statistics.

Gridwatch, 2022. National Grid Status. Available: https://www.gridwatch.templar.co.uk/ [Accessed 24.06.2022].

Harris, K., Michaels, C., Rose, S., Ying, D., Martin, V., Spry, W. & Spry, W. 2022. Energy Trends. Department for Business, Energy and Industrial Strategy (BEIS).

Hill, N., Bramwell, R., Karagianni, E., Jones, L., Maccarthy, J. & Hinton, S., 2020. Government greenhouse gas conversion factors for company reporting: Methodology paper. Department for Business, Energy and Industrial Strategy, 128.

IEA, 2022. IEA Data Browser; Electricity. Available: https://www.iea.org/fuels-and-technologies/electricity [Accessed 24.06.2022].

Kempton, W. & Tomić, J., 2005. Vehicle-to-grid power implementation: From stabilizing the grid to supporting large-scale renewable energy. Journal of power sources, 144, 280-294.

Kim, S. & Hur, J., 2020. A probabilistic modeling based on Monte Carlo simulation of wind powered EV charging stations for steady-states security analysis. Energies, 13, 5260.

Nationalgrid. Keeping 36 million electric vehicles on the move [Online]. National Grid Website. Available: https://www.nationalgrid.com/electricity-transmission/Keeping-36-million-electric-vehicles-on-the-mov [Accessed 24.06.2022].

Quirós-Tortós, J., Ochoa, L. F. & Lees, B., 2015. A statistical analysis of EV charging behavior in the UK. In 2015 IEEE PES Innovative Smart Grid Technologies Latin America (ISGT LATAM), IEEE, pp. 445-449.

Regen, 2018. Market insight series: Harnessing the electric vehicle revolution.

Sinsel, S. R., Riemke, R. L. & Hoffmann, V. H., 2020. Challenges and solution technologies for the integration of variable renewable energy sources—a review. renewable energy, 145, 2271-2285.

Ueckerdt, F. & Kempener, R., 2015. From baseload to peak: renewables provide a reliable solution. International Renewable Energy Agency, 505.

#82: Electric vehicle transition in a campus environment: a case study for short-dwell wireless charging

Sophie NAYLOR[1], Julie WALDRON[2], Lucelia RODRIGUES[3], Mark GILLOTT[4]

[1] University of Nottingham, NG7 2RD University Park, Nottingham, UK, sophie.naylor@nottingham.ac.uk
[2] University of Nottingham, NG7 2RD University Park, Nottingham, UK, julie.waldron@outlook.es
[3] University of Nottingham, NG7 2RD University Park, Nottingham, UK, lucelia.rodrigues@nottingham.ac.uk
[4] University of Nottingham, NG7 2RD University Park, Nottingham, UK, mark.gillott@nottingham.ac.uk

Abstract: The need to reduce greenhouse gas emissions from human activity in the city environment is well established, as reaffirmed in the recent report by the IPCC. For the transport sector, transition to electric in both private and commercial vehicles requires significant development of charging infrastructure. However, this presents a number of operational and infrastructural challenges for both vehicle owners and the local built environment. Some vehicle applications present a more challenging case for electric vehicles (EV): where utilisation is high and dwell time is low, the typical operational model of gradual overnight recharge is not always suitable. This paper covers the assessment of the potential for transition to electric vehicles in a challenging use case of a high utilisation vehicle fleet within a university campus environment. Vehicle charging demand was estimated and dwell locations analysed for the fleet based on one year of historic data from internal combustion engine (ICE) vehicles. The potential for wireless charging to be utilised for a charging approach targeting short-dwell events was then assessed. Simulation of charging cycles based on historic data suggested that a strategically placed set of wireless chargers could viably support this challenging use case where traditional wired charging may not allow sufficient charge or may place too much stress on local electrical infrastructure. The analysis conducted in this paper demonstrated that fleets seen as challenging for EV transition can have the technical capacity to be supported by EVs when provided with appropriate charging infrastructure. Key factors in the studied use case are dwell location and the ability to utilise short dwells for charging, where an overnight charging model is not possible.

Keywords: electric vehicles; wireless charging; EV infrastructure; clean transport; human behaviour

1. INTRODUCTION

The need to reduce carbon emissions from the use of energy across many sectors is well established, as reaffirmed in the recent report by the Intergovernmental Panel on Climate Change (Masson-Delmotte *et al.*, 2021). In the city environment, this requires co-ordination of several interconnected systems, including the built environment, transport and populations. As all sectors move towards decarbonised solutions, the existing electrical grid is likely to see an increase in demand on several fronts. It is therefore imperative to understand each system in the context of its implications for the wider environment. In the transport sector, the drive to transition traditional from the internal combustion engine (ICE) vehicles to electric is anticipated to increase electrical grid demand (*Future Energy Scenarios*, 2021, p. 149). In order to transition to electric in both private and commercial vehicles, significant electric vehicle (EV) charging infrastructure must be developed within existing built spaces.

Some transport applications present a more challenging case for EV transition: where vehicle utilisation is high and dwell time is low, the typical model of recharging the vehicle battery overnight is not always suitable. This paper investigates the charging infrastructural needs of one such challenging fleet, and the possibility of strategically placed wireless charging infrastructure to allow for a transition to EV in the context of a university campus environment. This builds upon previous work assessing other sections of the same fleet for suitability for Vehicle-to-Grid charging (Waldron *et al.*, 2022, 2020).

Studies on the barriers and motivators for EV uptake have suggested that a significant factor in the decision making process for EV transition is the lack of charging infrastructure (Biresselioglu *et al.*, 2018), contributing to the experience of 'range anxiety' (Pevec *et al.*, 2020). It is therefore key that vehicle users and decision makers can be assured that their charging needs can be met in order to operate vehicles according to fleet requirements. Factors influencing charging infrastructure for challenging fleet use cases include charging power, the ability to utilise potential charging dwell events, and location of charging infrastructure. Wireless power transfer (WPT) for electric vehicle charging has seen increasing research interest in recent years (Machura and Li, 2019). Wireless charging hardware falls broadly into two main categories: static wireless charging which, like traditional wired charging, is installed at a fixed parking location, and dynamic wireless charging, which aims to recharge vehicles during movement. The general principle of both technologies is to transfer energy to the vehicle battery without the need to physically connect a charging cable, thus minimising safety risks associated with cable connection (Machura and Li, 2019) and potentially minimising interaction time between a user wishing to start a charge session and the charger engaging. While in the relatively early stages of the technology, static wireless charging systems are commercially available and are thus considered for this study.

This work presents an analysis of required local charging infrastructure for the decarbonisation of a challenging use case for EV transition: a high-usage university vehicle fleet. It is proposed in this work that static wireless charging can facilitate EV transition by way of accessing shorter dwells for battery recharge than traditional wired charging, thereby allowing a charging infrastructure solution to be found for a high-usage fleet otherwise seen as challenging to decarbonise.

2. METHODOLOGY

The major objective of this work was to assess the feasibility of strategically placed wireless charging hardware to support the transition of an existing fleet of vehicles to electric within a university campus environment. Key to this assessment were the assumptions that vehicles from the proposed fleet spent sufficient dwell time at locations on the university campus to be able to recharge to meet demand during their stationary time, and the proposal that wireless charging systems could allow access to shorter dwell times for vehicle recharge than a traditional wired connection. The combination of these factors would allow more confidence in EV transition where fleet dwell times are low. It was therefore necessary to quantify the existing behaviours and requirements of the fleet through the following process:

- Generation of descriptive statistics of existing fleet activity, behavioural patterns and dwell locations;

- Estimation of projected EV charging demand and charging time requirements based on existing combustion vehicle activity;

- Assessment of feasibility of a wireless charging solution through potential charging capacity at strategic locations for the fleet based on calculated charging demand.

The vehicle fleet studied was the university campus fleet at the University of Nottingham, UK. While most sections of the university fleet have adopted some EVs to their roles, one section of the fleet has been identified by decision-makers as too challenging to transition due to its high usage over a 24-hour period, and subsequent low dwell times available for vehicle recharging. One year of historic vehicle telematics data was examined for 50 tracked vehicles within the university fleet, focussing on a high-usage, low-dwell sub-fleet of 7 ICE vehicles. The available dataset included a per-journey record of: start and end time, initial and finishing location, journey duration, and distance

travelled. A total of 57,007 journeys were analysed for the 7-vehicle fleet over the 1-year dataset. Locations and specific roles of the fleet were anonymised in accordance with the University of Nottingham data ethics policy.

Charging demand was estimated using data from an electric vehicle of equivalent size and function to the existing vehicles of the fleet. A Nissan e-NV200 model ("Nissan e-NV200 (2018) Charging Guide," n.d.) was selected for study, with a summary of statistics for this vehicle or the closest available equivalent shown in Table 1.

Table 1: Summary of Electric Vehicle Statistics used for Analysis

Total Battery Capacity	Estimated Usable Battery Capacity*	Maximum AC Charge Rate*	Maximum DC/Rapid Charge Rate*	Estimated Energy Used per Mile**		
				High (City/highway, cold weather)	Medium (EVDB real range)	Low (City, mild weather)
40 kWh	36 kWh	6.6 kW	46 kW	411 Wh/mi	352 Wh/mi	239 Wh/mi

*("Nissan e-NV200 (2018) Charging Guide," n.d.) **("Nissan e-NV200 Combi," n.d.)

In addition to the physical demands and availability of the fleet for charging, consideration must be made for the behavioural aspects of vehicle operation. It can reasonably be assumed that vehicle users will not make the effort to plug in and charge at every possible opportunity when dwell times are low, and when vehicles make a high number of unscheduled journeys such that the user will not know at the time of parking how long they expect to stay at their location. This is particularly true for vehicles that must attend quickly to events, for example vehicles used for medical assistance, security response etc., where users must be able to leave their parking location quickly without the need to unplug and pack away a charging cable. For the university fleet, specific information on which journeys were scheduled and which unscheduled was not available. Duration of dwell was therefore used as a proxy for assuming likelihood of the user to engage with a wired charging system. It was proposed that wireless charging can be operated with less direct interaction by the user, thus overcoming this behavioural barrier. Required charging time under different infrastructure scenarios were used to quantify the potential difference made by use of wireless charging.

In order to test the possible charge supplied to vehicles under a certain set of available charging locations and behavioural options, a simulation of vehicle battery charge cycles was conducted based on the observed vehicle behaviour in the historic data. Vehicle charging demand for an equivalent electric vehicle was estimated based on journey distance, and charge supplied to each vehicle from the proposed charging hardware was simulated under various scenarios.

3. RESULTS

3.1. Existing fleet vehicle activity

The first stage of analysis was to examine existing usage behaviours of the fleet to quantify the observed concerns about the suitability of the fleet for EV transition. Figure 1.a shows the 24-hour distribution of historic journeys made by each sub-fleet at the University of Nottingham, with the 7-vehicle sub-fleet represented as 'Fleet 3'. In contrast to the rest of the fleet, Fleet 3 was typically active over a full 24-hour period, meaning that the typical electric vehicle model of overnight recharging cannot be applied to this fleet. Duration of vehicle stationary time for each vehicle in Fleet 3 is shown in Figure 2.b, with a significant majority of dwell events under 30 minutes in duration. This was particularly true of Vehicles 2 and 4, for which the frequency of dwell events over 4 hours averaged approximately one every 6.6 and 4.6 days respectively. This further reinforces that charging models that rely on extended periods of gradual recharge will not be possible for all vehicles of the fleet.

It was also found that the vehicles of this fleet spend their stationary time across a high number of locations. Key sites per vehicle were selected based on total dwell time over a 1-year period. Across all vehicles in Fleet 3, a total of 17 sites across 4 university campuses were selected as shown in Table 2. Between these sites, 81% of all vehicle dwell time in the 1-year dataset was accounted for. It was noted that some vehicles spent a significant amount of dwell time off campus areas, identified as for servicing/repair work.
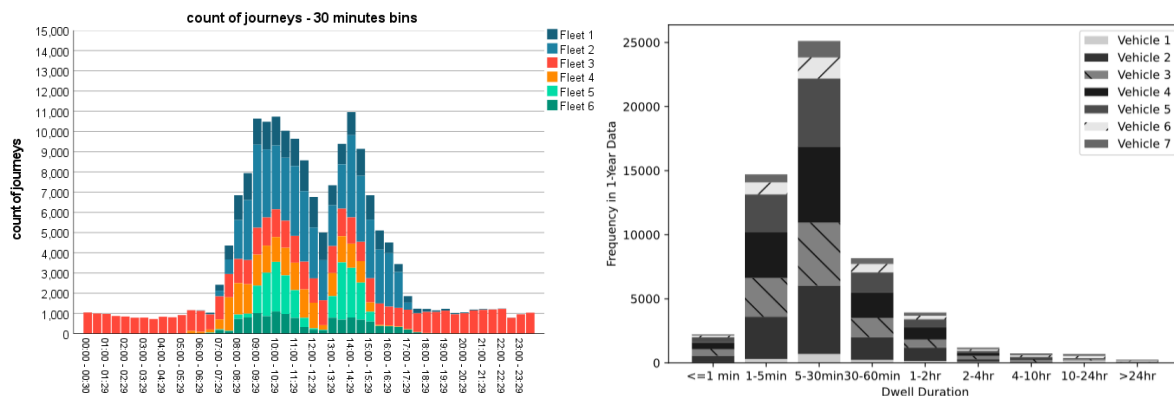
Figure 1: a) Stacked count of total fleet journeys according to their start time, 30-minute bin size, and b) Stacked count of Fleet 3 dwell events per vehicle according to their duration, varying bin size

. *Table 2: Dwell Time of Fleet 3 on Key Sites*

Campus Area	Location ID	Percentage total Fleet 3 Dwell Time
University Park Campus	UP1	46.4%
	UP2	0.7%
	UP3	9.8%
	UP4	0.8%
	UP5	0.4%
	UP6	0.5%
	UP7	0.5%
Jubilee Campus	JB1	12.2%
	JB2	1.0%
Kings Meadow Campus	KM1	0.1%
	KM2	0.0%
Sutton Bonington Campus	SB1	0.3%
	SB2	0.3%
	SB3	0.9%
	SB4	0.8%
	SB5	6.4%
	SB6	0.1%

Infrastructure challenges observed with this fleet therefore include:

- Low dwell time, meaning that the typical model of overnight charge is not possible for all vehicles;
- Diverse dwell locations, meaning that a larger number of chargers would be required to cover all high-use dwell locations;
- A number of differing roles within the highest-use vehicles in the fleet, each requiring different charging locations.

3.2. Projected charging demand and required charge times

The second stage of analysis was to establish how observed driving behaviours would likely translate into electrical demand for charging infrastructure on the university campus. Charging demand was estimated based on the behaviours observed in the historical ICE fleet data, applied to a Nissan e-NV200 electric vehicle model. Due to available data, the simulation of charging demand was limited to an estimation based on travel distance per journey. A 'high', 'medium' and 'low' scenario was simulated based on measured kWh per mile as observed in real-life operation on an e-NV200 in different environmental conditions as described in Section 2. An example of the results of this analysis for one vehicle in the fleet is shown in Figure 2. It can be seen that the depicted vehicle was projected to periodically exceed the estimated total usable battery capacity of 36kWh in daily charging demand. This means that the vehicle would likely need to recharge at multiple points during the day, further reinforcing that the single-charge model typically applied to lower usage vehicles would not be appropriate for this fleet. Further analysis was then conducted to assess whether a multi-charge model would feasibly be able to support the activity of this fleet.
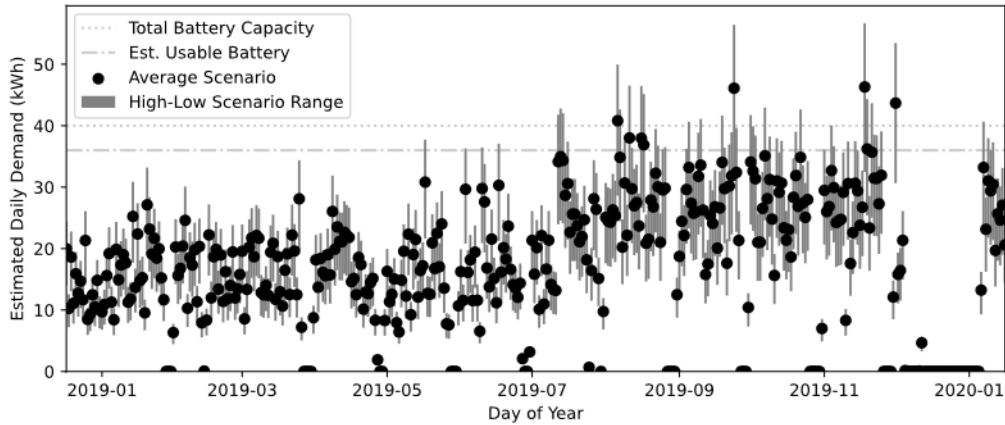
Figure 2: Estimated daily vehicle charging demand over 1-year period for Vehicle 2

Three charging rates were considered: a standard 7kW AC charger, for which the vehicle model studied would be able to receive a maximum of 6.6kW; a proposed wireless charger, which under the current standards adopted in the UK would be able to supply a maximum power of 11kW (SAE International, 2020); and a standard rapid charger, for which the vehicle model studied would be able to receive a maximum of 46kW. While the actual power received by vehicle charger varies throughout the charging cycle to best manage battery longevity, for the purpose of this comparison it was assumed that the vehicle could receive the full rated power throughout a charging session. The required charging time for each charger type was estimated using the calculated daily demand from the 'high usage' scenario. For this analysis, vehicles were defined as 'available' for charge during a dwell event if they were located within a 100-metre radius of one of the 17 identified common dwell locations, as calculated by the Haversine distance formula as described by Shipman *et al* (2020, p.3).

Table 3 summarises the mean estimated charging time requirements and available charging time of the studied fleet over the 1-year observation period. It can be seen that Vehicles 1, 6 and 7 had available charging time greater than the requirement by a significant margin. For the higher-usage vehicles in the fleet, in particular Vehicles 2 and 4, the difference between charging requirement and available time was smaller. It was found that, on average, all vehicles would have sufficient time to recharge to meet demand, even with lower-powered wired charging hardware, if chargers were available at all key locations and accessible during all dwell events. However, it should be noted that the daily charging demand per vehicle was variable throughout the observed year, as shown for Vehicle 2 in Figure 2. An inverse relationship between vehicle charging demand and available time for charging can be expected – where the vehicle spends more of the day active, less time will be available for charging. It was therefore necessary to examine the charging scenarios in further detail in order to determine whether a particular solution could consistently meet charging demand over the whole year.

Table 3: Average charging time requirements and available charging time for each vehicle over the 1-year dataset

	Vehicle 1	Vehicle 2	Vehicle 3	Vehicle 4	Vehicle 5	Vehicle 6	Vehicle 7
Mean daily charge time standard charger @6.6kW	0.57 hrs	3.15 hrs	2.80 hrs	3.50 hrs	3.14 hrs	1.63 hrs	1.09 hrs
Mean daily charge time DC charger @11kW	0.34 hrs	1.89 hrs	1.68 hrs	2.10 hrs	1.88 hrs	0.98 hrs	0.65 hrs
Mean daily charge time rapid wired @46kW	0.08 hrs	0.45 hrs	0.40 hrs	0.50 hrs	0.45 hrs	0.23 hrs	0.16 hrs
Mean available charging time (dwells >60minutes)	21.50 hrs	6.97 hrs	12.22 hrs	7.11 hrs	11.94 hrs	16.16 hrs	19.49 hrs
Mean available charging time (dwells >30minutes)	21.70 hrs	9.70 hrs	14.42 hrs	10.14 hrs	14.24 hrs	16.81 hrs	20.08 hrs
Mean available charging time (any dwell)	21.87 hrs	12.05 hrs	16.37 hrs	12.82 hrs	16.35 hrs	17.30 hrs	20.52 hrs

3.3. Projected infrastructure requirements

The above analysis suggested that a solution to operate this fleet as electric was theoretically possible, as vehicles were found to spend sufficient time to recharge between all 17 observed campus locations. However, there were three additional complicating factors. Firstly, as previously identified, the inverse relationship between demand and available charging time requires further analysis to ensure that all variations in usage behaviours of the fleet can be supported by the proposed charging infrastructure. Secondly, the assumption that charging facilities are available at all identified sites across university campuses was not feasible in application due to the high infrastructure costs associated with installing hardware at all locations. Thirdly, it was not guaranteed that all potential charging sessions can be utilised. For example, if the vehicle arrived at a charger with the battery already at 80% capacity, it will not be

able to charge any further than 100%, thus not utilising all available charging time. If this represents the only charging opportunity in that day, it is not guaranteed that the vehicle will have sufficient charge after this session to be able to meet its demand later on its route.

The final layer of analysis was to assess by simulation how charging events would actually be utilised by the fleet, and thus how many charger locations were needed to efficiently support this fleet. As described in Section 2, the simulation calculated the vehicle battery state of charge after each driving and charging event in the observed historic dataset as a continuous series of events.

The simulation of vehicle battery cycles over the 1-year dataset was completed under several possible charging scenarios. A sample of the calculated battery state of charge for Vehicle 4 over the same 24-hour period in two of the simulated scenarios is shown in Figure 3, comparing the state of the battery over the same high-demand day in the year. It can be seen that when the vehicle was limited to charging only when dwell times were greater than 60 minutes, the sparse nature of these events meant that a 46kW rapid charger was not able to sufficiently recharge the vehicle despite the short amount of time required to fully recharge. By contrast, a lower-powered charger, if able to utilise shorter dwells, was able to provide a 'little and often' charging model that allowed the battery to be topped up periodically throughout the day. This highlights the reliance on both behavioural factors to ensure that the vehicle battery can support existing use of the fleet, and the importance of planning infrastructure in existing built environments, as it must be assured that vehicles can receive charge at an appropriate place and time during their driving cycles.
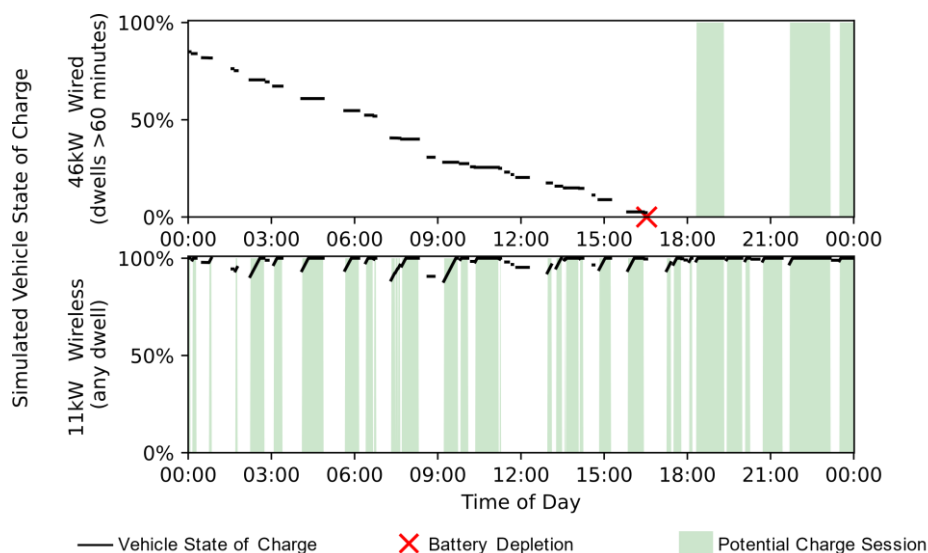
Figure 3: Comparison of sample day for Vehicle 4 Usage Activity from simulation of a) 46kW utilizing dwells > 60 minutes and b) 11kW charging utilising dwells of any duration

The sensitivity of charge demand coverage to such behavioural factors was explored through further simulation varying the available charge power, available dwell duration, percentage of missed potential charging events, and charger locations. For each scenario, one factor was varied while the others were held constant. The default values used are presented in Table 4.

Table 4: Default scenario values for sensitivity testing

Charger Power	Assumed Demand Scenario	Stop Duration Used for Charge	Missed Potential Charge Events	Available Charger Locations
6.6kW	High	>60 minutes	0%	All

Figure 4 shows the results of testing the simulation outcome's sensitivity to dwell duration, charge power and percentage of missed charging sessions. In these figures, 'total charge coverage' refers to the total energy supplied to each vehicle of the fleet by the simulated chargers as a percentage of that vehicle's estimated total charging demand. It was found that the highest-usage vehicles in the fleet (Vehicles 2 to 5) were most heavily affected by the dwell durations used for charge. It was only by accessing dwells of at least 30 minutes duration that chargers placed at all 17 locations were able to supply sufficient charge to the whole fleet consistently over the year of fleet behaviours. While higher powered charging hardware was able to supply a greater percentage of demand, if the behavioural assumption that a wired charge would be limited to dwell events greater than 60 minutes held, even a full set of wired rapid charging hardware would not be able to adequately supply this fleet due to the effect described in Figure 3. All

vehicles also showed some sensitivity to missed charging sessions – this effect was particularly pronounced for simulations charging only on longer dwells, as fewer total events were available for charge.
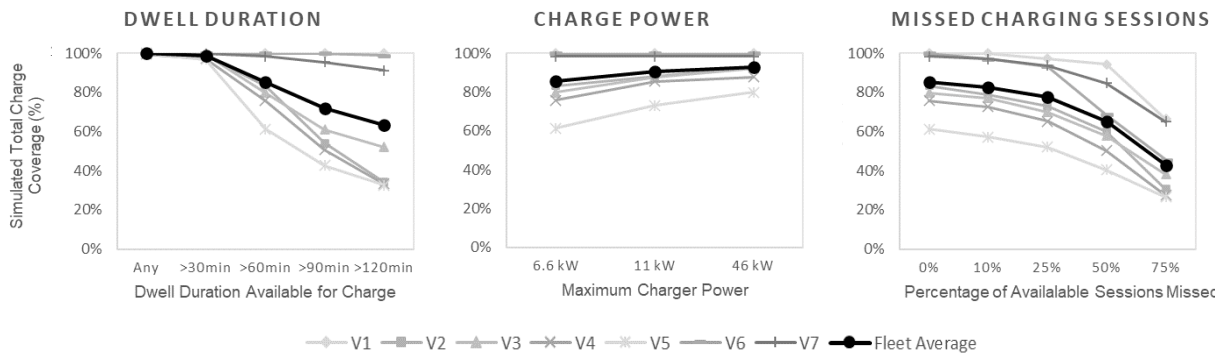
Figure 4: Fleet charge simulation results under varying charge availability scenarios

With the proposal that a wireless charging system would allow access to the use of shorter charging sessions, providing a feasible means to meet charging demand in this high-usage fleet, simulations were also run to assess the feasibility of an 11kW wireless EV charging solution in different charger location scenarios. The scenarios tested were as follows:

- Scenario A – One charger placed at each of the 17 identified highest-dwell locations.
- Scenario B – One charger per vehicle placed at the location with the highest dwell time for the total fleet.
- Scenario C – One charger per vehicle placed at each vehicle's primary dwell location.
- Scenario D – 'Best case' optimised charger location. Full detail of the optimisation process is not presented in this paper, but will be covered in a future publication.

A summary of the simulation results from these scenarios is presented in Table 5. As in Figure 4, the total charge coverage per vehicle represents the percentage of total charging demand that was supplied by the chargers in simulation. It was found that scenarios B and C, which might typically be used to identify locations for charging infrastructure, did not provide sufficient capacity to charge highest use vehicles, due to both a lack of dwell time and clashes of multiple vehicles needing to charge at one location at once. In contrast, scenarios A and D were both able to provide 99% of demand for the 7-vehicle fleet. However, the optimised solution D demonstrated that a set of six strategically placed 11kW wireless chargers was able to fulfil 98.8% of fleet charging demand, providing similar coverage to scenario A with significantly smaller infrastructure costs, requiring fewer than one charger per vehicle.

Table 5: Simulated charge coverage over 1-year period for the charger location scenarios

	A - All Locations	B - Single Location	C - Peak Locations	D - Optimal Locations
Vehicle 1	99.5%	99.9%	99.9%	99.6%
Vehicle 2	100.0%	57.9%	80.1%	100.0%
Vehicle 3	100.0%	61.4%	85.0%	98.6%
Vehicle 4	100.0%	61.6%	84.8%	98.9%
Vehicle 5	100.0%	68.1%	69.5%	99.4%
Vehicle 6	89.3%	100.0%	100.0%	95.1%
Vehicle 7	99.5%	99.8%	99.8%	99.4%
Total Coverage	98.9%	70.0%	84.0%	98.8%
Total Chargers	17	7	7	6
Effective Cover per Charger	5.8%	10.0%	12.0%	16.5%

4. DISCUSSION

While a solution to provide sufficient charge to support current vehicle behaviours was shown to be possible in the studied environment, a number of additional factors should be considered for practical application.

4.1. Factors affecting vehicles, fleet and behaviours

The results presented suggest that human behaviour is a significant factor in charging infrastructure requirements for challenging fleets. Given the high-use nature of this fleet and the unpredictability of the needs of drivers during short dwells, it was assumed that the practical requirements of consistent connection to a wired charger would be unlikely to provide decision-makers the confidence to transition to electric. The results of the charging simulations highlight the need to ensure that charge arrives at the right time in the vehicle's driving cycle, even if there is technically enough time during the day to recharge.

Analysis was based on the operation of an ICE vehicle fleet, with the assumption that the vehicle operators would require similar patterns of use from an electric fleet. Some additional assumptions were applied on the behaviour of vehicle operators, for example that users would be willing to park up to 100m away from their intended destination to charge their vehicle. It is possible that some issues with fleet charge could be resolved by enacting further behavioural policies in the fleet – by altering shift times, patterns or switching of vehicles between roles, it may be possible to access longer recharging periods with both wireless and wired charging systems.

While the focus of this study was static wireless charging as a direct alternative to traditional wired charging infrastructure, dynamic wireless charging systems designed to recharge vehicles during movement could also be a viable option for some applications, particularly where vehicle routes are limited such as in public transportation (Choi *et al.*, 2015). Dynamic charging was not considered here due to the relative cost of electrifying large areas of road, and the availability of full route data for this fleet. The benefit of either static or dynamic wireless charging in this application was established on the basis of wireless systems requiring lower interaction from the user in order to engage and disengage a charging session. However, there is to date a gap in existing research publication on the measured or perceived increase in usability to the vehicle driver.

It should be noted that this study did not consider the effect of different charging behaviours on the life of the vehicle battery. Aging of lithium-ion vehicle batteries is complex and can occur through multiple mechanisms, broadly described as 'cycle aging' and 'calendar aging' (Pelletier *et al.*, 2017). Existing literature suggests that use of rapid charging rates for charging cycles can increase battery degradation (Mothilal Bhagavathy *et al.*, 2021) suggesting that a charging model allowing for lower-power top ups through the day may have a less detrimental impact on the battery longevity than relying on long-term use of rapid charge. However, as calendar aging occurs faster when the battery is stored at a higher state of charge (Pelletier *et al.*, 2017), the 'charge at first available opportunity' model assumed in this study would likely not be the best approach to maximise battery life. The additional confidence provided by accessing a larger number of charging opportunities through the day should allow for management of vehicle batteries at a lower state of charge to minimise aging.

4.2. Impacts on local built environment

The number and placement of chargers must support the use case of the fleet, but also has implications for the local built environment and its electrical infrastructure. As a university campus, the environment studied had established patterns of energy use in the local buildings, use of onsite renewable energy generation etc. The introduction of additional vehicle charging hardware would cause an increase in local energy demand during charging cycles. Without management of charging through the day, timing of electrical demand may coincide with times of high demand from the local buildings, increasing stresses on local infrastructure and potentially increasing peak times of electrical demand. Access to a greater number of potential charging events throughout the day should allow charging demand to be offset to less intensive times of day where possible, reducing stress on the local system and potentially allowing for reduced carbon intensity of the fleet through charging management (Waldron *et al.*, 2022).

The introduction of additional vehicle charging hardware is likely to be limited by electrical capacity at the level of local substations. The current level of analysis for parking infrastructure did not account for the local capacity or physical space requirements in recommending charging locations. However, in practical application, both of these aspects must be considered. The impact on the local electrical infrastructure will also depend on the charging hardware used. The high-power infrastructure required to connect multiple rapid chargers would likely limit the possible locations available for charging and the number of chargers that can be operated concurrently at their rated power.

5. CONCLUSION

The decarbonisation of transport through transition of fleet vehicles to electric presents a number of challenges for the operation of charging infrastructure to suit the needs of fleet users, fleet managers, and the existing local environment. For use cases typically seen as challenging for transition, charging infrastructure planning must allow vehicles to access sufficient supply to ensure confidence in normal operation of the fleet. This study assessed the

potential requirements for charging infrastructure for a high-usage, low-dwell fleet within a university campus environment.

The analysis conducted in this paper demonstrated that fleets seen as challenging for electric transition can have the technical capacity to be supported by battery electric vehicles, dependent on a number of behavioural and infrastructural factors. Key factors in the studied use case were dwell location and the ability to utilise short dwells for charging, where an overnight charging model was not possible. This provided some validation to fleet decision makers' concerns that electric vehicle transition would be difficult to rely on for this high-usage role, highlighting that a larger proportion of dwell events comprising of shorter dwell durations must be utilised for charging in order to meet projected demand. Examination of varying charging scenarios showed that, while sufficient time for recharge was available in even the highest usage vehicles at a range of charge power rates, reliance on utilising longer-duration dwells cannot be guaranteed to supply charge at the right times of day to ensure vehicle batteries are charged through a full vehicle usage cycle. It was shown that reduced user interaction required by wireless charging systems would potentially allow for a more robust 'little and often' recharging model if shorter dwell events of this fleet can be accessed for charge. It was therefore key to ensure that charge could be supplied at the right place and time in addition to for the required duration. This has implications for the planning of charging hardware in environments such as the university campus studied. The need to balance charging availability against installation costs and the possibility of overwhelming existing infrastructure requires a strategic approach to charging infrastructure location planning.

A number of additional factors must be considered for best integration of vehicle charging hardware into existing built environments. This work forms the first stage of a larger project demonstrating the use of wireless charging hardware and applied intelligent algorithms for charging location planning.

6. ACKNOWLEDGEMENTS

7. REFERENCES

Biresselioglu, M.E., Demirbag Kaplan, M., Yilmaz, B.K., 2018. Electric mobility in Europe: A comprehensive review of motivators and barriers in decision making processes. Transp. Res. Part Policy Pract. 109, 1–13. https://doi.org/10.1016/j.tra.2018.01.017

Choi, S.Y., Gu, B.W., Jeong, S.Y., Rim, C.T., 2015. Advances in Wireless Power Transfer Systems for Roadway-Powered Electric Vehicles. IEEE J. Emerg. Sel. Top. Power Electron. 3, 18–36. https://doi.org/10.1109/JESTPE.2014.2343674

Future Energy Scenarios, 2021. , FES 2021. National Grid ESO.

Machura, P., Li, Q., 2019. A critical review on wireless charging for electric vehicles. Renew. Sustain. Energy Rev. 104, 209–234. https://doi.org/10.1016/j.rser.2019.01.027

Masson-Delmotte, V., Zhai, P., Pirani, A., Connors, S.L., Péan, C., Berger, S., Caud, N., Chen, Y., Goldfarb, L., Gomis, M.I., Huang, M., Leitzell, K., Lonnoy, E., Matthews, J.B.R., Maycock, T.K., Waterfield, T., Yelekçi, O., Yu, R., Zhou, B., 2021. Summary for Policymakers, Climate Change 2021: The Physical Science Basis. Contribution of Working Group I to the Sixth Assessment Report of the Intergovernmental Panel on Climate Change. IPCC.

Mothilal Bhagavathy, S., Budnitz, H., Schwanen, T., McCulloch, M., 2021. Impact of Charging Rates on Electric Vehicle Battery Life. Findings. https://doi.org/10.32866/001c.21459

Nissan e-NV200 (2018) Charging Guide [WWW Document], n.d. . Pod Point. URL https://pod-point.com/guides/vehicles/nissan/2018/e-nv200 (accessed 5.23.22).

Nissan e-NV200 Combi [WWW Document], n.d. . EV Database. URL https://ev-database.uk/car/1117/Nissan-e-NV200-Combi (accessed 1.29.21).

Pelletier, S., Jabali, O., Laporte, G., Veneroni, M., 2017. Battery degradation and behaviour for electric vehicles: Review and numerical analyses of several models. Transp. Res. Part B Methodol., Green Urban Transportation 103, 158–187. https://doi.org/10.1016/j.trb.2017.01.020

Pevec, D., Babic, J., Carvalho, A., Ghiassi-Farrokhfal, Y., Ketter, W., Podobnik, V., 2020. A survey-based assessment of how existing and potential electric vehicle owners perceive range anxiety. J. Clean. Prod. 276, 122779. https://doi.org/10.1016/j.jclepro.2020.122779

SAE International, 2020. Wireless Power Transfer for Light-Duty Plug-in/Electric Vehicles and Alignment Methodology, SAE Standard J2954. https://doi.org/10.4271/J2954_202010

Shipman, R., Waldron, J., Naylor, S., Pinchin, J., Rodrigues, L., Gillott, M., 2020. Where Will You Park? Predicting Vehicle Locations for Vehicle-to-Grid. Energies 13, 1933. https://doi.org/10.3390/en13081933

Waldron, J., Rodrigues, L., Gillott, M., Naylor, S., Shipman, R., 2022. The Role of Electric Vehicle Charging Technologies in the Decarbonisation of the Energy Grid. Energies 15, 2447. https://doi.org/10.3390/en15072447

Waldron, J., Rodrigues, L., Gillott, M., Naylor, S., Shipman, R., 2020. Decarbonising our transport system: Vehicle use behaviour analysis to assess the potential of transitioning to electric mobility 1. https://doi.org/10.17979/spudc.9788497497947

#83: Saving energy with kids; development of a toy for teaching building energy efficiency

Bahar Çınar[1], Batuhan Turan Öztürk[1], Rengin Köymen[1] İpek Tepe[1] Ata Şenel[1] Çağrı Can Yılmaz[1] Burçin Cavbeni[1] Abdalla Emeligy[1] Cihan Turhan[1]

Atılım University, Energy Systems Engineering, Incek/Ankara/Turkey, author email address, cinar.bahar@student.atilim.edu.tr ,ozturk.batuhanturan@student.atilim.edu.tr, koymen.rengin@student.atilim.edu.tr , tepe.ipek@student.atilim.edu.tr , senel.ata@student.atilim.edu.tr, yilmaz.cagrican@student.atilim.edu.tr ,cavbeni.burcin@student.atilim.edu.tr, abdalla.elmeligy@student.atilim.edu.tr, cihan.turhan@atilim.edu.tr

Abstract: Smart home systems, which aim to adjust thermal comfort in buildings via various sensors, are intended to increase energy efficiency in buildings. Adults can easily adjust the thermal comfort in their homes using these systems. Smart home systems, on the other hand, are neither useful nor educational for kids. Furthermore, their education on energy efficiency and thermal comfort in buildings is vital since they will use these systems from their middle childhood years. To this aim, this study proposed to teach pre-school kids, who were between 3 and 5 years, energy efficiency in buildings via a developed smart toy. The developed toy included various sensors such as air temperature, relative humidity and air pressure sensors, a microcontroller, a carbon dioxide sensor, light-emitting diode lamps, a text-to-speech module, a battery unit, and a precision clock module. The software of the toy was written on C-based programming language and the prototype of the toy was developed by undergraduate students of Atılım University in Turkey under an undergraduate project umbrella with the help of the supervisor of Dr. Turhan. The developed toy depicted the temperature with green, red, and blue colours representing neutral, hot, and cold environments. Additionally, the smart toy spoke to the kids to warn their adults to decrease/increase set-temperature of the heating and cooling system in the room. The developed toy also controlled the existence of open windows during operation of the heating system while staying in continued-communication with the kids. Moreover, the toy warned kids to check for lights during daytime. Since the main goal of the study was teaching energy efficiency to the kids, the outcome of the study would benefit development of self-skills and cognitive well-being, enhancing energy efficiency learning for the kids and improving the awareness of building energy efficiency for adults.

Keywords: teaching toys; building energy efficiency; energy saving; smart toy-based learning

1. INTRODUCTION

A significant world energy consumption increase, the huge difference between energy supply and demand, the accelerated depletion of useful energy resources, the excessive interest of states in energy in certain periods (such as war, technological developments, etc.) and environmental factors (global warming, ozone layer depletion, increased seasonal temperatures, etc.) have greatly increased concerns on energy consumption (Atmaca, 2016).

Three major sectors - industry, transportation, and buildings - are mainly responsible for the final energy consumption. The building sector includes residential and educational buildings together. Several projects to decrease energy consumption in residential and/or educational buildings have been developed in the literature and can be found in Pérez-Lombard, Ortiz & Pout (2008). The rapid population growth, the opportunities offered by living spaces, the increase in the level of comfort and the time spent in the residences (due to the COVID-19, the opportunities of online education, etc.) have rapidly increased the attention on building energy consumption (Khan *et al.*, 2021).

Developing countries, such as Turkey, have limited energy resources, therefore, reducing energy consumption in buildings is an important issue for these countries. On the other hand, even in developed countries, the impact of carbon dioxide (CO_2) emissions from buildings to the environment is increasing day by day. Keeping in mind that a building needs to consume a certain amount of energy depending on heating and cooling loads, zone, location, and type of building, decreasing energy consumption of the building is vital (Brugger *et al*, 2021).

The construction phase of buildings is also of great importance in terms of energy saving and consumption. However, operation of the building systems is more significant. For instance, heating, ventilation and air-conditioning (HVAC) systems provide thermal comfort to the occupants and this system has a 50% share of the energy consumption in buildings. However, thanks to the development of technology, the energy consumption of the HVAC system is decreasing by way of the smart system (Bac, Alaloosi & Turhan, 2021).

Smart home systems have become very common with the development of technology, however, these smart systems are only for adults: smart home systems are neither useful nor educational for kids. Kids do not know how to use these systems. The main question is do they have to know to use smart systems? The authors believe that the kids should be taught of the aim of smart systems before starting their education life. Energy consumption in kindergartens and nurseries is extremely high compared to other type of buildings (Doulas *et al.*, 2019). The reason could be because kids may leave the lights on and open the windows while operating heating system (Zhang & Liu, 2015).

There have been a lot of great reasons to increase energy efficiency in schools and kindergartens. As public institutions, schools and kindergartens should provide an example for other buildings not just in terms of design and creation, but also in terms of promoting energy efficiency. A study concluded that the average annual energy consumption for each school was between 400.000 and 1.750.000 kWh/year. Eighty-two percent of this consumption was due to electricity consumption (Alshibani, 2020). Projects on decreasing energy consumption are aimed only at adults, however, educating pre-school kids on energy efficiency is also possible (Airaksinen, 2011).

For this purpose, the aim of this study is to teach pre-school kids (between 3 and 5 years old) energy efficiency and thermal comfort. The prototype of the designed toy was developed in a laboratory at Ankara Atılım University and evaluated under real conditions.

2. METHODOLOGY

The study approach was composed of two major components: the primary section contained development of the toy with several sensors while the second section was developing the software for the toy.

2.1. Development of the toy

The proposed toy consisted of a microcontroller, a T&RH sensor, a carbon dioxide sensor, three light-emitting lamps, three resistors, a speaker, a text-to-speech module, a battery unit, and a precision clock module. As a microcontroller, an Arduino Mega was used in the project. Arduino Mega was a microcontroller board based on the ATmega2560 which had 54 digital pins Input /Output pairs, of which 15 pins could be used as a PWM outputs (Kusriyanto & Putra, 2016).

In the developed toy, TTEC brand power slim 2BB132MR model 5.000 mAh power bank was used as the battery unit, considering easy charging and safety precautions opportunities. The developed toy measured temperature and relative humidity (T&RH) via a BME280 type sensor that output a calibrated digital signal (Nasution *et al.*, 2020). The toy sent signals based on the temperature range of 18 to 22 degrees Celsius, which is the ideal room temperature for kids (Haiek, 2020). In addition, an open window warning was added to the developed toy in order to decrease energy consumption during heating season. The working logic of the system was that when the window was left open, the developed toy measured a 3°C temperature difference (Bhatia, 2015) with an air pressure difference of 20-30 Pa (Mikola, Simson & Kurnitski, 2019). Then, the toy started to communicate with the kid to warn about the open window.

However, if the CO_2 concentration measured above 1,000 ppm, the warning system was triggered due to the need of manual ventilation. Additionally, the MQ-135 sensor measured the amount of carbon dioxide in the air (Abbas *et al.*, 2020). According to ASHRAE 62.1 2016 standards, the top limit of indoor carbon dioxide concentration was determined as 1,000 ppm (ASHRAE Standard 62.1-2016, 2016). Thus, the system in the developed toy was programmed to issue a warning when the amount of carbon dioxide concentration exceeded 1,000 ppm. When the measured T&RH and CO_2 levels were in an unfavourable range, the toy gave an audible warning. A complete list of components of the toy and their specifications are shown in Table 1.

Table 1: Characteristics of all components of the produced toy
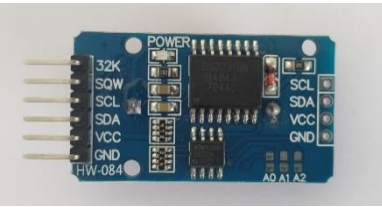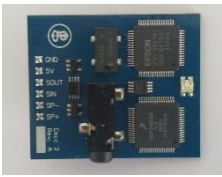
Components	Properties	Picture
Arduino Mega Microcontroller Card	Operating voltage: 5V Input voltage: 7-12 V (Zandamela, A. A., 2017)	
BME 280	Humidity measurement accuracy: ±3% RH Temperature measurement accuracy: +/-1.0ºC Air Pressure measurement accuracy: ±1.0 hPa (Day, R. J., & Salehi, H. S., 2018, April)	
MQ-135 For carbon dioxide concentration measurement	Operating Voltage: 5 V Measuring Range: 10 to 10000 ppm (Kumar, S., & Jasuja, A., 2017, May, p. 1343)	
DS3231	Real-Time Clock Counts Seconds, Minutes, Hours, Date of the Month, Month, Day of the Week, and Year, with Leap-Year Battery-Backup Input for Continuous 3.3V Operation	
EMİC 2 Text-to-speech	Power requirements: +5 VDC Communication- Asynchronous: 9600 bps serial (Dutta, D., 2014, p. 20)	
Li-Ion Battery	Capacity: 5.000 mAh Input: DC5V =1 A Output: DC5V = 1A Dimension: 68 * 134 * 10 mm Weight: 119 g	

Figure 1 depicts the circuit wiring diagram of the produced toy, and Figure 2 shows a sample screenshot of the data logger programming. The designed toy employed a C-based programming language that allowed the toy to be readily customised to the required characteristics. The developed toy incorporated a generated module after wiring and connections.
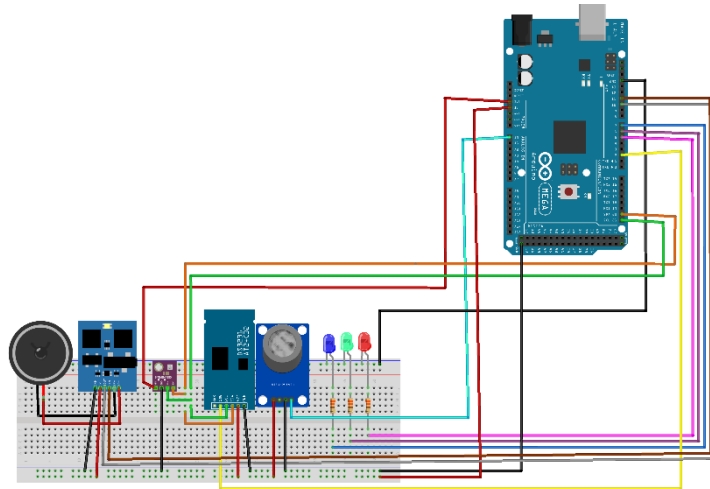
Figure1: Circuit connection diagram

```
77
78    void Update()
79    {
80      // check to see if it's time to change the state of the LED
81      unsigned long currentMillis = millis();
82
83      if(ledState == HIGH)
84      {
85        ledState = LOW;  // Turn it off
86
87        digitalWrite(ledPin, ledState);  // Update the actual LED
88      }
89      else if (ledState == LOW)
90      {
91        ledState = HIGH;  // turn it on
92        digitalWrite(ledPin, ledState);   // Update the actual LED
93      }
94    }
95  };
```

Figure 2: Screenshot of a part of the data logger programming

The T&RH sensor and the CO_2 sensors were placed in such a way that they were closest to the outer surface of the developed toy to minimise the margin of measurement errors. Figure 3(a) shows the location of the sensors inside the developed toy and the general circuit layour (3(b)).

(a)   *(b)*
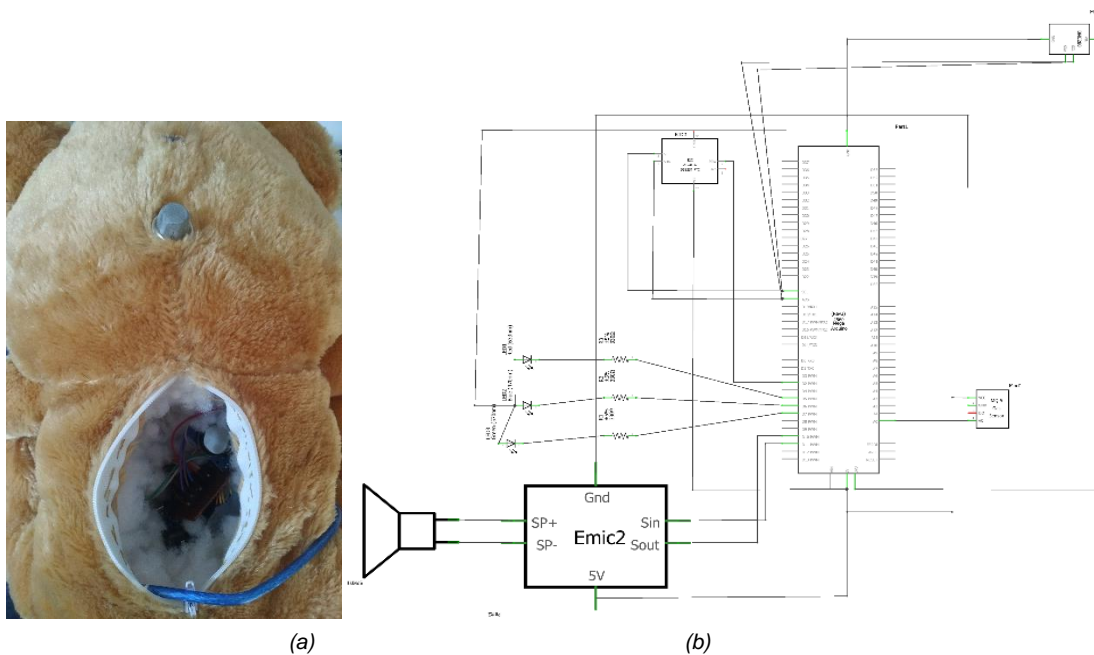
Figure 3: a) The inside, b) The electrical circuit of the developed data logger

3. RESULTS

This section describes the process related to the working logic of the toy, which was developed after the completed software process by using the C-based programming language. The final appearance of the toy will also be detailed.

Since the toy was light enough in weight for the kids to carry, it was suitable for usage in all zones of the buildings. The used materials are given in the methodology section and did not pose any risk to the kids. Moreover, the toy had a soft non-damaging surface.

In Table 2, the audio texts and LED warnings given by the toy based on the data obtained from the sensors inside the toy, are given in detail. For instance, if the measured temperature in the room was above 22°C in the winter season, the toy read an audio text "The room temperature is too high; can you tell your parents to turn off the thermostat?". Simultaneously, the LED in the middle of the toy lit red during the high temperature in the room. In normal cases, the light was green in order to teach kids energy efficiency.

Table 2: State-Condition Table

State	Living Room	Audio text	Colour
High room temperature	Temperature >22 °C	"The room temperature is too high; can you tell your parents to turn off the thermostat?"	Red
Low room temperature	Temperature <18 °C	"The room temperature is too low; can you tell your parents to turn on the thermostat?"	Blue
Poor air quality	CO_2 (ppm)>1000 ppm	"It's very stuffy inside, can you tell your family to ventilate the room?"	Red
Window warning based on the CO_2 and room temperature	Temperature-Current Temperature > 3°C and -3°C or Air pressure change 20-30 Pa) while CO_2 (ppm)<1000 ppm	"The window may be open; can you tell your parents to close the window?"	Red
Daytime lighting warning	Between 9:00-18:00	"Can you turn off unused lights?"	-
Normal	-	-	Green (except for adverse circumstances)

The developed toy was also energy-efficient and consumed 0.075 kWh during the day except during the sleeping time of the kids. The results of the measurements are shown in Table 3.

Table 3: Measurement results with the developed toy

Voltage	Ampere (A)	Energy Consumption (kWh)
5V	1A	0.075 kWh (07:00 am – 10:00 am)

Figure 4: Photo of the developed toy with the nephew of one author of this article (the permission was taken from the family of the kid to take a sample image before using the photo for an article)

The purpose of this toy was to raise awareness of kids on energy efficiency in buildings. The energy saving potential of the toy was out of the scope of this project. Unfortunately, due to the ethical limitations researching with the kids, the authors have not conducted any experiment with the kids but Figure 4 shows a kid and a toy together.The final version of the developed toy at the end of the project is shown in Figure 5.

Figure 4: The developed toy from the front (Left) and view from behind the developing toy (Right)

The total cost of the developed toy is shown in Table 4. The toy could be produced for approximately $110.

Table 4: Cost analysis of the developed toy

State	Price ($)
Arduino Mega Microcontroller Card	$19.50
BME 280	$4
MQ-135	$2.6
DS3231	$3.25
EMİC 2	$65
Li-Ion Battery	$4.55
Others (toys, speakers, LEDS, resistors, connecting cables)	$11.04
Total Price	$109.94

The aim of the developed toy was purely educational. Nevertheless, in order to see the energy saving potential of the developed toy, it must be compared with normal operations of the HVAC system during a day. However, it is worth noting that during the experiments, only adults were used due to the ethical issues with researching using kids. The developed toy was compared in two rooms with the same architectural configurations (total volume of 42 m^3), heating system (8800 Btu/h air conditioner for each) and internal gains. In one room, the adult obeyed the warnings of the developed toy while another adult in another room operated HVAC system as his thermal preferences. The energy consumption of the rooms was measured with two identical multifunctional energy meters. When using the developed toy, 13% of energy consumption was saved during the day. However, note that lower percentage savings could be achieved for spaces provided with thermostats. Furthermore, as the majority of heating systems in residential spaces are controlled by thermostats, it should be mentioned that monitoring when indoor air temperature is higher/lower than the set-point temperature has almost exclusively an educational purpose.

4. CONCLUSIONS

Adjustment of thermal comfort in buildings is very important nowadays. Therefore, increasing energy efficiency is vital for every passing day. Adults can comfortably adjust the thermal comfort using intelligent systems in homes, but kids will not be able to use these systems yet but should know about energy efficiency in buildings before starting their schools. The aim of the project was to educate or teach kids energy efficiency by an entertaining way. A toy was developed for this purpose, and included devices that measured the air temperature, air pressure and relative humidity inside, and that could communicate with the kids. The results showed that 13% of energy could be saved with using this toy. Future studies will cover the experiments with kids with ethical permission. Furthermore, the

possibility to include and monitor other parameters or conditions will be considered in the future developments of the toy.

5. REFERENCES

Abbas, F. N., Saadoon, M. I. M., Abdalrdha, Z. K., & Abud, E. N. (2020). Capable of gas sensor MQ-135 to monitor the air quality with Arduino Uno. Int J Eng Res Technol, 13(10). 2955-2959.

Airaksinen, M. (2011). Energy use in day care centers and schools. Energies, 4(6), 998-1009.

Alshibani, A. (2020). Prediction of the energy consumption of school buildings. Applied Sciences, 10(17), 5885.

ASHRAE Standard 62.1-2016. (2016). Ventilation for Acceptable Indoor Air Quality. Atlanta, GA. Atlanta, GA: Refrigerating and Air-Conditioning Engineers Inc.

Atmaca, A. (2016). Life cycle assessment and cost analysis of residential buildings in south east of Turkey: part 1—review and methodology. The International Journal of Life Cycle Assessment, 21, 831–846.

Bac, U., Alaloosi, K. A. M. S., & Turhan, C. (2021). A comprehensive evaluation of the most suitable HVAC system for an industrial building by using a hybrid building energy simulation and multi criteria decision making framework. Journal of Building Engineering, 37, 102153.

Bhatia, A. (2015). HVAC-Natural Ventilation Principles. Continuing Education and Development, Inc, 9.

Brugger, H., Eichhammer, W., Mikova, N., & Dönitz, E. (2021). Energy Efficiency Vision 2050: How will new societal trends influence future energy demand in the European countries?. Energy Policy, 152, 112216.

Day, R. J., & Salehi, H. S. (2018, April). Development of smart interior environmental mobile app for health monitoring. In 2018

IEEE Green Technologies Conference (GreenTech) IEEE., 115-118.

Doulas, L.T., Kontadakis, A., Madias, E.N., Sinou, M., & Tsangrassoulis, A. (2019). Minimizing energy consumption for artificial lighting in a typical classroom of a Hellenic public school aiming for near Zero Energy Building using LED DC luminaires and daylight harvesting systems. Energy and Buildings, 194, 201-217.

Dutta, D. (2014). Development of a personalized wireless attender calling system for critical patient management (Doctoral dissertation).

Haiek, C. (2020, June 9). Mum-approved advice for keeping your baby warm and safe on cold nights. Retrieved from Kidspot: https://www.kidspot.com.au/parenting/primary-school/how-to-keep-your-baby-warm-and-safe-on-cold-nights/news-story/5d583f265a36a729b3fd80957e6585de

Khan, I., Hou, F., Irfan, M., Zakari, A., & Le, H.P. (2021). Does energy trilemma a driver of economic growth? The roles of energy use, population growth, and financial development. Renewable and Sustainable Energy Reviews, 146, 111157.

Kumar, S., & Jasuja, A. (2017, May). Air quality monitoring system based on IoT using Raspberry Pi. In 2017 International conference on computing, communication and automation (ICCCA) IEEE, 1341-1346.

Kusriyanto, M., & Putra, B. D. . (2016, August). Smart home using local area network (LAN) based arduino mega 2560. In 2016 2nd international conference on wireless and telematics (ICWT) IEEE., 127-131.

Mikola, A., Simson, R., & Kurnitski, J. . (2019). The impact of air pressure conditions on the performance of single room ventilation units in multi-story buildings. Energies, 12(13), 2633.

Nasution, T. H., Hizriadi, A., Tanjung, K., & Nurmayadi, F. (2020). Design of indoor air quality monitoring systems. In 2020 4rd International Conference on Electrical, Telecommunication and Computer Engineering (ELTICOM) IEEE, 238-241.

Pérez-Lombard, L., Ortiz, J., & Pout, C. (2008). A review on buildings energy consumption information. Energy and buildings, 40(3), 394-398.

Zandamela, A. A. (2017). An approach to smart home security system using arduino. Electrical Engineering: An International Journal (EEIJ), 4 (2/3), 1-18.

Zhang, T., & Liu, X. (2015). An Energy Audit of Kindergarten Building in Vallbacksgården. Student thesis, Master degree (one year), 15 HE Energy Systems Master Programme in Energy Systems, University of Gavle, Sweden.

#94: Sustainable retrofit solutions for southern European residential buildings

Yangmin WANG[1], Janne HIRVONEN[1,2], Ke QU[3], Juha JOKISALO[1,4], Risto KOSONEN[1,4,5]

[1] Department of Mechanical Engineering, Aalto University, Espoo, Finland, yangmin.wang@aalto.fi
[2] Department of Civil Engineering, Tampere University, Tampere, Finland
[3] Department of Architecture and Built Environment, University of Nottingham, Nottingham, UK
[4] FinEst Centre for Smart Cities, TalTech, Tallinn, Estonia
[5] College of Urban Construction, Nanjing Tech University, Nanjing, China

Abstract: As the building sector is the largest single contributor for energy consumption and greenhouse gas (GHG) emissions in the EU, improving building energy efficiency plays a key role in achieving the ambitious goal of carbon neutrality. In addition to constructing new buildings with energy efficiency regulation, it is also important to renovate the existing building stock for lower energy consumption and GHG emissions.

This study aims at verifying the building level performance of several novel retrofit technologies and their combinations under southern European climate conditions. The novel retrofit technologies include bio-aerogel thermal insulation, photovoltaic vacuum window, phase change material, insulating breath membrane, room specific air handling unit with heat recovery, photovoltaic/thermal system and solar assisted heat pump. Three representative residential buildings in different southern European countries were chosen as the demo buildings to implement energy renovation in this study. These existing demo building models were simulated in IDA Indoor Climate and Energy simulation software (IDA ICE) and used as the reference cases for retrofit technology simulations. The retrofit technologies were classified into the passive package, ventilation package and generation package, and then integrated into the building models to examine their impact on primary energy and CO_2 emissions. Finally, different final combinations of retrofit technologies were simulated to achieve the lowest building energy consumption and CO_2 emissions after renovation.

According to the simulation results, the novel retrofit technologies all had a certain impact on primary energy and CO_2 emissions, while the impact of the same technology varied significantly in different demo buildings based on building type, climate conditions, heating schedules, etc. Regarding the performance of the final combinations, the maximum primary energy reduction after renovation was 48%, 58% and 64% in the Greek, Portuguese and Spanish demo buildings; the corresponding CO_2 emissions reduction was 48%, 58% and 66%, respectively. The lower reduction in the Greek and Portuguese demo building was caused by their heating schedules since energy renovation led to indoor air temperature level increase when the demo buildings were intermittently heated.

1. INTRODUCTION

The building sector accounts for 40% of total energy consumption and 36% of GHG emissions in the EU. Thus, improving building energy efficiency plays a key role in achieving the ambitious goal of carbon neutrality. New buildings constructed according to energy efficiency regulations (e.g., the Energy Performance of Buildings Directives) only account for little more than 1% of the EU building stock per year, while a substantial percentage of existing EU buildings was built without considering the energy efficiency as a priority (*EURIMA - New and Existing Buildings*, 2018). Consequently, it is more important to renovate the existing EU building stocks with low energy efficiency. However, the current renovation rate of existing buildings is only 1.2 - 1.4% per year which cannot ensure the EU building sector moves towards climate-neutral levels by 2050 (*A renovation wave*, 2021). Therefore, the EU commission published its Renovation Wave Strategy to accelerate the renovation steps.

With the background of Renovation Wave, the SUREFIT project, funded by the EU commission, is committed to finding sustainable solutions for affordable retrofit of EU residential buildings. A target of this project is to reduce heat loss of the building envelope and energy consumption of heating, cooling, ventilation and lighting, while increasing the share of renewable energy in the building to achieve near zero energy consumption. More specifically, the goal of the SUREFIT project is to reach a 60% reduction in primary energy consumption and CO_2 emissions of the demo buildings by retrofitting with different renovation measures.

In this study, the impact of SUREFIT retrofit technologies on primary energy and CO_2 emissions was evaluated in three representative residential buildings in southern European countries (Greece, Portugal and Spain) through building level simulations. In addition, the final combinations of retrofit technologies were also simulated to examine the maximum energy conservation potential of the demo buildings after renovation.

2. RESEARCH METHODS

2.1. Simulation setup

The demo buildings were modelled and simulated in a dynamic simulation tool IDA ICE, which is commonly used in Nordic countries. The building models were built up according to the floor plan of the demo buildings. The specific parameters of the building envelopes and energy systems were defined based on the input data from building owners and the online database TABULA WebTool (TABULA WebTool, 2021) in the user interface. The models were simulated on an hourly timescale to obtain hourly energy demand profiles and used as the reference cases for retrofit technology simulation.

The SUREFIT retrofit technologies were classified into different retrofit packages including the passive package, containing bio-aerogel thermal insulation, PV vacuum window, and phase change material; the ventilation package, consisting of insulating breath membrane and room specific air handling unit with heat recovery (RAHU); and generation package, including photovoltaic/thermal (PV/T) system and solar assisted heat pump (SAHP). As shown in Figure 1, they were integrated into the reference case models, and simulated separately by following the rule of starting from a single technology to all technologies in each package. Finally, the simulated final combinations contain all the technologies in the passive and ventilation package and either of the technologies included in the generation package.
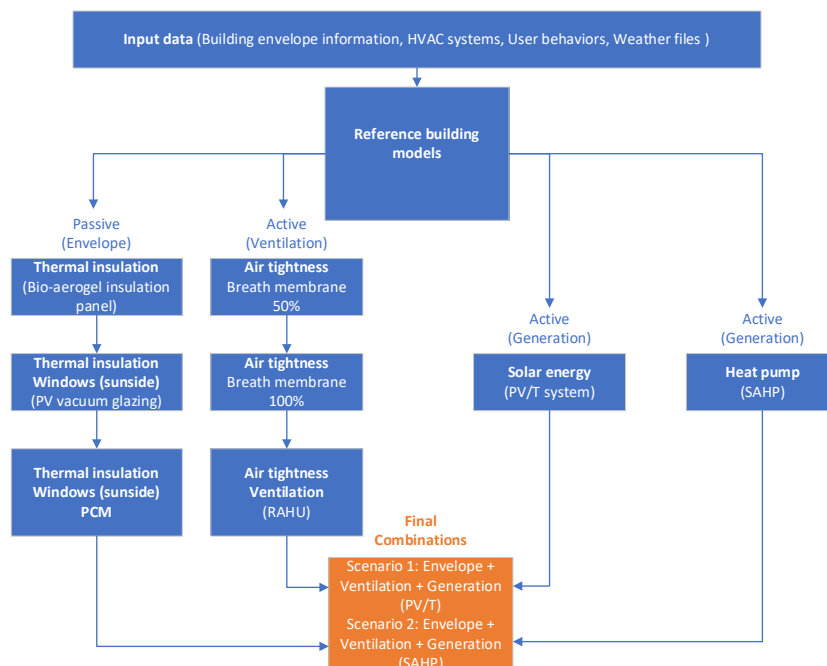
Figure 1: Simulation of retrofit packages in IDA ICE.

2.2. Demo building descriptions

The Greek demo located in Peristeri, Athens, was a small apartment building constructed in 1980s. This apartment building consisted of two apartment floors and a workshop. It was attached to two other buildings on the east and west sides. The apartment floors were heated with an oil boiler and water radiator system, and bedrooms and living rooms were equipped with electric air conditioners for cooling. Domestic hot water (DHW) is was by a solar thermal system.

The demo building in Portugal was a historic social house located in Lisbon. This demo building constructed in 1970s contained a ground floor as an apartment for one occupant and an upper floor as social space. All the living spaces were heated by portable electric heaters, while DHW heating was powered by a natural gas boiler.

The Spanish demo building was a terraced house in Valladolid. This demo house consisted of four apartments, each containing two residential floors and an unheated basement floor. It was heated by an independent heating system, which was a mix of gas boilers and electric heaters.

Table 1 and Table 2 shows the properties of the building envelope and parameters of HVAC systems in each demo building before renovation. Most of the input data were provided by the building owners, while the remaining unknown data were defined based on literature or TABULA WebTool (TABULA WebTool, 2021). As the field tests of airtightness were not implemented in these demo buildings, air leakage rate at 50 Pa pressure difference used for the simulation was an assumed value based on the typical airtightness of Spanish residential buildings (Feijó-Muñoz et al., 2019).

Table 1: Properties of building envelopes in the demo buildings before renovation.

Demo building	Greek apartment building	Portuguese social house	Spanish terraced house
U-values of envelope [W/m^{2}K]			
External wall	0.7	2.4	1.7
Roof	3.9	3.8	1.6
External floor	3.6	1.0	2.9
External door	1.1	3.6/3.7/3.9	2.2
Windows	5.9/3.0	5.1	5.8/2.8
Infiltration			
Air leakage rate, n_{50} [ACH]	6.7	6.7	6.7

Table 2: Parameters of HVAC systems in the demo buildings before renovation.

Demo building	Greek apartment building	Portuguese social house	Spanish terraced house
Ventilation system	Natural ventilation	Natural ventilation	Natural ventilation
Space heating system	Oil boiler and water radiators	Portable electric heaters	Gas boiler and water radiators/Electric heaters
Maximum heating capacity of boiler [kW]	65	-	65
Efficiency of boiler [%]	81	-	81
Power of electric heater [kW]	-	-	
Setpoint, living spaces [°C]	20	20	18-20
Setpoint, other rooms[°C]	20	20	18-20
Design temperature of water radiators [°C /°C]	90/60	-	70/40
Heating design outdoor temperature [°C]	1.8	4.9	-4.1
Cooling system	Split cooling units	No	No
Cooling capacity [kW]	2.6/7.0	-	-
Coefficient of performance	3.1/5.6/6.1	-	-
Setpoint [°C]	25	-	-
DHW	Solar collector and boiler	Gas heater	Gas boiler
Heating capacity [kW]	65.0	19.2	65.0
Efficiency [%]	81	90	81
Cold city water temperature [°C]	15	15	12
DHW outlet temperature [°C]	55	45	55
DHW use [L/day/person]	50	100	26
DHW recirculation loss [W/m^2]	0.5	-	-

As the energy demand for space heating accounts for most of the total energy consumption in residential buildings, it is important to define appropriate heating schedules to reflect energy consumption levels in the existing demo buildings. In southern European countries, residential buildings are commonly heated intermittently during certain hours of the day. The apartments in the Greek demo building were heated for two hours in the morning (7-9 am) and three hours in the evening (7-10 pm) from November to March. All the living spaces in the Portuguese social house were heated from 7-9 am and 7-10 pm from September to May. The Greek and Portuguese demo buildings were heated with a fixed heating setpoint (20°C), while the Spanish demo building was heated using a varying setpoint, 18 or 20°C during the day (2-11 pm) and 17°C in the evening and morning.

2.3. Primary energy and carbon emissions

The energy generation mix varies in different southern European countries, which affects the corresponding primary and CO_2 emissions factors of energy generation. Table 3 shows the primary and CO_2 emissions factors of energy carriers in Greece, Portugal and Spain.

Table 3: Primary energy factors and CO_2 emissions factors in Greece, Portugal and Spain.

	Primary Energy Factors (kWh/kWh)			CO_2 Emissions Factors (kg-CO_2/MWh)		
	Natural gas	Oil	Electricity	Natural gas	Oil	Electricity
Greece	1.05	1.10	1.79	196	264	572
Portugal	1.00	1.00	1.49	204	267	227
Spain	1.07	-	1.51	199	-	190

2.4. Retrofit packages

Passive package

The passive package included three technologies: bio-aerogel thermal insulation, PV vacuum glazing window and phase-change material (PCM). Bio-aerogel thermal insulation is an environmentally friendly insulating material made of starch-based aerogel. It was made into a prefabricated panel installed on the outside or inside of the external walls and roofs in the demo buildings. PV vacuum window is a daylight-management apparatus with photovoltaic solar cells embedded in a window (Jarimi *et al.*, 2020). It can not only generate electricity during daytime but also decrease heat transfer through windows due to its low U-value. To maximise the electricity generation of PV vacuum windows, they were installed on the south façade of the demo buildings. PCM is a substance which releases/absorbs sufficient energy at phase transition between solid and liquid to provide useful heat/cooling. PCM product S21, a salt hydrate, was chosen and treated as an independent PCM layer installed under the ceiling of demo buildings. The melting process started at 18°C, reached its peak at 27°C, and ended at 36°C (PCM Products, 2021). Table 4 shows more detailed parameters of these retrofit technologies.

Table 4: Parameters of retrofit technologies in the passive package.

Retrofit technology	Parameters
Bio-aerogel thermal insulation	Thermal conductivity [W/mK]: 0.037, Density [kg/m³]: 43, Specific heat [J/kgK]: 2260, Thickness of insulation panel [m]: 0.05
PV vacuum window	Solar heat gain coefficient (SHGC): 0.42, Solar transmittance: 0.3, Visible transmittance: 0.65, U-value of glazing [W/m²K]: 0.6, Efficiency of electricity generation [%]: 3.5, Area of PV vacuum windows [m²]: 11.2 (Greece), 1.1 (Portugal), 19.6 (Spain)
PCM Product S21	Layer density (solid) [kg/m³]: 1100, Layer specific heat (solid) [J/kgK]: 2300, Layer heat conductivity (solid) [W/mK]: 0.22, layer specific heat (liquid) [J/kgK]: 2300, Layer heat conductivity (liquid) [W/mK]: 0.22, Specific heat during reversing [J/kgK]: 300

Ventilation package

The ventilation package consisted of insulating breath membrane and room specific air handling unit with heat recovery (RAHU). Insulating breath membrane could be seen as a thermal insulating measure which can also improve airtightness of buildings after retrofit (WINCO Technologies, 2021). The breath membrane layer was installed over the external walls and roofs of the demo buildings. Since the air leakage rate of demo buildings after installing insulating breath membrane was unknown, two cases with different assumed air leakage rates were simulated in this study: 50% airtightness improvement (the average value of the infiltration rate of the existing building and the tested air leakage rate of insulating breath membrane) and 100% airtightness improvement (the tested air leakage rate of insulating breath membrane). RAHU was an independent mechanical ventilation device installed above the windows, consisting of heat pipes and fans (Barreto *et al.*, 2022). All rooms with windows except kitchens and bathrooms in the demo buildings were equipped with RAHU, and their ventilation rates were defined based on the European standard

for ventilation requirement. The efficiency of heat recovery depends on the air flow rate of ventilation systems. Detailed parameters of insulating breath membrane and RAHU are shown in Table 5.

Table 5: Parameters of retrofit technologies in the ventilation package.

Retrofit technology	Parameters
Insulating breath membrane	Thermal conductivity [W/mK]: 0.029, Density [kg/m^3]: 96.15, Specific heat [J/kgK]: 2260, Thickness of insulating breath membrane [m]: 0.026, Airtightness (50% improvement) at 50 Pa [ACH]: 3.4, Airtightness (100% improvement) at 50 Pa [ACH]: 0.07 (Greece), 0.15 (Portugal), 0.11 (Spain)
RAHU	Supply & Exhaust airflow rate [L/s]: Greece: Living room: 15/14 Bedroom: 8/7/4, Portugal: Bedroom: 7 Social space: 24, Spain: Living room: 8 Bedroom: 5, Efficiency of heat recovery: Greece: Living room: 0.64/0.66 Bedroom: 0.76, Portugal: Bedroom: 0.76 Social space: 0.59, Spain: Living room: 0.76 Bedroom: 0.76

Generation package

The generation package included two technologies: photovoltaic/thermal (PV/T) system and solar assisted heat pump (SAHP). PV/T system can convert solar radiation into usable thermal and electrical energy (Das, Kalita and Roy, 2018). As the most important component, the PV/T panel combines photovoltaic solar cells with a solar thermal collector. In this study, to maximise the energy return within limited installation space, the maximum available area for PV/T panel installation was used in the simulation to reduce the purchased energy as much as possible. Besides, the appropriate size of water tank and back up heater were defined according to the heating capacity. SAHP is a heat pump in which solar collectors act as the evaporator in a single integrated system (Huang and Chyng, 2001). The solar collector operates more like an ambient heat exchanger than a solar thermal collector because it also transfers heat from ambient air through convection. It was placed on the roof of the demo buildings to maximise the utilisation of solar radiation. In order to cover as much heating demand as possible, the SAHP with maximum thermal generation capacity and the largest available water tank were tested in the simulations. Table 6 presents parameters of PV/T system and SAHP in different demo buildings.

Table 6: Parameters of retrofit technologies in the generation package.

Retrofit technology	Parameters
PV/T system	Conversion factor of solar thermal: 0.486, Loss coefficient at collector fluid temperature equal to ambient temperature a_1 [W/m^{2}K]: 4.028, Loss coefficient of a collector depends on the temperature a_2 [W/m^{2}K]: 0.067, Electricity generation efficiency: 0.13, Area of PV/T panel [m^2]: 26 (Greece), 24 (Portugal), 10 (Spain), Volume of hot water tank [m^3]: 1 (Greece), 1.4 (Portugal), 1 (Spain)
SAHP	Total heating capacity [kW]: 11, COP: 4, Dimension of each solar collector panel [m]: 2.1×0.81, Panel number: 4, Conversion factor η_0: 0.7, Loss coefficient at collector fluid temperature equal to ambient temperature a_1 [W/m^{2}K]: 4, Loss coefficient of a collector depends on the temperature a_2 [W/m^{2}K]: 0.005

3. SIMULATED ENERGY CONSUMPTION AND CO_2 EMISSIONS

3.1. Greek apartment building

Table 7 shows the purchased fuel, electricity, primary energy as well as CO_2 emissions in the Greek apartment building. Regarding the passive package, bio-aerogel thermal insulation brought 15% reduction in both primary energy use and CO_2 emissions since it affected the space heating demand significantly, while the installation of PV vacuum windows and PCM only reduced the primary energy by 8% and 2%, the corresponding CO_2 emissions reduction of which were 8% and 1%. As for the first step in the ventilation package, the installation of insulating breath membrane could result in 14% and 15% primary energy reduction with 50% and 100% airtightness improvement assumption. Considering the slight difference between two cases, increasing the airtightness had only a minimal effect on energy, implying that the main energy efficiency impact came from the added thermal insulation. RAHU had a negative effect on primary energy consumption and CO_2 emissions, increasing primary energy by 7% and CO_2 emissions by 8%. In terms of generation technologies, primary energy and CO_2 emissions after installing the PV/T system were reduced by 26%, more than the 14% of installing SAHP. As SAHP consumed more electricity than the PV/T system and the CO_2 emissions factor is relatively high in Greece, the CO_2 emissions after retrofitting with the PV/T system were 1% higher than that before renovation. Thus, the final combination with the PV/T system resulted in a higher primary energy and CO_2 emissions reduction (48%) in the Greek apartment building.

Table 7: Energy consumption and CO_2 emissions in the Greek apartment building before and after retrofitting.

		Fuel [kWh/m²]	Electricity [kWh/m²]	Primary energy [kWh/m²]	CO_2 emissions [kg/m²]
	Reference case	36.8	14.8	67.0	18.2
Passive package	Insulation	30.6	13	56.9	15.5
	Insulation + PV window	27.9	11.7	51.6	14.1
	Insulation + PV window + PCM	27.2	11.5	50.5	13.8
Ventilation package	Membrane (50% improvement)	30.9	13.1	57.4	15.7
	Membrane (100% improvement)	30.2	13.1	56.7	15.5
	RAHU	32.1	14.6	61.4	16.8
Generation package	PV/T system	29.6	9.4	49.4	13.2
	SAHP	0.0	32	57.3	18.3
Final combination	Passive + Ventilation + PV/T system	17.7	8.4	34.5	9.5
	Passive + Ventilation + SAHP	0.0	27.8	49.8	15.9

3.2. Portuguese social house

As shown in Table 8, the retrofit technologies changed energy consumption and CO_2 emissions at different levels in the Portuguese social house. For the passive package, bio-aerogel thermal insulation had the most significant impact on primary energy (44% reduction) and CO_2 emissions (43% reduction), while PV vacuum windows and PCM basically had no impact on energy conservation. Compared with bio-aerogel thermal insulation, the impact of insulating breath membrane was slightly lower, leading to 38% and 39% reduction in primary energy and 37% and 38% reduction in CO_2 emissions. After installing RAHU, primary energy consumption and CO_2 emissions increased by 11% due to the increased space heating demand. As the PV/T system could produce electricity for electric heaters and thermal energy for DHW usage, while SAHP only covered DHW heating demand, the PV/T system conserved a larger energy conservation potential (16% reduction) than SAHP (4% reduction). Therefore, compared with the final combination including SAHP, the final combination including PV/T system was more effective in the Portuguese social house, reducing primary energy and CO_2 emissions by 58%.

Table 8: Energy consumption and CO_2 emissions in the Portuguese social house before and after retrofitting.

		Fuel [kWh/m²]	Electricity [kWh/m²]	Primary energy [kWh/m²]	CO_2 emissions [kg/m²]
	Reference case	18.3	97.1	163.0	28.3
Passive package	Insulation	18.3	49.5	92.1	16.3
	Insulation + PV window	18.3	49.2	91.6	16.2
	Insulation + PV window + PCM	18.3	48.7	90.9	16.1
Ventilation package	Membrane (50% improvement)	18.3	55.3	100.7	17.7
	Membrane (100% improvement)	18.3	54.3	99.2	17.5
	RAHU	18.3	66.8	117.8	20.6
Generation package	PV/T system	4.5	88.5	136.4	23.3
	SAHP	3.7	102	155.7	26.6
Final combination	Passive + Ventilation + PV/T system	4.5	43.1	68.7	11.8
	Passive + Ventilation + SAHP	3.7	57	88.6	15.2

3.3. Spanish terraced house

Table 9 presents the purchased energy consumption, primary energy and CO_2 emissions before and after retrofitting the Spanish terraced house. In the passive package, bio-aerogel thermal insulation was the most effective technology, resulting in 40% and 43% reduction in primary energy and CO_2 emissions. Compared with bio-aerogel thermal insulation, the impact of PV vacuum windows and PCM was much lower, leading to only a 6% and 1% reduction in primary energy. The installation of insulating breath membrane reduced the primary energy by 33% and 34% and CO_2 emissions by 35% and 36%, then to guarantee the indoor air quality, installing RAHU increased primary energy and CO_2 emissions by 8%. Regarding the generation measures, SAHP had a larger energy conservation

potential than the PV/T system, reducing primary energy by 29% and CO_2 emissions by 37%. Both final combination scenarios could reduce the primary energy and CO_2 emissions by over 60%. The primary energy and CO_2 emissions were reduced by 64% and 66% after retrofitting with the final combination including the PV/T system, while the final combination including SAHP brought 63% primary energy reduction and 72% CO_2 emissions decrease in the Spanish terraced house.

Table 9: Energy consumption and CO_2 emissions in the Spanish terraced house before and after retrofitting.

		Fuel [kWh/m^2]	Electricity [kWh/m^2]	Primary energy [kWh/m^2]	CO_2 emissions [kg/m^2]
	Reference case	115.0	19.4	152.4	26.6
Passive package	Insulation	58.0	19.3	91.1	15.2
	Insulation + PV window	51.1	18.2	82.1	13.6
	Insulation + PV window + PCM	50.2	18.2	81.2	13.4
Ventilation package	Membrane (50% improvement)	68.1	19.3	102.0	17.2
	Membrane (100% improvement)	67.2	19.3	101.0	17.0
	RAHU	77.5	19.8	112.8	19.2
Generation package	PV/T system	97.2	12.5	122.8	21.7
	SAHP	45.6	39.8	108.9	16.6
Final combination	Passive + Ventilation + PV/T system	33.1	12.7	54.6	9.0
	Passive + Ventilation + SAHP	5.9	33.3	56.6	7.5

4. CONCLUSION

According to the building level simulations of retrofit technologies, they have different levels of impact on primary energy and CO_2 emissions. Additional thermal insulation for external walls and roof was quite beneficial for reducing energy consumption for space heating. CO_2 emissions were reduced by 15-43% after adding bio-aerogel thermal insulation in all the demo buildings. The benefit acquired in different demo buildings varied depend on the ratio of heated spaces, heating schedules etc. The existing heating systems in the intermittently heated demo buildings could not ensure the heated spaces reach the heating setpoint during the limited daily heating time. Thus, even though the thermal insulation was improved significantly, the heating system still ran at high power to reach the heating setpoint, which means the space heating demand did not decrease as much as expected. Compared with the thermal conditions before renovation, thermal insulation improvement resulted in a significant indoor air temperature increase. In comparison, PV vacuum windows and PCM provided smaller energy conservation and emission reduction potential (lower than 10%) in all the demo buildings.

In terms of the ventilation package, similar to bio-aerogel thermal insulation, insulating breath membrane was also effective for cutting down space heating demand, while the brought emission reduction level was lower (14-38%) due to the different thermal characteristics and panel thickness. Comparing 50% and 100% airtightness improvement cases, it could be concluded that the building energy efficiency achieved by installing insulating breath membrane mainly came from thermal insulation improvement instead of airtightness increase. Although installing RAHU had a negative impact on space heating demand, it is important to include it in the retrofitting scenario for a better indoor air quality if insulating breath membrane is installed.

Regarding the generation measures, the PV/T system provided more benefit for primary energy conservation than SAHP in the Greek and Portuguese demo buildings. However, the installation of SAHP resulted in lower primary energy consumption and CO_2 emissions than the PV/T system in the Spanish demo building.

Correspondingly, the final combination including passive package, ventilation package and PV/T system was a better option for energy conservation in southern European countries. As the building energy efficiency acquired by thermal insulation was effectively affected by intermittent heating schedules, retrofitting with the final combination including PV/T system only reduced the primary energy and CO_2 emissions by 48% in the Greek apartment building and 58% in the Portuguese social house. Both final combination scenarios led to similar primary energy and CO_2 emissions reduction in the Spanish terraced house, which were 64% primary energy and 66% CO_2 emissions reduction after retrofitting with the final combination including PV/T system and 61% primary energy and 70% CO_2 emissions reduction after retrofitting with the final combination including SAHP.

5. ACKNOWLEDGEMENTS

6. REFERENCES

A Renovation Wave, 2021. Eurima. Available at: https://www.eurima.org.

Barreto, G. *et al.*, 2022. An innovative window heat recovery (WHR) system with heat pipe technology: Analytical, CFD, experimental analysis and building retrofit performance, *Energy Reports*, 8, pp. 3289–3305.

Das, D., Kalita, P. and Roy, O., 2018. Flat plate hybrid photovoltaic- thermal (PV/T) system: A review on design and development, *Renewable and Sustainable Energy Reviews*, 84, pp. 111–130.

EURIMA - New and Existing Buildings, 2018. Eurima. Available at: https://www.eurima.org/energy-efficiency-in-buildings/new-and-existing-buildings.html.

Feijó-Muñoz, J. *et al.*, 2019. Airtightness of residential buildings in the Continental area of Spain. *Building and Environment*, 148, pp. 299–308.

Huang, B.J. and Chyng, J.P., 2001. Performance characteristics of integral type solar-assisted heat pump, *Solar Energy*, 71(6), pp. 403–414.

Jarimi, H. *et al.*, 2020. Performance Analysis of a Hybrid Thin Film Photovoltaic (PV) Vacuum Glazing, *Future Cities and Environment*, 6(1), p. 2.

Skytech-Pro-XL-Non-combustible-and-insulating-breather-membrane, 2021. Available at: https://www.winco-tech.com/wordpress/wp-content/uploads/2022/01/Skytech-Pro-XL-Non-combustible-and-insulating-breather-membrane.pdf.

TABULA WebTool, 2021. Available at: https://webtool.building-typology.eu/#bm.

Thermal_storage_catalogue, 2021. PCM Products. Available at: https://www.pcmproducts.net/files/thermal_storage_catalogue.pdf.

#95: The impact of retrofitting in southern European residential buildings with intermittent or continuous heating

Yangmin Wang[1], Janne Hirvonen[1,2], Ke Qu[3], Juha Jokisalo[1,4], Risto Kosonen[1,4,5]

[1] Department of Mechanical Engineering, Aalto University, Espoo, Finland, yangmin.wang@aalto.fi
[2] Department of Civil Engineering, Tampere University, Tampere, Finland
[3] Department of Architecture and Built Environment, University of Nottingham, Nottingham, UK
[4] FinEst Centre for Smart Cities, TalTech, Tallinn, Estonia
[5] College of Urban Construction, Nanjing Tech University, Nanjing, China

Abstract: Renovating the existing building stock is important for the building sector to reach the carbon neutral level. However, in addition to evaluating energy conservation and emission reduction potential brought about by renovation, it is also important to pay much attention to the change in the indoor climate after retrofit since people spend approximately 90% of their time indoors. This study aims to compare building energy consumption and the indoor climate after implementing several novel renovation technologies and their packages in southern European residential buildings through building-level simulations. The novel technologies include bio-aerogel thermal insulation, photovoltaic vacuum window, phase change material, insulating breath membrane, room specific air handling unit with heat recovery, a photovoltaic/thermal system and solar assisted heat pump. Three representative residential buildings in different southern European countries were chosen as the demo buildings to implement energy renovation in this study. These existing demo building models were simulated with an intermittent or continuous heating schedule in IDA ICE and used as the reference cases for renovation technologies simulations. The novel renovation technologies were classified into the passive package, ventilation package and generation package, and then integrated into the building models to evaluate their impact on building energy consumption and indoor climate.

The novelty of this study was to assess energy consumption and indoor climate change brought by the combinations of retrofit technologies in different southern European countries. It also revealed the impact of intermittent or continuous heating schedules on the energy conservation potential of retrofit technologies. The impact of retrofit technologies on building energy consumption and indoor climate was significantly affected by heating schedules. The energy consumption reduction acquired by thermal insulation improvement under intermittent heating schedules was much lower than that under continuous heating schedules in all demo buildings since thermal insulation improvement resulted in an indoor air temperature increase when intermittently heated. Besides, when the intermittent heating schedule was switched to the continuous heating schedule, although the absolute energy consumption reduction brought by generation technologies increased, the relative reduction in percentage was diminished due to the increased backup energy demand for space heating.

Keywords: residential building; energy renovation; intermittent heating; energy conservation; indoor climate

1. INTRODUCTION

The building sector is the largest single contributor to energy consumption and carbon emissions in the EU, which accounts for 40% of total energy consumption and 36% of greenhouse gas (GHG) emissions. Thus, buildings hold a great potential for energy conservation and emission reduction. As new buildings are commonly constructed based on the energy efficiency regulations and only account for around 1% of the EU building stock, it is more important to renovate the existing building stock, especially those built without taking energy efficiency as a priority (*EURIMA - New and Existing Buildings*, 2018). Therefore, the EU commission published its Renovation Wave Strategy to accelerate building sectors towards climate-neutral levels by 2050 (*Renovation Wave*, 2020).

Following the Renovation Wave, the SUREFIT project aims at finding sustainable solutions for affordable retrofit of EU residential buildings. A target of this project is to reduce heat loss of the building envelope and energy consumption of heating, cooling, ventilation and lighting, while increasing share of renewable energy in the building to achieve near zero energy consumption. To explain the sustainable retrofit solutions intuitively, several representative residential buildings in different countries were chosen as the demo buildings to implement different energy-saving measures, including bio-aerogel thermal insulation, photovoltaic vacuum window, phase change material, insulating breath membrane, room specific air handling unit with heat recovery, photovoltaic/thermal system and solar assisted heat pump.

Although the performance of these retrofit technologies has been proved in several studies (Jarimi *et al.*, 2020; Barreto *et al.*, 2022), according to the authors' best knowledge, scientific research which combines them in different packages to assess their building level performance is unavailable. The study focused on comparing the impact of the combination of retrofit technologies on building energy consumption and indoor climate in southern European countries (Greece, Portugal and Spain). In addition, based on the simulations with different heating schedules, this study can also present the impact of intermittent or continuous heating schedules on the energy conservation potential of renovation technologies.

2. METHODOLOGY

2.1. Simulation setup

The demo buildings were modelled and simulated in a dynamic simulation tool IDA ICE, which is commonly used in Nordic countries. The building models were built up according to input data from building owners and online database TABULA WebTool (*TABULA WebTool*, 2021) and simulated on an hourly timescale to obtain hourly energy demand and indoor climate profiles. These demo building models were used as the reference cases for retrofit technology simulation.

The SUREFIT retrofit technologies were classified into different retrofit packages including the passive package, consisting of bio-aerogel thermal insulation, PV vacuum window, and phase change material; the ventilation package, consisting of insulating breath membrane and room specific air handling unit with heat recovery (RAHU); the generation package, consisting of photovoltaic/thermal (PV/T) system and solar assisted heat pump (SAHP). As shown in Figure 1, they were integrated into the reference case models with intermittent or continuous heating and simulated separately by following the rule of starting from a single technology to all technologies in each package. Finally, the simulated final combinations contain all the technologies in the passive and ventilation package and either of the technologies included in the generation package.

Figure 1: Simulation of retrofit packages in IDA ICE.

272

2.2. Demo building descriptions

The Greek demo located in Peristeri, Athens was a small apartment building constructed in 1980s. This apartment building consisted of two apartment floors and a workshop. It was attached to two other buildings on the east and west sides. The apartment floors were heated with an oil boiler and water radiator system, and bedrooms and living rooms were equipped with electric air conditioners for cooling. Domestic hot water (DHW) was supplied by a solar thermal system.

The Portuguese demo building was a historic social house located in Lisbon. This demo building constructed in 1970s contained a ground floor apartment for one occupant and an upper floor as social space. All the living spaces were heated by portable electric heaters, while DHW heating was powered by a natural gas boiler.

The Spanish demo building was a terraced house in Valladolid. It consisted of four apartments, and each apartment contained two residential floors and an unheated basement floor. Each apartment was heated by an independent heating system, which was a mix of gas boilers and electric heaters.

Table 1: Properties of building envelopes in the demo buildings before renovation.

Demo building	Greek apartment building	Portuguese social house	Spanish terraced house
U-values of envelope [W/m^{2}K]			
External wall	0.7	2.4	1.7
Roof	3.9	3.8	1.6
External floor	3.6	1.0	2.9
External door	1.1	3.6/3.7/3.9	2.2
Windows	5.9/3.0	5.1	5.8/2.8
Infiltration			
Air leakage rate, n_{50} [ACH]	6.7	6.7	6.7

Table 2: Parameters of HVAC systems in the demo buildings before renovation.

Demo building	Greek apartment building	Portuguese social house	Spanish terraced house
Ventilation system	Natural ventilation	Natural ventilation	Natural ventilation
Space heating system	Oil boiler and water radiators	Portable electric heaters	Gas boiler and water radiators/Electric heaters
Maximum heating capacity of boiler [kW]	65	-	65
Efficiency of boiler [%]	81	-	81
Power of electric heater [kW]	-	-	
Setpoint, living spaces [°C]	20	20	18-20
Setpoint, other rooms[°C]	20	20	18-20
Design temperature of water radiators [°C /°C]	90/60	-	70/40
Heating design outdoor temperature [°C]	1.8	4.9	-4.1
Cooling system	Split cooling units	No	No
Cooling capacity [kW]	2.6/7.0	-	-
Coefficient of performance	3.1/5.6/6.1	-	-
Setpoint [°C]	25	-	-
DHW	Solar collector and boiler	Gas heater	Gas boiler
Heating capacity [kW]	65.0	19.2	65.0
Efficiency [%]	81	90	81
Cold city water temperature [°C]	15	15	12
DHW outlet temperature [°C]	55	45	55
DHW use [L/day/person]	50	100	26
DHW recirculation loss [W/m^2]	0.5	-	-

Table 1 and Table 2 show the properties of the building envelope and parameters of HVAC systems in each demo building before renovation. Most of the input data were provided by building owners, while the remaining unknown

data were defined based on literature or TABULA WebTool. As field tests of airtightness were not implemented in these demo buildings, the air leakage rate at 50 Pa pressure difference used for the simulation was an assumed value based on typical airtightness of residential buildings in southern European countries (e.g., Spain) (Feijó-Muñoz et al., 2019).

2.3. Heating schedules

In this study, the building level simulations were implemented with both intermittent and continuous heating schedules. The intermittent heating schedules used for simulation were defined based on the occupant's feedback to reflect energy consumption level in the existing demo buildings, while the same continuous heating schedule was applicable for all demo buildings (see Table 3).

Table 3: Intermittent and continuous heating schedule in the different demo buildings.

Demo site	Heated space	Intermittent heating schedule	Continuous heating schedule
Greek apartment building	The whole apartment area	From 1 Nov to 31 Mar, 20°C [7-9, 19-22]	
Portuguese social house	All living spaces	From 1 Dec to 28 Feb, Weekdays: 20°C [7-8, 15-23], Weekends & Holidays: 20°C [8-23]	From 1 Sep to 31 May, 20°C
Spanish terraced house	Ground floor	All year round, 20°C [14-23], 17°C otherwise	
	Top floor	All year round, 18°C [14-23], 17°C otherwise	
	Attic	From 1 Oct to 30 Apr, 20°C [14-23]	

2.4. Retrofit packages

Passive package

The passive package included three technologies: bio-aerogel thermal insulation, PV vacuum glazing window and phase change material (PCM). Bio-aerogel thermal insulation is an environmentally friendly insulating material that is made of starch-based aerogel. It was made into a prefabricated panel installed on the outside or inside of the external walls and roofs in the demo buildings. PV vacuum window is a daylight-management apparatus with photovoltaic solar cells embedded in a window (Jarimi et al., 2020). It can not only generate electricity during the daytime but also decrease heat transfer through windows due to its low U-value. To maximise the electricity generation of PV vacuum windows, they were installed on the south façade of the demo buildings. PCM is a substance that releases/absorbs sufficient energy at the phase transition between solid and liquid to provide useful heat/cooling. PCM product S21, a salt hydrate, was chosen and treated as an independent PCM layer installed under the ceiling of the demo buildings. The melting process started at 18°C, reached its peak at 27°C, and ended at 36°C (PCM Products, 2021). Table 4 shows more detailed parameters of these retrofit technologies.

Table 4: Parameters of retrofit technologies in the passive package.

Retrofit technology	Parameters
Bio-aerogel thermal insulation	Thermal conductivity [W/mK]: 0.037, Density [kg/m^3]: 43, Specific heat [J/kgK]: 2260, Thickness of insulation panel [m]: 0.05
PV vacuum window	Solar heat gain coefficient (SHGC): 0.42, Solar transmittance: 0.3, Visible transmittance: 0.65, U-value of glazing [W/m^{2}K]: 0.6, Efficiency of electricity generation [%]: 3.5, Area of PV vacuum windows [m^2]: 11.2 (Greece), 1.1 (Portugal), 19.6 (Spain)
PCM Product S21	Layer density (solid) [kg/m^3]: 1100, Layer specific heat (solid) [J/kgK]: 2300, Layer heat conductivity (solid) [W/mK]: 0.22, layer specific heat (liquid) [J/kgK]: 2300, Layer heat conductivity (liquid) [W/mK]: 0.22, Specific heat during reversing [J/kgK]: 300

Ventilation package

The ventilation package consisted of insulating breath membrane and room specific air handling unit with heat recovery (RAHU). Insulating breath membrane could be seen as a thermal insulating measure which can also improve the airtightness of a building after retrofit (WINCO Technologies, 2021). The breath membrane layer was installed over the external walls and roofs of the demo buildings. Since the air leakage rate of demo houses after installing insulating breath membrane was unknown, two cases with different assumed air leakage rates were simulated in this study: 50% airtightness improvement (the average value of the infiltration rate of the existing building and the tested air leakage rate of insulating breath membrane) and 100% airtightness improvement (the tested air leakage rate of insulating breath membrane). RAHU is an independent mechanical ventilation device installed above the windows consisting of heat pipes and fans (Barreto *et al.*, 2022). All rooms with windows except kitchens and bathrooms in the demo buildings were equipped with RAHU, and their ventilation rates were defined based on the European standard for ventilation requirements. The efficiency of heat recovery depends on the airflow rate of ventilation systems. Detailed parameters of insulating breath membrane and RAHU are shown in Table 5.

Table 5: Parameters of retrofit technologies in the ventilation package.

Retrofit technology	Parameters
Insulating breath membrane	Thermal conductivity [W/mK]: 0.029, Density [kg/m^3]: 96.15, Specific heat [J/kgK]: 2260, Thickness of insulating breath membrane [m]: 0.026, Airtightness (50% improvement) at 50 Pa [ACH]: 3.4, Airtightness (100% improvement) at 50 Pa [ACH]: 0.07 (Greece), 0.15 (Portugal), 0.11 (Spain)
RAHU	Supply & Exhaust airflow rate [L/s]: Greece: Living room: 15/14 Bedroom: 8/7/4, Portugal: Bedroom: 7 Social space: 24, Spain: Living room: 8 Bedroom: 5, Efficiency of heat recovery: Greece: Living room: 0.64/0.66 Bedroom: 0.76, Portugal: Bedroom: 0.76 Social space: 0.59, Spain: Living room: 0.76 Bedroom: 0.76

Generation package

The generation package included two technologies: a photovoltaic/thermal (PV/T) system and solar assisted heat pump (SAHP). PV/T systems can convert solar radiation into usable thermal and electrical energy (Das, Kalita and Roy, 2018). As the most important component, the PV/T panel combined photovoltaic solar cells with a solar thermal collector. In this study, to maximise the energy return within limited installation space, the maximum available area for PV/T panel installation was used in the simulation to reduce the purchased energy as much as possible. Also, the appropriate size of the water tank and backup heater were defined according to the heating capacity. SAHP is a heat pump in which solar collectors act as the evaporator in a single integrated system (Huang and Chyng, 2001). The solar collector operates more like an ambient heat exchanger than a solar thermal collector because it also transfers heat from ambient air through convection. It was placed on the roof of demo buildings to maximise the utilisation of solar radiation. In order to cover as much heating demand as possible, the SAHP with maximum thermal generation capacity and the largest available water tank was tested in the simulations. Table 6 presents the parameters of the PV/T system and SAHP in different demo buildings.

Table 6: Parameters of retrofit technologies in the generation package.

Retrofit technology	Parameters
PV/T system	Conversion factor of solar thermal: 0.486, Loss coefficient a_1 [W/m^{2}K]: 4.028, Loss coefficient a_2 [W/m^{2}K]: 0.067, Electricity generation efficiency: 0.13, Area of PV/T panel [m^2]: 26 (Greece), 24 (Portugal), 10 (Spain), Volume of hot water tank [m^3]: 1 (Greece), 1.4 (Portugal), 1 (Spain)
SAHP	Total heating capacity [kW]: 11, COP: 4, Dimension of each solar collector panel [m]: 2.1×0.81, Panel number: 4, Conversion factor η_0: 0.7, Loss coefficient a_1 [W/m^{2}K]: 4, Loss coefficient a_2 [W/m^{2}K]: 0.005

3. SIMULATED ENERGY CONSUMPTION AND INDOOR CLIMATE

3.1. Greek apartment building

Table 7 presents the breakdown of purchased energy, indoor temperature, and CO_2 concentration in the Greek apartment building before and after renovation when it was intermittently heated. Regarding the passive package, bio-aerogel thermal insulation, PV vacuum window and PCM brought 16%, 7% and 2% reduction in total purchased energy, respectively. In terms of the ventilation package, installing insulating breath membrane over the building envelopes reduced the total purchased energy by 15% when 50% airtightness improvement was assumed and 16% when 100% airtightness improvement was assumed. As there was only 1% difference between two cases, increasing airtightness had only a minimal effect on energy, implying that the main energy efficiency impact came from the thermal insulation improvement. The installation of RAHU increased the space heating demand, which led to 7% increase in total purchased energy, while it also brought the CO_2 concentration, which had increased significantly due to the airtightness improvement, back to below 1,200 ppm again. Replacing the existing heating system with a PV/T

system or SAHP could reduce the total purchased energy by 24% or 38%. The final combination including the PV/T system gained a larger energy saving potential, which reduced the total purchased energy by 49%, than the final combination including SAHP, which reduced the total purchased energy by 46%.

Table 7: Simulated energy consumption and indoor climate in the intermittently heated Greek apartment building.

	Energy consumption			Indoor climate				
	Fuel [kWh/m^2]	Elec [kWh/m^2]	Total [kWh/m^2]	T < 20°C [%]	T > 25°C [%]	T_max [°C]	CO_2 < 1200 [%]	CO_2 < 1800 [%]
Ref	36.8	14.8	51.6	44.2	20.7	28.7	20.3	79.6
Ins	30.6	13.0	43.6	40.2	19.8	27.8	20.6	79.9
Ins+Win	27.9	11.7	39.6	34.3	24.4	28.6	20.8	80.8
Ins+Win+PCM	27.2	11.5	38.7	34.3	24.6	28.6	20.7	80.6
Mem 50%	30.9	13.1	44.0	40.0	19.9	27.8	12.8	66.4
Mem 100%	30.2	13.1	43.3	39.2	22.0	27.8	8.4	46.2
RAHU	32.1	14.6	46.7	42.5	19.5	28.2	100.0	100.0
PV/T	29.6	9.4	39.0	44.1	20.7	28.7	20.2	79.6
SAHP	0.0	32.0	32.0	44.2	20.7	28.7	20.3	79.6
Pas+Ven+PV/T	17.7	8.4	26.1	33.5	25.1	28.7	100.0	100.0
Pas+Ven+SAHP	0.0	27.8	27.8	33.2	25.1	28.7	100.0	100.0

*Ref: Reference case before renovation; **Ins**: Bio-aerogel thermal insulation; **Win**: PV vacuum window; **Mem**: Insulating breath membrane; **RAHU**: Room specific air handling unit with heat recovery; **PV/T**: Photovoltaic/Thermal system; **SAHP**: Solar assisted heat pump; **Pas**: All the technologies included in the passive package; **Ven**: All the technologies included in the ventilation package; **T < 20 °C/T > 25°C**: Proportion of time indoor temperature is lower than 20°C or higher than 25°C; **T_max**: Maximum air temperature; **CO_2 < 1200/1800**: Proportion of time CO_2 concentration is lower than 1200 or 1800 ppm.

Table 8: Simulated energy consumption and indoor climate in the continuously heated Greek apartment building.

	Energy consumption			Indoor climate				
	Fuel [kWh/m^2]	Elec [kWh/m^2]	Total [kWh/m^2]	T < 20°C [%]	T > 25°C [%]	T_max [°C]	CO_2 < 1200 [%]	CO_2 < 1800 [%]
Ref	109.3	18.2	127.5	0.6	0.0	25.0	21.7	79.7
Ins	56.5	14.3	70.8	0.9	0.0	25.0	21.4	80.2
Ins+Win	46.6	13.4	60	0.1	0.0	25.0	23.9	81.9
Ins+Win+PCM	45.9	13.4	59.3	0.0	0.0	25.0	23.6	81.7
Mem 50%	57.3	14.4	71.7	0.6	0.0	25.0	13.3	67.2
Mem 100%	54.2	14.4	68.6	0.5	0.0	25.0	10.4	48.6
RAHU	64.8	16.3	81.1	0.5	0.0	25.0	100.0	100.0
PV/T	99.2	10	109.2	0.0	0.0	25.0	22.0	61.8
SAHP	61.7	38.2	99.9	0.6	0.0	25.0	21.7	79.5
Pas+Ven+PV/T	35.7	7.5	43.2	0.4	0.0	25.0	100.0	100.0
Pas+Ven+SAHP	13.1	31.3	44.4	0.4	0.0	25.0	100.0	100.0

Table 8 shows the simulated energy consumption and indoor climate when the demo building was continuously heated. Due to the increased heating demand when it was continuously heated, the demo building consumed more than double the purchased energy under the intermittent heating schedule. The total purchased energy was reduced by 44%, 9% and below 1% after retrofitting with bio-aerogel thermal insulation, PV vacuum window and PCM, respectively. Installing insulating breath membrane conserved similar energy saving potential as bio-aerogel thermal insulation, which reduced the purchased energy by 44% with 50% airtightness improvement and 46% with 100% airtightness improvement, while it had a negative impact on indoor air quality, which meant CO_2 concentration was above 1,800 ppm for half of the year due to the improved airtightness. Thus, after installing insulating breath membrane, equipping the Greek demo building with RAHU could ensure the CO_2 concentration was always lower than 1,200 ppm at the cost of a 10% increase in purchased energy. As for the generation measures, installing SAHP had a larger impact on building energy consumption (14% reduction) than PV/T system (22% reduction). Finally, retrofitting with the final combination including PV/T system or SAHP led to 66% or 65% decrease in total purchased energy.

The technologies aimed at improving thermal insulation performance (e.g., bio-aerogel thermal insulation, insulating breath membrane) brought much higher energy saving potential when the intermittent heating schedule was switched to the continuous heating schedule. As shown in Table 7, when it was intermittently heated, around 44% of the year the indoor temperature was lower than 20°C before renovation, while this proportion became much lower after retrofitting the building envelopes. It meant that thermal insulation improvement led to the indoor temperature increasing. However, when the building was continuously heated, the indoor temperature was kept at the similar level before and after renovation. In addition, if the intermittent heating schedule was switched to the continuous heating schedule, although the absolute energy consumption reduction value became larger, the relative energy conservation

potential of generation measures in percentage would be reduced. The capacity of generation measures could not cover the increased heating demand due to the extended heating time. The backup heating demand increased dramatically to satisfy the heating demand. The share of backup energy in total energy consumption became much higher than that of the utilised energy from generation measures when the Greek apartment building was continuously heated.

3.2. Portuguese social house

Table 9 shows the simulated energy consumption and indoor climate when the Portuguese demo building was intermittently heated. The bio-aerogel thermal insulation was the most effective measure for energy conservation, resulting in 41% reduction in total purchased energy, while the impact of PV vacuum window and PCM was quite limited, only reducing the purchased energy by below 1%. When the insulating breath membrane was installed over the external walls and roof, the purchased energy was reduced by 36% with 50% airtightness improvement and 37% with 100% airtightness improvement. However, the airtightness improvement also made the CO_2 concentration level increase dramatically. After installing RAHU, the CO_2 concentration was controlled back to below 1,200 ppm all year round, while the purchased energy increased by 11%. As electric heaters were used for space heating in this demo house, SAHP only covered the heating demand for DHW, saving 8% of the purchased energy. Compared with SAHP, the PV/T system was a better option for energy conservation by reducing 19% of the purchased energy in this demo house since there were lots of spaces available for PV/T panels on the roof. Correspondingly, the purchased energy was reduced by 59% after retrofitting with the final combination including PV/T system, higher than 47% reduction achieved with the other scenario including SAHP.

Table 9: Simulated energy consumption and indoor climate in the intermittently heated Portuguese social house.

	Energy consumption			Indoor climate				
	Fuel [kWh/m^2]	Elec [kWh/m^2]	Total [kWh/m^2]	T < 20°C [%]	T > 25°C [%]	T_max [°C]	CO_2 < 1200 [%]	CO_2 < 1800 [%]
Ref	18.3	97.1	115.4	49.0	7.1	27.9	34.2	72.5
Ins	18.3	49.5	67.8	33.5	2.7	26.3	38.5	75.5
Ins+Win	18.3	49.2	67.5	33.6	2.2	26.2	39.0	75.7
Ins+Win+PCM	18.3	48.7	67	33.9	0.0	25.7	42.2	76.2
Mem 50%	18.3	55.3	73.6	36.7	3.8	26.5	23.6	61.6
Mem 100%	18.3	54.3	72.6	36.9	3.9	26.5	16.3	33.6
RAHU	18.3	66.8	85.1	42.9	2.0	26.8	100.0	100.0
PV/T	4.5	88.5	93	49.2	7.0	27.9	34.2	72.3
SAHP	3.7	102	105.7	49.1	7.1	27.9	34.1	72.4
Pas+Ven+PV/T	4.5	43.1	47.6	38.6	0.2	26.0	100.0	100.0
Pas+Ven+SAHP	3.7	57	60.7	38.4	0.5	26.1	100.0	100.0

Table 10: Simulated energy consumption and indoor climate in the continuously heated Portuguese social house.

	Energy consumption			Indoor climate				
	Fuel [kWh/m^2]	Elec [kWh/m^2]	Total [kWh/m^2]	T < 20°C [%]	T > 25°C [%]	T_max [°C]	CO_2 < 1200 [%]	CO_2 < 1800 [%]
Ref	18.3	210.8	229.1	0.0	7.1	27.9	35.5	73.3
Ins	18.3	66.6	84.9	0.0	2.7	26.3	39.5	75.8
Ins+Win	18.3	65.9	84.2	0.0	2.2	26.2	40.0	76.2
Ins+Win+PCM	18.3	65.9	84.2	0.0	0.0	25.7	43.2	76.9
Mem 50%	18.3	77.2	95.5	0.0	3.8	26.5	24.3	61.8
Mem 100%	18.3	75.1	93.4	0.0	3.9	26.5	16.3	32.6
RAHU	18.4	98	116.4	0.0	2.0	26.8	100.0	100.0
PV/T	4.5	189.8	194.3	0.0	7.0	27.9	35.4	73.3
SAHP	3.7	215.8	219.5	0.0	7.1	27.9	35.4	73.2
Pas+Ven+PV/T	4.6	53.8	58.4	0.0	0.2	26.0	100.0	100.0
Pas+Ven+SAHP	3.8	74.9	78.7	0.0	0.5	26.1	100.0	100.0

Table 10 presents the breakdown of purchased energy, indoor temperature, and CO_2 concentration in the Portuguese social house before and after renovation when it was continuously heated. The total purchased energy consumption before renovation doubled, and the indoor temperature was always above 20°C when the heating schedule was switched to the continuous heating schedule. Just covering the building envelopes with bio-aerogel thermal insulation resulted in 63% energy saving, compared to the negligible impact of PV vacuum window and PCM on energy consumption. Due to the excellent thermal and airtight properties, installation of insulating breath membrane led to 58-59% reduction in the total purchased energy and increased proportion (up to 67%) of the time CO_2 concentration was above 1,800 ppm. Then, equipping the living spaces with RAHU guaranteed the CO_2 concentration lower than 1,200 ppm, while increasing the purchased energy by 10%. Replacing the existing gas heater with PV/T system or

SAHP could reduce the total purchased energy by 15% or 4%. When these technologies were combined for renovation, the purchased energy was reduced by 75% or 66% after retrofitting with the final combination including PV/T system or SAHP.

Similar to the situation in the Greek apartment building, the energy conservation potential of thermal insulation improvement became more significant if the intermittent heating schedule was switched to the continuous heating schedule in the Portuguese social house. The indoor temperature before and after renovation was kept at a similar level (see Table 10) when the demo building was continuously heated, while thermal insulation improvement by bio-aerogel thermal insulation, insulating breath membrane etc. resulted in a significant indoor temperature increase (see Table 9) when it was intermittently heated. It meant that partial building efficiency achieved by thermal insulation was converted into the increased temperature level. However, the energy conservation potential of generation measures was reduced significantly when the intermittent heating schedule was switched to the continuous heating schedule. The space heating demand doubled due to the increased heating time. In this demo building, the capacity of SAHP could only cover DHW heating demand. The share of DHW heating in the total purchased energy decreased as the space heating demand increased, resulting in a corresponding decrease in the contribution of SAHP to energy conservation. For the PV/T system, although the increased heating time had led to more utilisation of electricity generated by PV/T panels, the share of increased electricity consumption for space heating in total energy consumption far exceeded that of the utilised solar energy.

3.3. Spanish terraced house

As shown in Table 11, the retrofitting technologies affected the purchased energy and indoor climate at different levels when the Spanish terraced house was intermittently heated. Regarding the passive package, bio-aerogel thermal insulation, the most effective measure for energy saving, reduced the purchased energy by 43%, while PV vacuum window and PCM only brought 5% and 1% reduction, respectively. In terms of the ventilation package, installing insulating breath membrane over building envelopes could reduce the total purchased energy by 35% when 50% airtightness improvement was assumed and 36% when 100% airtightness improvement was assumed. The installation of RAHU increased the electricity consumption and space heating demand, which led to 8% increase in total purchased energy, while it also ensured the CO_2 concentration was below 1,200 ppm almost all year round. Replacing the existing heating system with PV/T system or SAHP could reduce the total purchased energy by 18% or 36%. The final combination including SAHP conserved a larger energy saving potential, which reduced the total purchased energy by 71%, compare with the final combination including PV/T system, saving the purchased energy by 66%.

Table 11: Simulated energy consumption and indoor climate in the intermittently heated Spanish terraced house.

	Energy consumption			Indoor climate				
	Fuel [kWh/m²]	Elec [kWh/m²]	Total [kWh/m²]	T < 18°C [%]	T > 25°C [%]	T_max [°C]	CO_2 < 1200 [%]	CO_2 < 1800 [%]
Ref	115.0	19.4	134.4	5.1	11.9	30.5	41.3	98.1
Ins	58.0	19.3	77.2	0.0	11.4	29.6	43.9	98.6
Ins+Win	51.1	18.2	69.3	0.0	10.1	29.1	44.6	98.8
Ins+Win+PCM	50.2	18.2	68.4	0.0	10.5	28.5	45.4	98.9
Mem 50%	68.1	19.3	87.4	4.6	12.4	29.9	35.8	97.9
Mem 100%	67.2	19.3	86.5	0.0	12.0	30.2	24.2	95.7
RAHU	77.5	19.8	97.3	0.2	9.9	30.2	99.5	100.0
PV/T	97.1	12.5	109.6	5.1	11.7	30.4	41.2	98.1
SAHP	45.6	39.8	85.4	5.1	11.8	30.4	41.2	98.1
Pas+Ven+PV/T	33.1	12.7	45.8	0.0	8.3	28.3	99.5	100.0
Pas+Ven+SAHP	5.9	33.3	39.2	0.0	8.3	28.3	99.5	100.0

Table 12 shows the simulated building energy consumption and indoor climate before and after renovation when the heating schedule was switched to continuous heating. In terms of the passive package, the energy conservation potential brought by bio-aerogel thermal insulation, PV vacuum window and PCM was 45%, 6% and less than 1% reduction, respectively. As for the ventilation package, installing insulating breath membrane over building envelopes could reduce the total purchased energy by 37% when the airtightness was improved by 50%, and by 38% when the airtightness was improved by 100%. The installation of RAHU ensured CO_2 concentration below 1,200 ppm almost year-round at the expense of increased electricity consumption and space heating demand: 9% increase in total purchased energy. The total purchased energy was reduced by 14% or 36% when the existing heating system was replaced with PV/T system or SAHP. The final combination including SAHP saved more energy, 73% reduction in total purchased energy, than the final combination including PV/T system, saving the purchased energy by 65%.

Table 12: Simulated energy consumption and indoor climate in the continuously heated Spanish terraced house.

	Energy consumption			Indoor climate				
	Fuel [kWh/m²]	Elec [kWh/m²]	Total [kWh/m²]	T < 20°C [%]	T > 25°C [%]	T_max [°C]	CO₂ < 1200 [%]	CO₂ < 1800 [%]
Ref	145.5	19.4	164.9	0.1	9.9	30.5	43.8	98.2
Ins	72.2	19.3	91.5	0.0	9.3	29.6	47.0	98.8
Ins+Win	62.9	18.1	81	0.0	8.2	29.1	48.3	98.9
Ins+Win+PCM	62.1	18.1	80.2	0.0	8.4	28.5	49.4	99.0
Mem 50%	84.5	19.3	103.8	0.0	9.8	30.2	36.7	97.9
Mem 100%	83.6	19.3	102.9	0.0	9.9	30.2	24.5	96.5
RAHU	97.9	19.8	117.7	0.0	8.2	30.2	98.4	100.0
PV/T	128.6	12.4	141	0.2	9.9	30.4	43.9	98.2
SAHP	60.6	44.4	105	0.2	9.9	30.4	43.9	98.2
Pas+Ven+PV/T	45.6	12.7	58.3	0.0	6.7	28.4	98.4	100.0
Pas+Ven+SAHP	6.5	37.7	44.2	0.0	6.4	28.3	98.4	100.0

As the intermittent and continuous heating schedules applied in the Spanish terraced house were quite similar, the energy conservation potential of thermal insulation measures only increased by 1-2% when the intermittent heating schedule was switched to the continuous heating schedule. The space heating demand before renovation increased by 25%, which was much lower than that in other demo buildings, if the continuous heating schedule replaced the intermittent heating schedule. Thus, the energy-saving potential of generation technologies in the continuously heated Spanish demo building was only up to 2% lower than their energy conservation potential in the intermittently heated Spanish demo building.

4. CONCLUSION

The recommendation priority of renovation measures was concluded based on the simulation results under the same heating schedule. In terms of the passive package, insulating the external walls and roof with bio-aerogel was the most recommended measure for energy conservation, while the installation of PV vacuum windows and PCM only had a slight impact on energy consumption (up to 10% reduction). As a passive technology included in the ventilation package, insulating breath membrane had a similar energy saving potential to bio-aerogel thermal insulation and a negative impact on indoor air quality due to the improved airtightness. Considering the indoor air quality issue, it was necessary to install RAHU after renovating the building envelopes with insulating breath membrane. Regarding the generation measures, the energy saving potential of PV/T system and SAHP varied considerably across different southern European demo buildings, being 14-24% and 4-38%, respectively. The choice of generation measure depends on the actual conditions of the demo buildings. Finally, the maximum energy saving with the final combinations was up to 66%, 75% and 73% in the Greek, Portuguese and Spanish demo buildings when continuously heated.

The energy conservation potential of retrofit technologies was effectively affected by the heating schedules applied in the demo buildings. Commonly, the building energy efficiency achieved with thermal insulation improvement measures (e.g., bio-aerogel thermal insulation, insulating breath membrane etc.) was diminished when the continuous heating schedule was switched to the intermittent heating schedule. When the demo buildings were continuously heated, most of time the indoor temperature was maintained at heating setpoint before and after improving thermal insulation performance. However, when they were intermittently heated, for a considerable proportion of time the indoor temperature was lower than the heating setpoint due to the short heating period before renovation. Thus, although thermal insulation was improved significantly after renovation, the heating system still worked at a high power to approximate the heating setpoint which meant the space heating demand was not reduced as much as that in the continuously heated building. In brief, partial energy conservation potential brought by thermal insulation improvement was sacrificed for the improved indoor air temperature.

If the intermittent heating schedule was switched to the continuous heating schedule, the absolute energy consumption reduction brought by generation technologies increased, while the relative energy conservation potential in percentage became lower. The space heating demand was much higher under a continuous heating schedule than that under an intermittent heating schedule. The higher the space heating heat demand the lower the proportion of demand covered by generation measures and higher the proportion of backup heating demand. The energy conservation potential of generation measures lowered following the increased ratio of backup heating demand.

5. ACKNOWLEDGEMENTS

partners involved in R&D process of Surefit technologies, including PCM Products, WINCO Technologies, and Solimpeks.

6. REFERENCES

Barreto, G. *et al.*, 2022. An innovative window heat recovery (WHR) system with heat pipe technology: Analytical, CFD, experimental analysis and building retrofit performance. *Energy Reports*, 8, pp. 3289–3305.

Das, D., Kalita, P. and Roy, O., 2018. Flat plate hybrid photovoltaic- thermal (PV/T) system: A review on design and development. *Renewable and Sustainable Energy Reviews*, 84, pp. 111–130.

EURIMA - New and Existing Buildings, 2018. Eurima. Available at: https://www.eurima.org/energy-efficiency-in-buildings/new-and-existing-buildings.html.

Feijó-Muñoz, J. *et al.*, 2019. Airtightness of residential buildings in the Continental area of Spain. *Building and Environment*, 148, pp. 299–308.

Huang, B.J. and Chyng, J.P., 2001. Performance characteristics of integral type solar-assisted heat pump. *Solar Energy*, 71(6), pp. 403–414.

Jarimi, H. *et al.*, 2020. Performance Analysis of a Hybrid Thin Film Photovoltaic (PV) Vacuum Glazing. *Future Cities and Environment*, 6(1), p. 2.

Renovation Wave, 2020. European Commission. Available at: https://ec.europa.eu/commission/presscorner/detail/en/IP_20_1835.

Skytech-Pro-XL-Non-combustible-and-insulating-breather-membrane, 2021. Available at: https://www.winco-tech.com/wordpress/wp-content/uploads/2022/01/Skytech-Pro-XL-Non-combustible-and-insulating-breather-membrane.pdf.

TABULA WebTool, 2021. Available at: https://webtool.building-typology.eu/#bm.

Thermal_storage_catalogue, 2021. PCM Products. Available at: https://www.pcmproducts.net/files/thermal_storage_catalogue.pdf.

#96: A holistic energy planning tool for Danish cities and districts

Muhyiddine JRADI

University of Southern Denmark, Odense, Denmark, mjr@mmmi.sdu.dk

Abstract: Buildings and building blocks are considered to be a key component in most national and international legislation and initiatives aiming to reduce energy consumption and the corresponding emissions, and to achieve the energy and environmental goals. However, most of the efforts and investigations reported in recent years have concentrated on energy efficient design and performance improvement of single buildings or limited clusters of buildings. Considering the transition towards interconnected cities and communities and the widespread evolution of smart and flexible thermal and electrical grids and microgrids, there is an urgent need to scale up the effort from energy efficient single buildings and clusters to interconnected energy efficient and flexible cities and neighbourhoods. This work presents the first initiative towards developing a holistic energy planner tool for energy efficient and interconnected Danish cities and neighbourhoods. The tool methodology relies on two major pillars: dynamic building energy performance simulations in Energy Plus and data from the Danish building standard BR18. In addition, the tool considers the buildings type, age and use in predicting and reporting the corresponding heating and electricity demands. The paper presents the development and demonstration of the tool in two case study streets in Denmark, each comprising more than 85 buildings. The overall heating and electricity demand of the streets along with peak energy capacities needed and performance gap evaluations are reported and assessed along with highlighting the impacts of a selection of energy efficient design scenarios on the energy demand. Overall, the proposed tool serves not only as a comprehensive city energy planner but also as a simple to use, flexible and user-friendly tool that can be utilised by a wide range of engineers, planners, and decision makers.

1. INTRODUCTION

In the EU, the building sector is responsible for around 40% of total energy consumption, and 36% of the greenhouse gas emissions (Jradi *et al.*, 2017). To address this current and future energy challenge, buildings are considered a key component in most national and international legislation and initiatives, aiming to improve the overall performance and thus reduce energy consumption and corresponding emissions to achieve the set energy and environmental goals. In December 2018, the amended Energy Efficiency Directive (EU) 2018 (EU, 2018) set an EU energy efficiency target for 2030 of at least 32.5% improvement, compared to projections of the expected energy use in 2030. A large block of investigation and effort have reported in recent years dealing with various specifications and characteristics of the building sector, from conception and design to operation and maintenance. However, most of these investigations have targeted improving the design, construction and operation of single buildings or facilities (Li *et al.*, 2020; Dakheel *et al.*, 2020). Furthermore, dynamic energy modelling and simulation is a well validated and recognised approach with demonstrated major benefits in providing more accurate building models and predictions and the capability of characterising building response to various dynamic changes within the building environment (Yan *et al.*, 2019; Hagenau and Jradi, 2020). Overall, building energy modelling has been used extensively in the literature to aid designing, operating and optimising building performance. In addition, the use of building energy modelling and simulation as a basis for single buildings design, operational management and energy retrofitting is a mature domain and there are plenty of energy tools and modelling software in the market allowing accurate building modelling and performance predictions. When considering the global transition towards interconnected cities and communities and the widespread evolvement of smart and flexible grids, there is an urgent need for upscaling the effort from single buildings and clusters to interconnected energy efficient and flexible cities and neighbourhoods. There is currently a lack of validated procedures and standards when it comes to modelling large scale building clusters, such as on district or city level which affects the overall results accuracy and consistency. The complexity of building cluster simulations is addressed by Eicker (2018) who claimed that accurate cluster models need a large number of inputs and often the predictions are not as accurate as single building models as it is hard to schedule human behaviour, urban climate, and characterise the complexity of a single building on a larger basis. Delmastro *et al.* (2015) highlighted that when considering building clusters and areas, the energy consumption of the corresponding building stock is affected by many factors, including the design of the built environment, the interaction and integration between the buildings and open spaces, the type of materials and constructions used for the external surfaces, the socio-economic characteristics of the population in the specific area, the type of obstructions available, and most importantly , the climate and microclimate conditions

In recent years many models, with different methods and algorithms, have been developed for predicting energy consumption of building clusters at city level, including CitySim, UrbanSim "UCB", Urban Modeling Interface "UMI" and City Energy Analyst "CEA" (Mauree *et al.*, 2019; Sola *et al.*, 2020) which all estimate the energy demand of an area dependent on the climate and surroundings. In a recent work, Mutani and Todeschi (2020) presented an approach for Italian buildings energy modelling at neighbourhood scale based on data from district heating energy consumption. The reported findings showed that the proposed model was accurate for old buildings with an average error of 10% for buildings constructed before 1970, while the error reached 20% for newer buildings. Perera *et al.* (2018) presented an investigation using the CitySim tool which indicated that the prediction accuracy of the power consumption of buildings decreased when neglecting the urban climate. Today the district energy models are reliant upon many different data inputs. The data collection primarily consists of collecting data from GIS data, climate, morphology, and standardised energy consumptions. The databases are crucial for these models, as the predicted energy demand should be comparable with real energy demand. An example of a tool which incorporates vast amounts of data is the CityBES, developed by Chen *et al.* (2017), and used extensively in assessing energy retrofit scenarios and alternatives in addition to evaluating which measures improve the energy performance of building clusters in cities. Puglisi *et al.* (2016) introduced a method, based upon dynamic building models, which takes the variability of the climate and the internal loads into considerations. This model can be used for estimating the demand for heating, cooling, and domestic hot water and creates monthly load files for multiple buildings. Hedegaard *et al.* (2019) developed a building modelling framework using the bottom-up modelling approach. The proposed approach aimed at accurately modelling and predicting the energy consumption of a building cluster through modelling buildings individually first based upon smart meter data, characteristics, and climate conditions. Based on the single building data-driven models, the approach summed up all energy demands into a collective cluster demand, aiming to evaluate and analyse a cluster demand response to reduce peak consumption.

When it comes to energy consumption in the building sector, Denmark is not an exception and buildings of different types consume around 40% of the overall energy consumption with around 35% contribution to greenhouse gas emissions (Jradi *et al.*, 2020). Denmark has set an ambitious goal to attain an entirely fossil fuel-free energy sector by 2050 with major energy and environmental goals to be achieved by 2030 (Lund and Mathiesen, 2007). Overall, improving the design, construction and operation of the building sector is a key condition to attain the short and long-term goals. Thus, the Danish building energy regulations are continuously being tightened and upgraded, setting strict requirements and guidelines in terms of building constructions and materials, building energy systems design and operation, overall primary energy consumption and thermal comfort and indoor air quality. The standards and initiatives do not only target new builds but also existing and old buildings. In this context, the Danish government has launched the largest ever comprehensive Danish energy renovation strategy "Strategy for the energy renovation of the existing building stock" (2012) with multiple initiatives aiming to promote systematic and effective energy retrofitting of buildings and improving the existing building block performance.

To follow up with the standards and regulations in the field, a large block of theoretical and experimental investigations have been presented and demonstrated in the last two decades dealing with various aspects of building sector design, construction, operation and optimisation. However, the majority of these investigations target single buildings or facilities, building components, systems and services, where very few investigations are reported targeting the design, operation and retrofitting of Danish building clusters, streets and cities. This work presents DanCTPlan, the first initiative towards developing a holistic energy planner tool for energy efficient and interconnected cities and neighbourhoods in Denmark. The tool methodology relied on two major pillars: dynamic building energy performance simulations in Energy Plus and data from the Danish building standard BR18 (2018). In addition, the tool considered the buildings type, age and use in predicting and reporting the corresponding heating and electricity demands. The tool can incorporate data from the Danish Building and Housing Register (BBR) (2022) to get the building specifications of the area, and with this input, the tool predicted the overall area and building cluster energy consumption. In addition, it allowed comparing the predicted performance with the actual reported performance in the case of existing buildings, and thus estimating the performance gap between the expected consumption and the actual consumption of a defined area. The paper presents the development and design of the DanCTPlan tool along with a detailed description of the building cluster modelling and prediction approach and methodology. The tool was then demonstrated considering actual case study areas in Denmark. The overall heating and electricity demand of some streets and neighbourhoods were predicted and reported and evaluated along with suggestions for energy efficient operation.

2. APPROACH & METHODOLOGY

As stated in the review above, a massive amount of research and investigation have reported on single buildings and their design, operation, and performance improvement. However, there is a lack of tools targeting proper design and operation on streets, districts, or cities level. The main aim of this work was to design, develop and demonstrate a simple, user friendly, yet comprehensive tool to serve as a basis for Danish building clusters and neighbourhoods modelling and performance prediction. The main consideration in developing the tool methodology and approach was to establish a platform which would require very few inputs form the user and can automatically develop building clusters and streets models and provide heat and electricity demands as well as energy consumption predictions and automatic building information import. Figure 1 presents the overall methodology of the holistic energy planner tool for Danish cities and neighbourhoods, providing the inputs required, the information processing connections, the workflow and the outputs provided by the energy planner.

2.1. Methodology

The proposed city-level model delivery can be divided into three major features: the first is data collection and demand calculations, the second is fuel and energy resource consumption estimation, and the third is the performance gap evaluation.

Data collection and demand calculations

The first step was to insert a standard set of Danish BBR-data for a certain street or city from which the model would automatically extract the needed information for the performance prediction. With few mandatory manual inputs including the street and postal code, the model estimated the total energy consumption of the investigated street, considering the different building types and building year of construction/ last renovated. The outputs from this feature were:

- Heat consumption of the street
- Electricity consumption of the street
- Peak heating demand
- Peak electricity demand

Fuel and energy resource consumption estimations

The second feature of the city-level model was estimating the consumption of some of the standard fuel types and resources, e.g., wood pellets, oil, gas, district heating, depending on what inputs were provided. The estimation was performed considering an energy conversion factor and a fuel corresponding heating value incorporated as standard values based on validated calculations and estimations of the Danish Energy Agency (2019). The needed input data at this level was a general boiler efficiency and the COP of a heat pump, along with data read automatically from the Danish BBR-data concerning what fuel type was used in which buildings. The outputs from the model feature 2 were:

- Number of houses using the different fuel sources
- Actual consumption of the different fuels
- Evaluation of a specific fuel consumption in case the whole street switched to this fuel
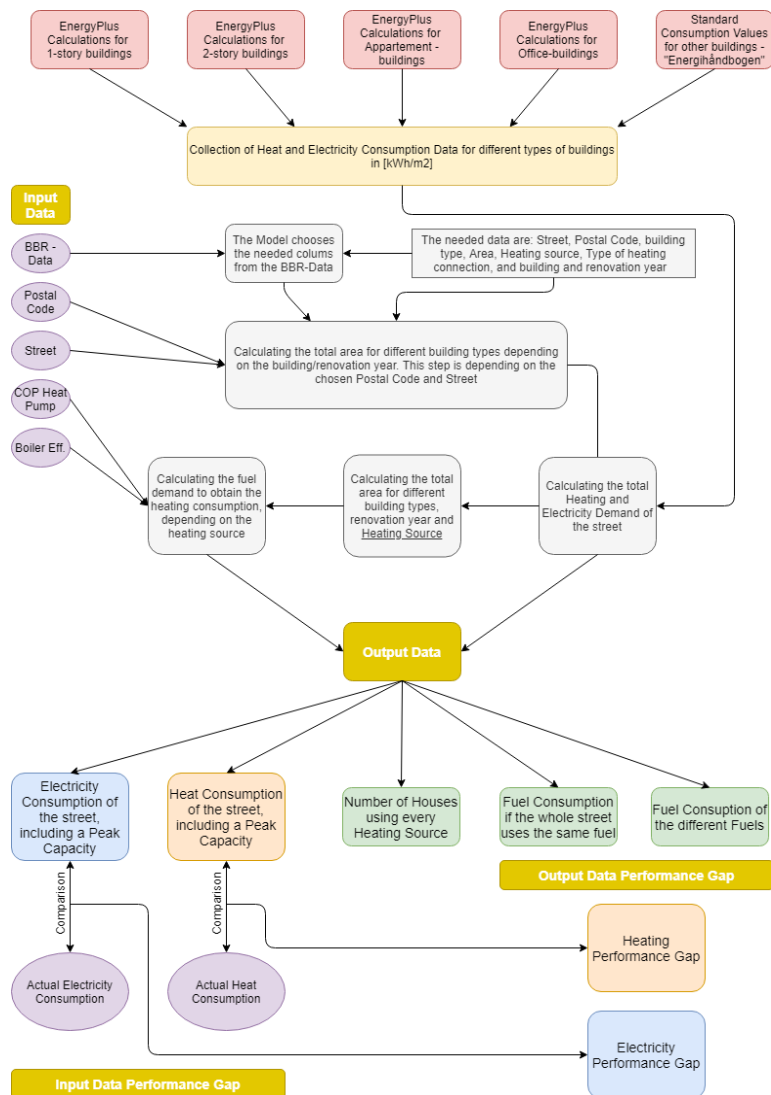
Figure 1: City energy planner tool methodology and evaluation approach

Performance gap evaluation

The third feature of the model was the ability to evaluate the performance gap between the actual consumption of the street in question and the predicted model consumption. Considering that the model predictions were validated based on inputs from the Danish Building Regulation, the predictions provided a proper baseline to evaluate if the street or building clusters was performing as expected, and to what level it deviated from the building regulations recommendations. To achieve this, two more inputs needed to be provided by the user:

- Actual heat consumption of the street/neighbourhood
- Actual electricity consumption of the street/neighbourhood

With these inputs, the model calculated two types of Performance Gap in [%]:

- Heating performance gap
- Electricity performance gap

In the following section, a more detailed explanation of the model inputs and workflow is provided.

2.2. Input data description

The first input to the proposed city-level model was data from the Danish Building and Housing Register (BBR) for the area. This is a standard large collection of information from the Danish building and housing ministry for all areas in Denmark. The information was a cluster of building relevant data e.g., building year, location, heating source,

usage, among others (BBR, 2022). This data was readily available and can be requested as an excel sheet by companies, experts or researchers operating in the building sector. The proposed model needed nine inputs:

  VEJ_NAVN,
  VARMEINSTAL_KODE
  BYG_BOLIG_ARL_SAML
  OPFOERELSE_AAR
  BYG_ANVEND_KODE
  PostNr
  OPVARMNING_KODE
  ERHV_ARL_SAML
  OMBYG_AAR

It should be noted that the inputs above were provided in Danish using the same term from the Danish building register BBR. VEJ_NAVN was the street name where PostNr was the postcode of the selected street. The BYG_ANVEND_KODE divided the building types into around 104 categories based upon their usage. Considering that many of these categories were similar and could be merged to simplify the workflow, we proposed reducing these categories to only eight being: 1-story-houses, 2-story-houses, apartments, offices, public institutions, stores with food, stores without food and others. OPVARMNING_KODE was a category which divided the heating fuel types into 7 categories: electricity, gas fired, liquid fuels, solid fuels, straw, natural gas, and others. The liquid fuels were assumed in the model to be fuel oil and the solid fuels were assumed to be wood pellets. One of the main inputs to the model was the building construction year or the performance year. This year was read automatically from the Danish BBR and was used as a basis to estimate the expected performance based on dynamic simulations and Danish building standard numbers. If the building had been renovated, OMBYG_AAR provided the energy renovation year and was therefore chosen as the energy performance year. The building construction year [OPFOERELSE_AAR] was the corresponding performance year if the building had not been renovated. The other inputs related to the building area divided into commercial building areas and residential buildings.

2.3. Single buildings energy consumption predictions

All buildings on the street were divided into eight building categories as highlighted above. Each category had a standardised energy consumption depending on the building age and year of construction. The first four categories, 1-story houses, 2-story houses, apartments, and offices were simulated using EnergyPlus to evaluate the overall heating and electricity consumption of each category depending on the year of construction. Years of construction were divided into six periods starting from buildings built before 1960 and the latest were buildings built after 2015. The dynamic simulations and the results were reported and validated by the authors in a previous study (Foldager *et al.*, 2019). For the other four building categories, static energy consumption data was used based on historical averages and reports from 1997 to 2002 collected in the Danish energy handbook 'Energihåndbogen' (2022). The standardised net consumption in kWh/m2 for the eight categories can be seen in Table 1. In addition to the energy consumption estimation, the model also reported the peak heating and electricity demand. The needed peak capacities for heating and electricity were also reported based on simulations carried out in EnergyPlus for the first four categories and interpolated to give a fitting estimate for the remaining categories considering the corresponding energy consumption. The heat and electricity capacity numbers in Watts per square metre can be seen in Table 2. The model placed all buildings within a category and a timeslot, e.g. all 1-story buildings built before the 1960s were grouped. Then it multiplied the corresponding consumption and capacity standardised number reported above in the tables with the area of each category to find the energy demand for the specific category. Lastly, it summed up the categories to find the total energy demand for the whole street/cluster.

Table 1: The standardised energy consumptions per square metre of different building categories and ages

[kWh/m^2]	Pre 1960s		60-70s		1980s		1990s		2000s		2015s	
	Elec	Heat	Elec	Heat	Elec	Heat	Elec	Heat	Elec	Heat	Elec	Heat
1-story	39.5	326.1	37.0	211.5	35.1	126.9	33.5	79.9	33.4	67.1	32.5	36.6
2-story	39.8	335.6	37.7	222.8	36.1	136.6	34.3	87.0	33.3	70.8	33.0	37.5
App	39.9	329.9	36.8	214.3	34.8	128.9	35.7	83.5	34.8	67.4	32.2	37.5
Office	45.5	384.2	42.3	250.3	41.3	152.6	40.6	93.9	40.1	81.0	38.5	43.5
Shop ÷ food	36.8	213.0	34.4	138.2	32.7	82.9	31.2	52.2	31.1	43.8	30.2	23.9
Shop + food	266.7	220.3	249.3	142.9	237.0	85.7	226.2	54.0	225.4	45.3	219.0	24.7
Public Inst.	33.3	292.6	31.1	189.8	29.6	113.9	28.2	71.7	28.1	60.2	27.3	32.8
					Not time specific							
Other buildings		Electricity 44.3						Heat 100.2				

Table 2: The standardised heating and electricity peak capacity for the eight different categories

Capacity [W/m²]	Pre 1960s		60-70s		1980s		1990s		2000s		2015s	
	Elec	Heat	Elec	Heat	Elec	Heat	Elec	Heat	Elec	Heat	Elec	Heat
1-story	9.0	105.3	8.6	70.2	8.4	46.5	7.4	31.6	7.5	27.4	8.0	16.7
2-story	9.2	107.9	9.0	79.9	8.8	54.9	8.0	19.5	7.8	15.6	7.7	8.2
App	9.3	110.9	8.8	75.0	8.5	50.3	8.3	33.4	8.1	27.6	7.8	16.3
Office	9.4	122.9	9.0	89.6	8.9	61.0	6.3	29.7	8.4	27.0	8.2	12.7
Shop ÷ food	7.6	122.9	7.1	89.6	6.7	61.0	6.4	29.7	6.4	27.0	6.2	12.7
Shop + food	55.0	122.9	51.5	89.6	48.9	61.0	46.7	29.7	46.5	27.0	45.2	12.7
Public Inst.	6.9	122.9	6.4	89.6	6.1	61.0	5.8	29.7	5.8	27.0	5.6	12.7
	Not time specific											
	Electricity						Heat					
Other buildings	9.1						31.7					

3. THE DANCTPLAN TOOL

The methodology and modelling approach described in the previous section were integrated and employed to develop a user-friendly and flexible tool to serve as an energy planning and designing tool on a street and city level in Denmark. DanCTPlan was developed as a collection of Microsoft Excel spreadsheets and was executed as a Google Sheet Application to make it easy to access, understand and implement by users. The tool consisted of an interface that showed input and output data, and a set of databases in the background with the model operation. The DanCTPlan interface can be seen in Figure 2.

On the left side of Figure 2, the section for the input data is located, where information needed to be inserted by the user in the yellow cells. The right section shows the output data, where the number of houses and their division into categories were shown along with estimations of heating and electricity peak capacity and energy consumption of the building cluster considered. The output data also included a section about the heating sources and fuels used in the buildings considered. In addition, estimations on the required fuel consumption was included if a certain energy source was to provide the heating demand of a specific street/cluster. The last part of the output section provided an overview and estimation of the performance gap of the building cluster considering heating consumption and electricity consumption, compared to actual numbers provided by the user. These inputs were not mandatory, but if provided, the performance gap could be calculated and reported. In addition to the input and output sections, two graphs were included as part of the DanCTPlan tool interface providing the overall energy consumption for heating and electricity in the different building categories, as well as the number of buildings accumulated based on the fuel and resource used to cover the heating demand.
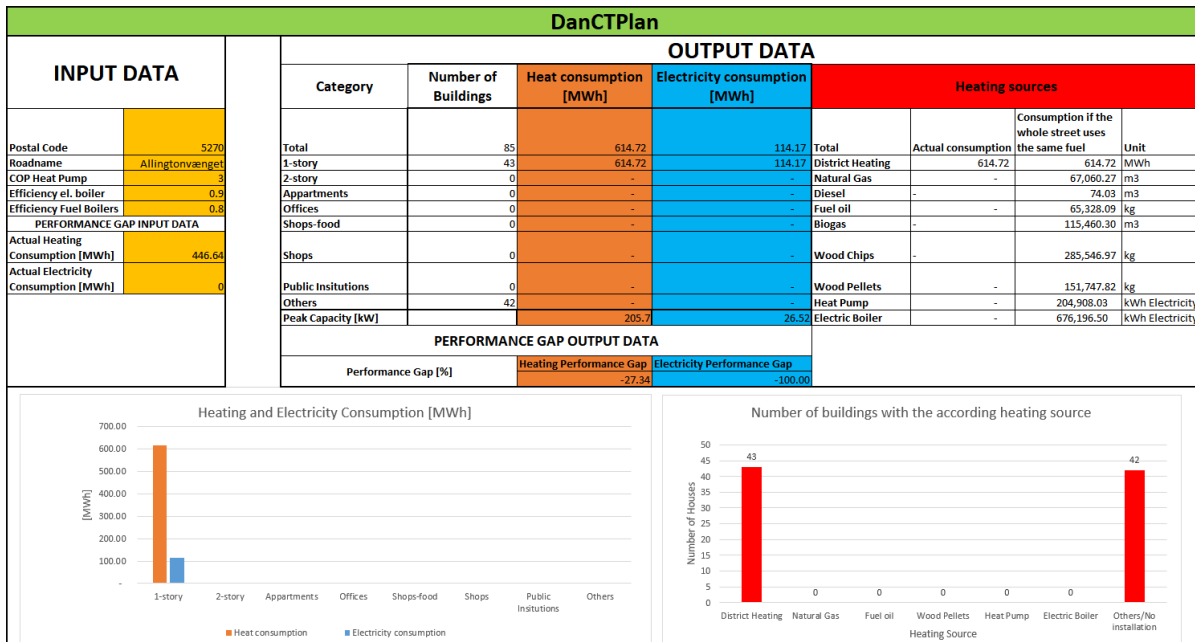

Figure 2: DanCTPlan tool interface

4. DANCTPLAN DEMONSTRATION

To demonstrate the tool, two case study areas in the city of Odense, Denmark were investigated. The first pilot case was Hjallesevej Street and the second was the street of Allingtonvænget. Each of these streets had different numbers of buildings of various types/uses/energy sources and construction year.

4.1. Hjallesevej Street

For the case of Hjallesevej Street, the manual inputs which needed to be provided by the user are listed in Figure 3. In addition, the corresponding Danish BBR sheet was also required as a major input to automatically read the type of buildings, area, heating source and other information as highlighted above in the methodology section. The actual heating and electricity consumption data were not available for this street which is why it was left empty. However, this did not hinder the tool from processing the information and inputs and provided the outputs mentioned above, except of the performance gap results.

The complete output data provided by DanCTPlan tool for the street of Hjallesevej is provided in Figure 4. As noted below, there were 101 buildings under the street tag with an estimated annual heating consumption of 4946 MWh and an annual electricity consumption of 975 MWh. The tool also estimated the peak capacities to be 1873 kW for heating, and 215 kW for electricity. These capacity outputs could provide a preliminary assessment on how big a future energy system designed and installed in the area would have to be, both in terms of a heating energy system and electricity generation system. This could provide a more accurate and better estimate for planning purposes, compared to tabulated static numbers currently in use which normally either oversize or undersize the system to be designed and implemented. In case of oversizing the system, additional unneeded cost is incurred, and in case of under sizing the system, energy demand cannot be met. Such information is key for energy planners, consultants, authorities and decision makers.

INPUT DATA

Postal Code	5000
Roadname	Hjallesevej
COP Heat Pump	3
Efficiency el. boiler	0.9
Efficiency Fuel Boilers	0.8
PERFORMANCE GAP INPUT DATA	
Actual Heating Consumption [MWh]	-
Actual Electricity Consumption [MWh]	-

Figure 3: DanCTPlan input data for the Hjallesevej Street case

OUTPUT DATA

Category	Number of Buildings	Heat consumption [MWh]	Electricity consumption [MWh]	Heating sources		
					Consumption if the whole street uses	
Total	101	4,946.40	974.82	Total	Actual consumption	the same fuel	Unit
1-story	10	430.60	56.93	District Heating	2,459.11	4,946.40	MWh
2-story	0	-	-	Natural Gas	-	539,602.80	m3
Appartments	34	3,581.13	613.93	Diesel	-	595.71	m3
Offices	1	15.75	1.87	Fuel oil	-	525,664.72	kg
Shops-food	3	115.46	20.36	Biogas	-	929,055.26	m3
Shops	2	71.84	108.90	Wood Chips	-	2,297,663.55	kg
Public Insitutions	5	714.89	165.44	Wood Pellets	-	1,221,044.06	kg
Others	46	16.73	7.39	Heat Pump		1,648,799.53	kWh Electricity
Peak Capacity [kW]		1873.1	214.65	Electric Boiler	45,100.61	5,441,038.46	kWh Electricity

PERFORMANCE GAP OUTPUT DATA		
Performance Gap [%]	Heating Performance Gap	Electricity Performance Gap
	-	-

Figure 4: DanCTPlan output data for the Hjallesevej Street case

Figure 4 shows that 10 buildings were categorised as 1-story houses, 34 as apartments, 1 office building, 2 shops with food and 5 public institutions, while 46 buildings were categorised as "others". Many of the ''others'' buildings do not have any energy consumption as these were mostly carports, storage boxes and sheds which were not conditioned. The current and predicted fuel consumption if a fuel were the sole provider is also illustrated in Figure 4. The actual consumption shows that the heating demands in Hjallesevej was currently supplied majorly by district heating with some additional electric boilers. The right column shows the amount of fuel the street would consume if the heating system was modified/retrofitted and the whole street used one specific fuel. If the whole street for example used electric boilers for heating, then 5441 MWh of electricity would be consumed. In terms of Wood Pellets, 1221 tons would be needed on an annual basis. This also provided a preliminary picture for authorities, decision-makers and consultants to decide on any future modification and upgrade of the current heating system in the area. The tool also provided graphs for the energy consumption for heating and electricity per building category as shown in Figure 5, along with the number of buildings accumulated by the heating source used, shown in Figure 6.

4.2. Allingtonvænget Street

To introduce the feature of the performance gap indicator in DanCTPlan tool, the street "Allingtonvænget" in the city of Odense in Denmark was chosen as the second case study. Figure 5 offers an overview on the outputs provided by DanCTPlan for this case, including energy consumption, capacity estimation and performance gap reporting. The actual heating consumption of the street was provided by the local district heating company in Odense (Figue 6), "Fjernvarme Fyn", where the electricity consumption was only available for part of the street and thus was not considered in the performance gap evaluation.
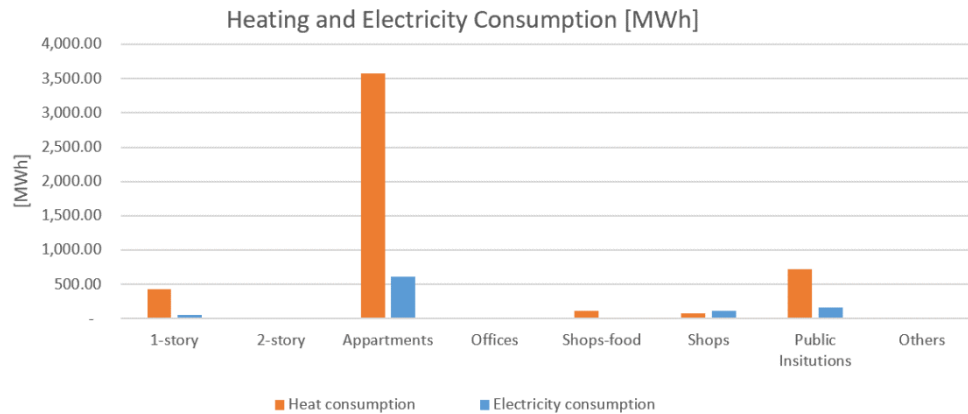

Figure 5: Predicted heating and electricity consumption numbers per building type in Hjallesevej Street
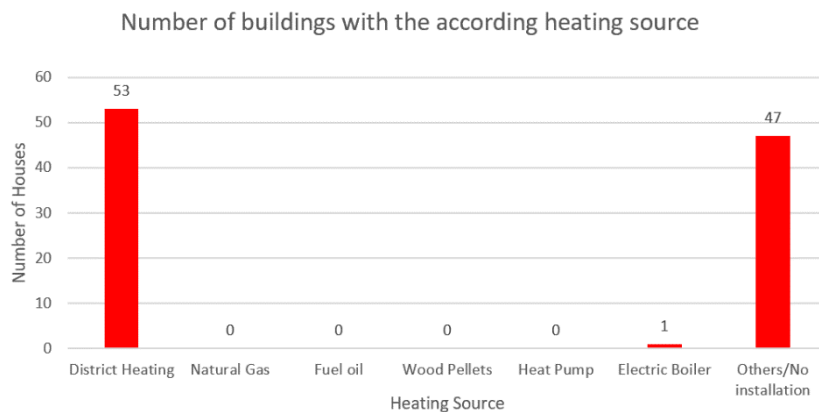

Figure 6: The number of buildings supplied by specific heating resource in Hjallesevej Street

OUTPUT DATA

Category	Number of Buildings	Heat consumption [MWh]	Electricity consumption [MWh]	Heating sources			
						Consumption if the whole street uses the same fuel	
				Total	Actual consumption		Unit
Total	85	614.72	114.17	District Heating	614.72	614.72	MWh
1-story	43	614.72	114.17	Natural Gas	-	67,060.27	m3
2-story	0	-	-	Diesel	-	74.03	m3
Appartments	0	-	-	Fuel oil	-	65,328.09	kg
Offices	0	-	-	Biogas	-	115,460.30	m3
Shops-food	0	-	-				
Shops	0	-	-	Wood Chips	-	285,546.97	kg
Public Insitutions	0	-	-	Wood Pellets	-	151,747.82	kg
Others	42	-	-	Heat Pump	-	204,908.03	kWh Electricity
Peak Capacity [kW]		205.7	26.52	Electric Boiler	-	676,196.50	kWh Electricity

PERFORMANCE GAP OUTPUT DATA

	Heating Performance Gap	Electricity Performance Gap
Performance Gap [%]	-27.34	-

Figure 7: DanCTPlan output data for the Allingtonvænget Street case

Overall, the street of Allingtonvænget had 43 buildings with an estimated heating consumption of 615 MWh and electricity consumption of 114 MWh. As presented in Figure 7, the expected peak capacities were estimated to be 205 kW for heating, and 26.5 kW for electricity, and these results would make it easier to plan and design energy supply systems or implement retrofitting and improvements. As only actual heating consumption was provided, the performance gap in terms of heating consumption was estimated and reported to be -28%, meaning that the building cluster in the street consumed 28% less heat than expected based on dynamic simulations and numbers from the Danish building regulations.

5. DISCUSSION

The major aim of this work was to develop the first of its kind DanCTPlan tool for energy planning of streets, neighbourhoods, and cities in Denmark. The tool used dynamic energy simulations and numbers from the Danish building regulations to provide an estimation of the energy consumption, in addition to information on the expected peak size of the heating and electricity supply system. The tool aimed to help energy planners to assess if there was a need for energy retrofitting in a specific area, or to indicate how much capacity a new supply system would need to satisfy the demands for heating and electricity. The intention was to have a comprehensive tool but at the same time for it to be user-friendly, robust, and easy to use. This aim was acheived with DanCTPlan which required minimal data input by the user and employed an automated approach for output generation. This comprehensive and flexible approach had the capability to serve as a basis for energy planning, design, system sizing and evaluating retrofits options by planners, consultants, authorities, and decision makers. In the development of the tool, some generic estimations and assumptions were considered to produce a simple and generic tool, which was easy to utilise and simple to comprehend. One of the strengths in the core approach of the tool was that it divided buildings into eight categories, providing the capability to accurately estimate the energy consumption of various building types. Regarding baselines for energy consumption and energy capacity estimations, four of the building categories made use of dynamic simulations in EnergyPlus and the other four categories use validated numbers and estimations from the Danish energy handbook 'Energihåndbogen'. Although these numbers were static to some extent, they were averaged and collected from many different samples over a period of five years.

The tool could estimate the fuel consumption for heating purposes based on the Danish BBR input-data. This data contained information about the heating installation and source, with the first defining whether the building was supplied by district heating, a boiler, or a heat pump and the second defining which fuel type was used e.g., electricity, gas, or others. For electricity as a fuel, the tool could distinguish between electric heaters and heat pumps. For the other sources, assumptions had to be made as the data were not complete enough; it only stated whether a liquid or a solid fuel was used. Hereby it was assumed that liquid fuels were always fuel oil while solid fuels were assumed to be wood pellets. This might cause some minor uncertainties in the results compared to the actual consumption. The performance gap was estimated based upon the standardised predicted data and the inputted actual data. This performance gap showed if the buildings in an area were operating properly as expected by simulations and regulations, considering the specific building sizes and the construction/renovation year. However, the current version of the tool only used an input on annual heat consumption. As climate conditions change from year to year, this would majorly affect the heating consumption and also have some effect on electricity consumption. The suggestion in the next versions of the tool is to use an average of the real energy consumption of the building cluster from several different years to minimise the impact of weather conditions swing, or the issue of having a specific year with very cold or warm weather compared to standard Danish weather. This method could help the user to estimate the real and accurate performance gap of the cluster/street. In addition, the performance gap evaluation allows planners and authorities to compare the performance of different streets in the same area, or different areas in the same city. This will aid informing future decisions and energy performance improvements in the whole district. In addition to the many positive impacts and benefits mentioned above for using and implementing DanCTPlan, the tool like any other tool has some limitations. Overall, the tool provided an estimate of the energy consumption and peak capacities of various building types from different construction years. However, the tool does not differentiate between two buildings built in 1965 and having the same area and same energy resource. This is due to the holistic approach which was intended to be used as a city-level planner and not as a single building investigation. Thus, the tool was not intended to be used to provide an accurate energy performance estimation for a specific building, but rather sees the building as one component in the big picture, the street/city. Moreover, the tool could be used as a preliminary assessment tool providing quick and straight forward estimations of energy consumptions and peak capacities and could be upgraded by additional specific and detailed calculations if the user needed to. Overall, DanCTPlan is a tool requiring very minimal inputs which can be used by a wide range of users including experienced consultants and junior engineers, providing an overall energy performance assessment on the level of streets and neighbourhoods, along with evaluating the performance gap compared to dynamic simulations and building regulation numbers baseline.

6. CONCLUSION

In recent decades, the majority of the theoretical and experimental investigations dealing with the Danish building sector have targeted different aspects and specifications of single and individual buildings. With the urgent need towards scaling up the effort from energy efficient single buildings and clusters to interconnected energy efficient and flexible cities and neighbourhoods, this work presented DanCTPlan, a city-level energy planning and performance gap evaluation tool. The tool was the first initiative towards developing a holistic energy planner for energy efficient and interconnected Danish cities and neighbourhoods. DanCTPlan used a comprehensive methodology for energy consumption and peak capacity evaluation of building clusters and streets but required very minimal inputs by the user with a very user-friendly and flexible interface. The tool methodology relied on two major pillars, dynamic building energy performance simulations in EnergyPlus and data from the Danish building standard BR18. It divided buildings into eight categories and took into account the building's use, type and year of construction/last renovation. The tool needed only a standard Danish BBR building registry sheet and it would then automatically calculate the expected energy consumption for heating and electricity, peak capacities and provide information on fuel consumption. In addition, the tool had an option where the user was able to insert the actual heating and electricity consumption and DanCTPlan would then evaluate the performance gap between the actual consumption of the street/area and the expected baseline predicted by simulations and Danish regulation numbers. The tool demonstration for two case

study streets was provided in this study. This was the first version of DanCTPlan and the aim is to implement it in multiple streets and areas and build up on the feedback and experiences to upgrade the tool and include additional features and capabilities. However, the goal will still be that DanCTPlan becomes a comprehensive city energy planner but a simple to use, flexible and user-friendly tool that can be utilised by a wide range of engineers, planners and decision makers.

7. ACKNOWLEDGEMENTS

8. REFERENCES

Chen, Y., Hong, T., Piette, M.A., 2017. Automatic generation and simulation of urban building energy models based on city datasets for city-scale building retrofit analysis. Applied Energy 205, 323-335.

Dakheel, A., Del Pero, C., Aste, N.O., Leonforte, F., 2020. Smart buildings features and key performance indicators: A review. Sustainable Cities and Society 61, 102328.

Danish Building Regulation (BR18) – Available at:< https://bygningsreglementet.dk/> [accessed 03.5.2022].

Danish Energy Agency, Calculation Assumptions for Energy Prices and Emissions – Available at:< https://ens.dk/sites/ens.dk/files/Analyser/samfundsoekonomiske_beregningsforudsaetninger_for_energipriser_og_e missioner_2019.pdf> [accessed 22.4.2022].

Delmastro, C., Mutani, G., Schranz, L., Vicentini, G., 2015. The role of urban form and socio-economic variables for estimating the building energy savings potential at the urban scale. International Journal of Heat and Technology 33, 91-100.

Eicker, U., 2018. Urban Energy Systems for Low-Carbon Cities, 1st Edition, Academic Press.

Energy Handbook 'Energihåndbogen', Foreningen for Energi & Miljø, Virum: Advice A/S, 2002.

Energy Performance of Buildings Directive (EU) 2018/844, European Commission, 2018.

Foldager, H.E., Jeppesen, R.C., Jradi, M., 2019. DanRETRO: a Decision-Making Tool for Energy Retrofit Design and Assessment of Danish Buildings. Sustainability 11, 3794-3813.

Hagenau, M., Jradi, M., 2020. Dynamic modeling and performance evaluation of building envelope enhanced with phase change material under Danish conditions. Journal of Energy Storage 30, 101536.

Hedegaard, R.E., Kristensen, M.H., Pedersen, T.H., Brun, A., Petersen, S., 2019. Bottom-up modelling methodology for urban-scale analysis of residential space heating demand response. Applied Energy 242, 181-204.

Jradi, M., Liu, N., Arendt, K., Mattera, C.G., 2020. An automated framework for buildings continuous commissioning and performance testing–A university building case study. Journal of Building Engineering 31, 101464.

Jradi, M., Veje, C., Jørgensen, B.N., 2017. Deep energy renovation of the Mærsk office building in Denmark using a holistic design approach. Energy and Buildings 151, 306-319.

Li, Y., Norda, N., Xiao, Q., Tereshchenko T., 2020. Building heating applications with phase change material: A comprehensive review. Journal of Energy Storage 31, 101634.

Lund, H., Mathiesen, B.V., 2007. Energy system analysis of 100 per cent renewable energy systems: the case of Denmark year 2030 and 2050. In: Dubrovnik conference on sustainable development of energy, water and environment systems, Dubrovnik, Croatia.

Mauree, D., Naboni, E., Coccolo, S., Perera, A.T.D., Nik, V.M., Scartezzini, J.L., 2019. A review of assessment methods for the urban environment and its energy sustainability to guarantee climate adaptation of future cities. Renewable and Sustainable Energy Reviews 112, 733-746.

Mutani, G., Todeschi, V., 2020. Building energy modeling at neighborhood scale. Energy Efficiency 13, 1353-1386.

Perera, A.T.D., Coccolo, S., Scartezzini, J.L., Mauree, D., 2018. Quantifying the impact of urban climate by extending the boundaries of urban energy system modeling. Applied Energy 222, 847-860.

Puglisi, G., Zanghirella, F., Ungaro, P., Cammarata, G., 2016. A methodology for the generation of energy consumption profiles in the residential sector. International Journal Heat and Technology 34(3), 491-497.

Sola, A., Corchero, C., Salom, J., Sanmarti, M., 2020. Multi-domain urban-scale energy modelling tools: A review. Sustainable Cities and Society 54, 101016.

Strategy for energy renovation of Buildings: The route to energy-efficient buildings in tomorrow's Denmark, The Ministry of Climate, Energy and Building in Denmark.
https://ec.europa.eu/energy/sites/ener/files/documents/2014_article4_en_denmark.pdf, May 2014.

The Central Register of Buildings and Dwellings (BBR) – Available at:<https://econ.au.dk/the-national-centre-for-register-based-research/danish-registers/the-central-register-of-buildings-and-dwellings-bbr> [accessed 02.5.2022].

Yan, T., Sun, X.W., Xu, X.H., Wan, H., Huang, G., 2019. Development of a simplified dynamic moisture transfer model of building wall layer of hygroscopic material. Energy 183, 1278-1294.

#100: Energy performance enhancement of solar assisted heat pump and building integrated PV/thermal storage system (PV-SAHP-TS) under different climate contexts

Ke Qu[1] [*], Yuhao Wang[2], Germilly Barreto[3], Muriel Iten[4], Yangmin Wang[5], Risto Kosonen[6], Saffa Riffat[7]

[1]Department of Architecture and Built Environment, the University of Nottingham, University Park, Nottingham, NG7 2RD, UK, ezzkq@nottingham.ac.uk
[2]Department of Architecture and Built Environment, the University of Nottingham, University Park, Nottingham, NG7 2RD, UK, ezxyw13@nottingham.ac.uk
[3]High Temperature Processes Unit, IMDEA Energy, Avda. Ramón de la Sagra 3, 28935, Móstoles, Spain, germilly.barreto@imdea.org
[4]Low Carbon & Resource Efficiency, R&Di, Instituto de Soldadura e Qualidade, 4415-491 Grijó, Portugal, mciten@isq.pt
[5]Department of Mechanical Engineering, Aalto University, Espoo, Finland, yangmin.wang@aalto.fi
[6]Department of Mechanical Engineering, Aalto University, Espoo, Finland, risto.kosonen@aalto.fi
[7]Department of Architecture and Built Environment, the University of Nottingham, University Park, Nottingham, NG7 2RD, UK, lazsbr@nottingham.ac.uk

Abstract: The solar-assisted heat pump (SAHP) is considered to be one of the most efficient and promising heating electrification technologies, while the research on improving its energy efficiency at night is insufficient. In this study, an innovative solar assisted heat pump and building integrated thermal storage/PV system (PV-SAHP-TS) was proposed to upgrade the heating efficiency during night-time and those periods when solar radiation is insufficient. Four building pilots were selected for installation to measure both the impact of different climate conditions on the integrated system energy and the economic performance after adopting this strategy. The pilot buildings were located in Nottingham (UK), Valladolid (Spain), Mafra Municipality (Portugal) and Peristeri Municipality (Greece), with warm, mild-temperate and slightly cold climate types, respectively. The SAHP system was working during the day to improve both electricity generation and solar heat extraction. The PV renewable electricity was used to support the compressor of the SAHP system in the full load operation. The water thermal storage tank was used to charge heat in the daytime to release at night-time. To investigate the annual operation performance of the proposed integrated PV-SAHP-TS system, hourly dynamic simulations in EnergyPro were conducted. The simulation results indicated that the hybrid heating COP could increase from 3.4-3.6 (SAHP alone) to 6.2-9.2 (integrated system), with net electricity savings of 27%, 50%, 57% and 61% in the four pilots, respectively. It was noticed that this proposed strategy could help reduce the peak electricity load by a maximum of 73% due to the thermal storage in the daytime. Besides, in the summertime, the system could operate independently without power input from the electrical grid.

Keywords: solar assisted heat pump; building energy; thermal storage; PV/thermal; heating COP.

1. INTRODUCTION

The solar-assisted heat pump (SAHP) has been widely investigated with theoretical, numerical simulation and experimental studies in recent years, applied in space heating and domestic hot water (DHW) supply. Differing from the conventional air-source heat pump (ASHP), refrigerant is circulated through the solar collector (thermodynamic panels) of the SAHP, serving as the evaporator of heat pumps (Kara, Ulgen *et al.,* 2008). Basically, the SAHP systems can be divided into direct and indirect expansion types (DX-SAHP and IDX-SAHP), regarding the usage of solar energy in heat pump refrigerant evaporation (Ito, Miura *et al.,* 1999). In the IDX-SAHP systems, the refrigerant does not circulate in solar collectors but is substituted by water antifreeze solution circulated between solar collectors and the heat storage tanks (Kamel, Fung *et al.,* 2015). In the DX-SAHP systems, the heat pump refrigerant evaporates directly without a heat transmitter fluid cycle, thereby simplifying the system and leading to the system's stability and durability with low maintenance requirements (Chaturvedi and Shen, 1984). To be beneficial, the lower freezing temperature refrigerant in the evaporator side (solar collector) could absorb the heat from both solar radiation and ambient air. Therefore, the surface temperature of the solar collector is crucial for the Coefficient of Performance (COP) of the SAHP systems. The effects of ambient conditions on the SAHP systems' heating performance have been investigated by Sezen *et al.,* (Sezen, Tuncer *et al.,* 2021), with solar radiation, ambient air temperature and wind velocity near the surface being key parameters affecting the system's COP. Thus, it is pivotal to determine the impact of the abovementioned ambient conditions on the SAHP systems' COP with correlations.

Much research has reported on the performance enhancement of the SAHP system by integrating Photovoltaic/Thermal (PVT) (Leonforte, Miglioli *et al.,* 2022), Phase Change Material (PCM) based solar thermal collector (Qv, Ni *et al.,* 2015), heat pipe-assisted solar collector (Chen, Zhang *et al.,* 2017) and phase change storage tank (Belmonte, Díaz-Heras *et al.,* 2022). Leonforte *et al.,* (Leonforte, Miglioli *et al.,* 2022) proposed an integrated PVT-SAHP system which benefited both systems due to their ability to produce electricity and thermal energy as well as increasing the efficiency of PV electricity generation. The average seasonal performance of the integrated system was maximised to 3.85 with the COP increased by 21.6%. Besides, the thermal energy production efficiency by PVT panels used to support the production of DHW in the summer was improved to 83.1%. Qv *et al.* (Qv, Ni *et al.,* 2015) proposed a PCM-based solar-assisted heat pump coupled with latent heat thermal energy storage resulting in remarkable advantage uncorrecting the mismatch between supply and demand of thermal energy and electricity. Results indicated that during the days when the outdoor temperature was below -10°C, heating COP of the PCM-SAHP system rose by 65% compared with that of the sole SAHP system, where the efficiency could be improved with the capacity lapse avoiding and exhaust cooling as well. In addition, Chen *et al.* (Chen, Zhang *et al.,* 2017) tested a heat pipe-based PVT-SAHP system with mathematical modelling where heat pipes were integrated with PV panels so that PV cells could be cooled down to a relatively low temperature. The heating COP was increased by 0.05 with the solar radiation increasing by 100W, meanwhile, it increased by 0.08 with the ambient temperature increasing by 0.5°C. Belmonte *et al.,* (Belmonte, Díaz-Heras *et al.,* 2022) simulated the performance of a SAHP system integrated with a phase-change storage tank for residential heating applications. The experimental test indicated that a PCM tank could store 14.5% more energy than a water tank but involved a longer charging/discharging time (around 4.6 times longer). Although the abovementioned technologies could enhance the SAHP system heating performance, there were several limitations such as: 1) Complexity of the whole system; 2) Expensive costs; 3) System degradation with longer operation period; 4) Frequent maintenance requirement. Therefore, it would be optimised if the existing PV panels and hot water storage tank could be integrated with the SAHP system rather than designing a novel compact SAHP system with enhanced technologies engagement.

The applications of the SAHP system for space heating and DHW have increased rapidly in recent years (Mohanraj, Belyayev *et al.,* 2018). Besides, many researchers have integrated renewable energy storage with heat pump systems to enhance the overall performance (Yang, Xu *et al.,* 2021). Miglioli *et al.,* (Miglioli, Aste *et al.,* 2021) reviewed the PVT-SAHP systems by integration methodologies, the possible configurations, the use of different sources and the design of sub-system components, and reviewed the availability and applicability of this technology as a building decarbonisation option. It is realised that even if the overall performance was promising and continued to be optimised, the actual performance of the whole system in a real case study building was still vague. Reda *et al.,* (Reda, Paiho *et al.,* 2020) also mentioned that to achieve better economic performance in real building applications, especially building retrofit with the SAHP systems where energy reduction rates were crucial for economic parameters, it was significant to set up advanced simulation procedures with real data to give realistic and credible correlation of the energy performance. By analysing the challenges remaining with the current SAHP systems, Fan *et al.,* (Fan, Zhao *et al.,* 2021) proposed that a fast responsible heat storage/exchanging unit needed to be integrated into the residential building application to avoid the mismatch between the heating demand of the building and the heat supply of the SAHP system.

Tetteh and Yazdani (Tetteh, Yazdani *et al.,* 2021) noted that energy storage had become essential in providing electricity and thermal energy when the demand was high for small-scale stand-alone renewable energy systems. Only a few technologies and strategies (Olivetti, Ceder *et al.,* 2017) have been applied for renewable energy storage in residential buildings. Among them, batteries and hot water storage tanks have been considered the most practical technologies for PV electricity and solar thermal short-time storage. However, battery electricity storage is limited due to its charging/discharging capacity and efficiency, short lifespan and degradation. Besides, hot water storage tanks for solar thermal storage is only used for DHW supply and would be insufficient for space heating applications.

Therefore, there is a lack of strategy for both electricity and thermal energy storage in an efficient and optimised manner.

This paper proposes an innovative PV-SAHP-TS integrated electro-thermal energy storage system for both space heating and DHW of residential buildings. The PV-generated electricity is used for the SAHP compressors' full-power operation combined with grid electricity import during sufficient solar radiation periods. In the meanwhile, the produced heat from the SAHP condenser side would be used to charge the hot water storage tank (TS) and discharge when required. It is advantageous to tackle the mismatch issue, system complexity and the efficient improvement of the whole system energy performance.

2. CONCEPT AND DESIGN OF SAHP-TS SYSTEM

The concept of a solar-assisted heat pump (SAHP) is the same as a traditional heat pump. The main difference is the use of a thermodynamic solar panel as evaporator which permits extraction of heat from the environment and the absorbed solar radiation in the solar panel. Figure 1 presents a typical configuration of a direct expansion solar assisted heat pump in a residential building. Solar-assisted heat pump systems can be divided in three main components: (i) solar thermodynamic panel; (ii) heat pump unit, which contains the expansion valve, compressor, and heat exchanger/condenser; and (iii) heat storage unit (water tank).
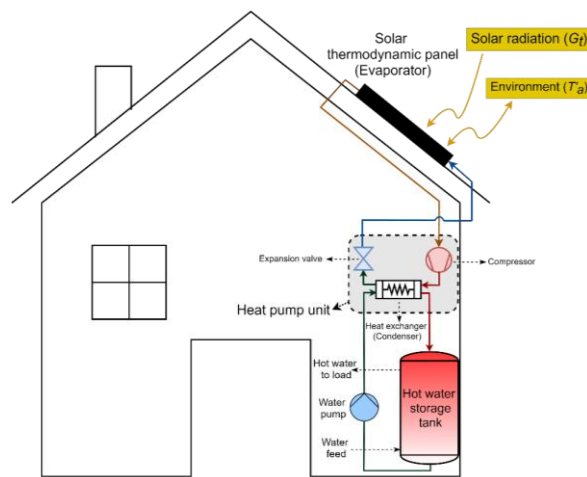

Figure 1: Solar-assisted heat pump system integrated in residential building

2.1. SAHP system configurations

Figure 2 presents the schematic diagram and the main components of the solar assisted heat pump (SAHP) considered in this work.
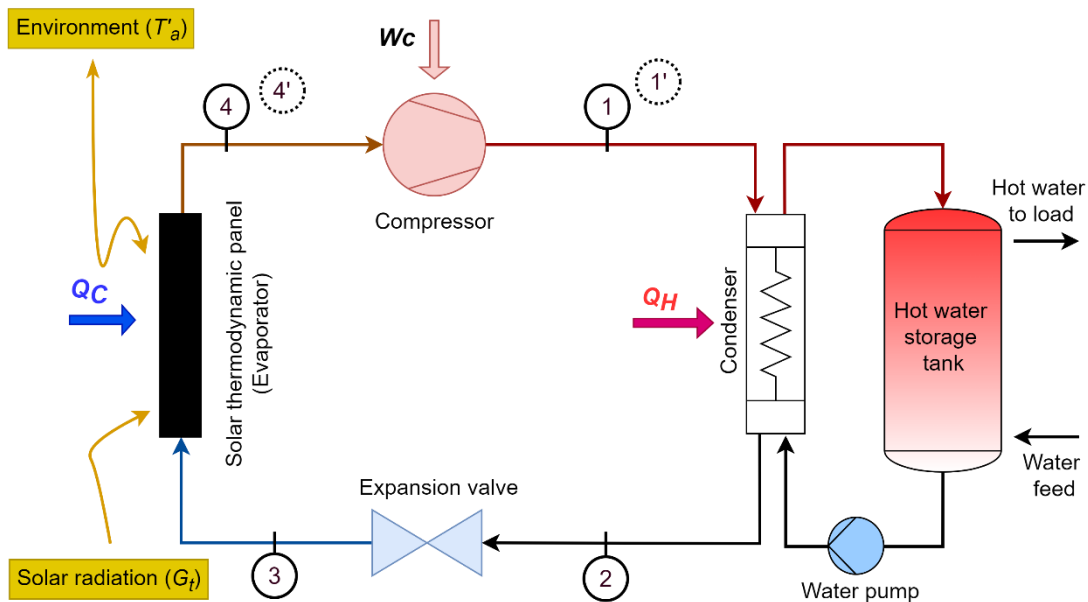

Figure 2: Schematic diagram of solar assisted heap pump

A hot water storage tank was used to store heat aiming at mitigating the mismatch between availability of solar radiation and building heat demand. Based in the schematic of Figure 2, the ideal thermodynamic cycle of the heat pump consisted of four processes:

- Between 1 or 1' and 2 (condensation of the refrigerant): the refrigerant hot gas was converted to liquid by releasing heat to the heat storage tank through the heat exchanger. During this process the pressure was kept constant (isobaric process).
- Between 2 and 3 (expansion of the refrigerant): the liquid refrigerant expanded in the expansion valve and its pressure and temperature decreased (isenthalpic process).
- Between 3 and 4 or 4' (evaporation of the refrigerant): the refrigerant was heated in the solar thermodynamic panel due to the aborted solar radiation and heat from environment. During this process the refrigerant was transformed into vapour at constant pressure (isobaric process).
- Between 4 and 1 (or 4' and 1') (compression of the refrigerant): the refrigerant gas was compressed in the compressor, causing its pressure and temperature to increase.

The heat absorbed in the solar panel can also be calculated using (Equation 1):

$$Q_C = F_R A \left[\eta_0 G_t - U(T_3 - T'_a) \right] \qquad \text{Equation (1)}$$

Where:

- F_R = ratio between actual power output and power output when $T_p = T_3$, being T_p (Equation (7)) the temperature of the plate of the solar thermodynamic panel;
- A = heat transfer area of the solar panel;
- η_0 = optical efficiency of the panel;
- G_t = solar radiation;
- U = heat transfer coefficient on the surface of the panel;
- T_3 = refrigerant temperature at inlet of the solar panel;
- T'_a = environment temperature near the panel.

The heat transfer coefficient U was calculated using (Kalogirou 2014):

$$U = 5.7 + 3.8V \qquad \text{Equation (2)}$$

Where V (m/s) = wind velocity. There can occurs cases of super-heated conditions of the refrigerant in the solar panel. This can occur in cases of high solar radiation intensity and/or high environment temperature. In these situations, the relation between the super-heated temperature and the absorbed heat in the solar panel is (Equation 3):

$$Q_C = \dot{m}[Q_{cL} + c'_p(T'_4 - T_4)] \qquad \text{Equation (3)}$$

Where:

- Q_{cL} = heat of evaporation of the refrigerant at the given pressure;
- c'_p i= heat capacity of the vapour at that pressure;
- T'_4 i= super-heated temperature at outlet of the solar panel (imposed to be at least equal to T'_a trough adjustments on the mass flow).

The power consumed in the compressor is also be calculated using Equation 4:

$$W_C = \dot{m} \left(\frac{P_4 v_4}{\eta_c} \left(\frac{k}{k+1} \right) \left[\left(\frac{P_1}{P_4} \right)^{\frac{k-1}{k}} - 1 \right] \right) \qquad \text{Equation (4)}$$

Where:

- P_4 = pressure at point 4 (same pressure if point 4' occurs);
- P_1 = pressure at point 1 (same pressure if point 1' occurs;
- v_4 = specific volume of the refrigerant at point 4 (or v'_4 if condition of point 4' occurs);
- η_c = efficiency of the compressor;
- k = ratio of specific heat of the refrigerant.

The heating coefficient of performance (COP_H) of the SAHP was calculated using Eqution 5:

$$COP_H = \frac{Q_H}{W_C}$$

2.2. Parameters and conditions used in the simulations

The following conditional between pressure before the solar thermodynamic panel and the solar radiation were used:

- If $0 \leq G_t < 200$ W m^{-2}, $P_3 = 320$ kPa ($T'_4 = 2.5$ ºC), $c'_p = 0.94$ kJ kg^{-1} K^{-1}
- If $200 \leq G_t < 400$ W m^{-2}, $P_3 = 400$ kPa ($T'_4 = 8.9$ ºC), $c'_p = 0.95$ kJ kg^{-1} K^{-1}
- If $400 \leq G_t < 600$ W m^{-2}, $P_3 = 500$ kPa ($T'_4 = 15.7$ ºC), $c'_p = 0.98$ kJ kg^{-1} K^{-1}
- If $G_t \geq 600$ W m^{-2}, $P_3 = 600$ kPa- ($T'_4 = 21.5$ ºC), $c'_p = 1$ kJ kg^{-1} K^{-1}

Table 1 presents the system geometric and thermal parameters and relevant thermodynamic properties of the R134a refrigerant.

Table 1: System geometric and thermal parameters and relevant thermodynamic properties of the R134a refrigerant

Parameter	Value
η_0	0.9
η_c	0.8
F_R	0.85
A (m^2)	1.6
k	1.2

All the other thermodynamics properties of the refrigerant (h, P, T, v, c_p) not presented below were obtained through interpolated data from (Urieli). The solar thermodynamic panel was south oriented with 30º of vertical inclination.

2.3. COP correlation

Solar radiation (G_t), environment temperature near the solar panel (T'_a) and wind speed (V) were combined in a single parameter and then used to describe the COP_H. This parameter was the plate temperature of the solar thermodynamic panel (T_p), which is presented in Equation (7), and was obtained by combining Equations (1), (2) and (6).

$$Q_C = A\left[\eta_0 G_t - U\left(T_p - T'_a\right)\right]$$

$$T_p = (1 - F_R)\left[T'_a + \frac{\eta_0 G_t}{5.7 + 3.8V}\right] + F_R T_3$$

Figures 3 presents the COP_H as a function of T_p and the respective linear correlated equations for the four pilots. The mean squared error (R^2) of the linear regressions were 0.946, 0.956, 0.973 and 0.920, respectively for UK, Greece, Portugal, and Spain. The general $\overline{COP_H}$ correlation, which was the mean of the four correlations, is shown in Equation (8):

$$\overline{COP_H} = 0.069T_p + 2.825$$

This correlation can be used to obtain the performance of the solar assisted heat pump for different climate conditions (solar radiation, environment temperature and wind speed).
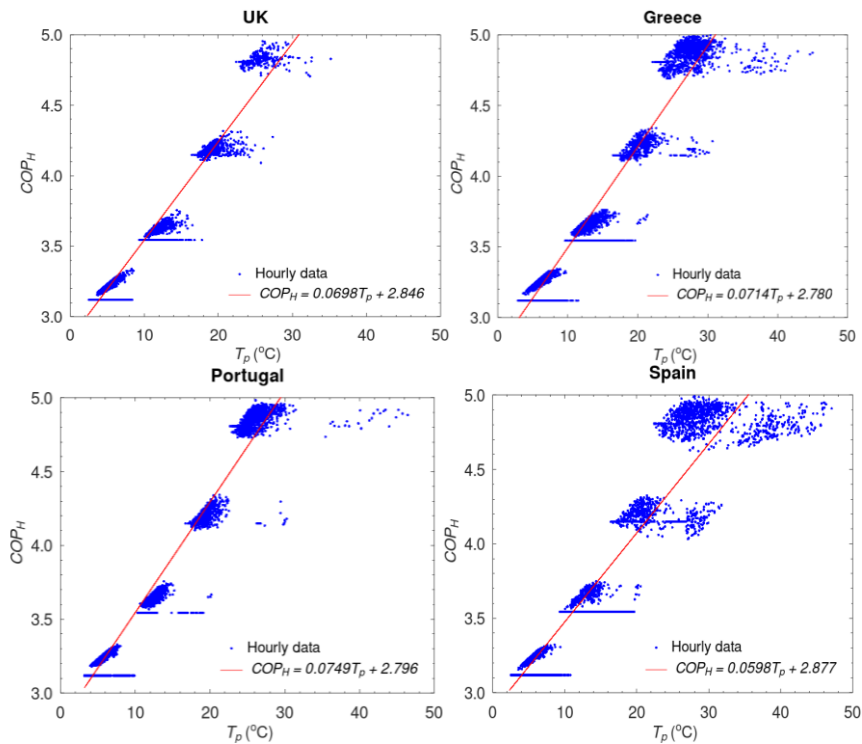
Figure 3: Linear regression of COP_H as function of T_p for the four different pilots

2.4. Simulation of the PV-SAHP-TS system

The energyPRO software was used to simulate the integrated PV-SAHP-TS system energy flow from energy source to energy demand via the integrated system, as shown in Figure 4. EnergyPRO is the leading software for modelling and analysing complex energy projects with combined supply of electricity and thermal energy (process heat, hot water and cooling), and is used for technical details of both existing and new energy projects in a very user-friendly interface providing the user with a clear overview of the project. The software offers a long range of technical and economic reports including graphical presentation of the simulated operation which provides an overview and in-depth understanding of the dynamics in a complex energy system.
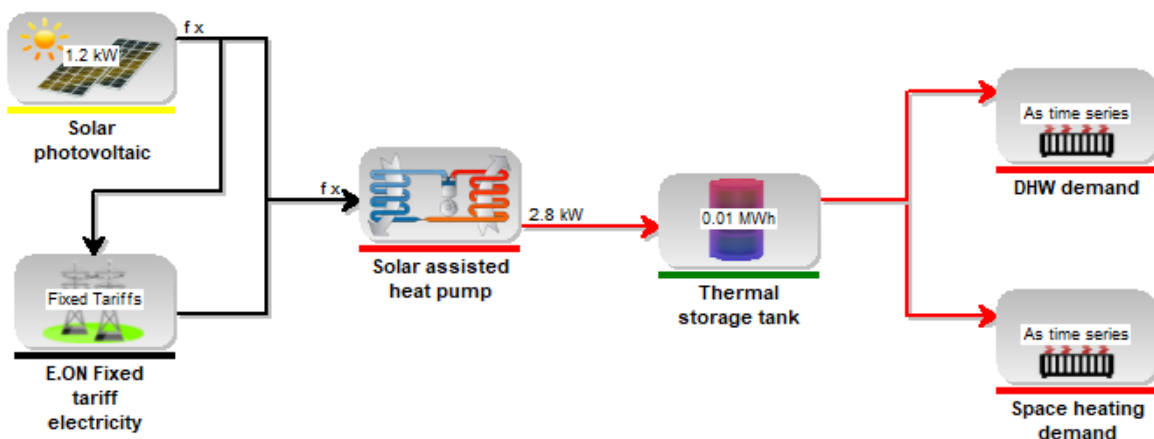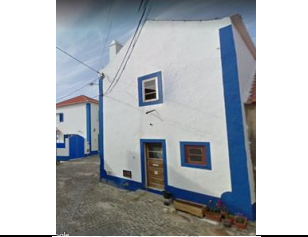
Figure 4: Energy flow work simulation process in energyPRO software

3. CASE STUDY

To demonstrate the energy performance of the PV-SAHP-TS system, four building pilots were selected from the SUREFIT project of UK, Spain, Portugal and Greece and the detailed information of the four buildings were obtained from the SUREFIT website (UNOTT). The heating and cooling demands were calculated via the IES VE simulation software by the Aalto University, with results of annual and peak space and DHW heating demands summarised in Table 2. Moreover, the hourly heating demands were served as inputs into the energyPRO simulation software to

297

calculate the final energy consumption, with the process described in Section 2.4, as well as the peak electrical power of the existing building electrical system.

Table 2: Results of annual and peak space and DHW heating demands and building introduction

Pilot cases	Space heating demand	DHW heating demand	
Semi-detached house Nottingham, **UK** Constructed in 1940s	Annual: 19818kWh Peak power: 6.9kW	Annual: 4518kWh Peak power: 9.3kW	
Terraced house Valladolid, **Spain** Constructed in 1950s	Annual: 24568kWh Peak power: 21.0kW)	Annual: 3174kWh Peak power: 1.3kW	
Social house Mafra Municipality, **Portugal** Constructed in 1960s	Annual: 1167kWh Peak power: 2.2kW	Annual: 1249kWh Peak power: 0.9kW	
Small apartment building Peristeri Municipality, **Greece** Constructed in 1970s	Annual: 6648kWh Peak power: 17.3kW	Annual: 4723kWh Peak power: 3.2kW	

4. POST-RETROFIT BUILDING ENERGY PERFORMANCE

4.1. Annual energy performance and COP

DHW and space heating demands of the four selected pilot buildings were simulated from the ICE-IDA with results summarised in Table 2. The required SAHP heating capacity was sized in the EnergyPro simulation software, which differed from the sole SAHP and PV-SAHP-TS integrated systems, as shown in Tables 3 and 4. It was noticeable that the SAHP sizes were reduced significantly in the PV-SAHP-TS integrated system being 4.1 - 5.6 kW compared to 7 – 26 kW, as a result of the peak heating demand of the SAHP system being mitigated by the discharge process of the thermal storage tank. Besides, the SAHP system was 100% operated during efficient solar radiation period in the integrated system. Moreover, the imported electricity from the grid was significantly reduced by 27%, 50%, 57% and 61% in the integrated system of the UK, Greece, Portugal and Spain buildings accordingly, due to the increasing PV electricity generation.

The heating COP was increased sharply in the integrated system due to the reduced electricity consumption of the whole system. As illustrated in Figure 5, the annual heating COP of the sole SAHP system remained at an almost constant value ranging from 3.4 to 3.6, independent of the ambient climate context. However, it increased by 72%, 100%, 135% and 156% in the four pilot buildings accordingly with the range of COP from 6.2 to 9.2.

Table 3: Building heating demand and imported electricity with sole SAHP system

Pilot location	DHW heating demand	Space heating demand	Annual heating demand	Required SAHP heating capacity	Imported electricity from the grid
UK	4.5MWh	5.9MWh	10.4MWh	11kW	8.1MWh
Greece	2.8MWh	1.4MWh	4.2MWh	20kW	1.2MWh
Portugal	1.2MWh	1.2MWh	2.4MWh	7kW	0.7MWh
Spain	3.2MWh	6.9MWh	10.1MWh	26kW	2.8MWh

Table 4: Building heating demand and imported/exported electricity with PV-SAHP-TS system

Pilot location	Annual heating demand	Required SAHP heating capacity	Hot water storage tank	Solar peak power	Imported electricity from the grid	PV exported electricity
UK	10.4MWh	6kW	800L	4.1kW	5.9MWh	2.9MWh
Greece	4.2MWh	5kW	400L	5.6kW	0.6MWh	8.9MWh
Portugal	2.4MWh	2.8kW	200L	5.6kW	0.3MWh	9.2MWh
Spain	10.1MWh	7kW	800L	5.2kW	1.1MWh	8.1MWh
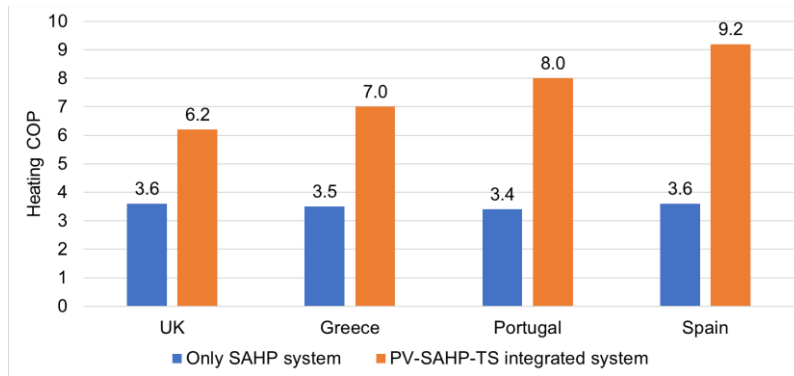
Figure 5: Heating COP of sole SAHP and PV-SAHP-TS integrated systems

4.2. Hourly heating and electricity demand, consumption, generation, and storage

For further operation performance comparison of the sole SAHP and the PV-SAHP-TS integrated systems, the hourly heating and electricity demand, consumption, generation, and storage of the UK pilot building are presented in Figures 6 and 7, during the coldest week from 25th December to 31st December 2021.

In Figure 6, the SAHP system was partially operated depending on the total heating demand with peak time occurring at night-time where the heating COP was relatively low due to insufficient solar radiation. As presented in Equation (8), the SAHP system's heating COP was related to the surface temperature of the thermodynamic panels which was considerably reduced without solar radiation and solely dependent on wind speed and environmental temperature near the thermodynamic panels. Consequently, the SAHP system's performance was limited to most residential buildings with those occupants who were absent during the daytime. Similar to the UK pilot building, although the solar radiation was sufficient in the other three countries, the SAHP system heating COP shows no apparent differences.

Unlike the sole SAHP system, the PV-SAHP-TS integrated system operated in an energy-efficient manner. The SAHP system was fully operated with heat generated and charged into hot water storage tanks when solar radiation was sufficient, as shown in Figure 7. During the heating required period, heat was discharged from hot water storage tanks to meet the building heating demand, especially at night-time. Therefore, the whole system heating COP was improved attributed to the increased surface temperature of the thermodynamic panels during operation time and direct feedback of PV electricity generation supporting the heat pump compressor.
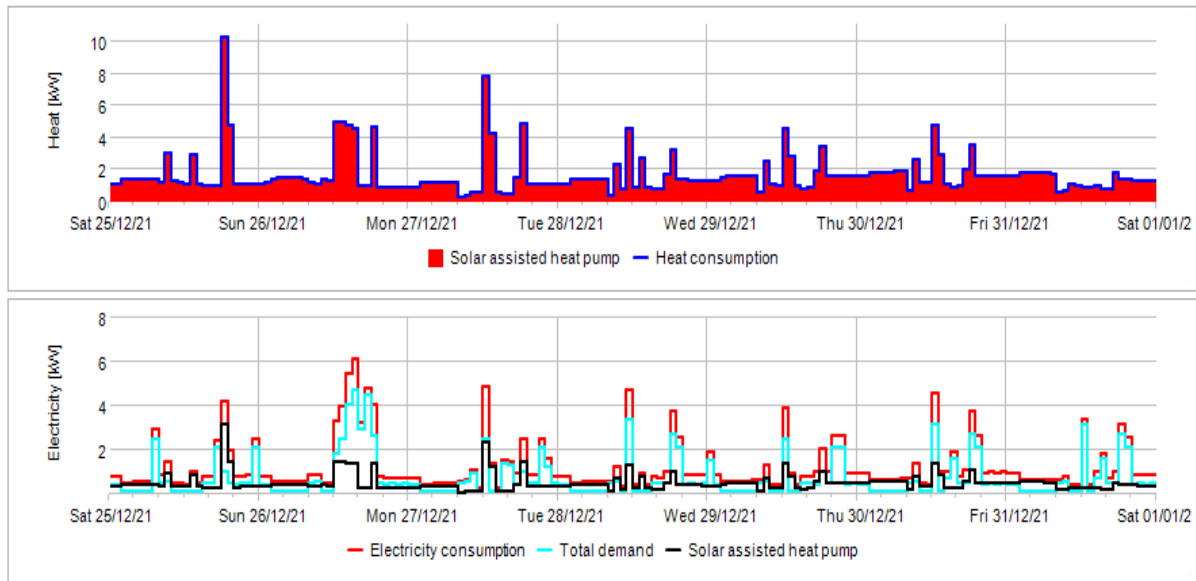
Figure 6: Hourly heat and electricity demand, consumption, generation, and storage in the coldest week (25th Dec to 31st Dec) of the sole SAHP system
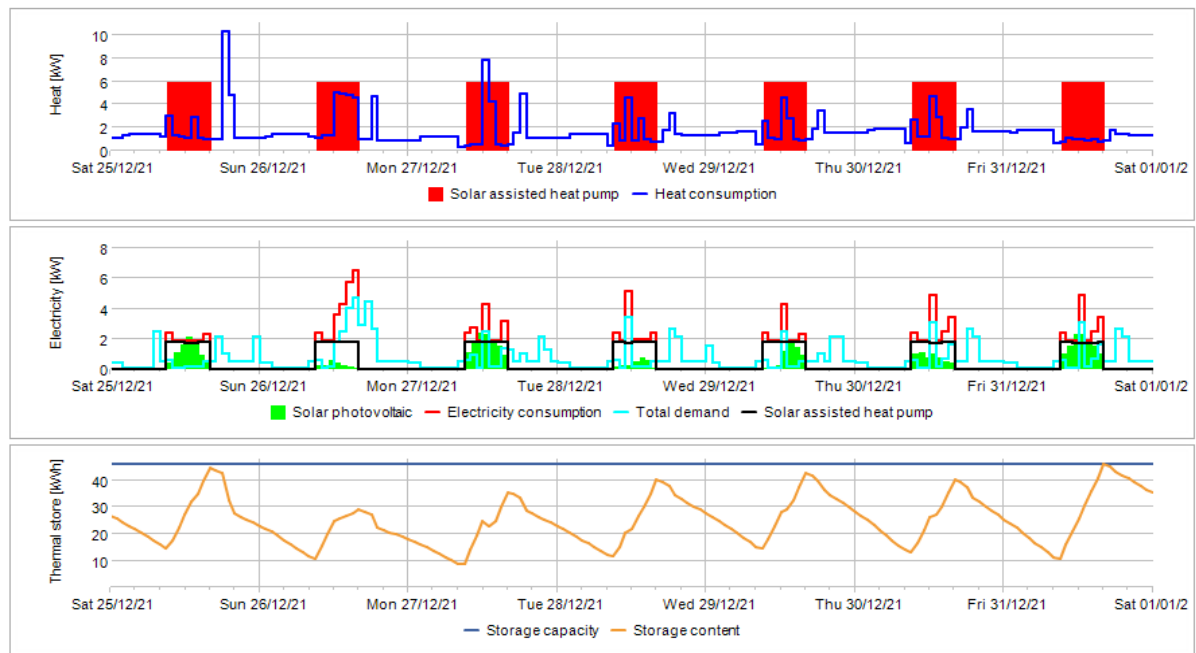
Figure 7: Hourly heat and electricity demand, consumption, generation, and storage in the coldest week (25th Dec to 31st Dec) of the PV-SAHP-TS system

5. CONCLUSION

An innovative PV-SAHP-TS integrated electro-thermal energy storage system was proposed in this research for both space heating and DHW of residential buildings. The COP correlation of the SAHP system was derived under different climate contexts with four pilot buildings in UK, Greece, Portugal and Spain. The annual energy performance was simulated via the IES VE - EnergyPro workflow with a comparison between the sole SAHP system and PV-SAHP-TS integrated system. Results indicated that there was a significant reduction of grid-imported electricity of 27%, 50%, 57% and 61% in the four pilots, respectively. In addition, the heating COP increased by 72%, 100%, 135% and 156% with the highest value of 9.2.

6. REFERENCES

(UNOTT), U. o. N. "WP4 - Deliverable D 2.5 Results of technology sizing."   Retrieved 12th Jan, 2022, from https://surefitproject.eu/wp-content/uploads/2022/05/D-2.5-Results-of-technology-sizing.pdf.

Belmonte, J. F., M. Díaz-Heras, J. A. Almendros-Ibáñez and L. F. Cabeza (2022). "Simulated performance of a solar-assisted heat pump system including a phase-change storage tank for residential heating applications: A case study in Madrid, Spain." Journal of Energy Storage **47**: 103615.

Chaturvedi, S. K. and J. Y. Shen (1984). "Thermal performance of a direct expansion solar-assisted heat pump." Solar Energy **33**(2): 155-162.

Chen, H., L. Zhang, P. Jie, Y. Xiong, P. Xu and H. Zhai (2017). "Performance study of heat-pipe solar photovoltaic/thermal heat pump system." Applied Energy **190**: 960-980.

Fan, Y., X. Zhao, Z. Han, J. Li, A. Badiei, Y. G. Akhlaghi and Z. Liu (2021). "Scientific and technological progress and future perspectives of the solar assisted heat pump (SAHP) system." Energy **229**: 120719.

Ito, S., N. Miura and K. Wang (1999). "PERFORMANCE OF A HEAT PUMP USING DIRECT EXPANSION SOLAR COLLECTORS1Paper presented at the ISES Solar World Congress, Taejon, South Korea, 24–29 August 1997.1." Solar Energy **65**(3): 189-196.

Kalogirou, S. A. (2014). Chapter 4 - Performance of Solar Collectors. Solar Energy Engineering (Second Edition). S. A. Kalogirou. Boston, Academic Press**:** 221-256.

Kamel, R. S., A. S. Fung and P. R. H. Dash (2015). "Solar systems and their integration with heat pumps: A review." Energy and Buildings **87**: 395-412.

Kara, O., K. Ulgen and A. Hepbasli (2008). "Exergetic assessment of direct-expansion solar-assisted heat pump systems: Review and modeling." Renewable and Sustainable Energy Reviews **12**(5): 1383-1401.

Leonforte, F., A. Miglioli, C. Del Pero, N. Aste, N. Cristiani, L. Croci and G. Besagni (2022). "Design and performance monitoring of a novel photovoltaic-thermal solar-assisted heat pump system for residential applications." Applied Thermal Engineering **210**: 118304.

Miglioli, A., N. Aste, C. Del Pero and F. Leonforte (2021). "Photovoltaic-thermal solar-assisted heat pump systems for building applications: Integration and design methods." Energy and Built Environment.

Mohanraj, M., Y. Belyayev, S. Jayaraj and A. Kaltayev (2018). "Research and developments on solar assisted compression heat pump systems – A comprehensive review (Part-B: Applications)." Renewable and Sustainable Energy Reviews **83**: 124-155.

Olivetti, E. A., G. Ceder, G. G. Gaustad and X. Fu (2017). "Lithium-Ion Battery Supply Chain Considerations: Analysis of Potential Bottlenecks in Critical Metals." Joule **1**(2): 229-243.

Qv, D., L. Ni, Y. Yao and W. Hu (2015). "Reliability verification of a solar–air source heat pump system with PCM energy storage in operating strategy transition." Renewable Energy **84**: 46-55.

Reda, F., S. Paiho, R. Pasonen, M. Helm, F. Menhart, R. Schex and A. Laitinen (2020). "Comparison of solar assisted heat pump solutions for office building applications in Northern climate." Renewable Energy **147**: 1392-1417.

Sezen, K., A. D. Tuncer, A. O. Akyuz and A. Gungor (2021). "Effects of ambient conditions on solar assisted heat pump systems: a review." Science of The Total Environment **778**: 146362.

Tetteh, S., M. R. Yazdani and A. Santasalo-Aarnio (2021). "Cost-effective Electro-Thermal Energy Storage to balance small scale renewable energy systems." Journal of Energy Storage **41**: 102829.

Urieli, I. "Thermodynamic Properties of R134a TetraFlouroEthane - CF3CH2F." from https://www.ohio.edu/mechanical/thermo/property_tables/R134a/.

Yang, L. W., R. J. Xu, N. Hua, Y. Xia, W. B. Zhou, T. Yang, Y. Belyayev and H. S. Wang (2021). "Review of the advances in solar-assisted air source heat pumps for the domestic sector." Energy Conversion and Management **247**: 114710.

#101: Deep energy retrofit of historic residential buildings with the integration of prefabricated transparent insulation facades (TIF)

Yuhao Wang[1], Tianhong Zheng[2], Ke Qu[3*], Man Luo[4], Saffa Riffat[5]

[1]Department of Architecture and Built Environment, the University of Nottingham, University Park, Nottingham, NG7 2RD, UK, ezxyw13@exmail.nottingham.ac.uk
[2]Department of Architecture and Built Environment, the University of Nottingham, University Park, Nottingham, NG7 2RD, UK, ezxtz4@exmail.nottingham.ac.uk
[3]Department of Architecture and Built Environment, the University of Nottingham, University Park, Nottingham, NG7 2RD, UK, ezzkq@exmail.nottingham.ac.uk
[4]Department of Architecture and Built Environment, the University of Nottingham, University Park, Nottingham, NG7 2RD, UK, laxml24@exmail.nottingham.ac.uk
[5]Department of Architecture and Built Environment, the University of Nottingham, University Park, Nottingham, NG7 2RD, UK, Lazsbr@exmail.nottingham.ac.uk

Abstract: The energy efficiency of a building façade is significant for the carbon emissions of the whole building and for the sizing of the building's energy system. However, it is challenging to insulate the façade of historic buildings due to the preservation of aesthetic, historical and cultural values of both interior and exterior surfaces of the wall which are typical in Victorian masonry residential buildings. This paper proposes an innovative deep energy retrofit strategy for Victorian residential buildings by integrating prefabricated transparent insulation panels (TIPs) with solar-assisted heat pumps (SAHP) and PV roof panels. Four alternative TIPs were investigated with single, double, triple, vacuum and PV glazing materials, which were applied to external masonry wall insulation with a 20mm air cavity between the external wall and glazing materials. Air convection was only allowed by the thermal buoyancy in the cavity for internally cooling of the transparent insulation facades (TIF) structures and to avoid the overheating issues in summer. Additionally, roof PV electricity could supply the SAHP system with stored hot water to provide both space heating (SPH) and domestic hot water (DHW). EnergyPro simulation was used to evaluate the carbon emission and economic performance with different retrofit packages. Results indicated that the integration of transparent PV glazing insulation façade (PVG), PVG roof and vacuum glazing window replacement with SAHP system, integrated with a water storage tank and batteries had the lowest payback period of 15-16 years with an initial investment of £323/m² - £538/m² and a 75.7% - 91.1% carbon emission reduction. In comparison, for with the scenario without façade insulation, the payback period was extended to 24-27 years, although the initial investment varied between £121/m² and £410/m².

1. INTRODUCTION

The building sector consumes an enormous amount of energy with residential buildings using more than 36% of total global energy consumption in 2018 and about 30% (9.95Gt) of global energy-related carbon dioxide emissions in 2019 (Ian Hamilton 2020). The European Union (EU) has legislated to reduce CO₂ emissions to 40% in 2030 and increase energy efficiency by 27% (Trotta 2019). Energy efficiency technologies could achieve these goals by reducing thermal losses, decreasing energy consumption and retrofitting building systems (Thomsen, Rose et al. 2016). Moreover, retrofitting existing buildings could be more effective than constructing new buildings with lower energy consumption (El-Darwish and Gomaa 2017). Those energy efficiency technologies used in existing buildings could help reduce energy consumption by about 35% and CO₂ emissions by 25% (González-Gil, Palacin et al. 2014).

Statistics reveal that 14% of building stock in Europe dates from before 1919 and that figure rises to 20.5% in the UK (Ozbalta, Yildiz et al. 2021). Therefore, energy retrofitting historic buildings is a critical challenge. However, historic buildings have unique cultural characteristics that should be protected, such as immovable architectural, historical, aesthetic, and archaeological features, consequently, historic buildings usually have old heating, ventilation and air conditioning (HVAC) systems with high-energy consumption (Cabeza, de Gracia et al. 2018). Besides, there is a lack of specific protocols to contribute well-balanced solutions for energy efficiency improvement and conservation requirements of historic buildings, and it is hard to provide a proper compromise (Mazzarella 2015). Therefore, protecting historic buildings whilst simultaneously improving the energy efficiency and achieving conservation requirements is crucial.

Some sustainable technologies have been proposed and developed for retrofitting historic residential buildings in previous studies. Generally, there are four main ways to improve the energy performance, (i) replacing the windows with low emissivity materials, (ii) increasing the thermal insulation of the walls and roof, (iii) improving the efficiency of the energy system, and (iv) improving the building airtightness insulation. The detailed information is summarised in Table 1.

Table 1: Literature of retrofitting historic residential buildings

Ref	Location	Building type	Construction year	Insulation method	Efficient energy system	Renewables	Energy reductions	Cost and PBT
(Ciulla, Galatioto et al. 2016)	Milano, Italy	Terraced house	Before 1919	IWI+RI+W	N/A	N/A	40.2%	€9833, 20 years
(Qu, Chen et al. 2021)	Nottingham, UK	Detached house	Before 1919	IWI+W+ATI	N/A	N/A	63.3%	£152,474, 24 years
(Seddiki, Anouche et al. 2016)	Oran, Algeria	Low-rise apartment	Late 19th century	IWI+W	N/A	N/A	23.5%	N/A
(Mukhopadhyay, Ore et al. 2019)	Havre, US	Detached house	between 1913 and 1919	IWI+W+ATI	HVAC	N/A	59.0%	More than 30 years
(Belpoliti, Bizzarri et al. 2018)	Caporciano, Italy	Terraced house	Before 1919	IWI+RI+GI+W	condensation boiler	N/A	41.5%	N/A
(Tink, Porritt et al. 2018)	Leicestershire, UK	Semi-detached house	1910s	IWI	N/A	N/A	23.5%	N/A
(Moran, Blight et al. 2014)	Bath, UK	Terraced house	1810	IWI+RI+ATI+W	AWHP	PV+SC	54%	N/A
(Şahin, Arsan et al. 2015)	Izmir, Turkey	Detached house	End of the 19th century	IWI+RI+GI+ATI+W	TC(Thermostat control)		34%	N/A
(Ascione, Cheche et al. 2015)	Naples, Italy	Detached house	Early 15th century	IWI+RI+WR	AWHP	N/A	45%	€559,044
(Tadeu, Rodrigues et al. 2015)	Coimbra, Spain	Terraced house	16th Century	IWI+RI+W	AC	N/A	40%	€52,800
(Lucchi, Tabak et al. 2017)	Lake of Como, Italy	Detached house	18th Century	IWI+RI	N/A	N/A	37.5%	€10000, 18 years
(Campbell, McGrath et al. 2017)	Belfast, Northern Ireland	Detached house	1878	IWI+LI+W	ASHP	N/A	N/A	N/A
(Caro and Sendra 2021)	Seville, Spain	Terraced house	Late 19th century	IWI+W+RI	ASHP	N/A	51	N/A

Although previous studies have already analysed improving the energy performance of historic residential buildings, more research is still required to develop the current knowledge of the specific characteristics and optimisation. There

is still a big challenge to properly retrofit historic buildings by adopting comprehensive sustainable strategies due to regulatory constraints on interior and exterior surfaces of the external wall while taking into account reasonable cost and payback period (PBP).

Therefore, this paper sets out to propose an innovative retrofit strategy integrating three different sustainable building technologies to analyse the energy preference in a Victorian masonry residential building. This new retrofit strategy combines the prefabricated transparent insulation façade (TIF) system with solar-assisted heat pumps (SAHP) and PV roof panels to achieve the deep energy retrofit aim. The TIF can provide significant thermal insulation and restrict infrared energy losses by re-radiation while transmitting short and long wavelengths of solar radiation. The semi-transparent photovoltaic glazing (PVG) has a low heat transfer coefficient (0.8 W/m2 K). It is used as roof PV to reduce solar heat gain, generate clean electricity, and admit comfortable daylight (Ghosh, Sundaram et al. 2018). Additionally, the roof PV electricity can supply the SAHP system with stored hot water to provide both space heating (SPH) and domestic hot water (DHW). In this paper, four alternative transparent insulation panels (TIPs) were designed and investigated with single, double, triple and vacuum glazing materials applied to external masonry wall insulation with a 20mm air cavity between the external wall and glazing materials. Air convection was only allowed by the thermal buoyancy in the cavity to remove the moisture inside and mitigate mould risks and external wall degradation. To carry out an environmental and economic assessment of energy efficiency retrofit measures, EnergyPro simulation was used to evaluate the carbon emission and economic performance with different combination sceneries.

2. METHODS

This research aimed to identify deep energy retrofit strategies for historic residential buildings based on the prefabricated transparent insulation facade (TIF) concept to minimise the impact of insulation retrofit measures on the building outlook, typical features and interior decoration. Five TIF construction types were proposed to be investigated including single glazing (SG), double glazing (DG), triple glazing (TG), vacuum glazing (VG) and PV glazing (PVG), integrated with air gaps between the glazing side and existing wall. In addition, a solar-assisted heat pump (SAHP) was used to replace the existing condensing gas boiler with thermal energy generated and stored in the water storage tank (WST), which would supply the heating demand when required. Also, the SAHP electricity demand could be partially supplied by the semi-transparent PV glazing panels installed as either TIF structures or roof sides. In order to maximise reducing the whole building heating demand, insulation was also applied on window glazing and roof. In this paper, vacuum glazing was selected to replace the existing glazing materials, and PV glazing roofs were selected for both insulation and solar electricity generation.

2.1. Concept, prototype, and structures of the TIF

Figure 1 illustrates a historical building before and after retrofit using transparent insulation façade (TIF) concept including three optical envelope insulation materials of transparent insulation façade (TIF), vacuum glazing (VG) window and a semi-transparent PV glazing (PVG) roof. The innovative PVG-based TIF prototype and its geometrical compositions are shown in Figure 2. The main structure (from inside to outside) of the TIF is based on:

- 240mm existing solid wall
- 200mm sealed air gap between the external glazing insulation and existing wall
- External glazing insulation with five alternatives: 6mm single glazing (SG), 18mm double glazing (DG), 30mm triple glazing (TG), 8mm vacuum glazing (VG) and 18mm PV glazing (PVG)
- Air inlet shutter at bottom of the external glazing structure
- Air outlet shutter at top of the sealed air gap

Among the single glazing (SG), double glazing (DG), triple glazing (TG) and vacuum glazing (VG) based TIF structures, the heat loss could be significantly reduced with the overall U-value modelled and calculated in the IES VE software. During wintertime, the air inlet and outlet shutters remain closed to insulate the existing wall with both air gaps and glazing structures. However, the shutters are open in the summertime to ensure the ambient air flowing from the bottom to the top because of the buoyancy force, leading to internal cooling of the TIF system, thereby avoiding overheating issues. The buoyancy force occurs when the strong solar radiation is absorbed by the air inside the sealed air gap layer. Meanwhile, the moisture condensation could be avoided at the original external wall surface due to the fact that air temperature inside the sealed cavity will be increasing and higher than the dew point temperature by incorporating the well-insulated TIF structure, serving as the preservation function to the external wall. The main objective of this study relied on:

- The determination of the thermal performance of various TIF structures and impacts on building heating demand reduction;
- The prediction of only SAHP and TIF-integrated system COP, as well as the whole building energy efficiency improvement;
- The optimisation of residential historic building retrofit packages for comprehensive energy, carbon and economic performances.
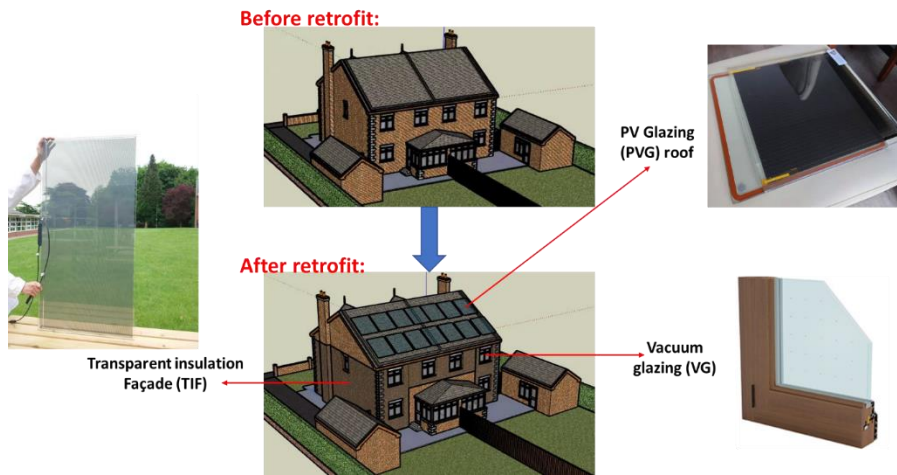
Figure 1: Historical building before and after retrofit using transparent insulation façade (TIF) concept
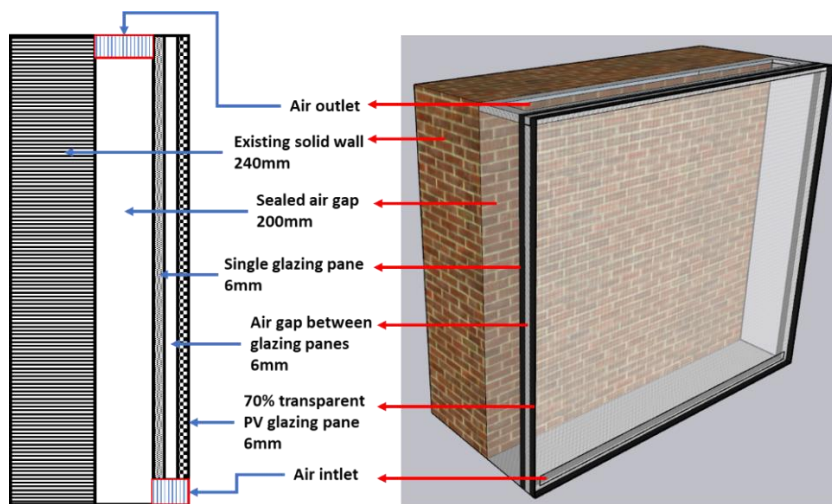
Figure 2: TIF prototype and its geometrical compositions

2.2. Case study

A semi-detached historical residential building located in Nottingham, UK, was constructed with SketchUp as the reference building with the model view shown in Figure 3. The thermal physical parameters of the envelope and energy systems were obtained from TABULA Webtool which provided the building information data for each typical building. The building envelope construction, U-values and surface areas are summarised in Table 2. The space heating and domestic hot water were supplied by an old natural gas condensing boiler with hot water radiator terminals. Due to the temperate weather conditions in the UK context, space cooling was not required in such historical buildings. However, due to the poor insulation and airtightness of this historical building, the heating energy consumption reached 16778.6 kWh accounting for approximately 76.5% of the final energy consumption (21939.0kWh). In addition, the total electricity consumption was 5160.4kWh. All the building energy consumption was calculated with the IES VE software.

Figure 3: SketchUp model view of a semi-detached historical residential building

Table 2: Thermal physical parameters of the building envelope

	Type of construction	U-value	Surface area
Roof	Pitched with gables	2.30 W/(m²K)	113.5 m²
Wall	Solid brick (as built)	2.10 W/(m²K)	200.3 m²
Ground floor	N/A	0.59 W/(m²K)	113.5 m²
Window	Wood frame with single glazing panel	4.80 W/(m²K)	46.5 m²
Door	Wood	3.00 W/(m²K)	3.8 m²

To investigate the impact of the proposed TIF retrofit systems, 18 retrofit packages (RP) were proposed and classified into three categories, as listed in Table 3.

- Category 1: RP1-RP10: To investigate the impact of different TIF construction types on the building energy performance, including single gazing (SG), double glazing (DG), triple glazing (TG), vacuum glazing (VG) and transparent PV glazing (PVG).
- Category 2: RP11-RP14: To investigate the impact of different insulation measures on the building energy performance, including transparent insulation façade (TIF), vacuum glazing (VG) window, and semi-transparent PV glazing (PVG) roof.
- Category 3: RP15-RP18: To investigate the impact of installation of energy-efficient systems of PV panels, solar-assisted heat pump (SAHP), hot water storage tank (WST) and battery on the building energy performance without any insulation technologies.

Table 3: Proposed retrofit packages with advanced insulation, efficient systems and renewable technologies

	SG-FIT	DG-TIF	TG-TIF	VG-TIF	PVG-TIF	VG window	PVG Roof	SAHP	WST	Battery
RP1	√					√	√	√	√	
RP2	√					√	√	√	√	√
RP3		√				√	√	√	√	
RP4		√				√	√	√	√	√
RP5			√			√	√	√	√	
RP6			√			√	√	√	√	√
RP7				√		√	√	√	√	
RP8				√		√	√	√	√	√
RP9					√	√	√	√	√	
RP10					√	√	√	√	√	√
RP11					√	√		√	√	
RP12					√	√		√	√	√
RP13					√			√	√	√
RP14					√			√	√	
RP15							√	√	√	√
RP16							√	√	√	
RP17					√			√	√	
RP18								√	√	√

The EnergyPro software was used to simulate the post-retrofit energy performance with energy-efficient systems, renewables and storage technologies based on the simulation results of building heating demand from the IES VE software. In Figure 4, the simulation flowchart of RP10 is illustrated as a case study demonstration in the EnergyPro interface before simulation.
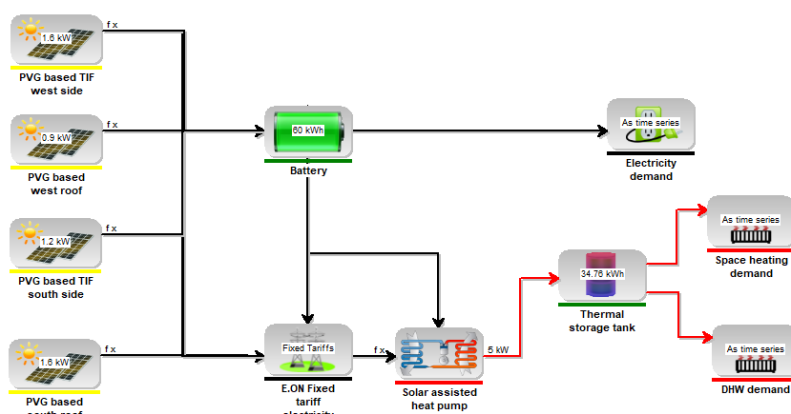

Figure 4: Simulation flowchart of RP10

2.3. Performance of retrofit technologies

The U-value of the integrated TIF structures, VG window and PVG roof were calculated in IES VE software according to their materials and compositions, with results included in Table 4. The PVG material solar electricity conversion rates were varied with the transparency rates, referenced to the Polysolar company's product. The number of the thermodynamic panels and the heating capacity of the SAHP were determined by the heating demand in each retrofit package with the SAHP system provided by the Arkaya (Energy) company. Moreover, the size of both WST and battery were considered by the SAHP heating generation and PVG electricity generation amount in each retrofit package. The overall cost is also summarised in Table 4 comprising of cost of components, installation and accessory fees.

Table 4: Specifications of retrofit technologies

Technologies	Compositions	Properties	Overall cost
SG-TIF	240mm existing wall + 200mm air gap + 6mm single glazing panel	U-value=1.23 W/m^{2}K	£3,411.24
DG-TIF	240mm existing wall + 200mm air gap + 6mm single glazing panel + 6mm air gap + 6mm single glazing panel	U-value=0.87 W/m^{2}K	£8,258.40
TG-TIF	240mm existing wall + 200mm air gap + 6mm single glazing panel + 6mm air gap + 6mm single glazing panel + 6mm air gap + 6mm single glazing panel	U-value=0.67 W/m^{2}K	£13,175
VG-TIF	240mm existing wall + 200mm air gap + 8mm vacuum glazing panel	U-value=0.41 W/m^{2}K	£15,500
PVG-TIF	240mm existing wall + 200mm air gap + 6mm single glazing panel + 6mm air gap + 70% transparent CdTe-PV glazing	U-value=0.76 W/m^{2}K, Solar electricity conversion rate=5.6%	£16,576.32
VG window	8mm vacuum glazing panel + 10mm air gap + 6mm single glazing panel	U-value=0.57 W/m^{2}K	£3,357.50
PVG roof	6mm single glazing panel + 20% transparent CdTe-PV glazing	U-value=1.52 W/m^{2}K, Solar electricity conversion rate=12%	£14,704.80
SAHP	Thermal dynamic panels + heat pump box	COP=0.069×Tp+2.825 (Tp: Surface temperature of the solar thermal dynamic panel) Maximum outlet temperature: 70°C (Energy)	£1,296 per 1kW heat capacity
WST	Water storage tank connected with condenser coils of heat pump	Inlet temperature: 30°C; outlet temperature: 80°C Insulation thickness:300mm	£180 per 100L water tank
Battery	Lithium battery	Charge and discharge efficiency: 85%	£3,514 per unit

3. RESULTS AND DISCUSSION

This section describes the comprehensive post-retrofit building energy, carbon emission and economic performance for the 18 listed retrofit packages. The energy, carbon and bills reduction rates are described in subsection 3.1, as well as the system COP and the building energy performance. The payback period and optimisation of retrofit packages are discussed in section 3.2.

3.1. Post-retrofit building energy and carbon performance

Figure 5 illustrates energy, carbon and bills reduction rate of the selected 18 retrofit packages compared with baseline with the range of 56.3% - 90.2%, 60.4% - 91.1% and 2.8% - 73.9%, respectively.
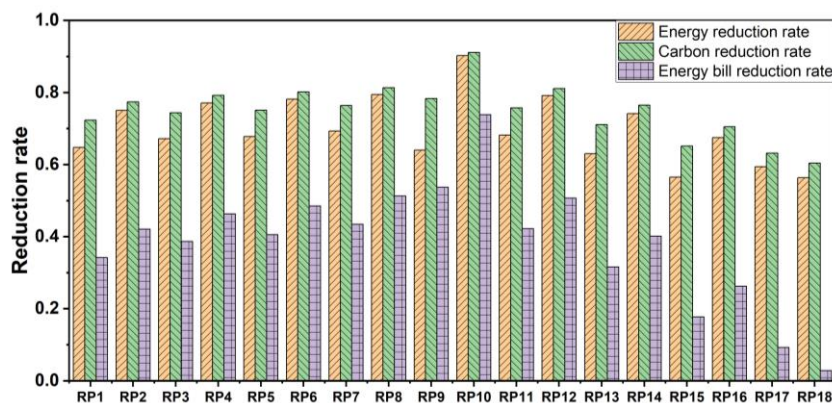

Figure 5: Energy, carbon and bills reduction rates

Among the 18 packages, RP10 had the maximum energy, carbon and bills reduction rate by integrating PVG-TIF, PVG roof, VG window, SAHP, WST and battery. Comparing RP1 and RP2, RP3 and RP4, RP5 and RP6, RP7 and RP8, RP9 and RP10, it was realised that the energy, carbon and bills reduction rates were higher for those with batteries than those without, although they had the same technologies of VG window, PVG roof, SAHP, WST and similar TIF construction type. In particular, the energy, carbon and bill reduction rates were significantly increased from 64.0% to 90.2%, 78.3% to 91.1% and 53.7% to 73.9% corresponding to RP9 (PVG-TIF without battery) and RP10 (PVG-TIF with battery). This may be attributed to the fact that batteries could mitigate the electricity peak load by charging the excessive PV-generated electricity and discharging during household appliances' operation time without sufficient PV electricity generation. By comparing different TIF construction types of SG (RP2), DG (RP4), TG (RP6), VG (RP8) and PVG (RP10), it was found that the energy, carbon and bill reduction rates increased with the U-value decline from 1.23 W/m^{2}K (SG-TIF) to 0.41 W/m^{2}K (VG-TIF) except for the PVG-TIF type with the U-value of 0.78 W/m^{2}K. Although the U-value of PVG-TIF was slightly higher than the VG-TIF causing a 356 kWh extra energy increase, the PVG-TIF could generate electricity of 2718 kWh which would evidently cover the increased energy consumption. Therefore, the PVG-TIF construction type was the most optimised selection among different TIF constructions. In the meanwhile, RP12 and RP13 had common technologies of PVG-TIF, SAHP, WST and battery in which the former package used the VG window technology. Results show that the energy, carbon and bills reduction rates decreased from 79.2% - 63.0%, 81.1% - 71.1%, 50.7% - 31.6%, respectively, indicating that VG window technology was essential. Compared with RP10, RP12 had similar technologies without PVG roof panels resulting in an 11.0%, 10.0% and 23.2% decrease in energy, carbon and bill reduction rates, respectively. Without using any construction type based TIF, RP15 – RP18 indicated the worst energy, carbon and bill performances compared with the optimised group of RP10, indicating that the TIFs could play an important role in historic building retrofit.

Figure 6 demonstrates the SAHP system COP, integrated heating COP and building energy efficiency of the selected 18 retrofit packages. Among all the retrofit packages, the SAHP system alone had similar heating COP ranges from 3.42 to 3.50. However, the integration of TIFs, WST and battery could take the heating COP up to 17.46 with approximately 400% improvement. Additionally, the building energy efficiency was significantly improved with the range of 2.02 (RP7) – 5.87 (RP10) compared with the baseline of 0.93.
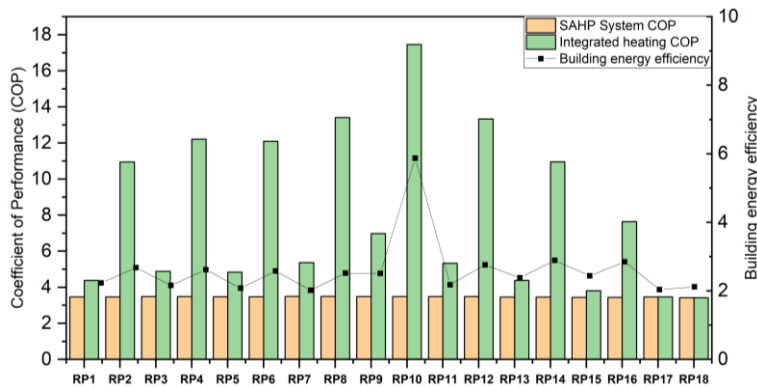
Figure 6: SAHP and integrated system heating COP and building energy efficiency

3.2. Post-retrofit building economic performance and optimisation

By analysing the lifecycle cost performance, the payback period was used as an economic performance indicator of the selected 18 retrofit packages with energy reduction rates ranging from 56.3% to 90.2%, as indicated in Figure 7. The payback periods were concentrated in three ranges: 1) 15 – 16 years, 2) 18 – 20 years and 3) 24 - 27 years. Without the TIFs (RP15 – RP18), the payback periods were much longer than those with TIF technologies. Within the shortest payback period range, RP10 – RP12 demonstrated the common retrofit technologies of PVG-TIF, VG window, SAHP and WST with alternatives of PVG roof and battery.
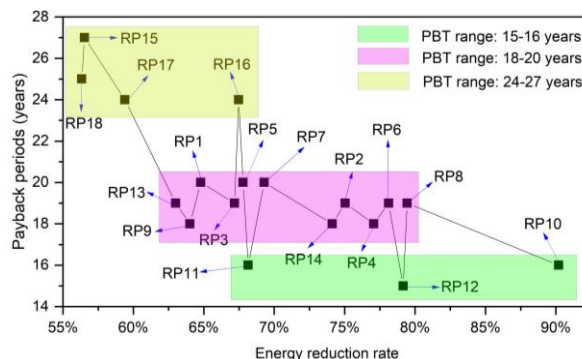
Figure 7: Payback periods with an increase in energy reduction rates

Figure 8 illustrates the combination flowchart of retrofit technologies and their relationship to comprehensive energy-economic performances, including the payback period (PBT), energy reduction rate (ERR), carbon reduction rate (CRR) and bill reduction rate (BRR), which could be used as optimisation guidance for different retrofit objectives. Considering the maximum ERR, CRR and BRR objectives, RP10 was recommended as the optimal retrofit package with ERR of 90.2%, CRR of 91.1% and BRR of 73.9%, whereas RP12 achieved the lowest PBT requirement with ERR of 79.2%, CRR of 81.1% and BRR of 50.7%. In addition, RP11 was an alternative with a PBT of 16 years and a relatively lower initial investment of £323/m^2 compared with £538/m^2 of RP10 and £365/m^2 of RP12.
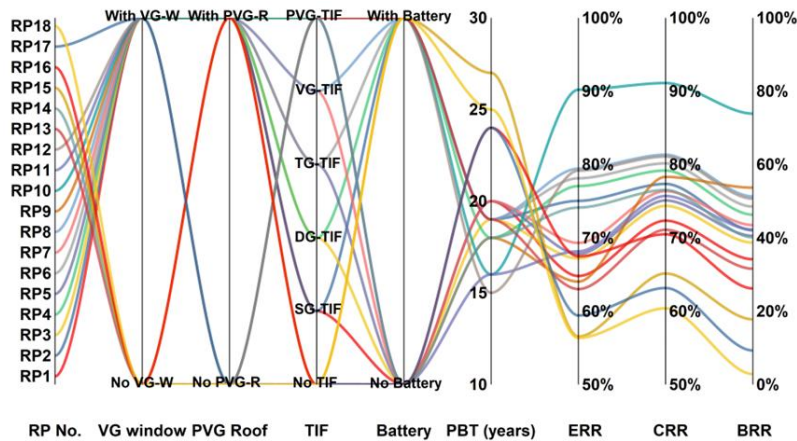
Figure 8: Comprehensive performance with retrofit technologies' flowchart

4. CONCLUSION

This paper identified deep energy strategies for historic residential buildings based on the prefabricated transparent insulation facades (TIF) concept to minimise the impact of insulation retrofit measures on the building outlook, typical features and interior decoration. The major conclusions could be drawn as below:

1) The determination of the thermal performance of various TIF structures and impacts on building heating demand reduction;

	SG-TIF	DG-TIF	TG-TIF	VG-TIF	PVG-TIF
Heating demand reduction rate	64.8%	67.2%	67.8%	69.3%	64.0%

2) The prediction of only SAHP and TIF-integrated system COP, as well as the whole building energy efficiency improvement;

Among all the retrofit packages, the SAHP system alone has similar heating COP ranges from 3.42 to 3.50. However, integrations of TIFs, WST and battery could lead the heating COP up to 17.46 with approximately 400% improvement. Besides, the building energy efficiency was significantly improved to the range of 2.02 (RP7) – 5.87 (RP10) compared with the baseline of 0.93.

3) The optimisation of residential historic building retrofit packages for comprehensive energy, carbon and economic performances.

Without the TIFs (RP15 – RP18), the payback periods were much longer than those with TIF technologies. Within the shortest payback period range, RP10 – RP12 demonstrated the common retrofit technologies of PVG-TIF, VG window, SAHP and WST with alternatives of PVG roof and battery.

5. REFERENCES

"Battery Inverters." from https://www.sma.de/en/products/battery-inverters.html.

"Direct water tanks." from https://www.directwatertanks.co.uk/water-storage-tanks.

"PRODUCT SPECIFICATIONS AND DATASHEETS." Retrieved 28th May, 2022, from https://www.polysolar.co.uk/technology/_domestic-info-specifications.

"TABULA WebTool."   Retrieved 28 May, 2022, from https://webtool.building-typology.eu/#bm.

Ascione, F., N. Cheche, R. F. D. Masi, F. Minichiello and G. P. Vanoli (2015). "Design the refurbishment of historic buildings with the cost-optimal methodology: The case study of a XV century Italian building." Energy and Buildings **99**: 162-176.

Belpoliti, V., G. Bizzarri, P. Boarin, M. Calzolari and P. Davoli (2018). "A parametric method to assess the energy performance of historical urban settlements. Evaluation of the current energy performance and simulation of retrofit strategies for an Italian case study." Journal of Cultural Heritage **30**: 155-167.

Cabeza, L. F., A. de Gracia and A. L. Pisello (2018). "Integration of renewable technologies in historical and heritage buildings: A review." Energy and Buildings **177**: 96-111.

Campbell, N., T. McGrath, S. Nanukuttan and S. Brown (2017). "Monitoring the hygrothermal and ventilation performance of retrofitted clay brick solid wall houses with internal insulation: Two UK case studies." Case Studies in Construction Materials **7**: 163-179.

Caro, R. and J. J. Sendra (2021). "Are the dwellings of historic Mediterranean cities cold in winter? A field assessment on their indoor environment and energy performance." Energy and Buildings **230**: 110567.

Ciulla, G., A. Galatioto and R. Ricciu (2016). "Energy and economic analysis and feasibility of retrofit actions in Italian residential historical buildings." Energy and Buildings **128**: 649-659.

El-Darwish, I. and M. Gomaa (2017). "Retrofitting strategy for building envelopes to achieve energy efficiency." Alexandria Engineering Journal **56**(4): 579-589.

Energy, A.   Retrieved 13/11/2021, from http://arkaya.co.uk/.

Ghosh, A., S. Sundaram and T. K. Mallick (2018). "Investigation of thermal and electrical performances of a combined semi-transparent PV-vacuum glazing." Applied energy **228**: 1591-1600.

González-Gil, A., R. Palacin, P. Batty and J. P. Powell (2014). "A systems approach to reduce urban rail energy consumption." Energy Conversion and Management **80**: 509-524.

Ian Hamilton, O. R. (2020). United Nations Environment Programme (2020). 2020 Global Status Report for Buildings and Construction: Towards a Zero-emission, Efficient and Resilient Buildings and Construction Sector. Nairobi, UCL, GlobalABC.

Lucchi, E., M. Tabak and A. Troi (2017). "The "Cost Optimality" Approach for the Internal Insulation of Historic Buildings." Energy Procedia **133**: 412-423.

Mazzarella, L. (2015). "Energy retrofit of historic and existing buildings. The legislative and regulatory point of view." Energy and Buildings **95**: 23-31.

Moran, F., T. Blight, S. Natarajan and A. Shea (2014). "The use of Passive House Planning Package to reduce energy use and CO2 emissions in historic dwellings." Energy and Buildings **75**: 216-227.

Mukhopadhyay, J., J. Ore and K. Amende (2019). "Assessing housing retrofits in historic districts in Havre Montana." Energy Reports **5**: 489-500.

Ozbalta, T. G., Y. Yildiz, I. Bayram and O. C. Yilmaz (2021). "Energy performance analysis of a historical building using cost-optimal assessment." Energy and Buildings **250**: 111301.

Qu, K., X. Chen, Y. Wang, J. Calautit, S. Riffat and X. Cui (2021). "Comprehensive energy, economic and thermal comfort assessments for the passive energy retrofit of historical buildings - A case study of a late nineteenth-century Victorian house renovation in the UK." Energy **220**: 119646.

Şahin, C. D., Z. D. Arsan, S. S. Tunçoku, T. Broström and G. G. Akkurt (2015). "A transdisciplinary approach on the energy efficient retrofitting of a historic building in the Aegean Region of Turkey." Energy and Buildings **96**: 128-139.

Seddiki, M., K. Anouche, A. Bennadji and P. Boateng (2016). "A multi-criteria group decision-making method for the thermal renovation of masonry buildings: The case of Algeria." Energy and Buildings **129**: 471-483.

Tadeu, S., C. Rodrigues, A. Tadeu, F. Freire and N. Simões (2015). "Energy retrofit of historic buildings: Environmental assessment of cost-optimal solutions." Journal of Building Engineering **4**: 167-176.

Thomsen, K. E., J. Rose, O. Mørck, S. Ø. Jensen, I. Østergaard, H. N. Knudsen and N. C. Bergsøe (2016). "Energy consumption and indoor climate in a residential building before and after comprehensive energy retrofitting." Energy and Buildings **123**: 8-16.

Tink, V., S. Porritt, D. Allinson and D. Loveday (2018). "Measuring and mitigating overheating risk in solid wall dwellings retrofitted with internal wall insulation." Building and Environment **141**: 247-261.

Trotta, G. (2019). "Assessing energy efficiency improvements, energy dependence, and CO2 emissions in the European Union using a decomposition method." Energy Efficiency **12**(7): 1873-1890.

#102: Sustainable energy technologies for sustainable agriculture: a review of current status and prospects for future challenges

Salih DINÇEL[1], Seçil Pelin AKA[2]

[1] Halic University, 34060 Eyup/Istanbul, salihdincel@halic.edu.tr
[2] Halic University, 3406 Eyup/Istanbul, secilpelinaka@halic.edu.tr

Abstract: Despite optimistic policies protecting agricultural lands for production both globally and specifically in Turkey, it draws attention to the fact that agricultural land areas are decreasing day by day and these policies are insufficient. While there are direct effects from the protection of agricultural lands, such as efficient use of such land and safeguarding from development, there are also indirect effects like change of climatic conditions and the protection and development of renewable energy-oriented agricultural lands. However, reasons such as insufficient collective effort and sensitivity in the current climate crisis, greenhouse gas emissions, and sudden seasonal changes increase the need for sustainable and renewable energy technologies.

This study aims to reveal the impact of renewable energy technologies on agricultural lands on the basis of innovation diffusion theory. By examining the dynamics of the sustainable energy technologies market in Turkey, it aims to reveal their use in agricultural lands and the adoption approaches of the users. These purposes will be explained with the use of secondary data over time series. Thus, it is aimed to present how renewable energy technologies are used in the agricultural sector, one of the most competitive areas in Turkey, their effects and application suggestions for the future.

Keywords: farmland; renewable energy; population; climate change

1. INTRODUCTION

One of the most important problems facing countries for economic and social development is to provide a cheap, clean, reliable, and easily obtainable energy source (Öztürk, 2021). Compared to the current situation, it is predicted that energy consumption will increase by 60% globally and by more than 100% in Turkey by 2030 (Satman, 2007). The increase in population and energy needs will be reflected on agricultural production. However, energy is also used directly in the agricultural production system. At this point, systems compatible with nature must support development and become a part of permanent growth and sustainability.

Agricultural lands, where crop production and animal husbandry activities are carried out, are a production resource and agricultural lands should be considered as a source of power in terms of sustainability (Lowder, 2021; BM, 2010; Li, 2017). There are 5 billion hectares of usable agricultural land in the world (World Bank, 2021) and in Turkey, there are 37,762 million hectares of agricultural land according to 2021 data (TUIK, 2021). However, agricultural land is decreasing both in Turkey and globally and there are fundamental reasons for this change. First, there is uncontrolled population growth in the world and in Turkey, and future projections reveal an ongoing situation. Unplanned settlements and urbanisation are one of the most important reasons that spoil and invade agricultural lands. In addition, studies have shown that increased greenhouse gas emissions will cause an increase in air temperature of around 1.5°C on average (IPCC, 2019; IEA, 2019) and will damage agricultural lands both now and in the future (Bayrac and Doğan, 2015). Studies have shown that it is possible to reduce the amount of gases which cause the greenhouse effect by making some changes in the production and use of energy (Öztürk, 2021).

According to the 2nd Special Study Report of the Intergovernmental Panel on Climate Change (IPCC) adopted in 2019, it has been stated that the air temperature on land has increased by approximately 1.5°C from the industrial revolution to the present day. If no measures are taken, it is estimated that the average temperature will increase by 1.8 - 4.0°C in 2100, even in the most favourable scenario (IPCC, 2019). The energy needs of the world increases by about 4-5% every year and it is known that the fossil fuel reserves are decreasing (Görez and Alkan, 2005).

2. RENEWABLE ENERGY SOURCES AND APPLICATION EXAMPLES ON AGRICULTURAL LANDS

Renewable energy sources and their use on agricultural lands differ widely (Şenpınar and Gençoğlu, 2016). Hydro Energy/Hydro Electricity generation power plants, which can prevent floods and overflows of dams and at the same time balance energy supply and demand by adjusting water amounts, stand at an important point among renewable energy sources that can be of use in agricultural lands (Uğur, 2000). Another renewable energy source is solar power plants: in addition to solar water heaters, which have become quite common, the construction of buildings that are heated by the sun, the conversion of solar energy to electricity, the use of solar water pumps in agricultural irrigation, the use of solar energy in the production of hydrogen from water - which is the fuel of the future – are all uses for solar energy (Gençoğlu and Cebeci, 2000). Solar power plant systems are used to mitigate the increasing fuel costs of irrigation agricultural lands that are far from electricity network lines (Taşkın and Vardar, 2016). At the same time, the availability of solar-powered sprayers have helped with costs. With solar-powered back pumps, pesticides can be applied in liquid form and a free energy system has been achieved instead of a fuel-based system (Joshua *et al.*, 2010). In addition, solar energy is applied in a balanced and conscious way for plant protection (Demir, 2005). It was realised that by replacing the air inside the greenhouse with the outside air, the movement of the air and the development of plant respiration takes place with the help of solar energy (Öztürk, 2006). With the solar-powered fence system, large herds of animals can be kept together, and predators that may harm production can be excluded. The generation of wind energy is possible on agricultural lands by installing wind turbines on the high points of hills. Also, thanks to the use of geothermal power plants, the consumption of fossil fuels and the greenhouse effect arising from their use together with the harmful effects caused by the discharge of acid rain gases into the atmosphere are decreasing. In modern geothermal power plants, there are reinjection systems that take the non-condensable gases from the steam and return them underground together with the used geothermal fluid. Nothing is thrown away or wasted by these geothermal power plants and geothermal heating systems (Güney and Karatepe, 2001).

Another important renewable energy source on agricultural land is bio-energy. Agricultural plants and wastes, industrial wood and log wastes, farm animal wastes and local organic matter wastes are sources of biomass (Saraçoğlu, 2004). In addition, the remaining waste following production is used as enriched fertilizer. Within the framework of the main title of agricultural development, the adaptation of agricultural products to the industry, creating a multiplier effect in agricultural development, reducing the environmental damage caused by fossil fuels, reducing the risks of exhaust emissions in terms of health, reducing foreign dependence on energy, being a safe fuel, finding solutions to the fossil fuel crises, reducing global warming, preventing the expansion of the ozone layer, being an independent fuel in war and mandatory situations, the advantage of not being a dangerous substance during transportation and storage are among the reasons that bring bioenergy to the agenda (Gizlenci, Acar and Şahin, 2012). The environmental damage caused by fossil fuels can be further reduced with carbon-free hydrogen energy (Ersöz *et al.*, 2001). Wave energy using the capacity of ocean waves (Aybers and Şahin, 1995) can alleviate energy problems of some countries and regions, as can nuclear energy and fusion energy (Parfit, 2005: 96), where a large part of the environment and alternative energy sources are provided by nuclear energy (Parfit, 2005: 96).

Renewable energy power plants (Efe and Kocaman, 2017) operating as hybrid energy production facilities using multiple energy types are among the renewable energy sources used on agricultural lands. Heat loss in greenhouses is very high, especially at night, and fossil fuel heating systems increase operating costs, therefore in regions with geothermal energy potential this source for greenhouse heating is favourable (Çanakçı and Acarer, 2010). The low depth of the geothermal energy source and the low temperatures (25-60°C) are the most suitable for greenhouse heating applications in terms of operation and maintenance. In this way, excavation and fluid pumping costs are reduced. In some applications, heat exchangers are used to provide heat transfer to the normal fluid (water) circulating in the greenhouse due to the chemical components in the geothermal fluid that cause corrosion (Yıldız, 2010). With geothermal energy, water can stay at a constant temperature (Günerhan, 2010; Erden, 2005).

In Turkey, between 2009-2019, the production of Wind+Solar+Geothermal+Biogas power plants excluding Hydro (Water) increased production by 13.5% of the total from 1.2% to 14.7% (TURKSTAT, 2021), while it increased from 8.7% to 11.2% in the rest of the world - 2.5% (WEC, 2021). Although Turkey is late according to the world trend, it was observed that Turkey has achieved a good output with the increase in recent years. It is important that this emerging trend is sustainable and continues. Obtaining electricity using nuclear power plants instead of fossil fuels is preferred in terms of preventing climate change and thus the destruction of agricultural lands. In Turkey, there is one nuclear power plant installation operating in Mersin (Aktaş, 2021; IAEA, 2022) and another is planned to be built in Sinop province (TC ÇŞİDB, 2021). Nuclear power plants are used extensively in Europe, Asia and America, and Turkey is late to benefit from such plants.

According to research conducted in Germany, the sale price of land around wind or bio gas power plants increase to a certain extent. When the power plant capacity doubled, land prices increased by about 0.4% (Myrna *et al.,* 2019). Another study conducted in England indicated that while trees and free-running animals were emphasized for naturalness in farmland and farm areas, renewable energy technology, trees and animal-free lands were perceived as the most "eco-friendly" use of farmlands, although wind turbines were not visually appealing (Rust *et al.*, 2021). In addition to the environmental aspects of a "Hybrid Renewable Energy System" proposed with the ready-made package program called HOMER, technical and economic research was emphasised to provide the highest energy capacity with the least land use and loss (Abid *et al.*, 2022).

Research revealed that in South Asia regional associations helped to attract investors to the region (Ghosh and Ghosh, 2018). However, there was still a lack of information and evidence to create an effective environment for the widespread use of renewable energy in the region (Gautam *et al.,* 2018). More research conducted in Japan suggested that the land be divided into 15 categories according to their location, usability and workability. In the same research, a study was conducted to establish solar power plants and wind power plants on the most inefficient lands specified (Obane *et al.*, 2020). Hatıra *et al.* (2005) revealed that there was an increase in the use of non-renewable energy in Turkish agriculture. At the same time, the researchers emphasised that new policy tools should be undertaken to ensure sustainability and efficient energy use.

The use of renewable energy in agriculture is becoming increasingly popular in Europe with government support. However, the reduction of state subsidies has had a devastating effect for poor agricultural economies in the face of unequal conditions such as quotas and restrictions where farmers had become dependent on state subsidies (Maroušek, 2013). Research conducted by Maroušek (2013) in the Czech Republic revealed that farmers do not care about ecological consequences. Among the reasons for this, it was assumed that the farmers were of a higher age.

In the last 10 years, rapid steps have been taken in the production of renewable energy in Turkey and in the world. While the production of Wind + Solar + Geothermal + Biogas power plants in Turkey in 2009 was 1.2% of the total production, this number was 14.7% in 2019 (TUIK, 2021). In the world, while the production of Wind + Solar + Geothermal + Biogas power plants was 8.7% of the total production in 2009, it increased to 11.2% in 2019. However, Turkey's 2020 "Renewable Energy Installed Power" was 25.58 MW in 2013, while renewable energy power plants increased by 100% to 49.58 MW in 2020 (TEİAŞ, 2021; TSKB 2021).

3. CONCLUSION

This study has tried to be explained within the framework of innovation diffusion theory. In the research conducted by Marangunić and Granić (2015) from 1986 to the present, the innovation acceptance theory was examined. The approach, which was derived from a psychology-based theory, has been discussed from different perspectives by different researchers with the development of technology. Chen *et al.* (2017) conducted research based on Technology Acceptance and Sustainable Energy Technology Acceptance Models. As a result of the research, it was determined that although the technological product was adopted at a low level, the technology was supported.

It is important to improve the investment environment, to keep the processes simple, to identify the problems faced by renewable energy investors in practice and to provide coordination and cooperation with the relevant institutions/organisations, to prepare and execute projects, and to implement and disseminate practices in the field of renewable energy.

The reason why energy consumption management in agriculture is a worldwide issue is because of the negative side effects caused by fossil fuels. The average temperature of the earth's surface is rising because of carbon dioxide and other greenhouse gases released by the use of fossil fuels. With this global warming, changes will be seen on the climatic characteristics of the world. For this reason, it is a priority requirement to introduce planned incentives for the use of green energy in order to protect today's energy availability in the agricultural sector and to prevent its negative effects on the environment. The widespread use of renewable energy sources in the agricultural sector will be beneficial for both socio-economic developments and sustainable agriculture.

4. REFERENCES

Abid, M. Z., Yousif, M., Ullah, S., & Hassan, M. 2022. Design, sizing and economic feasibility of a hybrid PV/diesel/battery based water pumping system for farmland. International Journal of Green Energy, 19(6), 614-637.

Aktaş, E. 2021. *Mersin Halkının Akkuyu Nükleer Santral Projesi ve Sektörel Etkileri Hakkındaki Görüşleri*. Journal of Applied And Theoretical Social Sciences, 3(2), 109-124.

Bayraç, H. N., & Doğan, E. 2016. *Türkiye'de iklim değişikliğinin tarım sektörü üzerine etkileri*. Eskişehir Osmangazi Üniversitesi İİBF Dergisi, 11(1), 23-48.

Boughali, S. Benmoussa, H. Bouchekima, B. Mennouche, D. Bouguettaia, H. and Bechki, D. 2009. *Crop drying by indirect active hybrid solar – Electrical dryer in the eastern Algerian Septentrional Sahara.* Solar Energy, 83: 2223–2232.

Chen, C. F., Xu, X., & Arpan, L. (2017). *Between the technology acceptance model and sustainable energy technology acceptance model: Investigating smart meter acceptance in the United States*. Energy research & social science, 25, 93-104Currie, D. J. 1993. *What shape is the relationship between body size and population density?*. Oikos, 353-358.

Çanakçı, C. ve Acarer, S. 2010. Jeotermal Enerji ile Sera Isıtma Sistemleri Tasarım Esasları.

Demir, C. 2005. Tekirdağ İli Tarım İşletmelerinde Kimyasal Savaşımda Kullanılan Bitki Koruma Alet Ve Makinelerinin Teknik Özellikleri Ve Uygulama Sorunlarının Saptanması Üzerine Bir Araştırma. Yüksek Lisans Tezi. Trakya Üniversitesi Fen Bilimleri Enstitüsü. Tekirdağ.

Efe, S. B., & Kocaman, B. 2017. *Yenilenebilir Enerji Kaynaklı Hibrit Sistemin Fiziksel Olarak Gerçeklenmesi ve Analizi*. In 5th International Symposium on Innovative Technologies in Engineering and Science 29-30 September 2017 (ISITES2017 Baku-Azerbaijan).

EİE, Elektrik İşleri Etüt İdaresi Genel Müdürlüğü. 2014. Rüzgar Enerjisi Su Pompalama Sistemleri Projesi.

Gizlenci, Ş., Mustafa, A. & Şahin, M. 2012. *Türkiye'de yenilenebilir enerji kaynaklarının (biyodizel, biyoetanol ve biyokütle) projeksiyonu*. Tarım Makinaları Bilimi Dergisi, 8(3), 337-344.

Gupta, J. G., De, S., Gautam, A., Dhar, A., & Pandey, A. 2018. Introduction to sustainable energy, transportation technologies, and policy. In Sustainable Energy and Transportation (pp. 3-7). Springer, Singapore.

Günerhan, H. 2010. Su Ürünleri Yetiştiriciliğinde Jeotermal Enerjiden Yararlanma. Url adress: http://www.mmo.org.tr/resimler/dosya_ekler/d8b65856ad9fc44_ek.pdf

Hatirli, S. A., Ozkan, B., & Fert, C. (2005). An econometric analysis of energy input–output in Turkish agriculture. *Renewable and sustainable energy reviews*, *9*(6), 608-623.

https://www.dunyaenerji.org.tr/2021-yenilenebilir-enerji-kuresel-durum-raporu-ozeti/

https://www.fao.org/home/en

https://www.tskb.com.tr/i/assets/document/pdf/enerji-sektor-gorunumu-2021.pdf

https://www.tuik.gov.tr/

IPCC. 2007. IPCC 4. Değerlendirme Raporu, (http://www.ipcc.ch).

IPCC. 2007. IPCC 4. Değerlendirme Raporu, (http://www.ipcc.ch).

IPCC. 2014. The Fifth Assessment Report (AR5), The Intergovernmental Panel on Climate Change, Geneva, Switzerland, (http://www.ipcc.ch.).

İAEA. 2022. https://pris.iaea.org/PRIS/CountryStatistics/CountryDetails.aspx?current=TR

Joshua, R. Vasu, V. and Vincent, P. 2010. *Solar Sprayer - An Agriculture Implement*. International Journal of Sustainable Agriculture, 2 (1): 16-19

Li, S., & Li, X. 2017. Global understanding of farmland abandonment: A review and prospects. Journal of Geographical Sciences, 27(9), 1123-1150.

Lowder, S. K., Sánchez, M. V., & Bertini, R. 2021. Which farms feed the world and has farmland become more concentrated?. World Development, 142, 105455.

Marangunić, N., & Granić, A. (2015). Technology acceptance model: a literature review from 1986 to 2013. Universal access in the information society, 14(1), 81-95.

Maroušek, J. (2013). Study on agriculture decision-makers behavior on sustainable energy utilization. Journal of agricultural and environmental ethics, 26(3), 679-689.

Myrna, O., Odening, M., & Ritter, M. (2019). The influence of wind energy and biogas on farmland prices. Land, 8(1), 19.

Obane, H., Nagai, Y., & Asano, K. 2020. Assessing land use and potential conflict in solar and onshore wind energy in Japan. Renewable Energy, 160, 842-851.

Öztürk, H. 2021. Yenilenebilir enerji kaynakları. Birsen Yayınevi, İstanbul.

Öztürk, H.H. 2006. *Tarımda Yenilenebilir Enerji Kaynaklarının Kullanımı*. http://www.emo.org.tr/ekler/85e48a43c7f63ac_ek.pdf

Rust, N. A., Rehackova, L., Naab, F., Abrams, A., Hughes, C., Merkle, B. G., ... & Tindale, S. (2021). What does the UK public want farmland to look like?. Land Use Policy, 106, 105445.

Satman, A. (2007). Türkiye'nin Enerji Vizyonu, Jeotermal Enerjiden Elektrik Üretimi Semineri, 3-18.

Şenpınar, A., & Gençoğlu, M. T. (2006). *Yenilenebilir Enerji Kaynaklarının Çevresel Etkileri Açısından Karşılaştırmasıl*. Fırat Üniversitesi Doğu Araştırmaları Dergisi, 4(2), 49-54.

T.C. ÇEVRE ŞEHİRCİLİK VE İKLİM DEĞİŞİKLİĞİ BAKANLIĞI. 2022. https://www.csb.gov.tr.

T.C. SAĞLIK BAKANLIĞI. 2021. https://saglik.gov.tr.

T.C. TARIM VE ORMAN BAKANLIĞI. 2022. https://www.tarimorman.gov.tr.

Taşkın, O., & Vardar, A. 2016. Tarımsal Üretimde Bazı Yenilenebilir Enerji Kaynakları Kullanımı. Uludağ Üniversitesi Ziraat Fakültesi Dergisi, 30(1), 179-184.

TMMOB.Ziraat Mühendisliği Odası. 2020. Türkiye Ziraat Mühendisliği VII. Teknik Kongresi. Bildiriler Kitabı-1, Ankara, 62-80.

TÜRKİYE İSTATİSTİK KURUMU. 2021. https://www.tuik.gov.tr/ (Erişim Tarihi:12.02.2022).

TÜRKİYE SINAİ KALKINMA BANKASI. 2021. https://www.tskb.com.tr.

Yıldız, M. 2010. Aydın İlindeki Jeotermal Enerji Kaynaklarının Sera Isıtmak Amacıyla Kullanımı Üzerine Bir Araştırma. Yüksek Lisans Tezi. Çukurova Üniversitesi Fen Bilimleri Enstitüsü. Adana.

#104: Experimental and numerical comparison of currently available reaction mechanisms for laminar flame speed in hydrogen/ammonia flames

A. Alnasif [1,2,*], S. Zitouni [3], S. Mashruk [1], P. Brequigny [3] M. Kovaleva [1]   C. Mounaim-Rousselle [3], A. Valera-Medina [1]

[1] College of Physical Sciences and Engineering, Cardiff University, Wales, CF243AA, UK, alnasifah@cardiff.ac.uk
[2] Engineering Technical College of Al-Najaf, Al-Furat Al-Awsat Technical University, Najaf, 31001, Iraq.
[3] Université Orléans, INSA-CVL, EA 4229 – PRISME, F-45072, France .

Abstract: The importance of ammonia as an alternative fuel for mitigating global warming emissions from the environment has become a growing topic in the research community. Due to the viability of ammonia as a hydrogen energy carrier, the molecule has encouraged considerable research towards its utilization as a combustion fuel. To understand the combustion characteristics of ammonia as a prospective fuel in internal combustion engines and gas turbines, the premixed laminar burning velocity of a binary fuel consisting of NH_3-H_2 has been investigated experimentally and numerically. A series of experiments using the spherical expanding flame set-up was employed to measure the laminar burning velocity of a $70NH_3/30H_2$ (%vol) blend of ammonia/hydrogen, at standard temperature and pressure across a wide range of equivalence ratios (0.8 – 1.4). ANSYS CHEMKIN-Pro software was used to perform an extensive numerical modelling analysis, appraising for 36 kinetic reaction mechanisms. Results show how some widely employed kinetic models were not able to accurately predict the Laminar flame speed, especially at leanest conditions. The kinetic mechanism of Duynslaegher et al. (2012) showed the ability to estimate lean conditions with minimal discrepancy and therefore has been identified as the best for estimation of premixed Laminar flame speed in such conditions. Meanwhile, the kinetic reaction mechanism of Nakamura et al. (2017) demonstrated a good estimation with a small error when the equivalence ratio varied from 1.2 and 1.4.

Keywords: ammonia; binary flames; kinetic modelling; laminar flame speed; reaction mechanisms

1. INTRODUCTION

Over the last century, the energy needs of our society have been largely supported by the abundance of cheap hydrocarbon-based fuels, accounting for nearly three-quarters of our global primary energy consumption (Ritchie and Roser, 2020). Declining indigenous resources coupled with the well-established environmental and ecological adversities resulting from hydrocarbon combustion have helped strive to focus on the study of alternative fuel sources (Riaz *et al.*, 2013). In this regard, ammonia (NH_3) has received a lot of attention lately (Chai *et al.*, 2021a; Valera-Medina *et al.*, 2018) as an efficient zero-carbon energy carrier. NH_3 offers higher gravimetric H_2 content than for example methanol, gasoline, and ethanol (Chatterjee *et al.*, 2021; Valera-Medina *et al.*, 2018) and can be synthesized from fossil fuels, or renewable energy sources coupled with an already mature infrastructure and storage system (Um *et al.*, 2014; Valera-Medina *et al.*, 2018). As such, NH_3 has became a promising alternative fuel with its utilization demonstrated in high-pressure energy systems such as industrial gas turbines and gas engines (Lhuillier *et al.*, 2021; Valera-Medina *et al.*, 2018, 2017). However, several combustion features of these flames require further understanding.

The Laminar flame speed is a fundamental physiochemical property of a premixed combustible mixture, resulting from the shared influence of mass and thermal diffusion of the reactants and mixture exothermicity (Law, 2006). The laminar flame speed reflects both the combustion process and a characterisation of a given fuel blend, rendering the laminar flame speed a key parameter in helping describe premixed operational instabilities (for example, flash-back, blow-off, and extinction). The laminar flame speed is defined as the velocity a steady one-dimensional adiabatic flame front propagates normal to itself in the doubly infinite domain. This definition renders the laminar flame speed particularly suitable for calculations in one-dimensional simulation which rely on thermodynamic and transport data, and thus by extension convenient in appraising and validating chemical kinetic mechanisms and models (Hu *et al.*, 2015; Law, 2006).

The laminar flame speed of NH_3 is very low, peaking at slightly rich conditions (equivalence ratio (Φ) of ~ 1.05-1.10), at a value of around 7cm/s (Chai *et al.*, 2021b). Such slow-burning velocities are often associated with low burning efficiencies in engines, potentially yielding poor flame stabilization resulting in local or global extinction. As such, to improve NH_3's combustion characteristics, blending with methane (CH_4) (Henshaw *et al.*, 2005; Pfahl *et al.*, 2000) or H_2 (Lee *et al.*, 2010), as well as oxy-combustion (Li *et al.*, 2015; Takeishi *et al.*, 2015) has been proposed. In this study, a NH_3-H_2 fuel mixture composition of 70%-30% (by vol.%) was chosen due to its stable performance in fuelling gas turbine combustors (Mørch *et al.*, 2011; Valera-Medina *et al.*, 2018). The addition of H_2 to NH_3 results in an increase in burning rate (Ichikawa *et al.*, 2015), enhanced reactivity of the mixture (Chen *et al.*, 2021), and widened flammability limits (Lhuillier *et al.*, 2020). However, the NH_3-H_2 fuel blend has several drawbacks, notably due to higher flame temperatures and abundance of radicals such as OH, O, and H, potentially causing an increase in NOx formation (Li *et al.*, 2017; Mei *et al.*, 2021b), a detrimental greenhouse gas pollutant.

Recently, significant efforts have been undertaken to establish kinetic models that are able to predict the combustion characteristics of NH_3-H_2 flames, including the commendable efforts to understand ammonia reaction chemistry from various groups worldwide (Glarborg *et al.*, 2018; Klippenstein *et al.*, 2018a; Shrestha *et al.*, 2021, 2018). The optimization process for NH_3-H_2 chemistry entails a specific understanding of the chemistry of each component of fuel and their interactions. Similarly, a chemical kinetic model has also been established by Mathieu and Petersen (2015) for ammonia oxidation based on experimental measurements taken inside a shock tube. The resulting mechanism has also been compared with 9 other kinetic mechanisms from the literature (Mathieu and Petersen, 2015). Glarborg *et al.* (2018) developed a comprehensive kinetic model including an overview of the most recent data in the kinetic modeling of ammonia combustion. The oxidation kinetic mechanism published by Shrestha *et al.* (2018) for pure ammonia and ammonia-hydrogen flames has also received considerable attention and been validated for a number of 0D and 1D energy systems. Li *et al.* (2019) led to the development of two reduced models for NH_3-H_2 and NH_3-CH_4-H_2 fuel mixtures. Similarly, many other research groups keep attempting to develop mechanisms that fully unravels the complexities of using ammonia blends with high accuracy for chemical and numerical studies.

As mentioned above, several numerical and experimental studies have been carried out to understand the combustion characteristics of NH_3-H_2 blends and their applicability in combustion-based systems. The present work deals with this problem by analyzing the Laminar flame speed of a highly stable 70%-30% (vol%) NH_3-H_2 binary fuel blend studied experimentally using a constant-volume spherical vessel, and numerically by modelling Laminar flame speed and comparing 36 currently used chemical kinetic mechanisms. This sheds light on the performance of these mechanisms and the key kinetic reactions that promote the laminar flame speed in the chemical kinetic environment for various equivalence ratios. The results denote the most accurate mechanisms for various combustion conditions, whilst directing efforts of future works to improve these models for further utilization.

2. METHODOLOGY

2.1. Experimental work

Laminar flame speed measurements were performed using a constant-volume spherical vessel (Figure 1). Details of the rig and post-processing technique can be found in Galmiche *et al.* (2012), updated for NH_3 specifications in

Lhuillier *et al.* (2020) and thus only a brief summary is presented here. The spherical vessel has a nominal internal volume of 4.2 L (ID 200mm), with four orthogonal 70mm quartz viewing windows with PID temperature control. High-speed Schlieren imaging of flame propagation was achieved using a CMOS high-speed camera (PHANTOM V1210) set to a suitable fast frame capture rate and facilitating a spatial resolution of ~0.1 mm per pixel. Flame propagation velocities were calculated by edge-detection algorithms written into a bespoke MATLAB script. Reactants were introduced into the chamber using batched thermal mass flow controllers (Brooks 5850S (±1%)). Mass fractions were calculated as a function of initial pressure (P), fuel-air equivalence ratio (Φ), and temperature (T), with mixture concentrations confirmed by partial pressure. Internal fans were used to pre-mix the reactants, and capacitor-discharge ignition was achieved via fine electrodes mounted to 45° to the measurement plane. Experiments were triggered by a simultaneous TTL signal to the ignition system and data acquisition systems after quiescence had been attained. High-

Figure 1: Schematic of Constant Volume Combustion Vessel

purity fuel components of H_2 (>99.95%) and NH_3 (99.95%) and dried compressed air were used to perform the experiments. Measurements were performed at initial conditions of 298 K (± 3K) and 0.1MPa (± 1x10-3Mpa).
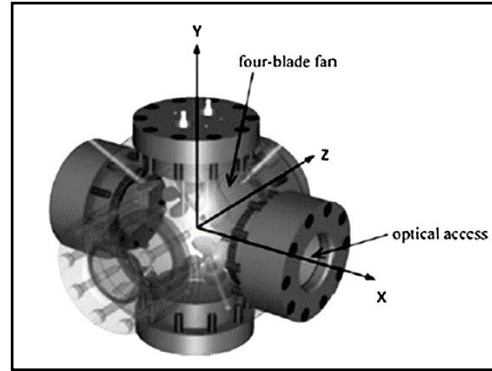
To investigate the influence of H_2 on NH_3 flame propagation, spherically expanding flame experiments were conducted for a set molar ratio of H_2 (30%, vol), evaluated across a wide range of equivalence ratio (Φ), to provide a comparison of the change in flame speed from lean to rich conditions. Schlieren measurements were undertaken to evaluate the laminar flame speed relative to the burned side and were experimentally determined by employing the same procedure as in previous studies (Lhuillier *et al.*, 2020; Zitouni *et al.*, 2022). Figure 2 illustrates an example of images underlining the quality of images taken using the Schlieren optical set-up.
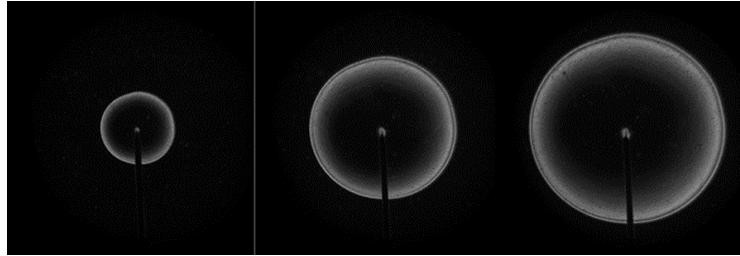

Figure 2: Temporal evolution of a spherically expanding flame using Schlieren imaging

For an outwardly propagating flame, the stretched flame speed (S_n) is expressed as the temporal derivative of the Schlieren flame radius (r_{sch}) as per Equation 1:

$$S_n = \frac{dr_{sch}}{dt}$$

(Equation 1)

A quasi-steady non-linear association between S_n and stretch as proposed by Kelley and Law (2009) was utilized to obtain an extrapolated unstretched flame speed (S_b) that allowed for arbitrary Lewis Number and accounts for deviations in adiabatic and planar assumptions prominent in flames which are heavily influenced by stretch such as lean H_2-based flames. To obtain an extrapolated unstretched flame speed, a quasi-steady non-linear association between S_n and α was employed (as in Equation 2), re-arranged with the error used for least square regression:

$$\left(\frac{S_n}{S_b}\right)^2 \cdot In\left(\frac{S_n}{S_b}\right)^2 = -\frac{2 \cdot L_b \cdot \alpha}{S_b}$$

(Equation 2)

Irrespective of the extrapolation methodology employed, to obtain representative values of laminar flame speed, the burned gas expansion must be factored as $U_L = S_b \cdot (\rho_b/\rho_u)$ with ρ_b and ρ_u, burnt and unburnt gases densities calculated using CHEMKIN-Pro.

Substantial efforts are being made to improve the accuracy of reaction mechanisms which depend on accurate laminar flame speed measurements (Chen, 2015). Uncertain quantification for the present measurements relies upon the methods outlined by Moffat (1988) employing a combination of the experimental facility specification and accuracy of the processing techniques chosen. It should be noted that the uncertainty was quantified for the unstretched flame speed (S_b), (and not as opposed to LBV itself), since this is the parameter measured. The total uncertainty estimate is given by Equation 3, where (B_{Sb}) represents the total bias uncertainty, ($t_{M-1,95}$) the student's t value at 95% confidence interval and M-1 degrees of freedom, (σ_{Sb}) is the standard deviation of the repeated experiments, and (M) the number of experimental repeats at each condition (Brequigny *et al.*, 2019; Lhuillier *et al.*, 2020):

$$U_{Sb} = \sqrt{B_{Sb}^2 + \left(\frac{t_{M-1,95}\sigma_{Su}}{\sqrt{M}}\right)^2}$$

(Equation 3)

The total bias uncertainty, given by Equation 4, relates changes in S_b with respect to an independent influential variable vi (i.e. temperature, ambient pressure, Φ) and the fixed error linked to that variable -yi-.

$$B_{Sb} = \sqrt{\sum_{i=1}^{n} \left(\frac{\partial S_b(v_i)}{\partial v_i} y_i \right)^2}$$

(Equation 4)

In order to employ Equation 4, the relationships between S_b and each independent variable must be established. The potential changes in S_b from several parameters were calculated as a function of Φ; such as temperature (±3 K), and pressure (±1 x 10^{-3} MPa), with the relationship proposed by Chen (2015) employed to evaluate the uncertainty in global Φ. Data modelling employing CHEMKIN-PRO was utilised to estimate these profiles. Uncertainty resulting from the optical system was evaluated from the summated fractional error of both the spatial resolution of the system (±0.05/25mm) and camera (± 1.5/3000fps). Additionally, Wu *et al.* (2015) quantified the uncertainty in extrapolation, with corresponding MalinKamid values for data presented in this work falling within the recommended range of -0.05 – 0.15. Accordingly, error bars on all subsequent plots illustrating laminar flame speed measurements were derived from Equations 3 and 4, with the error for U$_{Su}$ scaled with respect to the density ratio. A minimum of 5 repeats were conducted per each experimental condition.

2.2. Kinetic modelling

The analysis of 36 kinetic reaction mechanisms were performed by ANSYS CHEMKIN-PRO software. A premixed laminar flame-speed calculation model was applied for all reaction mechanisms. The numerical calculations for all model tests were done in a one-dimensional computational domain of length 10cm, with a maximum grid size of 5000. The adaptive grid control based on solution gradient and curvature was set to 0.02. The grid dependency was taken into account and the accuracy for all cases was tested and adjusted to give precise results. Table 1 illustrates each mechanism's details regarding the number of reactions and species adopted.

Table 1: Chemical kinetic mechanisms used in the present work

NO.	Kinetic mechanisms reference	No. of Reactions	No. of species	NO.	Kinetic mechanisms reference	No. of Reactions	No. of species
1	(Bertolino *et al.*, 2021)	264	38	19	(U. Mechanism, 2018)	41	20
2	(Mei *et al.*, 2021a)	264	38	20	(Klippenstein *et al.*, 2018b)	211	33
3	(Han *et al.*, 2021)	298	36	21	(Nakamura *et al.*, 2017)	232	33
4	(Mei *et al.*, 2021b)	257	40	22	(Zhang *et al.*, 2017)	251	44
5	(Gotama *et al.*, 2022)	119	26	23	(Lamoureux *et al.*, 2016)	934	123
6	(Shrestha *et al.*, 2021)	1099	125	24	(Xiao *et al.*, 2016)	276	55
7	(Wang *et al.*, 2021)	444	91	25	(Song *et al.*, 2016)	204	32
8	(Zhang *et al.*, 2021)	263	38	26	(Nozari and Karabeyoǐlu, 2015)	91	21
9	(Arunthanayothin *et al.*, 2021)	2444	157	27	(Mathieu and Petersen, 2015)	278	54
10	(Stagni *et al.*, 2020)	203	31	28	(Duynslaegher *et al.*, 2012)	80	19
11	(Han *et al.*, 2019b)	177	35	29	(Klippenstein *et al.*, 2011)	202	31
12	(De Persis *et al.*, 2020)	647	103	30	(Zhang *et al.*, 2011)	701	88
13	(Mei *et al.*, 2019)	265	38	31	(Lamoureux *et al.*, 2010)	883	119
14	(Li *et al.*, 2019)	957	128	32	(Konnov, 2009)	1207	127
15	(Okafor *et al.*, 2019)	356	59	33	(Mendiara and Glarborg, 2009)	779	79
16	(Glarborg *et al.*, 2018)	231	39	34	(Tian *et al.*, 2009)	703	84
17	(Shrestha *et al.*, 2018)	1081	124	35	(Dagaut *et al.*, 2008)	250	41
18	(Otomo *et al.*, 2018)	213	32	36	(Smith *et al.*, 2000)	325	53

3. RESULTS AND DISCUSSION

This section addresses the Laminar flame speed modelled by 36 kinetic reaction mechanisms, compared to the experimental results conducted in the present study. To determine the best performing kinetic mechanism for predicting the laminar flame speed of NH_3/H_2 flames at atmospheric conditions, the absolute percentage error (APE) function was adopted (Armstrong and Collopy, 1992) to calculate the error percentage between the predicted numerical data and experimental results for various equivalence ratios (lean and rich conditions).

3.1. Lean condition flames

Figure 3 shows that Duynslaegher's model provided good agreement with experimental results with an error equal to approximately 2% followed by that of Song, Klippenstein, and Nakamura with around 4% of relative error for each mechanism. For an equivalence ratio of 0.8, Lamoureux *et al.* (2010) mechanism demonstrated to be the best mechanism in the estimation of laminar flame speed with a minor error of just 1%. On the other side, the relative error for Duynslaegher was recorded at around 6%, as illustrated in Figure 3. When the equivalence ratio was at stoichiometry, Duynslaegher was the best performing mechanism with 0% relative error. Therefore, the Duynslaegher mechanism showed an excellent prediction for the laminar flame speed measurement not only in the stoichiometric conditions but also along with the lean conditions (0.6-1.0).
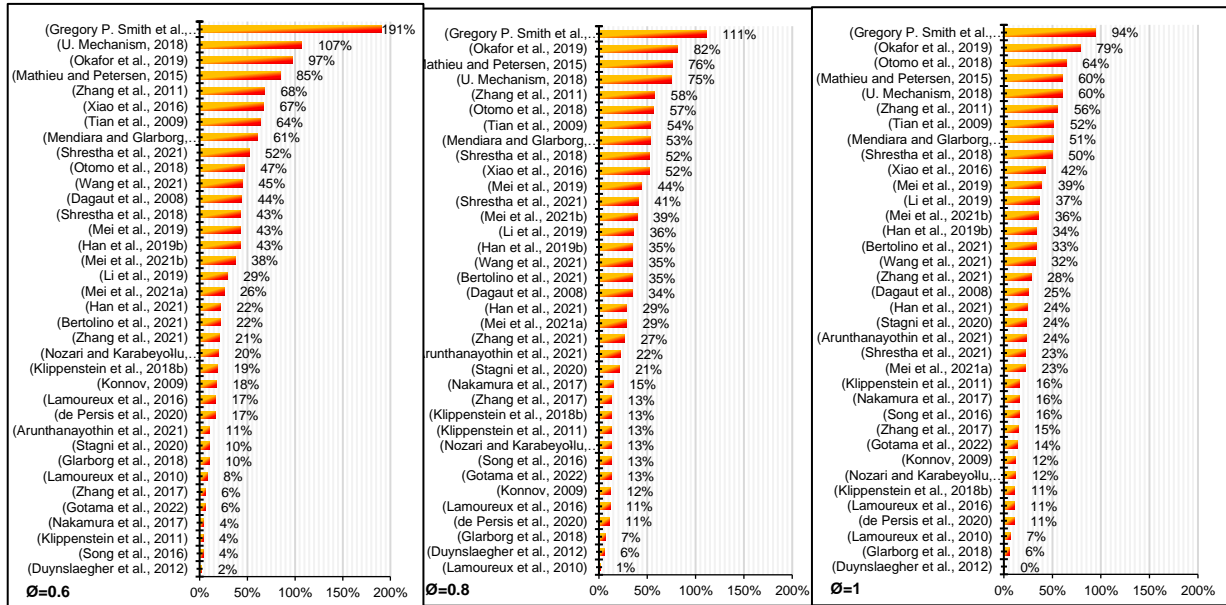
Ø=0.6

Mechanism	Relative error
(Gregory P. Smith et al.,	191%
(U. Mechanism, 2018)	107%
(Okafor et al., 2019)	97%
(Mathieu and Petersen, 2015)	85%
(Zhang et al., 2011)	68%
(Xiao et al., 2016)	67%
(Tian et al., 2009)	64%
(Mendiara and Glarborg,	61%
(Shrestha et al., 2021)	52%
(Otomo et al., 2018)	47%
(Wang et al., 2021)	45%
(Dagaut et al., 2008)	44%
(Shrestha et al., 2018)	43%
(Mei et al., 2019)	43%
(Han et al., 2019b)	43%
(Mei et al., 2021b)	38%
(Li et al., 2019)	29%
(Mei et al., 2021a)	26%
(Han et al., 2021)	22%
(Bertolino et al., 2021)	22%
(Zhang et al., 2021)	21%
(Nozari and Karabeyollu,	20%
(Klippenstein et al., 2018b)	19%
(Konnov, 2009)	18%
(Lamoureux et al., 2016)	17%
(de Persis et al., 2020)	17%
(Arunthanayothin et al., 2021)	11%
(Stagni et al., 2020)	10%
(Glarborg et al., 2018)	10%
(Lamoureux et al., 2010)	8%
(Zhang et al., 2017)	6%
(Gotama et al., 2022)	6%
(Nakamura et al., 2017)	4%
(Klippenstein et al., 2011)	4%
(Song et al., 2016)	4%
(Duynslaegher et al., 2012)	2%

Ø=0.8

Mechanism	Relative error
(Gregory P. Smith et al.,	111%
(Okafor et al., 2019)	82%
(Mathieu and Petersen, 2015)	76%
(U. Mechanism, 2018)	75%
(Zhang et al., 2011)	58%
(Otomo et al., 2018)	57%
(Tian et al., 2009)	54%
(Mendiara and Glarborg,	53%
(Shrestha et al., 2018)	52%
(Xiao et al., 2016)	52%
(Mei et al., 2019)	44%
(Shrestha et al., 2021)	41%
(Li et al., 2019)	39%
(Han et al., 2019b)	35%
(Wang et al., 2021)	35%
(Bertolino et al., 2021)	35%
(Dagaut et al., 2008)	34%
(Han et al., 2021)	29%
(Mei et al., 2021a)	29%
(Arunthanayothin et al., 2021)	22%
(Stagni et al., 2020)	21%
(Nakamura et al., 2017)	15%
(Zhang et al., 2017)	13%
(Klippenstein et al., 2018b)	13%
(Klippenstein et al., 2011)	13%
(Nozari and Karabeyollu,	13%
(Song et al., 2016)	13%
(Gotama et al., 2022)	13%
(Konnov, 2009)	12%
(Lamoureux et al., 2016)	11%
(de Persis et al., 2020)	11%
(Glarborg et al., 2018)	7%
(Duynslaegher et al., 2012)	6%
(Lamoureux et al., 2010)	1%

Ø=1

Mechanism	Relative error
(Gregory P. Smith et al.,	94%
(Okafor et al., 2019)	79%
(Otomo et al., 2018)	64%
(Mathieu and Petersen, 2015)	60%
(U. Mechanism, 2018)	60%
(Zhang et al., 2011)	56%
(Tian et al., 2009)	52%
(Mendiara and Glarborg,	51%
(Shrestha et al., 2018)	50%
(Xiao et al., 2016)	42%
(Mei et al., 2019)	39%
(Li et al., 2019)	37%
(Mei et al., 2021b)	36%
(Han et al., 2019b)	34%
(Bertolino et al., 2021)	33%
(Wang et al., 2021)	32%
(Zhang et al., 2021)	28%
(Dagaut et al., 2008)	25%
(Han et al., 2021)	24%
(Stagni et al., 2020)	24%
(Arunthanayothin et al., 2021)	24%
(Shrestha et al., 2021)	23%
(Mei et al., 2021a)	23%
(Klippenstein et al., 2011)	16%
(Nakamura et al., 2017)	16%
(Song et al., 2016)	16%
(Zhang et al., 2017)	15%
(Gotama et al., 2022)	14%
(Konnov, 2009)	12%
(Nozari and Karabeyollu,	12%
(Klippenstein et al., 2018b)	11%
(Lamoureux et al., 2016)	11%
(de Persis et al., 2020)	11%
(Lamoureux et al., 2010)	7%
(Glarborg et al., 2018)	6%
(Duynslaegher et al., 2012)	0%

Figure 3: The relative error for 36 kinetic mechanisms for an equivalence ratio range of 0.6-1.0 (lean conditions)

Figure 4 shows the laminar flame speed of the kinetic mechanisms with the lowest error, compared to experimental measurements for the full range of equivalence ratios. As can be seen from Figure 4, the mechanisms of Glarborg, Lamoureux, and Duynslaegher gave a good agreement with the experimental measurements in the lean conditions. In spite of there being an underestimation of the laminar flame speed when the equivalence ratio was equal to 0.8, the mechanism of Duynslaegher had a minimum level of discrepancy against the experimental data. The Lamoureux mechanism had good performance at lean conditions and gave only a slight underestimate of laminar flame speed at an equivalence ratio of 0.6, with the error increasing at stoichiometry to give an overestimate of around 7% compared to experimental measurements. The Glarborg kinetic model had a consistent trend line along with the experimental results with an overestimation value for the laminar flame speed between 6% to 10% and for all lean conditions. Finally, the Gotama model showed peak divergence at stoichiometry, but performed fairly well at rich and lean equivalence ratio conditions.
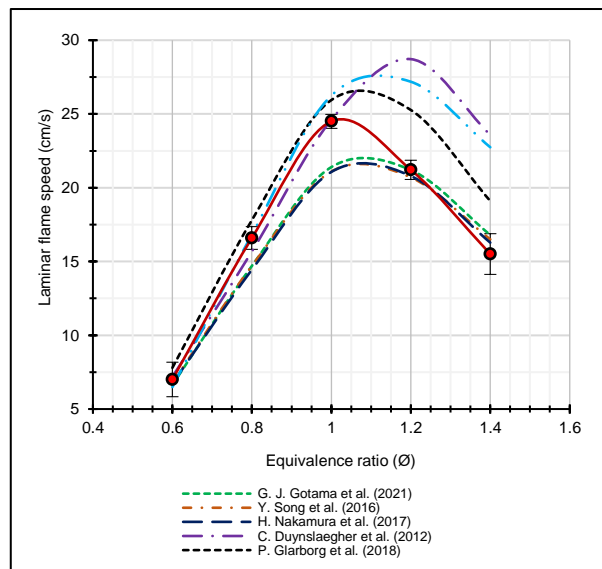
Figure 4: The laminar flame speed for NH$_3$-H$_2$ flames predicted by the six best kinetic reaction mechanisms for the full range of equivalence ratios (0.6-1.4).

Legend (Figure 4):
- G. J. Gotama et al. (2021)
- Y. Song et al. (2016)
- H. Nakamura et al. (2017)
- C. Duynslaegher et al. (2012)
- P. Glarborg et al. (2018)

To analyse the flame speed sensitivity of NH$_3$-H$_2$ mixtures, three kinetic reaction mechanisms were selected (Gotama, Duynslaegher, and Glarborg) based on their performance in lean to stoichiometric equivalence ratios. These mechanisms were chosen because the mechanism of Glarborg slightly overestimated the Laminar flame speed, and the Gotama mechanism slightly underestimated the Laminar flame speed, while the kinetic mechanism of Duynslaegher was inbetween both, with the lowest error of all.

As shown in Figure 5, each of the bar charts presents the most 10 important reactions in the above selected kinetic mechanisms tested for NH_3-H_2 flames. Since the mechanism of Duynslaegher had a better prediction of the experimental data of laminar flame speed and with a minimum level of error values between 0% to 2% in the full range of the lean condition, the reaction 'NH+H_2O↔HNO+H_2' recorded a high level of sensitivity and resulted as the second most important kinetic reaction in the promotion of the flame speed in NH_3-H_2 blends in the Duynslaegher reaction model, with sensitivity coefficient values between 0.12 and 0.4 in the lean conditions. It was also noticed that this reaction was missing in the database of both Glarborg and Gotama mechanisms. Instead, the previous mechanisms demonstrated the reaction 'NH+O_2↔HNO+O' as one of the three most effective reactions in the range of 0.6 and 0.8 of the equivalence ratio.

At an equivalence ratio of 0.6, all three kinetic mechanisms presented the chemical reaction 'NH_2+OH↔NH+H_2O' as a dominant reaction having high sensitivity. Also the sensitivity coefficient values of the mentioned reaction differed from one mechanism to another, where the Glarborg mechanism gave a high level followed by Duynslaegher and Gotama respectively. This was because of the variation of Arrhenius parameters such as rate constant.
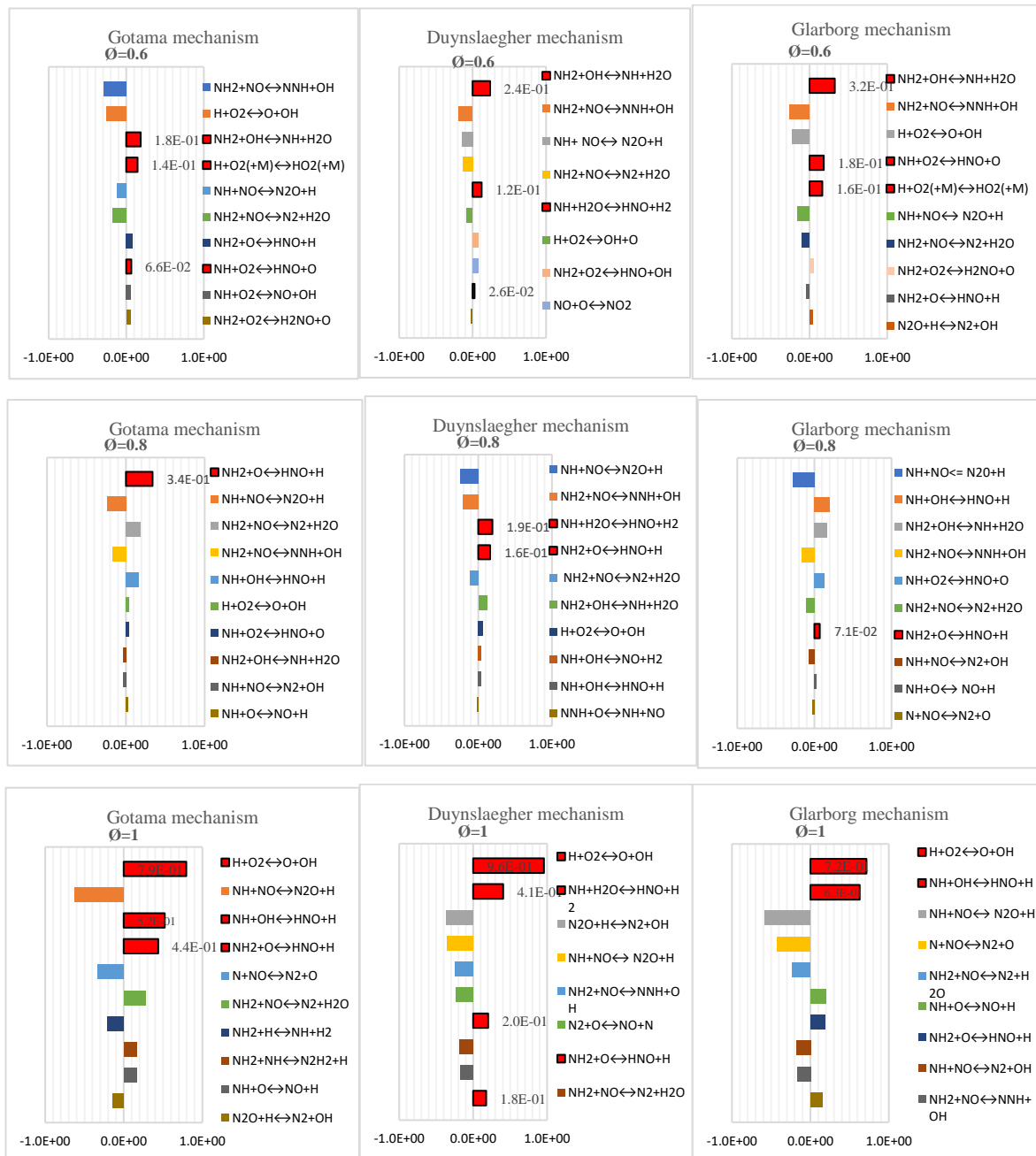
Figure 5: Sensitivity analysis for laminar flame speed of 70NH₃/30H₂ (vo;%) under atmospheric conditions and for three kinetic mechanisms (Gotama et al. 2022, Duynslaegher et al. 2012, and Glarborg et al. 2018) that give a minimum discrepancy value at a lean range of equivalence ratio of 0.6-1.0. Critical reactions for the laminar flame speed are marked in red colour.

As shown in Table 2, the kinetic reaction 'NH$_2$+OH↔NH+H$_2$O' estimated by Gotama had large temperature dependence because of its large value of activation energy, while the same reaction that had been listed in both Duynslaegher and Glarborg mechanism database showed low-temperature dependency due to low activation energy. So, the fact that most kinetic reactions were temperature dependent might be the reason behind the discrepancy matter in the prediction of laminar flame speed from one mechanism to another. Also, the difference in which kinetic reactions were included substantially affected the performance of the kinetic mechanism.

At stoichiometric conditions, Duynslaegher mechanism gave an excellent prediction of Laminar flame speed, with an error percentage equal to 0%. As can be seen from Figure 5, in addition to the kinetic reaction 'NH+H$_2$O↔HNO+H$_2$' mentioned previously, the Duynslaegher reaction model presented another reaction 'NH+OH↔NO+H$_2$'. This was also the case of the Gotama and Glarborg mechanisms but they did not list this kinetic reaction among the ten most important reactions of laminar flame speed. Rather, both mechanisms introduced the kinetic reaction 'NH$_2$+OH↔HNO+H' as the second important reaction for the promotion of laminar flame speed in stoichiometric conditions. Furthermore, All kinetic models demonstrated a substantial activity of the reaction 'H+O$_2$↔O+OH', Therefore, this reaction could be considered the dominant kinetic reaction in the laminar flame speed of NH$_3$-H$_2$ flames when the blend met the stoichiometric conditions. That the sensitivity coefficient values for the same kinetic reaction were varied because of the difference in Arrhenius parameters was also noticed. As seen in Table 2, the reaction 'H+O$_2$↔O+OH' was a temperature-dependent reaction and its activity was controlled by the activation energy value where Dyunslaegher mechanism had higher sensitivity coefficient compared to Gotama and Glarborg kinetic mechanisms due to the low activation energy value of this reaction, which was listed in the database of the Duyenslaegher mechanism.

Table 2: Key reactions for NH$_3$-H$_2$ flames generated from Gotama, Duynslaegher, and Glarborg mechanisms

NO.	Reaction	Gotama *et al.* (2022)			Duynslaegher *et al.* (2012)			Glarborg *et al.* (2018)		
		A	n	E	A	n	E	A	n	E
1	NH$_2$+OH↔NH+H$_2$O	9.60E+06	2	669	9.00E+07	1.5	-460	3.30E+06	1.90	-217
2	H+O$_2$(+M) ↔HO$_2$(+M)	4.65E+12	0.4	0	1.48E+12	0.6	0	4.70E+12	0.40	0
3	NH+O$_2$↔HNO+O	3.92E+13	0	17885	-	-	-	2.40E+13	0.00	13850

To see the effect of Arrhenius parameters on the laminar flame speed, the Rate of Reaction for the most effective chemical reactions has been plotted at 0.6 of the equivalence ratio. As shown in Figure 6, the reaction rate of NH$_2$+OH↔NH+H$_2$O, H+O$_2$(+M)↔HO$_2$(+M), and NH+O$_2$↔HNO+O predicted by the Glarborg mechanism were larger than those estimated by both Gotama and Duynslaegher mechanisms and this effect was also reflected on the temperature plots for the mentioned mechanisms, where the temperature profile estimated by Glarborg model reaction recorded a higher value than the other two reaction mechanisms at the position where maximum heat release rate took place. In addition to that, the peak values of the reaction rate for the mentioned reactions that were estimated by Gotama's mechanism nearly swept to the right compared with peak values for the same reactions calculated by Glarborg and Duynslaegher which were aligned. Further, the reaction rate profiles of 'H+O$_2$(+M)↔HO$_2$(+M)' for all three mechanisms gave the same trend, which was in spite of the peak values of this reaction taking place in the reaction zone, the kinetic reaction had the reaction continuous and in progress in the post flame region. Along with that, the reaction rate of the mentioned kinetic reaction predicted by the Duynslaegher mechanism rapidly decreased and reached almost zero around 5.13cm in comparison to the same kinetic reaction calculated by the Gotama and Glarbourg mechanisms that showed a higher reaction rate in the same location and decreased gradually to reach nearly zero above 5.3cm.
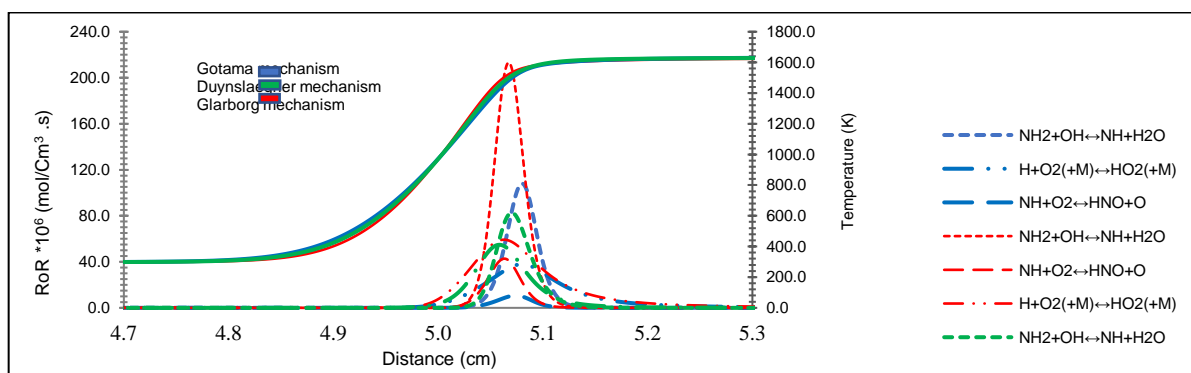

Figure 6: The reaction rate profiles of the key reactions and temperature profiles for NH$_3$-H$_2$ flames at Ø= 0.6.

3.2. Rich condition flames

Figure 7 refers to the relative error for laminar flame speed in the rich equivalence ratio range (1.2 and 1.4). As can be seen, the Nakamura mechanism gave a good estimate of flame speed with error values between 2% and 5% for 1.2 and 1.4 of Ø respectively. The Song mechanism had a similar performance, with some overestimation at 1.4

equivalence ratio. While Gotama's kinetic model provided an excellent estimate at Ø=1.2, this percentage was increased with increasing equivalence ratio to reach 8% at 1.4. Although Duynslaegher kinetic mechanism demonstrated a good estimation in the lean conditions, its performance deteriorated in the rich conditions with errors between 26% to 34%, as was highlighted in Figure 4.
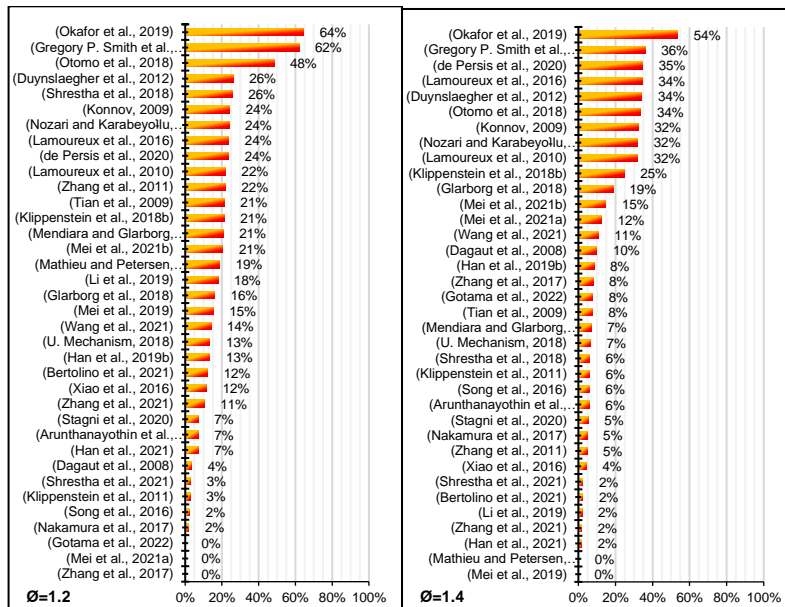

Figure 7: The relative errors for the laminar flame speed predicted by 36 kinetic reaction mechanisms under the rich condition of the equivalence ratio 1.2 and 1.4 respectively.

To analyse the origins of these discrepancies between the kinetic mechanisms at rich conditions, Figure 8 shows the sensitivity analysis of the laminar flame speed for rich conditions. When Ø=1.2, the Gotama and Song kinetic mechanisms presented the same most sensitive kinetic reactions for the laminar flame speed of NH_3-H_2 with nearly the same estimated sensitivity coefficients. $NH+OH \leftrightarrow HNO+H$ was the kinetic reaction on the top of the list with a higher positive value, while this reaction was in the second order in the Nakamura mechanism. Along with that, the Nakamura mechanism presented three kinetic reactions ($NH_3+H \leftrightarrow NH_2+H_2$, $NH_2+N \leftrightarrow N_2+2H$, and $2NH_2 \leftrightarrow N_2H_2+H_2$) that were not listed in either Gotama and Song reaction models.
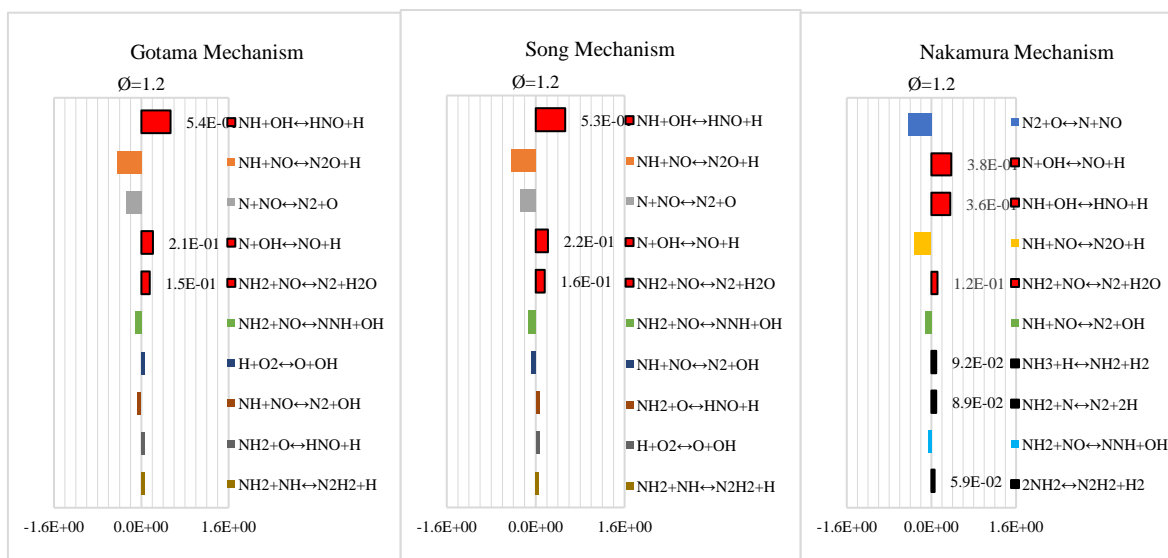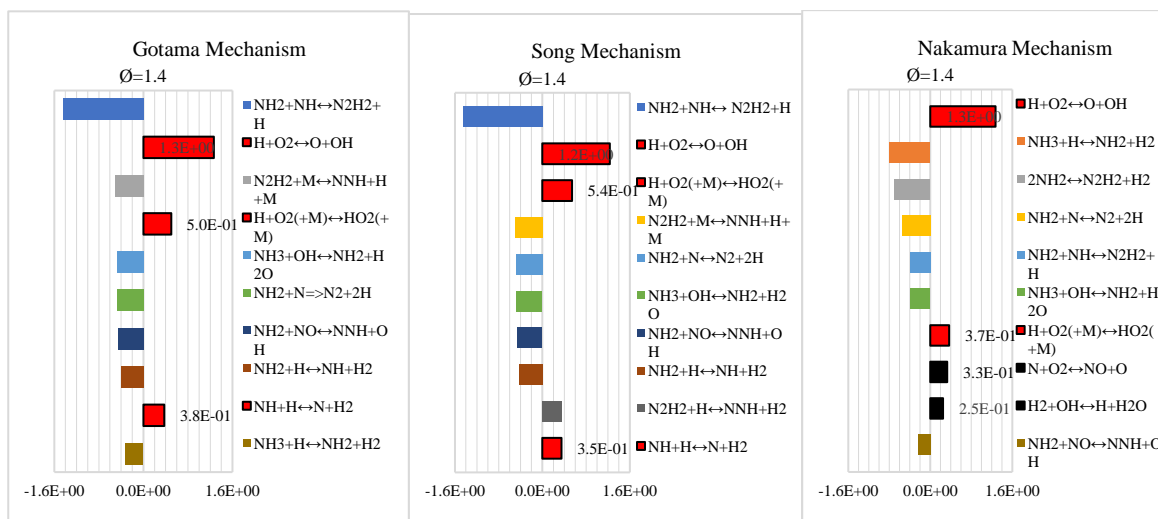

Figure 8 (part 1)

Figure 8 (part 2): Sensitivity analysis for laminar flame speed of 70NH3/30H2 (%vol) under atmospheric conditions and for three kinetic reaction mechanisms (Gotama, Song, and Nakamura) that give a minimum discrepancy value at a rich range of equivalence ratio of 1.2 -1.4. Critical reactions for the laminar flame speed are marked in red colour.

As can be noticed in Figure 8, the reaction models of Gotama, Song and Nakamura all overestimated the laminar flame speed under high rich conditions (Ø=1.4). However, the Nakamura kinetic model was the one that had a better prediction for the experimental data with a low discrepancy value. The sensitivity analysis for Nakamura kinetic model showed that $H+O_2 \leftrightarrow O+OH$ presented high positive sensitivity values among other 10 important kinetic reactions followed by $H+O_2(+M) \leftrightarrow HO_2(+M)$. A similar case was noticed in both Gotama and Song but with different values. Most importantly, the Nakamura mechanism showd the role of both $N+O_2 \leftrightarrow NO+O$ and $H_2+OH \leftrightarrow H+H_2O$ in the promotion of the flame speed in NH_3-H_2 mixtures. While the absence of the effect of the above-mentioned reactions in the other two mechanisms was apparent, both Gotama and Song's kinetic mechanisms showed the importance of $NH+H \leftrightarrow N+H_2$ with a sensitivity value between 0.35 and 0.38.

Table 3: Key reactions for the promotion of flame speed of NH_3-H_2 flames at rich conditions and for 3 kinetic mechanisms

NO.	Reaction	Gotama *et al.* (2022)			Song *et al.* (2016)			Nakamura *et al.* (2017)		
		A	n	E	A	n	E	A	n	E
1	$H+O_2 \leftrightarrow O+OH$	5.07E+15	-0.5	16126.7	1.00E+14	0	15286	1.04E+14	0	15286.0
2	$NH+H \leftrightarrow N+H_2$	3.01E+13	0	0	3.00E+13	0	0	1.00E+14	0	0
3	$H+O_2(+M) \leftrightarrow HO_2(+M)$	4.65E+12	0.4	0	4.70E+12	0.4	0	4.65E+12	0.4	0

To investigate the reasons behind the discrepancy among the kinetic mechanisms in estimating the flame speed, Figure 9 illustrates the reaction rate for the most important kinetic reactions affecting the laminar flame speed for the Gotama, Song and Nakamura kinetic mechanisms in terms of temperature and distance for Ø =1.4. The Figure shows that the kinetic reaction $H+O_2 <=> O+OH$, which was governed by the Gotama mechanism, gave the maximum value of reaction rate compared with Song and Nakamura. Along with that, this type of reaction was highly dependent on temperature, as shown in Table 3. Further, as the Gotama mechanism presented a higher reaction rate for $H+O_2 <=> O+OH$ at the reaction zone among other mechanisms, its reaction value decreased sharply when moving away from the reaction zone, as was the case for all reaction mechanisms, and hence dropped berneath Nakamura's reaction rate for the same kinetic reaction. While both reactions $NH+H \leftrightarrow N+H_2$ and $H+O_2(+M) \leftrightarrow HO_2(+M)$ were not temperature-dependent (because they had zero activation energy), the kinetic mechanisms for the last two kinetic reactions had nearly the same values of pre-exponential factor (A) and activation energy (E).
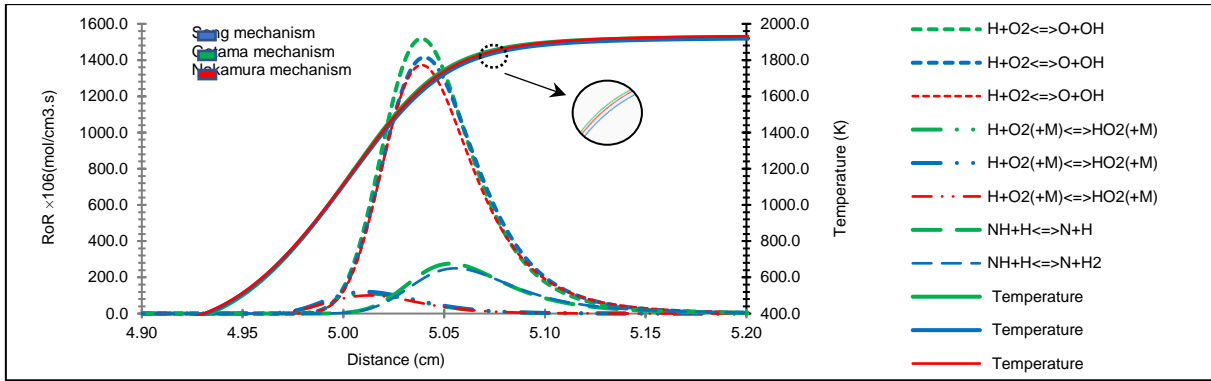
Figure 9: The reaction rate profiles of the key reactions for the laminar flame speed of NH_3-H_2 flames at Ø= 1.4.

Finally, Figure 10 shows the performance of the 36 kinetic reaction mechanisms in the prediction of flame speed of NH_3-H_2 flames and indicated the improvement of the prediction of the kinetic reaction when the mixture took place in the rich conditions with an error between 15% to 13%. Meanwhile, the flame speed prediction accuracy for the kinetic mechanisms deteriorated at the lean range of the equivalence ratio and reached a high value of under/overestimation close to 38% at 0.6 (Ø). It also revealed the importance of the oxygenated species, such as O, O_2, OH, and NO in the reaction with ammonia major decomposition products NH_2 and NH.
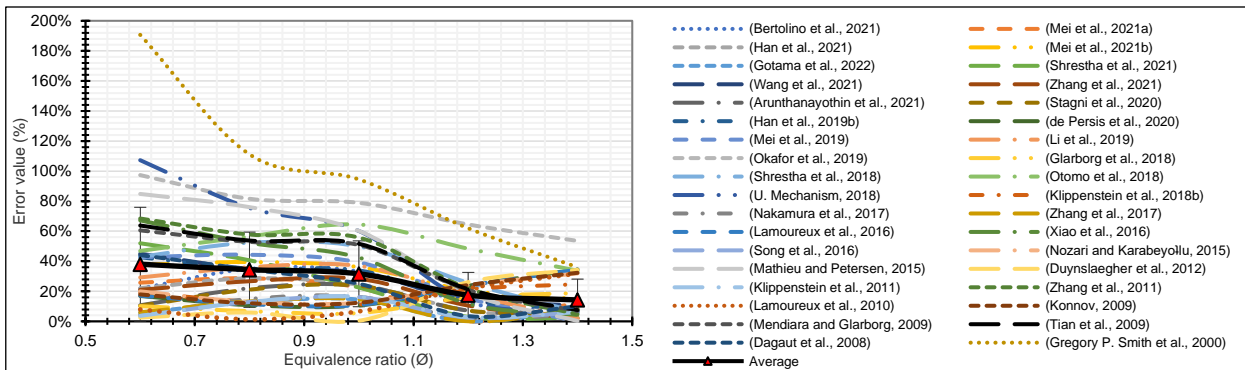

Figure 10: Tthe trend line of prediction error related to the experimental data on the laminar flame speed of NH_3-H_2 flames estimated by all kinetic mechanisms as a function of the equivalence ratio. Symbols denote the average prediction error of 36 kinetic model.

4. CONCLUSION

The present work investigated the laminar flame speed of $70NH_3/30H_2$ (vol%) blended flames for a broad range of equivalence ratios (0.8-1.4) at atmospheric conditions of pressure and temperature. 36 chemical kinetic mechanisms from the literature were evaluated for their ability to predict Laminar flame speed based on experimental data measured in the present work. The main conclusions are listed as follows:

- The mechanism of Duynslager *et al*. provided a very good prediction in comparison to the experimental data in the lean range of the equivalence ratio (0.6-1.0) with only low levels of a discrepancy between 0% to 6% being observed. Alongside this comparison, the sensitivity analysis of the laminar flame speed for the Duynslaegher kinetic mechanism revealed the important role of the kinetic reaction 'NH+H_2O↔HNO+H_2' in the promotion of laminar flame speed at lean conditions.

- The temperature dependency due to the effect of the activation energy of various kinetic reactions was observed to be the reason behind the discrepancy among the kinetic mechanisms, where the activation energy differed in values from one mechanism to another, and this difference affected the reaction rate of each kinetic reaction and hence the laminar flame speed estimation.

- Nakamura kinetic mechanism gave a better prediction of laminar flame speed at rich conditions with low levels of discrepancy (between 2% and 5%). In addition, the Nakamura mechanism showed reactions NH_3+H↔NH_2+H_2, NH_2+N↔N_2+H_2, and $2NH_2$↔N_2H_2+H_2 at 1.2 of Ø; and N+O_2↔NO+O and H_2+OH↔H+H_2O at 1.4 equivalence ratios as having some of the highest sensitivities to flame speed, compared to the mechanisms of Gotama and Song, which showed different sensitive reactions.

- The estimation accuracy for the 36 kinetic mechanisms varied along with the equivalence ratio. The majority of kinetic mechanisms over- or underestimated the laminar flame speed in the lean conditions, especially at 0.6 of equavelance ratio, where the error bars fluctuated close to 38% of the experimental flame speed.

However, the performance of these mechanisms improved at rich conditions with a percentage error close to 13% at 1.4 of Ø.

The variation in the estimation of Laminar flame speed from 36 kinetic models has been documented and only a few of these kinetic mechanisms were able to predict accurately the laminar flame speed for a broad range of equivalence ratios. Therefore, modifying and updating these models over time would enable the improvement of future reaction mechanisms for more complex tasks (ie. turbulence industrial modelling).

5. ACKNOWLEDGEMENTS

6. REFERENCES

Armstrong, J.S., Collopy, F., 1992. Error measures for generalizing about forecasting methods: Empirical comparisons *, International Journal of Forecasting.

Arunthanayothin, S., Stagni, A., Song, Y., Herbinet, O., Faravelli, T., Battin-Leclerc, F., 2021. Ammonia-methane interaction in jet-stirred and flow reactors: An experimental and kinetic modeling study, in: Proceedings of the Combustion Institute. Elsevier Ltd, pp. 345–353. https://doi.org/10.1016/j.proci.2020.07.061

Bertolino, A., Fürst, M., Stagni, A., Frassoldati, A., Pelucchi, M., Cavallotti, C., Faravelli, T., Parente, A., 2021. An evolutionary, data-driven approach for mechanism optimization: theory and application to ammonia combustion. Combustion and Flame 229. https://doi.org/10.1016/j.combustflame.2021.02.012

Brequigny, P., Uesaka, H., Sliti, Z., Segawa, D., Foucher, F., Dayma, G., Mounaïm-Rousselle, C., n.d. Uncertainty in measuring laminar burning velocity from expanding methane-air flames at low pressures.

Chai, W.S., Bao, Y., Jin, P., Tang, G., Zhou, L., 2021a. A review on ammonia, ammonia-hydrogen and ammonia-methane fuels. Renewable and Sustainable Energy Reviews. https://doi.org/10.1016/j.rser.2021.111254

Chai, W.S., Bao, Y., Jin, P., Tang, G., Zhou, L., 2021b. A review on ammonia, ammonia-hydrogen and ammonia-methane fuels. Renewable and Sustainable Energy Reviews. https://doi.org/10.1016/j.rser.2021.111254

Chatterjee, S., Parsapur, R.K., Huang, K.W., 2021. Limitations of Ammonia as a Hydrogen Energy Carrier for the Transportation Sector. ACS Energy Letters 6, 4390–4394. https://doi.org/10.1021/acsenergylett.1c02189

Chen, J., Jiang, X., Qin, X., Huang, Z., 2021. Effect of hydrogen blending on the high temperature auto-ignition of ammonia at elevated pressure. Fuel 287. https://doi.org/10.1016/j.fuel.2020.119563

Chen, Z., 2015. On the accuracy of laminar flame speeds measured from outwardly propagating spherical flames: Methane/air at normal temperature and pressure. Combustion and Flame 162, 2442–2453. https://doi.org/10.1016/j.combustflame.2015.02.012

Dagaut, P., Glarborg, P., Alzueta, M.U., 2008. The oxidation of hydrogen cyanide and related chemistry. Progress in Energy and Combustion Science. https://doi.org/10.1016/j.pecs.2007.02.004

de Persis, S., Pillier, L., Idir, M., Molet, J., Lamoureux, N., Desgroux, P., 2020. NO formation in high pressure premixed flames: Experimental results and validation of a new revised reaction mechanism. Fuel 260. https://doi.org/10.1016/j.fuel.2019.116331

Duynslaegher, C., Contino, F., Vandooren, J., Jeanmart, H., 2012. Modeling of ammonia combustion at low pressure. Combustion and Flame 159, 2799–2805. https://doi.org/10.1016/j.combustflame.2012.06.003

Galmiche, B., Halter, F., Foucher, F., 2012. Effects of high pressure, high temperature and dilution on laminar burning velocities and Markstein lengths of iso-octane/air mixtures. Combustion and Flame 159, 3286–3299. https://doi.org/10.1016/j.combustflame.2012.06.008

Glarborg, P., Miller, J.A., Ruscic, B., Klippenstein, S.J., 2018. Modeling nitrogen chemistry in combustion. Progress in Energy and Combustion Science. https://doi.org/10.1016/j.pecs.2018.01.002

Gotama, G.J., Hayakawa, A., Okafor, E.C., Kanoshima, R., Hayashi, M., Kudo, T., Kobayashi, H., 2022. Measurement of the laminar burning velocity and kinetics study of the importance of the hydrogen recovery mechanism of ammonia/hydrogen/air premixed flames. Combustion and Flame 236. https://doi.org/10.1016/j.combustflame.2021.111753

Gregory P. Smith, David M. Golden, Michael Frenklach, Nigel W. Moriarty, Boris Eiteneer, Mikhail Goldenberg, C. Thomas Bowman, Ronald K. Hanson, Soonho Song, William C. Gardiner, Jr., V.V.L., Zhiwei Qin, 2000. GRI-Mech 3.0 [WWW Document]. http://www.me.berkeley.edu/gri_mech/.

H. Ritchie, M. Roser, 2020. Our World in Data [WWW Document]. Available: https://ourworldindata.org/energy-production-and-changing-energy-sources.

Han, X., Lavadera, L., Konnov, A.A., 2021. An experimental and kinetic modeling study on the laminar burning velocity of NH3+N2O+air flames. Combustion and Flame 228, 13–28. https://doi.org/10.1016/j.combustflame.2021.01.027

Han, X., Wang, Z., Costa, M., Sun, Z., He, Y., Cen, K., 2019. Experimental and kinetic modeling study of laminar burning velocities of NH3/air, NH3/H2/air, NH3/CO/air and NH3/CH4/air premixed flames. Combustion and Flame 206, 214–226. https://doi.org/10.1016/j.combustflame.2019.05.003

Henshaw, P.F., D'Andrea, T., Mann, K.R.C., Ting, D.S.K., 2005. Premixed ammonia-methane-air combustion. Combustion Science and Technology 177, 2151–2170. https://doi.org/10.1080/00102200500240695

Hu, E., Li, X., Meng, X., Chen, Y., Cheng, Y., Xie, Y., Huang, Z., 2015. Laminar flame speeds and ignition delay times of methane-air mixtures at elevated temperatures and pressures. Fuel 158, 1–10. https://doi.org/10.1016/j.fuel.2015.05.010

Ichikawa, A., Hayakawa, A., Kitagawa, Y., Kunkuma Amila Somarathne, K.D., Kudo, T., Kobayashi, H., 2015. Laminar burning velocity and Markstein length of ammonia/hydrogen/air premixed flames at elevated pressures. International Journal of Hydrogen Energy 40, 9570–9578. https://doi.org/10.1016/j.ijhydene.2015.04.024

Kelley, A.P., Law, C.K., 2009. Nonlinear effects in the extraction of laminar flame speeds from expanding spherical flames. Combustion and Flame 156, 1844–1851. https://doi.org/10.1016/j.combustflame.2009.04.004

Klippenstein, S.J., Harding, L.B., Glarborg, P., Miller, J.A., 2011. The role of NNH in NO formation and control. Combustion and Flame 158, 774–789. https://doi.org/10.1016/j.combustflame.2010.12.013

Klippenstein, S.J., Pfeifle, M., Jasper, A.W., Glarborg, P., 2018a. Theory and modeling of relevance to prompt-NO formation at high pressure. Combustion and Flame 195, 3–17. https://doi.org/10.1016/j.combustflame.2018.04.029

Klippenstein, S.J., Pfeifle, M., Jasper, A.W., Glarborg, P., 2018b. Theory and modeling of relevance to prompt-NO formation at high pressure. Combustion and Flame 195, 3–17. https://doi.org/10.1016/j.combustflame.2018.04.029

Konnov, A.A., 2009. Implementation of the NCN pathway of prompt-NO formation in the detailed reaction mechanism. Combustion and Flame 156, 2093–2105. https://doi.org/10.1016/j.combustflame.2009.03.016

Lamoureux, N., Desgroux, P., el Bakali, A., Pauwels, J.F., 2010. Experimental and numerical study of the role of NCN in prompt-NO formation in low-pressure CH4-O2-N2 and C2H2-O2-N2 flames. Combustion and Flame 157, 1929–1941. https://doi.org/10.1016/j.combustflame.2010.03.013

Lamoureux, N., Merhubi, H. el, Pillier, L., de Persis, S., Desgroux, P., 2016. Modeling of NO formation in low pressure premixed flames. Combustion and Flame 163, 557–575. https://doi.org/10.1016/j.combustflame.2015.11.007

Law, C.K., 2006. Combustion physics. Cambridge University Press.

Lee, J.H., Kim, J.H., Park, J.H., Kwon, O.C., 2010. Studies on properties of laminar premixed hydrogen-added ammonia/air flames for hydrogen production. International Journal of Hydrogen Energy 35, 1054–1064. https://doi.org/10.1016/j.ijhydene.2009.11.071

Lhuillier, C., Brequigny, P., Contino, F., Mounaïm-Rousselle, C., 2021. Experimental investigation on ammonia combustion behavior in a spark-ignition engine by means of laminar and turbulent expanding flames, in: Proceedings of the Combustion Institute. Elsevier Ltd, pp. 6671–6678. https://doi.org/10.1016/j.proci.2020.08.058

Lhuillier, C., Brequigny, P., Contino, F., Mounaïm-Rousselle, C., 2020. Experimental study on ammonia/hydrogen/air combustion in spark ignition engine conditions. Fuel 269. https://doi.org/10.1016/j.fuel.2020.117448

Li, J., Huang, H., Kobayashi, N., He, Z., Osaka, Y., Zeng, T., 2015. Numerical study on effect of oxygen content in combustion air on ammonia combustion. Energy 93, 2053–2068. https://doi.org/10.1016/j.energy.2015.10.060

Li, J., Huang, H., Kobayashi, N., Wang, C., Yuan, H., 2017. Numerical study on laminar burning velocity and ignition delay time of ammonia flame with hydrogen addition. Energy 126, 796–809. https://doi.org/10.1016/j.energy.2017.03.085

Li, R., Konnov, A.A., He, G., Qin, F., Zhang, D., 2019. Chemical mechanism development and reduction for combustion of NH3/H2/CH4 mixtures. Fuel 257. https://doi.org/10.1016/j.fuel.2019.116059

Mathieu, O., Petersen, E.L., 2015. Experimental and modeling study on the high-temperature oxidation of Ammonia and related NOx chemistry. Combustion and Flame 162, 554–570. https://doi.org/10.1016/j.combustflame.2014.08.022

Mei, B., Ma, S., Zhang, X., Li, Y., 2021a. Characterizing ammonia and nitric oxide interaction with outwardly propagating spherical flame method. Proceedings of the Combustion Institute 38, 2477–2485. https://doi.org/10.1016/j.proci.2020.07.133

Mei, B., Zhang, J., Shi, X., Xi, Z., Li, Y., 2021b. Enhancement of ammonia combustion with partial fuel cracking strategy: Laminar flame propagation and kinetic modeling investigation of NH3/H2/N2/air mixtures up to 10 atm. Combustion and Flame 231. https://doi.org/10.1016/j.combustflame.2021.111472

Mei, B., Zhang, X., Ma, S., Cui, M., Guo, H., Cao, Z., Li, Y., 2019. Experimental and kinetic modeling investigation on the laminar flame propagation of ammonia under oxygen enrichment and elevated pressure conditions. Combustion and Flame 210, 236–246. https://doi.org/10.1016/j.combustflame.2019.08.033

Mendiara, T., Glarborg, P., 2009. Ammonia chemistry in oxy-fuel combustion of methane. Combustion and Flame 156, 1937–1949. https://doi.org/10.1016/j.combustflame.2009.07.006

Moffat, R.J., 1988. Describing the uncertainties in experimental results. Experimental Thermal and Fluid Science 1, 3–17. https://doi.org/10.1016/0894-1777(88)90043-X

Mørch, C.S., Bjerre, A., Gøttrup, M.P., Sorenson, S.C., Schramm, J., 2011. Ammonia/hydrogen mixtures in an SI-engine: Engine performance and analysis of a proposed fuel system. Fuel 90, 854–864. https://doi.org/10.1016/j.fuel.2010.09.042

Nakamura, H., Hasegawa, S., Tezuka, T., 2017. Kinetic modeling of ammonia/air weak flames in a micro flow reactor with a controlled temperature profile. Combustion and Flame 185, 16–27. https://doi.org/10.1016/j.combustflame.2017.06.021

Nozari, H., Karabeyołlu, A., 2015. Numerical study of combustion characteristics of ammonia as a renewable fuel and establishment of reduced reaction mechanisms. Fuel 159, 223–233. https://doi.org/10.1016/j.fuel.2015.06.075

Okafor, E.C., Naito, Y., Colson, S., Ichikawa, A., Kudo, T., Hayakawa, A., Kobayashi, H., 2019. Measurement and modelling of the laminar burning velocity of methane-ammonia-air flames at high pressures using a reduced reaction mechanism. Combustion and Flame 204, 162–175. https://doi.org/10.1016/j.combustflame.2019.03.008

Otomo, J., Koshi, M., Mitsumori, T., Iwasaki, H., Yamada, K., 2018. Chemical kinetic modeling of ammonia oxidation with improved reaction mechanism for ammonia/air and ammonia/hydrogen/air combustion. International Journal of Hydrogen Energy 43, 3004–3014. https://doi.org/10.1016/j.ijhydene.2017.12.066

Pfahl, U.J., Ross, M.C., Shepherd, J.E., Pasamehmetoglu, K.O., Unal, C., 2000. Flammability Limits, Ignition Energy, and Flame Speeds in H 2-CH 4-NH 3-N 2 O-O 2-N 2 Mixtures.

Riaz, A., Zahedi, G., Klemeš, J.J., 2013. A review of cleaner production methods for the manufacture of methanol. Journal of Cleaner Production. https://doi.org/10.1016/j.jclepro.2013.06.017

Shrestha, K.P., Lhuillier, C., Barbosa, A.A., Brequigny, P., Contino, F., Mounaïm-Rousselle, C., Seidel, L., Mauss, F., 2021. An experimental and modeling study of ammonia with enriched oxygen content and ammonia/hydrogen laminar flame speed at elevated pressure and temperature. Proceedings of the Combustion Institute 38, 2163–2174. https://doi.org/10.1016/j.proci.2020.06.197

Shrestha, K.P., Seidel, L., Zeuch, T., Mauss, F., 2018. Detailed Kinetic Mechanism for the Oxidation of Ammonia Including the Formation and Reduction of Nitrogen Oxides. Energy and Fuels 32, 10202–10217. https://doi.org/10.1021/acs.energyfuels.8b01056

Song, Y., Hashemi, H., Christensen, J.M., Zou, C., Marshall, P., Glarborg, P., 2016. Ammonia oxidation at high pressure and intermediate temperatures. Fuel 181, 358–365. https://doi.org/10.1016/j.fuel.2016.04.100

Stagni, A., Cavallotti, C., Arunthanayothin, S., Song, Y., Herbinet, O., Battin-Leclerc, F., Faravelli, T., 2020. An experimental, theoretical and kinetic-modeling study of the gas-phase oxidation of ammonia. Reaction Chemistry and Engineering 5, 696–711. https://doi.org/10.1039/c9re00429g

TAKEISHI, H., HAYASHI, J., KONO, S., ARITA, W., IINO, K., AKAMATSU, F., 2015. Characteristics of ammonia/N2/O2 laminar flame in oxygen-enriched air condition. Transactions of the JSME (in Japanese) 81, 14-00423-14–00423. https://doi.org/10.1299/transjsme.14-00423

Tian, Z., Li, Y., Zhang, L., Glarborg, P., Qi, F., 2009. An experimental and kinetic modeling study of premixed NH3/CH4/O2/Ar flames at low pressure. Combustion and Flame 156, 1413–1426. https://doi.org/10.1016/j.combustflame.2009.03.005

U. Mechanism, 2018. Chemical-kinetic mechanisms for combustion applications [WWW Document]. mechanical and aerospace engineering (combustion research), University of California at San Diego.

Um, D.H., Kim, T.Y., Kwon, O.C., 2014. Power and hydrogen production from ammonia in a micro-thermophotovoltaic device integrated with a micro-reformer. Energy 73, 531–542. https://doi.org/10.1016/j.energy.2014.06.053

Valera-Medina, A., Pugh, D.G., Marsh, P., Bulat, G., Bowen, P., 2017. Preliminary study on lean premixed combustion of ammonia-hydrogen for swirling gas turbine combustors. International Journal of Hydrogen Energy 42, 24495–24503. https://doi.org/10.1016/j.ijhydene.2017.08.028

Valera-Medina, A., Xiao, H., Owen-Jones, M., David, W.I.F., Bowen, P.J., 2018. Ammonia for power. Progress in Energy and Combustion Science. https://doi.org/10.1016/j.pecs.2018.07.001

Wang, Z., Han, X., He, Y., Zhu, R., Zhu, Y., Zhou, Z., Cen, K., 2021. Experimental and kinetic study on the laminar burning velocities of NH3 mixing with CH3OH and C2H5OH in premixed flames. Combustion and Flame 229. https://doi.org/10.1016/j.combustflame.2021.02.038

Wu, F., Liang, W., Chen, Z., Ju, Y., Law, C.K., 2015. Uncertainty in stretch extrapolation of laminar flame speed from expanding spherical flames. Proceedings of the Combustion Institute 35, 663–670. https://doi.org/10.1016/j.proci.2014.05.065

Xiao, H., Howard, M., Valera-Medina, A., Dooley, S., Bowen, P.J., 2016. Study on Reduced Chemical Mechanisms of Ammonia/Methane Combustion under Gas Turbine Conditions. Energy and Fuels 30, 8701–8710. https://doi.org/10.1021/acs.energyfuels.6b01556

Zhang, K., Li, Y., Yuan, T., Cai, J., Glarborg, P., Qi, F., 2011. An experimental and kinetic modeling study of premixed nitromethane flames at low pressure. Proceedings of the Combustion Institute 33, 407–414. https://doi.org/10.1016/j.proci.2010.06.002

Zhang, X., Moosakutty, S.P., Rajan, R.P., Younes, M., Sarathy, S.M., 2021. Combustion chemistry of ammonia/hydrogen mixtures: Jet-stirred reactor measurements and comprehensive kinetic modeling. Combustion and Flame 234. https://doi.org/10.1016/j.combustflame.2021.111653

Zhang, Y., Mathieu, O., Petersen, E.L., Bourque, G., Curran, H.J., 2017. Assessing the predictions of a NOx kinetic mechanism on recent hydrogen and syngas experimental data. Combustion and Flame 182, 122–141. https://doi.org/10.1016/j.combustflame.2017.03.019

Zitouni, S., Pugh, D., Crayford, A., Bowen, P.J., Runyon, J., 2022. Lewis number effects on lean premixed combustion characteristics of multi-component fuel blends. Combustion and Flame 238. https://doi.org/10.1016/j.combustflame.2021.111932

#107: Encouraging net-zero energy retrofit adoption for apartment buildings:

An upscaling guideline

Hua Du[1], Qi Han[2], Bauke De Vries[3], Joris Pepijn Van Den Heiligenberg[4]

[1] Information Systems in the Built Environment, Eindhoven University of Technology, h.du@tue.nl
[2] Information Systems in the Built Environment, Eindhoven University of Technology, q.han@tue.nl
[3] Information Systems in the Built Environment, Eindhoven University of Technology, b.d.vries@tue.nl
[4] Information Systems in the Built Environment, Eindhoven University of Technology, j.p.v.d.heiligenberg@student.tue.nl

Abstract: It is proposed in Dutch and EU policy to be carbon neutral by 2050 to mitigate climate change. Hence, it is important to improve the energy efficiency in existing real estate as the built environment is responsible for 16% of total energy use in The Netherlands. Net-zero energy building (NZEB) retrofit concepts have been developed and are being tested as one promising solution. However, the NZEB retrofit industry is still in its infancy, and upscaling these concepts faces difficulties. Influences for upscaling were investigated by doing case-study research substantiated by two frameworks from the transition studies field: the socio-technical system analysis and innovation niche analysis. The two frameworks were adopted to identify the origin of the upscaling barriers and understand the development of the NZEB high-rise retrofit niche. A list of 30 upscaling barriers, barrier solutions, and seven upscaling drivers were identified through literature review and interviews with industry professionals from the two project cases. The barriers from the literature review and case study were compared and double-checked. Furthermore, the management quality of the important innovation-niche building processes were evaluated, and improvements presented. The results of the analyses were then connected to answer what is thwarting upscaling and what can be done to enhance upscaling by presenting strategic recommendations. An upscaling guide for both consortia and government is demonstrated. More specifically, recommendations for developing consortia are: forming complete

networks; setting clear and aligned expectations; experimenting with small manageable elements; adding system integration and modularity to the design criteria; and forming new business models and perspectives. Suggestions for policymakers include the following: 1) more experimental space and rule exemptions should be available for NZEB projects; 2) the 70% decision rule for housing associations should be simplified for the NZEB project; 3) updating the energy efficiency fee act (in Dutch: EPV wetgeving) and virtual energy balancing rules are suitable for boosting the upscaling of NZEB high-rise projects; 4) Furthermore, criticism has been provided on the subsidy policy in the Netherlands.

Keywords: net-zero energy building; building energy retrofit; high-rise building; transition theory

1. INTRODUCTION

Energy transition must be accelerated as it is proceeding too slowly to reach the goals of the Paris Agreement (IPCC, 2018). Existing housing stock has large energy-saving potential as buildings are responsible for about 40% of energy consumption and 38% of CO_2 emissions in the EU (European Commision, 2019). In the Netherlands, the government set the goal of reducing CO_2 emissions to a level 80% to 95% lower than that in 1990 (Government of the Netherlands, n.d.). Hence, the housing industry is seeking solutions to achieving carbon neutrality.

Solutions for reducing energy consumption and CO_2 emissions in buildings include energy retrofits and adopting sustainable energy. Achieving net-zero energy building (NZEB) through retrofitting existing building stock is one of the applications of the solutions. In the meantime, the diffusion of energy-retrofit and sustainable energy falls behind expectations (Du *et al.*, 2021, 2022). The uptake of these technologies often faces constraints and barriers such as social and regional factors (van den Heiligenberg *et al.*, 2017) and financial factors in innovative and experimental technologies. Foreseeing certain constraints and barriers has proven supportive of effectively encouraging the acceptance of innovations in the design of urban experiments (Dijk *et al.*, 2018; van den Bosch, 2010). The adoption of technologies in individual houses is often decided by the house owner, involveing fewer stakeholders. On the contrary, high-rise buildings often involve more stakeholders and might face more social barriers. This study investigated the barriers to net-zero energy retrofit adoption for high-rise buildings in the Netherlands. Two cases were analysed to identify barriers in practice and to gain insights into tackling the barriers and encouraging the adoption of such technologies.

2. LITERATURE REVIEW

The concept of NZEB has been evolving since it found the spotlight. Attia (2018) defined an NZEB as an ultra-low energy building that meets its energy needs annually from renewable sources, produced on-site or nearby. Besides energy use, the site boundary is another important part of the definition. The site boundary for single building use in this study is the boundary of the property (Kent Peterson *et al.*, 2015). Attia (2018) proposed four design principles that can be used for NZEB design: 1) reduce energy demand; 2) improve indoor environmental quality; 3) provide renewable energy share; 4) reduce primary energy and carbon emissions.

Moreover, the NZEB concept has also been used in the housing retrofit sector. Van Oorschot *et al.* (2018) summarised the characteristic retrofit concept for high-rise buildings, which included integral concept, modular, and product-based. The integral concept indicated that building elements are designed from a multi-disciplinary aspect, such as a façade element providing several building services. The modular and product characteristics suggested that the elements should follow standard module design so that elements can be easily replaced and suitable for various situations.

After new technology has been developed, the adoption and spread is important for innovations such as NZEB in order to survive in the market. This process depends on multiple factors. Rogers (1962) proposed that the diffusion of innovations was influenced by the relative advantage, complexity to use, compatibility with the existing system, trialability, and the observed effects. Innovation adoption and diffusion are elements of upscaling. However, upscaling is interpreted as merely the broader adoption of innovative products over time in practice and research. No consistent definition of upscaling exists in the literature. In the innovation literature, scaling up is considered an important part of the innovation trajectory. Upscaling innovations are intertwined with the success of those innovations. Dijk *et al.* (2018) defined upscaling from innovation experiments or projects as not only the growing level of adoption but also the changing social and institutional context. This definition was further elaborated by Kent Peterson *et al.* (2015) who stated that upscaling was about developing knowledge, obtaining a voice and a face, and becoming accepted and institutionalised in society. Jolly *et al.* (2012) proposed an overview of 7 dimensions of upscaling of business models, which were quantitative, organisational, geographical, deep, functional, replication, and institutional. Afterward, it was concluded that the definition of upscaling was that the adoption number of the innovation was increasing and being

diffused to different locations. This definition included replicating initiatives on the same or on a larger scale and the changing social and institutional context when the upscaling occurred.

3. METHODOLOGY

In this study, two cases were selected for performing quantitative research through the survey. Then, multi-level perspective analysis and Innovation-niche analysis were adopted for developing the upscaling guideline for NZEB among high-rise residential buildings.

3.1. Case study

First, a case selection was performed to include only the cases suitable for the following analysis. The selection criteria were as follows: 1) The consortium must have the intention to scale up the NZEB concept after the first experimental project; 2) The developing consortium must be progressed in the development of the NZEB concept, which can be distinguished by having a detailed design, a client and an available 8-story or higher building for prototyping/retrofit; 3) The plan for the available building must have the ambition of Net Zero Energy Building based on the energy calculations; 4) The consortium and the retrofit project must be in the Netherlands; 5) The consortium must be willing to share knowledge about their technology and the process. These criteria lead to two projects: Inside-out and Happy Balance.

After the selection, interviews and consulting project documents were conducted for data collection. An interview guide was used to ensure that the important topics on which data was to be collected were addressed in the interview. The first section of the interview focused on finding upscaling factors for NZEB retrofit concepts for a high-rise. The answers provided case-specific information and factors for the innovation itself. Case information about the retrofit concept, consortium, and upscaling information was obtained by asking the first eight questions of the interview guide. The interview guide was also used to minimalise the bias of both interviewees and the interviewer. By keeping the same structure for the interviews and not providing too much information in the conversation, the interviewee answered the question with their own beliefs and perspectives. The following subsections introduced theories used for designing and structuring the survey.

3.2. Multi-level perspective framework

The core of the multi-level perspective was that transitions come from interactions between processes at different levels. A socio-technical system is a dynamically stable interplay of technical and social elements to fulfill societal functions. In the case of NZEB retrofit, the socio-technical system in this study was "housing". The three levels of the multi-level perspective were landscape, regime, and niche. The three levels were interconnected with each other and interacted in the following way when transitions happened: "a) niche-innovations build up internal momentum; b) changes at the landscape level create pressure on the regime; c) destabilization of the regime creates windows of opportunity for niche-innovations" (Geels & Schot, 2010). This process is illustrated in Figure 1.
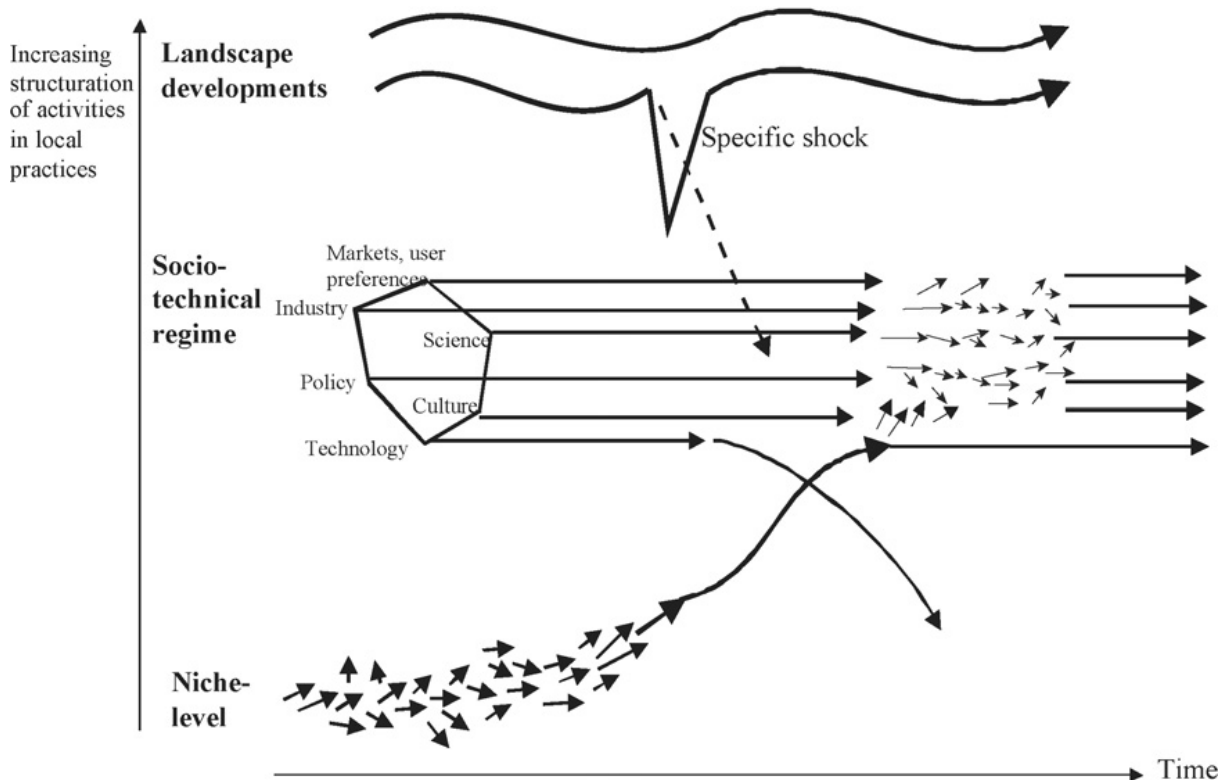
Figure 1: Technological substitution pathway (Geels & Schot, 2010)

The socio-technical landscape is a broad, exogenous environment in which autonomous trends and major crises take place that put pressure on the system (regime and niche). These landscape developments are mostly long-term, which can be demographic, environmental, macro-economy, political, culture, and world-level situations. Under the absence of landscape pressure, the regime is likely to remain dynamically stable. When landscape pressure is present, the regime can either be opened or sustained. Landscape developments that open the regime can create opportunities for innovations（niches). Thus, when niches experience favorable external conditions in the regime caused by landscape pressure, niche innovations have the chance of competing and even replacing existing main steam technology.

The middle part in Figure 1 is the socio-technical regime, which helps to understand the sociological category of rules (Geels & Schot, 2010). There are many things stabilising the existing socio-technical systems. However, changes are needed to make transitions happen. Regimes contain three types of rules: cognitive, regulative, and normative. Cognitive rules are guiding principles, goals, innovative ideas, and belief systems. Regulative rules are regulations, laws, and standards. Normative rules are role relationships, behavioural norms, and values (Geels, 2004). The socio-technical regime is the established and mainstream method of performing projects (Smith *et al.*, 2010). In other words, the regime and its rules determine how things are done. Innovations such as NZEB retrofit for high-rises often emerge at the niche-level outside of the existing regimes (Geels & Schot, 2010). This niche-level act as an incubation space where innovations are protected from mainstream market selection. In the space, the selection criteria differ from the regime.

3.3. Strategic Niche Management

The Strategic Niche Management (SNM) approach (Schot & Geels, 2008) was developed to understand the process of niche creation and how niche innovations can become mainstream. SNM focused on how to stimulate the emergence of innovations (or niches) and distinguished three critical processes for the successful development of a niche: social network building, articulation of visions and expectations, and learning processes. These processes were combined under the concept of nurturing, which targeted to ensure the protective space for innovation (Verhees *et al.*, 2013). The nurturing process should include three critical elements for successful development: social network building, articulation of visions and expectations, and learning processes (Smith & Raven, 2012).

The framework was later expanded by adding two other essential processes: shielding and empowerment. The function of shielding was to protect innovation from selection pressures from socio-technical regimes and provide room for experimentation. This can prevent innovation development from mismatches with the current socio-technical configurations of the regime (Verhees *et al.,* 2013). Shielding can be divided into active and passive shielding. Active shielding was about creating protection for innovation by actively supporting the development of the innovation. Passive shielding was about finding spaces where the selection pressure was less for conditional reasons.

Empowerment was when an innovation developed into a market niche and was adapted to fit the needs of a specific market segment without requiring further support from shielding measures. This means that the innovation must be strengthened by being successfully nurtured. Empowerment can occur in two forms: 'fit and conform' or 'stretch and transform'. Fit and conform is when the innovation becomes competitive with mainstream socio-technical practices in equal selection environments. The second form of empowerment is to stretch and transform. This form aims to undermine the incumbent regime and transform the selection environment to favor innovations (Smith & Raven, 2012). This entails that the innovation changes conventional selection criteria (Verhees *et al.*, 2013). A key aspect of strategically managed niches is to design socio-technical experiments. Experiments can be defined as: "inclusive, practice-based and challenge-led initiatives designed to promote system innovation through social learning under uncertainty and ambiguity" (Sengers *et al.*, 2019).

4. RESULTS

Two cases (Inside-Out and Happy Balance) were selected based on the criteria described in section 3.1. Project consortia provided the basic information about the projects. The Inside-out project aimed at developing and testing a modular retrofit system for high-rise buildings. In this project, the components were mainly on the outside of the building and were connected. Happy Balance project focussed on developing an NZEB strategy specifically for high-rise apartment buildings. One of the goals for Happy Balance was accelerating the retrofit of apartment complexes by standardisation and industrialisation and cleverly designing the processes surrounding retrofit, completion, and maintenance. Another goal was to create tailor-made solutions with promised performance.

4.1. Multi-level perspective analysis

The socio-technical system for NZEB in this study was housing. Although the innovation under observation during this analysis was rather specific, it was being developed in a large socio-technical system with many alternatives that generate guiding principles. The socio-technical system was chosen to incorporate the entire overview of what the configurations and guiding principles were in society.

The six dimensions of the MLP framework were used to describe the regime, and upscaling barriers and drivers were then coupled to different dimensions. Some barriers were multi-dimensional but were categorised under the most suitable dimension. An overview of all barriers is presented in Table 1. This table also includes solutions that were given by the interviewees.

Table 1: Upscaling barriers and solutions

Dimension	Code	Upscaling barrier	Barrier solution
Technological	T1	Energy behavior of occupants cannot be modeled	Monitor energy use in executed projects carefully
	T2	Lack of knowledge on practical execution of NZEB retrofit projects	Experiment with the construction process on a small scale
	T3	Lack of knowledge on system integration	Include system integrators (consultants) in the consortium
	T4	Lack of modularity in retrofit concept	Use modularity as design criteria from the start
Market, user	M1	NZEB retrofit concept costs too high for home-owners	Lease agreements instead of buying. Loan on the dwelling industrialize manufacturing
	M2	Reluctant or unaware occupant	Informing, marketing, branding. Show the (financial) advantages to the resident.
	M3	Length of the customer journey	Prepare customer journey, make use of online information tools such as a website with AI.
	M4	Financial agenda of housing association	Lease agreements instead of buying, inform about total cost of Ownership thinking, show benefits, make retrofit profitable
	M5	New property added on existing property for home-owners	Make arrangements with the notary
	M6	No future perspective of multiple projects	Create an overview of the existing housing stock and make offers to real estate owners
Policy	P1	70% decision rule	Invest in the relationship with the occupant, lobby for change in legislation for sustainable projects
	P2	Current rules are not suitable for high-rise	Lobby for legislation adaption in cooperation with non-profit organizations
	P3	Different policies in regions	Visualize differences, find similar regions
	P4	Lack of European organizing	-
	P5	The municipal policy is not in line with national ambitions	Lobby for legislation adaption in cooperation with non-profit organizations
	P6	No room for experimentation	Lobby for legislation adaption in cooperation with non-profit organizations
	P7	Lack of subsidies	Lobby for more subsidy options in cooperation with non-profit organizations
	P8	Subsidy process to complex	Include subsidy consultant
	P9	Virtual energy balancing regulations	The housing association can take the role of ESCo, Lobby for legislation adaption in cooperation with non-profit organizations
Industry	I1	Closed-innovation mindset	Create networks of trust by forming new entities with cooperation agreements
	I2	Ending the business model of the housing association	New financial structures
	I3	Changing business model ESCo	
	I4	Lack of industrial designers in consortia	Include industrial designers in consortia from the start
	I5	Trust issues in consortia	A new contractual agreement, form a new entity
	I6	Lack of international perspective	-
	I7	Lack of networks	Create networks of trust
	I8	More consortia needed	-
	I9	No revenues for the government in the energy transition	Include government in the consortium; government should invest in themselves and do more than just facilitate
Culture	C1	The traditional character of the industry	Create networks of trust
	C2	Risk avoiding attitude in the sector	Create networks of trust

4.2. Innovation-niche analysis

In this subsection, the innovation niche was reviewed to find out to what extent the niche was developed and available to fill this window of opportunity. The strategic niche management (SNM) framework was used as guidance.

Shielding

One of the shielding measures for the two cases was the subsidy. Both cases received substantial subsidies from the government for R&D and execution. Multiple actors stated that the projects would not even exist without these subsidies. Another shielding factor for the two cases was the location factor. Both Utrecht and Amersfoort have set high ambitions relative to other locations in the Netherlands. For project Inside-Out, this has entailed the rule exemption in the building permit procedure. Although the design did not comply with the municipality's policy, Aldermen overruled the spatial plan regulations and approved the project. Without this rule exemption, the entire retrofit concept could not have been applied, and the building would not be net-zero energy after the retrofit.

Nurturing

The analysed consortia were assembled with much care and contained many actors. By reviewing the list of included stakeholders in the consortia/network, one would think these networks were broad and deep. The network implied that enough actors and resources (knowledge, finances) would be available. However, a different perception was received from the consortium members during the interviews. It was stated that actors such as the municipality should have been involved in the project much earlier or even be included in the consortium. These actors seemed much more powerful than expected. It was stated that when the project progressed to becoming concrete, the network somewhat expanded, but the stakeholder resource commitment decreased.

The vision and expectations were clear from the beginning because both consortia used a project plan that was obliged to receive the TKI subsidy. However, expectations were not 'robust' as they did not align between the different actors. For example, different answers were received when asked about their expectations during the interviews. Some actors of the Inside-Out consortium thought the project would remain in theory as theoretical research into the possibilities of retrofitting a high-rise apartment building to net-zero energy. Other actors were convinced it would become an actual construction project.

Learning processes were also arranged by the use of the project plan obliged for receiving the TKI subsidy. Learning took place mostly on the first-order level. Learning included technology, financial feasibility, and finding out what retrofitting an entire building entailed. By doing small experiments, the learning process was divided into smaller elements. Both consortia manufactured façades and tested them in a climate chamber. In addition, Inside-Out tested their prototype retrofit concept on one dwelling at the actual apartment building. Few social aspects were incorporated into the learning process. An example where much relevant knowledge could be obtained was the process involving the occupants who were essential stakeholders in the process. For Inside-Out, the occupants voted 90% in favour of the retrofit plans, which is very high, especially for such an ambitious project. During the interviews, it was asked why this percentage was reached, but it turned out there was no learning plan for this aspect of the project even though this knowledge can change the assumptions for the start of the following projects, which would generate second-order learning.

Empowerment

The two forms of empowerment were 'fit and conform' and 'stretch and transform'. The interviewees were asked about the upscaling barriers from literature and the barriers that were mentioned during the interview. They were asked if these barriers could be overcome by further developing technological and social innovation (fit and conform) or changing the configurations of the current system (stretch and transform). This strategy gave insight into the empowerment that was needed to upscale the NZEB retrofit. A mixture of both forms of empowerment was also possible. The form of empowerment for each upscaling barrier is presented in Table 2. It can be noted that the experts classified most upscaling barriers to be overcome as 'stretch and transform'. This meant that regime changes were needed to make NZEB retrofit concepts for high-rise scale-up.

Table 2: Forms of empowerment to overcome upscaling barriers

Upscaling barrier	Fit and conform – Stretch and transform
The insufficient capacity energy grid	Mixture
Mismatch energy production/ consumption building level	Mixture
The traditional character of the industry	Stretch and transform
Reluctant occupant	Stretch and transform
Unaware occupants and home-owners	Stretch and transform
Financial agenda of housing associations	Mixture
Costs of the NZEB concept	Fit and conform
70% decision rule	Mixture
Lack of trust between stakeholders	Stretch and transform
Incompetent municipal apparatus	Stretch and transform

The multi-level perspective analysis and the strategic niche management analysis contributed to researching the upscaling influences and then analysing to what extent the niche was developed. The results showed that there were challenges for upscaling NZEB high-rise retrofits. However, when pressure on the regime becomes more severe of the described landscape developments, which was predicted, innovation can become a more attractive alternative. NZEB retrofit concepts for high-rises are starting to emerge more, and the number of experimental projects has increased. This indicates that innovation is on the rise and could be the preferred alternative when there are fewer barriers. For upscaling, it is important that experimental NZEB projects are being executed because the niche is still in its infancy. Increasing the experiments will strengthen the niche. Strategic recommendations for future development and advice to policymakers based on analysis results are presented in the next section.

5. UPSCALING GUIDELINE

5.1. Strategic recommendations

Different recommendations based on the results from the case studies are presented in Table 3. Recommendations contain practical recommendations for further experiments and retrofit projects as well as recommendations that drive upscaling.

Table 3: Strategic recommendations

Category	Actor	Recommendation
Network & stakeholders	Housing association	End-user participation can be a crucial element in having a successful project. Make the end-user participate during the early phases of the project to find out worries and complaints as these might concern other issues than sustainability. This should be done by housing association in cooperation with the consortium/contractor.
	Consortium	1) Include large entity in the consortium to carry costs needed for the investments for large scale production. 2) Include net operator early in the process for streamlined cooperation. 3) Include governmental institutions in the consortium to keep them informed and participate them in the design process. This will smoothen bureaucratic processes and speed up the process. 4) Include research institutes to the consortium to ensure a proper learning process with second-order learning. 5) Include an innovative architect or product designer in the network to ensure aesthetics and be able to do branding of the concept/product. 6) Include an independent mediator into the consortium who keeps track of the goals and can solve trust issues between actors. 7) Form cooperation contracts with consortium or form new entity to resolve trust issues.
Learning processes	Consortium	Learning by doing will help to reach the learning objectives better. Experiment with smaller parts of the retrofit concept to make it manageable.
	Research institutes	Include learning targets on social aspects such as end-user behavior.
Expectations alignment	Mediator	1) Make sure that expectations are clearly defined and supported by the consortium members. This can solve trust issues in later phases of the process. 2) Have an independent actor keep track of responsibilities and confront actors in the consortium whenever someone is not acting according to the responsibilities.
Resources	Consortium	Include actors with knowledge on system integration in the consortium. System integration is complex and an important element for the feasibility of the retrofit concept.
	Subsidy consultant	Subsidies are possible to obtain for R&D and realization of NZEB retrofit projects. It is important to check for possibilities early in the process because these procedures can consume much time and energy before subsidies are allocated.
Technology	Consortium	1) To be able to create multiple product-market combinations' modularity' must be add to the design criteria to ensure this is incorporated in all building elements; 2) Make system integration one of the design criteria for higher feasibility
Business model	Contractor	Focus on Total cost of ownership (TCO) to overcome the fear of high initial investment costs of real estate owners such as housing associations. Emphasize the financial benefits of this perspective.
	Consortium	Develop the option for lease agreements with customers. Involve suppliers that can deliver products based on lease-agreements instead of full ownership.
Policy related	Mediator	Involve municipality, welfare committee and other governmental stakeholders to inform them about what is happening and request support.

5.2. Policy implications

In the Netherlands and many other western countries, the national objective is to become net-zero energy before 2050. Many elements of society must be changed to encourage more sustainable alternatives to achieve this goal. The transition to greener forms of energy provision is happening slowly as the built environment still accounts for 16% of energy use. This chapter advises policymakers in the Netherlands and possibly other countries to support the energy transition in the housing sector by accelerating the introduction of NZEB high-rise retrofit concepts.

Strategic role

The interviewee from Province Utrecht stated that the government should play a role in facilitating consortia with knowledge and organising management processes. Firstly, the government could support high-potential pilots by enlarging legitimacy. Furthermore, more effort should be put into supporting consortia and networks by organising learning processes and knowledge-sharing initiatives. Some initiatives on knowledge-sharing have been organised by organisations such as the economic board.

Adjust 70% decision rule

Most of the interviewed experts in the industry agreed with the 70% decision rule as a democratic tool for the occupants to have a voice in the decisions of housing associations and owner associations. However, in some cases, renovation plans have been cancelled because occupants do not cooperate with housing associations because of previous disagreements. All experts agreed that when a certain level of sustainability is part of the plans, the rule should be downsized. The advice was to downsize the rule for NZEB retrofit projects. However, to protect occupants, it must be shown that the situation is financially equal to pre-retrofit or post-retrofit.

Create energy efficiency fee act rules suitable for high-rise

Because the NZEB high-rise innovation is in its infancy, regulations and laws are not aligned with high-rise apartments. The energy efficiency fee act (in Dutch: wet energieprestatievergoeding) is an example of this situation. Minimal demands for energy use and generation are mentioned in this act. However, it turned out this was based on row (terraced) houses and does not represent high-rise apartments. The dwellings received too much energy according to this act, making the NZEB high-rise projects unfeasible. The act should be extended with a section that considered energy consumption for high-rise apartments based on their energy use data (heating, hot water, electricity).

Align municipal policy with national ambitions

National objectives on sustainability are ambitious and have changed rapidly in the last few years. What is being experienced during NZEB projects is that the municipal policy does not correspond with national objectives. The municipal policy has not changed along with the national policy. For instance, the welfare committee and municipality are still doing what they were always doing, which is following the policy. The rules that are used for judging an architectural design of an NZEB high-rise retrofit project are the same for all other projects and do not comply with innovative solutions. It was advised that governmental institutes act flexibly for these experimental projects with a large positive influence on energy transition. This would be more in line with the national policy. Creating more room for experimentation could also be the solution to comply with national ambitions.

Adjust regulations on virtual energy balancing

In the Netherlands, rules are very strict on energy provision and how the check-out works. Happy Balance and Inside-Out tried to generate the energy collectively and then virtually divide the energy over the dwellings by a 'smart meter'. National legislation does not allow this because only an Energy Service Company (ESCo) is allowed to do this according to Dutch legislation. This led to the consortium having to physically connect solar panels to each dwelling by installing inverters and wiring separately, which caused high material and labour costs. This legislative barrier could be relieved if the policy on this aspect was changed. For instance, the housing association could be allowed to virtually balance the generated renewable energy, possibly in cooperation with an ESCo.

Provide more room for experimentation

From the data, it was noted that not enough room for experimentation was available in the housing sector. Obtaining rule exemptions for regulations such as virtual energy balancing regulations are available in the Netherlands. However, to make use of these exemptions, it is necessary to go through a long process that prevents consortia from using these experimentation options due to project deadlines. Hence, more experimentation space and easier application procedures are needed.

Provide more subsidies

More subsidies should be available to accelerate the energy transition, which was substantiated by the interviewed expert of the Province Utrecht. It was stated that many subsidies were requested. However, it is complex to choose who should be subsidised; therefore, few subsidies were allocated. The analysed consortia during the case study stated that subsidy was needed for experimental projects. Providing subsidies for innovation projects could help the NZEB retrofit industry innovate faster. Therefore, providing more subsidies to high-potential transformative (R&D) energy, housing, and agriculture projects was advised.

Simplify subsidy procedure

Besides the lack of subsidies, the procedures of subsidy allocation were too complex. The analysed consortia both needed a subsidy specialist to obtain the subsidies. This specialist would be paid from the subsidy funding, which was money that could have been invested in the retrofit concept. A simpler procedure was needed. Besides, many subsidies requested deadlines which meant that many sustainable start-ups that are driving the energy transition are obliged to wait for a long time before being able to request a subsidy. This could mean the start-up can go bankrupt

while they are waiting for the subsidy. It was advised to make the request for some subsidies available year-round so that start-ups can use them.

5.3. Validation

First, the upscaling guideline was validated by a project manager. The recommendations to consortia in the industry were presented to the project manager of the case 'Inside-Out'. Positive feedback was received to the recommendations. It was stated that some recommendations were somewhat obvious, but the inclusion of specific stakeholders in the consortium, such as the mediator and architect, solved certain barriers to the project. Especially the inclusion of a mediator was essential. In project Inside-Out, many responsibilities were not tracked, and when the mediator became involved, the debate about responsibilities became much more streamlined. Positive feedback was received on the timeline as well. It was stated that it was very helpful to be guided in an uncommon process. One suggestion made by the project manager was that the timeline could be expanded with leading actors for each phase concerning the actions needed.

The policy implications were validated by the interviewee from Province Utrecht. The proposed advice had been presented to check whether the advice was clear and usable. Overall, the advice as described was clear, and it was stated that most advice was directed to specialists among policymakers. The policymaker provided extra information about the enlargement of legitimacy, assisting network building, and organising learning processes and knowledge sharing. These elements were added to the policy advice.

6. CONCLUSION

This research contributes to the scientific field by providing insights into what influences the upscaling of net-zero energy retrofit for high-rise buildings. This is important for the energy transition and to mitigate climate change. Besides, this paper studied the dynamics and mechanisms driving the adoption and diffusion of module-based and product-based innovations.

This research presented lease agreements as a solution for upscaling barriers such as the fear of high initial costs for an NZEB high-rise retrofit project. Future research could investigate the possibilities for lease agreements for retrofit concepts. Another suggestion is to study the industrialisation of the manufacturing process. It is frequently mentioned that the optimal strategy can substantially lower the NZEB retrofit concept's manufacturing costs. Future research could also look at the adoption mechanisms of end-users in NZEB retrofit projects. The case study in this paper showed that learning processes mostly include learning about technology and practical execution. Little learning was done on the social aspects of the retrofit projects.

7. REFERENCES

Attia, S. (2018). Net Zero Energy Buildings (NZEB): Concepts, frameworks and roadmap for project analysis and implementation. https://books.google.nl/books?hl=en&lr=&id=w084DwAAQBAJ&oi=fnd&pg=PP1&dq=Net+Zero +Energy+Buildings+(NZEB)+Concepts,+Frameworks+and+Roadmap+for+Project+Analysis+and+Implementation& ots=1NUX0G7GOZ&sig=M8S12Xn5oSml50KGKTj2OzD15ho

Dijk, M., de Kraker, J., & Hommels, A. (2018). Anticipating Constraints on Upscaling from Urban Innovation Experiments. Sustainability 2018, Vol. 10, Page 2796, 10(8), 2796. https://doi.org/10.3390/SU10082796

Du, H., Han, Q., & de Vries, B. (2022). Modelling energy-efficient renovation adoption and diffusion process for households: A review and a way forward. Sustainable Cities and Society, 77, 103560. https://doi.org/10.1016/J.SCS.2021.103560

Du, H., Han, Q., & Vries, B. de. (2021). Housing energy-efficient renovation adoption and diffusion: a conceptual model for household decision-making process. ECPPM 2021 – EWORKAND EBUSINESS IN ARCHITECTURE, ENGINEERINGAND CONSTRUCTION, 232–241. https://doi.org/10.2/JQUERY.MIN.JS

European Commision. (2019). Energy performance of buildings. https://ec.europa.eu/energy/en/topics/energy-efficiency/energy-performance-of-buildings/overview

Frank W. Geels, & Johan Schot. (2010). The dynamics of socio-technical transitions: A socio-technical perspective. https://www.researchgate.net/publication/309174050_The_dynamics_of_socio-technical_transitions_A_socio-technical_perspective

Geels, F. W. (2004). From sectoral systems of innovation to socio-technical systems: Insights about dynamics and change from sociology and institutional theory. Research Policy, 33(6–7), 897–920. https://doi.org/10.1016/J.RESPOL.2004.01.015

Government of the Netherlands. (n.d.). Central government encourages sustainable energy. Retrieved May 9, 2022, from https://www.government.nl/topics/renewable-energy/central-government-encourages-sustainable-energy

IPCC. (2018). An IPCC Special Report on the Impacts of Global Warming of 1.5°C above Pre-Industrial Levels and Related Global Greenhouse Gas Emission Pathways, in the Context of Strengthening the Global Response to the Threat of Climate Change.

Jolly, S., Raven, R., & Romijn, H. (2012). Upscaling of business model experiments in off-grid PV solar energy in India. Sustainability Science, 7(2), 199–212. https://doi.org/10.1007/S11625-012-0163-7/TABLES/4

Kent Peterson, Paul Torcellini, & Roger Grant. (2015). A COMMON DEFINITION FOR ZERO ENERGY BUILDINGS.

Rogers, E. M. (1962). DIFFUSION OF INNOVATIONS. Simon and Schuster. https://books.google.nl/books?hl=en&lr=&id=v1ii4QsB7jIC&oi=fnd&pg=PR15&dq=diffusion+of+innovations+rogers&ots=DMSxuMZt9U&sig=hsPCe-JCyCyRHmKzj-8ZGwjKbM8#v=onepage&q=diffusion of innovations rogers&f=false

Schot, J., & Geels, F. W. (2008). Strategic niche management and sustainable innovation journeys: theory, findings, research agenda, and policy. Https://Doi.Org/10.1080/09537320802292651, 20(5), 537–554. https://doi.org/10.1080/09537320802292651

Sengers, F., Wieczorek, A. J., & Raven, R. (2019). Experimenting for sustainability transitions: A systematic literature review. Technological Forecasting and Social Change, 145, 153–164. https://doi.org/10.1016/J.TECHFORE.2016.08.031

Smith, A., & Raven, R. (2012). What is protective space? Reconsidering niches in transitions to sustainability. Research Policy, 41(6), 1025–1036. https://doi.org/10.1016/J.RESPOL.2011.12.012

Smith, A., Voß, J. P., & Grin, J. (2010). Innovation studies and sustainability transitions: The allure of the multi-level perspective and its challenges. Research Policy, 39(4), 435–448. https://doi.org/10.1016/J.RESPOL.2010.01.023

van den Bosch, S. (2010). Transition experiments: exploring societal changes towards sustainability. https://repub.eur.nl/pub/20714/

van den Heiligenberg, H. A. R. M., Heimeriks, G. J., Hekkert, M. P., & van Oort, F. G. (2017). A habitat for sustainability experiments: Success factors for innovations in their local and regional contexts. Journal of Cleaner Production, 169, 204–215. https://doi.org/10.1016/J.JCLEPRO.2017.06.177

van Oorschot, J. A. W. H., Hofman, E., & Halman, J. I. M. (2018). A bibliometric review of the innovation adoption literature. Technological Forecasting and Social Change, 134, 1–21. https://doi.org/10.1016/J.TECHFORE.2018.04.032

Verhees, B., Raven, R., Veraart, F., Smith, A., & Kern, F. (2013). The development of solar PV in The Netherlands: A case of survival in unfriendly contexts. Renewable and Sustainable Energy Reviews, 19, 275–289. https://doi.org/10.1016/J.RSER.2012.11.011

#113: Mycorrhizal inoculant and bamboo biochar amendment promoted mycorrhizal population and soil nutrients for sustainable cacao farming

Emer C. GESTIADA, Lea Joy M. MORONG, Kristel S. VICTORIA, Nelly S. AGGANGAN

National Institute of Molecular Biology and Biotechnology
Office of the Vice Chancellor for Research and Extension
University of the Philippines Los Baños
College, Laguna, Philippines, 4031
ecgestiada@up.edu.ph
lmmorong@up.edu.ph
ksvictoria@up.edu.ph
nsaggangan@up.edu.ph

Abstract: Poor soil nutrient levels and acidity negatively impact the production of high value crops that constitute the food economy and security background in most countries. Arbuscular mycorrhizal fungi (AMF) are proven to have biological activities that improve soil fertility and productivity of many crops, including cacao (Theobroma cacao). In this study, the long-term effects of AMF and biochar applied singly or in combination on rhizosphere mycorrhizal population was investigated. Grafted cacao seedlings (var UF18, K1, and K2) bought from an accredited cacao grower were inoculated with AMF (MYKORICH®, coded as MR) during transfer into bigger polybags filled with 1.5 kgs of soil sand mixture (1:1 v/v) and grown in a nursery of UPLB-BIOTECH. Field planting was done after six months where biochar was added as a treatment. The initial mycorrhizal spore level and soil fertility were assessed during field planting. Rhizosphere soil samples were collected every 12 months for over 5 years to assess any improvement of mycorrhizal population and soil fertility. Overall, MR+/-BB significantly improved the mycorrhizal sporulation as compared to its uninoculated counterparts, especially in K1 variety. In addition soil physico-chemical properties in UF18 and K2 varieties significantly improved two years after inoculation. Correlation analysis showed the significant positive effects of MR+/-BB to mycorrhizal population build up and to soil fertility. Moreover, regression analysis showed that AMF density predicts the variation in soil nutrients. Increase in AMF a year after inoculation has contributed to overall significant impact on soil physico-chemical characteristics and nutrients in the succeeding years. AMF density significantly (p<0.0001) predicted 87% in the variation of soil pH (F=74.28, b=0.433); 90% of OM (F=94.48); 89% of N (F=86.4); 71% of P (F=26.94); and 89% of soil CEC (F=85.78). Results show that mycorrhizal inoculant can enhance soil fertility even under stressed environmental conditions. Findings support the value of the technology as a renewable biological solution to agricultural problems arising from soil nutrient deficiency and acidity. Results must be verified in other high value crops and in other ecosystems with similar structure to demonstrate and establish the effectiveness of the technology for wider use by various sectors.

Keywords: AMF; biochar; physico-chemical properties; mycorrhizal spore build up

1. INTRODUCTION

Soil acidity reduces the availability of all essential elements causing high mortality, retarded growth, and low crop yield particularly of high value crops that constitute the global food economy. Problems in soil degradation including poor health and increased erosion are a major concern in sustainable production systems (Jianping, 1999). Hence, improving soil quality and fertility in the most sustainable, safe, and cost-effective way is of worldwide concern.

The use of biofertilizers has gained significant interest in sustainable farming systems and as a safe replacement for chemical fertilizers. They contain microorganisms, such as mycorrhizae, that when applied to seed, plant surfaces or soil increase supply of nutrients, root biomass or root area, and nutrient uptake capacity (Vessey, 2003). They are widespread in nature and associated with more than 80% of plants (Atluntas, 2021). As such they can be harnessed for their growth and yield-promoting potential as well as provide a renewable resource that is economical, eco-friendly, more efficient, productive, and accessible to marginal and small farmers (Kumar *et al.*, 2017).

The use of biochar technology has also gained attention due to its ability to promote plant growth and productivity and improve poor soil conditions (Biederman and Harpole, 2012). When added to soil, biochar increases water and nutrient retention, lowers bulk density, increases pH (Laird, 2008) and increases CEC (Cation exchange capacity), thereby enhancing the uptake and assimilation of nutrients and promoting the beneficial microbial elements like rhizobacteria (PGPR) and AMF present in the rhizosphere (Soudek *et al.*, 2017) and improving the production of phytohormones (Mehari *et al.*, 2015). The impact of biochar in regulating growth through direct or indirect mechanisms can vary with plant species. Chukwuka *et al.* (2020) reported positive effects of biochar application on soil beneficial microbes, soil quality and crop yield.

Cacao is one of the high value crops in the Philippines planted by small farm-holders and can be seen intercropped with other crops like coconut, lanzones, and banana, among other perennial crops. Cacao has high diversified uses from food to non-food that cannot be substituted by other products or raw materials, thus, it warrants a sustainable marketing opportunity. The Philippines ranks 24th among the top countries producing cacao beans but placed 72nd among the exporting countries with less than 0.01% global market share. Philippine earnings from exports reached USD 17,449,939 in 2020 with 82% from cacao beans. However, import of cacao exceeds the export value with an average of USD 168.3-M and USD 22.1-M, respectively, as major chocolate manufacturers in the country prefer to use imported powder and cacao butter for their raw materials over local produce. The Philippine Cacao Industry had predicted the cocoa shortage at 1-M metric tons (MT) in 2020. This was due to the increase in global demand of about 4.7 million to 5 million metric tons (MT) and the annual local consumption of 50,000 metric tons (MT) far exceeded the local supply of around 10,000 metric tons (MT). To be globally competitive and sustainable, the cacao industry in the Philippines needs to be revitalised to create greater impact on poverty alleviation and inclusive growth of small-scale farm holders and thereby contribute to overall growth of the Philippine economy. Nevertheless, despite the increasing trend in cacao production, there is still a supply shortage to meet the increasing market demand both locally and internationally. This is due to the high mortality of planting materials and the lack of knowledge of the cacao growers resulting to low productivity (2016-2022 Philippine Cacao Roadmap). While the cacao industry needs to be reinvigorated, the health of the agroecosystem is of the utmost importance to achieve a sustainable cacao production.

The increasing price of fossil fuel-based commercial fertilizers and the ecological and health risks associated with its application has prompted the Philippine government to look for a cost efficient and safe alternative. Several studies had proven the effectiveness of biofertilizers as a renewable source of plant nutrients (Pandey and Singh, 2019). Specifically, microbial fertilizers can play a vital part of sustainable agricultural practices (Chukwuka *et al.*, 2020; Djenatou *et al.*, 2018), for example in cacao farming (Djenatou *et al.,* 2018; Aggangan *et al.,* 2019). Other studies showed the significant effects of combining biofertilizers and other soil amendments to enhance the physical and chemical properties of soil for successful revegetation (Singh *et al.*, 2011).

Several studies have discussed the response of number of agricultural crops, including cacao, to AMF technology. Notwithstanding, studies on the effects of biochar technology particularly on AMF population and soil nutrients status, specifically with cacao seedlings, is very limited if not lacking and therefore needs to be investigated. Soumaila *et al.* (2012) determined that cacao can be highly associated with AMF. Further, mycorrhizal treatment promoted a 73% root colonisation in cacao seedlings (Chulan and Ragu, 1986).

Cacao has a very wide ecological and geographical range as it grows in regions within the equatorial range and can tolerate soil ranging from extremely acidic to slightly alkaline (Wood, 1985). However, it will never thrive in poor nutrient areas. Acidic upland in the Philippines comprise 32% of its total land area with a topsoil pH ranging from 5.0 to 5.5. According to Scher (1999), the problem with low pH was that soluble metal ions like aluminum and manganese become toxic. Much greater areas in the country could become productive with the application of biofertilizers on this high value crop. With the mycorrhizae, plants in critical areas and in nutrient depleted zone can effectively reach the nutrient rich areas to absorb the needed nutrients.

MYKORICH® is an inoculant containing 12 species of arbuscular mycorrhizal fungi (AMF) produced by the National Institute of Molecular Biology and Biotechnology of the University of the Philippines Los Baños, Philippines (BIOTECH-UPLB). Using this technology, researchers from the Institute have successfully bioremediated mined out areas in Marinduque province of the Philippines. Moon and Aggangan (2019) and Anarna and Aggangan (2019)

proved that MYKORICH® was effective in promoting growth, survival, biomass, and nutrient uptakes of several reforestation and plantation species such as *Eucalyptus pellita*, *Pterocarpus indicus, Acacia mangium,* and *Eucalyptus urophylla* in the former copper mined areas of Mogpog in Marinduque. These studies led to the conduct of succeeding research using MYKORICH®, with and without the biochar technology in fruit bearing agricultural crops to produce a healthy and nutritious source of food safe for human consumption, despite its exposure to extreme environmental conditions, such as high acidity.

In nursery studies, Jomao-as and Aggangan (2019) showed that MYKORICH® gave the significantly highest increment in height, stem diameter, and dry weight of the roots, stems, and leaves of cacao seedlings after 6 months. The combination of MYKORICH+15% bamboo biochar synergistically improved the total biomass by 111% and nutrient (N and P) uptake compared to uninoculated cacao at 0% BB. Meanwhile, spore count from the rhizosphere as well as the chemical properties of the soil such as pH, available P, exchangeable K, and CEC were consistently improved by 15% BB. After six months, these cacao seedlings were planted in an acidic agroforest ecosystem and bore fruits after a year. Field studies showed that cacao seedlings treated with MYKORICH® gave the highest height and stem diameter increments as compared to untreated counterparts (Victoria and Aggangan, 2019). Meanwhile, in grafted cacao varieties, K1 variety that received MYKORICH with 15% bamboo biochar amendment gave the highest height increment as compared to other treatments 1-2 years after field planting but was outgrown by MR treatment alone after 3 years. For stem diameter, MR+15% BB and MR inoculated K1 variety gave the highest increment on the first and third year, respectively. Highest plant survival was also observed in MR-treated UF18 and K2 varieties (100% and 87%, respectively) throughout the 3-year experiment. Aggangan and Aguilar (2019) further showed that MR-treated UF18 variety had the highest mycorrhizal spore count. The long-term effects of mycorrhizal inoculants in rhizosphere mycorrhizal population and soil fertility five years after receiving the inoculation treatments in 2016 needed to be understood, hence this study. It was concluded that mycorrhizal inoculant not only had a positive effect on mycorrhizal build up but on physico-chemical properties of soil as well during the early reproductive stage of grafted cacao varieties.

This study generally aimed to introduce to cacao farm growers in the local area and across the country an economical and environment-safe farming technology using MYKORICH® alone or in combination with bamboo biochar as a promising renewable natural energy sources for a successful agriculture. Specifically, in this study, the authors have determined the effects of mycorrhizal inoculation on grafted cacao varieties in terms of rhizosphere mycorrhizal build up and soil physico-chemical properties and how the variation in the former can affect the latter parameter in the long run. Moreover, it aimed to assess the effect of bamboo biochar technology as an amendment to the AMF fertilizer.

2.   METHODOLOGY

2.1   Experimental Design

The field experiment was arranged in two factor Randomised Complete Block Design (RCBD) with three blocks and 5 plants per treatment per variety (UF18, K1 and K2). Factor 1 was AMF treatment [with MYKORICH® (+MR) or without (-MR)] amended with bamboo biochar (BB) [0% (-BB) and 15% (+BB)]. Factor 2 was the three varieties: namely, UF18, K1 and K2.

2.2   Biofertilizer, Bamboo Biochar and Vermicompost

MYKORICH® is a soil-less capsulated AMF inoculant developed and commercialised by BIOTECH-UPLB. It contains 12 species of beneficial AMF belonging to the genera *Glomus, Gigaspora, Acaulospora, Scutellospora* and *Entrophospora* which have proven effective for promoting growth, yield, and survival of a wide range of agricultural crops and forest tree species and improve soil nutrient status and productivity. Biochar is an organic material developed from pyrolyzed agricultural waste materials. It is characteristically porous and a carbon-stable material that can provide a suitable habitat for AMF and other soil microbes. Bamboo wastes were collected from the bamboo industries, sun dried, chopped and pyrolyzed at 500°C inside a fabricated closed tank under limited oxygen supply. After an overnight cooling, the pyrolyzed bamboo wastes were soaked in water for 24 hours, air-dried and then pulverized in a stainless mill crushing and mixing machine installed at the Pilot Plant of BIOTECH-UPLB. Meanwhile, the vermicompost was purchased from an accredited commercial producer.

2.3   Clone Preparation and Inoculation

Grafted cacao (var UF18, K1, and K2) were bought from an accredited cacao grower and brought into the screenhouse of BIOTECH-UPLB. These were either uninoculated (Control or -MR) or inoculated with 2 capsules each of MYKORICH® (+MR) during transfer into bigger polybags filled with 1.5 kgs of soil sand mixture (1:1 v/v) and grown for 6 months. Half of the treated plants received 15% bamboo biochar (60g) per hole during field planting in an acidic farmland in Calauan, Laguna in July 2016. All seedlings were applied with 1kg vermicompost organic soil conditioner (100% natural fertilizer). Biochar and vermicompost were mixed thoroughly with the excavated soil from the planting hole prior to backfilling the hole.

2.4 Parameters gathered

Mycorrhizal Spore Population.

A 50g rhizosphere soil sample was taken at random from three trees per treatment to assess the mycorrhizal spore count. The spores were extracted following the wet sieving and centrifugation technique of Brundrett *et al.* (1996). Soil samples were suspended in water, mixed thoroughly, and then decanted three times through a series of steel sieves with pore openings of 0.5mm, 100 µm, and 325 µm. After the first centrifugation, the supernatant was discarded as the spores were left in the pellet. The pellet was re-suspended with 60% sucrose. After centrifugation, spores in the sucrose solution were collected in a fine-mesh sieve (325 µm), washed several times with water, and then placed in Petri dishes with grid lines. Mycorrhizal spores were counted in ten field views under a stereomicroscope and expressed as spores per 50g soil.

Soil Chemical Properties.

Soil samples for chemical analysis were taken at 0-20 cm depth using an auger. The soil was analysed for pH, OM%, N%, available P, exchangeable K, and CEC using standard practice. Soil pH was measured with a compound electrode using a soil-to-water ratio of 1:1. Soil CEC was determined by ammonium acetate distillation, exchangeable K by ammonium displacement of the exchangeable cations, and available P was determined by the Bray method.

2.5 Statistical Analysis

All data gathered were subjected to two-way ANOVA procedure using MSTATC program (Michigan State University, 1989). Treatment means were compared using LSD at $p<0.05$. Correlation and regression analysis between AMF density and soil physico-chemical properties at each monitoring period were done using SPSS ver. 18.3. To find out the extent of variations brought about by the changes in AMF spore count (2017-2019) to soil nutrient status in 2019, regression weights used the former as the independent variable while the latter, the dependent variable.

3. RESULTS AND DISCUSSION

3.1 Mycorrhizal spore population

There was no significant difference in AMF spore count in the 1st and 2nd year among treatment or variety (Table 1). Significant difference in spores per g (spg) however was obtained in treatment and variety interaction in 2017, 2019 and 2022.

AMF population changed through time. The 1st and 2nd year showed an increase in spg reaching its peak in 2018 and declined in the succeeding years (Table 1). A significant decrease in AMF spore density in 2019-2022 was observed in all clones except in MR treated K1. This indicated that biochar addition can either give positive or negative effect to AMF abundance. This result was consistent with the findings of Spokas *et al.* (2012).

Table 1: AMF density in UF18, K1 and K2 clones from 2017-2022 after inoculation with MYKORICH (MR) while in the nursery and amended with bamboo biochar (BB) during field planting in an acidic agroforest ecosystem in Calauan

Source of Variation	BB level	AMF Spore Count 50g⁻¹ soil*			
		2017	2018	2019	2022
Treatment (Factor A)					
-MR	-BB	70±30a	139±62a	17±5c	21±2c
	+BB	67±19a	118±28a	22±6c	27±6c
+MR	-BB	85±29a	116±30a	87±22a	105±17a
	+BB	85±39a	112±46a	49±9b	57±14b
p-value (Factor A)				*<0.0001*	*<0.0001*
Variety (Factor B)					
UF18		85+42a	119±26a	28±8b	43±9b
K1		85±23a	101±38a	61±7a	66±11a
K2		61±24a	144±59a	42±16ab	49±9ab
p-value (factor B)		*0.24*	*0.16*	*<0.0001*	*<0.0001*
p-value (factor A x B)		*0.02*	*0.10*	*<0.0001*	*<0.0001*

*. Analysed using 2-way ANOVA in MSTATC. Values with the same letter/s are not significantly different.

Values in boldface are mean difference between-subjects factors significant at the 0.05, 0.01 and 0.001 level.

Table 2 shows the mycorrhizal density per year. In general, highest AMF density was observed in UF18 with MR (134±39 spg) in 2017, in uninoculated and BB treated K2 in 2018 (167±67 & 169±67 spg) and in MR treated K1 in the succeeding years (136±19 and 174±35 spg, respectively). There was no collection in 2020 due to the pandemic. With respect to effects of AMF and biochar co-amendment, a significant result was noted in UF18 in 2017. MR co-amended with 15% BB gave a 17.34% increase in spg relative to its counterpart without BB (134±39 spg). Likewise, BB amendment had increased the spg by 45% in MR treated K1. By contrast, BB reduced the spg by 63% in MR treated K2.

Table 2: AMF spore count from 50g rhizosphere soil samples recorded from 2017-2022 from UF18, K1 and K2 varieties planted in an acidic agroforest ecosystem in Calauan, Laguna, Philippines after inoculation with MYKORICH® (MR) and amended with +/- bamboo biochar (BB)

Variety	Treatment	AMF Spore Count 50g⁻¹ soil*			
		2017	2018	2019	2022
UF18	CONTROL	53±13bd	105±20ac	14±3d	5±2g
	BB	37±27d	114±11ac	12±2d	18±6fg
	MR	134±39a	142±19ab	60±26b	67±2bc
	MR+BB	115±88ab	116±56ab	25±3d	83±26b
K1	CONTROL	111±67ac	145±100ab	19±3d	28±4ef
	BB	100±5ad	72±6bc	20±1d	23±4eg
	MR	39±16d	53±5c	136±19a	174±35a
	MR+BB	89±3ad	136±43ac	69±5b	38±4df
K2	CONTROL	45±11d	167±67a	18±8d	31±2df
	BB	66±27bd	169±67a	33±16cd	42±8de
	MR	83±31ad	155±66ab	65±22b	73±16b
	MR+BB	51±cd	84±38ac	52±18bc	49±12cd

. Analyzed using 2-way ANOVA in MSTATC. Values with the same letter/s are not significantly different.

In 2018, K2 with BB alone gave the highest spg (169±69) but did not significantly differ with that of untreated control (167±67 spg). BB amendment had increased the spg by 97% in MR treated K1. By contrast, BB reduced the spg by 60% in MR treated UF18.

In 2019, highest spg (136±19) was recorded in K1 with MR alone and lowest in uninoculated UF18, K1 and K2. BB amendment reduced the spg of MR treated K1 by 86%, by 18% in UF18, and 19% in K2.

In 2022, MR without BB gave the highest spg (174±35) in K1 while the untreated UF18 gave the lowest spg (5±2). BB amendment in MR treated K1 and K2 reduced the spg by 152% and 6%, respectively. By contrast, BB amendment increased the spg by 23% in MR treated UF18.

Jomao-as and Aggangan (2019), reported that biochar alone did not improve the number of spore propagules in UF18 cacao seedlings grown in the nursery for six months, instead, an increase was observed in its co-amendment with AMF. AMF+15% BB had the highest spore population in the soil, with up to 549 spores 10 g⁻¹ soil, followed by AMF + 3.75% BB and AMF + 7.5% BB. In another study, bahia grass with MYKORICH + 7.5% BB amended sand gave 176 spg, while 3.75% BB gave 250 spg (Aggangan and Iringan, 2019)

A parallel field experiment on cacao-mycorrhizal fungi association in the present study site using another commercial biofertilizers MYKOVAM® (MV) and BioN™ (containing nitrogen-fixing bacteria) also produced by the UPLB-BIOTECH and endoROOT (eR from the USA) revealed that highest (188.5 per 50 g soil) spore count was when inoculated with MV+eR+BioN™ and 15% biochar. The lowest count was obtained from MR+BioN™ treated plants without biochar (Victoria and Aggangan, 2019).

3.2 Soil Chemical Properties

The physico-chemical properties of the soil (required and study site), biochar and vermicompost are shown in Table 3. Based on previous studies (Villason and Olguerra, 2020), the ideal soil for cacao should be 50% sand and 30-40% clay. Further, it should be friable, non-plastic and non-sticky, and be more than 100cm deep. They further describe the other soil properties that would be ideal for cacao. Based on these, we can see that the study site falls short of the requirements, especially in CEC (+25.72 me/100g), P (-87.42ppm) and K (-100.4 mg/kg).

Table 3: Physico-chemical properties of the soil, biochar and vermicompost used in the study

HYSICO-CHEMICAL CHARACTERISTICS	PORTED REQUIREMENTS FOR CACAO (cited by Villason & Olguera, 2020)	STUDY SITE (Agangan & Aguilar, 2019)	BIOCHAR (Agangan & Aguilar, 2019)	VERMICOMPOST (Agangan & Aguilar, 2019)
CEC (me/100g)	12.00	37.72	7.29	54.24 - 57.15
pH	5.0-6.5	4.72	8.21	6.80
OM (%)	3.50	3.16	9.60	0.36
N (%)	0.09	0.18	0.48	0.19
P (ppm)	100.00	12.58	0.3%	0.25%
K (mg/kg)	117.30	16.90	1.15%	0.14%

Table 4 shows that the variation in soil OM, P, and K was due to interactions between treatments and varieties, while for CEC, varietal differences was the main source of variation. Soil pH and N, however, were not significantly affected by treatment or variety. Overall, there was a significant improvement in soil nutrients and physico-chemical properties, especially in UF18 and K2 varieties. Highest (5.1 ppm) pH was recorded in MR+BB inoculated K2. Three other soil chemical properties were found to be significantly higher in UF18 than any other variety that received MR+/-BB, or with BB alone: specifically, OM in MR, P in MR+BB, and K in BB. Inoculation treatments had no effect on CEC in all varieties (Table 5).

Table 4: Results of ANOVA on soil parameters as affected by inoculation treatments [MYKORICH (MR) with or without bamboo biochar (BB) amendment], variety (UF18, K1 and K2) and its interaction

Source of Variation	BB level	Soil Parameters (Mean ± SD)					
		pH	OM %	N %	P ppm	K (cmolc/kg soil)	CEC (cmolc/kg soil)
Treatments (Factor A)							
-MR	-BB	4.49±0.37a	2.65±0.52b	0.14±0.02a	11.53±1.94c	1.68±0.32b	26.62±1.46a
	+BB	4.47±0.41a	3.09±0.34ab	0.15±0.02a	14.34±2.62bc	2.80±0.35a	27.46±1.12a
+MR	-BB	4.46±0.47a	3.58±0.60a	0.16±0.03a	20.48±3.37ab	1.85±0.43b	27.85±2.34a
	+BB	5.01±0.24a	3.10±0.15ab	0.17±0.03a	26.06±5.65a	1.76±0.63b	27.78±1.31a
p-value (Factor A)			*0.003*	*0.29*	*<0.0001*	*0.0001*	
Variety (Factor B)							
UF18		4.33±0.39a	3.03±0.34a	0.16±0.03a	18.76±4.3ab	3.14±0.45a	30.03±2.11a
K1		4.67±0.35a	3.00±0.44a	0.15±0.02a	21.08±2.57a	1.38±0.14b	25.59±1.57b
K2		4.51±0.37a	3.29±0.43a	0.15±0.02a	14.46±3.31b	1.54±0.71b	26.67±1.01b
p-value (Factor B)		*0.19*	*0.24*	*0.38*	*0.002*	*<0.0001*	*<0.0001*
p-value (A x B)		*0.19*	*0.03*	*0.2*	*<0.0001*	*<0.0001*	

Values in boldface are mean difference between-subjects factors significant at the 0.05 level

With respect to effects of co-amendment of biochar and AMF, soil pH in UF18 (4.03) and K1 (4.63) treated with MR+BB had no significant improvement and was just comparable with MR alone. On the contrary, K2 treated with MR+BB (5.1) had 15% higher pH than its counterpart with MR alone (4.33). The same trend was observed for OM. Addition of BB had reduced OM in UF18 and K1 treated with MR by 24.37% and 23.83%, respectively. Only K2 treated with MR had an increased OM (11%) when amended with 15% BB as compared to its counterpart with MR alone (3.21).

A synergistic effect of biochar and AMF co-amendment had improved soil N by 15% and 2% in MR+BB treated UF18 and K2 relative to its counterpart with MR alone. For K1, effect of MR and MR+BB was just comparable. The same trend was observed for soil P in MR+BB treated UF18 and K2 that had an increased P (71% and 9%, respectively) relative to its counterparts with MR alone. By contrast, amendment of BB to MR treated K1 reduced P by 54%.

For soil K, the effect of biochar and AMF co-amendment was positive in K2 (1.87 cmolc/kg soil or 7% higher) but not in UF18 with 18% decrease when compared with MR alone. For K1, the effect of MR and MR+BB was just comparable. Finally, inoculation treatments had no effect to CEC.

Table 5: Results of soil physico-chemical analysis after inoculation of UF18, K1 and K2 var with MYKORICH (MR) while in the nursery and amendment of bamboo biochar (BB) during field planting in an acidic agroforest ecosystem in Calauan, Laguna - measured as: pH, OM %, N %, P (ppm), K (cmolc/kg soil), and CEC (cmolc/kg soil)

Variety	Treatment	Soil Parameters					
		pH	OM %	N %	P ppm	K (cmolc/kg soil)	CEC (cmolc/kg soil)
UF18	Control	4.37±0.21ab	2.26±0.19d	0.13±0.01b	5.93±0.29f	1.64±0.44ce	28.50±1.71ab
	BB	4.57±0.80ab	2.93±0.32bd	0.16±0.01ab	10.50±1.50ef	6.02±0.14a	30.31±1.89a
	MR	4.33±0.49b	3.95±0.84a	0.17±0.03ab	13.10±4.90de	2.70±0.34b	30.60±3.86a
	MR+BB	4.03±0.06b	2.99±0.01bd	0.20±0.06a	45.50±10.50a	2.21±0.90bc	30.72±0.97a
K1	Control	4.63±0.47ab	2.98±0.92bd	0.15±0.03ab	16.00±3.00ce	2.22±0.19bc	25.19±2.12c
	BB	4.70±0.26ab	2.73±0.29cd	0.14±0.01b	21.67±3.21c	1.00±0.17e	25.34±0.35c
	MR	4.70±0.61ab	3.57±0.30ab	0.16±0.03ab	32.00±2.00b	1.10±0.11de	26.18±2.19bc
	MR+BB	4.63±0.06ab	2.72±0.24cd	0.16±0.01ab	14.67±2.08de	1.19±0.09de	25.64±1.61bc
K2	Control	4.47±0.42ab	2.72±0.44cd	0.15±0.02ab	12.67±2.52de	1.16±0.31de	26.18±0.54bc
	BB	4.13±0.15b	3.62±0.42ab	0.17±0.03ab	10.85±3.15ef	1.39±0.76de	26.74±1.14bc
	MR	4.33±0.31b	3.21±0.65ac	0.14±0.02b	16.33±3.21ce	1.74±0.85ce	26.77±0.98bc
	MR+BB	5.10±0.61a	3.59±0.20ab	0.15±0.01ab	18.00±4.36cd	1.87±0.91cd	26.98±1.37bc

Ishii and Kadoya (1994) revealed that co-amendment of biochar and AMF enhanced access of roots to available soil nutrients that translated to improved microbial population, stimulated mycorrhizal performance, and enhanced physical and chemical properties of soil. The tiny pores in the biochar serve as a haven for mycorrhizal hyphae and various symbiotic bacteria that protect them from microbial predators, thus enhancing plant host-fungus symbiosis. Also, biochar favourably influenced the complex chemical communications between plants and mycorrhizae and made certain inhibitory compounds ineffective (Warnock *et al.*, 2010). Addition of biochar in the soil may improve bulk density, water holding capacity, soil pH and cation exchange capacity resulting to a more favourable environment for mycorrhizal colonization and activities that could give beneficial effects on plant growth (Atkinson *et al.*, 2010; Yamato *et al.*, 2006); and improved nutrient content and nutrient retention (Lehmann *et al.*, 2003).

3.3   Correlation Analysis

Table 6 shows the significant correlation *(p<0.05 – p<0.001)* between mycorrhizal spore count at different monitoring periods (2017-2019) and soil chemical properties (2019). Result shows that soil pH and N, pH and AMF spore count in 2018 and pH and P have negative correlation. By contrast, pH and K, OM and CEC, OM and AMF spore count in 2019, N and AMF spore count in 2017, K and CEC, AMF spore count in 2017 and 2018, N and OM, OM and P, P and N, and P and AMF spore count in 2017 were all positively correlated.

Table 6: Results of correlation analysis between mycorrhizal spore count in 2017-2019, nutrient status, and chemical properties of soil (2019) after inoculation of UF18, K1 and K2 var with MYKORICH (MR) while in the nursery and amendment of bamboo biochar (BB) during field planting in 2016 in an acidic agroforest ecosystem in Calauan, Laguna, Philippines

Variables	1.	2.	3.	4.	5.	6.	7.	8.	9.
1. pH		-0.113	-0.314	-0.238***	0.478	-0.066	-0.193	-0.337*	0.206
2. OM	-0.113		0.817***	0.541***	0.169	0.34*	0.219	0.124	0.323*
3. N	-0.314*	0.817***		0.557	0.098	0.252	0.278*	0.174	0.012
4. P	-0.238	0.541***	0.557***		0.077	0.042	0.488***	0.274	-0.014
5. K	0.478*	0.169	0.098	0.077		0.477*	-0.101	-0.246	-0.107
6. CEC	-0.066	0.34*	0.252	0.042	0.477*		0.119	0.083	-0.024
7. AMF_2017	-0.193	0.219	0.278*	0.488***	-0.101	0.119		0.476**	-0.087
8. AMF_2018	-0.337*	0.124	0.174	0.274	-0.246	0.083	0.476**		-0.142
9. AMF_2019	0.206	0.323*	0.012	-0.014	-0.107	-0.024	-0.087	-0.142	

*Significant at 0.05 level, **Significant at 0.01 level, ***Significant at 0.001 level

3.4   Regression Analysis

AMF spore population has significantly *(p<0.05 - p<0.0001)* contributed to overall variation in soil nutrient status, except in soil K (Table 7). Increase in AMF a year after inoculation has therefore contributed to overall significant impact on soil physico-chemical characteristics thus, AMF density can serve as a predictor of changes in the latter variables.

For the variation in all soil chemical composition other than K, AMF spore population was a significant contributory variable. Specifically, AMF population build up in 2018 and 2019 significantly predicted the soil pH *(F=74.28; b=433, p<0.00 in 2018 and b=0.367, p <0.0001 in 2019)*. Moreover, *r²=0.87* depicts that the model explains 87% of the variance in soil pH was due to changes in AMF population between those periods.

AMF density during the entire monitoring period significantly *(F= 94.48)* contributed to 90% variation in soil OM; to 89% variation in N; to 71% variation in P; and to 89% variation in CEC.

The positive relationships of mycorrhizal spore count with all the essential soil nutrients except K and the former's negative relationship with the soil acidity (pH) was consistent with the potential synergism between biochar additions and mycorrhizal abundance – that result in increased nutrient availability in the soil (Yamato *et al.,* 2006). Combined mycorrhizal fungi and biochar could be a more effective and efficient soil amendment strategy for a higher crop productivity and sustainability (Warnock *et al.,* 2010).

Table 7: Results of regression analysis between mycorrhizal spore count in 2017-2019, nutrient status, and chemical properties of soil (2019) after inoculation of UF18, K1 and K2 var with MYKORICH (MR) while in the nursery and amendment of bamboo biochar (BB) during field planting in 2016 in an acidic agroforest ecosystem in Calauan, Laguna, Philippines

Independent Variable	Dependent Variable	Beta Coefficient	r²	F	*t-value*	*p-value*
AMF Spore Count	Soil Nutrients					
2017		0.222			1.63	0.11
2018		0.433	0.87	74.28	3.11	0.00
2019	pH	0.367			4.15	<0.001
2017		0.262			2.15	0.04
2018		0.397	0.90	94.48	3.17	0.00
2019	OM	0.378			4.77	<0.001
2017		0.281			2.21	0.03
2018		0.446	0.89	86.41	3.42	0.00
2019	N	0.299			3.62	<0.001
2017		0.611			3.00	0.01
2018		0.177	0.71	26.94	0.85	0.40
2019	P	0.099			0.75	0.46
2017		0.293			1.16	0.25
2018		0.251	0.56	13.74	0.97	0.34
2019	K	0.272			1.66	0.11
2017		0.234			1.83	0.08
2018		0.476	0.89	85.78	3.64	<0.001
2019	CEC	0.316			3.82	<0.001

Results of our study were consistent with the findings of Syib'li *et al.* (2013) pointing to the influence of AMF as an indicator of soil fertility through the enhancement of chemical, biological and physical content of soil with *Tithonia difersivolia.* He observed that the most fertile soil had the highest AMF spores density and confirmed that AMF had high interaction with organic carbon, organic matter, total phosphorus, cation exchange capacity, water level, soil fungi and soil bacteria.

In this study, we also revealed that mycorrhizal inoculant and biochar technology applied alone or in combination had either positively or negatively affected the AMF spore density and soil nutrients status on grafted cacao varieties. Further, we confirmed that farm practice can be different by plant species or by varieties, whether from seeds or from clones. In general, findings revealed the viability and sustainability of the mycorrhizal-biochar technology in cacao farming.

4.   SUMMARY AND CONCLUSION

UF18, K1 and K2 cacao varieties responded differently to inoculation treatments. UF18 and K2 inoculated with MR+/-BB and with BB alone, respectively had an improved soil nutrient status, while K1 inoculated with MR alone had improved mycorrhizal density over time.

For K1, MR was the most effective inoculant that promoted mycorrhizal sporulation and density. This was so because the amendment of BB to MR, or with BB alone, just led to decreased capacity of K1 to sporulate hence its lowered AMF spore count. For UF18, MR+BB was the most effective since the addition of BB resulted in increased AMF density and improved OM, N, P and CEC. With BB alone, UF18 had the highest K, especially needed during the onset of flowering and the fruiting stage. Re-application of BB before the flowering season is therefore recommended. MR+BB is recommended for K2. Amendment of BB to MR contributed to an improved soil pH. Replication of the study in other areas in the country with similar ecosystem can be explored to understand how the beneficial microbes from these inoculants can symbiotically co-exist with different plant species and promote mutualistic biological action for improved AMF density and abundance and soil fertility. The timing of application of the inoculants in combination with the bamboo biochar and the re-application of biochar before the flowering season should also be explored for a more successful soil amelioration practice.

Findings showed that AMF-biochar technology can be a viable and sustainable solution to address food insecurity and renewable energy security problem of the country. The authors offer a promising technology for a more sustainable agricultural practice in place of the highly expensive synthetic commercial fertilizers. Nonetheless, results must be verified with other high value crops and in other ecosystems with similar structure to demonstrate and establish the effectiveness of the technology for wider use by various sectors.

5. ACKNOWLEDGEMENT

6. REFERENCES

Aggangan, N.S. & Irigan, D.S. (2019). Spore Production and Root Colonization of Arbuscular Mycorrhizal Fungi in Different Media and Levels of Biochar: Their Effect on Growth of *Paspalum notatum*. Philippine Journal of Crop Science (PJCS) Special Issue, 44: 28-38.

Aggangan, N.S., & Aguilar, E.A. (2019). Response of three cacao (Theobroma cacao L.) varieties to biochar and microbial inoculation. Philippine *Journal of Science,* 44: 89-97.

Atkinson C.J., Fitzgerald J.D., & Hipps, N.A. (2010). Potential mechanisms for achieving agricultural benefits from biochar application to temperate soils: a review. *Plant Soil*, 337(1- 2):1-18.

Atluntas, O. (2021). Production of vegetable crops by using arbuscular mycorrhizae. In: Radhakrishnan, R. (eds). 2021. Mycorrhizal Fungi Utilization in Agriculture and Forestry, DOI: 10.5772/intechopen.97552

Berruti, A., Lumini, E., Balestrini, R., & Bianciotto, V. (2016). Arbuscular mycorrhizal fungi as natural biofertilizers: let's benefit from past successes. *Frontiers in Microbiology,* 6: 1559. doi:10.3389/fmicb.2015.01559

Biederman, L.A. & Harpole, W.S. (2012). Biochar and its effects on plant productivity and nutrient cycling: a meta-analysis. GCB-Bioenergy 5(2): 202-214.

Brundrett,. M.C., Bougher, N.D.B., Grove, T, & Malajczuk N. (1996). Working with mycorrhizas in forestry and agriculture. ACIAR Monograph 32. *Canberra: Australian Centre for International Agricultural Research,* 374 p.

Chukwuka, K.S., Akanmu, A.O., Umukoro, O.B., Asemoloye, M.D. & Odebode, A.C. (2020). Biochar: a vital source for sustainable agriculture. *Biostimulants in Plant Science*.

Chulan, H.A., & Ragu, P. (1986). Growth response of *Theobroma cacao.* L seedlings to inoculation with vesicular-arbuscular mycorrhizal fungi. Plant and Soil 96:279-285

Djenatou P, Tchétchoua YH, Kosma P, & Ngonkeu MEL. (2018). Precocious screening tests of the resistance of two varieties of cocoa seedlings *(Theobroma cacao L.)* from combinations of fertilizers against *Phytophthora megakarya* (Brasier and Griffin) in nursery. *African Journal of Agricultural Research, 13* (11): 518-525.

Elad Y, Rav-David D, Harel YM, Borenshtein M, Kalifa HB, Silber A, & Graber, E.R. (2010). Induction of systemic resistance in plants by biochar, a soil applied carbon sequestering agent. *Phytopathol.,* 100: 913– 921.

Ishii T, & Kadoya, K. (1994). Effects of charcoal as a soil conditioner on citrus growth and vesicular -arbuscular mycorrhizal development. *J Jpn Soc Hortic Sci*. 63:529-535.

Jomao-as JG, & Aggangan NS. (2019). Growth, nutrient uptake, and soil chemical properties of cacao seedlings using biochar or AMF grown in acidic soil. *Philippine Journal of Science*, 44: 76-82.

Kumar, A., Sah, B., Singh, A.R., Deng, Y., He, X., Kumar, P., & Bansal, R.C. (2017). A Review of Multi Criteria Decision Making (MCDM) towards Sustainable Renewable Energy Development. Renewable and Sustainable Energy Reviews 69: 596-609. https://doi.org/10.1016/j.rser.2016.11.191

Laird, A.D. (2008) The Charcoal Vision: A Win-Win-Win Scenario for Simultaneously Producing Bioenergy, Permanently Sequestering Carbon, While Improving Soil and Water Quality. Agronomy Journal, 100, 178-184.

Lehmann J, Da Silva JP jr, Steiner C, Nehls T, Zech W, & Glaser, B. (2003). Nutrient availability and leaching in an archaeological Anthrosol and a Ferralsol of the Central Amazon basin: fertilizer, manure, and charcoal amendments. *Plant Soil,* 249:343-357.

Lim SL, Wu TY, Lim PN, & Shak KPY. (2014). The use of vermicompost in organic farming: overview, effects on soil and economics. *Journal of the Science of Food and Agriculture,* 95(6):1143– 1156.

Mehari, Z.H., Elad, Y., Rav-David, D., Graber, E.R., & Harel, Y.M. (2015). Induced systemic resistance in tomato (*Solanum lycopersicum*) against *Botrytis cinerea* by biochar amendment involves jasmonic acid signaling. Plant Soil 395: 31-44. 10.1007/s11104-015-2445-1

Pandey VC & Singh V. (2019). Chapter 20-Exploring the Potential and Opportunities of Current Tools for Removal of Hazardous Materials from Environments. In: Phytomanagement of Polluted Sites, eds. Pandey VC, Bauddh K, *Elsevier*, pp. 501-516, ISBN 9780128139127, https://doi.org/10.1016/B978-0-12-813912-7.00020-X.

Scherr, SJ. (1999). Soil degradation: a threat to developing country food security by 2020? 2020 Brief No. 58, IFRI, Washington, D.C.

Singh JS, Pandey VC, & Singh DP. (2011). Efficient soil microorganisms: A new dimension for sustainable agriculture and environmental development. *Agriculture, Ecosystems and Environmental,* 140:339-353.

Soudek, P., Rodriquez Valesca, I. M., Petrová, Š., Song, J., & Vaněk, T. (2017). Characteristics of different types of biochar and effects on the toxicity of heavy metals to germinating sorghum seeds. Journal of Geochemical Exploration 182 Part B:157–65.

Soumaila, Z. B. I.-M., Tra, T. B., Noêl, Z. G., Claude, K. Z., Ghislaine, F. K. R., & Zézé, A. (2012). Arbuscular mycorrhizal fungi associated with Theobroma cacao L. in the region of Yamoussoukro (Cote d'Ivoire). African Journal of Agricultural Research, 7(6), 993–1001.

Spokas KA, Cantrell KB, Novak JM, Archer DW, Ippolito JA, Collins HP, Boateng, A.A., Lima, I.M., Lamb, M.C., McAloon, A.J., Lentz, R.D., & Nichols, K.A. (2012). Biochar: a synthesis of its agronomic impact beyond carbon sequestration. *J Environ Qual.,* 41: 973–989.

Syib'li, M.A., Muhibuddin, A., & Djauhari, S. 2013. Arbuscular mycorrhiza fungi as an indicator of soil fertility. Agrivita 35(1): 44-53.

Uchida, R., (2000). Essential nutrients for plant growth: nutrient functions and deficiency symptoms. *Plant nutrient management in Hawaii's soils,* 4, pp.31-55.

Vessey, J. (2003). Plant Growth Promoting Rhizobacteria as Biofertilizers. Plant and Soil, 255, 571-586. http://dx.doi.org/10.1023/A:1026037216893

Villason, N.A., & Olguera, D.T. (2020). Physico-chemical characteristics of soils under cacao production system in Davao de Oro, Philippines. *Southeastern Philippines Journal of Research and Development,* 115-134.

Warnock, D., Mummey, D.L, McBride, B., Major, J., Lehmann, J., & Rillig, M.C. (2010). Influences of non-herbaceous biochar on arbuscular mycorrhyzal fungal abundances in roots and soils: Results from growth-chamber and field experiments. *Appl Soil Ecol.*, 46: 450-456.

Whipps J.M. (2004). Prospects and limitations for mycorrhizas in biocontrol of root pathogens. *Canadian J Bot.*

Wood, G.A.R. (1985) History and development. In: Wood, G.A.R. and Lass, R.A. (eds) Cocoa. Longman, London, pp. 1–10

Yamato, M., Okimori, Y., Wibowo, I.F., Anshori, S., & Ogawa, M. (2006). Effects of the application of charred bark of Acacia mangium on the yield of maize, cowpea and peanut, and soil chemical properties in South Sumatra, Indonesia. *Soil Sci Plant Nutr.,* 52:489–495.

2016-2022 Philippine Cacao Roadmap. Department of Trade and Industry, September 2016. Available: https://pef.ph/index.php/2016/09/29/2016-2022-philippine-cacao-industry-roadmap/ Accessed on June 3, 2022.

#115: Endemic microbes and biochar technology increased above-ground biomass and carbon stock of *Pterocarpus indicus* Willd. in a mined-out area

Emer C. Gestiada, Lea Joy M. Morong, Kristel S. Victoria, Nelly S. Aggangan

National Institute of Molecular Biology and Biotechnology
Office of the Vice Chancellor for Research and Extension
University of the Philippines Los Baños
College, Laguna, Philippines, 4031
ecgestiada@up.edu.ph
ljmorong@up.edu.ph
ksvictoria@up.edu.ph
nsaggangan@up.edu.ph

Abstract: This study aimed to develop a technology to bring mined-out areas back to life and thereby contribute to shaping priority areas towards sustainable development and energy security of the country. In this study, growth and development, above-ground biomass, and carbon stocking of Pterocarpus indicus were investigated 24 months after field planting on mine tailings. Five months prior to outplanting, the nursery-grown seedlings were treated with the UPLB-BIOTECH developed inoculants such as the MYKOVAM®, MYKORICH® and BioN™ and the newly developed inoculants containing endemic isolates of arbuscular mycorrhizal fungi (NewMyc) and nitrogen fixing bacteria (NewNFB); applied singly or in combination, and either amended or not with biochar from bamboo (BB) wastes. Except for BioN- and NewMyc-treated plants, amendment of biochar in treated P. indicus resulted in significantly higher growth increment, basal area, biomass density (Mg ha^{-1}), and carbon dioxide sequestered (Mg ha^{-1}). Overall, NFB+NewMyc+BB promoted the highest growth increment, basal area, biomass density, and carbon stock. Amendment of BB in NFB+NewMyc increased the biomass density by 210.33% (from 5.37 Mg ha^{-1} to 16.66 Mg ha^{-1}) and the carbon stock by 79.34% (from 8.86 Mg ha^{-1} to 15.89 Mg ha^{-1}) relative to the control. Meanwhile, its counterpart without BB was just 13.4% higher in biomass and carbon stock relative to the control. With BB alone, plant biomass and carbon stock were just 12% higher relative to the control. This implied a better growth performance of P. indicus with biofertilizers containing endemic AMF and NFB than with BioN, MYKOVAM, MYKORICH, or NFB alone. Results show the value of these new inoculants in developing biofertilizers for an integrated bioremediation protocol for mined-out sites in the country and other countries with similar ecosystems. Further, the findings can support a relevant policy for the adoption, resourcing and dissemination of the technology and/or protocol. Finally, the technology/protocol contributes to the country's efforts in developing a sustainable economy.

Keywords: biomass density; carbon storage; bioremediation; beneficial microbes; biochar

1. INTRODUCTION

Explorations and mining of mineral resources contribute to economic growth and create job opportunities in the local and international scale; however, the resulting exacerbated ecological and health damage have been of major concerns due to limited funds and sustainable restoration technologies, especially for abandoned mines. Bringing back these mined-out areas into its original state or near state is costly and a major challenge worldwide, especially in third world countries like the Philippines. Without any sustainable technological interventions, reforestation plants can barely survive from the biotic and abiotic stresses in the mined-out areas and restoration efforts would always be a failure.

Heavy metal pollution in soil is an unavoidable problem following mining activities. Posing hazards to both humans and wildlife, it contaminates receiving water bodies and, through earth excavation, damages landscapes making them unfit for other land uses. Removal of vegetation and earth excavation depletes the carbon dioxide (CO_2) stored in plant biomass both above- and below-ground. Once abandoned, these mines present another environmental challenge – pollution of vital waterways from heavy metals released from underground and surface mine workings, acid mine drainage from the reaction of exposed pyrites and sulphide materials present in the natural environment, and siltation due to exposed mined-out areas (Alforte, 2017). These then undermine the Government's strategy for sustainable development by destroying or severely damaging critical ecosystems including watersheds, rivers, marine ecosystems and important agricultural production areas.

There are 31 mines in the Philippines that are considered abandoned, inactive or closed (Aggangan *et al.*, 2019, p.482), which because of the total area covered present a challenge to rehabilitate. The Philippine Mining Act of 1995 (Republic Act 7942) stipulated that "contractors and permittees shall technically and biologically rehabilitate the excavated, mined-out tailings covered, and disturbed areas to the condition of environmental safety." However, returning the mined-out area to its original, or near to its pre-mining state, can incur huge costs with many companies committing PhP25B in 2016 for mine rehabilitation and another PhP14B for social development and management (Teves, 2018). Top environment officials, nongovernment and special interest groups, as well as impacted communities stress the urgency of these undertakings, stating the 'need to properly manage natural resources and protect the environment' (Teves, 2018). Various technologies are available for rehabilitating mined out areas. However, the success of any of these technologies depends on the appropriateness of technology, its cost, and the timing of its execution.

Rehabilitation of highly degraded areas is costly, although this cost is thought to be lower than the losses that would result from inaction. The high cost of rehabilitation calls for the development of a more sustainable, energy efficient, environment-safe and cost-effective technology such as bioremediation and phytoremediation - the use of pollutant-accumulating microbes and plants to contain/reduce pollutants. Using plants alone is affordable and easily implementable (Aggangan *et al.,* 2015), but plant growth may be hampered by the pollutants in the soil which is why arbuscular mycorrhizal fungi (AMF) and ectomycorrhizal fungi (ECMF) are used to enhance plant growth and survival especially in acidic soils with high heavy metal content. These microbes are used in biofertilizers which are biological products containing live microorganisms that, when applied to seed, plant surfaces, or soil, promote growth by several mechanisms such as increasing the supply of nutrients, increasing root biomass or root area and increasing nutrient uptake capacity of the plant (Vessey, 2003). They are economical, eco-friendly, more efficient, productive and accessible to marginal and small farmers (Kumar *et al.*, 2017)

The mine tailings pits in Mogpog, Marinduque have been abandoned for more than 35 years now but still pose a threat to people and even to wildlife. Past rehabilitation efforts of the Local Government Unit (LGU) in the abandoned mined-out areas in have failed. Planted seedlings did not survive in the acidic mine tailings with deficient nutrients and ladened with heavy metals, such as, copper, cadmium, lead and zinc. Considering the high cost incurred from the past rehabilitation projects and with the recurring failures in mines restoration, the Local Government Unit sought expert technical assistance and technological innovation in the restoration. The preliminary bioremediation efforts using microbial fertilizers were successful and this bioremediation approach gave the local community a hope for the future of the country's environment.

For the succeeding phytoremediation of another site, researchers planted narra, *Pterocarpus indicus*, due to its very high tolerance to a wide range of environmental conditions. Although critically endangered due to rampant illegal logging and habitat destruction, it is widely used as a reforestation species in the country due to its premium quality and high ability to fix atmospheric N (Combalicer *et al.,* 2011) and thus offers a viable option for bioremediation of the mined-out site.

Several short-duration studies have looked at the effects of biofertilizers in agriculture, in rehabilitating degraded lands, and in remediating mined-out areas. Most have been limited to the nursery with very few conducted in the field to verify the beneficial effects of microorganisms in reducing heavy metal toxicity and lessening the soil pollution. In this study, we investigated the efficacy of newly developed inoculants, containing endemic AMF and nitrogen-fixing bacteria (NFB), and bamboo biochar amendment in promoting *P. indicus* growth and development, survival, biomass density, and carbon sequestration capacity in the field. We then compared the performance of the effects of newly-developed inoculants with the effects of the commercial inoculants on the said species.

2. METHODOLOGY

2.1 Study site

The 2-ha mined-out area (N 13º29'54" and S 121º 52'12" E) was located 60 masl on a plateau-like hill in Brgy. Capayang, Mogpog, Marinduque, Philippines. It was abandoned by the Consolidated Mines Inc. after more than three decades of copper (Cu) and gold (Au) extraction in an open pit mine. The hazards from the pit can be deduced from the results of the physico-chemical analysis of the soil from the mined-out area. It was highly acidic with low organic matter and nutrient content (Table 1). Heavy metal (HMs) and Cu content exceeded the maximum allowable limit of 36 mg kg^{-1} soil when compared to the Dutch standards for soil contamination assessment.

Table 1: The soil physico-chemical analysis conducted in June 2016 in a 2-ha mine tailing in Brgy. Capayang, Mogpog, Marinduque, Philippines planted to P. indicus in 2019

Properties	Values
pH (1:1, soil:water)	4.6±0.25
CEC	18.53±3.52 me 100 g^{-1} soil
% Organic matter	0.34±0.14%
Total N	0.22±0.02%
Available P	75.5±62ppm
Exchangeable K	0.12±0.08 me 100 g^{-1} soil
Ca	6.78±2.45 me 100 g^{-1} soil
Mg	3.48±1.13 me 100 g^{-1} soil
Cu	100 mg kg^{-1} soil

Source: Morong LJM and Aggangan NS, 2019.

2.2 Preparation of biofertilizers, biochar and vermicompost

Microbial inoculants developed by the National Institute of Molecular Biology and Biotechnology (BIOTECH), of the University of the Philippines Los Baños (UPLB) - MYKOVAM®, MYKORICH® and BIO-N™ - were used in the study. They have been proven effective for the growth and development, survival, and yield performance of several agricultural species (Paguntalan, 2020) and forest trees, and for reforestation and bioremediation (Moon and Aggangan, 2019). MYKOVAM® and MYKORICH® both contain 12 species of AMF belonging to the genera *Glomus, Gigaspora, Acaulospora, Scutellospora*, and *Entrophospora* collected and isolated from stressed sites such as grasslands and abandoned mine tailings. MYKOVAM®, developed in 1980, is effective in promoting growth and yield of a variety of agricultural crops, including fruit crops, ornamentals, and forest species. MYKORICH® contains the same mycorrhizal species as MYKOVAM but it is in capsule form and has a different carrier composition. A capsulized (1g) MYKORICH contains a spore count of 100-150. BIO-N™ contains *Azospirillum* spp., a nitrogen-fixing bacteria (NFB) isolated from the roots of *Saccharum spontaneum* (Aggangan *et al.*, 2019). The new inoculants contain endemic AMF (NewMyc) and NFB species (NewNFB) isolated from the copper mine tailings in the site. These were first tested in this study to determine its potential in promoting the growth, survival, biomass accumulation, and carbon dioxide sequestration capacity of *P. indicus*.

The authors believed that utilisation of biofertilizers in ecological restoration can address concerns for long term soil productivity and ecological sustainability that arise from problems in using fossil fuel-based inorganic fertilizers. According to Okon (1985), biofertilizers have several benefits such as the increase in nutrient availability and uptake by the agricultural plants, production of plant growth-promoting substances, suppressions of growth and pathogenic microorganisms, better plant growth and development, increased yield, and enhanced soil quality and nutrients status. Specifically, AMF has positive association with about 80% of plants. They constitute a group of root obligate biotrophs that can provide the host with water, nutrients, and pathogen protection in exchange for photosynthetic products. According to Berruti *et al.* (2016), restoring the natural level of AMF richness warrants a sustainable agricultural practice that lessens dependence on the use of agrochemicals and strengthens the defence system of the AMF-mediated plants to promote growth and development even in soils contaminated with HMs.

The present study has benefitted from the successful results of previous bioremediation and studies on cacao using the locally produced commercial microbial fertilizers. The authors explored the potential of the biochar technology in addition to the established bioremediation approach. A study reported that biochar improved not only soil chemical and physical properties but also soil microbial properties. Addition of biochar to soil could improve soil structure, increase porosity, decrease bulk density, and enhance aggregation and water retention (Baiamonte *et al.*, 2015). Another past study showed that biochar application in nutrient-poor agroecosystems increased plant nutrient availability and carbon dioxide sequestered (Jiang *et al.,* 2012).

For this study we used bamboo biochar from pyrolyzed trimmings collected from local businesses which specialised in making furniture and novelty products. Chopped and sundried wastes were pyrolyzed at 500°C inside a closed tank under limited oxygen supply, then cooled overnight. Finally, pyrolyzed bamboo wastes were soaked in water for

24 hours, air-dried and then pulverized in a stainless mill. The vermicompost, on the other hand, was purchased from an accredited commercial producer.

In the Philippines, biochar technology is widely adopted in the agricultural farm practices and in remediation of polluted environments but not much in bioremediation. The authors used the biochar technology in bioremediation for the first time believing that this would contribute to environmental sustainability and food security. Biochar can cause changes in soil health – on its physical, chemical, and biological features - and maintains the functions of both natural and managed ecosystems essential for sustainable agricultural fertility and productivity (Chintala *et al.*, 2016). The use of biochar on a large scale will also promote sustainable waste management of the community. Turning agricultural waste materials into biochar can help in recycling abundant waste from the environment and provide the surest source of high-quality organic materials for soil amelioration purposes.

Biochar is loaded with ammonium, nitrate, and phosphate hence a promising resource for soil's fertility management (Kammann *et al.*, 2015). Biochar's elemental composition generally include carbon, nitrogen, hydrogen, and some trace elements, such as K, Ca, Na, and Mg (Zhang *et al.*, 2015). Biochar can contain amounts of extractable humic-like and fluvic-like substances (Lin *et al.*, 2012). With this, biochar can provide a healthy habitat for the microbes to increase their population and diversity and enhance their enzyme activities (Ding, 2016). Therefore, the authors concluded that biochar-microbial technology could bring out synergistic effects and could enhance *P. indicus* growth, biomass and carbon dioxide sequestration capacity.

2.3   Experimental design, treatment, and inoculation

We planted on the mine tailings five-month old seedlings of *P. indicus* obtained from a nursery in Gasan, Marinduque, Philippines, that was accredited by the Bureau of Plant Industry. A total of 560 vigorous seedlings of uniform height were selected for the two-factorial experiments (15% or 0% biochar) with eight (8) treatments and seven (7) seedlings per treatment in five (5) blocks.

T1	Control (no additives)	T5	Mykorich
T2	New Nitrogen-Fixing Bacteria (NFB)	T6	Mykovam
T3	New mycorrhiza (Nmyc)	T7	BioN
T4	NFB + Nmyc	T8	New NFB + NMyc +Mrich + BioN

One-month old seedlings were transplanted into individual polybags with 1:2 coir dust and garden soil. For treatment with mycorrhiza and NFB, 5g each of these microbial biofertilizers was added to the polybag with soil medium prior to the placement of the seedlings. Those with MYKORICH® received 2 capsules per seedling. Five months after inoculation, experimental plants were planted out on mine tailings in Barangay Capayang in September 2019. One-ft^2 holes were dug and soil from each of these holes was mixed with 500g lime and 1kg vermicompost before backfilling the mixture into the hole. One month after field planting, 5g of complete fertilizer (14-14-14) plus 500g vermicompost were applied per seedling.

2.4   Soil sampling and analysis

Rhizosphere soil samples randomly selected from three blocks per treatment were digested via dry ashing, and then analysed at the Analytical Services Laboratory of the Agricultural Systems Institute, College of Agriculture and Food Science, UPLB, College, Laguna, for soil nutrients, physico-chemical properties and heavy metals (HMs).

2.5 Parameters gathered

The following parameters were gathered. All data were subjected to ANOVA using MSTATC computer program (MSU 1996). Treatment means were compared using LSD at $p < 0.05$.

Height and stem diameter: a year after field planting, height and stem diameter increments were obtained using a meter stick placed on the soil surface up to the tip of the main stem while stem diameter was measured using a Vernier calliper exactly 3 inches above the soil surface.

Plant biomass density and carbon sequestration: above-ground tree biomass for trees with diameter <5 cm, measured 30cm above the ground, was estimated using the allometric equation developed by Martines-Yrizar *et al.* (1992) for tropical dry forest (Equation 1):

Equation 1:
$$TB = 10^{\{-0.535 + log10\ (BA)\}}$$

Where:

- TB = biomass per tree in kg (kg tree-1)
- BA = basal area in cm2

Root biomass (RB)(kg) was calculated using the regression model developed by Pearson *et al.* (2005), which is based on the calculated TB of individual tree:

Equation 2:
$$RB = exp\ (-1.0587 + 0.8836\ x\ ln(TB)$$

The total tree biomass (TTB) in ton ha-1 was calculated as the sum of above-ground tree and root biomass (Heriansyah *et al.,* 2007):

Equation 3:
$$TTB\ (t\ ha-1) = TTB\ (Mg)/area\ of\ the\ plot\ (sq.m)\ x\ 10,000\ sq.m/ha$$

Where:

- TTB (Mg) = (TB + RB) kg × 1 Mg/ 1000 kg

Biomass conversion to carbon stock: to determine the carbon stock of the trees in the area, a default value of 45% was assumed, being the average carbon content of wood samples growing in secondary forests from the different parts of the Philippines (Lasco and Pulhin, 2000).

The amount of total carbon stored (TCTB) and CO_2 content in the wood biomass was derived using the following:

Equations 4 & 5: $$TCTB = TTB\ x\ \%\ C\ content$$ CO_2 *content = C stored* ✗ *44/12*

Where:

- CO2 = 1 molecule of Carbon and 2 molecules of Oxygen
- Atomic weight C = 12; O = 1
- Weight of CO_2 is C + 2*O = 43.999915 or 44

3.   RESULTS AND DISCUSSION
3.1   Growth performance

In almost all cases, amendment with bamboo biochar in seedlings treated with microbial fertilizers significantly increased stem diameter except when combined with BioN and NewMyc (Figure 1). Overall, NewNFB+NewMyc+BB had the highest stem diameter increment (1.96cm). This was 46.27% higher than its counterpart without biochar (1.34cm) and 51.94% higher than the control. Without BB, NFB+NewMyc was just 3.88% higher than the control. The same trend held true for height increment (Figure 2), with NFB+NewMyc+BB growing 10.71% higher than its counterpart without biochar. Amendment of biochar in almost all treated seedlings significantly increased stem height, except for those with NewMyc, Mykovam, or BioN alone. Lowest height increment was recorded in seedlings with BB alone.
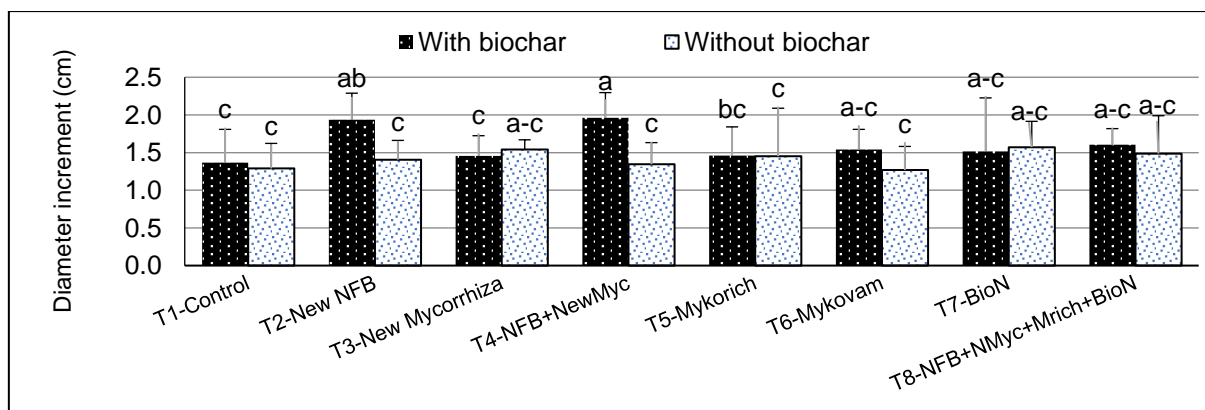
Figure 1: Stem diameter increment of P. indicus 24 mo after field planting in a mined-out area in Brgy. Capayang, Mogpog, Marinduque, Philippines using the microbial inoculants and biochar technology in remediation
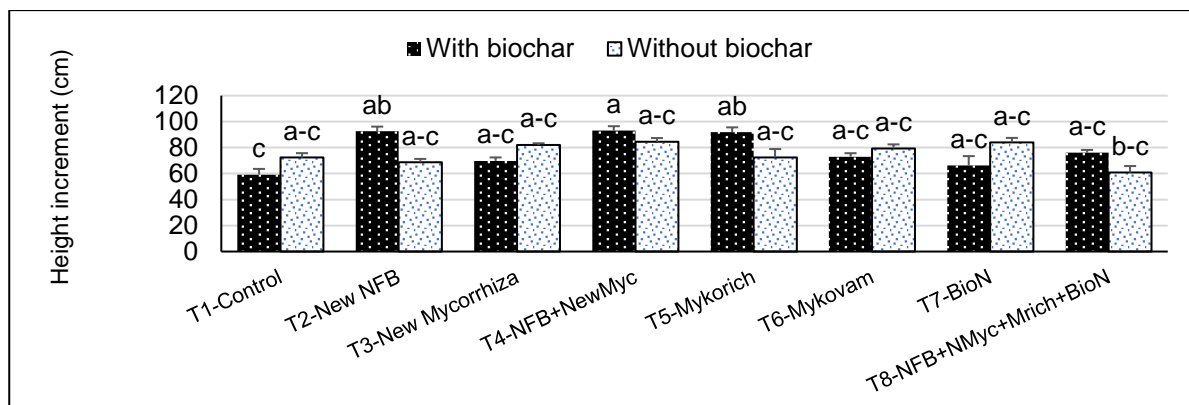
Figure 2: Stem height increment of P. indicus 24 mo after field planting in a mined-out area in Brgy. Capayang, Mogpog, Marinduque, Philippines using the microbial inoculants and biochar technology in remediation

In a 2019 study conducted by Algabre *et al.* at an adjacent site, they concluded that NFB and mycorrhiza did enhance plant growth based on stem height and diameter, and that biological activities of microbes varied depending on the associated host plants species and its synergism with other microorganisms present in the soil amendments. They used commercial mycorrhizal and NFB inoculants in 27-month-old *Acacia mangium, Pterocarpus indicus* and *Eucalyptus urophylla*.

3.2   Biomass density and carbon dioxide sequestration

Overall, basal area coverage, biomass density and carbon dioxide sequestered *by P. indicus* was highest in NFB+NewMyc+BB ($11cm^2$, $16.66Mg$ ha^{-1} and $15.89Mg$ ha^{-1}, respectively). Amendment of biochar had a positive significant effect on the said parameters in almost all seedlings but not with NewMyc, or BioN alone, and even in those with a mixture of all inoculants (Figure 3). Basal area of seedlings inoculated with NFB+NewMyc+BB ($11cm^2$) was 103.74% higher than the control ($6cm^2$); without BB, NFB+NewMyc ($7cm^2$) gave only a 19% increase in basal area relative to the control. Specifically, basal area of seedlings with NFB+NewMyc+BB ($11cm^2$) was 71.28% higher than its counterpart without BB ($7cm^2$).

Except for BioN- and NewMyc-treated plants, amendment of biochar in treated *P. indicus* resulted in significantly higher growth increment, basal area, biomass density (Mg ha^1), and carbon dioxide sequestered (Mg ha^{-1}). As for growth performance, NFB+NewMyc+BB promoted the highest growth increment, basal area, biomass density and carbon stock. Amendment of BB in NFB+NewMyc increased the biomass density by 210.33% (from 5.37 Mg ha^{-1} to 16.66 Mg ha^{-1}) and the carbon stock by 79.34% (from 8.86 Mg ha^{-1} to 15.89 Mg ha^{-1}) relative to the control. Meanwhile, its counterpart without BB was just 13.4% higher in biomass and carbon stock relative to the control. With BB alone, plant biomass and carbon stock were just 12% higher relative to the control. This implied a better growth performance of *P. indicus* with biofertilizers containing endemic AMF and NFB than with BioN, MYKOVAM, MYKORICH, or NFB alone.

Carbon dioxide sequestered was derived from the plant biomass density hence it followed the same trends. Relative to the control, *P. indicus'* biomass density (Figure 4) increased up to 210.33% (from 5.37 Mg ha^{-1} to 16.66 Mg ha^{-1}) while carbon dioxide sequestered (Figure 5) increased up to 79.34% (from 8.86 Mg ha^{-1} to 15.89 Mg ha^{-1}) when inoculated with NFB+NewMyc with BB amendment. Without BB, NFB+NewMyc contributed an increase of around 13.4% (from 5.37 Mg ha^{-1} to 6.09 Mg ha^{-1}) in biomass density and carbon stock (from 8.86 Mg ha^{-1} to 10.05 Mg ha^{-1}) relative to control. Specifically, NFB+NewMyc+BB had 173.45% higher biomass density and 58.03% higher carbon stock than its counterpart without BB. The untreated seedlings had 12% lower biomass and carbon stock than their counterpart with BB amendment.
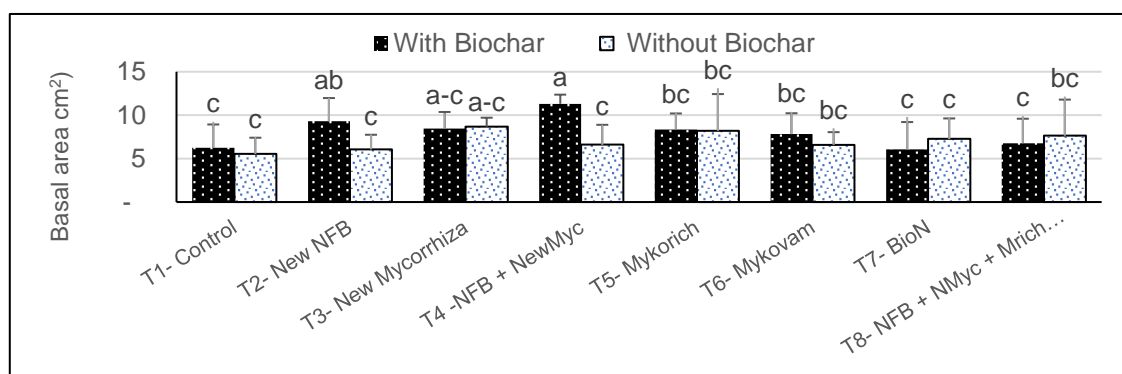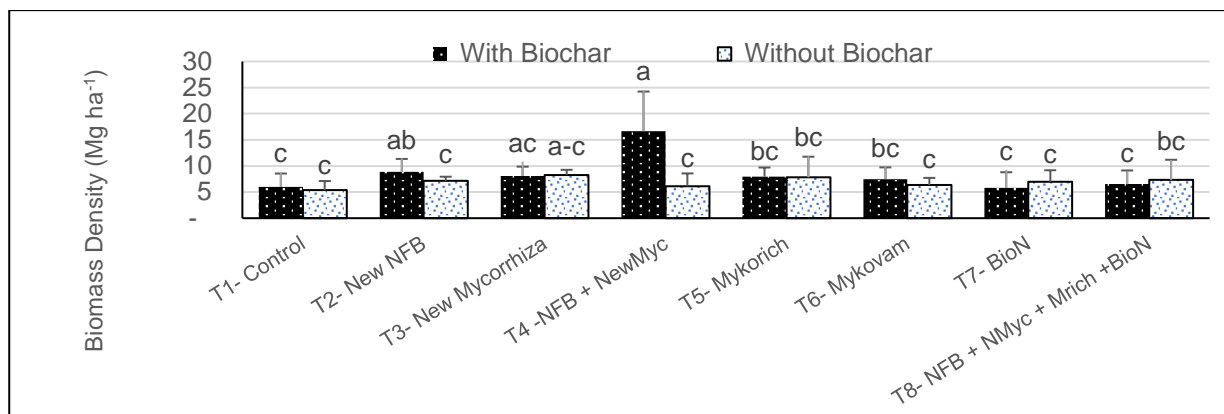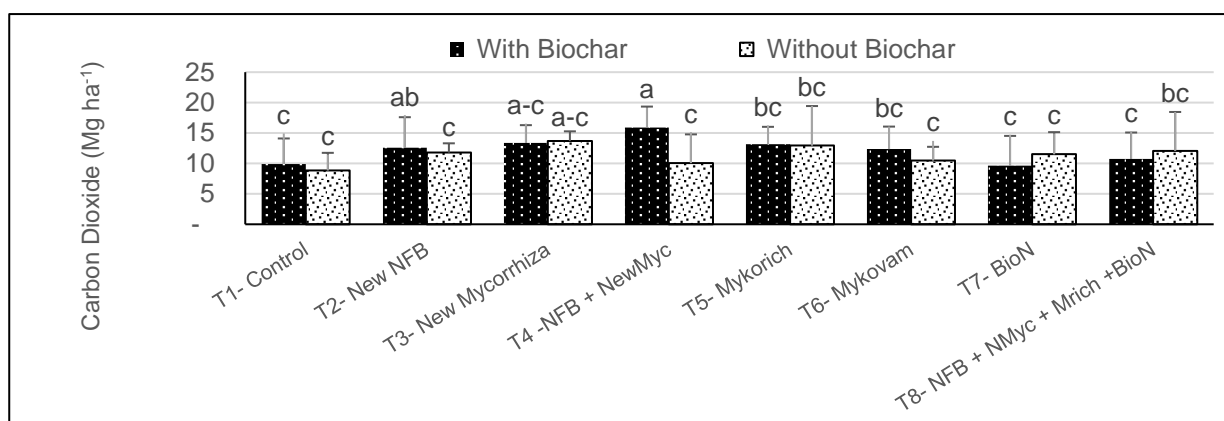

Figure 3: Basal area computed from the stem diameter of P. indicus 24 mo after field planting in a mined-out area in Brgy. Capayang, Mogpog, Marinduque, Philippines using the microbial inoculants and biochar technology in remediation

Figure 4: The biomass density of P. indicus 24 mo after field planting in a mined-out area in Brgy. Capayang, Mogpog, Marinduque, Philippines using the microbial inoculants and biochar technology in remediation

Figure 5: The carbon dioxide sequestered by P. indicus 24 mo after field planting in a mined-out area in Brgy. Capayang, Mogpog, Marinduque, Philippines using the microbial inoculants and biochar technology in remediation

Various authors (Guo *et al.*, 2021) have reported that biochar amendment increased microbial biomass, diversity and enzyme activities. Biochar provided a conducive environment for the microbes, which then enhanced the host plants' growth and increased the plant biomass and its carbon dioxide sequestration capacity. Biochar amendment can reduce soil CO_2 emissions and increase soil organic carbon (SOC) for the long term (Lehmann *et al.*, 2011), with SOC and CO_2 efflux increasing on average by 61 and 19%, respectively (Wang *et al.*, 2015). According to Qingyuan and Chunbo (2016), the glomalin released after AMF hyphal death helped bind soil particles to form soil aggregates that may contribute to long-term carbon storage by protecting soil organic matter from oxygen and microbial decomposers.

According to Chan *et al.* (2006), application of biochar to soils can impact soil GHG fluxes by changing the composition and activity of soil microbes, soil pH and soil biogeochemical processes. Meanwhile, biochar-plant-microbe interaction enhances plants nitrogen fixation capacity thus resulting in enriched soil microbial populations and increased colonisation of the host plant roots by AMF (Yamato *et al.*, 2006). In the present study, the combined effects of biochar-plant-microbe interaction in building up microbial population and improving soil fertility were not studied hence it is recommended for future studies.

As mentioned by Algabre *et al.* (2019), biomass production of a 27-month old *A. mangium* was highest after Mycorrhiza+NFB inoculation (50.87 Mg ha-1) and lowest in the control (36.77 Mg ha-1). Meanwhile, *P. indicus* seedlings with Mycorrhiza+NFB also produced higher biomass (17.03%) as compared to the control (15.32 Mg ha-1). Findings also showed that accumulated biomass and CO_2 content in *A. mangium* and *P. indicus* inoculated with mycorrhiza + NFB increased by 128% and 17%, respectively. The biomass of *E. urophylla* increased by 83% with mycorrhizal inoculation alone. The mycorrhizal inoculant and NFB used in that study were commercially sold and differ from that used in the present study which contained endemic isolates of AMF and NFB.

Biochar has been widely applied to remediate polluted environments (Lyu *et al.*, 2016), however, there is a dearth of information on its use to enhance bioremediation in the country. Valizadeh *et al.* (2021) described the potential of biochar for the remediation of soils contaminated by polychlorinated biphenyls (PCBs). Hammond (2021) observed increased degradation of diesel oil in oil-contaminated soil. Earlier, Lyu *et al* (2016) described applications of biochar produced from various biomasses for remediation of contaminated systems including soils, wastewater, and groundwater.

On the other hand, there are many challenges to the use of biochar technology in the field and especially on heavily polluted soil where the environmental conditions cannot be controlled. Nandy *et al.* (2021) stressed that taking lab-scale research into the field is challenging due to gaps in understanding microbial processes at the polluted niche, bioavailability of the pollutant, survival of non-native species, and lack of an integrated multi-disciplinary approach with the challenges brought about handling the microbes and their continuous monitoring for *in situ* bioremediation.

To ensure success in bioremediation, the timing of application of biochar must be considered. Here, we applied the inoculants and the bamboo biochar to the medium in the nursery. They were placed on the medium in individual polybags during seedling transplanting. Early application ensures better plant growth and nutrient uptake performance once the seedlings are planted in the field. The treated seedlings were planted out in the field after five months to ensure that microbes had already formed synergistic mutual symbiosis with the living microorganisms in the biochar. A blanket application of lime and vermicompost during field planting helped in ameliorating the otherwise compacted and highly acidic mine tailings. Commercial fertilizer was added a month after field planting to correct yellowing of leaves. This technique therefore lessened the application of too much synthetic fertilizers during remediation. This procedure was carried out just once in the entire bioremediation activity implying technological cost-efficiency, effectiveness, sustainability, and environmental safety.

Our previous studies on cacao support benefits gained from the application of microbes+biochar. Victoria and Aggangan (2019) showed that amendment of 15% biochar increased NFB population compared to seedlings without biochar, while the combination of AMF+15% BB improved the total biomass by 111%, and N and P uptake compared to uninoculated cacao without BB. Jomao-as and Aggangan (2019) showed that the amendment of 15% bamboo biochar together with other inoculants significantly increased the mycorrhizal spore count from the rhizosphere and enhanced root infection in the cacao roots. It also improved the pH, available P, exchangeable K and CEC of the soil.

In general, *P.* indicus that received the newly developed bioremediation combination - NFB+NewMyc+BB – performed better than the control and the other plants receiving other treatments in terms of growth and development, biomass accumulation and carbon sequestration capacity. Containing endemic AMF and NFB isolated from the study site, this newly developed inoculant produced compounded effects, especially when amended with 15% bamboo biochar. However, this was the first reported use of the new inoculant and therefore, these results must be validated in other mined-out areas in the Philippines and other ecosystems with similar structure.

4. CONCLUSION AND RECOMMENDATION

This study demonstrated the beneficial effects of the microbial-based fertilizers and the biochar technology in the bioremediation of abandoned mined-out areas in Mogpog, Marinduque. Noteworthy was the better growth performance of *P. indicus* and its enhanced biomass density and carbon dioxide sequestration capacity using the technology with endemic AMF and NFB amended with bamboo biochar. The seedlings inoculated with the new inoculants with 15% biochar gave 46.27% higher diameter increment than its counterpart without biochar and 51.94% higher than the control. Without biochar, the new inoculants just gave 3.88% higher diameter increment relative to the control. Likewise, the new inoculants with 15% biochar gave 10.71% higher increment in the stem height compared to the control. With the biochar alone, seedlings were quite stunted. Plant biomass density and carbon stocks were 210.33% and 79.34% higher in seedlings that received new inoculants with 15% biochar than its respective untreated counterparts. Without biochar, the new technology gave just 13.4% higher biomass and carbon stock relative to the control. Nevertheless, with biochar alone, plant biomass and carbon stock were just 12% higher relative to the control. This newly developed technology is a more sustainable alternative to address soil degradation due to pollution with HMs and land use conversions. This technology and the appropriate protocol are viable, accessible and easily implementable.

A policy recommendation supported by the necessary funding and training will provide the enabling environment for technology dissemination and adoption. Success in the bioremediation of the whole abandoned mined-out area in Mogpog, Marinduque, would be ensured with the integration of the technology into the rehabilitation initiatives of the local government unit, as well as the legislation of biochar production using locally available agricultural biomasses. The protocol and technology developed from this study must also be tested in other mined-out areas in the country to explore its applicability even in places with other environmental conditions. Finally, avenues for continued research include determination of microbial population dynamics during the bioremediation process, as well as determination of costs for specific sites and/or severity of contamination including values accruing to the environment as a result of the bioremediation.

5. ACKNOWLEDGEMENTS

6. REFERENCES

Aggangan NS, Anarna JA and Cadiz NM (2019). Tree Legume -Microbial Symbiosis and Other Soil Amendments as Rehabilitation Strategies in Mine Tailings in the Philippines. *Philippine Journal of Science*, 14(3):481-491.

Aggangan NS, Pampolina NM, Cadiz NM and Raymundo AK (2015). Assessment of plant diversity and associated mycorrhizal fungi in the mined-out sites of Atlas Mines in Toledo City, Cebu for Bioremediation. *Journal of Environmental Science and Management* 18(1): 71-86.

Algabre, IC, Racelis EL, and Aggangan NS (2019). Biomass and Carbon Sequestration of Forest Tree Species in Response to Microbial Biofertilizers. *Philippine Journal of Crop Science (PJCS)* Special Issue, 44: 83-88

Alforte, R (2017). Proposed mine rehabilitation of the abandoned mine of Zambales Base Metals situated at Upper Baluno, Zamboanga City. [online] Mines and Geoscience Bureau, Regional Office No. IX. Available at: https://region9.mgb.gov.ph/index.php/services/49-proposed-mine-rehabilitation-of-the-abandoned-mine-of-zambales-base-metals-situated-at-upper-baluno-zamboanga-city?msclkid=00ddba35cfe711ec9b0f863074786b28 [Accessed on 10 May 2022].

Baiamonte G, De Pasquale C, Marsala V, Cimò G, Alonzo G, Crescimanno G, Conte P (2015) Structure alteration of a sandy- clay soil by biochar amendments. *J Soils Sediments* 15:816–824. doi:10.1007/s11368-014-0960-y

Berruti A, Lumini E, Balestrini R, and Bianciotto V (2016). Arbuscular Mycorrhizal Fungi as Natural Biofertilizers: Let's Benefit from Past Successes. *Frontiers in Microbiology* 6: Available at https://www.frontiersin.org/article/10.3389/fmicb.2015.01559. doi: 10.3389/fmicb.2015.01559

Chan KY, van Zwieten L, Meszaros I, Downie A, and Joseph S (2006). Using poultry litter biochars as soil amendments. *Australian Journal of Soil Research*, 46:437-444.

Chintala R, Owen R, Kumar S, Schumacher TE, Malo D (2016). Biochar impacts on denitrification under different soil water contents. *World Congress of Soil Science,* 6:157-167

Combalicer MS, Lee DK, Woo SY, Park PS, Lee KW, Tolentino EL, and Park YD (2011). Above-ground biomass and productivity of nitrogen-fixing tree species in the Philippines. *Sci Res Essays*. 6(27):5820-5836.

Chukwuka, K. S., Akanmu, A. O., Umukoro, O. B., Asemoloye, M. D., & Odebode, A. C. (2020). Biochar: a vital source for sustainable agriculture. *Biostimulants in Plant Science.*

Ding, Y., Liu, Y., Liu, S. et al (2016). Biochar to improve soil fertility. A review. *Agron. Sustain. Dev.* 36, 36. https://doi.org/10.1007/s13593-016-0372-z

Hammond, A. (2021). Use of biochar to enhance bioremediation of an oxisol contaminated with disel oil. [online] Afribary. Available at: https://afribary.com/works/use-of-biochar-to-enhance-bioremediation-of-an-oxisol-contaminated-with-diesel-oil [Accessed 10 May 2022].

Heriansyah I, Miyakuni K, Kato T, Kiyono Y, and Kanazawa Y. (2007). Growth Characteristics and Biomass Accumulations of Acacia mangium under Different Management Practices in Indonesia. *Journal of Tropical Forest Science*, 19, 226-235.

Jiang C, Yu G, Li Y, Cao G, Yang ZP, Sheng W, Yu W (2012) Nutrient resorption of coexistence species in alpine meadow of the Qinghai- Tibetan Plateau explains plant adaptation to nutrient-poor environment. *Ecol Eng* 44:1–9. doi:10.1016/j.ecoleng.2012.04.006

Jomao-as JG and Aggangan NS. (2019). Growth, nutrient uptake, and soil chemical properties of cacao seedlings using biochar or AMF grown in acidic soil. *Philippine Journal of Science*, 44: 76-82.

Kammann CI, Schmidt HP, Messerschmidt N, Linsel S, Steffens D, Müller C, Koyro HW, Conte P, Joseph S (2015) Plant growth im- provement mediated by nitrate capture in co-composted biochar. *Sci Report* 5:11080. doi:10.1038/srep11080

Kumar S, Nakajima T, Mbonimpa EG, Gautam S, Somireddy UR, Kadono A, et al. (2014). Long-term tillage and drainage influences on soil organic carbon dynamics, aggregate stability, and carbon yield. *Soil Science & Plant Nutrition,* 60:108-118

Kumar R, Kumawat N and Sahu YK. (2017). Role of biofertilizers in Agriculture. *Popular Kheti* 5(4): 63-66. Available at: https://www.researchgate.net/profile/Narendra-Kumawat/publication/323185331_Role_of_Biofertilizers_in_Agriculture/links/5a851abc4585159152b81679/Role-of-Biofertilizers-in-Agriculture.pdf [Accessed on 10 May 2022].

Lasco, R. D., & Pulhin, F. B. (2000). Forest land use change in the Philippines and climate change mitigation. Mitigation and adaptation strategies for global change, 5(1), 81-97.

Lehmann J, Rillig MC, Thies J, Masiello CA, Hockaday WC, and Crowley D. (2011). Biochar effects on soil biota—A review. *Soil Biology and Biochemistry*, 43:1812-1836. DOI: 10.1016/j.soilbio.2011.04.022

Lin Y, Munroe P, Joseph S, Henderson R, Ziolkowski A (2012) Water extractable organic carbon in untreated and chemical treated bio- chars. *Chemosphere* 87:151–157. doi:10.1016/j.chemosphere. 2011.12.007

Lyu H, Gong Y, Gurav R and Tang J. (2016). Chapter 9 – Potential application of biochar for bioremediation of contaminated systems. In. Ralebitso-Senior, TK and Orr, CH (eds.). Biochar Application: *Essential Soil Microbial Ecology.* Pp221-246.

Martinez-Yrizar A, Sarukhan J, Perez-Jimenez A, Rincon E, Maass JM, Solis-Magallanes A, and Cervantes L. (1992). Above-ground phytomass of a tropical deciduous forest on the coast of Jalisco, Mexico. *J Trop Ecol.*, 8(1):87-96.

Moon H and Aggangan NS. (2019). Seedling Growth and Mineral Uptake of *Eucalyptus pellita* with Different Mycorrhizal Inoculants in Central Kalimantan, Indonesia. *Philippine Journal of Crop Science* (PJCS), 44:1-8.

Nandy S, Andraskar J, Lanjewar K and Kapley A. (2020). Chapter 23 - Challenges in bioremediation: from lab to land. In Saxena G, Kumar V & Shah MP (eds.). 2020. Bioremediation for Environmental sustainability: Toxicity, Mechanisms of Contaminants Degradation, Detoxification, and Challenges. Pp 561-583.

Paguntalan DP, Buot IE, and Aggangan NS. (2020). Cacao – Arbuscular Mycorrhizal Fungi Association: A review on its increased potential in improving the ecology of cacao plantations in the Philippines. *Philippine Journal of Science*, 149 (3-a): 903-914.

Qingyuan L and Cunbo H. (2016). AMF helps in carbon sequestration in soil. *Marine Geology Frontiers* 32(8): 41-46. Doi: 10.16028/j.1009-2722.2016.08005

Teves C. (2018). DENR raises urgency for mine rehabilitation. [online] Philippine News Agency. Available at: https://www.pna.gov.ph/articles/1024785?msclkid=a23c2d52cfe911ecbcfa5c5b6b2dc90a [Accessed 10 May 2022].

Valizadeh S, Lee SS, Baek K, Choi YJ, Jeon B, Rhee GH, Lin KA, and Park Y. (2021). Bioremediation strategies with biochjar for polychlorinated biphenyls (PCBs)-contaminated soils: A review. *Environmental Research* 200:111757, doi:10.1016/j.envres.2021.111757.

Vessey JK. (2003). Plant growth promoting rhizobacteria as biofertilizers. *Plant Soil.* 255:571–586. doi: 10.1023/A:1026037216893.

Victoria KS and Aggangan NS. (2019). Effect of Mycorrhizal Inoculation on Growth, Nutrient Status, and Rhizosphere Microbes of *Acacia mangium* and *Eucalyptus urophylla*. *Philippine Journal of Crop Science* (PJCS), 44:9-17.

Wang J, Chen Z, Xiong Z, Chen C, Xu X, Zhou Q and Kuzyakov Y. (2015). Effects of biochar amendment on greenhouse gas emissions, net ecosystem carbon budget and properties of an acidic soil under intensive vegetable production. *Soil Use and Management*, 31:375-383

Yamato M, Okimori Y, Wibowo IF, Anshori S, and Ogawa M. (2006). Effects of the application of charred bark of *Acacia mangium* on the yield of maize, cowpea and peanut, and soil chemical properties in South Sumatra, Indonesia. *Soil Sci Plant Nutr.,* 52:489–495.

Zhang H, Voroney R, Price G (2015) Effects of temperature and process- ing conditions on biochar chemical properties and their influence on soil C and N transformations. *Soil Biol Biochem* 83:19–28. doi:10. 1016/j.soilbio.2015.01.006

#116: Experimental comparison of asymmetric compound parabolic concentrator (ACPC), symmetrical CPC and non-concentrating solar photovoltaic

Wan Nur Adilah WAN ROSHDAN[1], Hasila JARIMI[2], Ali.H.A. AL-WAELI[3], Adnan IBRAHIM[4], Kamaruzzaman SOPIAN[5]

[1] Solar Energy Research Institute (SERI), Universiti Kebangsaan Malaysia, 43600 Bangi, Selangor, Malaysia, adilahroshdan25@gmail.com
[2] Solar Energy Research Institute (SERI), Universiti Kebangsaan Malaysia, 43600 Bangi, Selangor, Malaysia, hasila.jarimi@ukm.edu.my
[3] Department of Engineering, American University of Iraq - Sulaimani (AUIS), 46001, Kirkuk Rd, Sulaymaniyah, ali.alwaeli@auis.edu.krd
[4] Solar Energy Research Institute (SERI), Universiti Kebangsaan Malaysia, 43600 Bangi, Selangor, Malaysia, iadnan@ukm.edu.my
[5] Solar Energy Research Institute (SERI), Universiti Kebangsaan Malaysia, 43600 Bangi, Selangor, Malaysia, ksopian@ukm.edu.my

Abstract: Compound parabolic concentrator (CPC) photovoltaic (PV) technology is a promising concept because it is a low-concentrating concentrator collector that can concentrate the solar energy onto solar panels and increase the efficiency of the solar panel at a lower cost. However, the incidence angle is not symmetrical across geographical regions and is not consistent throughout the year. As a result, an asymmetrical CPC configuration was used in this study to account for variations in the sun irradiation angle. This paper discusses the performance of asymmetrical CPC PV solar collectors in comparison to symmetrical CPC and non-concentrating solar PV (flat type). A novel high-performance low-concentration concentrator known as asymmetric CPC was introduced, designed and characterised experimentally to compare with symmetrical CPC and flat type solar PV panels. The electrical performance of the concentrators was analysed through an indoor experiment. The sun simulator was set to irradiance at 600W/m^2. The asymmetric CPC was designed and constructed at an acceptance angle of 5° and 65° in pairs. The symmetric CPC was paired at 65° and 65° acceptance angles. Experiments show that the use of an asymmetric CPC outperforms the maximum power of symmetric CPC and flat type by 2.73% and 6.5%, respectively. The novel asymmetric CPC in this study significantly maximised the output power of both the conventional symmetric CPC and flat type non-concentrating PV panels. It has good potential as a low-cost static concentrator for building integration. In this study, the innovative asymmetric CPC outperforms the standard symmetric CPC and flat type non-concentrating PV panels in terms of maximum output power.

Keywords: Photovoltaics (PV); asymmetric; compound parabolic concentrator (CPC); maximum output power

1. INTRODUCTION

Conventional sources of energy supplies such as coal, oil, natural gas, fossil fuels and others are depleting globally (Shafiee and Topal, 2009). Commercial sectors used 80% of the conventional sources of energy (Zayed *et al.*, 2019) and 38% contributes to the development of the country (Murillo-torres and Montero-izquierdo, 2022). Other forms of energy, such as nuclear power, have their downside with nuclear waste disposal issues; the construction of vast water reservoirs for hydroelectricity generating causes migration and disruption in the whole ecosystem (Renewables 2014 Global Status Report, 2014). As a result, other energy sources are being explored. One of the most promising sources of energy that is easily accessible is solar energy which accounts for a wide range of applications such as solar thermal collectors and solar PV systems.

One approach to increase the intensity of the solar panel is by adding reflectors or concentrators (Qiu *et al.*, 2021). Low-concentrating solar concentrators such as compound parabolic concentrator (CPC) collectors are non-imaging static concentrators that serve a potential for solar energy applications due to their capacity to capture incident solar radiation within the acceptance angle (Parupudi *et al.*, 2021). Based on literature, the application of CPC is categorised into several categories: solar PV systems, solar thermal, daylighting, and others. For photovoltaic systems, there are 2D through CPC, lens-walled, crossed, 3D revolved, VPF and RACPC (Tian *et al.*, 2018). Asymmetric configuration of the CPC (ACPC) accounts for the variation in the solar incidence angle throughout the year at different time and location (Rabl, 1976). Much research on ACPC PV/T has been carried out in order to find the optimum half acceptance angle. Based on the analysis, it was found that 5° and 65°were the optimum pair of acceptance angles for low and middle latitude countries (Wan Roshdan *et al.*, 2022).

2. METHODOLOGY

2.1. Geometric design of the CPCs

Important components to consider in CPCs are the half acceptance angle θ_c, the aperture a, the CPC's height h, the absorber area S and the focal point f. The CPC reflectors will reflect any radiation that strikes within the angles of the reflectors (Duffy and Beckman, 1982).The height of the CPC can be truncated in order to lower the cost of construction without contributing to a significant impact on the performance.

Figures 1 and 2 show the geometric structure of the CPC and ACPC. The CPC consists of two parabola curves of specific angles of incidence. Based on the mathematical modelling computed using MATLAB software, the optimum acceptance angles are 5° and 65° for low, mid and high latitude countries. Hence, for the experiment, the pairing configuration of the CPC was 65° and 65°, whereas for ACPC they were 5° and 65°. Table 1 shows the parameters used for the CPCs and PV panel.

Table 1: Parameters of CPCs and PV panel

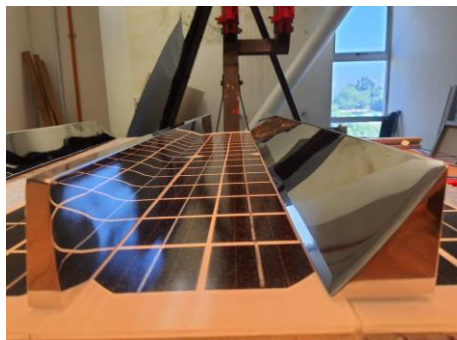| Parameter	Value
Acceptance angle (θ_c) of the CPC	65° and 65° (for CPC)
	5° and 65° (for ACPC)
Truncated height ratio H_R	0.95
Solar irradiance	600 W/m²
Size of PV panel	Size : 1.2m (L) x 0.9m (W)
	Nominal power at STC : 17W
	Voc : 19.2V
	Isc : 1.28A
	Type : Monocrystalline

Figure 1: ACPC of 5° and 65°   *Figure 2: CPC of 65° and 65°*

2.2. Experimental setup

Figure 3 shows the experimental setup of the experiment. The CPCs were attached to the solar PV panel. The experiment was done indoor by setting up the solar sun simulator into irradiance of 600 W/m². The PV panel was attached with the CPC. In order to find out the electrical characteristics of the PV-CPC and PV-ACPC, the positive and negative terminals of the PV panel were connected to a PV system analyser (PROVA 1011).

Figure 3: Experimental setup

3.   RESULTS AND DISCUSSION

From the experimental setup, several results were obtained by combining different arrangements of CPC with the solar PV panel.

3.1. The performance of CPC and ACPC on solar PV panel

The effect of concentrating solar cells with CPC can be shown in the graph in Figure 4. By having just a flat type, the maximum power output at 600W/m² was 4.39W. Solar PV panel that were concentrated by CPC achieved 4.51W maximum power and asymmetric CPC achieved 4.68W. PV-CPC outperformed the flat type by 2.73% and PV-ACPC outperformed the PV-CPC by 3.77%. Overall, with ACPC design configuration, it increased the maximum power output by 6.5%. This showed that concentrated PV types are a promising method to increase the maximum power output (P_{max}).
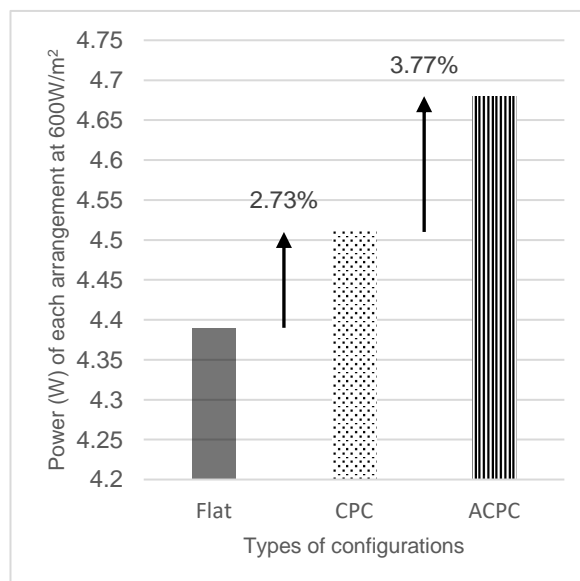
Figure 4: The performance of solar PV based on the configuration of different CPC and ACPC pairings

3.2. I-V Curve and P-V Curve

Figure 5 presents the I-V curve and P-V curve of the ACPC, CPC and flat-type (non-concentrated). The power output of the flat type was significantly lower compared to the CPC and ACPC.
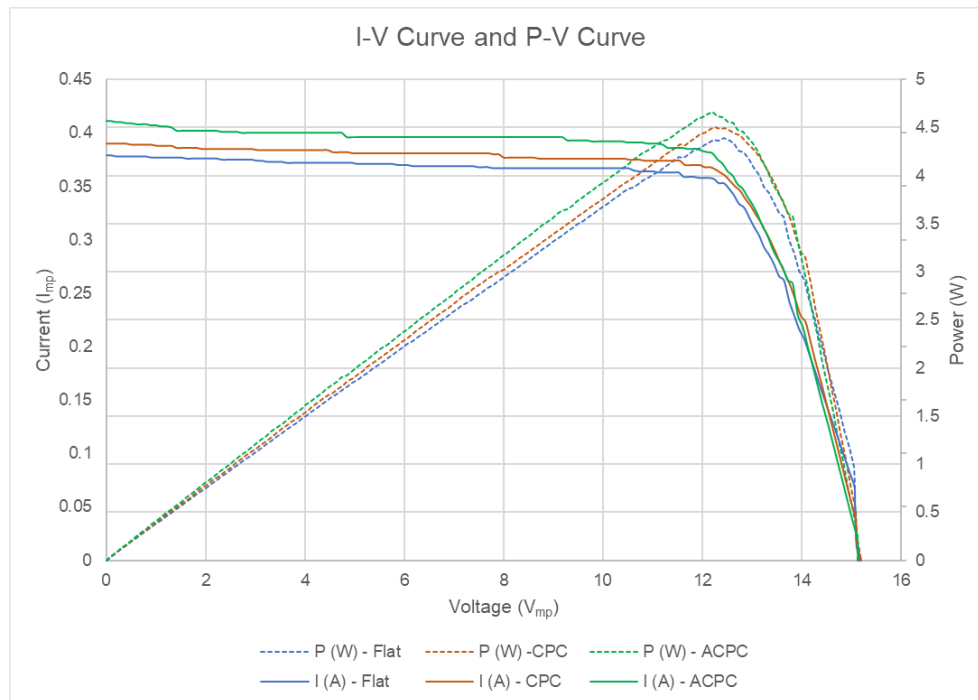
Figure 5: I-V and P-V curves of PV-ACPC, PV-CPC and Flat type

4. CONCLUSION

The solar PV panel was analysed with different configurations and pairings of CPCs. An asymmetric CPC configuration was proposed in this experiment to overcome the limitations of the symmetric CPC. At irradiance of 600W/m^2, the maximum power (P$_{max}$) obtained by PV-ACPC, PV-CPC and flat type PV was 4.68W, 4.51W and 4.39W respectively. Comparatively, PV-ACPC was 3.77% higher than PV-CPC and 6.5% higher than the flat type. This shows that PV-ACPC design significantly outperformed the conventional CPC and flat type solar PV panels. The asymmetrical half acceptance angles at full and truncated heights of the ACPC showed the highest performance.

5. REFERENCES

Duffy and Beckman (1982) *Solar engineering of thermal processes, Design Studies*. doi: 10.1016/0142-694x(82)90016-3.

Murillo-torres, W. and Montero-izquierdo, A. (2022) 'A review of the state-of-the-art of solar thermal collectors applied in the industry Una revisión de los últimos avances de los colectores solares térmicos aplicados en la industria', (January).

Parupudi, R. V. *et al.* (2021) 'Long term performance analysis of low concentrating photovoltaic (LCPV) systems for building retrofit', *Applied Energy*, 300, p. 117412. doi: 10.1016/j.apenergy.2021.117412.

Qiu, G. *et al.* (2021) 'Comparative study on solar flat-plate collectors coupled with three types of reflectors not requiring solar tracking for space heating', *Renewable Energy*, 169, pp. 104–116. doi: 10.1016/j.renene.2020.12.134.

Rabl, A. (1976) 'Comparison of solar concentrators', *Solar Energy*, 18(2), pp. 93–111. doi: 10.1016/0038-092X(76)90043-8.

REN21,P.S.,Renewables 2014:Global Status Report (2014) : Secretariat Renewable Energy Policy Network for the 21st Century (REN21) Paris.

Shafiee, S. and Ã, E. T. (2009) 'When will fossil fuel reserves be diminished ?', 37, pp. 181–189. doi: 10.1016/j.enpol.2008.08.016.

Tian, M. *et al.* (2018) 'A review on the recent research progress in the compound parabolic concentrator (CPC) for solar energy applications', 82(September 2017), pp. 1272–1296. doi: 10.1016/j.rser.2017.09.050.

Wan Roshdan, *et al.* (2022) 'Case Studies in Thermal Engineering Performance enhancement of double pass photovoltaic / thermal solar collector using asymmetric compound parabolic concentrator (PV / T-ACPC) for façade application in different climates', (April), pp. 1–16.

Zayed, M. E. *et al.* (2019) 'Applications of cascaded phase change materials in solar water collector storage tanks: A review', *Solar Energy Materials and Solar Cells*, 199(December 2018), pp. 24–49. doi: 10.1016/j.solmat.2019.04.018.

#117: Finding biological solutions on greening nickel areas in Claver, Surigao del Norte, Mindanao, Philippines

Nelly S. Aggangan[1], Julieta A. Anarna[1], Emer C. Gestiada[1], Dennis M. Gilbero[2], Bethlehem T. Magsayo[3], Mitz C.Tapi-on[3], Van Justine A. Podiotan[3], Christopher M. Salud[3], Lynlee Ross J. Cuesta[3], Ruben F. Amparado[3]

[1]National Institute of Molecular Biology and Biotechnology, University of the Philippines Los Baños, Laguna 4031, nsaggangan@up.edu.ph; janarna@up.edu.ph; ecgestiada@up.edu.ph
[2]Ecosystem Research and Development Bureau, Department of Environment and Natural Resources, Bislig, Surigao del Sur 8311, forgilbero@gmail.com
[3]Department of Biological Science, College of Science and Mathematics, MSU-Iligan Institute of Technology, Iligan City 9200, ruben.amparado@g.msuiit.edu.ph; bethlehemmarie.magsayo@g.msuiit.edu.ph mitz.tapi-on@g.msuiit.edu.ph; vanjustine.podiotan@g.msuiit.edu.ph; christopher.salud@g.msuiit.edu.ph; lynleeross.cuesta@g.msuiit.edu.ph

Abstract: Successful and fast rehabilitation of areas have been a challenge internationally including in the Philippines. Areas may be devoid of plants due to many biotic and abiotic factors, one of which is the presence of residual heavy metals from mining waste. Three concurrent nursery experiments were conducted on Philippines native tree species namely: narra (Pterocarpus indicus), lahilahi (Syzygium acuminatissimum) and mangkono (Xanthostemon verdugonianus) to determine the best beneficial biofertilizers to promote plant growth in nickel (Ni) soil collected in Claver, Surigao. This study aimed to find biological solutions to successfully rehabilitate barren areas of Claver, Surigao. Six month old seedlings raised in a nursery were inoculated with either MYKORICH®, MYKOVAM®, new mycorrhiza (NewMYC), new nitrogen-fixing bacteria (NewNFB), combined NewMYC and NewNFB or not inoculated (control). Inoculation rates followed the recommended dosages indicated on the labels. The NewMYC and NewNFB were isolated from a copper (Cu) mined–out area in Marinduque, Luzon, while the first two were commercial inoculants containing arbuscular mycorrhizal fungi (AMF) developed and produced locally. Growth response at 6 months after inoculation in the nursery differed to that obtained at 12 months in the field. In the nursery, MYKORICH promoted (p<0.01) the tallest narra, lahilahi and mangkono. In the field, NewMYC promoted the tallest narra and mangkono, while NewMYC and NewNFB gave the tallest lahilahi. NewMYC promoted the biggest (p<0.05) stem diameter of lahilahi and mangkono while NewMYC and NewNFB equally gave the biggest stem diameter of narra. Microbial biofertilizers also improved the root and plant dry weight, and root to shoot ratio relative to the control due to good colonisation by AMF with numerous hyphae to absorb nutrients and water. In the field, NewMYC gave 90% seedling survival on narra, while NewNFB gave 90 and 77% on lahilahi and mangkono, respectively. The established field trials showed the applicability of MBP in greening Ni mined-out area in Claver, Surigao. The NewNFB and NewMYC indigenous in a Cu mined-out area, also worked in Ni mined-out soil, in association with narra, lahilahi and mangkono with high survival rates for a successful rehabilitation and bioremediation.

Keywords: nickel; mined-out area; arbuscular mycorrhizal fungi; nitrogen fixing bacteria

1. INTRODUCTION

Successful and fast rehabilitation of areas has been a challenge internationally including in the Philippines. There are 27 abandoned mined-out areas that are devoid of plants due to many biotic and abiotic factors, one of which is the presence of residual heavy metals in the mining waste.

Responsibility for greening mined-out areas in the Philippines (GMAP) falls under Sustainable Communities, the top priority of the National Research Council of the Philippines Department of Science and Technology's National Basic Research agenda. Sustainable communities have research areas on vulnerable ecosystems, data analytics and natural phenomena and environmental and anthropogenic activities where bioremediation studies are included.

Bioremediation is a branch of environmental biotechnology that treats contaminated soil, air and water with living organisms. Bioremediation is the use of live microbes and plants as biological solutions to clean up and rehabilitate stressed environments such as mined-out or mine tailing areas. Plant-microbe association can accelerate rehabilitation of unproductive areas like mined-out or mine tailing sites employing bioremediation strategies.

There are more than 300ha in 27 abandoned mines in the Philippines as reported by the Mines and Geoscience Bureau, Department of Environment and Natural Resources, but there could be more created by small scale miners. Our first GMAP project was conducted in Marinduque, in Luzon Island, that aimed to develop bioremediation protocol for rehabilitating abandoned mined-out areas, to select plants that were more appropriate for such areas and to possibly discover indigenous new beneficial microbes for their potential use as biofertilizers.

The experimental field site was on a 2ha waste dumpsite, 600m above sea level. It was part of the 32ha open pit mined for copper (Cu) and gold (Au) by the Consolidated Mining Inc. in Barangay Capayang, Mogpog, Marinduque. This area had been abandoned for more than 35 years (Mahusay 2014). The field site overlooked the open pit where farmers got water for irrigation, surrounded by agricultural lands, communities, elementary and secondary schools just below the dumpsite, fresh and marine bodies where milkfish and shrimps were cultured.

There were no plants on the area because the soil was acidic, deficient in nutrients, and contained heavy metals such as Cu, cadmium (Cd), lead (Pb) and zinc (Zn). These heavy metals can contaminate surrounding agricultural lands and marine bodies and may post health risks to residents, teachers, students and all forms of living organisms.

With our innovation, the barren land was transformed into a young mini forest planted with narra (*Pterocarpus indicus*), *Acacia mangium* and *Eucalyptus urophylla* within three years. Planting materials were inoculated with microbial biofertilizers in the nursery and applied with vermicompost, lime and basal NPK fertilizers during field planting.

The microbial biofertilizers used in this project were developed and produced at the National Institute of Molecular Biology, University of the Philippines Los Baños (BIOTECH-UPLB), and contained nitrogen fixing bacteria (NFB) or arbuscular mycorrhizal fungi (AMF). NFB fix atmospheric nitrogen (N_2) and convert the fixed N into forms that plants can utilise. AMF infect the fine roots and help the plants absorb nutrients and water. They act as biological control against root pathogens and can increase plant tolerance to heavy metals and other stresses (Smith and Read, 2010).

In the Marinduque Cu area, growth of biofertilizer-inoculated seedlings was very impressive with 95% survival after 12 months, while the growth of untreated seedlings was stunted and unhealthy, with only 50% survival (Aggangan *et al.*, 2019). After 22 months, 95% survival was obtained in seedling treated with microbial biofertilizers plus other soil amendment as compared with 26% in the untreated control (no amendments) (Aggangan and Anarna, 2019). After 27 months, plant survival was 92% if the seedlings were applied with microbial biofertilizers plus other soil amendment as compared with only 15% in the control (no amendments) (Aggangan and Anarna, 2019). After three years, all un-inoculated seedlings were dead.

The microbial biofertilizer technology in our Marinduque Bioremediation Protocol (MBP) re-greened the barren area and also reduced the exposure to health-related diseases caused by heavy metals. It was concluded that the beneficial soil microbes in this bioremediation technology can hasten the rehabilitation and transformation of barren mine tailings that had been unproductive for many decades into a productive one - a young healthy forest stand. The brown barren and mine tailing areas were transformed into green vegetative cover using microbial biofertilizers such as AMF and NFB combined with other soil amendments such as compost, lime and basal NPK fertilizers.

The success of the MBP has led to test its effectivity in a Ni mined-out area in Claver, Surigao del Norte, on the island of Mindanao. The objectives were to verify the effectiveness of the MBP, to assess the potential of Marinduque isolates (NewNFB and NewMYC) as biofertilizers and to determine the best tree species-microbial partners to be recommended for use in rehabilitation of such areas.

2. METHODOLOGY

2.1. Soil characteristics in the nickel mined-out area

Soil for the nursery experiments was collected from the Ni mining waste dumpsite in Taga1 rehabilitation area of Taganito Mining Corporation (TMC), Claver, Surigao. The soil was air-dried and passed through a screen wire to discard bulk soil and unwanted debris. Soil samples were analysed at the Department of Agriculture, Butuan City. The initial soil physico-chemical analyses indicated a neutral of pH 7.17±0.38, low level OM (0.40±0.2%), low available P (1.30±0.58 ppm), deficient exchangeable K (6.0±0 ppm), N was below detection limit, electrical conductivity of 113.3±38 µS/cm, Fe of 326,600±139.29 ppm and Ni of 7,166.66±1342.88 ppm. The Dutch Standard for Soil Contamination listed the target value or allowable value of 35mg Ni kg^{-1} soil and the intervention value was 210mg Ni kg^{-1} soil (1ppm = 1mg kg^{-1}). The intervention value indicates serious contamination of soils where remediation is necessary.

2.2. Experimental Design

The experiments were established in a plastic shaded roof nursery following RCBD with 10 blocks and 10 replicates per treatment per block. The field experiments also followed RCBD with 10 blocks and 10 seedlings per row plot per treatment per block. Planting distance in the row plot was 2m, 3m between rows and 4m between blocks.

2.3. Selection of tree species

Three tree species, narra (*Pterocarpus indicus*), lahilahi (*Syzygium acuminatissimum*) and mangkono (*Xanthostemon verdugonianus*) were selected, all being indigenous in the country and were preferred by the collaborating mining company. Narra belongs to Leguminosae, a N$_2$ fixer through its *Rhizobium* association forming nodules. It can be seen throughout the country producing premium quality wood which is excellent for furniture, house walling, and many other purposes. Lahilahi and mangkono are native in Mindanao and both classified under Myrtaceae. Lahilahi has a wide range of habitat from the high mountains to the beach forests. Mangkono is an evergreen tree growing to 50m tall and the bole can be up to 115cm in diameter. It is also known as the ironwood, a slow grower but accordingly, the oldest standing trees in Surigao are about 200 years old with a stem diameter of more than a metre. It is commonly found in an ultramafic area with height of a meter (Ocon *et al.,* 2018). These three species can form association with AMF.

2.4. Nursery and field experiments

Three concurrent nursery experiments were conducted using Philippines native tree species, namely narra, lahilahi and mangkono, to determine the best beneficial biofertilizers to promote plant growth in Ni mined-out soil collected in Claver (Ni content of 0.72% and pH of 7.1), Surigao del Norte.

After six months in the nursery, the treated seedlings were field planted in a Ni waste dumpsite area in the Taga1 rehabilitation area of TMC, Claver, Surigao, following a RCBD with 10 blocks and 10 seedlings per row per treatment per block. The Ni mined-out soil was mixed with vermicompost and NPK during the establishment of nursery and field experiments.

2.5. Inoculation with biofertilizers

Inoculation with biofertilizers was carried out on the 6-month-old nursery-raised seedlings provided by TMC (for lahilahi and mangkono) and by the Department of Environment and Natural Resources (for narra). Inoculants used were either MYKORICH®, MYKOVAM®, new mycorrhiza (NewMYC), new nitrogen-fixing bacteria (NewNFB), combined NewMYC and NewNFB or not inoculated (control). Inoculation rates followed the recommended dosages as indicated on the label. NewMYC and NewNFB were Marinduque isolates from a Cu mined–out area in Marinduque, Luzon island, while the first two were commercial AMF inoculants developed and produced by the National Institute of Molecular Biology and Biotechnology, University of the Philippines, Los Baños (BIOTECH-UPLB).

MYKORICH® is a soil-less capsulated AMF inoculant containing 12 species of beneficial AMF belonging to the genera *Glomus, Gigaspora, Acaulospora, Scutellospora* and *Entrophospora* and proven effective for promoting growth, yield, and survival of a wide range of agricultural crops and forest tree species and improves soil nutrient status and productivity. MYKOVAM is a soil-based powder consists of the same AMF as in MYKORICH.

2.6. Parameters gathered

Initial height and stem diameter were measured just after inoculation and the monthly growth increments were computed (difference of the last measurements from the initial). After six months, representative experimental seedlings in the nursery experiments were harvested for the determination of plant biomass. Likewise, destructive sampling was also done in the

field at six months after field planting. Seedlings were randomly chosen and excavated. The roots were cleaned under running water. Fine (<0.5 mm diameter) roots were detached and processed for the assessment of mycorrhizal root colonisation on the harvested and excavated seedlings. Fine roots were processed following the technique of Brundrett *et al.* (1996). Stained roots were assessed under a microscope following the technique of Giovannetti and Mosse (1980). Seedling survival was monitored periodically in both nursery and field experiments.

2.7. Statistical Analysis

All data gathered were subjected to one-way ANOVA using MSTATC program (Michigan State University, 1989). Treatment means were compared using LSD at $p<0.05$.

3. RESULTS

3.1. Plant growth in the nursery

Better growth of seedlings inoculated with biofertilizers than the control or un-inoculated counterpart was observed on narra (Figure 1A), and mangkono (Figure 1B) six months after inoculation. The root system of inoculated plants was denser and longer than the control counterpart (Figures 1C and 1D) and MYKORICH doubled the height of narra followed by the NewMYC (Figure 1A). NMYC and NFB improved the growth of mangkono (Figure 1B) and lahilahi (not shown).
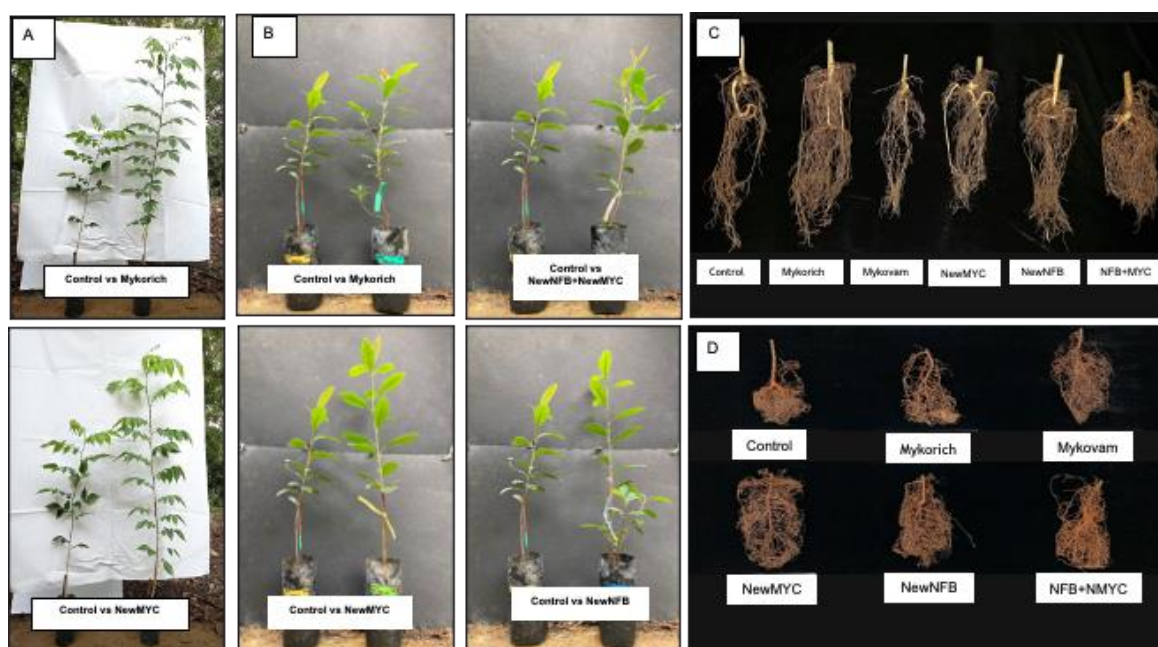
Figure 1: Comparative vegetative growth and root structures of narra (A), mangkono (B) and roots of narra (C) and mangkono (D) of un-inoculated (control) or inoculated with mycorrhizal inoculants. NewMYC, NewNFB are indigenous isolates from a Cu mined-out area and MYKORICH is a commercial mycorrhizal inoculant.

Inoculation with MYKORICH® gave the tallest height of narra, lahilahi and mangkono six months after inoculation in the nursery and during field planting (Figure 2A). MYKORICH® gave the tallest height of narra but comparative with those inoculated with combined Marinduque isolates. MYKORICH® also promoted the biggest stem diameter of narra (Figure 3A) while the biggest stem diameter of lahilahi and mangkono was obtained from inoculation with MYKOVAM®. MYKORICH-inoculated seedlings gave significant increases in height from 16 to 190% and stem diameter from 2 to 135%, relative to the un-inoculated control.
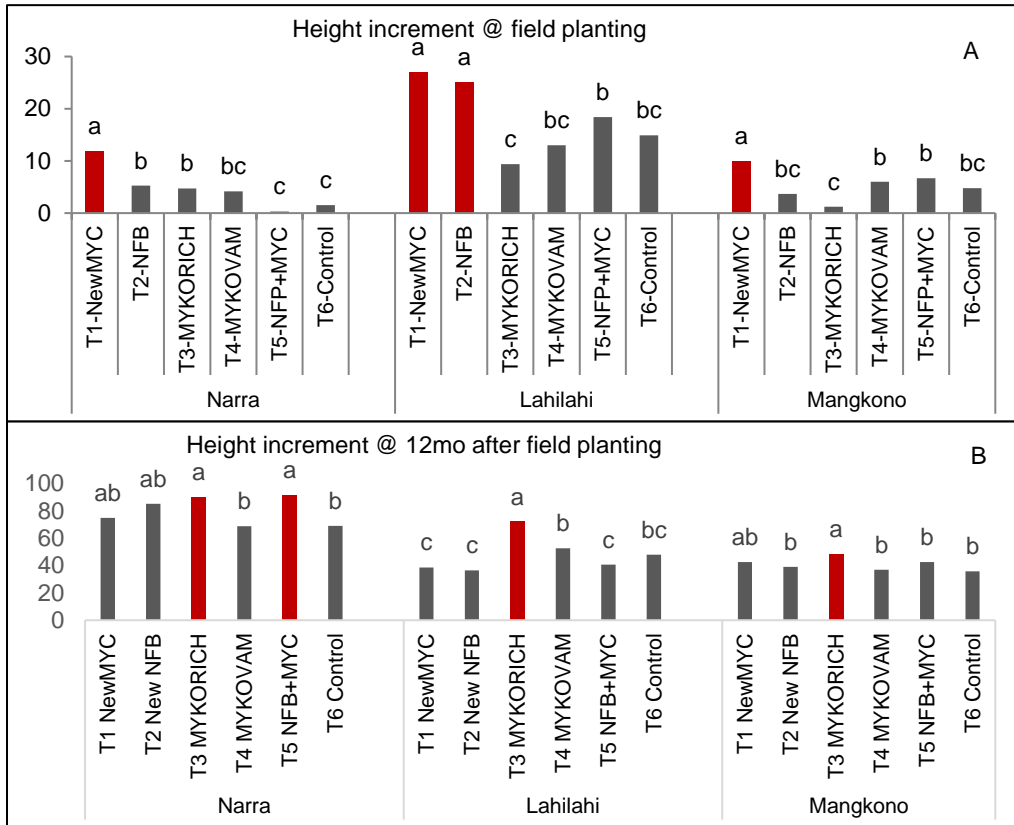
Figure 2: Height increment of narra, lahilahi and mangkono seedlings after six months inoculation in the nursery (A) and in the field (B).
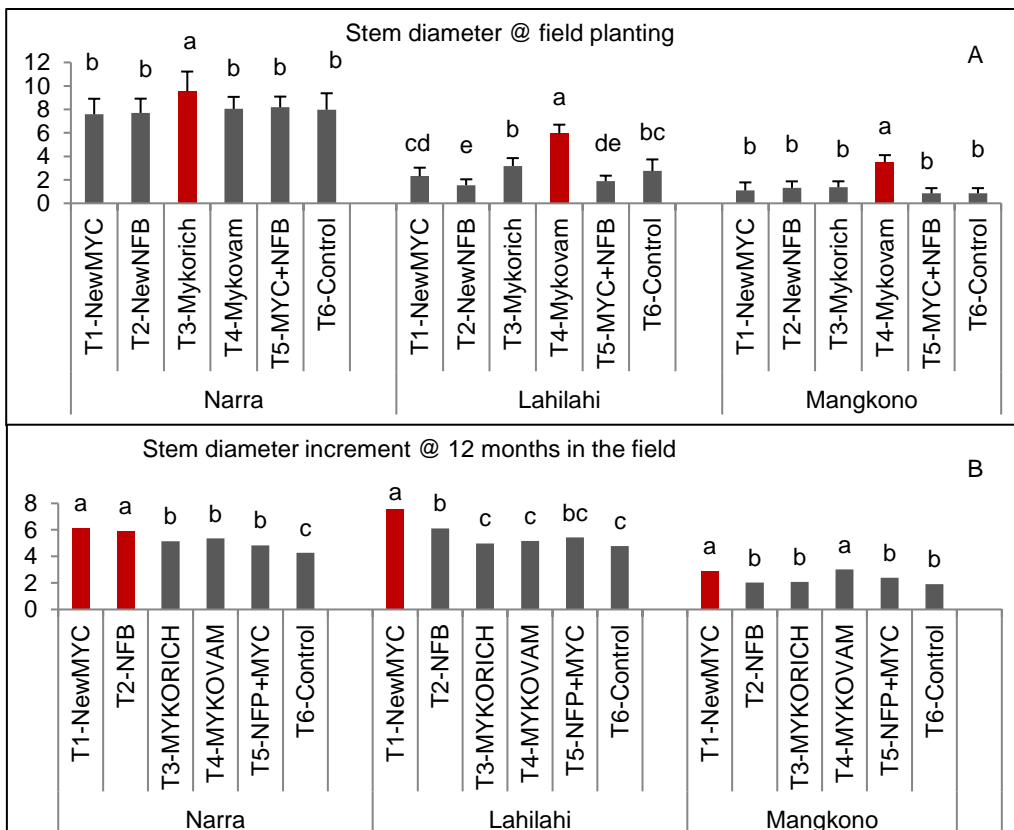
Figure 3: Stem diameter increment just after field planting (A) and after 12 months in the field (B) in a Ni area in Claver, Surigao del Norte, Mindanao island.

3.2. Plant biomass

The heaviest total and root dry weights of narra and lahilahi was obtained from seedlings inoculated with MYKORICH® (Figure 4). The total and root dry weights obtained from MYKORICH® inoculated narra, were comparable with those observed from the other inoculation treatments except NewNFB which had the lowest (18.43 cm) (Figures 4A and 4B). On lahilahi, MYKORICH® gave the heaviest (28.30 g plant^{-1}) which was 39% higher (p<0.05) than the control (20.03 g plant-1). On mangkono, MYKORICH® and NewNFB gave comparable total plant dry weights that were significant as compared with those inoculated with NewMYC. In terms of root dry weight, MYKORICH® promoted the heaviest and again significantly higher than those inoculated with NewMYC (Figure 4B).
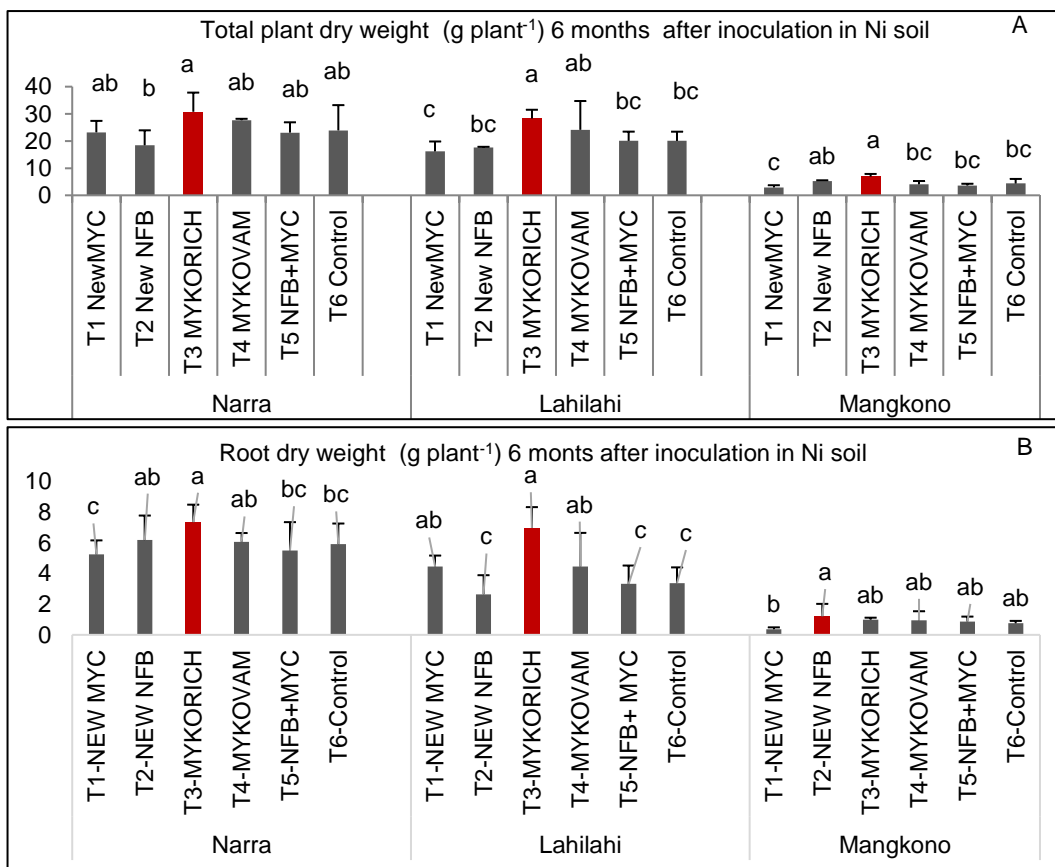
Figure 4: Total plant (A) and root (B) dry weights of narra, lahilahi and mangkono seedlings after six months growth in Ni mined-out soil as affected by the inoculation with biofertilizers and grown under nursery conditions.

3.3. Plant survival

The highest survival rate was 95% and 97% when narra and lahilahi were inoculated with the combined NewMYC and NewNFB (Table 1). NewMYC gave the highest survival rate (93%) on mangkono at the end of 6 months in the nursery.

After 12 months in the field, the seedling survival rate were 90% on NewMYC inoculated narra, 90% when lahilahi were inoculated with NewNFB and 77% on NewNFB-inoculated mangkono. Irrespective of inoculation treatment, lahilahi gave the highest seedling survival rate in the nursery and in the field of 87% and 84%, respectively, and the lowest was on mangkono with 82% in the nursery and 69% 12 months after field planting (Table 1).

3.4. Plant growth in the field

Growth of lahilahi was greatly improved when inoculated with biofertilizers (Figure 5A). The control seedlings exhibited yellowing of leaves (Figure 5B) while the leaves of those with microbes were green and broader than the control (Figures 5C and 5D). In the field, NewMYC increased height of narra by 6x, NewMYC and NewNFB gave 1.8x for lahilahi, and NewMYC increased height of mangkono by 2x (Figure 2B)., The Marinduque isolates gave a 1.5x stem diameter increase of narra, 1.6x increase by NewMYC on lahilahi and 1.5x increase by NewMYC and MYKOVAM® on mangkono (Figure 3B).

Table 1: Seedling survival in the nursery prior to field planting and after 12 months in Ni mined-out area in Claver, Surigao del Norte, Mindanao.

Treatment	Narra	Lahilahi	Mangkono	Narra	Lahilahi	Mangkono
	Survival in the nursery before field planting			Survival 12 months after field planting		
T1-NewMYC	92	87	**93**	**90**	74	67
T2-NewNFB	94	95	87	85	**90**	**77**
T3-MYKORICH	84	93	76	82	70	67
T4-MYKOVAM	92	95	70	88	77	65
T5-NewNFB+NewMYC	**95**	**97**	87	79	69	71
T6-Control	63	91	81	81	71	67
Mean	**87**	**93**	**82**	**84**	**75**	**69**

Figure 5: Growth of lahilahi after six months in a Ni area of Taganito Mining Company, Claver, Surigao.

In terms of total and root dry weight of narra and lahilahi excavated in the field after 6 months, the best inoculant for Narra were NewNFB and MYKOVAM® while the best inoculants for Lahilahi were the combined Marinduque isolates, MYKOVAM and MYKORICH® (Table 2). Irrespective of inoculation treatment, biomass was higher on narra than lahilahi and the lowest was on mangkono. Narra inoculated with NewNFB gave higher (p<0.05) than the control (20.03 g plant^{-1}). On mangkono, MYKORICH® and NewNFB gave comparable total plant biomass which was significant as compared with those inoculated with NewMYC.

Table 2: Total plant and root biomass of narra and lahilahi, excavated 6 months after field planting in a Ni mined-out area in Claver, Surigao, Mindanao.

Treatment	Narra	Lahilahi	Narra	Lahilahi
	Total plant dry weight (g plant^{-1})		Root dry weight (g plant^{-1})	
T1-NewMYC	58.84 ab	27.68 bc	18.34 c	9.48 bc
T2-NewNFB	**60.74 a**	18.99 c	27.1 b	7.22 c
T3-MYKORICH	39.81 c	42.52 b	8.64 d	11.01 ab
T4-MYKOVAM	**61.4 a**	**47.34 a**	**30.09 a**	**12.99 a**
T5-NewNFB+NewMYC	42.59 bc	43.02 b	15.51	**12.09 a**
T6-Control	53.11 bc	31.39 bc	19.82 c	8.62 bc
Mean	**52.75**	**35.16**	**19.92**	**10.23**

Root shoot ratios due to inoculation treatments under nursery and field conditions are presented in Table 3. In the nursery, the highest (0.50) R/S ratio was obtained from narra, 0.29 R/S ratio on NewMYC on lahilahi and on mangkono, the combined NFB and MYC gave the highest R/S ratio 0.32 followed by those inoculated with MYKOVAM® (0.31). In the field, MYKOVAM® inoculated narra excavated six months after field planting gave a perfect root shoot ratio of 1.0 which was the highest in all treated plants (Table 3). For lahilahi, the highest was obtained from those inoculated with NewNFB which was 0.61 (Table 3). It should be noted that R/S ratio were twice as high in the field than in the nursery (Table 3).

Table 3: Root shoot ratio of selected tree species six months after inoculation in the nursery or six months after field planting in a Ni mined-out area in Claver, Surigao, Mindanao.

Treatment	Narra	Lahilahi	Mangkono	Narra	Lahilahi
	R/S ratio in the nursery			R/S ratio in the field	
T1-NewMYC	0.29	**0.29**	0.14	0.50	0.52
T2-NewNFB	**0.50**	0.16	0.30	0.64	**0.61**
T3-MYKORICH	0.31	0.23	0.17	0.32	0.35
T4-MYKOVAM	0.28	0.23	**0.31**	**1.00**	0.38
T5-NewNFB+NewMYC	0.34	0.17	**0.32**	0.53	0.39
T6-Control	0.33	0.17	0.21	0.62	0.38
Mean	**0.34**	**0.21**	**0.24**	**0.60**	**0.44**

3.5. Mycorrhizal root colonisation

The un-inoculated control narra and lahilahi did not show any root colonisation inherent in the soil (Table 4). Roots of mangkono were colonised by an unknown mycorrhizal fungi but the level of colonisation was low (9%). Moreover, roots of NewNFB (no mycorrhiza) inoculated narra, lahilahi and mangkono had mycorrhiza colonised roots ranging from 1% to 3% implying the presence of indigenous AMF in the growing medium.

Root colonisation in mycorrhizal narra ranged from 36% to 39%, 31% to 42% in mycorrhizal lahilahi and 14% to 35% in mycorrhiza inoculated mangkono (Table 4). Irrespective of inoculation treatment, mycorrhizal root colonisation was 25% in both narra and lahilahi and lower in mangkono (17%) (Table 4). Roots of NewMYC inoculated narra showed numerous hyphae inside and outside the roots as compared to the roots of un-inoculated counterparts where there was no trace of colonisation by mycorrhizal fungi (Figure 6).

Table 4: Mycorrhizal root colonisation after 6 months in a Ni mined-out soil.

Treatment	Narra	Lahilahi	Mangkono
T1-NewMYC	37	**42**	14
T2-NewNFB	1	3	3
T3-MYKORICH	**39**	31	19
T4-MYKOVAM	36	34	**35**
T5-NewNFB+NewMYC	**39**	38	23
T6-Control	0	0	9
Mean	**25**	**25**	**17.12**
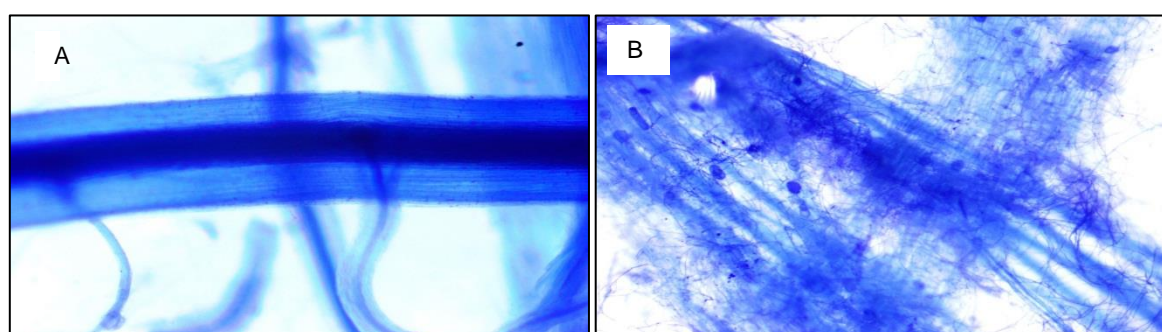
Figure 6: Roots of narra un-inoculated (A) or inoculated with NewMYC (B) and grown in Ni mined-out soil for 6 months in the nursery showing vesicles (dark blue oval shape structures) and numerous hyphae of arbuscular mycorrhizal fungi.

4. DISCUSSION

In this study, biological solutions were used with different tree species native in the country (such as narra) or indigenous in the planting site (lahilahi and mangkono) and different microbes from different environment. Biological solutions such as finding the best synergistic association between indigenous tree species and the most appropriate microbial biofertilizers offer successful rehabilitation of unproductive areas. This strategy or protocol is often called bioremediation. Bioremediation is a process that uses mainly microorganisms, plants, or microbial or plant enzymes

to detoxify contaminants in the soil and other environment (Pande *et al.,* 2022). Bioremediation uses micro-organisms to reduce pollution through the biological degradation of pollutants into non-toxic substances (Vieira and Stefenon, 2017).

The two Marinduque isolates, NewNFB and NewMYC, were isolated from a Cu mined-out area in Marinduque while the 12 AMF species present in the commercial mycorrhizal inoculants MYKORICH® and MYKOVAM® came from marginal, abandoned mined-out areas throughout the Philippines particularly areas that were routinely subjected to excessive drought coupled with high temperature especially during summer.

Microbes such as AMF probe for nutrients and water in soil with little or no essential nutrients and at the same time protect the plants from damage caused by the presence of heavy metals. Thus, the plant grows in environmentally stressed sites due to the presence of AMF and other beneficial microbes (Smith and Read, 2010). These beneficial microorganisms make the plants grow healthier as a result of the nutrients and water passed on to them. The above-ground biomass on the other hand, provides the fungi with the manufactured carbohydrates for the microbes to survive and proliferate (Smith and Read, 2010).

Root colonisation by mycorrhizal fungi play a significant role in promoting growth and survival especially in a very stressful environment (e.g. mined-out areas). In this study, the field site lacked essential nutrients and was prone to high temperatures: most mine waste dumpsites and mined-out areas are barren with very few grasses. In Marinduque, there were few ferns in the gullies containing high heavy metals contents. Ferns (where NewNFB and NewMYC were isolated) are known to be heavy metal accumulators. This could be the reason why these mixed microbes grew well in the Ni soil and colonised the roots of the three native tree species. In the same manner, some of the AMF in the commercial mycorrhizal inoculants MYKORICH® and MYKOVAM® were also collected in stressed environments thus proliferated in Ni soil. These mycorrhizal inoculants promoted height, stem diameter, total and root dry weight and root shoot ratio under nursery and field conditions. Seedling survival one year after field planting, was generally higher when the narra, lahilahi and mangkono were inoculated with microbes, implying the importance of the symbioses.

The results obtained from this study conformed to an earlier study by Aggangan *et al.* (2016), where seedlings of *Acacia mangium*, falcata (*Paraserianthes falcataria*) and mangkono (*Xanthostemon verdugonianus*) were inoculated with mixed spores of AMF native in the Cu-Au mined-out site in Placer, Surigao or mycorrhizal inoculants MYKOVAM® and Mycogroe (containing ectomycorrhizal fungi *Pisolithus* sp. and *Scleroderma* sp.) and grown in marginal or Cu-Au mine waste soils. Plants inoculated with the native ECM or AMF outperformed the un-inoculated counterpart. The native mycorrhizal fungi promoted the best growth of *A. mangium* and mangkono. On the other hand, inoculation did not promote growth of falcata seedlings.

The above results also conformed to another study of Aggangan and Cortes (2018). AMF associated with ferns and grasses growing in the mine tailings were screened for potential use in rehabilitating a 3-decade abandoned area in Mogpog, Marinduque. Narra was used as the host plant to establish mycorrhizal fungi association. Among the treatments, indigenous AMF associated with Ferns 1, 2 and 5 generally improved the height, stem diameter and total dry weight of the narra seedlings and the effect was comparable with commercially available AMF inoculants, MYKOVAM® and MYKORICH®. The dry weight of the roots and nodules was consistently improved by the indigenous AMF from Fern2 and Grass1, which had a comparable effect with MYKOVAM® and MYKORICH®. Thus, it was concluded that the mined-out indigenous AMF were potential agents to rehabilitate the abandoned mine tailings in the Philippines.

A similar approach has been tested in Indonesia with the isolation of native mycorrhizal fungi. Prayudyaningsih *et al.* (2019) studied the AMF species on Ni post mining land and its association with pioneer plant roots. The authors reported that of the 163 pioneer plant species studied, the roots were all colonised by AMF. It was further reported that grass species had the highest AMF colonisation level similar to where the Marinduque isolates NewNFB and NewMYC used in this study came from. Thus, all the above results indicated successful rehabilitation of heavy metal mine-out areas if the promising indigenous microbes are used for inoculation. It is also important that the seedlings should have fully colonised roots before planting in the field. Soil amendments such as compost and lime were very important to provide initial nutrient requirements of the plants during establishment stage while the microbes were adapting to the environments.

5. SUMMARY AND CONCLUSION

The Marinduque Bioremediation Protocol developed in a Cu area also worked in a Ni mined-out area in Claver, Surigao del Norte, on the island of Mindanao. The MBP used commercial microbial biofertilizers (MYKOVAM® and MYKORICH®), those isolated from the Cu area in Marinduque and native tree species which were applied with vermicompost and minimal amounts of chemical fertilizers (14N:14P:14K) during field planting. Growth response at 6 months after inoculation in the nursery differed to that obtained at 12 months in the field. In the nursery, MYKORICH® promoted (p<0.01) the highest plant height on narra, lahilahi and mangkono. In the field, NewMYC promoted the tallest narra and mangkono, and NewMYC and NewNFB gave the tallest lahilahi. NewMYC promoted the biggest (p<0.05) stem diameter of lahilahi and mangkono while NewMYC and NewMYC equally gave the biggest stem diameter of narra. MYKORICH® gave the heaviest (p<0.05) total plant dry weight on narra and lahilahi. Microbial biofertilizers also improved the root and plant dry weight, and root to shoot ratio relative to the control as a result of

the good root colonisation by the mycorrhizal symbionts with numerous hyphae to mine nutrients and water from the Ni mined-out soil. In the field, NewMYC gave 90% seedling survival on narra, while NewNFB gave 90% and 77% survival for lahilahi and mangkono, respectively. Microbial biofertilizers also improved the root and plant dry weight, and higher root-to-shoot ratio relative to the control as a result of the good root colonisation by the mycorrhizal symbionts with numerous hyphae to absorb nutrients and water from the Ni soil. In the field, NewMYC gave 90% seedling survival on narra, while NewNFB gave 90% and 77% survival rates for lahilahi and mangkono, respectively. The established field trials showed the effectiveness of the MBP in greening Ni areas in Claver, Surigao. The Marinduque isolates NewNFB and NewMYC indigenous in Cu mined-out area also showed potential in the rehabilitation of Ni mined-out soil under nursery and field conditions, thus could be further studied to prove their potential as biofertilizers for bioremediation.

6. ACKNOWLEDGEMENT

7. REFERENCES

Aggangan NS, Anarna JA, Cadiz NM. 2019. Tree legume-microbial symbiosis and other soil amendments as rehabilitation strategies in mine tailings in the Philippines. Philippine Journal of Science 143(3): 481-491.

Aggangan NS, Anarna JA. 2019. Microbial biofertilizers and other soil amendments enhanced tree growth and survival in a barren area. Journal of Environmental Science and Management 22(2): 77-88.

Aggangan NS, Cortes AD. 2018. Screening indigenous mycorrhizal fungi for the rehabilitation of mine tailing areas in the Philippines. REFORESTA 6: 71-85

Aggangan NS, Edradan MRR, Alvarado GB, Macana PPC, Noel LKS, Edradan DRR. 2013. Mycorrhizal fungi from mine sites and rehabilitation of marginal and mine sites in Surigao, Philippines. Chapter 18 p. 343-356, Ed by Dr. Carlos Alberto Busso. In: From Seed Germination to Young Seedlings: Ecology, Growth and Environmental Influences. Nova Science Publishers, Inc. New York. ISBN: 978-1-62618-653-8, 369 p.

Brundrett M, Bougher NL, Dell B, Grove T, Malajczuk N. 1996. Working with Mycorrhizas in Forestry and Agriculture. *ACIAR Monograp*h 32: 374 pp.

Giovannetti M, Mosse B. 1980. An evaluation of techniques for measuring vesicular-arbuscular infection in roots. New Phytol 84: 489–500.

Mahusay JR. 2014. Marinduque still being targeted by mine firms. Island sentinel. Retrieved April 3, 2015 from http://islandsentinel.com/2014/06/09/marinduque-still-being-targeted-by-mine-firms/

[MSU] Michigan State University. 1996. User's guide to MSTAT-C. Design, Management and Statistical Research Tool. East Lansing, Michigan: Michigan State University.

Ocon J, Ampan P, Mora-Garcia C, Cuidad KL, Buenaflor EM. 2018. Diversity assessment of floral species and screening of potential nickel hyperaccumulator in nickel-rich Kinalablaban Delta, Cagdianao, Claver, Surigao del Norte, Philippines. Journal of Environment and Earth Science www.iiste.org ISSN 2224-3216 (Paper) ISSN 2225-0948 (Online) Vol.8(7): 14.

Pande V, Pandey SC, Sati D, Bhatt P, Samat M. 2022. Microbial interventions in bioremediation of heavy metal contaminants in agroecosystem. Frontier Microbiology. 06 May 2022. https://doi.org/10.3389/fmicb.2022.824084

Prayudyaningsih R, Sari R, Mangopangi AD. 2019. Isolation of indigenous arbuscular mycorrhizal fungi (AMF) to support revegetation on the nickel post-mining land. IOP Conf. Series: Earth and Environmental Science 308 (2019) 012038 IOP Publishing doi:10.1088/1755-1315/308/1/012038.

Smith SE, Read DJ. 2010. Mycorrhizal symbiosis. London, UK: Academic Press.

Vieira JD, Stefenon VM. 2017. Soil Bioremediation in Heavy Metal Contaminated Mining Areas: A Microbiological/Biotechnological Point of View. Journal of Advances in Microbiology 4(1): 1-10.

#118: Improving energy efficiency of a ventilated tiled roof by using phase change materials

Eleonora Baccega[1*], Michele Bottarelli[1], Francisco Javier González Gallero[2], Giovanni Zannoni[1]

[1] Department of Architecture, University of Ferrara, Via Quartieri 8, 44121 Ferrara, Italy,
[2] Escuela Técnica Superior de Ingeniería de Algeciras, University of Cádiz, 11202 Algeciras, Spain
*Corresponding author: eleonora.baccega@unife.it

Abstract: The adoption of ventilated roofs and facades, as well as the integration of phase change materials (PCMs) in the building envelope, have proved to be effective as passive cooling techniques in reducing solar heat gain through the building envelope during the summer period and, therefore, reducing the energy requirement for cooling. Even though much research has focused on each of these strategies individually, their combination has not been deeply studied yet. Preliminary numerical studies were carried out on the application of PCMs on a pitched ventilated tiled roof and the most effective position turned out to be suspension in the middle of the above sheathing ventilation (ASV) channel. Based on this conclusion and exploiting an existing mock-up facility, two equivalent pitched ventilated roofs with an air gap of 4cm were built to cover two identical rooms, each one equipped with a fan coil; one with a 0.007m PCM layer suspended in the middle of the ASV and the other one without. They were then tested under real conditions at the TekneHub Laboratory at the University of Ferrara. The PCM supplied was an inorganic PCM with a melting temperature of 25°C and the roofs had a steel structure upon which a wooden deck covered by a polyolefin membrane was installed, with a cladding layer of Portuguese tiles. The behaviour of the two configurations were compared in terms of temperature, heat flux, velocity of the air in the ASV, and energy requirement for cooling, which were monitored through T-type thermocouples, heat flow meter, anemometers and energy meters, respectively. The aim of the research was to validate the numerical results and confirm that the combination of the two strategies allows further improvement of roof performance. Results showed consistent differences between the two configurations corresponding with the melting range of the PCM, which brought variances in the temperature of the extrados of the wooden deck of more than 5K and a reduction of the HVAC system operating time in the room with the PCM roof.

Keywords: passive cooling; phase change materials; ventilated roof; energy efficiency of buildings

1. INTRODUCTION

Accounting for 40% of the EU's energy consumption, 36% of its CO_2 emissions and 55% of the electricity consumption, the building sector consistently affects the total global energy demand (Boosting Building renovation, 2016). The major areas responsible for this are heating and cooling systems (IEA, 2019) and, with special regard to cooling, air conditioning is the main contributor to peak electricity demand both in hot climates and during summer (Chan, 2010). The ever increasing expectation of higher living standards together with the decrease of the cost of cooling equipment and the impact of the urban heat island effect, especially in crowded cities, are additional burdens to the actual scenario and will lead to a further growth of energy requirement for HVAC systems that is expected to increase by 80% by 2050 compared to 2010 levels (Ürge-Vorsatz, 2015). Among the possible solutions to counteract this behaviour are passive cooling techniques, through which it is sometimes possible to improve building performance and indoor comfort without any additional energy demand. Song, among others, classified the main passive cooling methods and identified three main categories, namely solar and heat control, heat exchange reduction, and heat removal (Song *et al.,* 2021). Solar control is mainly done through shading which can be integrated within the building or made with vegetation. As regards heat exchange reduction, methods are divided between those with and without thermal mass; the former consists in the addition of insulation layers, while the latter includes, for instance, the use of phase change materials (PCMs). PCMs have high latent heat capacity and can absorb and release a large amount of heat in a shorter temperature range around the phase change temperature, when compared to sensible heat storage (Lizana, 2017). Heat removal can be achieved, for instance, through natural ventilation in ventilated roofs and facades. These are particularly effective in decreasing the heat transfer through the envelope thus reducing the energy requirement for cooling, and are particularly effective in roofs where heat transfer has been estimated to be around three times greater than that through a south facing façade (Chang, 2008).

In hot climates, such as the Mediterranean, ventilated roofs allow the dissipation of the incoming heat during summer (Ciampi, 2005) and create an insulated layer around the building inner envelope in winter (Dimoudi, 2006). Their efficacy has been demonstrated by different experimental observations (Lee, 2009, Baccega, 2022). In addition to this, the project LIFE Climate Change Adaptation HEROTILE (High Energy savings in building cooling by ROof TILEs shape optimization toward a better above sheathing ventilation) (HEROTILE) aimed at improving the performance of ventilated roofs by designing new tiles, namely Marsigliese and Portoghese, that could improve the airflow through the tiles overlaps. The project consisted of numerical investigations and experimental activities, as documented in Bottarelli, 2018; Bottarelli, 2017a; and Bottarelli, 2017b. Further improvements on the performance of ventilated roofs might be obtained by the integration of PCM as already proposed by some researchers. For instance, Kosny *et al.* (Kosny, 2012) carried out tests on an experimental ventilated roof in which the PCM was positioned under the fiberglass, below the air cavity, and obtained a reduction of 55% in the cooling load in summer. Hou *et al.* (Hou, 2021) proposed a ventilated roof composed of multiple PCMs, one positioned above the roof and the other one under the ventilation layer, above the indoor environment. They carried out different summer tests, obtaining a reduction of the peak indoor temperature of up to 47% and an increase of the minimum indoor temperature of between 19% and 40%. Yu *et al.* (Yu, 2020) studied numerically a three-dimensional model of a ventilated roof in which, above the ventilation channel, a 0.03m layer of form-stable PCM was embedded between two cement mortars, and obtained a reduction of the peak indoor temperature of more than 4K. Bottarelli *et al.* (Bottarelli, 2020) carried out a numerical investigation of the integration of a layer of PCM inside the ventilation channel in two different positions, namely one laid on the roof deck and the other one suspended in the middle of the air gap. They concluded that, by allowing air to flow both above and below the PCM layer, a reduction of the energy load of about 18% could be obtained. The research given here started from the conclusions drawn by Bottarelli *et al.* (Bottarelli, 2020) and consisted in arranging and monitoring two ventilated roofs, one used as a benchmark and the other in which a layer of PCM was suspended in the middle of the air channel. Plastic containers filled with inorganic salt with a melting temperature of 25°C were placed in the middle of a 0.04m air channel. The behaviour of the two roof configurations were monitored in terms of temperature, heat flux and ASV (Above Sheathing Ventilation) velocity. Experimental results were in accordance with the numerical results previously obtained, with a reduction of about 15% of the heat load. The experimental data were then used to calibrate a Computational Fluid Dynamic (CFD) numerical model implemented in COMSOL Multiphysics v5.6 (COMSOL) to be used later to investigate the performance and to help in the design of other ventilated roofs: by varying the ASV channel height, the PCM layer height or its thermal properties, i.e., melting and solidification temperature and relative ranges, etc.

2. METHODOLOGY

The research reported here was carried out in two steps. The first step consisted of a simultaneous and thorough experimental monitoring of two roof configurations (with and without PCM layer) and the analysis of the thermal and airflow data obtained. Then, a CFD model of the roof configuration with the PCM layer was implemented in COMSOL Multiphysics, following the work of Bottarelli *et al.* (Bottarelli, 2020). This numerical model, whose results have been compared with experimental measurements, aimed to be a first approach to the problem and it was expected that more sophisticated versions would allow new scenarios to be simulated with a suitable level of uncertainty.

2.1. Experimental mock-up

The experimental activity consisted of the monitoring and further comparison of the performances of two equivalent ventilated roofs, one containing a layer of PCM and the other one not, which exploited an existing mock-up facility

located at the TekneHub Laboratory of the University of Ferrara. This mock-up building (Figure 1a) was originally constructed for the European project LIFE Climate Change Adaptation – HEROTILE (High Energy savings in building cooling by ROof TILEs shape optimization toward a better above sheathing ventilation), and was partially modified for this research.

a)   b)

Figure 1: (a) Mock up building at the TekneHub Laboratory at the University of Ferrara; (b) Arrangement of the PCM plastic containers in the ASV layer of the roof.

The mock-up had an 8 x 10 m² rectangular plan and was made of seven equivalent rooms, with five of them being the actual test rooms, north-south oriented, and the remaining two at the ends being guard rooms, used to ensure the same conditions in each of the test rooms. The structure was of steel and was clad with sandwich panels both for exterior and interior walls. The roof, which was tilted 20° with north-south oriented pitches, was made of steel beams covered by a 0.03m wooden deck and a waterproof polyolefin membrane upon which the tile supports were arranged. The two rooms set for the monitoring both had 0.04m tiles supports, which formed the ASV, and the cladding layer made of Portoghese tiles. In one of the two roofs a 0.007m layer of PCM was arranged in the middle of the air cavity. The layer consisted of 0.30 x 0.30m² plastic containers each filled in with about 0.42kg of inorganic PCM with a melting point of about 25°C. In Figure 1b, the arrangement of the PCM plastic containers is depicted. Several sensors were installed to monitor the behaviour of the two configurations. In terms of boundary conditions, a weather station was installed outside the laboratory and collected data about solar radiation, air temperature and humidity, wind speed and direction every 15 minutes.

a)   b)
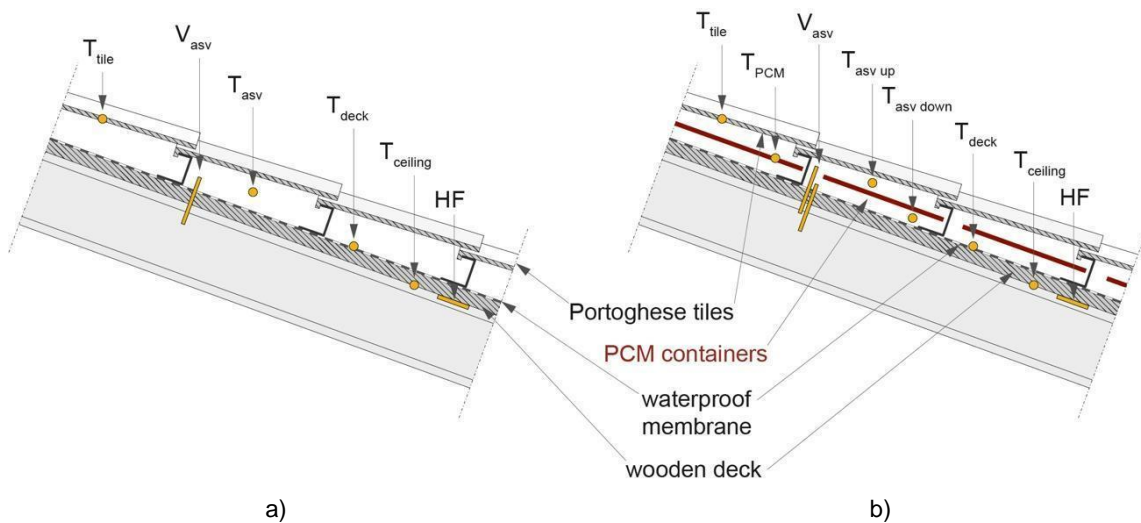
Figure 2: Section of the roof configurations (a) without the PCM layer; (b) with the PCM layer.

For more accurate measurements, additional sensors were installed, namely a pyranometer parallel to the south pitch to measure the solar radiation, a RTD Pt100 outside the north wall to measure air temperature, and cup anemometers at different heights (1.50 – 2.50 – 4.00 – 6.00 m) for the wind profile. For monitoring the two roof configurations, temperature and heat flux sensors together with hot wire anemometers were used, and their position is shown in Figure 2a and 2b. T-type thermocouples (accuracy: 0.5 K) were installed on the tile intrados, in the middle of the ASV channel above and below the PCM layer, underneath one of the plastic containers, on the extrados and intrados of the wooden deck and inside the rooms. Each room had a fan coil unit to regulate indoor temperature, which during the period of the test was set to 26°C. The heat flux meter (accuracy: 3%) was installed on the intrados of the wooden deck next to the thermocouple, while two anemometers (operating range: 0.1-2.5 m/s, accuracy: 3% of reading +1% of full scale) were installed in the middle of the ASV channel, above and below the PCM layer. With respect to the roof without PCM, only one thermocouple and anemometer was positioned in the middle of the only ASV channel. In general, all the above-mentioned sensors were installed in the south facing pitch and were connected to a datalogger, and data about temperatures and heat fluxes were collected with a time step of two minutes, while wind speed data were collected every minute.

2.2. CFD model

In order to reduce computational cost, the CFD model reproduced a 2D section of the south pitch (Figure 3), including in a 5m x 8m external environment. Due to the low thermal inertia of the system, 24 hours (10-11 May 2022) of simulation were selected among those of the experimental campaign in which the air conditioning system operated in cooling mode.
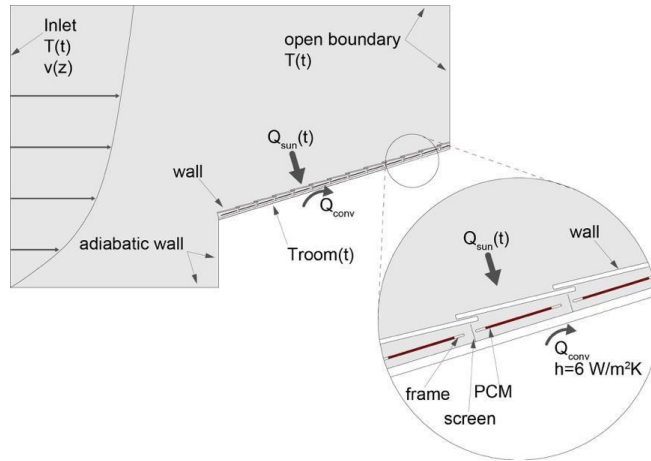

Figure 3: Description of CFD domain and boundary conditions.

The Portoghese tiles of the covering were modelled as 0.41m x 0.015m rectangles and the metal supports through which the ASV channel was built were modelled as a 1D screen layer to which a 70% of solidity, with an average hole dimension of 0.003m, was assigned. The PCM plastic containers were modelled as 0.23m x 0.007m rectangles of PCM material surrounded by plastic rectangular frames (0.035m x 0.007m). The properties assigned to the different materials are given in Table 1. For what concerns the PCM density, a value of 1560 kg/m^3 was experimentally estimated. However, since the default model length is of 1 m and that the layer of PCM is not a continuous layer but it consists of separated plastic containers (4 in a pitch width of 1.3 m), the density applied to the material was proportionally reduced in order to consider in the model the same PCM mass as in the actual roof. Hence, the value assigned to the PCM material is 600 kg/m^3.

Table 1: Physical properties of the building materials.

Material	Thickness [m]	Density [kg/m3]	Thermal conductivity [W/m/K]	Specific heat [J/kg/K]	Latent heat [kJ/kg]	Phase change temperature [°C]	Emissivity [-]
Tiles	0.015	1600	0.5	800	-	-	0.8
PCM	0.007	600*	0.6	1800	100	24 melting 23 solidification (span 5K)	0.8
Wooden deck	0.03	532	0.4	1000	-	-	0.8

Regarding boundary conditions, indoor and outdoor temperatures and solar radiation were expressed as time dependent functions according to the experimental data acquired (Figure 4).
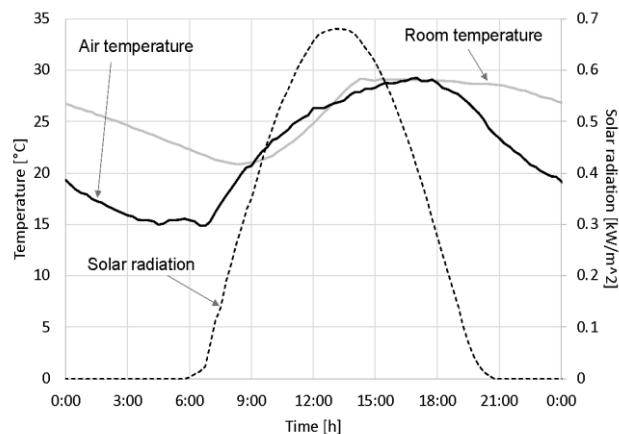
Figure 4: Boundary conditions applied to the model.

For what concerns the wind velocity profile assigned to the inlet of the fluid domain, the following power law (Equation 1) was used:

Equation 1: Wind speed profile.

$$v(z) = v_0 \left(\frac{z}{z_0}\right)^{\alpha}$$

where:

- $v(z)$ = wind speed at height z (m/s)
- z = height
- v_0 = wind speed at a reference height, equal to 1 m/s
- z_0 = reference height
- α = empirical non-dimensional exponent, equal to 0.3 (Masters, 2004).

The k–ε model with standard wall functions was used to simulate turbulence within the fluid domain. The numerical problem was solved in two stages. First, a steady-state solution of the airflow was sought in the thermal conditions formerly described. Then, from the steady-state airflow solution, the heat transfer transient problem with relative tolerance of 10-3 was set for residuals. Meshes were locally refined in areas with high temperature and velocity gradients. After an independence grid study in which temperatures and air flow velocities were analysed, an unstructured mesh made of 48127 elements was used, which showed an average element quality of 0.79.

3. EXPERIMENTAL RESULTS

The roofs were arranged at the beginning of March 2022, and the monitoring activity has been carried out ever since. A period of 5 consecutive days (from 10 to 14 May 2022), with similar ambient conditions, was chosen for the purpose of this article and the results are presented here. As regards the indoor conditions, the fan coil unit operated in cooling mode when indoor temperature exceeded the set point of 26°C, while for the outdoor conditions, air temperature and solar radiation are reported in Figure 5a and wind speed and direction in Figure 5b. Air temperature fluctuated between a minimum of 12-15°C during the night up to almost 30°C during the day, with a horizontal solar radiation that reached peaks of nearly 900 W/m². As for the wind, the velocity was around 1m/s during the first and the last days, while for the rest of the days it was slightly higher (between 1.5m/s and 2m/s). The prevalent wind directions were south and west. From the comparison of the two roof configurations, the effect of the PCM is clearly visible. Temperatures inside the ASV are depicted in Figure 6a. During the day, the temperature within the ASV channel in the roof with PCM above the PCM layer (Tasv-up) was almost the same as that in the roof without PCM, while the temperature under the PCM (Tasv-down) was lower, with differences of about 5K during the hottest hours of the day and which reached peaks up to 7K during the morning, when, based on the external conditions, the PCM was melting. On the contrary, during night-time both (up and down) ASV temperatures in the roof with PCM were higher than ASV temperature on the roof without, with differences up to 5K between midnight and 3 a.m. Again, this is likely due to the effect of the solidification of the PCM, which can be seen in the graph (Figure 6a) as sharp temperature changes around 25°C.
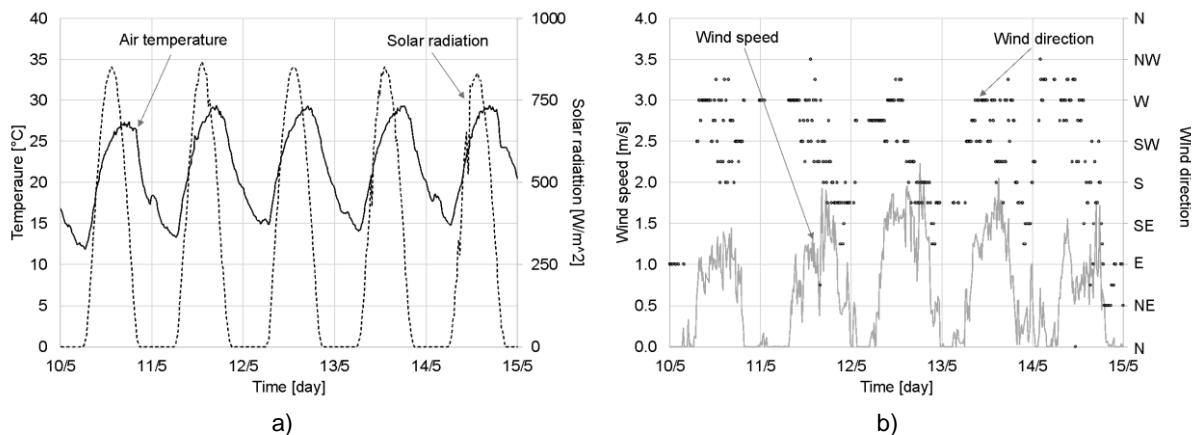

a)   b)

Figure 5: 15 min average ambient conditions during the monitoring activity: (a) air temperature and solar radiation; (b) wind speed and direction.

A similar behaviour can be observed on deck temperatures, depicted in Figure 5b, where during the day the deck temperature of the roof with PCM was up to 3K lower than that of the roof without PCM, while during the night it was up to 2K higher, in correspondence with the phase change of the PCM. Furthermore, and according to Fisher's F-test for comparing variances, temperature fluctuations at deck in the roof with PCM were significantly smaller than those in the roof without PCM, which agreed with the results of a previous CFD numerical study of this kind of roof

configurations (Bottarelli *et al.,* 2020). The standard deviation of deck temperature for the roof with PCM was 19% smaller than for the roof without. Thus, a slower degradation of the outer surface of the insulation layer caused by extreme temperatures was expected in the roof with PCM. There were no significant statistical differences between the average values according to z-test. Regarding heat fluxes (Figure 6b), outgoing (positive) heat fluxes were measured mainly during night time, remaining nearly constant most of the time (4 W/m^2 on average, approximately), and starting about two hours after sunset and vanishing about three hours after sunrise. The roof with PCM showed a smaller variance (F-test) but a statistically greater average (just 0,4 W/m^2; z-test) of these outgoing heat fluxes than the roof without PCM. Incoming (negative) heat fluxes took place three hours after sunrise and two hours before sunset, with peak values of around 35 and 31 W/m^2 for the roofs without and with PCM, respectively.

a)   b)
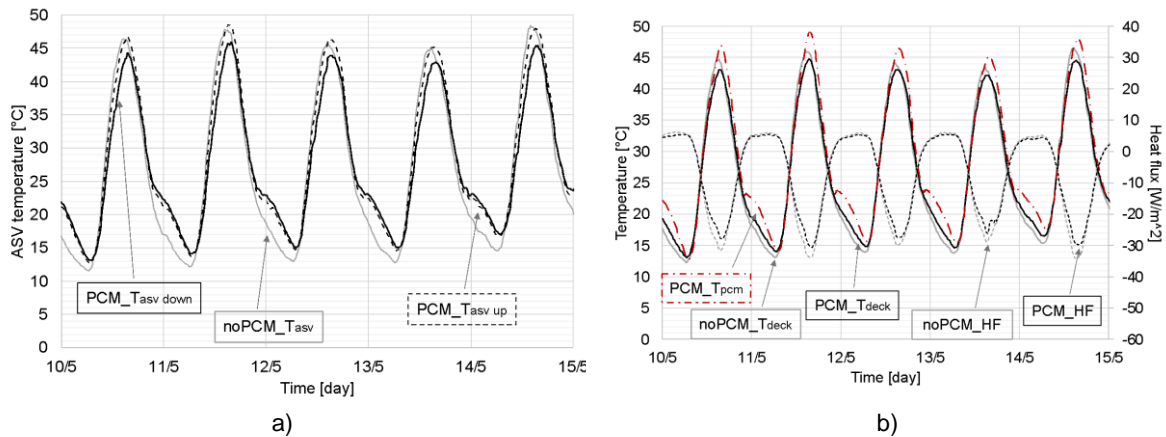
Figure 6: 15 min average of (a) ASV temperature and (b) deck temperatures and heat fluxes of both the roof configurations monitored.

In Figure 7, a detailed view of the heat flux through the roofs is depicted for one of the five days considered, more specifically May 14th. It was observed that peak values of incoming heat fluxes through the roof with PCM showed a delay of about 20 to 30 minutes with respect to the roof without PCM. Again, variances of these incoming fluxes were significantly smaller for the roof with PCM (F-test), showing a smaller average value as well (-10%; z-test). The addition of the PCM layer resulted in a reduction of about 5 W/m^2 in the hottest hours of the day, which corresponded to about 15% of the incoming flux through the roof without PCM.
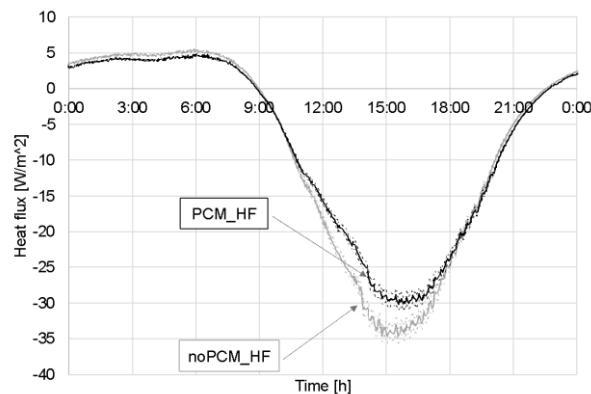
Figure 7: Detail of the heat fluxes on May 14th. Ranges of experimental uncertainty are shown with dashed lines. Raw data acquired with a time step of 2 min.

The total incoming energy during the five days considered were calculated from the incoming heat flux and shown in Figure 8a. In the case with PCM there was about 8% less incoming energy through the roof, which meant lower energy demand for cooling in the room. Regarding room temperature, during the day the rooms had the same indoor temperature which were kept constant with the help of fan coils. However, during the night, when the temperature was lower than the set point temperature and therefore the fan coil units were off, the presence of the PCM layer kept the room warmer, with temperature increases that reached almost 2K.

The velocity of air inside the ASV is depicted in Figure 8b. In the case of the roof without PCM, the velocity of the ASV was almost the same as that of the other roof under the PCM containers, with values that were lower than 0.1 m/s on average except for some peaks during the second and third days that reached 0.2 m/s. The velocity of air inside the ASV above the PCM containers was completely different, more than double than the one under the PCM containers on average and with peaks higher than 0.4 m/s. However, it was noticed that, in general, these air velocities were all quite low since Ferrara is characterised by frequent low wind speeds.
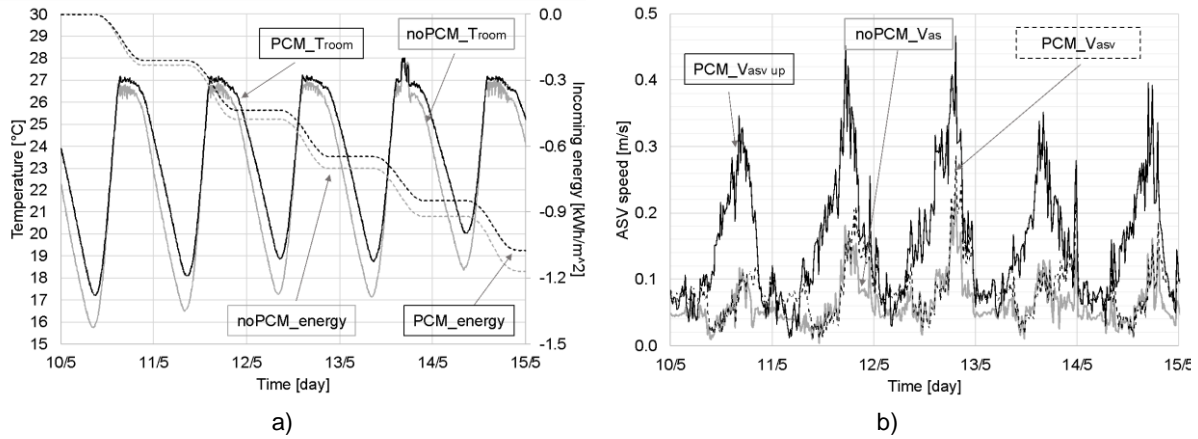
<div align="center">a)   b)</div>

Figure 8: 15 min average of (a) room temperature and total incoming energy from the roof; (b) air velocity in the ASV.

From the experimental measurements for a longer period (3 May to 16 June 2022), a multiple regression model (MLR) was carried out as in Equation 2 in order to estimate heat flux (HF) through the roof (for both configurations), under cooling mode operation of the fan coil unit, in terms of outdoor air temperature (T_{out}) and solar radiation (SR). Table 2 shows the parameters of the MLR model. The fitting can be considered statistically good (R^2 around 0,82 for both cases).

Equation 2: Multiple Linear Regression Model. $$HF = \beta 0 + \beta 1 \cdot T_{out} + \beta 2 \cdot SR$$

where:

- HF= heat flux (W/m^2);
- T_{out} = Outdoor ambient temperature (ºC);
- SR = Solar radiation (W/m^2)

Table 2: Values of MLR model parameters.

MLR model parameter	No PCM	PCM
$\beta 0$	25,92948	24,53770
$\beta 1$	-1,25896	-1,21624
$\beta 2$	-0,01843	-0,01459
R2	0,824	0,820

In order to highlight the actual effect of PCM on the performance of the roofs, only data collected in the range between midday and 3 p.m. were considered in a second analysis, since ambient conditions are the most critical at that period. As reported in Table 3, during the selected five days the average air temperature, solar radiation and wind speed were about 27.3°C, 820 W/m^2 and 1.3 m/s, respectively. Under these conditions, the differences already observed on deck and ASV temperatures were emphasised. Regarding the deck, the average temperature in the roof without PCM was 42.3°C, while that in the roof with PCM was 2.2K lower, with a corresponding reduction of 5.2%. A greater reduction was visible in terms of ASV temperature, where the average in the roof without PCM was 44.5°C while in the roof with PCM, under the PCM containers, it was 39.4°C, corresponding to a reduction of 11.4%. The temperature of the tile was almost the same in the two configurations, with differences lower than 0.5K. The same behaviour can be observed in the temperatures of the ceiling and the room, where the differences between the two configurations were lower than sensor uncertainty. Eventually, the energy incoming through the roof with PCM was 15.1% smaller than that through the roof without PCM, with an average daily difference of 11.6 Wh/m^2 during the hottest hours of the day, and nearly 20 Wh/m^2 when considering the whole day.

Table 3: Average data during the selected period in the range 12:00-15:00.

	Air temperature [°C]	Solar Radiation [W/m^2]	Wind speed [m/s]	T_{tile} [°C]	T_{asv} [°C]	T_{deck} [°C]	$T_{ceiling}$ [°C]	T_{room} [°C]	Incoming energy [Wh/m^2]
noPCM	27.3	820.2	1.3	52.6	44.5	42.3	28.9	24.9	77.0
PCM				52.2	39.4	40.1	29.2	25.1	65.4
difference	-	-	-	-0.9%	-11.4%	-5.2%	+1.1%	+0.8%	-15.1%

4. NUMERICAL RESULTS

Comparisons between numerical and experimental results have focused particularly on thermal variables (temperature and heat flux). Thus, regarding the temperatures inside the ASV channel, the differences between the experimental and the simulated data were of about 0.6K on average. More specifically, if compared to the experimental values, during the night and between 3p.m. and 6 p.m. the simulated values were about 1K lower, while during the morning and after sunset the simulated values were between 2K and 4K higher. Concerning the temperature of the PCM tile, the average difference between the experimental and simulated values was about 1.5K, while during the night the simulated values were about 2K higher than the experimental one, and, on the contrary, during the day they were 5K higher. As for the deck temperature, the difference between the experimental and the simulated values was almost constant, with simulated values always between 2K and 3K higher than the experimental ones. Regarding the heat flux, the average difference between the experimental and simulated values was 0.2 W/m^2, with simulated values lower than the experimental ones during the morning and after 3 p.m. but higher between 9 a.m. and 13 p.m. The root mean square errors (RMSE) were also estimated and values are reported in Table 4. Regarding temperatures, RMSE values ranged between 3 and 5 times the experimental uncertainty, with lower values for the temperatures inside the ASV channel, while as for the heat flux, the RMSE value was between 2 and 3 times the experimental uncertainty. Figure 9 shows the simulated and experimental values of a) ASV temperatures and b) PCM and deck temperatures and heat flux.

Table 4: RMSE values estimated

	Tpcm	Tasv up	Tasv down	Tdeck	Heat flux
RMSE	2.52K	1.53K	1.56K	2.55K	2.16 W/m^2
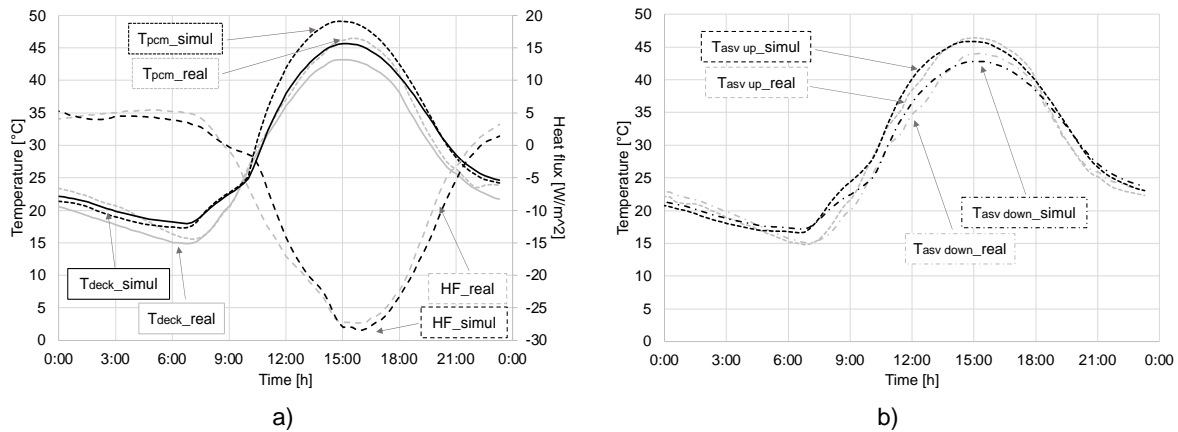
Figure 9: Simulated and experimental values of a) ASV temperatures and b) PCM and deck temperatures and heat flux.

5. CONCLUSIONS

An experimental activity was carried out at the TekneHub Laboratory at the University of Ferrara where two equivalent ventilated roofs were arranged, one with a layer of PCM suspended in the middle of the air channel and the other one without PCM layer. The layer of PCM consisted of an inorganic PCM with a melting temperature of about 24-25°C and contained in plastic containers. The roofs were constantly monitored from March 2022. The experimental results confirmed the effect of the PCM layer in reducing the peak temperatures as well as reducing the incoming heat fluxes. In fact, the addition of PCM inside the ASV channel brought a reduction of the maximum temperature of up to 5K during the hottest hours of the day, corresponding to a reduction of 11.4%, while below the ASV channel and above the wooden deck, the maximum temperature reached was 2K lower during the day, corresponding to a reduction of 5.2%. It was up to 3K higher during the night. Concerning the incoming energy, with the PCM layer brought an average reduction of 8% over the whole day, and of up to 15% during the hottest hours of the day. In terms of air velocity in the ASV channel, the velocity monitored below the PCM layer was the same as in the roof without PCM, while the velocity above the PCM layer was more than double. These velocities, however, were all quite low due to the low wind speed. Moreover, from a closer look on the PCM plastic container, the maximum temperature reached was very high which might indicate an undersized PCM layer or a too low melting temperature. The experimental results were then used to validate a simplified 2D numerical model of the south pitch, which could be considered an approach to the problem and a first step for the development of more advanced CFD models to be used for further investigations considering different boundary conditions, climatic zones, as well as changing the geometry and PCM thermal characteristics.

6. ACKNOWLEDGEMENTS

7. REFERENCES

Baccega, E., Bortoloni, M., Bottarelli, M., Dino, G.E., Zannoni, G. 2022. Improving the air permeability of ventilated roofs. Future Cities and Environment, 8(1), 1-8.

Boosting Building renovation, 2016. Available online: https://www.europarl.europa.eu/RegData/etudes/STUD/2016/587326/IPOL_STU(2016)587326_EN.pdf (accessed on 27 March 2022).

Bottarelli, M., Bortoloni, M., Zannoni, G., Allen, R., Cherry, N. 2017a. CFD analysis of roof tile coverings. Energy, 137, 391-398. http://dx.doi.org/10.1016/j.energy.2017.03.081

Bottarelli, M., Bortoloni, M. 2017b. On the heat transfer through roof tile coverings. International Journal of Heat and Technology, 35, 316-321. http://doi.org/10.1820/ijht.35Sp0143

Bottarelli, M., Bortoloni, M., Dino, G. 2018. Experimental analysis of an innovative tile covering for ventilated pitched roofs. International Journal of Low Carbon Technologies, 13, 6-14. http://dx.doi.org/10.1093/ijlct/ctx014

Bottarelli, M., González Gallero, J.F., Rodríguez Maestre, I., Pei, G., Su, Y. 2020. Solar gain mitigation in ventilated tiled roofs by using phase change materials. International Journal of Low Carbon Technologies, 00, 1-9. http://doi.org/10.1093/ijlct/ctaa001

Chan, H.Y., Riffat, S.B., Zhu, J. 2010. Review of passive solar heating and cooling technologies. Renewable and Sustainable Energy Reviews, 14, 781-789. http://doi.org/10.1016/j.rser.2009.10.030

Ciampi, M., Leccese, F., Tuoni, G. 2005. Energy analysis of ventilated and microventilated roofs. Solar Energy, 79, 183-192. http://doi.org/10.1016/j.solener.2004.08.014

COMSOL Multiphysics Reference Manual. Available online: http://www.comsol.com (accessed on 19 November 2020).

Dimoudi A., Androutsopoulos A., Lykoudis S. 2006. Summer performance of a ventilated roof component. Energy and Buildings, 38, 610-617. http://doi.org/10.1016/j.enbuild.2005.09.006

HEROTILE. https://www.lifeherotile.eu/it/

Hou, M., Kong, X., Li, H., Yang, H., Chen, W. 2021. Experimental study on the thermal performance of composite phase change ventilated roof. Journal of Energy Storage, 33. https://doi.org/10.1016/j.est.2020.102060

IEA, 2019. IEA website: https://www.iea.org/topics/energy-efficiency

Kosny, J., Biswas, K., Miller, W., Kriner S. 2012. Field thermal performance of naturally ventilated solar roof with PCM heat sink. Solar Energy, 86, 2504-2514. http://dx.doi.org/10.1016/j.solener.2012.05.020

Lee, S., Park, S.H., Yeo, M.S., Kim, K.W. 2009. An experimental study on airflow in the cavity of a ventilated roof. Building and Environment, 44, 1431-1439. http://doi.org/10.1016/j.buildenv.2008.09.009

Lizana, J., Chacartegui, R., Barrios-Padura, A., Valverde, J.M. 2017. Advances in thermal energy storage materilas and their applications towards zero energy buildings: A critical review. Applied Energy, 203, 219-239. http://dx.doi.org/10.1016/j.apenergy.2017.06.008

Masters, G.M. 2004. Renewable and Efficient Electric Power Systems. New York: John Wiley and Sons.

Song, Y., Darani, K.S., Khdair, A.I., Abu-Rumman, G., Kalbasi, R. 2021. A review on conventional passive cooling methods applicable to arid and warm climates considering economic cost and efficiency analysis in resource-based cities. Energy Reports, 7, 2784-2820. https://doi.org/10.1016/j.egyr.2021.04.056

Ürge-Vorsatz, D., Cabeza, L.F., Serrano, S., Barreneche, C., Petrichenko, K. 2015. Heating and cooling energy trends and drivers in buildings. Renewable and Sustainable Energy Reviews, 41, 85-98. http://dx.doi.org/10.1016/j.rser.2014.08.039

Yu, J., Leng, K., Wang, F., Ye, H., Luo, Y. 2020. Simulation study on dynamic thermal performance of a new ventilated roof with form stable PCM in Southern China. Sustainability, 12. http://doi.org/10.3390/su12229315

#122: Modelling of the hydraulic power take-off system at the wave-to-energy station installed in Gaza Strip

Taleb Alrayyes[1], Mohammed Jarad[2], Ahmed Abutabaq[3], Khair Ghunaim[4], Mohammad Abuhaiba[5]

[1]Islamic University of Gaza, Centre of Excellence for Renewable Energy (CERE-IUG), Gaza Strip, talrayyes@iugaza.edu.ps
[2]Islamic University of Gaza, Centre of Excellence for Renewable Energy (CERE-IUG), Gaza Strip, mohjarad.98@gmail.com
[3]Islamic University of Gaza, Centre of Excellence for Renewable Energy (CERE-IUG), Gaza Strip, ahtabaq@gmail.com
[4]Islamic University of Gaza, Centre of Excellence for Renewable Energy (CERE-IUG), Gaza Strip, khghunaim@gmail.com
[5]Islamic University of Gaza, Centre of Excellence for Renewable Energy (CERE-IUG), Gaza Strip, mhaiba@iugaza.edu.ps

Abstract: Wave energy from seas and oceans is among the most promising sources of renewable energy. A point absorber wave energy converter (WEC) was constructed at the Gaza-Palestine fishing port. A hydraulic circuit was used as the Power Take-Off (PTO) system to convert kinetic energy from floaters to useful electricity. The hydraulic PTO is well suited for dealing with the sea wave's excessive forces applied on the WEC's floaters at low frequencies. The efficiency of the PTO, and subsequently the WEC, depends on many parameters and operating conditions. Developing a control system is essential for enhancing PTO efficiency. The purpose of this study was to simulate both the hydraulic and control systems with the future aim to optimize the PTO by developing a control system and modifying the hydraulic circuit. SEIMENS SIMCENTER AMESIM software was used to replicate the installed hydraulic PTO. The main advantage of SIMCENTER AMESIM was the ability to deal with complex input data coming from irregular sea waves. The model was validated by comparing the simulation results with experimental data. The input for the model was real data taken at the different wave conditions (wave height and angles) and power output. The comparison was based on pressure and flow rate behaviours at different locations of the hydraulic circuit. This was especially important for critical components such as the accumulator and the pressure compensating valve. Both have an important role in the stability and efficiency of the circuit by absorbing flow pulsation and regulating the variability of pressure, subsequently, smoothing the power delivered to the electrical generator. The results showed an identical behaviour between the experimental data and results from the simulation. The model will be used for continuous improvement of the circuit, and for developing an improved control strategy.

Keywords: renewable energy, wave energy converter, hydraulic, power take-off, optimization.

1. INTRODUCTION

The global energy situation is receiving a lot of attention these days due to the war in Ukraine. The world is still highly dependent on using fossil fuels to produce energy. Over the last few years, there has been an increase in using renewable energy sources, especially wind and solar (Lund, 2007). However, the ocean covers over 70% of the planet's surface and is regarded as one of the most promising renewable energy sources. Ocean waves have a significant amount of energy and have the potential to contribute significantly to worldwide renewable energy (Kalogirou, 2005). Wave energy has some advantages over other sources of renewable energy including higher energy density, substantial availability, and source reliability. If the technology develops, it might be able to solve the energy needs of the planet (Esteban and Leary, 2012).

The wave energy conversion consists of four phases of conversion: absorption, transmission, generation, and conditioning. In the absorption stage, the kinetic energy stored in the sea waves is transferred to the floating bodies. In the transmission stage, the absorbed energy is primarily transformed into a generator where it is converted to electricity. This is the generation stage. Finally, in the conditioning stage, the generated electricity is converted to the right type of current and voltage to be delivered to the grid (Van Der Jagt, 2018).

Wave Energy Converters (WEC) are devices designed to convert wave energy to electrical energy or another kind of useful energy. WECs are classified according to different types of conversion concepts. They are attenuators, point absorbers, oscillating water surge converters, oscillating water columns, overtopping/terminator devices, submerged pressure differential, bulge wave, and rotating mass, (Liu, 2016; Alamian, Shafaghat *et al.*, 2017; Falcão, Henriques *et al.*, 2017; Malara, Gomes *et al.*, 2017; EMEC 2021). Point absorbers depend on floating structures that absorb energy from all directions through their movements at the water surface. Point absorbers, such as the installed WEC in the fishing port of Gaza, account for 40% of research and development efforts in wave energy technology (Magagna and Uihlein, 2015).

A Power Take-Off (PTO) system is used for the transmission stage. The PTO is a crucial component in wave energy conversion. It should be robust, and reliable and should require as little maintenance as possible in the harsh sea environment (Têtu, 2017). There are many types of PTO systems; the most commonly used is the hydraulic one. It employs incompressible fluid to transfer kinetic energy stored in the floating body into fluid power, which can be transferred to useful work. The oil-hydraulic PTO is adapted for dealing with especially high forces normally induced by waves, particularly at low frequencies (Ponce de León, Bettencourt *et al.*, 2011).

The sea rarely shows unidirectional, regular sinusoidal wave patterns. The waves on the seas are, by their nature, random and of irregular shapes (Zhao, Han *et al.*, 2019). Many studies have been performed to model the behaviour of sea waves by either observing them as a mixture of regular waves or making use of numerical methods. Nevertheless, none of them have accurately represented the behaviour of seas. Furthermore, when waves approach coastlines, they can experience transformations due to refraction and diffraction as a result of the changes in depth and the presence of currents. Wave energy loss can occur due to bottom friction and depth-induced wave breaking (Ponce de León, Bettencourt *et al.*, 2011). All the aforementioned reasons make the prediction of waves' behaviour real challenging.

The majority of studies on wave energy have focused on the hydrodynamic performance of wave energy converters assuming a linear PTO system. Fewer studies have focused on PTO, for example, Beirão *et al.* used FluidSim software to design a simple hydraulic PTO as a part of a student project. The study built a pilot circuit using dedicated materials to compare simulation results with the circuit data. In their work, a hydraulic pump (with a reciprocation sinusoidal flow) was used to resemble the behaviour of sea waves (Beirão and Malça. 2011). Ke Sun *et al.* proposed a design of a hybrid WEC equipped with a hydraulic PTO unit. AMESIM Software was used to model the hydraulic system. Steady system pressure and an essentially constant motor speed was obtained with the help of accumulators. Their study confirmed that the stability of the hydraulic system was influenced by the size of the accumulator and the number of cylinders. However, their work was a simulation and not based on any experimental work (Sun, Ge *et al.*, 2016).

In this study, a wave-to-energy pilot station was installed at the Gaza fishing port to produce electricity from sea waves. The produced electricity was used to lighten the fishing port at night. In addition, the station is becoming part of the Centre of Excellence for Renewable Energy (CERE-IUG) at the Islamic University of Gaza. The station is heavily instrumented to act as a research facility for wave energy.

In this paper, a hydraulic simulation of the PTO system that was used in the wave-to-energy pilot station in Gaza is presented (Figure 1). Real wave data is used as input data for the simulation. The complex hydraulic was validated for future optimization of the circuit and for the ongoing development of a control system that will be used to increase the efficiency of the hydraulic circuit. An example of continuous improvement is reducing cut-in wave height and increasing cut-out wave height. Cut-in wave height is defined as the minimum wave height that a wave-to-energy station can use to produce electricity. Cut-out wave height, on the other hand, is defined as the maximum wave height that the wave-to-energy station can operate in without affecting its structural integrity. Both parameters can be improved by developing a control strategy that will link wave height to different operating conditions in the PTO.
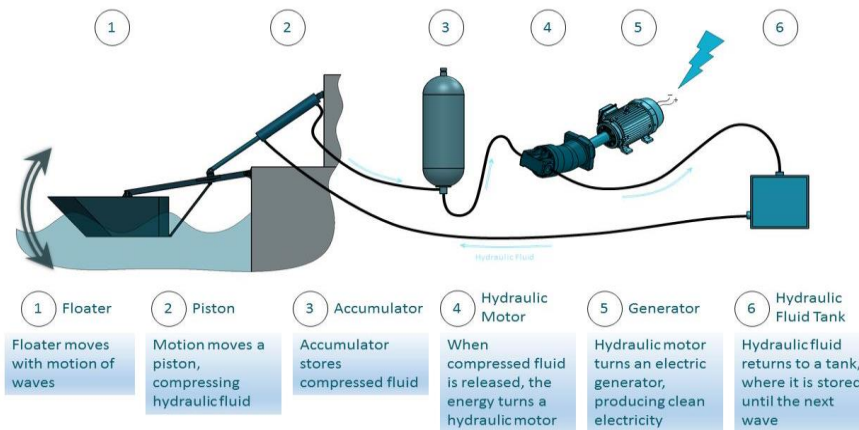
Figure 1: Wave-to-energy converter concept

Another method is to optimize the sizing of different components to fit the input of the floaters. Both can be done through accurate modelling of PTO. In this paper, the hydraulic motor was sized using the hydraulic circuit model as an example of the continuous improvement that the hydraulic circuit model will be used for.

2. METHODOLOGY

The investigation was carried out as follows.

2.1. Wave-to-energy converter in Gaza

The installed wave-to-energy converter (WEC) in Gaza was a point absorber with a single degree of freedom. The stored kinetic energy in the sea waves was transferred via the floaters into a flow energy (pressure and flow rate). This flowing energy then can be transported to a generator through a power take-off (PTO) system as shown in Figure 1. The installed PTO was a hydraulic circuit. The PTO started with a hydraulic cylinder that was connected to each floater. The Cylinders acted as pumps to pressurise oil.

Directional control valves (DCVs) were used to switch between three modes of operations in the hydraulic PTO. The first one was the power mode where the oil was transferred to the hydraulic motor/generator. The second mode was the neutral mode (no load) where the oil circulated freely from the cylinder to the oil tank and vice versa without going to the motor to allow for maintenance and any emergency. Finally, emergency mode, which lifted the floaters above the water level to avoid rough weather and high wave conditions (See Figure 2). The DCVs were solenoid operated. Switching between the different modes of operation was operated from a signal from the PLC controller.
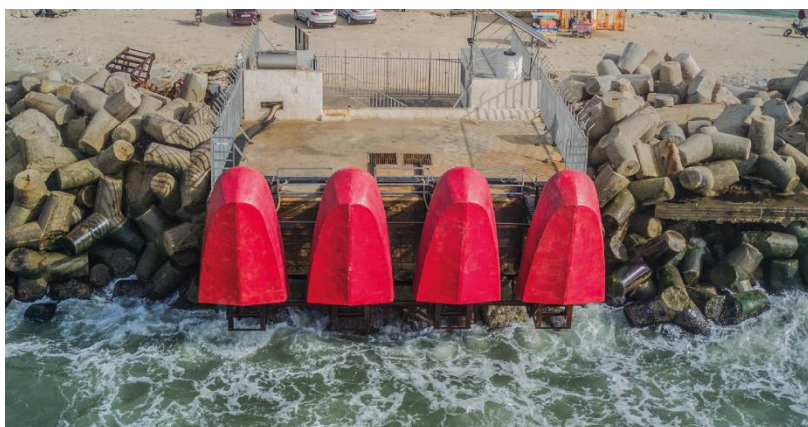
Figure 2: Floaters in the emergency mode

Due to sea wave random behaviour, accumulators were installed to act as energy storage devices and dampers. Furthermore, a pressure compensated valve was used to keep a steady flow of oil regardless of the pressure difference in the circuit. Change pressure difference occurred due to a change in energy supply (different wave heights) and/or change in power demand (change in hydraulic motor load). Both the accumulator and pressure compensated valve ensured the stability of flow and consequently the speed of the hydraulic motor. Constant speed was required to maintain a constant AC frequency supplied to the grid. The installed hydraulic circuit is shown in Figure 3.
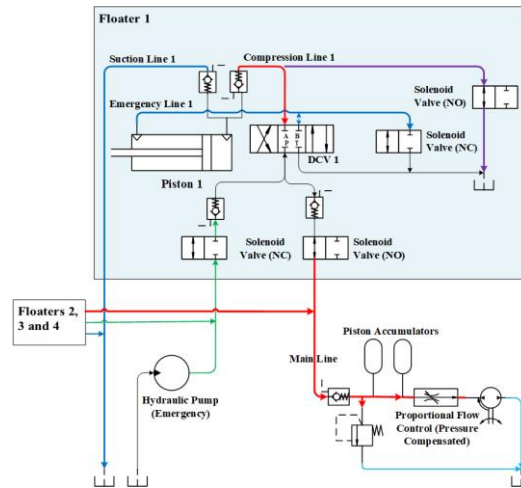
Figure 3: The installed hydraulic circuit in Gaza

Figure 4: Hydraulic power take-off (PTO) system

Several pressure sensors were mounted at different locations of the hydraulic circuits as illustrated in Figure 4. Pressure was measured at the cylinder's outlet, mainline, hydraulic motor, and accumulators. A flow rate meter was used to monitor the flow in the main line. Experimental measurements were taken using the Data Acquisition system (DAQ). A sample of the data plotted is shown in Figure 5. During experiments, different loads were applied to the hydraulic motor/generator combination using a load panel.
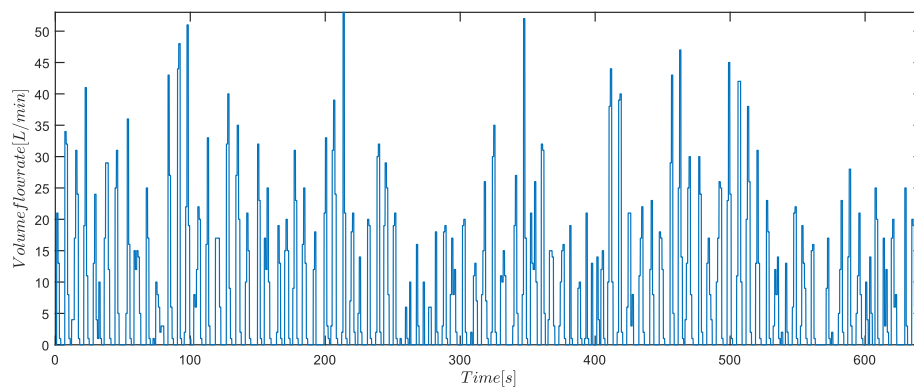
Figure 5: Flow meter data

2.2. Modelling of the hydraulic circuit

Hydraulic equipment is expensive and is hard to be found in Gaza Strip due to political reasons. Therefore, it is extremely hard to investigate and research based on real experiments. An Accurate model for a hydraulic circuit is important for continuous improvement of the circuit, particularly in the development and optimization of the control system.

AMESIM software was selected for this study. The selection criterion was based on many aspects, the ease of use, the library of components, accuracy of results, and the ability to use experimental data as input signals. That is, the behaviour of sea waves is random, and therefore, using regular sinusoidal waves can be misleading.

Few limitations appeared in the simulation software. For example, the hydraulic library did not include any piston accumulators. Accumulators are important components in the hydraulic circuit and it is essential to accurately model them. The piston accumulator was replaced by a bladder accumulator. Several experiments were carried out to obtain the working parameters of the accumulators in the software that are closest to the real ones. In addition, several concepts were employed to facilitate the process of modelling the PTO in the software environment. The in-circuit control system is a PLC that has been simplified and considered a classic control system. Furthermore, the cylinders in the real model were replicated as signal inputs. The model is shown in Figure 6.
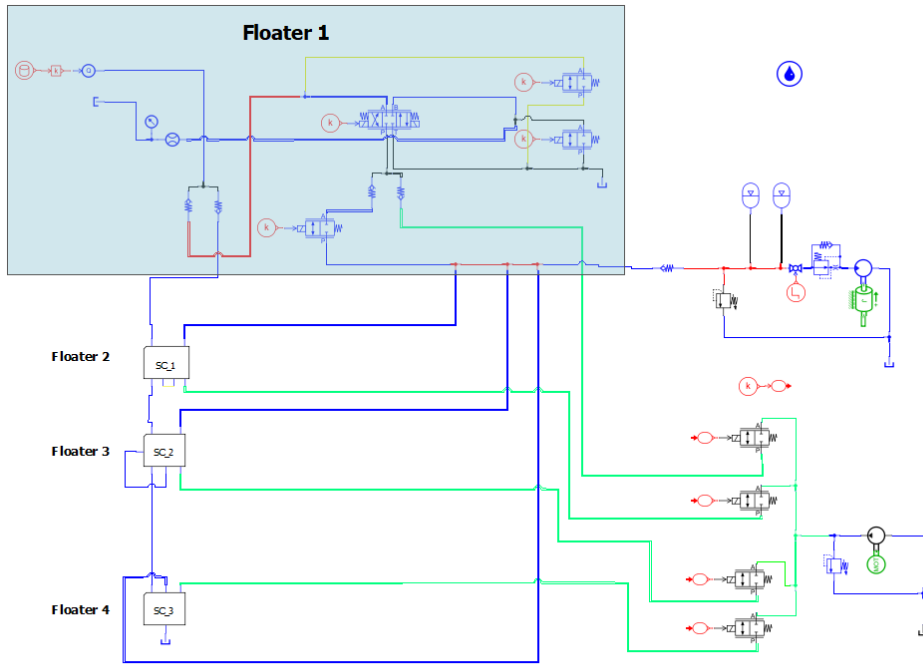
Figure 6: AMESIM SIMCENTER Model

2.3. Optimization of the motor size and kinematic model of the floaters

Size optimization of the hydraulic motor is extremely important. The main parameter that affects the sizing of the hydraulic motor is the flow rate that is affected by wave height. The hydraulic motor has to rotate at a constant speed to allow for constant AC production. According to historical data, wave height in Gaza ranges between 0.3m and 1.5m. In this study, the cut-in and cut-out wave heights were based on the most common wave heights in Gaza. The sizing of the hydraulic motor was based on the hydraulic model. Different hydraulic motor sizes were examined with real data. At each wave height increment between 0.1m and 1m, different motor sizes were examined for continuous rpm running.

A kinematic model was built to link the flow meter data with the response of the floater and consequently the height of the waves in the location of the rig. Testing data for a single day in the flowmeter is shown in Figure 5. The link between flowrate and wave height allowed linking between wave height and the performance of the hydraulic circuit.

The installed WEC was considered a slider-crank four-bar mechanism as illustrated in Figure 7. Links R_1 and R_2 were of constant lengths. On the other hand, link R_3 changed with time as the floater rose or fell. Point ξ was the frontest most point in the area of interaction between the floater body and the seawater (See Figure 8). Symbol ξ_Z was defined as the predicted vertical translational of point ξ and thus, the floater's response with respect to the bottom line of sea waves. This response emulated the wave height of sea waves in the location of the rig.
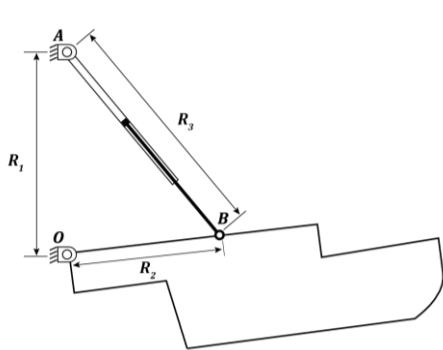

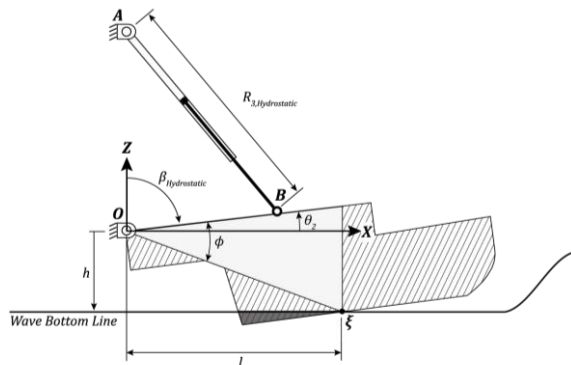Figure 7: Geometry of the slider-crack four-bar mechanism

Figure 8: Hydrostatic position of the floater

A formula of ξ_Z can be derived such that:

Equation 3: Floater's response
$$\xi_Z = \sqrt{h^2 + l^2}\, \sin(\theta_2 - \phi)$$

Where:

- ξ_Z= vertical displacement of point ξ from hinge O (m)
- h= vertical distance from point O to the wave bottom line (m)
- l= horizontal distance between the wall and point ξ in the hydrostatic equilibrium position of the floater (m)
- θ_2= angle by which floater's arm rotates about hinge O (rad)
- ϕ= position angle of point ξ (rad)

Length l depended on both the water depth, h, and $\beta_{Hydrostatic}$ which was the angle at which the buoyancy force on the floater equalised the floater's weight. Furthermore, ϕ was the position angle of point ξ. Now ϕ, l and $\beta_{Hydrostatic}$ are calculated using Meshmagick.

The rotation of the floater's arm is represented by angle θ_2. It depends on many parameters, all of which are constants except for R_3

Equation 4: Arm's rotation
$$\theta_2 = \sin^{-1}\left(\frac{R_1^2 + R_2^2 - R_3^2}{2R_1R_2}\right)$$

Where:

- R_1= distance from point O to point A. (m)
- R_2= distance from point O to point B. (m)
- R_3= distance from point A to point B. (m)

In other words, R_3 changes by the extension and retraction of the hydraulic cylinder. This term is intended to be derived from the experimental flow rate data inside one of the cylinders. It is given by

Equation 5: Derivation of R_3
$$R_3 = R_{3,Hydrostatic} - \int_{t_i}^{t_{i+1}} \frac{4Q}{\pi d^2} dt$$

Where:

- $R_{3,Hydrostatic}$= reference length of the hydraulic cylinder (to be at the hydrostatic equilibrium at no wave condition and at $\beta_{Hydrostatic}$ (m)
- Q= experimental flow rate data taken from the rig (L/min)
- d= inside diameter of the hydraulic cylinder (m)

3. RESULTS

The validation of the hydraulic model was carried out by comparing simulation results with real reading data taken from the wave-to-energy station. The model can then be used for further development of the PTO and control system.
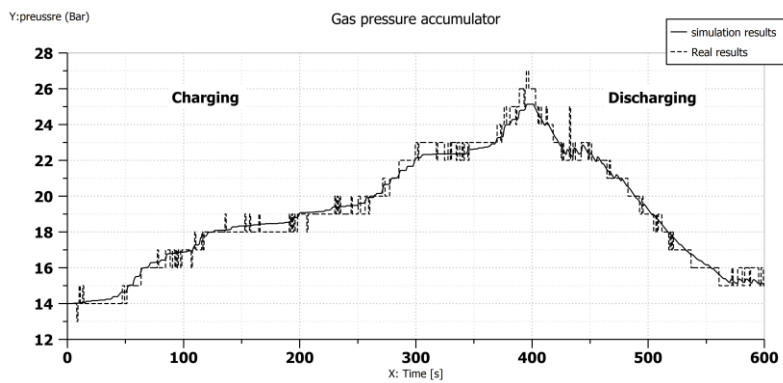
3.1. Validation of the model

Inside the model, the measurements were set up at the same locations as in the real circuit. The measurements include gas pressure in the accumulators and the mainline, and the speed of the hydraulic motor.
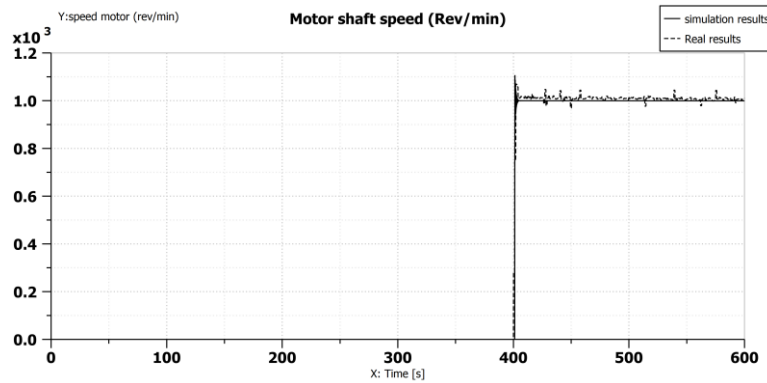
The results in Figure 9 (A) clearly show that the behaviour of the pressure in the mainline was almost identical between the simulation and test data. This was an indication that the simulation was able to replicate the minor and major losses in the circuits.
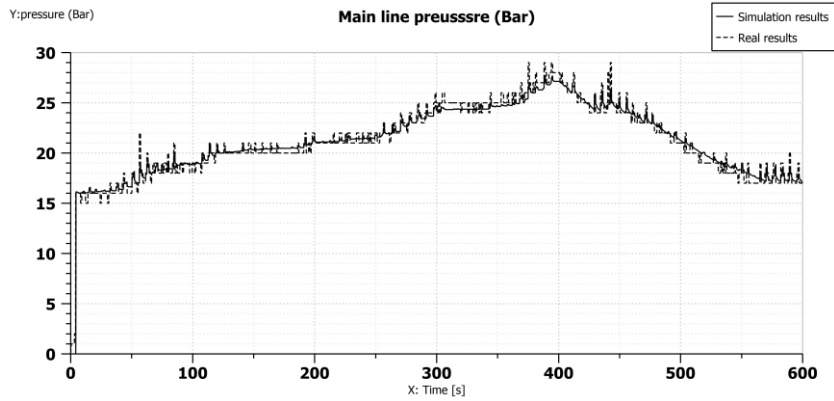
(A) Main line pressure

(B) Accumulator gas pressure

(C)   Motor speed results

Figure 9: Validation of the hydraulic model

In (C)   Motor speed results

Figure 9 (B), the accumulator behaviour was captured during charging from empty status until fully charged then discharging until empty again. Capturing this behaviour was important because charging and discharging happen very frequently during operation. As mentioned in the methodology section, the piston accumulators were replaced by bladder ones. Theoretically, bladder accumulators should respond more quickly to system pressure variations than piston types. In bladder accumulators, there is no static friction to be overcome as with a piston seal, and there is no piston mass to be accelerated and decelerated. In practice, however, the difference in response was insignificant and had no effect on our application as shown in the result. (C)   Motor speed results

Figure 9 (B) shows the exact replication of piston accumulator and model data from AMESIM outcome.

Motor speed results, shown in Figure 9 (C), are an indication of flow rate through pressure compensated valve. The pressure compensated valve was switched off to allow for accumulators charging. During accumulator discharging, the pressure compensated valve was used to maintain a constant flow. Different loads were applied during the

experiment. The speed of the motor and subsequently the behaviour of the pressure compensated valve was identical in both experimental and simulation results.

3.2. Size optimization for the hydraulic motor

Different hydraulic motor sizes were included in the model. Test flow data on different days and wave conditions were used for the model. At each flow data set and motor size, the maximum speed that would allow for continuous running was calculated from the model. The floater response, i.e., wave height for each flow data set was calculated using the kinematic model. The wave height for each daily flow rate test data is shown in Figure 10.
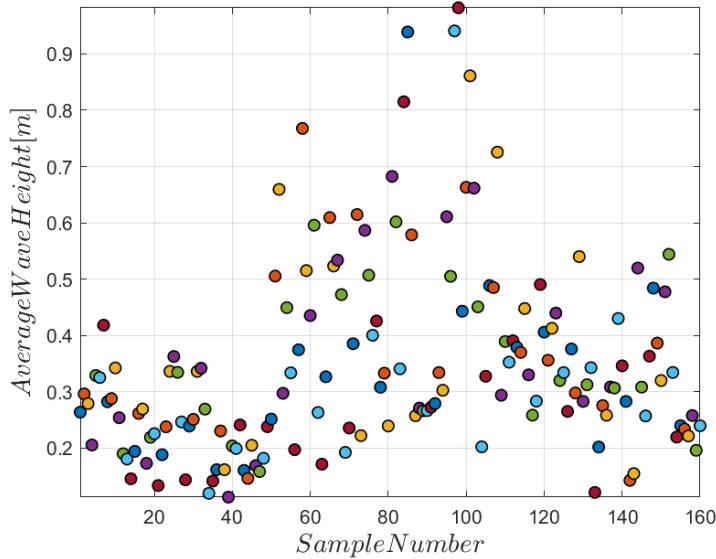
Figure 10: Average response for each day

The relationship between wave height and motor capacity running at constant speed is shown in Figure 11. Assuming that the targeted cut-in wave height is 0.3 m, the motor has to have a capacity of 18 ccs per rev to be able to run at a constant speed of 1500 rpm (50 Hz). Assuming a cut out of 1.5 m that allows for continuous running without any back pressure on the system. The required hydraulic motor capacity is 26 cc. This means using a variable displacement hydraulic motor will increase the wave range that the current facility is running and increase the efficiency of the system with a total increase in power output.
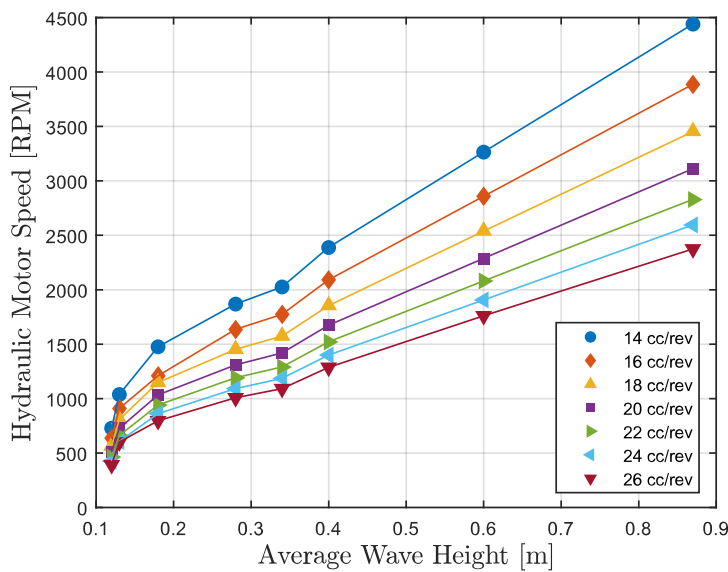

Figure 11: Average response vs motor speed

4. CONCLUSION

This paper fully describes the PTO system that was installed in the wave-to-energy Gaza station. A complete model of the PTO has been presented using AMESIM software. The comparison between test data obtained from the station and the model shows clearly that model reflected the accurate behaviour of the hydraulic circuit under different running conditions. The simulation results have demonstrated that the model can be used to optimize the size of the hydraulic components with an example of optimization of the motor size to suit the specific wave characteristics in the Gaza strip. Future work will focus on the dynamic simulation of the wave-to-energy station using this PTO to analyse optimal control algorithms to maximise power extraction.

5. ACKNOWLEDGEMENTS

6. REFERENCES

Alamian, R., R. Shafaghat, M. S. Shadloo, R. Bayani and A. H. Amouei (2017). "An empirical evaluation of the sea depth effects for various wave characteristics on the performance of a point absorber wave energy converter." Ocean Engineering **137**: 13-21.

Beirão, P. and C. Malça (2011). Hydraulic power take-off prototype for a wave energy converter. Proceedings of the 4th International Congress of Energy and Environment Engineering and Management, Mérida, Spain.

EMEC. (2021). "Wave devices." from http://www.emec.org.uk/marine-energy/wave-devices/.

Esteban, M. and D. Leary (2012). "Current developments and future prospects of offshore wind and ocean energy." Applied Energy **90**(1): 128-136.

Falcão, A. F. O., J. C. C. Henriques and L. M. C. Gato (2017). "Rotational speed control and electrical rated power of an oscillating-water-column wave energy converter." Energy **120**: 253-261.

Kalogirou, S. A. (2005). "Seawater desalination using renewable energy sources." Progress in energy and combustion science **31**(3): 242-281.

Liu, C. (2016). "A tunable resonant oscillating water column wave energy converter." Ocean Engineering **116**: 82-89.

Lund, H. (2007). "Renewable energy strategies for sustainable development." Energy **32**(6): 912-919.

Magagna, D. and A. Uihlein (2015). "Ocean energy development in Europe: Current status and future perspectives." International Journal of Marine Energy **11**: 84-104.

Malara, G., R. P. F. Gomes, F. Arena, J. C. C. Henriques, L. M. C. Gato and A. F. O. Falcão (2017). "The influence of three-dimensional effects on the performance of U-type oscillating water column wave energy harvesters." Renewable Energy **111**: 506-522.

Ponce de León, S., J. H. Bettencourt and N. Kjerstad (2011). "Simulation of irregular waves in an offshore wind farm with a spectral wave model." Continental Shelf Research **31**(15): 1541-1557.

Sun, K., W. Ge, L. Luo, H. Liang, C. Xu, J. Leng, Z. Yuan and H. Huang (2016). Research on the hydraulic power take-off unit of a hybrid wave energy converter. OCEANS 2016-Shanghai, IEEE.

Têtu, A. (2017). Power Take-Off Systems for WECs. Handbook of Ocean Wave Energy: 203-220.

Van Der Jagt, J. (2018). "A methodology for assessing power performance of Wave Energy Converters, applied to a quasi-rigid submerged pressure differential device."

Zhao, D., N. Han, E. Goh, J. Cater and A. Reinecke (2019). Chapter 6 - Analysis codes for floating offshore wind turbines. Wind Turbines and Aerodynamics Energy Harvesters. D. Zhao, N. Han, E. Goh, J. Cater and A. Reinecke, Academic Press**: 401-430.